N85-27414

MEASUREMENT OF ELEMENTS IN THE STRATOSPHERE

Final Technical Report

In Fulfillment of NASA Grant NASW 3242

Submitted to the National Aeronautics and Space Administration

by

The President and Fellows of Harvard College
Office for Sponsored Research
Holyoke Center
1350 Massachusetts Avenue
Cambridge, Massachusetts 02138

Prepared by

James G. Anderson
Principal Investigator

CONTENTS

I. INTRODUCTION

The distribution of ozone in the Earth's stratosphere controls both the amount of ultraviolet radiation reaching ground level and the heating/cooling rates of the middle atmosphere. With the advent of global scale release of synthetic molecules not present during the evolution of the earth-atmosphere system, it becomes critically important to define the photochemical structure of the stratosphere to a level of detail required to confidently predict secular trends in global ozone, a responsibility delivered by Congress to NASA by

The key to constructing the foundation of our scientific understanding to satisfy the intent of this congressional mandate depends upon our ability to (1) detect key free radicals, and (2) define the mechanisms controlling the concentration of the free radicals that accelerate the recombination of ozone (and atomic oxygen) to reform molecular oxygen. Techniques for the detection of free radicals in the gas phase at the part-per-trillion level are just being developed for laboratory studies; it is the purpose of the research reported here to develop the techniques and experimental approach to achieve similar detection levels throughout the entire altitude interval encompassed by the stratosphere.

We can summarize the required objectives for the key free radicals $O(^3P)$, OH, HO_2, N, Cℓ, CℓO, NO, and NO_2, along with the major "reservoir" terms, H_2O, HCℓ and $HONO_2$, as follows:

Vertical Resolution	0.25 km
S/N into the Lower Stratosphere	$\geq$ 50/1
Experimental Accuracy	± 10 - 15%
Experimental Precision	± 5%
Restriction on Solar Zenith Angle	None; all solar zenith angles must be investigated

During the period 10/01/78 to 03/31/84, three major areas of research were pursued:

1. Design, development, fabrication, and test of a new Reel Down/Reel Up approach to stratospheric measurements in which a Kevlar filament is employed to lower and retrieve over a vertical segment 10 km or greater, an instrument array capable of detecting free radicals at the ppt level. That system must be deployable from any balloon float altitude between 25 and 40 km. That, coupled with the $\geq$ 10 km range of the Reel Down phase, will encompass all altitudes between 15 and 40 km. That system must be capable of four or more vertical soundings from a single balloon launch. Section II of this report details the development and successful test of that system.
2. Design, development, fabrication, and test of a new Copper Vapor Laser system for the in situ detection of OH and HO_2. That system must achieve the objectives noted in the introduction for those two radicals at all altitudes between 15 and 40 km, and be capable of making those measurements simultaneously with in situ observations of H_2O, O_3, NO, NO_2, ClO, total pressure, and absolute temperature. Section III of this report describes the successful accomplishment of these objectives.
3. An array of new instruments to complete the complement of observations required to constrain current theories of

ozone depletion trends, including instruments for the *in situ* detection of NO_2, O_3 and H_2O. Section IV details this research and development.

The final section of this report (Section V) presents a series of manuscripts written and presented during the course of this contract which provides an interpretation of the evolving scientific understanding of stratospheric chemistry.

II. THE REEL DOWN/REEL UP SYSTEM

The following reports detail the design, development, fabrication, and test of a new Reel Down/Reel Up approach to stratospheric measurements.

FREE RADICALS IN THE STRATOSPHERE: A NEW OBSERVATIONAL TECHNIQUE

J.G. Anderson, N.L. Hazen, B.E. McLaren, S.P. Rowe,
C.M. Schiller, M.J. Schwab, L. Solomon, E.E. Thompson, and E.M. Weinstock

Harvard University
Department of Chemistry
and
Center for Earth and Planetary Physics

November 1984

ABSTRACT

A new approach to in situ observations of trace reactive species in the stratosphere is presented. A balloon-borne system, floating 40 km above the Earth's surface, successfully lowered and then retracted a cluster of instruments, capable of detecting gas phase free radicals present at the part-per-trillion level, 12 km on a 1.8 mm diameter filament of Kevlar. Excellent stability of the suspended instrument array is reported as are the first observations of atomic oxygen in the stratosphere obtained with the new approach.

The photochemistry of stratospheric ozone has received intense, interdisciplinary attention for more than a decade following the realization that global scale chemical changes in the lower atmosphere, amplified by homogeneous gas phase catalysis in the stratosphere, are mechanistically linked to future changes in stratospheric ozone. This decade of development has been comprehensively summarized.[1] Concern has centered primarily on the catalytic effects of nitrogen[2] and chlorine compounds,[3] which are photochemical biproducts of N_2O oxidation and halogen substituted hydrocarbon photodecomposition, respectively. Recently, however, the chemical ramifications of global increases in CO_2 and CH_4, with requisite effects on temperature and reactive hydrogen compounds, has broadened the scope of the problem considerably.[4]

A clearly perceived need to forecast secular trends in the column concentration of ozone has focussed attention on developing an integrated understanding of global chemical cycles: (1) biogeochemical, (2) tropospheric, and (3) stratospheric. Of the three, stratospheric photochemistry is much the simplest, not only because many of the subtle interactions among biological, chemical and physical processes are diminished in the stratosphere, but also because tropospheric removal processes vastly restrict the spectrum of molecules which traverse the dynamically stable region separating the troposphere and stratosphere.

While the stratosphere stands today as a potentially tractable photochemical system, it is nevertheless characterized by approximately 200 elementary reactions, a vast majority of which involve free radicals present at the part-per-billion to part-per-trillion level. It is these radicals which dictate the pathways and rates of chemical transformation

within the stratosphere. Their concentration distribution as a function of altitude, latitude and time of day, as well as their kinetics and photochemistry establishes the mechanistic link between the introduction of stable molecules from the troposphere and the catalyzed conversion of ozone to molecular oxygen in the stratosphere.

Detection of these radicals in carefully selected sets holds the key to disentangling the chemical structure of the stratosphere. In situ studies can provide mechanistic information concerning free radical exchange reactions because concentration differences between adjoining atmospheric layers can be spatially resolved. Given the exceedingly short time constants linking the free radicals chemically, an analysis of variance can be used to diagnose cause and effect. This approach depends upon the simultaneous detection of a complement of interrelated stratospheric free radicals. Such correlation measurements require detailed control over the dominant experimental variables, as well as repetitive observations carried out under "identical" conditions to test reproducibility.

While previously obtained "snap shots" of the free radical concentration provided first order information on concentration regimes as a function of altitude, there were several drawbacks. Problems centered primarily on inadequate control over flow conditions, platform instability on a given flight and, for the chemical conversion experiments (such as for $C\ell O$ and HO_2 where nitric oxide was used to convert the radicals to $C\ell$ and OH, respectively), reactant gas mixing times.

We report here a new approach which has been developed to eliminate these impediments. Designated the "Reel Down" technique and depicted in

Figure 1, the system consists of (1) a winching system borne by a helium research balloon to an altitude of $\leq$ 40 km (where the atmospheric pressure is approximately 2 mm Hg) and (2) an instrument cluster which is lowered on a filament of Kevlar a distance of $\sim$ 10 km and then retracted back to the winch platform. Vertical soundings can be repeated several times for a given balloon launch.[5]

The architecture of the individual instruments used to detect atoms and small free radicals by atomic and molecular resonance fluorescence or by laser induced fluorescence is shown in Figure 1. Briefly, a nacelle, hollow through the core from nose to tail with an impeller in the anterior section, provides for the laminar flow of stratospheric air around and through the instrument. Detection of trace species is carried out at one (or more) optical axes within the nacelle.

A major subset of the important stratospheric radicals can be detected using the configuration shown in Figure 1. For the first flight of the Reel Down system, we selected atomic oxygen, $O(^3P)$, because (1) it is a reactant in the rate limiting step of virtually every important catalytic cycle in stratospheric ozone removal, and (2) it is the easiest free radical experiment to execute in the stratosphere.

Calibration of the instrument is carried out in the laboratory using the detector head and lamp module/photodiode combination installed in a fast flow system. This provides a direct measure of the proportionality factor between the atomic oxygen concentration and the detector count rate for a broad range of conditions. The fast flow reactor reproduces the pressure and flow velocity conditions encountered during the stratospheric observations; a detailed discussion of the calibration technique appears elsehwere.[6]

The first flight of the Reel Down system took place on September 15, 1982 from the National Scientific Balloon Facility in Palestine, Texas. The balloon-winch-suspended payload ascended to 133,000 ft ($\sim$ 40 km) in 3 hours and 20 minutes. Controlled descent of the suspended instrument cluster was initiated by releasing a magnetically controlled brake, transferring descent rate control to a generator in series with resistively heated radiation panels.

Dynamical behavior of the suspended payload and winching platform were documented in real time by a combination of accelerometers, gyros, load cells, solar sensors and a downward looking video monitor on the winch platform. Longitudinal and azimuthal motion was virtually absent; acceleration of $<$ 1% of g with a period of $\sim$ 15 sec at full extension and one full rotation on descent were recorded. No pendulum motion and no measurable body centered perturbation developed during any phase of the descent or ascent.

We next examine the implications of the atomic oxygen data obtained on the first flight of the system. Figure 2 superposes those data with previous rapid descent parachute controlled measurements[1] and with the most recent photochemical model calculations which incorporate vertical transport with a comprehensive reaction set including all recent developments in the kinetics and photochemistry of oxygen, hydrogen, nitrogen and halogen compounds.[7] To first order, both the gradient and absolute concentration of the in situ data substantiate the mechanism used in the model for oxygen atom production and destruction. There are, however, clear differences which become important when the results are critically appraised at the level required to confidently use the model to predict the behavior of the stratosphere into the next century. While space

does not allow a thorough discussion here, we sketch the highlights.

Atomic oxygen is photochemically coupled to ozone by

$$O_3 + h\nu \xrightarrow{J_{O_3}} O + O_2$$
$$O + O_2 + M \xrightarrow{k_1} O_3 + M \qquad (1)$$

which establishes a steady state between $O(^3P)$ and O_3 on the time scale of seconds throughout the stratosphere. The sum of atomic oxygen and ozone, $[O_x] = [O(^3P)] + [O_3]$, is produced by direct photolysis of O_2 by radiation shortward of 242 nm, $O_2 + h\nu \xrightarrow{J_{O_2}} O + O$, and destroyed by recombination, $O + O_3 \xrightarrow{k_2} O_2 + O_2$. In the middle and upper stratosphere, this last reaction is accelerated by a series of two-step homogeneous, gas phase catalytic cycles involving hydrogen, nitrogen and chlorine radicals of the form $X + O_3 \rightarrow XO + O_2$ and $XO + O \rightarrow X + O_2$, where $X \equiv$ OH, NO, Cℓ, respectively.

The important point to note is that atomic oxygen is involved in each of the major rate limiting steps so that detailed knowledge of its concentration is required to test our understanding of O_x destruction rates.

Returning to Figure 2, we note that the mean of the previously published data lies above the calculated concentration by ~ 50% between 29 and 35 km, and then slowly converges up to 40 km. Results obtained from the Reel Down experiment follow the same trend but fall ~ 25% above the calculated distribution up to 35 km.

A recent and rather thorough analysis of midlatitude O_3 observations, wherein all available balloon, rocket and satellite data were used, concluded that observed O_3 concentrations at midlatitudes substantiate calculated densities up to 30 km, but monotonically diverge above 35 km

such that observed ozone concentrations (from a broad class of experiments) fall 30 to 50% above calculated concentrations between 40 and 50 km.[8]

Taken together, these results imply a serious discrepancy because (1) the relevant cross sections and reaction rate constants, which appear in Equation (1), have been carefully studied and, with the exception of the O_2 photolysis rate, J_{O_2}, are known to ± 10 percent or better; (2) recent in situ measurements defining the penetration of solar radiation into the middle stratosphere have narrowed considerably the uncertainty in J_{O_2}[9]; and (3) ozone can be measured to an accuracy of ± 5 percent at these altitudes. If we hope to predict changes in ozone in the next century to an accuracy of 10 percent, it is imperative that we be able to "predict" its present concentration with considerably better accuracy than that cited above, particularly in the photochemically controlled regime above 30 km.

With the experimental control and repeatability afforded by Reel Down, we can now systematically examine each of the chlorine, nitrogen and hydrogen rate limiting steps in the catalytic destruction of ozone. An analysis of variance between ozone and the rate limiting radicals as well as the diurnal, latitudinal and seasonal trends can be used to establish cause and effect within and between the chemical cycles, providing a significantly more rigorous test of the dominant catalytic mechanisms.

ADDED NOTE

The Reel Down system was launched for the second time on September 14, 1984 from Palestine, Texas. Two vertical scans of 8 km each were executed, each exhibiting the striking dynamic stability reported in this paper. That flight began a series of experiments investigating the free chlorine radical, ClO, which rate limits the chlorine catalyzed recombination of ozone and atomic oxygen to molecular oxygen.

ACKNOWLEDGMENTS

A large number of people contributed to this development, both within and outside the Harvard community.[10] Support for the development of this technique came from the NASA Environmental Observations Program of the Office of Space Science and Applications under the direction of Drs. S.G. Tilford and R.T. Watson, Contracts NASW 3242 and NAS6 3061.

REFERENCES

1. See, for example: World Meteorological Office/National Aeronautics and Space Administration, The Stratosphere 1981: Theory and Measurements, WMO Global Ozone Research and Monitoring Project, Report #11; National Academy of Sciences Causes and Effects of Changes in Stratospheric Ozone: Update 1983, National Academy Press, Washington D.C., 1984; G. Brasseur and S. Solomon, Aeronomy of the Middle Atmosphere, Reidel, 1984.

2. Johnston, H.S., Chapter 4, Stratospheric Ozone and Man, F.A. Bower and Richard B. Ward, eds., CRC Press, Inc., Boca Raton, 1982.

3. Rowland, F.S. and M.J. Molina, Rev. of Geophys. and Space Phys. 13, 1, 1975. Also see the entire two-volume series, Stratospheric Ozone and Man, Vols, I and II, F.A. Bower and R.B. Ward, eds., CRC Press, Boca Raton, 1982.

4. The Major Biochemical Cycles and Their Interactions, B. Bolen and R.B. Cook, eds., SCOPE, 1983.

5. Hazen, N.L. and J.G. Anderson, American Institute of Aeronautics and Astronautics, 22nd Aerospace Sciences Meeting, 9-12 January 1984, Reno, Nevada.

6. Anderson, J.G., H.J. Grassl, R.E. Shetter and J.J. Margitan, J. Geophys. Res. 85, 2869, 1980.

7. Prather, M.J., provided the $O(^3P)$ profile calculated for the conditions of the flight using the model which provided the calculations for the results reported in Causes and Effects of

Changes in Stratospheric Ozone: Update 1983, National Academy Press, Washington, D.C., 1984.

8. See, for example: Ko, M.K.W. and N.D. Sze, Geophys. Res. Lett. 10, 341, 1983; and Crutzen, P.J. and V. Schmailzl, Planet. Space Sci. 31, 1009, 1983.

9. Anderson, G.P. and L.A. Hall, J. Geophys. Res. 88, 6801, 1983.

10. Acknowledgments extend to a broad community: Jacques Blamont of the Centre National d'Estudes Spatiales, Paris, France, first used cables to tether balloons in the troposphere; Fred Kaufman of the University of Pittsburgh first suggested using cables in the stratosphere; and the Dupont Corporation developed Kevlar with a strength-to-weight ratio of 10 over that of steel. That development allowed us to take the approach described in this report. Mark Titchener and Kelly Roney developed much of the hardware/software used in the data acquisition and reduction. Terry Schiller and Ed Dobbyn contributed significantly to the fabrication of the flight electronics. Members of the National Scientific Balloon Facility call for special recognition: Robert Kubara, Operations Director; Keith Hazelwood, Engineering; Al Shipley, Base Director; and Grady Cole, Launch Chief were particularly critical contributors during many difficult periods.

FIGURES LEGENDS

Figure 1. Rendering of the Reel Down system showing the winching system and suspended payload. A helium filled research balloon is used to lift the combination to any altitude up to 40 km from which vertical scans of greater than 10 km are executed. Panel (a) displays the geometry of the experiment at float altitude in the docked position. Panel (b) shows a schematic of the suspended instrument array indicating the optical

system and flow system used to obtain the in situ free radical observation.

Figure 2. Comparison between (a) the $O(^3P)$ concentration profile obtained from the Reel Down experiment described here; (b) the mean of all previous in situ observations of $O(^3P)$; and (c) the most recent calculations of atomic oxygen for the conditions corresponding to those of the Reel Down observation.

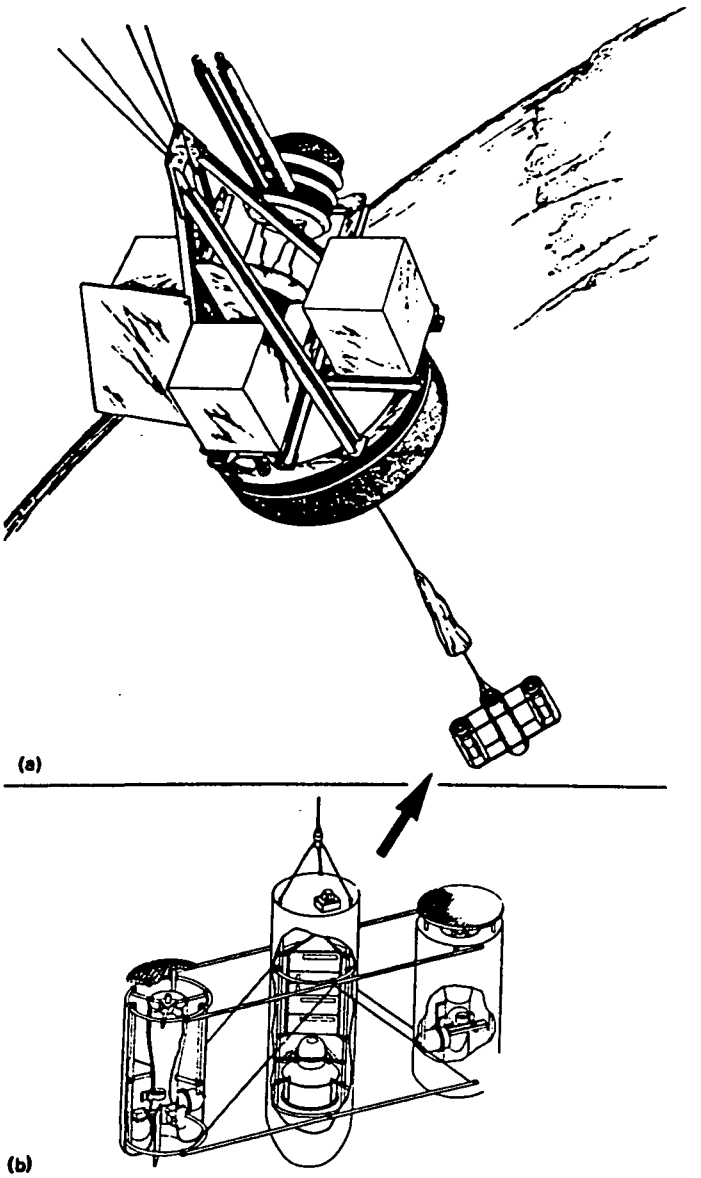
(a)
(b)

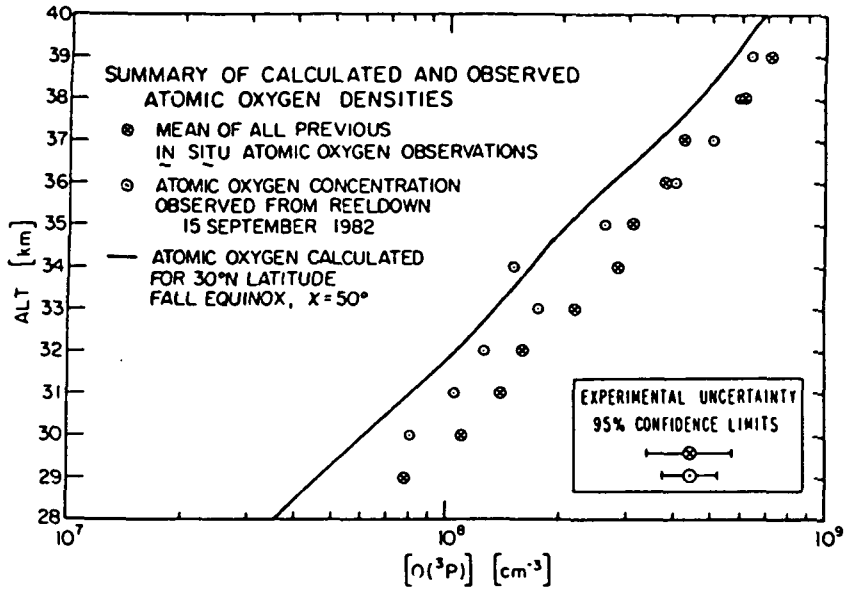
SUMMARY OF CALCULATED AND OBSERVED
ATOMIC OXYGEN DENSITIES
MEAN OF ALL PREVIOUS
IN SITU ATOMIC OXYGEN OBSERVATIONS
ATOMIC OXYGEN CONCENTRATION
OBSERVED FROM REELDOWN
15 SEPTEMBER 1982
ATOMIC OXYGEN CALCULATED
FOR 30°N LATITUDE
FALL EQUINOX, X=50°
EXPERIMENTAL UNCERTAINTY
95% CONFIDENCE LIMITS
ALT [km]
40
39
38
37
36
35
34
33
32
31
30
29
28
10^7
10^8
10^9
[O(3P)] [cm^-3]

AIAA'84

AIAA-84-0027

Reel Down: A Balloon-Borne Winch System for Stratospheric Sounding From Above

N.L. Hazen and J.G. Anderson, Harvard Univ., Cambridge, MA

AIAA 22nd Aerospace Sciences Meeting

January 9-12, 1984/Reno, Nevada

REEL DOWN: A BALLOON BORNE WINCH SYSTEM FOR STRATOSPHERIC SOUNDING FROM ABOVE

N.L. Hazen and J.G. Anderson
Harvard University
Cambridge, Massachusetts 02138

Abstract

A balloon-borne winch system has been developed and flight tested which permits the repetitive lowering and hoisting of a stratospheric sampling payload for distances of up to 20 km from a float altitude of 35-40 km. This new approach to in situ stratospheric measurements permits multiple scans of various depths and velocities, closely spaced over a period of hours or days, thus dramatically increasing observational effectiveness. The motor driven winch permits control of ascent velocities from 0-9 m/s with energy derived from a large battery; for descent, the motors are used as generators, velocity is controlled over the same range, and the energy is dumped radiatively to space. The 1.75 mm diameter tether is of braided Kevlar construction with a nylon jacket; it exhibits a 2900 N break strength. Both the winch and the payload suspended by the tether are fully instrumented to evaluate potentially destructive system-induced dynamics and the effects of stratospheric wind shears. The system was successfully flight tested by lowering a 62 kg payload for a distance of 12 km from a float altitude of 38.5 km and hoisting it back up again, both at velocities ranging between 5-9 m/s. Observations indicated minimal system-induced dynamical effects, and no adverse effects due to the 8 m/s wind shear present during flight.

Introduction

Studies of the chemical composition of the upper atmosphere, in particular the stratosphere, have utilized two broad classes of experimental technique heretofore. Remote sensing techniques such as absorption measurements through the atmosphere from satellites, or laser sounding techniques such as Lidars provide excellent large scale morphological information, but suffer as a result of relatively limited altitude or geographic resolution. Alternatively, in situ techniques employing balloon vehicles, while suited for providing spatially and temporally correlated observations on the "microscopic" level, have been generally limited by the inability to make more than one rapid scan or limited set of measurements for each flight. These provide only brief glimpses into the complex chemistry of reactive species that is known to vary rapidly in the dimensions of time, space and solar illumination. The technique we describe here provides a whole new avenue of approach to the experimental observation of the stratosphere.

Conceived by one of the authors (J. Anderson) in 1977 after a frustrating balloon flight providing just such a brief glimpse at a promising observation, the Reel Down system was developed at Harvard with NASA sponsorship over the period 1980-1982. It is comprised of a Winch Platform held by balloon at a float altitude high in the stratosphere and an instrumented Suspended Payload which is lowered and raised on a tether. These are shown in Fig. 1 hanging from the launch vehicle prior to flight. The most unusual aspect of the system is the length of the tether, 12 km deployed and recovered in the first flight, and a system capacity of 20 km. For the first time, Reel Down provides opportunity for stratospheric examination with command-selected instrument scan velocities and altitude limits, in a number of vertical scans or small altitude increments. Coupled with in situ chemical abundance experiments and real time data telemetry and display, Reel Down represents a powerful new tool for advancing stratospheric chemistry. This paper describes the evolution of the Winch Platform design, the nature of the tether and the subsystem designs, and presents system performance data obtained on the first flight in September, 1982.

System Design Definition

The basic performance requirements for the Reel Down system derive from the observational needs in stratospheric chemistry; they are listed in Table 1. Although the system should be capable of achieving these requirements, the goal of one 12

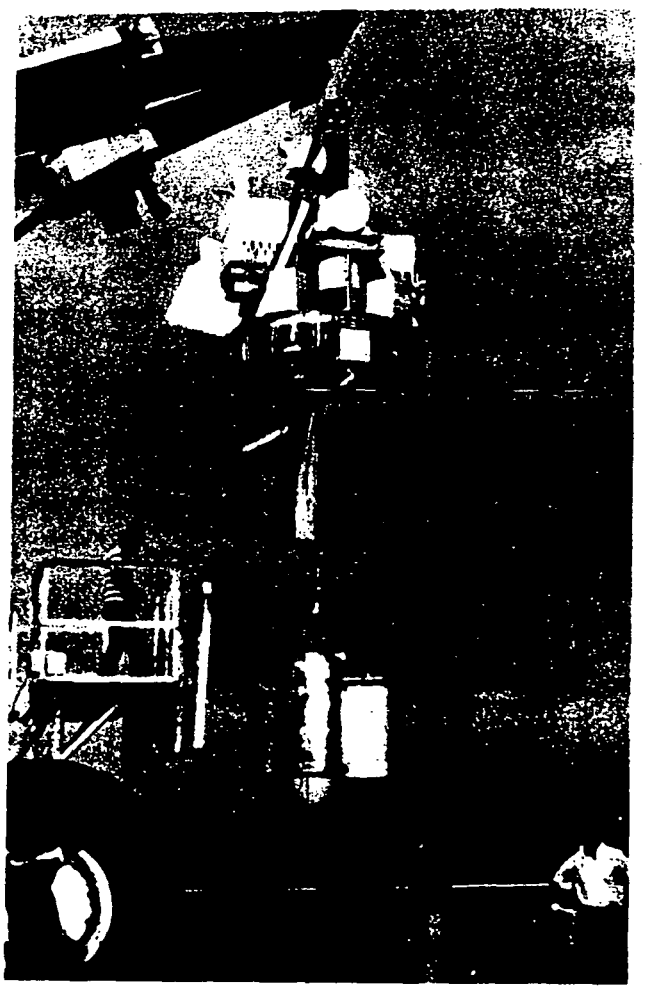

Fig. 1. Reel Down System in Launch Position

Table I System Performance Requirements

Float Altitude	40 km +
Scan Distance	≤ 20 km
Scan Velocity	≤ 10 m/s
Payload Mass	≥ 50 kg
Number of Scans	Flight selectable

km scan, down and up, was chosen for the first flight; here the immediate system objectives were (a) to demonstrate the feasibility of the concept in actual flight; (b) to evaluate the effects of stratospheric winds on the line and payload; and (c) to evaluate the character and magnitude of self-excited effects on the system. Additional goals related to observational methods in the Suspended Payload.

The choice of the tether is central to the design definition process; the availability of the Kevlar material described in the next section, in fact, made this system possible. Given the material, system considerations strongly favor the choice of the smallest diameter (lightest) line capable of providing the chosen margin of safety. In systems where the line's own weight is a substantial factor, there is disappointing payload gain in choosing a larger (heavier) line and the hoist energy requirement goes up very rapidly. The small line also permits a compact storage drum; our 20 km of line requires less than 0.06 m^3 of volume. Given the tether and the previously fixed payload mass and scan velocities, then the system power handling requirements are fully defined. In our case a net steady state power of 520 kg-m/sec (6.8 HP) was required for the first flight.

Early development efforts for the Reel Down system were centered on traction winches where a capstan system is used for line take up, and the storage is accomplished separately on a drum at low tension. The system complexity to achieve stable control at high velocities soon became overbearing, however, and we shifted our attention to a simple winch operating at full tension. Analysis was done to indicate that a suitable sturdy (but massive) storage drum could be built, and misgivings about damage to the line resulting from deep wrapping at high tension were allayed through empirical laboratory similation on drums of reduced scale.

Given the line length and weight and the payload weight, the single storage drum can be dimensioned for its inner diameter, flange diameter and distance between flanges, so that (to the first order) it will operate at constant torque (i.e., greater line weight overboard will be compensated by a smaller instantaneous winding radius). Furthermore, by operating the system at constant peak shaft speed (allowing the resulting ~ 40% variation in line velocity), one can operate, by and large, at a constant power level and further simplify the system. These strategies were used to minimize the control system complexity. We also avoided attempts at energy recovery from the descent phase for the first block of flights, although this may be used to realize long term economies later on. The resulting system has proven to be remarkably trouble-free and easy to operate.

Tether

The Reel Down concept is possible because of the extraordinary properties of the recent plastic fiber material manufactured by DuPont, tradenamed Kevlar. It is one of a family of aromatic polyamide fibers which exhibit an exceptionally high strength-to-weight ratio and a modulus of elasticity approaching steel.[1] Table 2 lists some of the pertinent properties of Kevlar 29 in constrast with some of the other commonly used cable structural materials.

As it has become increasingly available and understood, Kevlar has found applications as mooring pendants for offshore oil rigs, oceanographic instrumentation cables, aerostat tethers, yacht sails, composite structural panels and even bullet-proof vests. It is available from DuPont in yarn form of various specific weights (deniers) for processing into its end form (cloth, cable, braided line) by specialty firms such as the Cortland Cable Company.[2]

Table II Properties* of Several Tether Materials

	Kevlar 29	Steel	Nylon	Dacron
Density (lbs/in^3)	0.052	0.28	0.041	0.050
Tensile Strength (10^3 psi)	375	275	145	163
Specific Strength (10^6 in)	7.2	1.0	3.5	3.3
Elastic Modulus (10^6 psi)	9.1	30	0.8	1.5
Specific Modulus (10^8 in)	1.75	1.07	0.19	0.30
Breaking Length (10^3 ft)	~ 500	~ 80	~ 290	~ 275

*representative typical values

Flight Tether

The specific line chosen for the flight system is braided of Kevlar 29 and is a variant of Cortland's type B29/12-15, meaning that the braid consists of 12 yarn ends, each of 1500 denier weight. It is made in one continuous length, although the braiding equipment requires finite yarn lengths and therefore yarn splicing (by doubling the yarns over a certain length). Splices of each yarn occur at about 600 m intervals, but have no adverse effect on strength. The braiding is done at a low helix angle, then bound in place with a non-structural braided nylon jacket, and the whole is bonded with a highly-diluted water-dispersed acrylic adhesive. This construction offered the best combination of strength and handling properties, while being readily available.

As finished for flight, the tether exhibits a 2900 N minimum breaking strength, has a diameter of about 1.75 mm and specific mass of 3.13 kg/km. The low helix angle braided line results in low initial stretch and high stiffness while being intrinsically "torque balanced." The jacket produces a quite rigid line and protects the underlying Kevlar from abrasion and damage due to modest mishandling.

Tether Testing

Early work focussed on line termination techniques, as all subsequent tests require terminated line. Capstan grips, epoxy-filled sockets and eye splices were all found to yield adequate strengths when properly done, but eye splices[3] were more reproducible and chosen for final tests and flight. The statistical expectations for breaking strength were evaluated by numerous tensile tests over the course of the program; these have yielded a mean break strength of 3102 N with a standard deviation of 121 N. The lowest break strength recorded in formal test was 2878 N. Elastic properties were measured both statically and dynamically (spring-mass); normalized spring constants varied between 0.94×10^5 and 1.54×10^5 N as a function of loading. A long term creep test was also performed at a loading of 33% of minimum break strength; creep strain was found to be about 0.14% per decade of time, although less in the first 200 hours. Finally, because of the Reel Down System design concept of winding at full tension directly onto the drum, a series of spooling tests were performed on a subscale drum to achieve comparable depths (60-80 layers) at a tension of 780 N. No damage to the line was observed, although both general and localized flattening occurred.

Tether Management and Storage

The elements of the system concerned with management of the tether are shown schematically in Fig. 2. The power handling elements will be discussed in the next section.

Drum

The tether line is stored on a supply drum after being loaded at nearly operational tension prior to flight. Thus the innermost layers are wound at the highest tension, while the outer layers are tensioned comparable to the payload weight alone. A design analysis for the drum was done[4], assuming a full 20 km was loaded at a uniform tension of 890 N, with wall thicknesses determined to assure that an arbitrary maximum stress of 50,000 psi was not exceeded. The conclusions were sobering and resulted in a drum with a wall thickness greater than 38 mm (1.5 inches), flanges of similar root thickness and substantial fastenings to join the two. Welded flanges were avoided both to gain higher reliability and to allow adjustment of the final drum face width. 7075-T6 aluminum with a yield strength of 70,000 psi was used for both drum and flanges. Actual use conditions have been significantly less severe than the design assumptions for this drum, and all deformations observed have proven to be elastic.

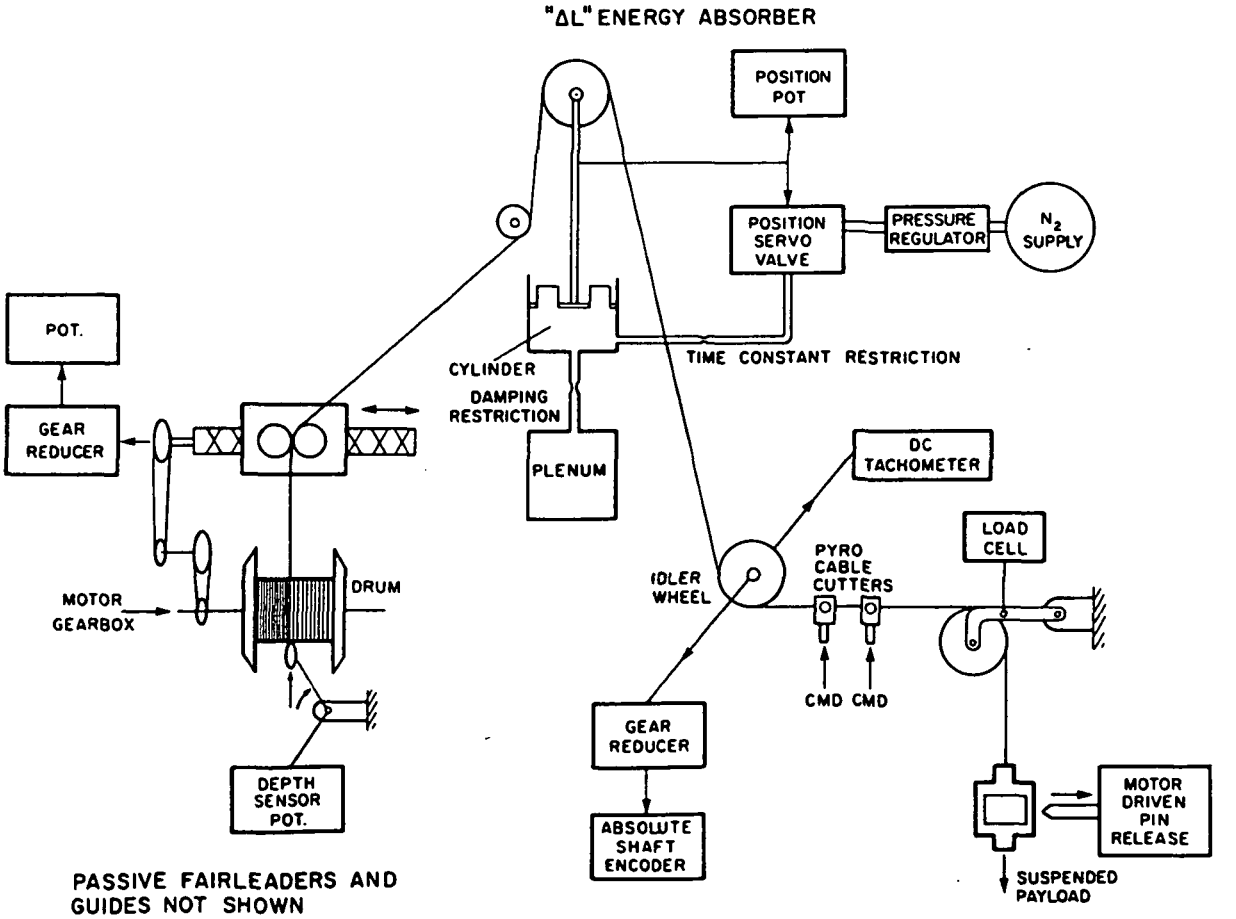

Fig. 2. Tether Management and Instrumentation

Level Wind

The line is guided onto and off of the drum by a gear-driven diamond-screw level winder whose travel is adjusted to match the interflange distance (allowing for line thickness). A series of laboratory experiments indicated that the most orderly winding at flight tension in deep layers occurred with an advance of about two line diameters per drum revolution; this value has been used for flight. Note that, although approximately 80 close packed "layers" are theoretically necessary to contain 15 km of tether, 160 traverses of the drum face are necessary with this level wind advance. Experience has also shown that synchronism between the guide and the line on the drum is maintained for the whole line length during unreeling even when the line tension is dramatically lower (a factor of 10) than the loading tension.

ΔL Energy Absorber

Early analytical work on the Reel Down System tether dynamics concentrated on the question of elastic energy build up in the tether due to the periodic inputs from a high speed winch and the high modulus of the line. Calculation and measurement identify an accoustical wave velocity in the Kevlar line of around 8500 m/s, and data suggest relatively little damping at low frequencies.[5] It was our fear that standing wave accoustical energy build up over the frequency range of 0.25-20 Hz (as might be expected from a high speed rotating winch system) might be far more detrimental to safety than the effects of simple mass-spring-mass elastic motion between the winch and the suspended payload. Application of transmission line theory pointed in the direction of a line "termination" device (a dancer/damper) having very low mass and spring constant, with a high impedance (flywheel) between it and the disturbing device (supply winch). The achievement of these properties and the complexity were problematical, so a compromise energy absorber ("ΔL" to accommodate longitudinal velocity irregularities) was incorporated into the system, as shown in Fig. 3.

This device has a low mass shuttle-mounted pulley, over which the line passes, supported by a pneumatic cylinder. The cylinder with its interconnected plenum volume (see Fig. 2) determine the spring constant of the device, while a restriction in the connection introduces the damping. However, the average load on the device varies by nearly a factor of two during the course of the tether deployment; this is accommodated by incorporating a pneumatic position servo which senses the piston's average position and increases or decreases the average pressure to restore the shuttle to mid-position. The time constant for this servo is adjusted to about 3 minutes; the commercial servo valve* was modified to achieve this and to reduce gas consumption to a reasonable level. The absorber exhibited considerable low amplitude activity, both during tether loading and during flight reeling.

Instrumentation and Security Devices

After passing over the energy absorber, the tether engages two other pulleys before exiting from the payload. The first, with a circumference

*Bellofram Type 80 Positioner

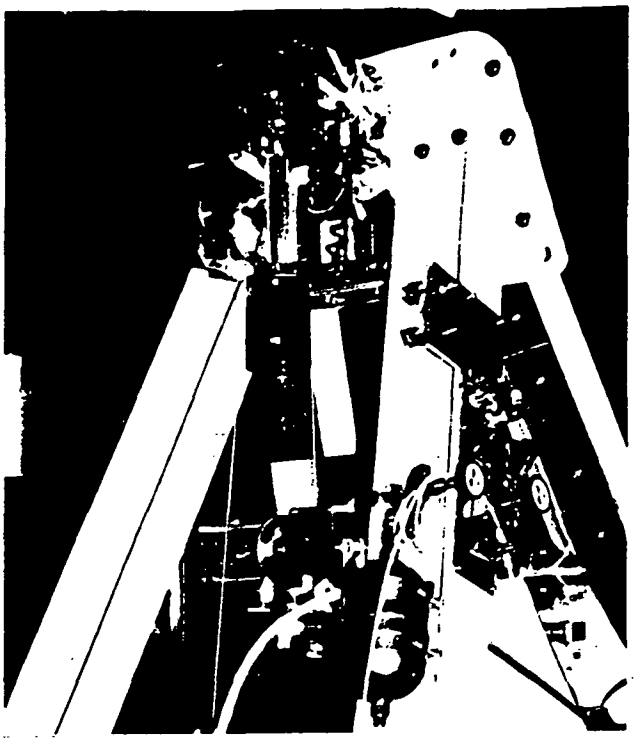

Fig. 3. ΔL Energy Absorber

of 1/3 meter, is instrumented with a DC tachometer with dual ranging to measure line velocity from < 0.1 m/s up to 10 m/s. It also drives a gear-reduced absolute shaft encoder which accounts for deployed line length, monotonically, with a resolution of 2 meters (0.02%). The second (exit) idler pulley is equipped with a strain gauge type load cell with a range encompassing the maximum breaking strength of the tether. Another measure of line tension is the average pressure in the "ΔL" energy absorber; this is also telemetered for comparison with the load cell.

Two further absolute measures of deployed line length are incorporated. The first is a feeler arm sensing the wrap depth on the drum, while the second evaluates the total number of revolutions of the drum (via the level wind screw). Although neither of these is linear, they are monotonic and are calibrated (0.5%) during line loading.

In order to protect the tether from launch and flight damage prior to use, a pin-engaged toggle is used at the junction of the line and the parachute above the Suspended Payload. The pin completely supports the payload up to the time of reeling down, although it is not equipped to reengage (capture) the toggle after reeling up. The winch system is also equipped with a redundant pair of pyrotechnic cable cutters to sever the tether at the exit point in the case of fouling or other malfunction.

As a final note on line security, all elements of the line handling system in direct contact with the tether are in the form of grooved or flat face pulleys with diameters at least 50 times the tether diameter. In addition, numerous (non-contacting) fairleaders and guides are incorporated to insure that if the line went momentarily slack it could return only to the appropriate pulleys.

Power Handling

Early in the payload development effort, a quantity of a certain candidate motor of the right power rating became available under very favorable circumstances. Although other candidates were identified and compared during the course of the effort, none proved to have outstanding superiority in combined performance, efficiency, availability, maintainability, ruggedness and cost. Hence, the power handling system design was an evolution of accommodation to the prime mover.

Motors and Control Protocol

The flight motors are traditional series-wound DC traction motors rated at 4 HP at 4500 RPM with an input of 60 V and 65 A. They weigh 75 pounds each. Comparison with the flight speed and line tension (i.e., power) requirements immediately suggested a tandem motor arrangement. This was further reinforced by the awareness that, because of the shunt motor characteristics, either alone is capable of tether control at low speed or stall for limited periods of time, thus substantially improving mission reliability.

A great deal of laboratory effort was devoted to testing these motors, one against another, in a motor/generator dynamometer arrangement. Tests explored various combinations of series excited and separately excited fields, DC power sources and pulse-modulated SCR controllers of two types. The control arrangements finally employed, although by no means the only possibilities, are shown in Fig. 4. In the reel up (motor) mode each series-connected motor is controlled by a conventional SCR motor drive providing very high torques at low speed and smooth proportional control all the way to full power (equivalent to the battery being directly connected to the motor). In the reel down mode, each motor is connected as a separately-excited generator with a fixed field current, a fixed load resistor providing a limiting speed at constant torque, and an SCR modulated control resistor providing speed reduction to about 10% of the limiting speed. The generator mode cannot provide power absorption down to zero speed, of course, (the limit being the armature resistance) and the SCR needs a back EMF sufficient to support forward conduction, so stopping the winch completely requires a separate brake. Note that in the reel down (descent) mode, very little power is required from the batteries.

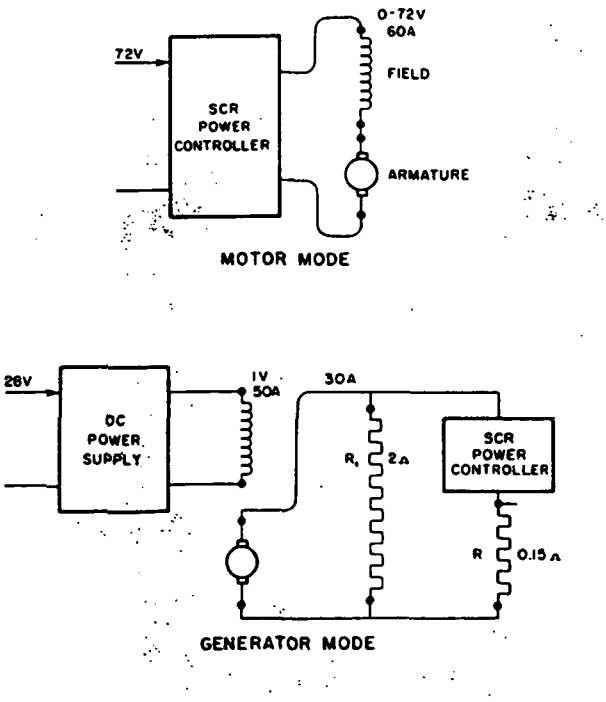

Fig. 4. Winch Motor Control Arrangements

Flight Power Handling System

An overall power handling system block diagram is shown in Fig. 5. The physical arrangement of the power train, including the drum, is best illustrated in Fig. 6, taken before installation of much of the surrounding equipment. The two traction motor/generators are geared together in tandem within a heavy-duty two-pass gear box providing a 17.5:1 reduction to the winch drum drive shaft. Nominal full operating speed is 320 RPM at the drum, and 5600 RPM at the motors. Mode switching is accomplished with DC contactors, 5 poles per motor, rated at 100 A (continuous). Switching, however, is customarily done at zero power with the winch stopped. Both the motors and the contactors are enclosed in pressurized containers for cooling and arc suppression on the brushes and contacts.

Motor power control (reel up) is implemented with an SCR switching controller employing both pulse frequency and width modulation. The units finally flown, General Electric's EV-1B, are rated at 250 A and came straight from the electric vehicle market. They have been modified only as necessary to achieve electronic command control of power level, and they have evidenced no distress at being exposed to the aerospace environment. Traction power for the ascent phase comes from batteries. For the first flight the complement was 275 lb of silver-zinc cells providing 120 A at 72 V (steady state) with a capacity of over 10 kw-hours, enough for two complete 12 km ascents.

In the descent phase, the generator fields are excited by two current-regulated DC-DC converters, unusual only in that they must provide a high current at a very low voltage. At maximum steady state descent velocity, the generator outputs are routed to two 2 ohm resistor panels, each a one-meter square metal-clad silicone imbedded resistor blanket rated at 2.5 kw. These radiate the power to space. To decelerate the winch, the SCR controllers are used to modulate a pair of resistor sets each having a net resistance of 0.15 ohms. These need have only a modest power rating, however, because when they are fully modulated the speed is low; the power of < 200 watts is absorbed conductively by the winch gondola. Care must be taken in the choice of the control resistor value, such that the power absorbed when fully modulated doesn't reduce the winch speed, and therefore the generator EMF, below the SCR minimum forward conduction voltage.

To bring the winch to a full stop, control the starting and stopping transients generally, and to lock the system in a power-off condition, a single "fail-safe" electromagnetic brake is used. This

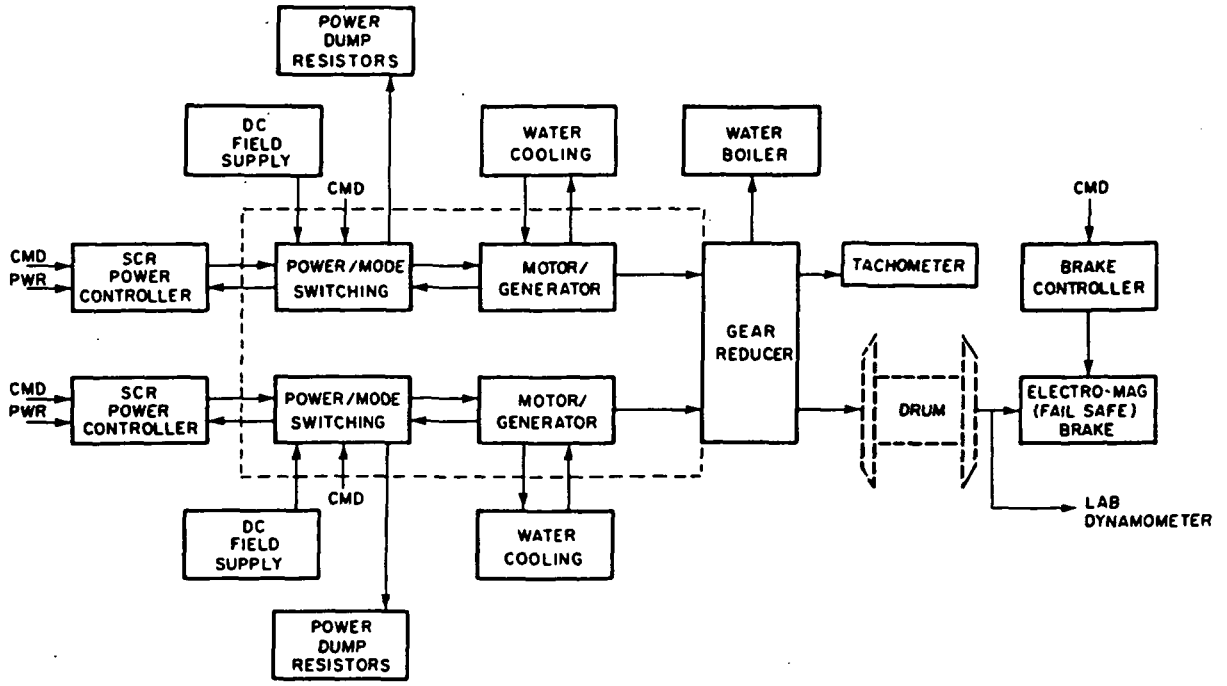

Fig. 5. Winch Power Handling Block Diagram

unit, a Warner ER 1225 commercial brake, has built in ceramic magnets which provide three times the braking torque necessary to lock the drum against line tension. It is released by providing the excitation necessary to counteract the permanent magnetic field. For flight, it is equipped with a pulse-width-modulated proportional controller, with input from a command-initiated ramp generator to achieve smooth stops and starts.

When handling such large amounts of power, temperature control is a problem. Elements like the SCR controllers, DC power supplies, brake and brake controller have proven to exhibit low losses, and thus are kept cool simply by care in mounting. The motors and gearbox, however, dissipate substantial heat. Three strategies have been used to keep the temperature rises under control. First, as noted earlier, the motors are contained in a pressurized housing so that their internal fans can maintain circulation for rotor cooling. Second, each motor is fitted with a water-cooled shroud, and the gondola has two closed fluid cooling loops in which pumps cause the water to transport the heat to the gondola frame. Third, the gearbox is encircled with a water filled shroud having a pressure relief poppet valve (much like a pressure cooker) set at 20.7 kPa (3 psid). At float altitude in the stratosphere, this permits the water to boil, and steam to escape, at a temperature of 60°C, thus removing heat from the gearbox at that temperature.

As a final, but very important, aspect of the power handling system design, the winch drum backshaft has been equipped to drive into and out of a laboratory dynamometer for system development and test. Such a dynamometer was assembled and used in every aspect of the test program; it also allowed exercise and practice of all phases of the operational control protocol prior to flight. This was a crucial factor in the success of the first flight.

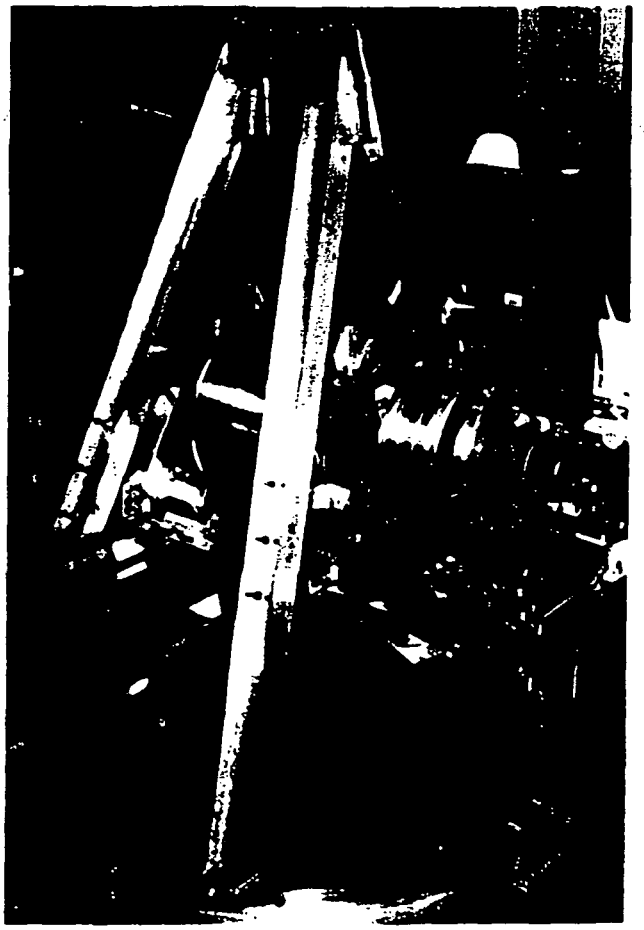

Fig. 6. Power Train During Construction

Command and Telemetry

The essential parts of the Winch Platform command and telemetry system are shown in Fig. 7. A bit-coded command transmission is received by the VHF command receiver and routed to the LARSE decoder which, if address is correct, further decodes the command into steering and information codes. Two classes of commanded functions are used: (a) on-off switch closures of which 21 are contained on 3 cards; and (b) voltage magnitude generators, with digitally derived rate limiting, to provide command input to the three proportional controllers for the motors and brake. Each specific function can be separately commanded with its unique code, and the voltage generator magnitudes are set with a 6 bit code yielding 64 discrete voltage levels into the power controllers. A back up command capability, with a separate receiver and decoder, accesses the switched functions only.

Telemetry is conveyed through a conventional PCM/FM system, supplemented with subcarrier oscillators (SCOs), with transmission in the L band. The PCM encoder operates at a 4096 bps clock rate, samples 8 bit digital words 32 times per second and subcommutates 128 channels of analog information with a repetition time of 2 seconds. Higher bandwidth analog information is transmitted via the SCOs.

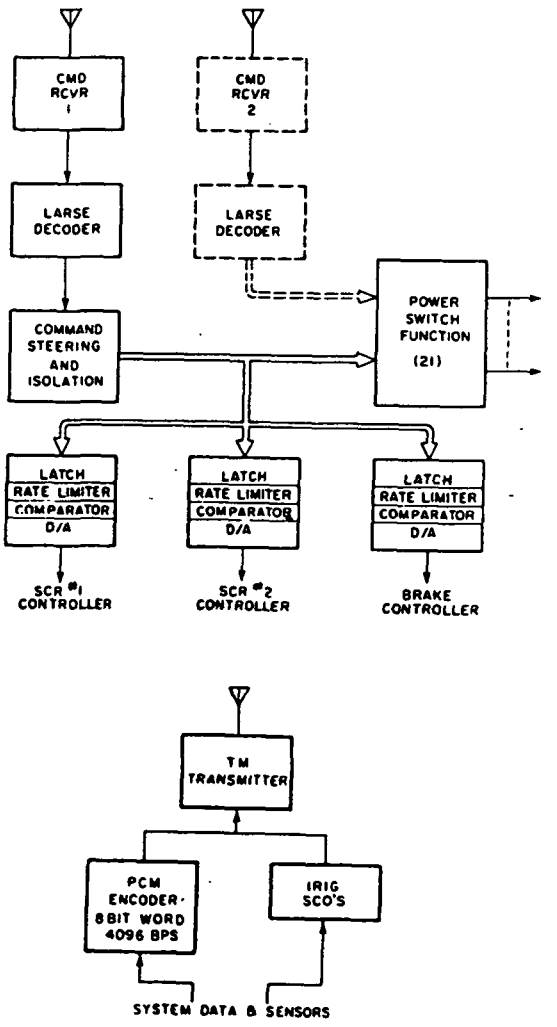

Fig. 7. Command and Telemetry Block Diagram

For flight operations (and for preflight testing) a small self-contained set of ground support equipment is used. Commanding is performed through a LARSE command encoder and a VHF transmitter. The telemetry signals are received and demodulated, the PCM data decoded, and the information presented on CRT displays and strip chart recordings in real time. All data are tape-recorded for later detail reduction.

An additional feature enhancing command control on the Winch Platform is a closed circuit TV camera which can be pointed by command to allow observation of the action (for example, the pulling of the locking pin, or the incoming payload during the ascent phase). Automatic film cameras are also placed onboard to support post-flight diagnostic review.

Similar command and telemetry links with their associated ground support equipment are used for the Suspended Payload. These are completely independent from the Winch Platform equipment.

Suspended Payload

For the first flight of the Reel Down system, a Suspended Payload was constructed which, in addition to scientific instruments for measuring atomic oxygen concentration, carries sensors to evaluate the dynamics associated with the flight activities. The scientific complement of the payload and its performance are described elsewhere.[6] The attitude of the payload is sensed by a vertical gyro having a range of ±60° in pitch and roll and a resolution of about 1°. Vertical accelerations are measured by two accelerometers, and line tension by a load cell at the attachment point. The 62 kg (137 lb) payload is attached to a 16 foot diameter parachute, the top of which is connected to the tether by means of a pyrotechnic separation device. Thus, a vertically stretched parachute is always present at the bottom of the tether during reeling operations, the tether velocity and air density being insufficient to cause the canopy to inflate.

First Flight

The first flight of the Reel Down System took place on September 15, 1982 from Palestine, Texas. The Suspended Payload was supported by the foreshortened parachute below the Winch Platform (Fig. 1), isolated from the tether by a locking pin. After launch, the small parachute was extended to full length and the whole system ascended to the initial float altitude of 40.5 km (133,000 ft). Tracking during ascent permitted a computation of wind speed and direction as a function of altitude, to be used later to evaluate wind shear effects on the lowered tethered payload.

After the balloon drifted to an acceptable test area, the tether tension was adjusted using one of the motors and the brake; then the locking pin was pulled, placing the Suspended Payload directly onto the tether. Shortly thereafter, the brake was released and descent at limiting velocity started (see Fig. 8). The spool velocity gradually increased from 220 RPM to 350 RPM during the descent due to warming of the gearbox; but because of the drum geometry the line velocity remained relatively

constant. (The dashed lines in the figure indicate the descent performance expected, had the gearbox been already warmed up.) Deceleration was initiated at about 11.5 km extension, and the winch brought to a full stop at 12.03 km. It was immediately apparent from real-time telemetry that no dramatic dynamic effects were present in the tether or the Suspended Payload either during descent or stationary at the bottom. During the steady state portion of the descent, power output level for each of the two generators was 1.8 kw, and each of the two resistive radiator panels heated to a plateau temperature of about 130°C.

After 10 minutes wait, the motor connections were reconfigured, the ascent started and the system was brought to full power. The input power to each motor was approximately 60 Amps at 72 volts during most of the ascent period. Spool angular velocity was relatively constant during the ascent and yielded a tether velocity which gradually increased from 5 to 8.2 m/s.

The total time for descent was 28 minutes; for ascent it was 35 minutes including slow recovery of the last 0.5 km. Eight meters more of tether were retrieved than were dispensed, attributable to creep under tension which peaked at 1020 N (at the top).

Longitudinal dynamics in the tethered system were the foremost concern of the flight, being previously unexplored in the stratosphere and not subject to testing in the laboratory. Instrumentation for these observations included tensiometers at the top and bottom of the tether, two accelerometers in the Suspended Payload, and an amplitude sensor on the ΔL energy absorber described earlier.

Oscillations of the simple mass-spring-mass sort were observed at the expected periods (up to 15.2 sec at 12.03 km), although the amplitudes were small and variable. Self excited harmonic motion and most transients associated with commanded power level changes had double amplitudes below 3% of the static (1 g) tension level and durations of a fraction of a minute to several minutes. One transient — that associated with the first commanded deceleration towards the end of the descent — had a double amplitude of 6%, and damped out in about 5 cycles. No evidence was observed for the presence of acoustical energy in the line.

Wind data were obtained during the balloon's ascent to float altitude which, presuming validity for the period of reeling approximately 5 hours later, indicate a shear (with respect to the floating balloon) growing from 0 to 7 m/s in the first 5 km of reel down descent, and then remaining in the range of 7-9 m/s for the remaining distance. The relative wind direction was the same within ±40° over the whole descent trajectory. The Suspended Payload was equipped with a vertical gyro to measure pitch and roll attitude. During the course of the reel down and reel up portions of the flight these evidenced no measurable body centered perturbations, although limited data suggest a hang off angle of 4° due to the wind shear above. Around the azimuthal axis, the payload described one revolution during the first half of the descent, stabilized from there to the bottom and until half way up, then described three revolutions in opposite direction in the last half of the ascent. The Winch Platform meanwhile was describing 8 revolutions in the second direction, at relatively constant velocity.

At the conclusion of the reel up phase, the tether connection to the Suspended Payload was within one meter of the Winch Platform. Two hours later, the Suspended Payload was separated from the tether with a pyrotechnic device, and descended to the ground on its attached small parachute. The Winch Platform was "cut away" from the balloon shortly thereafter for descent on its larger parachute. Both were recovered with only minor damage.

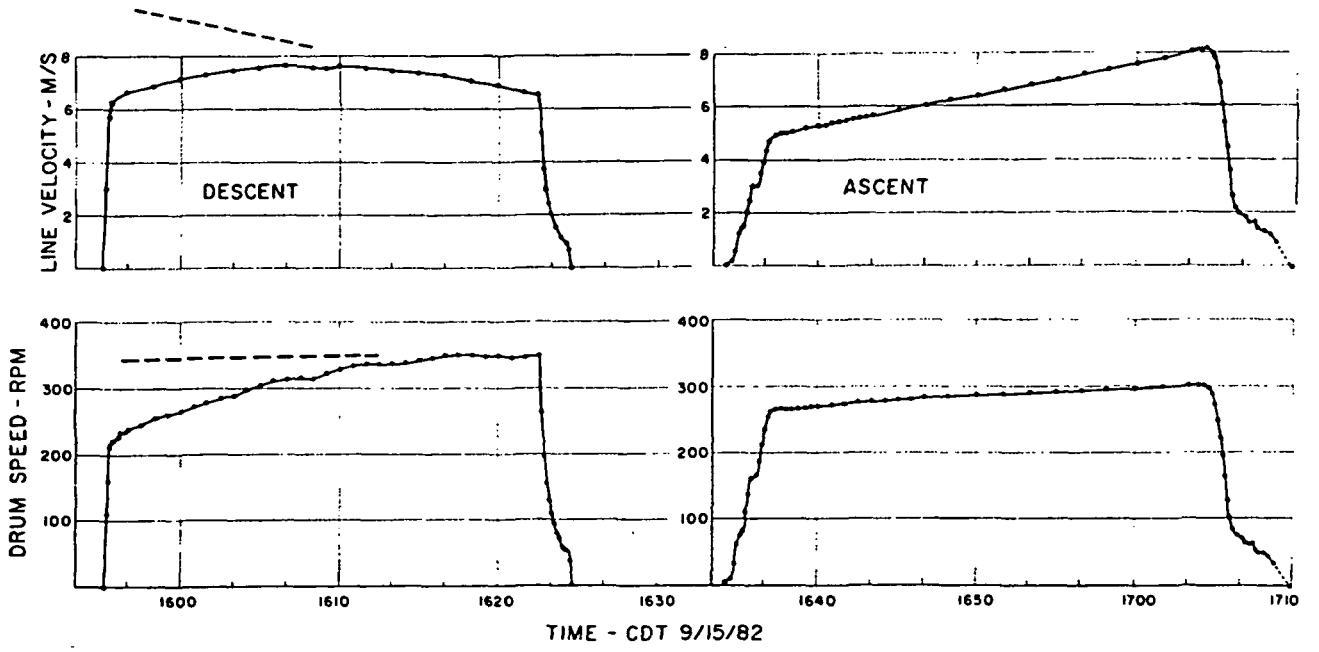

Fig. 8. Descent and Ascent Velocities

Conclusions

Having finished the development effort and the conduct of the first flight test, we can now make the following observations:

(a) The Reel Down Winch System appears to be an effective tool for stratospheric chemistry research through the means of repetitive deep soundings from above employing high scan velocities. The system performed flawlessly during the first flight and presented far fewer difficulties during development and test than expected.

(b) System instabilities or tether risk due to self-excited dynamic effects have proven not to be a significant factor within the operational realm explored.

(c) Moderate stratospheric wind shears have not produced any detrimental effect on system operation or observational effectiveness.

Given these findings, we are now preparing the Reel Down System for more productive use. In its second flight a somewhat heavier payload will be reeled down and up four times, with a tether length of 8 km. Additional battery capacity will be installed to provide the necessary energy. The Suspended Payload will contain a more extensive complement of scientific experiments, in addition to the dynamic sensors previously flown. We will continue to critically monitor stratospheric and self-induced effects on the system during the course of the next flights.

Acknowledgments

Design, development and final preparation of this equipment took place within the Atmospheric Research Project, Harvard University; Leonard Solomon, Manager. Especially valuable were the efforts of Bill McLaren, Stod Rowe, Craig Schiller and Edward Thompson. Janie P. Schwab and Elliot Weinstock prepared the Suspended Payload. Virtually all construction was done by the Division of Applied Sciences Machine Shop; George Pisiello, Manager. Flight support under demanding circumstances was willingly provided by the National Scientific Balloon Facility including, particularly, Robert Kubara and Keith Hazelwood. This work was supported under NASA contracts NASW 3061 and NASW 3242.

References

1. Strength and Durability Characteristics of Ropes and Cables from Kevlar™ Aramid Fibers; M.H. Horn, P.G. Riewald, C.H. Zweben; in Proceedings of OCEANS 77 Conference. Marine Technology Society/IEEE; 1978.
2. Cortland Kevlar Ropes and Cables; E. Scala; Sea Technology, July 1977.
3. Technical Data Sheet #121; available from Cortland Line Company, 1981.
4. Report #8964-048; Otis Engineering Corp. 1981.
5. P.G. Riewald, E.I. DuPont de Nemours, private communication.
6. In Situ Detection of Free Radicals in the Stratosphere: A New Approach; J.G. Anderson et al., Science, in preparation.

Stratospheric ClO: In-Situ Detection with a New Approach

Wm. H. Brune, E.M. Weinstock, M.J. Schwab,
R.M. Stimpfle and J.G. Anderson
Department of Chemistry and
Center for Earth and Planetary Physics
Harvard University
Cambridge, Massachusetts 02138

March 1985

Abstract

Stratospheric chlorine monoxide concentrations were measured in situ using a new and improved observational method in which the detection package is lowered on a tether from a balloon-borne platform floating near 40 km altitude and then reeled back up. Two reel down and reel up sequences covering 38 to 31 km produced [ClO] profiles which agree with each other to ± 12%. The measured [ClO] profile falls within the envelope of nine previous "fast" parachute drop results, but exhibits a different shape, peaking near 32 km as opposed to ~ 39 km for the average of the previous profiles. These results are lower than but consistent with the profiles derived from remote sensing methods, and indicate the need for simultaneous measurements of relevant species.

Early optimism that computer simulations could accurately depict the photochemistry of stratospheric chlorine and hence predict secular trends has given way to a more sobering but realistic view that a more judicious mix of observations and calculations must guide our conclusions. For example, the concept of a free radical "titration" in which the catalytic control of global ozone transits from nitrogen control to chlorine control (Prather et al., 1984) has reemphasized the need to firmly establish within the real atmosphere a limited number of essential mechanistic links.

Another major concern, the observed variability of [ClO], greatly limits the utility of comparisons between computer simulations and observations as tests for valid photochemistry because the large range of [ClO] values "agrees" with the results of models containing different photochemical assumptions. From simple photochemical considerations, these [ClO] fluctuations appear to be related primarily to fluctuations in stratospheric methane and, to a lesser extent, water vapor (Solomon and Garcia, 1985). Unknown chemistry or chemical sources, either constant or sporatic, terrestrial or extraterrestrial, may also play a role. Unfortunately, no attempt has been made to systematically rule out unusual chemistry or sources on physical or chemical grounds.

It is clear that substantial progress in our understanding of stratospheric chlorine photochemistry requires simultaneous observations of ClO and other related species which remain approximately in photochemical steady state. Two types of experiments should be performed: measurements made in widely differing atmospheric conditions, such as low latitude summer and high latitude late winter, or sunrise and sunset transitions; and in-situ kinetics experiments which directly observe the rate of internal conversion within the free radical cycles. In this

letter we discuss a new observation system designed to carry stratospheric research from the age of species concentration measurement to one of mechanistic diagnosis. We also include the results of the first CℓO measurements made with this system as a first step toward more meaningful simultaneous observations of CℓO with other species.

All previous in-situ CℓO measurements were made with the "fast" drop method, in which the instrument was carried to $\sim$ 40 km by a balloon and then dropped through the stratosphere on a parachute at 30 - 100 meters per second. These "snapshots" of the CℓO distribution often lacked other simultaneous measurements and instrument-induced fluctuations and low altitude resolution made separation of atmospheric variations and instrument effects difficult. Clearly, a new technique with better altitude resolution, higher sensitivity, better control of the experimental variables, and the ability to make repetitive scans was required. Since the last "fast" drop CℓO experiment in September, 1979, our laboratory has been working on new approaches to in-situ measurements. One result is the reel down technique which is illustrated in Figure 1a and has been discussed in detail elsewhere (Hazen and Anderson, 1984; Anderson et al., 1985). In summary, measurements are made when a suspended payload containing the measurement array is lowered at a controlled rate (5 - 7 meters per second) on a Kevlar filament by a winching platform attached to the balloon. The payload is slowed to a halt at the end of the scan and is reeled back up for another measurement. One measurement of 10 km takes approximately one hour; present energy capability allows $\sim$ 4 complete scans. In addition to the reel down method, substantial improvements have been incorporated into the suspended array. Impellers mounted at the top of each detection flow tube provide independent control over the flow conditions and minimize

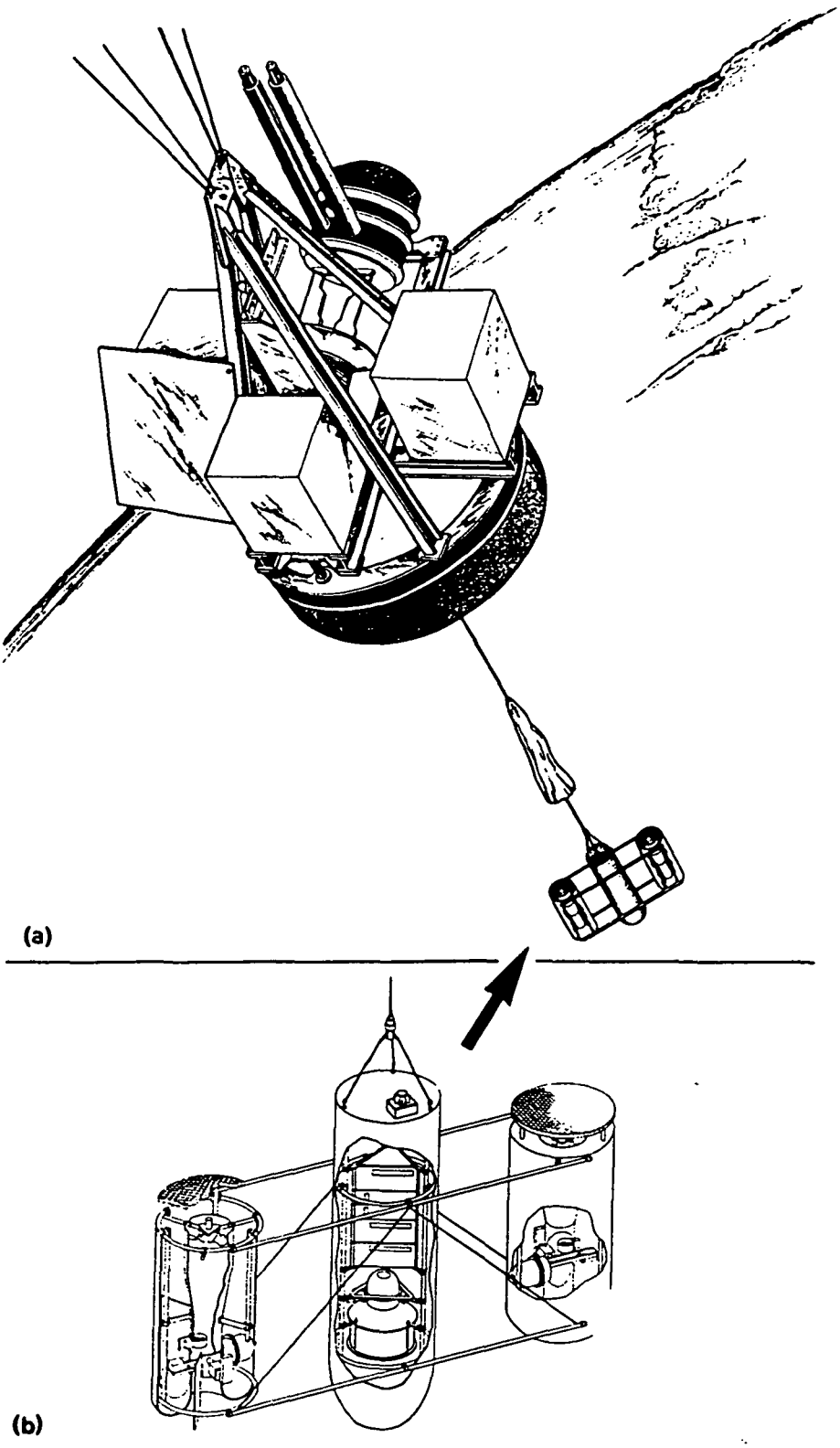

Figure 1. Rendering of the Reel Down system showing the winching system and suspended payload. A helium filled research balloon is used to lift the combination to any altitude up to 40 km from which vertical scans of greater than 10 km are executed. Panel (a) displays the geometry of the experiment at float altitude in the docked position. Panel (b) shows a schematic of the suspended instrument array indicating the optical system and flow system used to obtain the in-situ free radical observation.

the effects of horizontal wind shear, thermistor arrays above and below the resonance fluorescence detection axis in each flow tube indicate the character of the flow, and anemometers mounted above the detection axis monitor gas flow velocity. The first flight of reel down incorporationg these improvements was a successful measurement of the atomic oxygen concentration from 39 to 30 km with a single reel down/reel up sequence on 15 September 1982 (Anderson et al., 1985).

Further improvements have been made in the ClO detection scheme itself. Presently, the most sensitive method for in-situ ClO detection is the chemical conversion of ClO to Cl by reaction with excess added NO and the subsequent resonance fluorescence detection of the Cl atoms with 118.9 nm Cl resonance radiation. An additional sensitivity gain of 20 to 50 is achieved by increasing the optical collection efficiency with a 14 cm diameter condensing mirror which focusses the scattered resonance radiation onto a photomultiplier. Greater control is gained in the NO chemical conversion because the time required for the complete mixing of NO in the ambient air becomes much less than the time required for the chemical conversion, and the NO flows necessary for 95% ClO to Cl conversion are greatly reduced from values used in the fast drop method. Finally, a photoionization detector to measure absolute injected NO concentrations has been added just above the Cl detection axis. A summary of experimental parameters highlighting the differences between the reel down and "fast" drop methods is given in Table 1.

In addition to absolute [ClO] and [Cl] altitude profiles, some simple in-situ chemical kinetics experiments similar to laboratory discharge flow studies become feasible. The reaction rate constant between ClO and NO is measured by adding to the flow enough NO to only

Technique	Reel Down	"Fast" drop
Altitude range	42 - 15 km	44 - 20 km
Descent velocity	0 - 7 m/sec	30 - 100 m/sec
Altitude resolution at S/N = 20	< 50 meters	0.5 km
Flow control	Descent and impellers	Descent
[NO] required for 95% ClO to Cl conversion	$5 \times 10^{12} - 5 \times 10^{13}$ molec/cm^3	$1.5 \times 10^{14} - 1 \times 10^{15}$ molec/cm^3
Detection sensitivity	$10^{-5} - 10^{-4}$ ct/sec/cm^3	$5 \times 10^{-7} - 1 \times 10^{-5}$
Background signal	< 100 ct/s	< 50 ct/s
Diagnostics	UV flux; thermistor array; NO photoionization; NO concentration variation	UV flux

Table 1. Experiment parameters for two in-situ methods.

partially convert ClO to Cl. A plot of [Cl]/[ClO] against [NO] · [reaction time] yields the reaction rate constant. The objective is to test the consistency of the in-situ method with laboratory controlled results. Another experiment, the interrogation of the rate of conversion with a chemical cycle, requires addition of a reactant to the ambient flow. The shifted steady state values of the ambient concentrations are then measured. An example is the addition of NO to repartition Cl and ClO which allows the conversion rate of $Cl + O_3 \rightarrow ClO + O$ to be measured.

This first ClO experiment using the reel down approach was designed to measure at least two [ClO] altitude profiles from 40 to 32 km. The primary objective was to provide data for comparison with the profiles taken by the substantially different "fast" drop technique. Secondary objectives were to test the dependence of measured [ClO] on experiment variables, such as the impeller rotation speed, the descent velocity, and the NO flow rate, as well as the performance of the more sensitive mirror/photomultiplier detector. To this end, the instrument shown in Figure 1b was flown with

two ClO detection flow tubes, one placed on either side of a center section containing all the electronics, batteries, and regulated NO and O_2 gas supplies. One flow tube housed the mirror/photomultiplier detector; the other just a photomultiplier. They both contain the new NO injection and detection systems and the flow diagnostics.

The experiment was launched from Palestine, Texas (latitude = 31.5°N) on 14 September 1984, and achieved an initial float altitude of 39 km. Two successful measurements of the ClO altitude profile were made from 38 km to 31 km at (20:00 - 20:30) UT and (21:35 - 22:00) UT, with average solar zenith angles of 39° and 55°, respectively. Descent velocities were 4 to 5 meters per second for the first descent and 5 to 7 meters per second for the second, so the eight second gas on/off cycle provided an ultimate altitude resolution of ~ 50 meters. Prior to the first descent, the radio frequency power for the chlorine light sources degraded from 34 watts to ~10 watts. A slight further shift occurred prior to the second descent, and the less sensitive detection system light source became unstable during the second descent. These shifts were fortunately not catastrophic because post-flight calibrations at pre-flight power levels showed less than a 5% degradation of detection sensitivity, and careful post-flight calibration at the lower flight power levels was possible.

The three independent ClO altitude profiles, two taken on the first descent with the two detection systems and one taken on the second descent with the more sensitive system are shown together in Figure 2. The data from the less sensitive system (Pod 1) are averaged over 0.5 km intervals to give a signal-to-noise ratio of 14; the data from the other (Pod 2) are averaged over 0.2 km intervals to give a signal-to-noise ratio of 32. The three profiles agree to within ± 12% at all altitudes, but descents 1 and

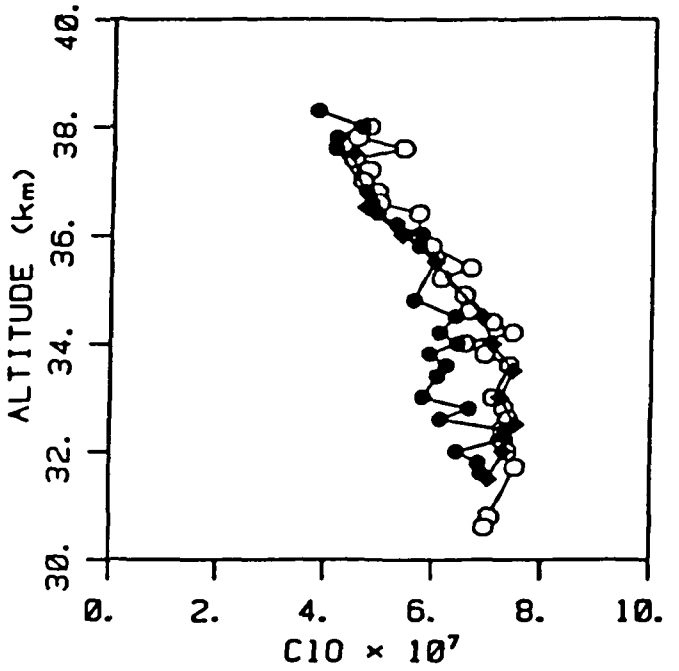

Figure 2. The observed ClO concentrations from the Reel Down flight. Closed diamonds are the 0.5 km averages from Pod 1 on the first descent. Closed and open circles are 0.2 km averages from Pod 2 on the first and second descents, respectively.

2 for Pod 2 show statistically meaningful variations on the 0.2 km scale of as much as ± 10%. Since these variations do not occur at the same altitude for the two descents, they are assumed to be instrument effects, either undetected sensitivity changes or "losses" of ClO in the perturbed flow. An error analysis for the precision gives ± 12% precision for Pod 2 and ± 15% for Pod 1, with the uncertainty primarily due to the degradation of the resonant lamp fluxes for this flight, and the resulting lack of resolution of the light source flux monitors (± 10%). Losses of ClO or Cl either on the flow tube surfaces or by recombination of Cl with NO to form ClNO reduce the measured [ClO] by less than 5%, according to an analysis of the effects of impeller speed and thermistor array data on the derived profiles. Thus the total precision of ~ ± 15% adequately explains the difference in the profiles shown in the figure. For future experiments, and under normal operating conditions, the precision should be ± 5%, with counting statistics being the largest contribution. The absolute uncertainty will be improved from the present ± 25%, based on

the errors discussed by Anderson et al. (1980), to less than ± 15%, an accuracy now routinely obtained in laboratory rate constant studies.

The reel down measurements, averaged together in one kilometer intervals, are given in Figure 3, together with all "fast" drop in-situ measurements (Weinstock et al., 1981). The reel down profile lies within

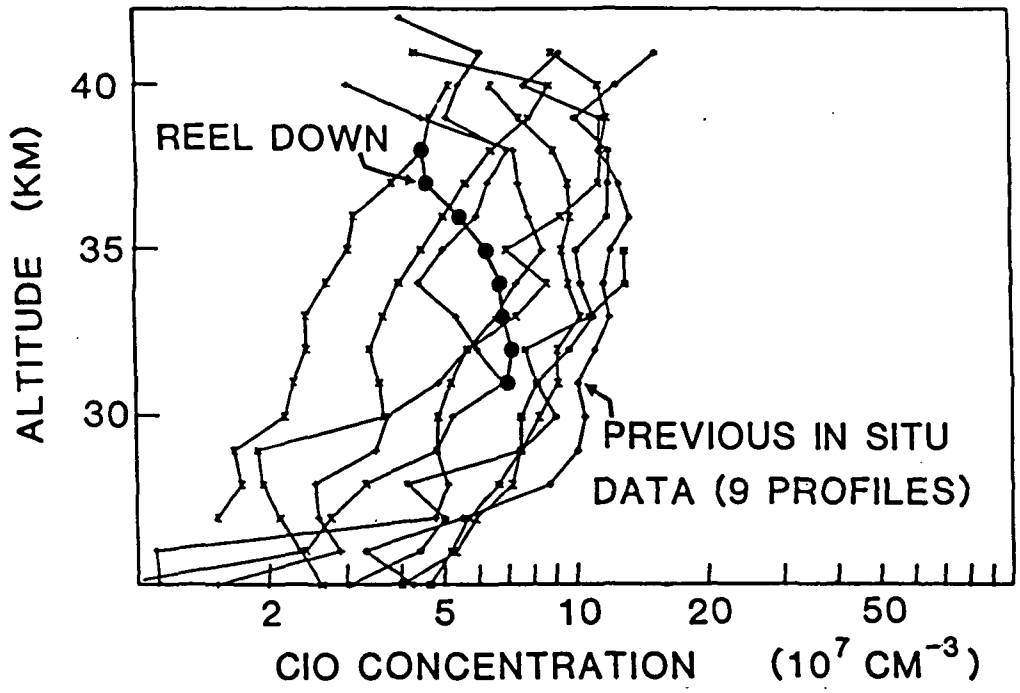

Figure 3. Comparison of the average Reel Down (large closed circles) [ClO] results with 9 "fast" parachute drop profiles (see Weinstock et al., 1981 and Anderson et al., 1980 for the specifics of each measurement).

the envelope defined by the earlier measurements, but it exhibits a distinctly different shape, particularly above 35 km. It is interesting to speculate on why this ClO profile has [ClO] one half of the mean of previous in-situ measurements at 38 km and approximately equal to the mean below 35 km. Careful reexamination of both experimental methods reveals no errors large enough to result in such a discrepancy; nevertheless, a future flight in which a "fast" drop measurement is made between two reel down observations is being planned. Furthermore, this profile is probably not a result of changes in atmospheric parameters such as

solar flux variations over the eleven year solar cycle or a gradual change in a trace constituent. The most likely candidate is a $[CH_4]$ profile similar to the high side of the envelope of observed methane values, since the methane deviation is greatest at ~ 40 km and becomes substantially less below 35 km. Another possibility in the framework of known photochemistry is a low [OH] profile, perhaps similar to that measured by Heaps and McGee (1985), since OH liberates active chlorine from the HCℓ reservoir. An aberrant $[O]/[O_3]$ ratio, which partitions reactive chlorine into Cℓ and CℓO, cannot be responsible since the Cℓ atoms would have been detected as a much larger background than expected from chamber and Rayleigh scatter alone.

The status of atmospheric CℓO research is summarized by a comparison among the in-situ and remote sensing observations and a computer simulation as shown in Figure 4. The data are plotted as mixing ratios, where the Anderson and co-workers in-situ profile is the average of all flights except 07/26/76 and 07/15/77, and the balloon-borne mm-wave results of Waters et al. (1981) and the ground-based mm-wave results of deZafra et al. (1984) were both converted from CℓO column densities to mixing ratios by the authors. Not included on the plot are the early results from the promising infrared laser heterodyne technique which requires improvement in sensitivity and laboratory calibrations to be useful. While no attempt has been made to correct these observations to the same conditions, such as latitude, solar zenith angle, or season, there is generally good agreement among the techniques, and a somewhat less satisfying agreement with the model. The appearance of greatest divergence above 35 km is disconcerting because chlorine chemistry has its greatest impact on ozone in that altitude range; but it is also illusory,

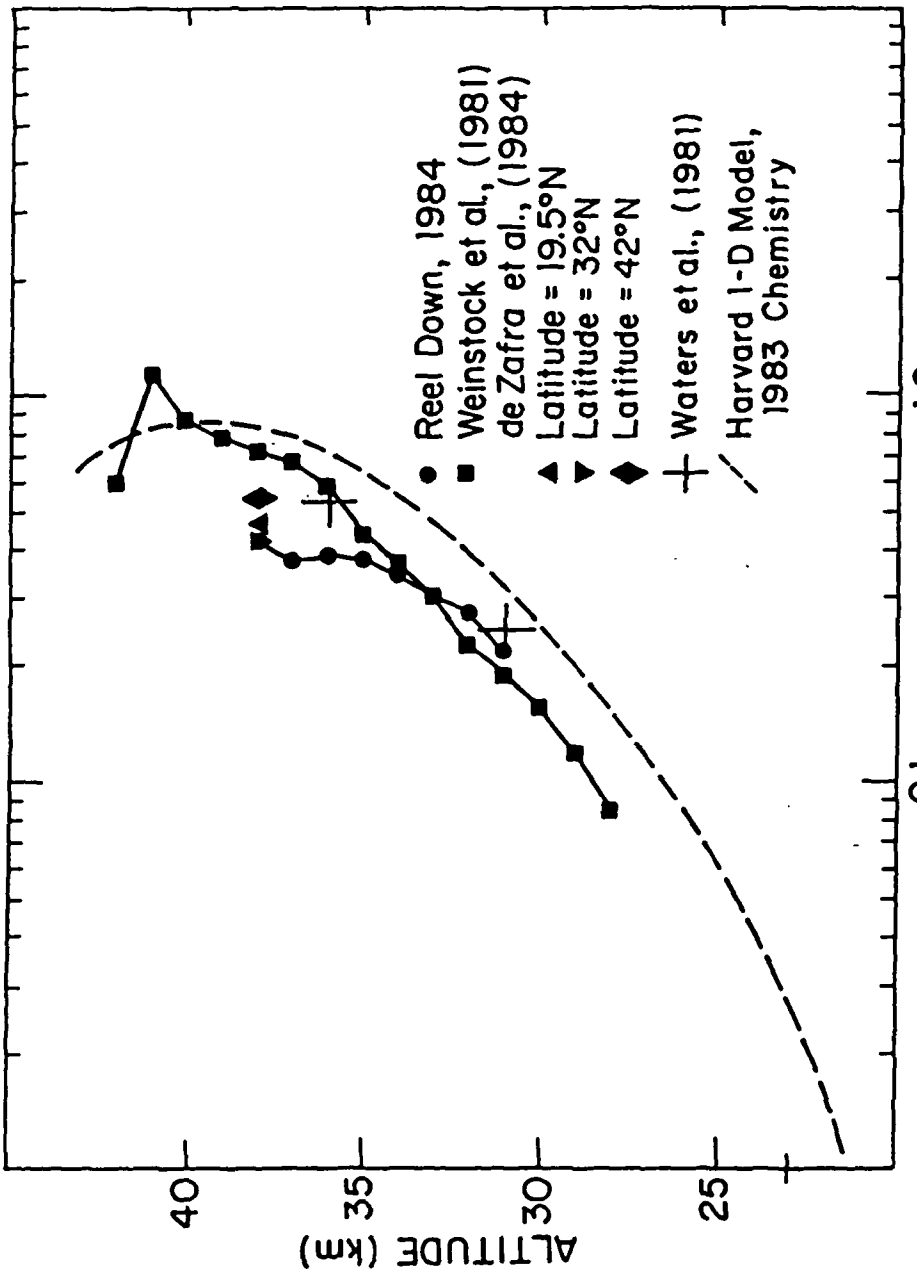

Figure 4. ClO mixing ratios from experiments, both in-situ and remote, and the Harvard 1-D model (NAS report, 1984), 30°N, 3:00 PM conditions. Remote measurements were converted from total column to mixing ratios by the authors.

since plausible variations in methane and other species may account for it.

We conclude that, while some differences between observations may be instrument related, atmospheric changes now dominate. Clearly, measurements of stratospheric CℓO alone will not be able to resolve the differences between observations and simulations; simultaneous measurements of other species, HCℓ, CH_4, H_2O, and others, are required. This first CℓO flight was a step in that direction.

Acknowledgments

We thank all those who made this experiment possible: Nathan Hazen, Stoddard Rowe, Joe Demusz, Ed Thompson, and Lenny Solomon, in particular, from the Atmospheric Research Project at Harvard; the Harvard Scientific Instrument Shop; and the National Scientific Balloon Facility. This project is supported by the NASA Upper Atmospheric Program (NASA grant NASW 3242) and received funds from the Chemical Manufacturers' Association for Reel Down development, all of which is gratefully acknowledged.

References

Anderson, J.G., H.G. Grassl, R.E. Shetter and J.J. Margitan, Stratospheric free chlorine measured by balloon-borne in-situ resonance fluorescence, J. Geophys. Res. 85, 2869, 1980.

Anderson, J.G., N.L. Hazen, B.E. McLaren, S.P. Rowe, C.M. Schiller, M.J. Schwab, L. Solomon, E.E. Thompson and E.M. Weinstock, Free radicals in the stratosphere: a new observational technique, Science , , 1985.

Hazen, N.L. and J.G. Anderson, Reel down: a balloon-borne winch system for stratospheric sounding from above, 22nd Aerospace Sciences Meeting, 9-12 January 1984, Reno, Nevada.

Heaps, W.S. and T.J. McGee, Progress in stratospheric hydroxyl measurement by balloon-borne LIDAR, J. Geophys. Res., in press.

National Academy of Sciences, Causes and Effects of Changes in Stratospheric Ozone: Update 1983, National Academy Press, Washington, D.C., 1984.

Prather, M.J., M.B. McElroy and S.C. Wofsy, Reductions in ozone at high concentrations of stratospheric halogens, Nature 312, 27, 1984.

Solomon, P.M., R. deZafra, A. Parrish and J.W. Barnett, Observation of diurnal variation of stratospheric chlorine oxide: a critical test of chlorine chemistry in the ozone layer, Science , , .

Solomon, S. and R.R. Garcia, On the distribution of long lived tracers and chlorine species in the middle stratosphere, J. Geophys. Res., in press.

Waters, J.W., J.C. Hardy, R.F. Jarnot and H.M. Pickett, Chlorine monoxide radical, ozone and hydrogen peroxide: stratospheric measurements by microwave limb sounding, Science 214, 61, 1981.

Weinstock, E.M., M.J. Phillips and J.G. Anderson, In-situ observations of ClO in the stratosphere: a review of recent results, J. Geophys. Res. 86, 7273, 1981.

III. THE COPPER VAPOR LASER

The single most important free radical in the stratosphere in terms of bounding predictions of ozone depletion is the hydroxyl radical. It is particularly important to establish both the absolute concentration of OH and simultaneously the absolute concentration of H_2O within the same volume element. We have therefore placed particular emphasis on the development of a laser system which will provide adequate detection sensitivity to yield 0.25 km resolution at any solar zenith angle with $S/N \geq 50$.

In order to achieve the required performance it was necessary to combine very high average power with low peak power. That requirement could not be met by any commercial unit (by two orders of magnitude), so we began in 1979 the development of a copper vapor laser which could pump a dye laser at a repetition rate of 20 kilohertz and achieve an average power at 5106 Å of 10 watts. We present here the results of that development through the first flight test of the system in the stratosphere. The report is broken into the following sections:

A. Theory of Operation

B. Experimental

C. Results and Discussion

A. Theory of Operation

The technique of laser induced fluroescence has been used extensively for the detection of trace species in the gas phase and is well documented in the literature. The technique is extremely versatile, thus a variety of excitation and observation schemes are possible, depending on details of the molecule and the experimental hardware.

In this experiment a particular rotational level in the $X^2\Pi_{3/2}$, v = 0 ground state of OH is pumped at λ = 2820 Å into the $A^2\Sigma$, v = 1 excited state. The upper level of the selected transition undergoes rapid radiative and collisional relaxation by a variety of different pathways as indicated in Figure 1 and summarized by the five major processes below which focus on the vibrational levels involved:

Radiation Relaxation	$OH(A^2\Sigma, v=1) \rightarrow OH(X^2\Pi, v=1,0) + h\nu$	(1)
Electronic Quenching	$OH(A^2\Sigma, v=1) + M \rightarrow OH(X^2\Pi) + M$	(2)
v-v Transfer	$OH(A^2\Sigma, v=1) + M \rightarrow OH(A^2\Sigma, v=0) + M$	(3)
Radiative Relaxation	$OH(A^2\Sigma, v=0) \rightarrow OH(X^2\Pi, v=0) + h\nu$	(4)
Electronic Quenching	$OH(A^2\Sigma, v=0) + M \rightarrow OH(X^2\Pi) + M$	(5)

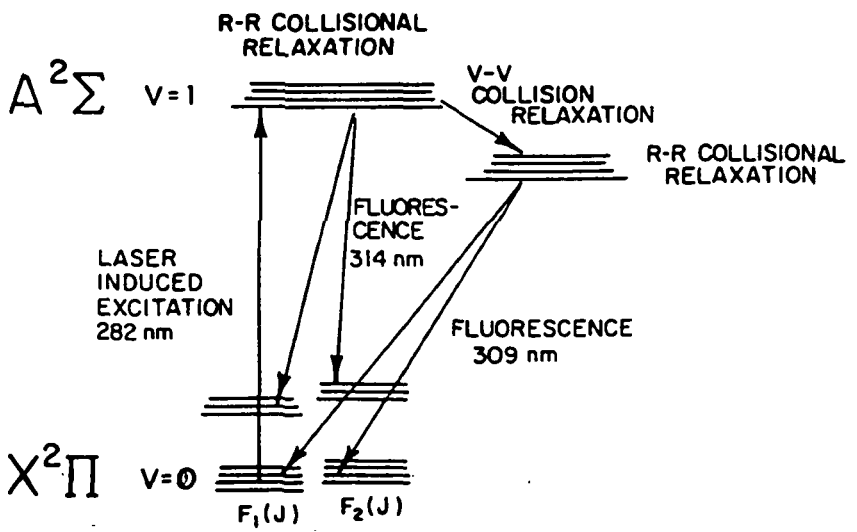

Figure 1

The fraction of excited state molecules that radiate and the partitioning of the emi-ted fluorescence into the most favored bands, (1,1), (1,0) and (0,0), is determined by the relative rates for the above processes. The v = 1, v = 0 collision-induced vibrational relaxation rate is of particular importance since its magnitude relative to processes 1 and 2 leads to significant population in the v = 0 level of the $A^2\Sigma$ state. The primary fluorescence signal observed in this experiment is emitted from this level via the (0,0) band, centered around 3090 Å. This detection scheme, pumping a rovibronic line in the (1,0) band and observation of the (0,0) band fluorescence is chosen because of its simplicity with regard to experimental hardware required. The OH molecule provides a convienient wavelength shift between the laser pumping frequency and the observation band, thus scattered laser light is not a competing background signal superimposed on the OH fluorescence signal.

Signal Equation

The relationship between the observed OH fluorescence signal on the 3090 detector, S_{OH}^{3090}, and the OH number density in the sample volume is given by the signal equation below:

$$S_{OH}^{3090}(\text{cts/sec}) = \int F(\lambda)\sigma(\lambda)d\lambda \; [OH] \; VQ\varepsilon T\eta \qquad (6)$$

where $F(\lambda)$ = the laser flux (photons/cm^2sec cm^{-1});

$\sigma(\lambda)$ = the OH absorption cross section (cm^2/cm^{-1});

[OH] = the OH number density (molec/cm^3);

V = the volume of the sample element interrogated by laser, defined by the overlap of the projected area of the laser beam and projected area of the 3090 detector field of view (cm^3);

Q = the fluorescence efficiency, that is the fraction of $OH(A^2\Sigma, v=1, J)$ molecules produced by the laser that fluoresce in the (0,0) band rather than collisionally deactivate or fluoresce in other bands;

ε = the geometric collection efficiency of the 3090 detector;

T = the transmission of the 3090 detector optics; and

η = the efficiency of converting a photon incident on the photocathode surface into an observed count.

The signal equation is represented more concisely by our working expression

$$S_{OH}^{3090} = C_{OH}EQ[OH] \tag{7}$$

where E represents a dimensionless measure of the intensity of the laser beam in the sample volume element. In the working expression the nonvariable terms in the signal equation, those that are fixed by knowledge of the transition being pumped by the geometry of the experiment, or by the optical hardware, are expressed as a single product, C_{OH}^{3090},

$$C_{OH}^{3090}\left(\frac{cts/sec}{Q \cdot [OH]}\right) = \int g_{laser}(\lambda)\sigma(\lambda)d\lambda \; V \; \varepsilon T\eta \tag{8}$$

where $g_{laser}(\lambda)$ represents a normalized laser linewidth function.

In practice the value of C_{OH} is determined by direct measurement of S_{OH}^{3090} with a known OH density in the sample volume elment, at a known power, E, and a known quenching environment, Q, as explained in the experimental section. Detailed evaluation of each of the terms in Eq. (8) is not required for derivation of OH density from the observed count rate. However, comparison of measured and estimated values of C_{OH}^{3090} provides a valuable diagnostic on system performance.

Laser Spectral Characteristics

The linewidth of the frequency doubled output of the dye laser is approximately 5 cm^{-1}. In comparison the OH absorption lines in the A - X band are primarily Doppler broadened in the pressure and temperature environment of the stratosphere resulting in a width slightly less than 0.1 cm^{-1}. The longitudinal mode spacing of the dye laser is considerably less, 0.012 cm^{-1}, thus many modes act to pump the absorption transition during a given pulse. The width of an individual mode has not been measured explicitly but it must be greater than 4×10^{-4} cm^{-1} which is the Fourier transform limit for a 15 nsec FWHM pulse length, characteristic of our system. The width of an individual mode is not particularly important provided the flux per unit cm^{-1} interval does not lead to population depletion of the lower level of the transition being pumped. Absorption saturation was never observed when conditions of low pressure and high laser power were explored using the calibration facility.

OH Molecular Characteristics

Several different rovibronic transitions are suitable candidates for OH detection, as shown in Figure 2. The indicated transitions are those that lie within our remote tuning range and have the most favorable product of transition moment strength and population in the lower quantum level.

The wavelengths and the relative absorption intensity of these lines is shown in Figure 3. The Q branch lines are accompanied by satellite lines ($\Delta K \neq \Delta J$) of significant intensity. The splittings from the parent lines, ranging from .1 to .9 cm^{-1}, are small compared to laser linewidth. Therefore, when a pure Q branch line ($\Delta K = \Delta J$) is pumped, the accompanying satellite line is also pumped. Note that the $P_1 1$ line has no satellite structure associated with it. Pumping a neighboring satellite line does not adversely impact the analysis of the fluorescence data since at pressure encountered in the stratosphere extensive collision-induced rotational redistribution occurs within the excited state. Thus the technique is not sensitive to the spin components of the upper state.

The fluorescence efficiency, Q, is the fraction of initially excited OH molecules that fluoresce in the (0,0) band. The issue of the overlap of the detector band width with the fluorescence emission band is not considered in this term, but is included in the net transmission of the detector optics. The functional form of Q is conceptualized most simply as the product of two terms: (1) the efficiency for v-v transfer out of the v = 1 level and into the v = 0 level of the A state; and (2) the efficiency for fluorescence from the v = 0 level in the (0,0) band. Thus, we have,

$$Q = \frac{k^{VV}[M[}{k_{Rad}^{v=1} + k^{VV}[M] + k^{Q,v=1}[M]} \times \frac{k_{Rad}^{0,0}}{k_{Rad}^{v=0} + k^{Q,v=0}[M]} \qquad (9)$$

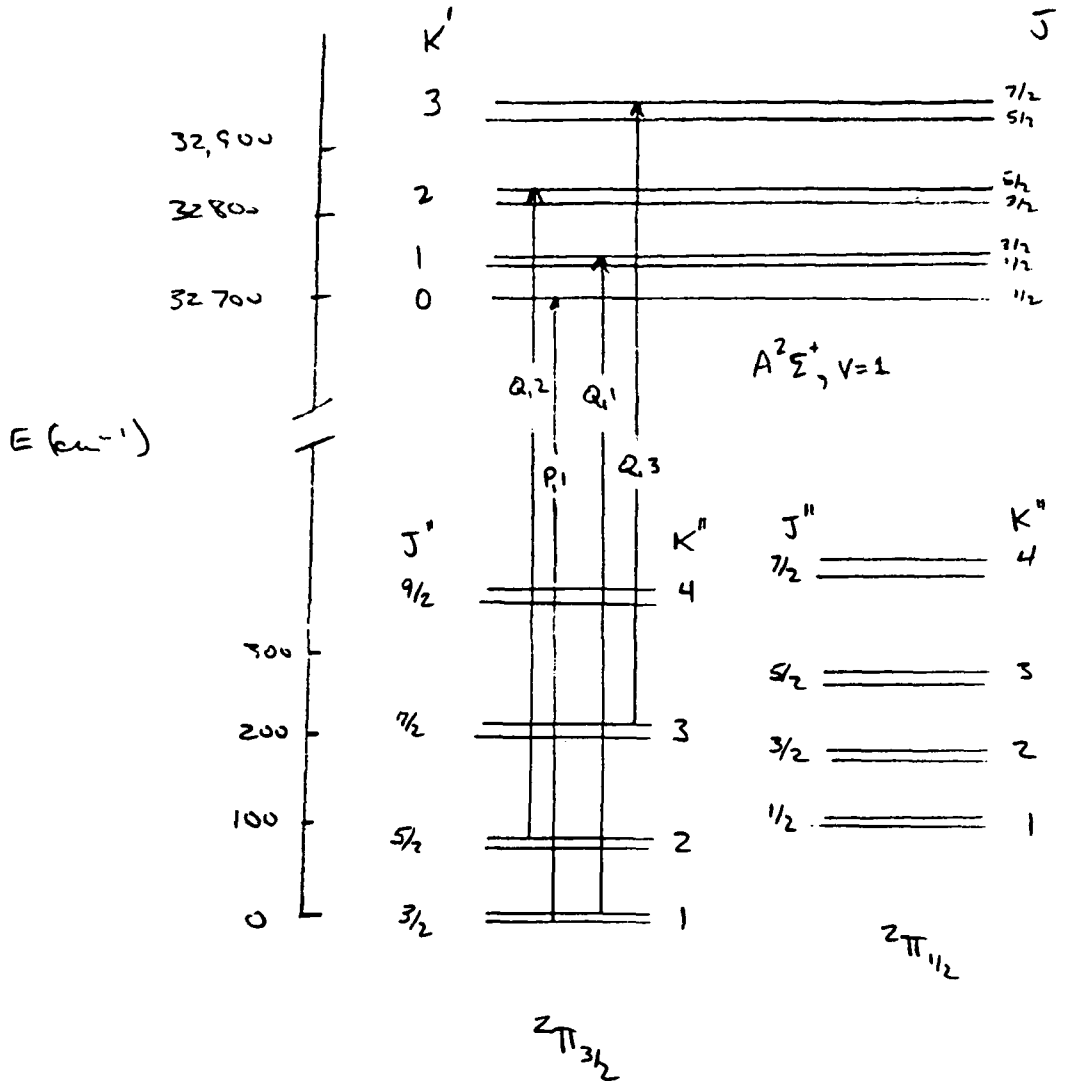

Figure 2. Energy level diagram of OH. After [Coxon, 1980].

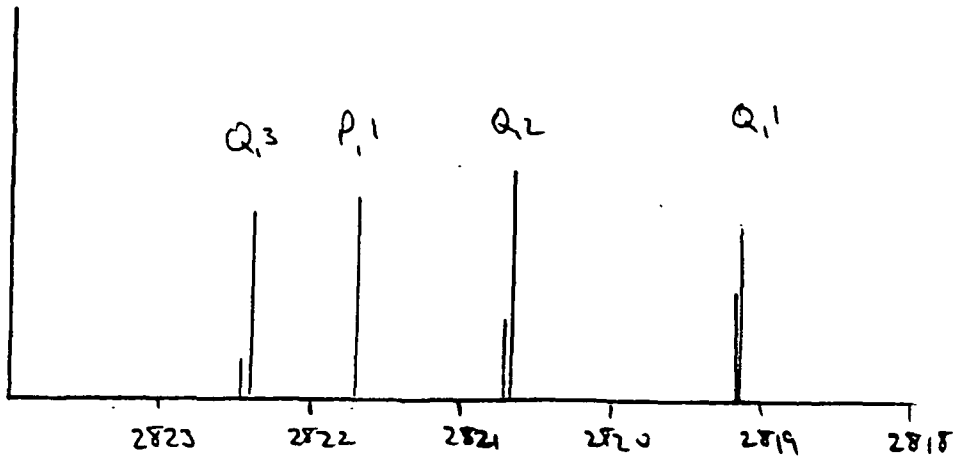

Figure 3. The OH absorption in the 2823-2818 Å region. Line heights are proportional to intensity. [Chidsey and Crosley, 1980].

where the bimolecular rate constants, k^{VV} for v-v transfer and $k^{Q,v=1}$ and $k^{Q,v=0}$ for collisional quenching of the v = 1 and v = 0 levels, respectively, are weighted averages, of experimentally measured values, for the natural abundances of N_2 and O_2 in air. [M] is the density of air (molec/cm^3). The values adopted for the bimolecular rate constants are given in Table 1, based on the cumulative results of four different determinations which when taken together provide the complete set of measurements required. $k_{Rad}^{v=1}$ and $k_{Rad}^{v=0}$ are total radiative decay rates of the v = 1 and v = 0 vibrational levels without reference to the bands structure. $k_{Rad}^{0,0}$ is the radiative decay rate in the (0,0) band. The values used for the radative rates are necessarily experimentally determined values that represent averages over thermal rotational distributions. The value adopted for the radiative rates are:

$$k_{Rad}^{v=1} \approx k_{Rad}^{1,0} + k_{Rad}^{1,1} = 1.4 \times 10^6 \text{ sec}^{-1}$$

$$k_{Rad}^{v=0} \approx k_{Rad}^{0,0} = 1.4 \times 10^6 \text{ sec}^{-1}$$

[German, 1975; McDermid and Laudenslager, 1982].

The rate constant determinations used to compose Table 1 consist of two distinct but complementary types, depending on the overall pressure at which the measurements are made. The low pressure studies, in the mtorr range obtain quenching and radiation rates for an individual rotational level that is the upper level of the transition initially pumped. The bimolecular collision rate is too slow to thermalize the rotational distribution in the upper state in this case. The high pressure studies, in the 1 to 25 torr range, observe a broader, more complex fluorescence spectrum comprised of many lines since appreciable R - R

	K^{VV}	$K^{Q,v=1}$	$K^{Q,v=0}$
N_2	1.6 (-10)	3.0 (-11)	3.0 (-11)
O_2	1.4 (-11)	1.6 (-10)	1.0 (-10)

Table 1. Bimolecular collisional rate constants. Units are $cm^3 molec^{-1} sec^{-1}$. Based on results of [Selzer and Wang, 1979; German, 1976; Lengel and Crosley, 1978; and McDermid and Laudenslager, 1982].

transfer takes place in the upper state as radiative decay occurs. Thus, the high pressure studies produce rate constants averaged over the rotational distribution that forms following pumping into a single rotational level.

The pressure environment in the stratosphere is similar to the high pressure studies; thus it is appropriate to use the rate constants that average the effect of many different emitting levels. Consistent results are obtained if the low pressure results are weighted and summed to produce a thermally averaged rate constant. Note that, since the B value of OH is relatively large (~ 17 cm^{-1}), a fully thermalized distribution of rotational levels will only appreciably populate levels up to K = 7 (15% total population), with the maximum population almost equally divided between the K = 1 and 2 levels.

The magnitude of the bimolecular rate constants in Table 1 and, in particular, the extremely rapid v-v transfer rate for N_2 leads to a relatively simple altitude dependence for Q through most of the stratosphere. For example, Figure 3 shows the altitude dependence of the fraction of the total emitted fluorescence that occurs via the (0,0) band. The partitioning of the fluorescence into the three main bands does not change by more than 10% from the ground level up to ~ 40 km. Above this altitude, the v-v transfer rate begins to slow appreciably with altitude, and the fluorescence spectrum increasingly favors emission from the v = 1 level.

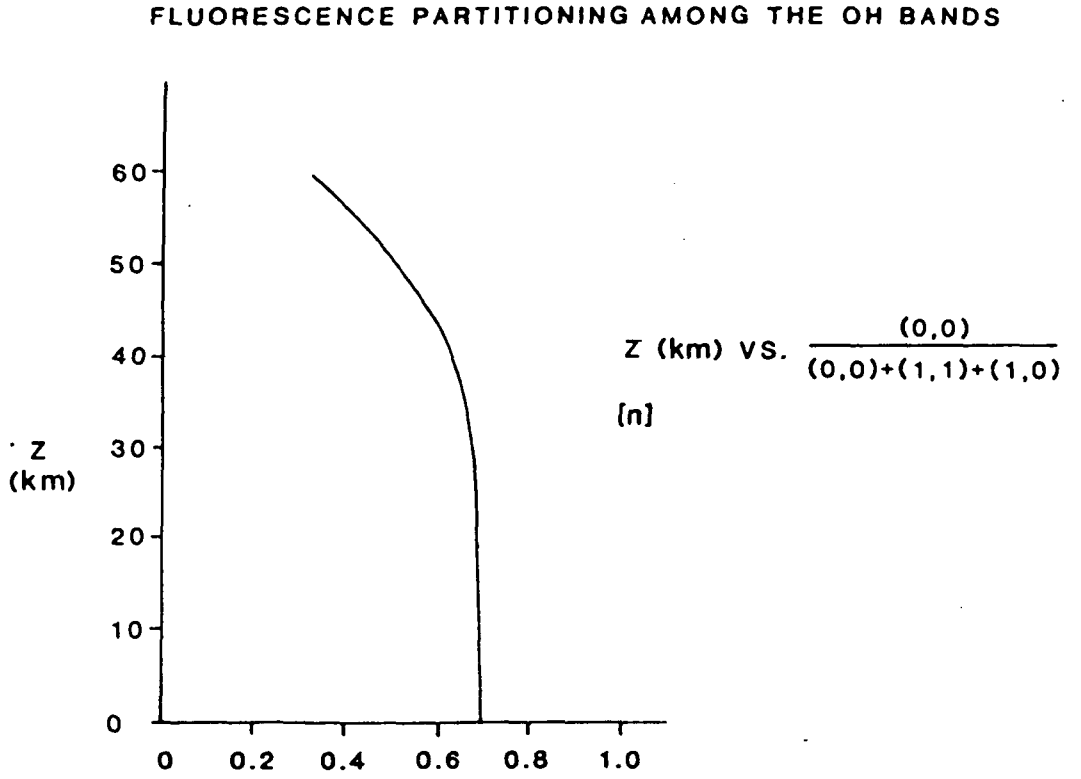
FLUORESCENCE PARTITIONING AMONG THE OH BANDS
Z (km) VS. (0,0) / (0,0)+(1,1)+(1,0)
[n]
Z (km)
60
50
40
30
20
10
0
0
0.2
0.4
0.6
0.8
1.0

Figure 3.

The value of Q is plotted against altitude in Figure 4. Again, since the collisional processes dominate the radiative rates, Q has a simple inverse [M] dependence through the tropopause and well into the stratosphere.

We have not attempted to apply a temperature correction to the rate constants since there have not been any temperature dependence measurements below room temperature, and the resulting uncertainty in a temperature correction cannot be reliably estimated.

The remaining terms in the signal equation, $V_e T$ and η, are discussed in the Experimental Section.

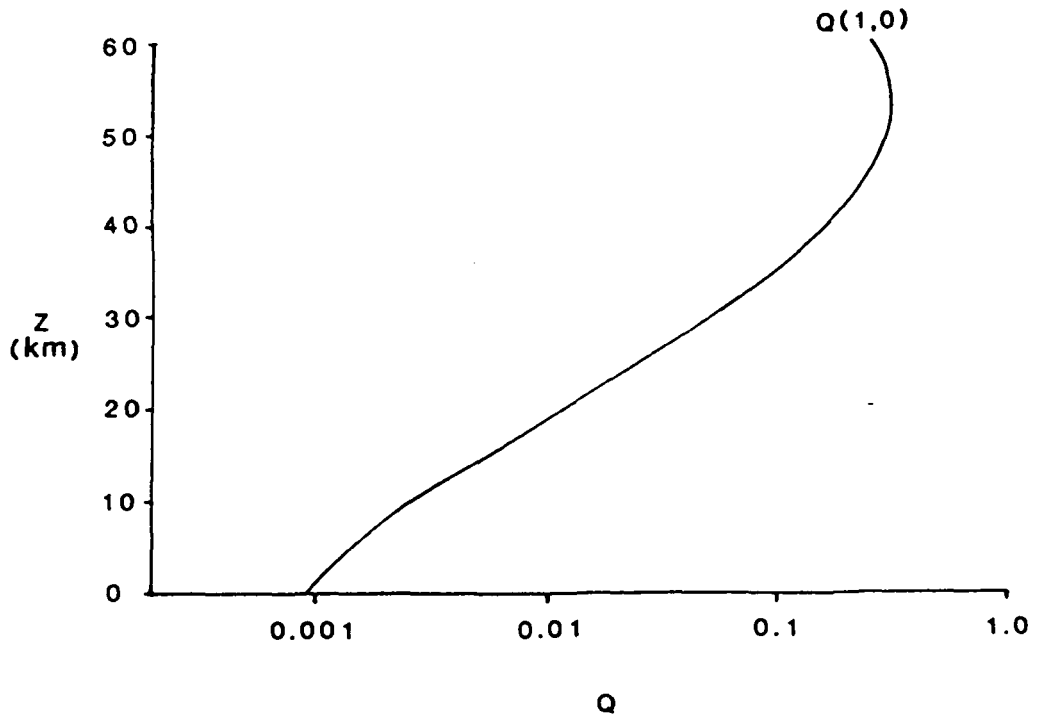

Figure 4.

Power Measurement

The calculation of the OH density from the observed count rate due to OH fluorescence, Eq. (7), requires a simultaneous measurement of E, the laser power delivered to the sample volume element. The E measurement is accomplished with a second photomultiplier tube detector that views the sample volume element, but is optically filtered to detect Rayleigh scattering at the laser wavelength. The signal equation for the 2820 detector is analogous to the 3090 detector signal equation, the difference being only in the nature of the scattering event observed,

$$S_{Ray}^{2820}\ (\text{cts/sec}) = F(\lambda)\sigma_{Ray}(\lambda)[M]V\epsilon T\eta \qquad (10)$$

The overlap integral need not be represented since the frequency dependence of the Rayleigh scattering cross section is extremely weak. The working expression for Eq. (10) is

$$S_{Ray}^{2820}\ (\text{cts/sec}) = C_{Ray}E[M] \qquad (11)$$

where C_{Ray} is easily determined during the laboratory calibration. Finally, E is recorded as

$$E = \frac{1}{C_{Ray}} \frac{S_{Ray}^{2820}}{[M]} \qquad (12)$$

Null Experiments

The observed count rates on the 3090 and 2820 detectors are in principle composed of a number of different contributions. The sought after signals must be differentiated from the remaining background signals by suitably designed null experiments.

The null experiment for the 3090 detector is carried out by tuning the laser wavelength on and off the OH absorption line at constant E and observing the difference in S^{3090},

$$S_{OH}^{3090} = S^{3090}(\text{on resonance}) - S^{3090}(\text{off resonance})$$

This method for obtaining S_{OH}^{3090} implicitly assumes that all laser dependent non-OH sources of detector counts are wavelength independent over the small excursion in wavelength required to tune off an OH absorption line. In general, this assumption is well founded and by pumping at least two different OH lines our confidence that there is no other molecule that mimics OH is greatly increased.

This method cannot differentiate against an OH signal that might arise from OH that may be produced photochemically by the laser flux itself since this is a resonant signal. Although this possibility is unlikely in the stratosphere, care must be taken to demonstrate that this background is negligible.

A null experiment for the 2820 detector is required to differentiate gas phase Rayleigh scattering from other background sources such as laser scattering off chamber walls. In the laboratory this is accomplished by evaucating the sample chamber and measuring the chamber scatter directly. In flight the analysis is carried out by studying the pressure dependence of the 2820 count rate.

B. Experimental

A block diagram of the optical system is shown in Figure 6. The lasers and other optical accessories necessary for remote operation are mounted on an optical bench supported by a three point kinematic mount within the walls of the flight gondola. The scattering chamber through which the atmosphere sample flows is rigidly attached to the optical bench through three support arms which also serve to place the flow axis of the sample chamber 36" from the outside wall of the gondola. The distinguishing features of the subsystems involved are discussed here.

Cu Vapor Metal Atom Laser

The key characteristics of the Cu vapor laser are the capability of operation at high repetition rate, and generation of high average power with excellent conversion efficiency [Nerheim et al., 1978; Smilanski et al., 1978; Chen et al., 1978]. Our laser is operated at a pulse rate of 17 kHz. The choice of the Cu laser is based upon the design goal of minimizing the peak power while simultaneously allowing for high average power. High average power is advantageous since the fluorescence signal is directly proportional to the average power. On the other hand, peak power or more appropriately peak flux, in the sample volume element, should be minimized in order to avoid absorption saturation phenomena which, in turn, can lead to nonlinear fluorescence strength, an avoidable complication.

The laser, diagrammed in Figure 7, consists of an insulated 1 in i.d. quartz tube, vacuum sealed at each end with Brewster angle windows

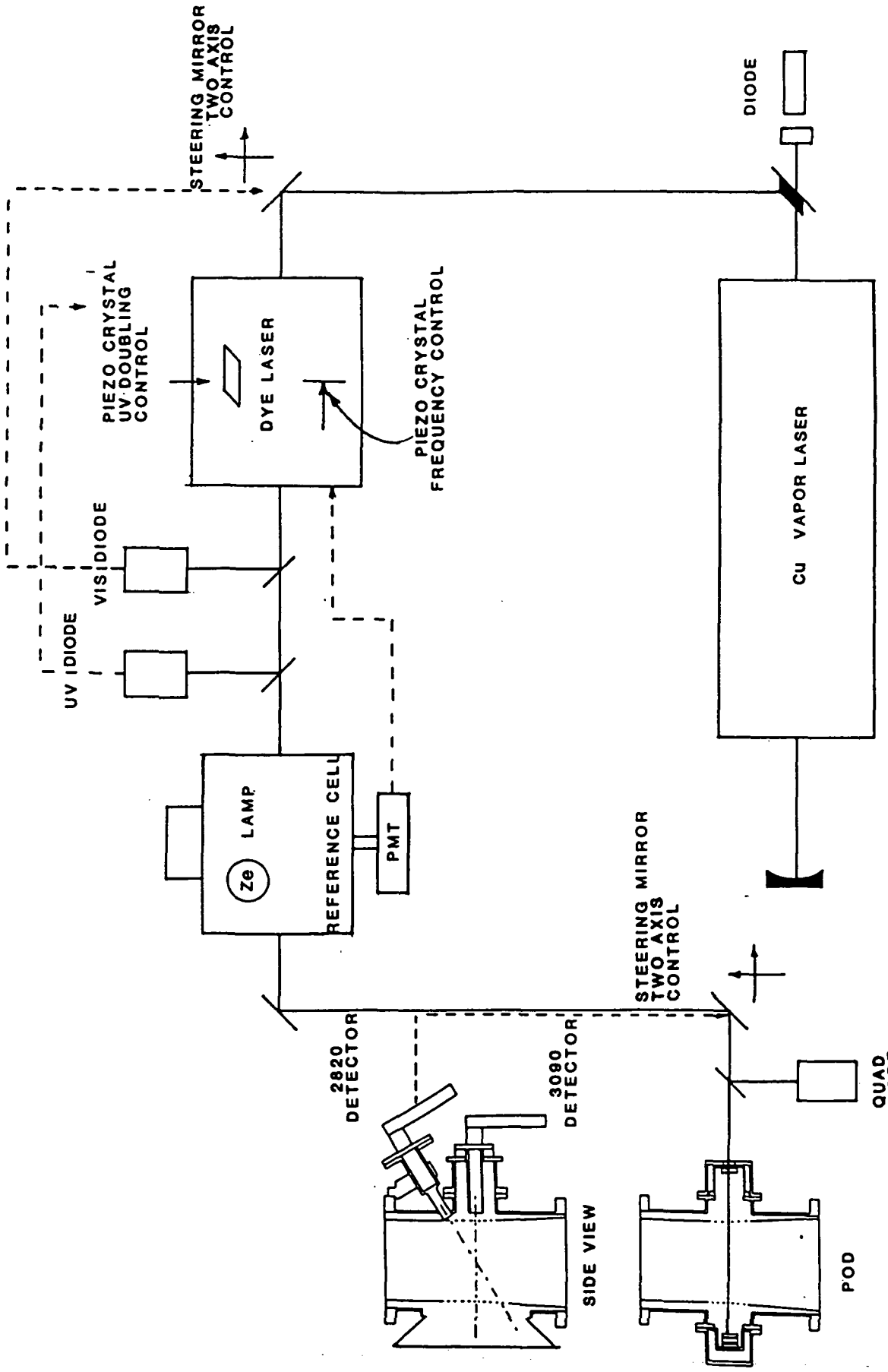

Figure 6. Block diagram of the optical system.

mounted to two hollow, cylindrical copper electrodes. A 10 kV, coaxial discharge takes place between the electrodes at the 17 kHz pulse rate. The pulse width is about 20 nsec, with a 10^6 V/μsec rise time on the cathode. The buffer gas is flowing Ne held at about 12 torr. The source of Cu atoms is a temperature controlled furnace containing CuCℓ powder, m.p. ≈ 450 C, through which flows ~ 20% of the carrier gas. Since extremely high optical gain in the plasma leads to super radiant conditions, the external cavity mirrors utilize an unstable resonator design in order to extract a well collimated (< 0.2 mrad divergence) 0.5 cm diameter beam [Siegman, 1965].

Laser emission occurs mainly at λ = 5160 Å, as shown in Figure 8, with approximately 30% of the output at λ = 5780 Å. Typical wall plug efficiency is 0.4%, that is 5 - 6 Watts average output power and 1300 Watts input to the high voltage power supply. The output power is monitored by a photodiode located behind the convex mirror at the output end of the optical cavity. The laser tube and power supply share a common pressure containment vessel cooled by forced circulation of an ethylene glycol-water mixture through closed loops provided.

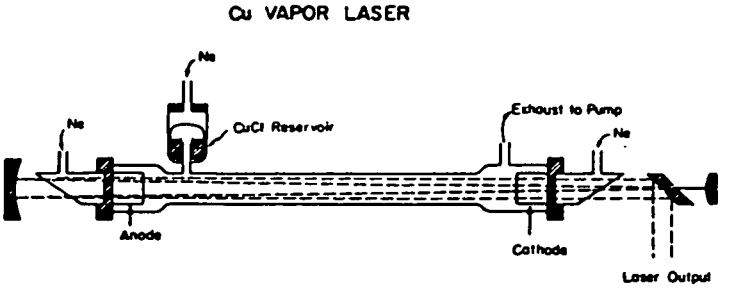

Figure 7. Diagram detailing the basic physical assembly of the Cu vapor laser.

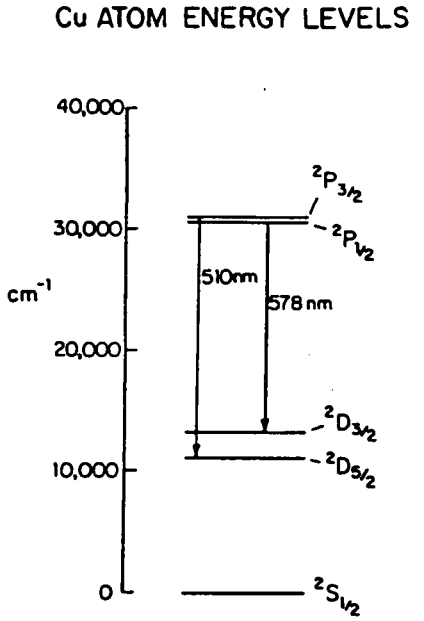

Figure 8. Identity of the Cu atom transitions through which laser emission takes place.

Dye Laser

Since the peak power of the Cu vapor laser is relatively low, about 15 kw, the dye laser must employ a low-loss design with a correspondingly low threshold power required for turn-on. These requirements are met with the axially pumped dye laser diagrammed in Figure 9, which consists of the core optical components from a Chromatix model 1052 dye laser [Wallace, 1971]. The pump beam, which is focussed onto the flowing dye cell, enters the dye laser through a dichroic input mirror. Rhodamine 6G dissolved in ethyl alcohol is used as the dye. The fundamental at 5640 Å is frequency narrowed by three Brewster angle prisms placed in the optical cavity. The fundamental is frequency tuned by rotating the back mirror about an axis normal to the plane of oscillation with a piezo-electric crystal. UV laser emission is obtained by intracavity doubling with a Brewster cut KDP crystal, phase-matched by angle tuning, which is also controlled with a pizeo-electric crystal. The crystal actuators are powered by microprocessor controlled high voltage power supplies contained within the pressure-temprature enclosure housing the dye laser. Typical output power at $\lambda \sim 2820$ Å is 15 mW with a 5 W input beam, giving the net power conversion efficiency of approximately 0.3%. The full scale frequency tuning range fixed by the effective throw of the piezo crystal is 3.2 Å.

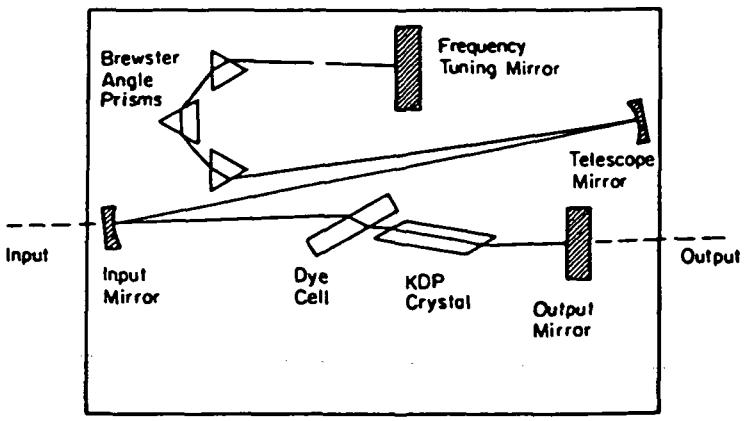

Figure 9. Optical diagram of the dye laser.

Dye laser performance is monitored by two photodiodes located adjacent to the dye laser housing using thin quartz beam splitters to sample the output. The first photodiode monitors the fundamental output at 5640 Å and serves as the feedback element for optimization of dye laser circulating power by steering the Cu vapor laser pump beam into the dye laser at the optimal angle. The steering mirror is one of two microprocessor controlled, cam-actuated mirror drives, operable in the horizontal and vertical axes. The second photodiode monitors the second harmonic output at 2820 Å and serves as the feedback element for optimization of the UV power by angle tuning the doubling crystal. The feedback element used for tuning the frequency of the dye laser is the OH reference cell which is described next.

OH Reference Cell

The OH reference cell is a self-contained, scattering chamber containing an estimated 10^9 OH molec cm^{-3} that functions as a frequency reference for fine tuning the dye laser wavelength for maximum overlap with a specific OH absorption line. The laser beam passes through the cell along an axis of symmetry. Fluorescence from OH is observed with a PMT oriented perpendicular to the laser beam and equippped with a 3085 Å FWHM interference filter, for observation of the (0,0) band. The steady state OH density is formed by photolysis of water vapor by an RF powered, RF powered, sealed Xe lamp whose spectrum consists of a band centered at 1650 Å and FWHM width of 200 Å. The static gas mixture within the cell is predominantly Ar at 600 torr pressure. The water vapor is supplied from a molecular sieve source, which may be heated, if necessary, to maintain the partial pressure of water at about 0.5 torr.

Under typical conditions the count rate from the cell is 5000 cts sec^{-1} when the laser is tuned to an OH line and 100 cts sec^{-1} off line. The identity of the absorption lines can be made by tuning the dye laser frequency across its full range and comparing the resulting fluorescence spectrum with the known OH absorption spectrum, as shown in Figure 10. Since the laser power does not remain constant as frequency is turned, unless the doubling crystal is tuned simultaneously (which, in general, it is not), the relative intensities of the lines should not be used to identify a line. The absorption line identification was frequently verified on the ground by measuring the laser wavelength with .5 meter spectrometer.

Following the OH cell the laser beam is redirected by a stationary mirror onto the second microprocessor controlled two-axis steering mirror that directs the beam outboard of the gondola towards the sample chamber.

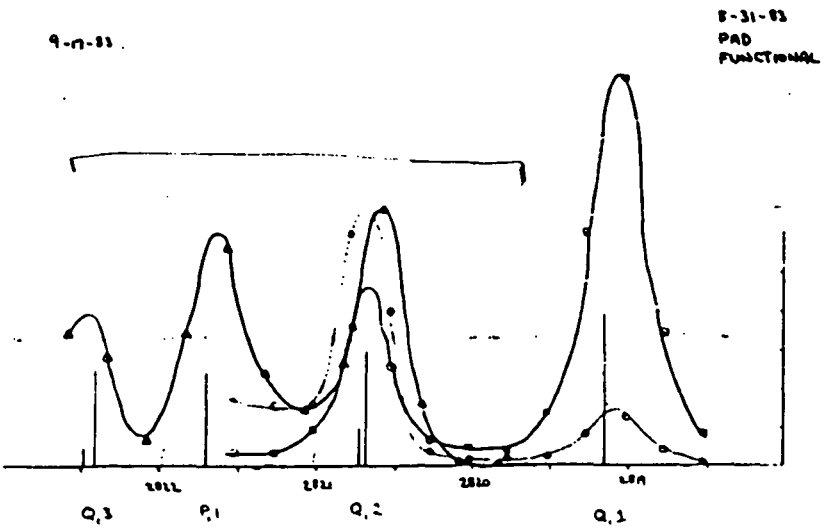

Figure 10. Composite course spectrum of three separate wavelength scans with fixed KDP crystal angles. The tuning range of the dye laser is indicated.

Enclosed-Flow Sample Chamber

Optical System

The optical components making up the sample pod are the entrance aperture, the light trapping mirrors, the 2820 and 3090 detector heads, and various baffle structures.

The entrance aperture assembly is fit with a beam splitter that directs a fraction of the laser beam onto a photodiode which is divided into four quadrants. The quad cell provides a target with medium resolution X - Y spatial information yielding a measure of the alignment of the laser beam with respect to the light trapping cell. A lens is also present that focuses the beam into the light trapping cell with an f number which matches the light trapping cell.

The light trapping cell consists of two, 2 in diameter spherical mirrors of 5 in radius of curvature mounted in a near concentric spacing arrangement, approximately 10 in apart [Herriot et al., 1964; Perry et al., 1980]. The laser beam enters the optical cavity through a .125 in diameter hole drilled through one of the mirrors about 0.6 in radially from the mirror axis. The mirrors are mounted on spring steel rings, independently adjustable in two axes.

The beam trajectory in the light trapping cell normally is such that the pattern formed by returning beams on each mirror is a circle composed of 22 individual reflections. The total number of passes, 44, is fixed by the mirror separation. The internal pattern described by the multipassed beam is an hourglass shape, the diameter of the beam package being about 0.25 in at the flow tube axis and 1.2 in at the mirrors. It is possible to achieve an alignment whereby after one complete circuit of 44 passes, the beam nearly misses the exit (entrance)

aperture and completes additional circuits at diminished intensity due to some of the beam being lost through the exit aperture. Since this alignment condition leads to increased power in the sample volume, it was regularly used.

Two bi-alkali photomultiplier tubes view the scattering volume, each equipped to view a different wavelength band, as illustrated in Figure 6. The 3090 detector, used to observe OH fluorescence is oriented mutually perpendicular to the flow tube axis and the optical axis of the light trapping cells. The photocathode surface is located about 5 in from the flow tube axis. The 3090 detector is fitted with an optical assembly tube that houses the optical components which define the light collection properties and bandwidth of the detector. The optical components include a quartz 1 in diameter f/1 lens which images the sample volume onto the photocathode, an interference filter 50 Å FWHM centered at 3080 Å which isolates the (0,0) band fluorescence, and a liquid pyridine/ethyl alchohol filter in a 1 mm path length sealed quartz cell. The liquid filter functions as a cut-off filter to eliminate detection of scattered laser photons. The collection efficiency is estimated by ray tracing calculations to be $\varepsilon^{3090} \sim .002$ or an equivalent f number of 5.6. The net transmission of the system is $T^{3090} \approx .14$ at 3080 Å.

The 2820 detector is used for observing Rayleigh scattering at the laser wavelength. The axis of the 2820 detector is in the plane containing the flow tube axis and axis of the 3090 detector. The 2820 detector views the center of the scattering volume inclined at a 30° angle with respect to the flow tube axis, inclined such that the viewing direction is towards the throat of the pod. The photocathode is located about 7 in from the scattering center.

The band width is established by two back-to-back 30 Å FWHM interference filters centered at 2832 Å. Imaging optics are not used. The net transmission of the system is $T^{2820} = 0.009$. The collection efficiency is estimated to be $\varepsilon^{2820} = 7 \times 10^{-5}$ or an equivalent f number of 30. The spectral relationship of the detectors, the laser, and the OH molecule is summarized in Figure 11.

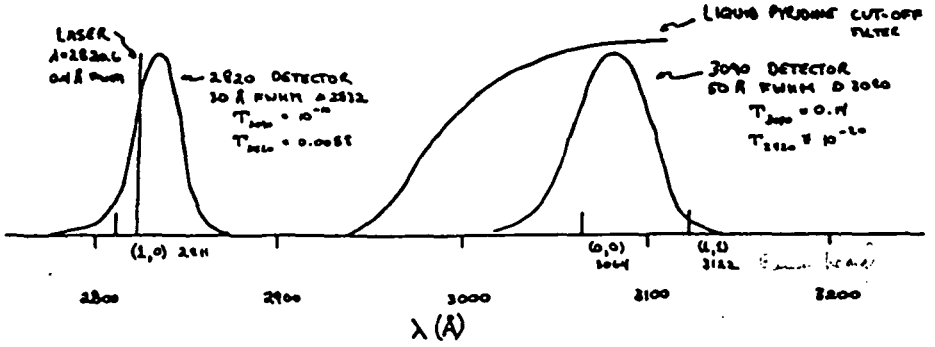

Figure 11. Detector band passes and spectral relationship to OH emission band.

The wall opposite the detector heads is recessed 5 inches from the surrounding flow tube wall, forming a dark inner chamber that is the backdrop for both detectors. The walls of the interior baffle fall away from the flow tube walls at an acute angle so light entering from either direction along the axis is trapped in the corners of the baffle. The surface inside the baffle are upholstered with black velvet which was found to give the darkest surface. All other surfaces in the sample chamber are coated with a flat black paint.

Pod-Sample System

The geometry of the sample pod establishes the fluid dynamic character of the flow as well as shields the detectors from the ambient solar radiation environment. The main components of the sample pod are identified in Figure 12.

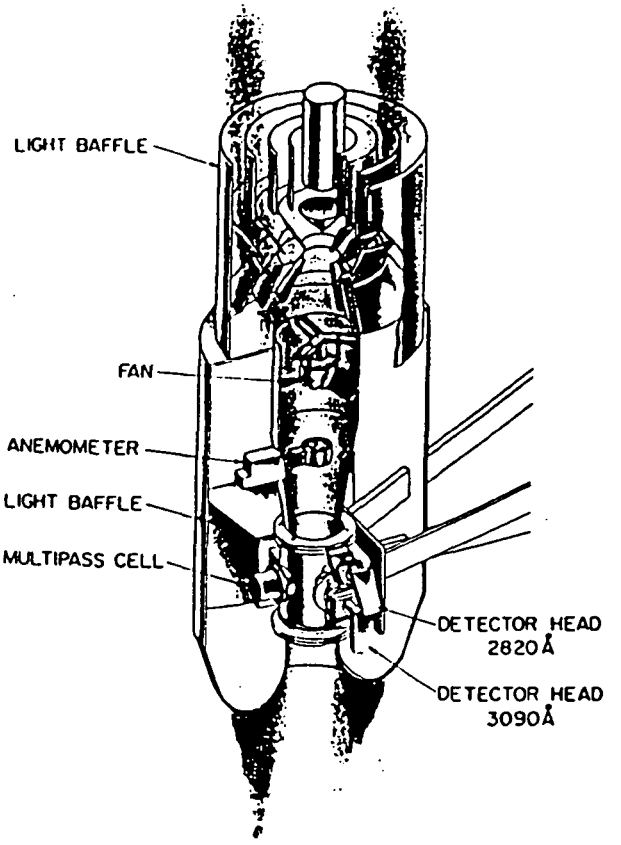

Figure 12. Cut-away illustration of the sample pod.

A fan is axially mounted near the top of the cylindrical structure which forms the inside walls of the flow tube. The fan ensures that an adequate flow velocity can be established independent of the drop velocity of the gondola. The fan control interface allows for several preselected rotation speeds.

The anemometer provides independent verification that a gas flow is established in the sample tube. The shape of the flow tube, i.e., the inside diameter, is designed to ensure laminar flow through the

instrument. The nose cone incorporates a gentle curve aiding the passage of nonturbulent flow into the tube. The inside diameter decreases steadily to a 5 inch minimum at the optical plane. The slowly decreasing diameter tends to accelerate the flow and suppresses boundary layer growth. Over the next five inches the i.d. is fixed; then it begins to open steady to a 12 inch diameter to accept the fan. The flow tube wall is smooth throughout the structure. Above the fan the structure immediately opens up into a large cylindrical light baffle which prevents direct solar illumination from penetrating into the sample pod. The openness of the baffle provides a high conductance path for the exiting flow.

The temperature of the air in the flow tube is monitored by five, 0.010 inch diameter thermistors located in a plane four inches above the optical plane. The thermistors are supported from two black threads spanning the flow tube at right angles to one another, as shown in Figure 13. The air temperature of the flow is a very sensitive test for the perturbation of the atmospheric sample by the presence of the sample chamber.

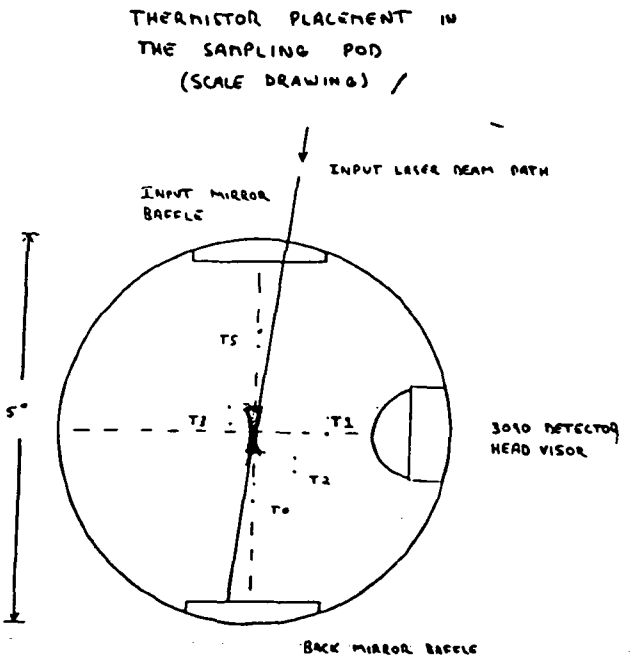

Figure 13. The location of five thermistors that sample the sample air temperature.

In general, the inside wall of the flow tube is never in equilibrium with the ambient air temperature, thus the incursion of boundary layer air into the core of the flow is readily observable by marked temperature excursions. The ambient air temperature is monitored by two thermistors suspended below the gondola from two opposite walls.

Calibration Facility

The calibration facility provides a method to form a known OH number density in the sample chamber in the laboratory under conditions that approach the stratospheric environment and which maintains the optical system in a state unaltered from the flight configuration. An overview of the calibration facility is shown in Figure 14.

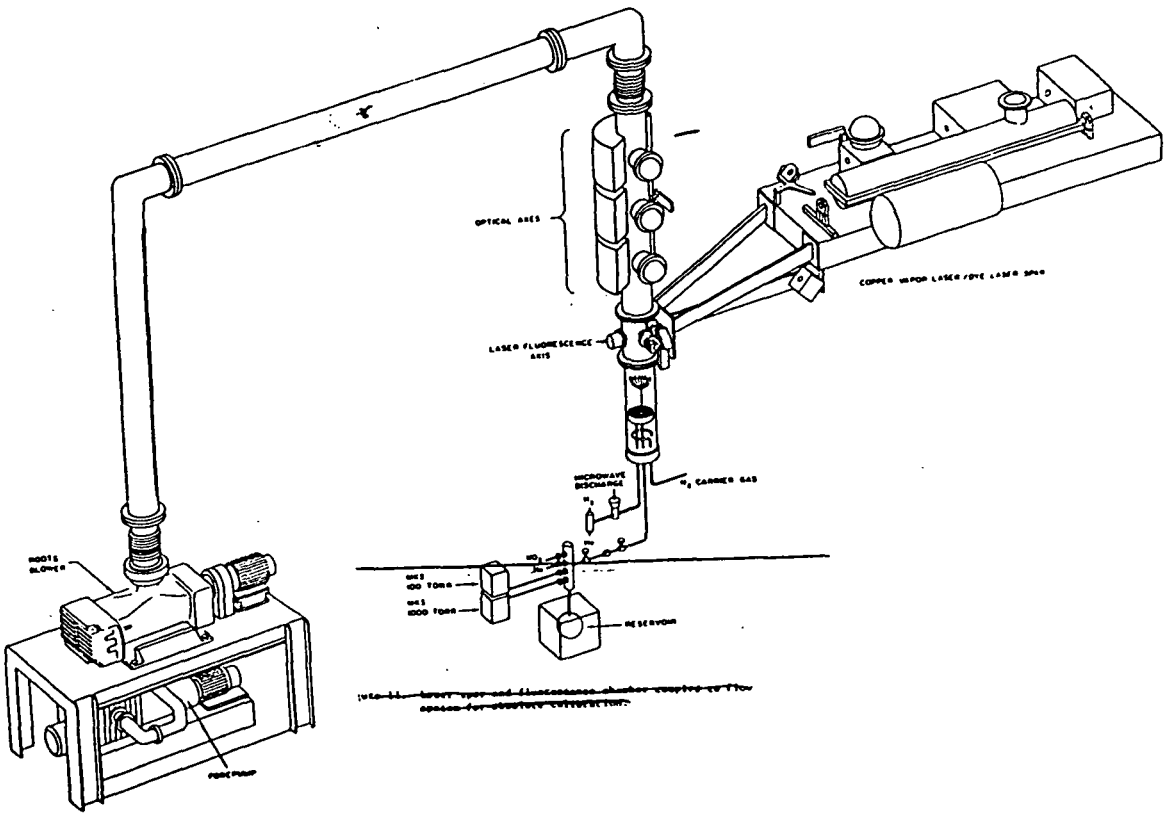

Figure 14. Laser spar and smaple chamber coupled to the flow system for absolute calibration.

A Roots blower-forepump combination, Lebold Hereaus MA-2002, is used to establish a low pressure(1 to 20 torr) high velocity (5 - 20 m sec^{-1}) flow through a 6 in i.d. stainless steel pipe. The center section of the sample pod, which houses the optical components discussed, fits into the flow tube as indicated. The laser spar resides in the flight gondola (not shown) as it is configured for flight. To accommodate the height

requirement at the pod, the gondola is raised and supported on a wood pedestal. Vibrations from the pump are damped to an imperceptible level at the pod by bellows and a steel box filled with 500 lbs of glass shot that encases a 6 ft horizontal section of the flow tube. The horizontal crossover section is supported by independent means such that there is no loading on the sample pod and optical spar.

All gas additions to the sample flow are made through the head of the 4 ft section of pyrex tube below the sample pod. The carrier gas, N_2, is added through a loop injector just inside the backing plate at about 3 SCFM (760 torr, 25°C), as measured with a 0 - 5 SCFM Matheson flow meter.

A known density of OH is formed using standard gas phase kinetics techniques based upon the reaction,

$$H + NO_2 \rightarrow OH + NO \qquad k = 1.2 \times 10^{-10}\ cm^3 molec^{-1} sec^{-1}$$

(see, for example, [Setser, 1979]). A carefully measured flow of NO_2 is reacted to completion in excess H. Hydrogen atoms are produced by combining a flow of liquid N_2 trapped He with a trace amount of H_2 and passing the mixture through a 20 watt, 2547 MHz discharge; the resulting flow is admitted to the flow tube immediately downstream of the carrier gas injection loop. NO_2 flows are determined by measuring the rate of pressure change in a reservoir of known volume containing a few tenths of a percent mixture of NO_2 in He. NO_2 flows are added through a moveable injector equipped with a teflon coated shower-head like injector to facilitate rapid mixing into the flow. Pressures in the reservoir and the flow tube are measured with MKS capacitance manometers calibrated against oil and mercury manometers.

In the present configuration, the NO_2 addition technique is used to form calibrated OH densities in the 10^9 to 10^{12} molecules cm^{-3} range. In order to extend the calibration range to 10^7 in a convenient and accurate manner, the first auxilliary optical axis above the laser fluorescence axis is used with a RF powered, OH resonance lamp-induced fluorescence system similar to the type used on previous stratospheric flights by this research group. This system has proven linearity over 10^7 to 10^{12} density range. The lower end of this range overlaps the upper end of the laser fluorescence system operating at full power. The remaining optical axes were not used in this work, but they may be used, for example, in a H_2O - O_3 sensitivity study by measuring H_2O by photofragment fluorescence and O_3 by molecular absorption.

Calibration

The flight system was calibrated at the balloon launching facility following final assembly in preparation for the flight. Time constraints prevented acquisition of a large data base; however, sufficient number of experiments were performed to verify the correct operation of the calibration facility and to characterize the sensitivity of the flight instrument.

The calibration data is summarized in Table 2. These measurements were made at a pressure of 3.8 torr of N_2. The power in the UV laser beam was 10 mW. The $Q_1 2$ absorption line was used to pump OH. The average value of the ratio of S_{OH}^{3090} to [OH] is

$$\frac{S_{OH}^{3090}}{[OH]} = C_{OH}^{3090}{}_{EQ} = 1.2 \pm 0.2 \times 10^{-4} \frac{\text{cts sec}^{-1}}{\text{molec cm}^{-3}} \tag{13}$$

At 3.8 torr total pressure, the 3090 count rate was observed to be linear at least through 23,000 counts sec^{-1} by varying OH density.

The average value of S_{Ray}^{2820} is 580 cts sec^{-1}. The ratio of S^{2820} to the gas chamber density represents the power measurement

$$\frac{S_{Ray}^{2820}}{[M]} = \frac{580}{3.8 \times 3.26 \times 10^{16}} = 4.7 \times 10^{-15} \frac{\text{cts sec}^{-1}}{\text{molec cm}^{-3}} \tag{14}$$

or approximately 150 $\frac{\text{cts sec}^{-1}}{\text{torr}}$.

The value of Q at 3.8 torr of N_2 is given by Eq. (6) and found to be 0.22. Thus we may write the working expression:

$$S_{OH}^{3090} = C_{OH}^{3090}{}_{EQ}[OH] \tag{15}$$

with the measured value of C_{OH} normalized to the power and quenching environment:

Resonance S_{OH}^{3090} Lamp	[OH]	S_{OH}^{3090}	S_{Ray}^{2820}	$S_{OH}^{3090}/[OH]$
34	6.8×10^{7}	7000	570	1.03×10^{-4}
84	1.6×10^{8}	18400	590	1.15×10^{-4}
30	6×10^{7}	8500	570	1.4×10^{-4}

Table 2. Calibration for the copper vapor laser system. These measurements were made at a pressure of 3.8 torr of N_2.

$$S_{OH}^{3090} = 1.2 \times 10^{-4} \left(\frac{Q}{0.22}\right) \frac{S_{Ray}^{2820}/[M]}{4.7 \times 10^{-15}} [OH] \tag{16}$$

Upon solving for [OH] we derive an exceedingly simple expression for the OH density,

$$[OH] = S_{OH}^{3090} \frac{[M]}{S_{Ray}^{2820}} \frac{1}{Q} 8.6 \times 10^{-12} \frac{\text{molec}}{\text{cm}^3} \tag{17}$$

Thus in addition to the appropriate signal count rates from the 3090 and 2820 detectors, a density measurement and knowledge of the OH line being pumped are all that is required to derive the OH density.

The error introduced by the need to calculate a value of Q is less than implied by Eq. (17) since Eq. (6) is used to scale Q from the laboratory pressure environment to the encountered stratospheric environment. The effect of inclusion of 20% O_2 in the required value of Q is minimal. Future laboratory calibrations will incorporate N_2/O_2 carrier gas flow in the correct atmospheric ratio and cooled to stratospheric temperatures.

The method of measuring power with the 2820 detector requires that both detectors have an identical functional dependence on power for any light trapping pattern that may form. This requirement was examined experimentally by observing S_{Ray}^{2820} and S_{OH}^{3090} in the presence of OH while walking the laser beam across the input aperture to the sample pod with

the steering mirror. The ratio of S_{OH}^{2820} to S_{OH}^{3090} was found to be constant for all mirror positions where laser light was admitted to the scattering volume. This is the expected result since both detectors are aligned precisely on the intersection of the flow tube axis and the light trapping optical axis and the waist of the resulting light trapping pattern underfills the acceptance angle of both detectors. The detector bodies are fixed to the pod housing by relatively massive mechanical assemblies, precluding the possibility of accidental collisions leading to detector misalignment.

Checks of possible saturation of the OH absorption profile were performed at input laser powers up to 20 mW and 1.7 torr total pressure in the flow tube. Nonlinearity in S_{OH}^{3090} was not observed.

Counter saturation is a function of both pressure and count rate. Under the worst scenario, the high pressure limit counter saturation would not become important below S^{3090} equal to ~70% the pulse rate. During the flight peak count rate of both pod detectors never exceeded 600 cts sec^{-1}, well below this limit.

It is a valuable exercise to compare the calibrated sensitivities of the 2820 and 3090 detectors with a calculation of the same quantities based on independent measurements or best estimates for the parameters involved.

The 2820 detector sensitivity is given by

$$\frac{S^{2820}}{[M]} = F\sigma_{Ray}\varepsilon T\eta\ V \qquad (18)$$

Since $F = \frac{E}{A}$, where E is the average power and A is the beam area, and $V = A \times \ell \times \#passes$, where ℓ is the length of a beam that is viewed by the detector, and # is the number of passes in the light trapping cell,

we may write,

$$\frac{S^{2820}}{[M]} = E\sigma_{Ray}\varepsilon T\eta\ell \ \#passes \tag{19}$$

Using E = 8 mW, taking into account reflection losses on the light trapping mirrors, value of ε and ℓ estimated by ray tracing techniques, known values of T and η, and #passes = 66, appropriate when the light trapping cell exhibits multicircuiting behavior, we obtain:

$$\frac{S^{2820}}{[M]} = 8\ mW\ 1.4 \times 10^{15}\ \frac{photons}{mW}\ 4 \times 10^{-27}\ \frac{cm^2}{molec \cdot Sr}\ 8.2 \times 10^{-4}\ Sr$$

$$\times\ .009 \times .2 \times 1.5\ cm \times 66$$

$$= 6.5 \times 10^{-15}\ cts\ sec^{-1}/molec\ cm^{-3} \tag{20}$$

The measured value is 4.7×10^{-15}.

The sensitivity of the 3090 detector is given by

$$C_{OH} = F\sigma d\lambda\ \varepsilon T\eta V$$

$$= E\ \frac{\Delta\nu_{OH}}{\Delta\nu_{laser}}\ \sigma\ \varepsilon T\eta\ell\ \#passes \tag{21}$$

Using ray tracing estimates for the optical quantities and known values of T and η, we obtain:

$$C_{OH} = 8\ mW\ 1.4 \times 10^{15}\ \frac{photon}{mW} \times \frac{1}{40}\ 1.4 \times 10^{-16}\ \frac{cm^2}{molec}$$

$$\times\ .002 \times .14 \times .2 \times 1.5\ cm \times 66$$

$$C_{OH} = 2.1 \times 10^{-4}\ cts\ sec^{-1}/Q \tag{22}$$

This compares with the calibrated value of 5.4×10^{-4}. The estimated values for both detectors are in reasonable agreement with the calibrated values indicating that the optical system is well understood.

evidence pertaining to the question of perturbation of the sample by the experimental platform.

Pod thermistor data for two different twenty-minute segments of the flight are shown in Figures 15 and 16. The first example shows data around the period when the pod fan was first commanded on. At this point, the platform is suspended at 35 km and has been at float for twenty minutes. Prior to the fan turn-on, the thermistors are measuring the temperature of more or less stationary air within the pod, showing highly correlated fluctuations about a mean.

The effect of turning on the fan is readily apparent. The temperature immediately drops for all thermistors, from 260 to 240 C. The temperature does not remain low since at float the pod is drawing in air which obviously is influenced by the presence of the gondola. For example, the ambient air thermistors, also shown, exhibit random fluctuations uncorrelated with any other thermistor.

This type of random behavior observed by both sets of thermistors is characteristic of the float period. It arises from the combination of gondola rotation in the presence of solar illumination, variable horizontal wind shears, and slow rising and sinking of the platform about the mean height. Therefore, it is likely that the observed fluctuations in the pod are due to nonuniformity in the temperature of the air entering the pod and not to a nonuniform velocity through the pod. The anemometer data support this conclusion.

The second example, Figure 16, shows the thermistor data during the drop period. The start of the drop is cleared demarked by the simultaneous decrease in all thermistor readings to nearly identical temperatures. The gondola is dropping through unperturbed stratospheric air.

Figure 16a shows the response of the three thermistors that sample the core of the flow, closest to the flow tube axes, T0, T2 and T3. They form a highly correlated set with essentially identical temperature readings. The ambient air thermistors which are also shown in Figure 16a show an identical lapse rate and the same mean fluctuations as the temperature in the flow pod four inches above the optical axis. The offset between the ambient and pod thermistors is believed to be a systematic error in one of the thermistor calibrations, and is not real. The change in the mean slope at 62500 seconds occurs at the time of parachute deployment where the drop velocity is instantly doubled. Note that the indicated temperature is continuous through the velocity change and all thermistor readings remain correlated.

Figure 16b shows the measurements of the remaining two thermistors, T5 and T1, which are located nearer to proturberances in the flow tube wall as well as nearer to the wall itself. Thermistor T5 tracks the T2 trace well, but shows several major short-term departures from the core flow temperature. Here we see dramatic evidence of boundary layer air intrusion into the flow stream. The occurrence may indicate a wind shear at the pod entrance causing boundary layer separation off that side of the flow tube, aided by the presence of the input mirror light baffle on the wall.

The remaining trace is that of T1, which is located over the 3090 detector baffle, the mechanical assembly that extends into the flow tube by the greatest amount. At this position, there are fewer but notable excursions form the mean. The average temperature remains locked at a markedly higher value, yet the mean fluctuations are correlated with the core thermistors. Evidently air that encounters the 3090 detector head

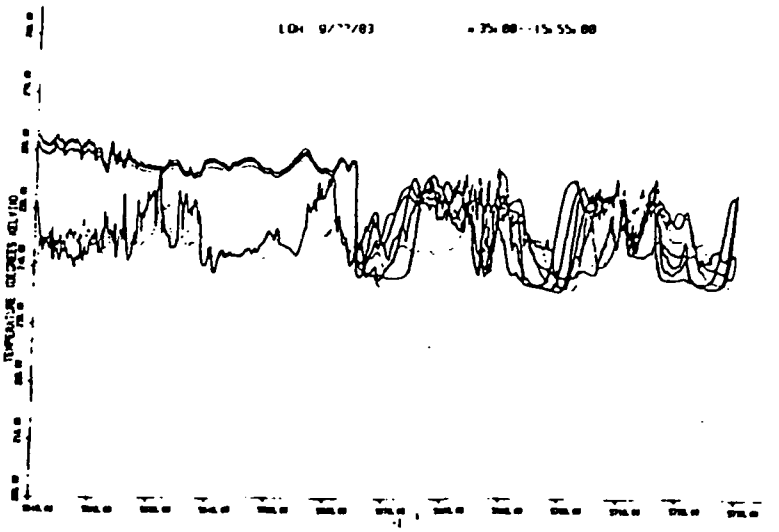

Figure 15.

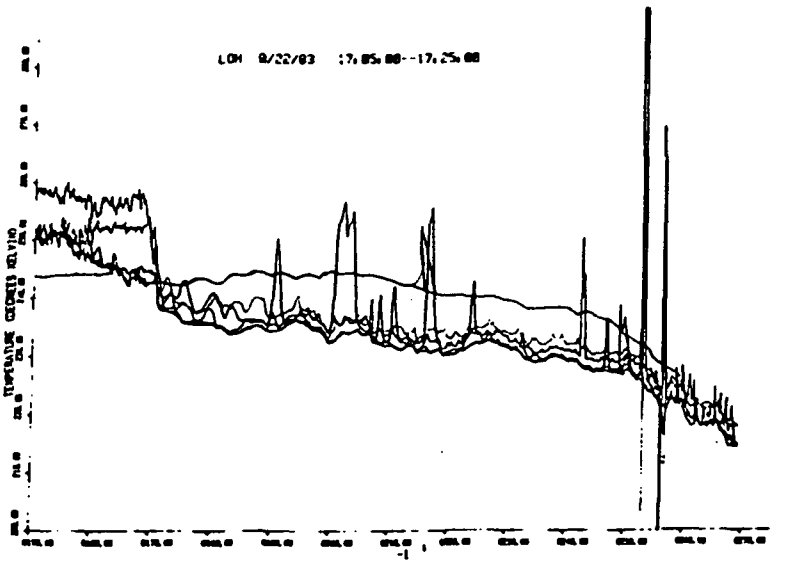

Figure 16a and b

is warmed significantly. The high correlation with the ambient air temperature indicates that at the low Reynolds numbers of this experiment the turbulence caused by the detector head is rapidly damped and we see a temperature trace indicative of reestablished laminar flow. In conclusion, we note that since the pod thermistor observations are made four inches above the detection zone, the inferred boundary layer intrusions at the optical axis must be significantly less than those observed. Since the core of the flow shows no intrusions at the thermistory plane, the detection zone must be sampling unperturbed stratospheric air during the drop.

Detector Count Rates — At Float

One of the experiments performed while the instrument was at float involved a check of the flow velocity dependence of the 3090 detector count rate. In this test the system was fully operational for the detection of OH fluorescence, with the laser tuned to the $Q_1 2$ absorption line. The sole commoands sent during the test were a pod fan off command followed by a fan on command two minutes later. Prior to the test, there was essentially no detectable OH in the air sample being drawn into the sample pod. The count rates of the 3090 and 2820 detectors is shown in Figure 17.

The response of the 3090 detector is striking, rising immediately with the termination of the flow velocity through the pod. The 3090 detector signal continues to increase with time through the period the fan remains off, and vanishes the instant the flow velocity is reestablished with a fan on command. The 2820 detector signal remains essentially constant through the test. Unfortunately, we did not tune the laser off resonance during the test, so we cannot unequivocally defend

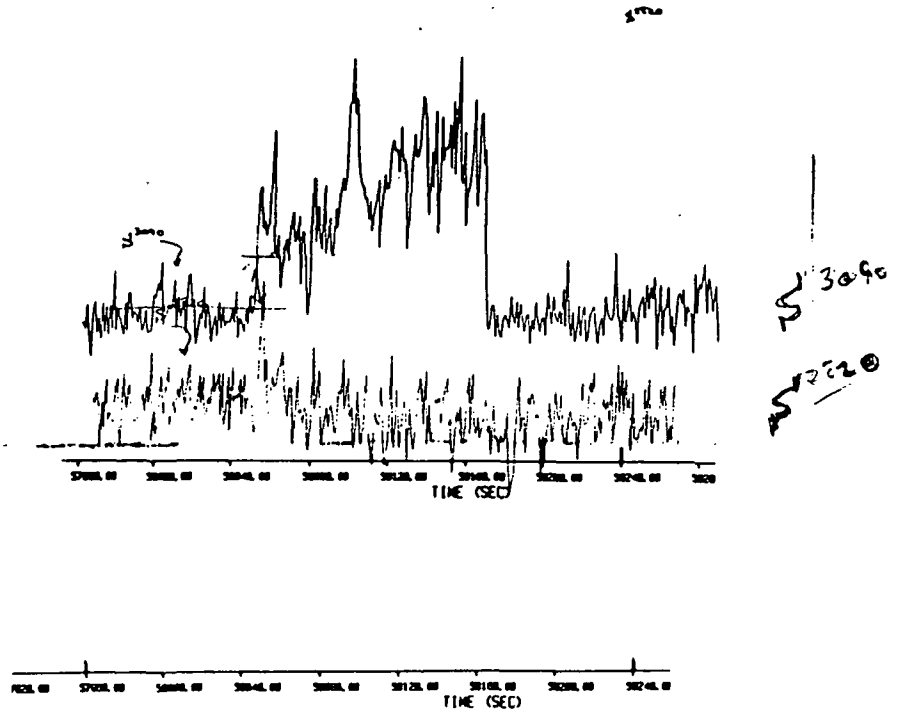

Figure 17.

the resonant character of the signal. On the other hand, there is no question that the laser was tuned to an OH line since the reference cell output averaged 4000 cts sec^{-1} through this period.

The most probable source of the observed signal is photochemical production of OH by the laser beam in the presence of ozone and water vapor. The mechanism involves the photolysis of ozone at 2820 Å to produce $O(^1D)$, which reacts with water vapor to form OH.

$$O_3 + h\nu \rightarrow O(^1D) + O_2$$

$$O(^1D) + H_2O \xrightarrow{k} 2OH$$

The steadily increasing signal is presumably due to increasing water vapor concentration controlled by instrument outgassing rate. At the same time, ozone is being lost at the walls but at an unknown efficiency. The velocity dependence arises simply as a consequence of its control of sample volume clearing times. The steady state concentration of laser produced OH rises to detectable levels when the loss out of the sample volume is diffusion controlled.

The steady state concentration of OH formed may be estimated for the conditions at float. The rate of OH formation in the laser beam is given by the product of the $O(^1D)$ production rate and the fraction which reacts with water vapor to produce OH,

$$\text{Source} = F\sigma\Phi[O_3] \times \frac{2k[H_2O]}{k[H_2O] + k^Q[M]} = 9 \times 10^8 \frac{\text{molec}}{\text{cm}^3\text{sec}}$$

where we have use the following values:

F, the laser flux for a beam of .025 cm radius =

$$\frac{6\ (mW)\ 1.4 \times 10^{15}\ (photons\ mW^{-1})}{\pi\ .025\ (cm)^2}$$

σ, the O_3 absorption cross section = 4×10^{-18} (cm^2)

Φ, the quantum yield for $O(^1D)$ production = 0.9

$[O_3] = 1 \times 10^{12}$ molec cm^{-3})

k, the $O(^1D) + H_2O$ reaction rate constant = 2.3×10^{-10} $cm^3 molec^{-1} sec^{-1}$

k^Q, the $O(^1D)$ quenching rate constant in air =

$(0.8 \times 3 \times 10^{-11}) + (0.2 \times 3.6 \times 10^{-10}) =$

9.6×10^{-11} $cm^3 molec^{-1} sec^{-1}$

$[M] = 1.7 \times 10^{17}$ molec cm^{-3}

$[H_2O] = 8.5 \times 10^{11}$ molec cm^{-3}

We are using an estimated value of 5 ppm for the ambient water vapor concentration in the stratosphere.

The diffusion controlled loss rate out of the sample volume is approximated by

$$\text{Loss} = \frac{2D}{x^2} = 4.8 \times 10^2\ sec^{-1}$$

where we have used

$D = 60\ cm^2 sec^{-1}$ for the diffusion of OH in N_2

x, the diameter of the beam pattern at the sample volume =

0.5 cm

The steady state OH concentration is given by

$$[OH] = \frac{9 \times 10^8}{4.8 \times 10^2} = 2.0 \times 10^6\ \text{molec}\ cm^{-3}$$

The observed signal change at the start of the fan off period is taken as 30 cts sec^{-1} by putting a straight line through the fan off 3090 detector data and taking the difference from the fan on signal at the point where the fan was first turned off.

This signal represents the instantaneous change in S^{3090} due to velocity effects alone before the sample chamber alters the presumed ambient concentration of H_2O and O_3. Using Eq. (17) to solve for the observed OH density, we have

$$[OH] = 30 \text{ (cts sec}^{-1}) \frac{1.7 \times 10^{17} \text{ (molec cm}^{-3})}{150 \text{ (cts sec}^{-1})} \frac{1}{0.10} \; 8.6 \times 10^{-12}$$

$$[OH] = 2.9 \times 10^{6} \text{ molec cm}^{-3}$$

The agreement between the observed and estimated values is good given the obvious uncertaintly in the large number of parameters needed to carry out the calculation. However, the origin of the observed signal can be considered as understood and taken as evidence that the instrument is operating in a predictable manner.

Drop Phase

The detector count rate data from the drop phase of the flight is shown in Figure 18. The abscissa scale is identical with the thermistor data plot in Figure 16. As the drop commenced, the system was operating stably, with the fan on and the laser tuned to the $Q_1 2$ absorption line. The laser was tuned off of the $Q_1 2$ line twice during the drop at the points indicated by the sharp drops in the count rate from the OH reference cell. The termination of the balloon descent phase is marked by the simultaneous and precipitous drops of the reference cell and 2820 detector count rates since the chute deployment detuned the laser alignment and terminated the dye laser output.

The 2820 detector count rate shown has been normalized to the power in the UV laser beam, given by the UV monitor, to remove the fluctations due to this source. The clean, increasing exponential behavior in S^{2820} indicates that the efficiency of the light trapping cell was to a large degree constant through the drop. This conclusion is further supported by plot of S^{2820} versus gas density shown in Figure 19. More important, however, the zero intercept of this plot establishes that the observed signal is due entirely to gas phase Rayleight scattering. There is no chamber scattering component which, if it had been present, would have indicated a pathological laser beam entry condition. The zero intercept also indicates the absence of a solar scattering component, as observed whenever the laser is off, such as after chute deployment in Figure 18. Thus, the 2820 detector provided a very sensitive, direct measurement of the laser power delivered to the sample volume.

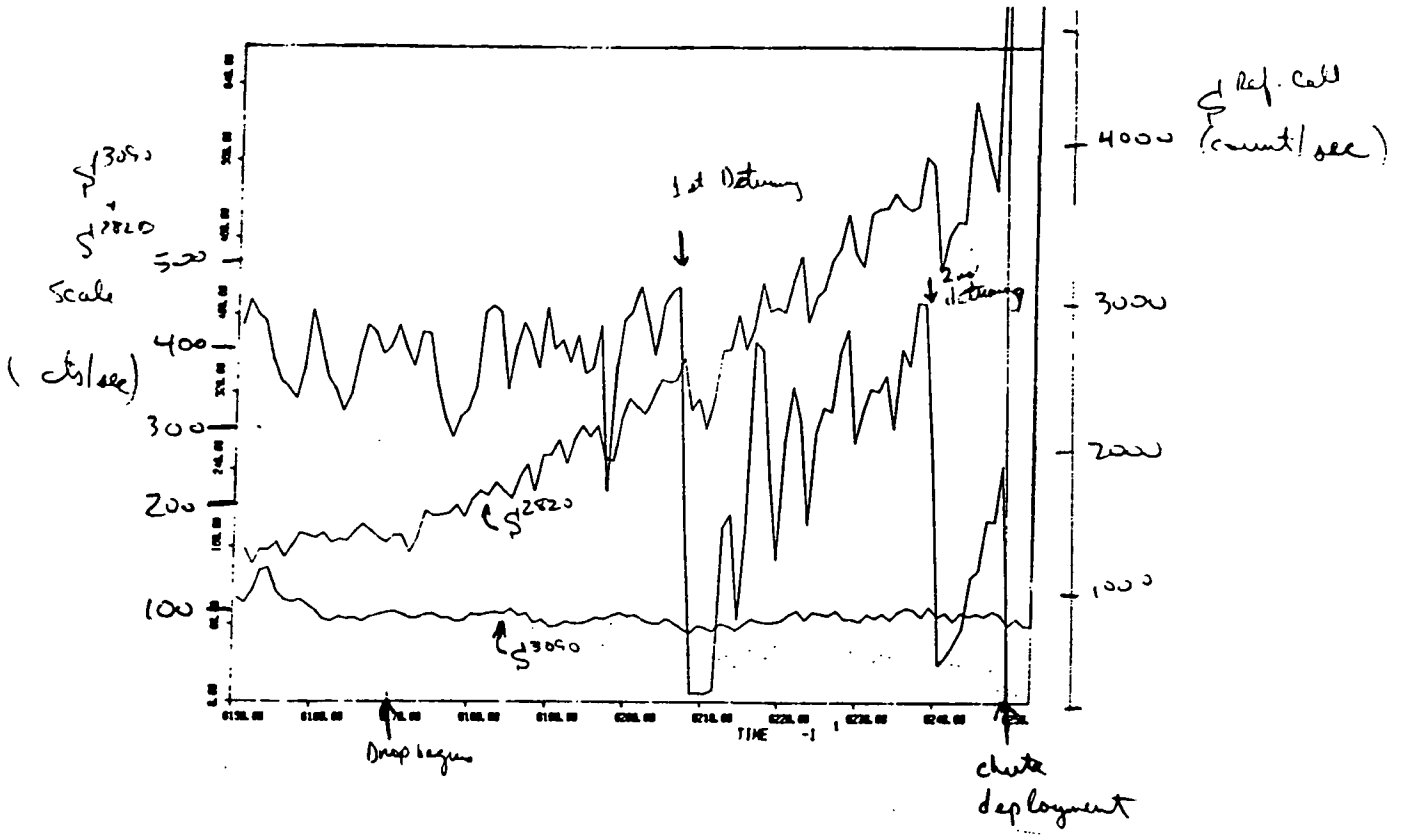

Figure 18. Detector count rates during the drop period. Count rates are averaged over and plotted at 10 sec intervals S^{2820} and $S^{Ref\ Cell}$ have been normalized to the laser power.

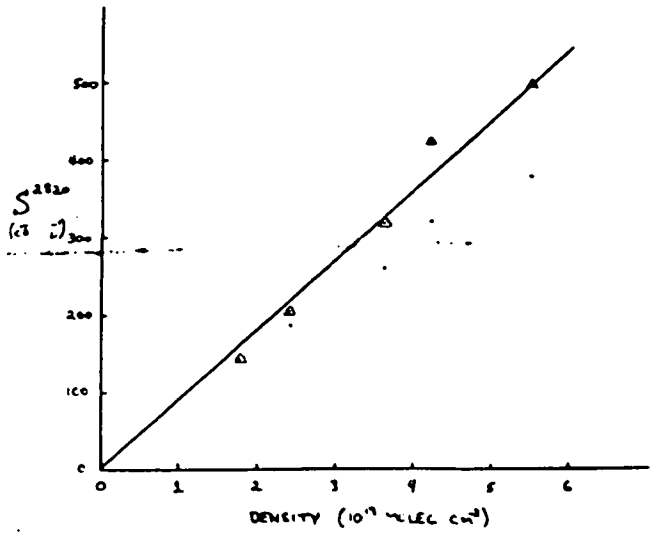

Figure 19. Plot of S^{2820} against density at various altitudes during the drop.

The slope of the plot in Figure 19 yields a direct measure of the peformance of the optical system in flight. The 2820 detector sensitivity during the drop is 1×10^{-15} cts sec^{-1}/molec cm^{-3}. This is about 20% of the performance achieved during the calibration phase which was 4.7×10^{-15} cts sec^{-1}/molec cm^{-3}. About half of this decline is due to lower output from the dye laser. The remainder is attributed to having achieved less than the maximum number of passes in the light trapping cell.

The OH reference cell count rate, $S^{ref\ cell}$, has also been normalized to the laser UV beam energy in an identical manner to the 2820 normalization. The source of the remaining observed fluctuation has not been positively identifed, but most probably is either fluctuation in the Xe lamp output which produces the OH in the reference cell, or direct frequency fluctuation in the dye laser output. In any case, the performance of the OH reference cell and the dye laser does not adversely impact the interpretation of the results from this flight. The absolute frequency of the laser and the character of the on-resonance and off-resonance modes is well established.

The observed 3090 detector count rate shown in Figure 18 does not have a significant dependence on the laser frequency and was observed in general to be only slightly dependent on the presence of laser light in the sample volume element. The observed count rate is predominantly due to solar scattering off the atmosphere. The solar scattering signal can be seen explicitly in Figure 18 after the chute deployment point.

The observed, unnormalized count rates from each detector are given in Table 3 for the two periods where the laser was tuned off the OH absorption line. In each case, the relative change in S^{3090} is surprisingly small, less than 10%.

Altitude interval = 33 - 32 km Q = .074 [M] = 2.5×10^{17}

	S^{Ref}_{Cell}	S^{2820}	S^{3090}	S^{3090}_{OH} see text (upper limit)	[OH] upper limit
On Resonance[1]	2820[2]	234	82.4	7.8	1.0×10^6
Off Resonance	47	162	74.6		
Altitude interval = 29 - 28 km Q = .044 [M] = 5.0×10^{17}					
On Resonance	2888	349	94.4	4.4	1.2×10^6
Off Resonance	189	204	90.0		

NOTES: 1. Q_12 line is used.
2. All count rates are averaged over 30 sec and reported on a per sec basis.

Table 3. Data Summary

The count rate due to OH fluorescence is given by the difference in the on-resonance and off-resonance 3090 detector count rate.

$$S^{3090}_{OH} = S^{3090,on} - S^{3090,off} \qquad (23)$$

only when the difference between between the two measurements is strictly the laser frequency. However, in these measurements the laser power dropped significant, 30% and 40%, after the first and second detuning events, respectively. Although the drops were greater than we had planned, they arose simply because we did not choose to reoptimize the doubling crystal angle for the off-resonance measurement. In the future, the doubling crystal will be slaved to the frequency drive in a manner such that the UV power will remain optimized over the entire tunable frequency interval.

Accordingly, an ambiguity arises since, as the off-resonance signal is made at a lower overall power, the difference equation will under-correct for the presence of non-resonant laser dependent background sources. This situation is more evident if we explicitly account for the various signal sources on the 3090 detector:

$$S_{OH}^{3090} = S^{3090,on} - S^{3090,off}$$

$$= S_{OH}^{3090} + S_{\Sigma laser}^{3090,on} + S_{\Sigma nonlaser}^{3090} - (S_{\Sigma laser}^{3090,off} + S_{\Sigma nonlaser}^{3090,off})$$

where $S_{\Sigma laser}^{3090}$ represents the sum of all background sources that arise from scattered laser light that are frequency independent:

$$S_{laser}^{3090} = S_{\substack{\text{Rayleigh +} \\ \text{Raman scattering}}}^{3090} + S_{\substack{\text{Nonresonant fluorescence} \\ \text{of unidentified molecules}}}^{3090}$$

$$+ S_{\substack{\text{Chamber wall} \\ \text{fluorescence}}}^{3090}$$

and $S_{\Sigma nonlaser}^{3090}$ represents all nonlaser dependent background sources,

$$S_{\Sigma nonlaser}^{3090} = S_{\substack{\text{detector dark} \\ \text{count}}}^{3090} + S_{\substack{\text{solar atmosphere} \\ \text{backscatter}}}^{3090}$$

The anticipated and observed magnitudes of the background signals are summarized in Table 4.

	$S_{\substack{\text{Solar} \\ \text{backscatter}}}^{3090}$	$S_{\Sigma laser}^{3090}$	$S_{\substack{\text{Solar} \\ \text{backscatter}}}^{2820}$	$S_{\substack{\text{Chamber} \\ \text{scatter}}}^{2820}$
Anticipated	< 2	< 2	< 2	< 2
Observed	66 - 80	0 - 10	< 2	< 2

Detector dark counts rates are < 1 cts sec^{-1}.

Table 4. Anticipated and observed background count rates, counts counts sec^{-1}.

The 2820 detector provides an excellent means to normalize the $S_{\Sigma laser}^{3090,off}$ signal to the resonance condition. However, this correction requires partitioning of $S^{3090,off}$ measurements into its laser-induced and non-laser induced components. This assignment can only be done if

one of these is independently measured. During this flight, the $S_{nonlaser}^{3090,off}$ signal was found to be more variable than originally anticipated. Eighteen minutes before the drop the solar background was observed to 66 cts sec^{-1}, and at chute deployment it had risen to 80 cts sec^{-1}. While the measurement at chute deployment is close in time and altitude to the second detuning event, the value in the vicinity of the first detuning event is less certain. Unfortunately, during the drop we did not anticipate the need to incorporate solar scatter measurements by effectively blocking laser light entry to the sample pod.

In future flights, the $S_{\Sigma nonlaser}^{3090}$ signal will be measured essentially simultaneously, with the fluorescence measurement yet, in the absence of laser light, by additionally gating both detectors a second period per pulse at a point within the 60 μsec interval between laser pulses when laser induced effects are absent. Secondly, it is possible to decrease the solar backscatter signal significantly after a second iteration on the optical design of various baffles and surface treatments.

Considering the magnitude of the observed signals, we will not attempt to argue a best value for the relevant background signals, but instead consider the directly observed difference on the 3090 count rate as an upper limit to the S_{OH}^{3090} signal. Using Eq. (17), the OH number densities given in Table 2 are calculated. These results are considerably lower than what was expected based on model calculations and what previous measurements indicate.

Even with the reduced performance levels of this flight, an OH concentration of 1×10^7 would have led to count rates of 83 and 36 cts sec^{-1}, respectively, at the first and second detuning events. Given the strengths

of the background signals achieved in this flight, OH fluorescence signals of this magnitude should have been readily observable. The effect of lower laser power during the off-resonance measurement would cause the detector counts rate differences to appear greater.

References

Nerheim, N.M., A.M. Bhanji, G.R. Russell, A continuously pulsed copper halide laser with a cable-capacitor Blumlein discharge circuit, IEEE J. Quant. Electr. 14, 686, 1978.

Smilanski, I., A. Kerman, L.A. Levin, G. Erez, Scaling of the discharge heated copper vapor laser, Op. Comm. 25, 79, 1978.

Chen, C.J., A.M. Bhanji, G.R. Russell, Long-duration, high-efficiency operation of a continuously pulsed copper laser utilizing copper bromide as a lasant, Appl. Phys. Lett. 32 146, 1978.

Siegmann, A.E., Unstable optical resonators for laser applications, Proc. IEEE 53, 277, 1965.

Wallace, R.W., Generation of tunable UV from 2610 to 3150 Å, Opt. Comm. 4, 316, 1971.

Herriott, D., H. Kogelnik, R. Kompfner, Off-axis paths in spherical mirror interferometers, Appl. Opt. 3, 523, 1964.

Perry, B., R.O. Brickman, A. Stein, E.B. Treacy, P. Rabinowitz, Controllable pulse compression in a multiple-pass-cell Raman laser, Opt. Lett. 5, 288, 1980.

Hazlewood, K., Instantaneous, predictable balloon system descent from high altitude, Adv. Space Res. 3, 49, 1983.

Selzer, P.M., C.C. Wang, Quenching rates and fluorescence efficiency in the $A^2\Sigma^+$ state of OH, J. Chem. Phys. 71, 3786, 1979.

German, K.R., Collision and quenching cross sections in the $A^2\Sigma^+$ state of OH and OD, J. Chem. Phys. 64, 4065, 1976.

Lengel, R.K., D.R. Crosley, Energy transfer in the $A^2\Sigma^+$ OH. II. Vibrational, J. Chem. Phys. 68, 5309, 1978.

McDermid, I.S., J.B. Laudenslager, Radiative lifetimes and quenching rate coefficients for directly excited rotational levels of OH($A^2\Sigma^+$, v=0), J. Chem. Phys. 76, 1824, 1982.

Coxoñ, J.A., Optimum molecular constants and term values for the $X^2\Pi$ ($v \leq 5$) and $A^2\Sigma^+$ ($v \leq 3$) states of OH, Can. J. Phys. 58, 933 1980.

Chidsey, I.L., D.R. Crosley, Calculated rotational transition probabilities for the A - X system of OH, J. Quan. Spectrosc. Radiat. Transfer 23, 187, 1980.

German, K.R., Radiative and predissociative lifetimes of the $v' = 0,1$ and 2 levels of the $A^2\Sigma^+$ state of OH and OD, J. Chem. Phys. 63, 5252, 1975.

Setser, D.W., ed., Reactive intermediates in the gas phase, generation and monitoring, Academc Press, New York, NY, 1979.

Reprinted from Preprint Volume: Second Symposium on the Composition of the Nonurban Troposphere, May 25-28, 1982; Williamsburg, Va. Published by the American Meteorological Society, Boston, Mass.

12.6

TROPOSPHERIC OH OBSERVATIONS: APPLICATION OF THE HIGH REPETITION RATE ATOMIC COPPER VAPOR LASER

Richard M. Stimpfle and James G. Anderson
Department of Chemistry and Center for Earth and Planetary Physics
Harvard University
Cambridge, Massachusetts

1. INTRODUCTION

The observation of OH in the troposphere has become a highly controversial topic both because of the importance of the observation and because of the difficulties associated with experimental execution (see Davis et al., 1981; Wang et al., 1981; Penner et al., 1976; Campbell et al., 1980; Ortgies et al., 1981). The difficulties hinge on three interrelated aspects of the experiment:

a. Sensitivity: At predicted OH concentrations of 10^5-10^7 molecules cm^{-3}, the radical constitutes less than one part in 10^{13} of the atmosphere in the middle and lower troposphere, but it is crucial that the observational technique achieve an acceptable signal-to-noise ratio (i.e., > 10/1) for a given observation within a short period compared with the time corresponding to sizable concentration fluctuations. Long integration time dramatically reduces the value of the observation. It is also essential that sufficient sensitivity be available to test whether the inferred OH concentration is independent of laser flux.

b. Photochemical Interference: At the optimal pumping frequency for OH fluorescence, 282 nm, the photolysis of ozone in the laser pulse forms $O(^1D)$ where reacts with H_2O to form OH in concentrations equal to or larger than that originally present in the atmospheric sample, unless the laser system is designed specifically to eliminate the problem.

c. Absolute Calibration: A direct determination of absolute sensitivity under controlled laboratory conditions and a method for verifying each of the critical quantities related to the absolute calibration during the field observations on a pulse-by-pulse basis is a prerequisite for unambiguously referenced cross calibration. Since no single measurement technique can cope with the scale of the required global OH measurement program, the measurement techniques must be amenable to direct intercomparison prior to field deployment.

We present results of a state-to-state model calculation of the laser-induced fluorescence detection of OH under tropospheric conditions paired with the results of laboratory experiments obtained using a laser system designed to provide high detection sensitivity while simultaneously minimizing photochemical interference. A corollary objective is to condense the detailed calculations relating laser sensitivity and photochemical interference into a form which can be used to appraise any tropospheric laser-induced fluorescence experiment. In several instances in the literature, controversy has resulted simply from an incomplete definition of experimental parameters.

2. DESCRIPTION OF THE MODEL

A time-dependent calculation of the state-to-state kinetics during and after the interrogation of a tropospheric sample by a laser pulse used to induce fluorescence in the OH radical was carried out with three objectives in mind. First, since there are a large number of chemical species and quantum states involved, with characteristic time constants on the order of the laser pulse length, details of the temporal development are essential. A thorough understanding of the energy transfer rates and photochemical interference terms can only be achieved by a detailed comparison between calculated and observed behavior. Second, it is possible, with the aid of the calculation, to define the minimum aggregate of experimental parameters which comprise a complete description of a given experiment. There has been considerable controversy created regarding tropospheric OH observations which results directly from incomplete specification of experimental quantities. What we will show is that the results of the fully time-dependent model can be condensed into an analytical expression which affords rapid analysis of photochemical interference effects for any tropospheric laser-induced fluorescence experiment if the minimum set of experimental parameters are provided. Third, the model provides direct guidance for maximizing the design of the experimental hardware.

The kinetic model follows the time evolution of the laser flux, the concentration of twenty specific internal energy states of the OH radical including those formed by the reaction of $O(^1D)$ with H_2O, the $O(^1D)$ concentration, and the fluorescence emission rate from each state under a variety of experimental conditions.

The laser pulse is simulated by a time-dependent Gaussian function with variable amplitude and width. The time-dependent populations and photon emission rates for each of the quantities noted in the schematic below are calculated with ~10 psec time resolution.

The results from a series of calculations carried out with a fixed laser pulse width of approximately 15 nsec and three different pressure regimes in the absence of O_3 and H_2O are shown in Figure 2.

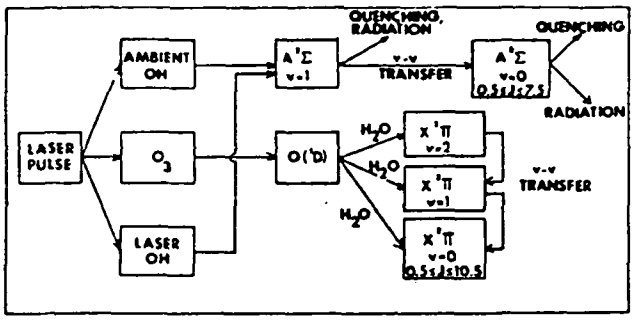

Figure 1.

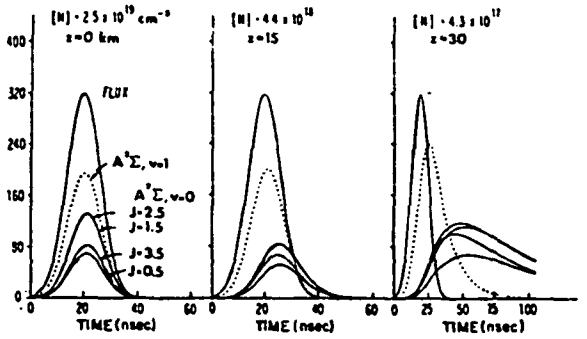

Figure 2.

These three pressure regimes summarize the points that: (a) at ground level the $A^2\Sigma$ v-v transfer rates occur on a time scale short compared with the pulse length, as does electonic quenching; (b) at the tropopause, electronic quenching is on the order of the laser pulse length and v-v transfer into the ground vibrational level of the $A^2\Sigma$ state shifts the population peak of the v=0 state toward the trailing edge of the pulse; and, finally, (c) at the mid-stratosphere, the quenching and v-v transfer rates are significantly longer than the laser pulse length.

Inclusion of O_3 and H_2O into the model allows one to determine the temporal development of fluorescence from ambient and photochemically induced OH, as in Figure 3, below.

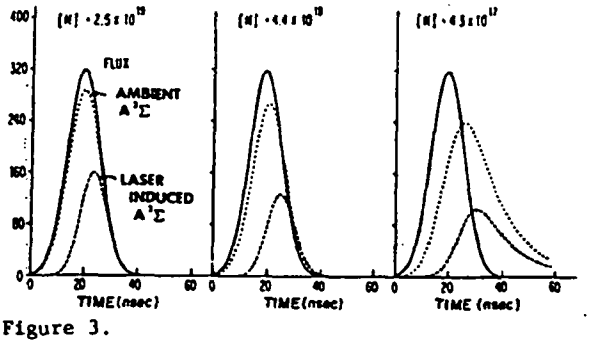

Figure 3.

Fluorescence from photochemically formed OH in the laser pulse peaks at slightly greater times than direct fluorescence of ambient OH because the time constant for formation of OH from

$$O(^1D) + H_2O \rightarrow OH + OH$$

occurs on the time scale of the laser pulse.

The quantity of particular interest for tropospheric observations is the ratio of the fluorescence from OH formed photochemically in the laser pulse to that from ambient OH

$$R = \int_{OH}^{Laser} \Big/ \int_{OH}^{Ambient}$$

This ratio may be written in the condensed form:

$$R = (\text{constant})\left\{\int F(t)dt\right\}\frac{\mu_{O_3}\mu_{H_2O}}{\mu_{OH}} \times [M]\frac{\left(\int [A100]^{Laser}dt\right)}{\left(\int [A100]^{Ambient}dt\right)} \quad (1)$$

where μ is the mixing ratio of each constituent, $\int F(t)dt$ is the integral of the laser flux, and $\int [A100]^{Laser}dt$ is the integral of the fluorescence from the $A^2\Sigma$, v=1 state of OH formed in the laser beam, and the remaining integral is for the identical quantity from ambient OH. Note that R is directly proportional to μ_{O_3} and μ_{H_2O} and inversely proportional to μ_{OH}. The dependence of R on total pressure, however, is not exclusively linear, nor easily predictable since [M] dominates the characteristic time constants for relaxation of the excited atomic and molecular species above a few torr. If the total pressure changes, the ratio

$$\int [A100]^{Laser}dt \Big/ \int [A100]^{Ambient}dt$$

will change, depending on the balance between the chemical relaxation time constants and the laser pulse width. Thus, the pressure and pulse width dependence of R are coupled and are investigated by considering the partial derivation of R with respect to pulse width and pressure.

Of particular importance is the fact that R is directly proportional to the peak flux. It is crucial to recognize the different roles played by the peak flux and the pulse width since these two quantities are not independent when describing a laser pulse of a specified energy. The pulse width imposes a time constant on the system, as noted previously. The peak flux dependence arises from the quadratic dependence of fluorescence emission rates from OH formed in the laser pulse and the linear dependence from ambient OH.

We consider next how these results can be used to analyze <u>any</u> laser-induced fluorescence experiment for tropospheric OH. The first problem is to define the minimum set of experimental parameters needed to uniquely specify the signal-to-noise ratio fo the experiment and the effect of photochemical interference on the results. That <u>minimum</u> set includes:

a. The proportionality factor, C_{OH}, <u>per unit average power</u> between the observed count rate from OH fluorescence, S_{OH}, and the OH concentration in the sample, [OH]. This quantity is fundamental to the absolute calibration of the experiment regardless of the optical arrangement.

b. The laser pumping wavelength which specifies the particular rovibronic transition used to induce fluorescence;

c. The laser pulse width, T_ℓ, in seconds;

d. The average power, $\bar{E}$, of the laser in mw,

e. The average flux, $\bar{F}$, of the laser in mw/cm^2;

f. The repetition rate of the laser, N_p, in pulses/sec;

g. The product of the ozone and water vapor concentration and the total pressure of the interrogated sample; and, finally,

h. The background count rate of the experiment in the absence of OH fluorescence.

Given these data, we are in a position to calculate:

a. The absolute count rate from OH fluorescence for a given [OH];

b. The contribution to the total count rate from OH formed in the laser beam; and

c. The signal-to-noise ratio of the experiment for a given observation period.

The analysis proceeds as follows.

Absolute Count Rate from Ambient OH Fluorescence

It is first necessary to use the correct value for the fluorescence efficiency which is readily calculable from known rate constants for the various relaxation processes.

The product $C_{OH}Q$ is then multiplied by the average power of the laser system, $\bar{E}$, to yield directly the proportionality between the ambient OH concentration and the observed count rate, $S_{OH}^{Ambient}$, such that

$$S_{OH}^{Ambient} = C_{OH}Q\bar{E}[OH]_{Ambient}$$

Contribution to the Total Count Rate from OH Formed in the Laser Beam

Equation (1) provides the functional form of the ratio of the count rate resulting from OH formed in the laser pulse to that from ambient OH. That expression can be reduced to the simple form:

$$R = S_{OH}^{Laser}/S_{OH}^{Ambient} = (3.4 \times 10^{-2}) \frac{\mu_{O_3}\mu_{H_2O}}{\mu_{OH}}(\bar{F}/N_p)f(x)$$

where:

μ_{O_3}, μ_{H_2O} and μ_{OH} are the volume mixing ratios of ozone, water vapor and OH, respectively;

$\bar{F}$ is the laser flux in mw cm^{-2};

N_p is the number of pulses per second; and

$f(x)$ is a polynomial which expresses the ratio of the laser pulse length to the chemical time constant for OH formation from $O(^1D) + H_2O$ in terms of the parameter

$x = 3 + \log(k^I T_\ell)$ where

$k^I = 3 \times 10^{-11}[M]$ sec^{-1}

T_ℓ = FWHM of the laser pulse

Figure 4 presents f(x) as a function of altitude for a number of different laser pluse widths.

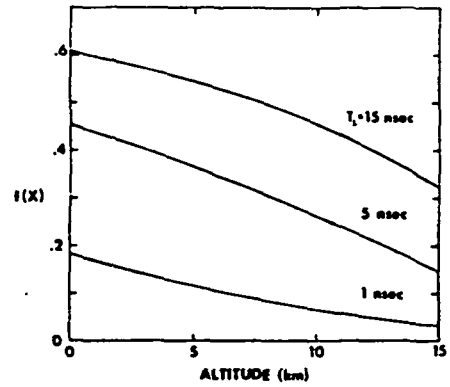

Figure 4.

The influence of varying the pulse repetition frequency, N_p, at a fixed E is summarized in Figure 5, below, assuming each pulse interrogates a different sample volume element.

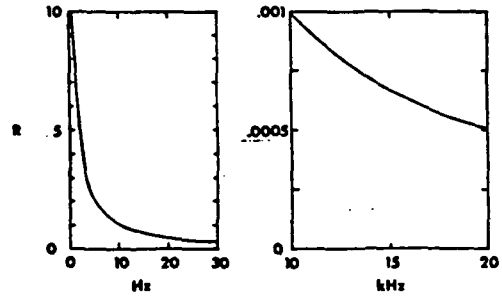

Figure 5.

The analysis of a given experiment for photochemical interference is now simply a matter of:

a. Specifying the altitude and laser pulse width;

b. Reading off the appropriate value of f(x) from Figure 4;

c. Inserting the laser flux, $\bar{F}$, and the pulse rate, N_p;

d. Inserting the mixing ratio of ozone, water and OH; and

e. Calculating $R = S_{OH}^{Laser}/S_{OH}^{Ambient}$

The relationship betwen the fluorescence count rate from ambient OH and that from laser-generated OH is most succinctly represented by a plot of $S_{OH}/\bar{E}$ vs. $\bar{E}$ for both $S_{OH}^{Ambient}$ and S_{OH}^{Laser} which will

have the general form displayed in Figure 6, below.

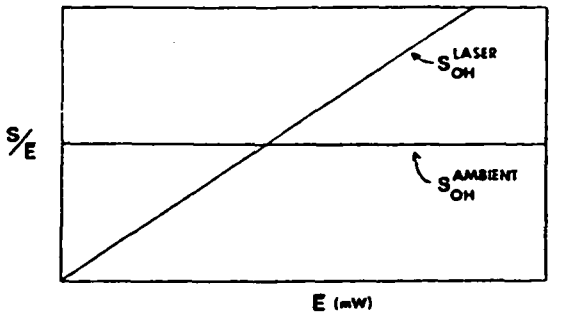

Figure 6.

What such a graph defines, of course, is the point at which the observed signal from laser-generated OH becomes comparable to that from ambient OH for a given laser power and ambient OH concentration. It is instructive to attempt the construction of such a graph, which is central to the quantitative analysis of any tropospheric OH observation, using the information provided in articles discussing LIF measurements of OH.

Signal-to-Noise Ratio

To complete the analysis, one must compare the fluorescence count rate from Figure 6 with the background count rate in the absence of OH for a given $C_{OH}\bar{E}Q$. Such a comparison will establish the period of time required to obtain an OH observation.

3. EXPERIMENTAL SYSTEM

The experimental strategy we have selected for the detection of OH in the stratosphere and troposphere is to minimize photochemical interference effects and maximize instrumental sensitivity by using an extremely high repetition rate pulsed laser. Such a system has been successfully developed for use on a balloon-borne package which employs a 17 kHz atomic copper vapor laser pumping a low-loss dye laser which is doubled into the ultraviolet to pump the $X^2\pi(v=0) \rightarrow A^2\Sigma(v=1)$ transition at 2820 Å. This pulse rate, which is approximately two thousand times greater than that used for previous experiments, affords large average powers (and thus low detection thresholds) with very low peak powers (and thus minimization of photochemical interference). The system has been used to test the calculations cited above, and those results will be discussed in detail.

4. REFERENCES

Davis, D.D., S.D. Fischer and M.O. Rodgers, Reply to Wang and Davis, Geophys. Res. Lett., 9, 101 (1982).

Campbell, M.J., J.C. Sheppard and B.F. Au, Measurement of Hydroxyl Concentration in Boundary Layer Air by Monitoring CO Oxidation, Geophys. Res. Lett., 6, 175 (1979).

Ortgies, G., K.H. Geriche and F.J. Comes, Optical Measurements of Tropospheric Hydroxyl with Lasers, Z. Naturforsch., 36a, 177 (1981).

Penner, D., D.H. Ehhalt, H.W. Patz, U. Platt, E.P. Roth and A. Volz, OH Radicals in the Lower Troposphere, Geophys. Res. Lett., 3, 466 (1976).

Wang, C.C., L.I. Davis, P.M. Selzer and R. Munoz, Improved Airborne Measurements of OH in the Atmosphere Using the Technique of Laser Induced Fluorescence, J. Geophys. Res., 86, 1181 (1981).

IV. RESEARCH AND DEVELOPMENT OF NEW INSTRUMENTS

NO_2: Analysis of Techniques and a New Instrument Design

Nitrogen dioxide is an enigma within the small molecule community in that its manifold of overlapping electronic and vibrational states yields a spectroscopic complexity comparable to molecules significantly larger. This behavior has hindered the development of optical detection techniques with sufficient sensitivity to achieve the experimental specifications outlined in the introduction to this report.

On the other hand, NO_2 stands in the rate limiting position in the catalytic couplet which is responsible for 70 percent of the globally integrated conversion of ozone to molecular oxygen:

$$O_3 + NO \rightarrow NO2 + O_2$$

$$O + NO_2 \rightarrow NO + O_2 \quad \leftarrow \text{Rate Determining}$$

$$O_3 + O \rightarrow O_2 + O_2$$

It is thus essential that we develop a method for detecting NO_2 within a highly confined volume element such that the detection technique is fully compatible with the other in situ methods discussed here. We present this development in the following sections:

A. Candidate Techniques

B. An Evaluation

C. Quantification of the Laser Induced Fluorescence Technique

D. Design and Evaluation of a Prototype Flight Instrument.

A. Candidate Techniques

There are of course a large number of possible detection techniques. The low concentration of NO_2 in the stratosphere eliminates as insensitive many of these possible techniques. For example, the powerful resonance fluorescence technique is much less sensitive with polyatomic molecules than with atoms or diatomic molecules, since polyatomic molecules in general possess few strong electronic transitions. The following sections critically analyze four possible techniques, developing upper bound signal rates for each of the techniques since the lowest order criterion is that of adequate sensitivity.

Laser Induced Fluorescence (LIF)

This technique is well known. Laser photons at a specified wavelength coherently excite the species of interest to an upper electronic state, whereupon the molecule fluoresces to the ground state. Subsequently, some fraction of the absorbed energy is actually radiated as light. This fraction is dependent upon microphysical processes such as radiationless transitions and energy transfer (rotational, vibrational, or electronic). The technique can be quite specific; if there are well separated rovibronic transitions from the molecule's ground state to an upper state, one can in theory shift the frequency of the exciting laser photons slightly and drastically reduce the amount of emitted fluorescent photons. The logic of this as a 'null experiment' rests on the improbability of an interfering species having a similar

absorption maximum and minimum at exactly the same place. The sensitivity of LIF depends principally on the strength of the electronic transition and on the efficiency with which the molecule radiates into a particular experimental bandpass. A strength of laser induced fluorescence as a detection technique is its simplicity; in particular, the fundamental character of the physical process.

LIF applied to NO_2 is unfortunately a complicated phenomenon at the detailed level. The complexity of the visible absorption spectrum even at high resolution has been well documented by Zare and coworkers[4]. Figure 1 depicts a representative section of the NO_2 visible absorption spectrum. Even under supersonic cooling, the molecule exhibits approximately a factor of 10 more transitions in the visible[10] than is predicted by ab initio calculations[11]. The canonical view, due to Douglas[12], is that the $\tilde{A}\ ^2B_2$ electronic state is significantly diluted by admixture with upper vibrational levels of the ground state $\tilde{X}\ ^2A_1$. Furthermore, the $\tilde{A}'\ ^2B_1$ and $\tilde{A}''\ ^2A_2$ electronic states interact vibronically; the $^2B_1$ and $^2A_1$ states, and the $^2B_2$ and $^2A_2$ states may be coupled by the Renner-Teller interaction, and the unpaired electron induces spin splittings[13] (visible in Figure 1, for example). It is difficult to say whether the calculated Born-Oppenheimer states are even approximate eigenfunctions of the molecular Hamiltonian. Fluorescence from the molecule is also anomalous: the radiative lifetime is an order of magnitude longer than that expected from computation of the integrated absorption coefficient[14]; and fluoresence from the molecule is strongly red-shifted, displaying vibrational peaks superposed on a quasicontinuum (see Figure 2). The peaks in the fluorescence spectrum of Figure 2 are the result of radiation from the initially populated level in the

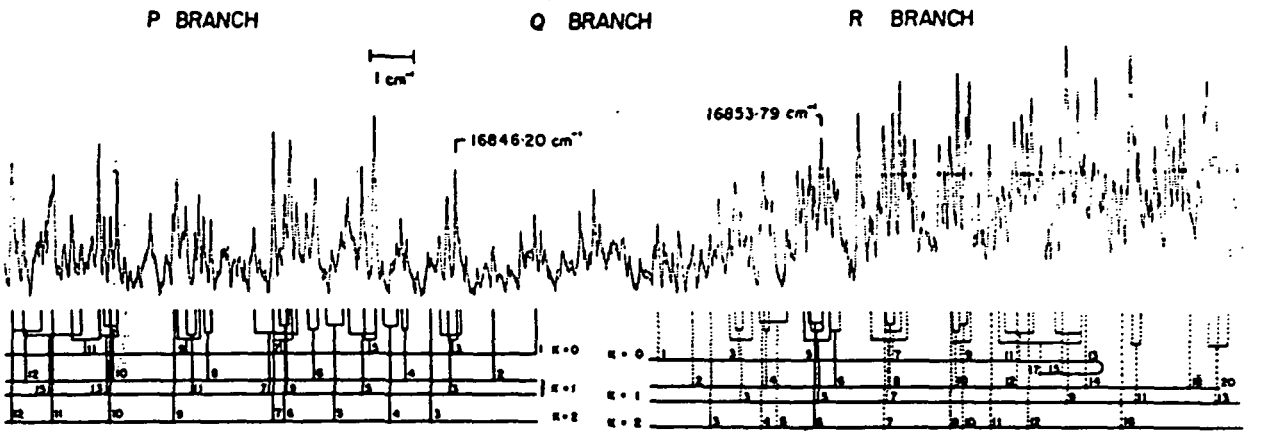

Figure 1. High resolution absorption spectrum of NO_2 near 593 nm.

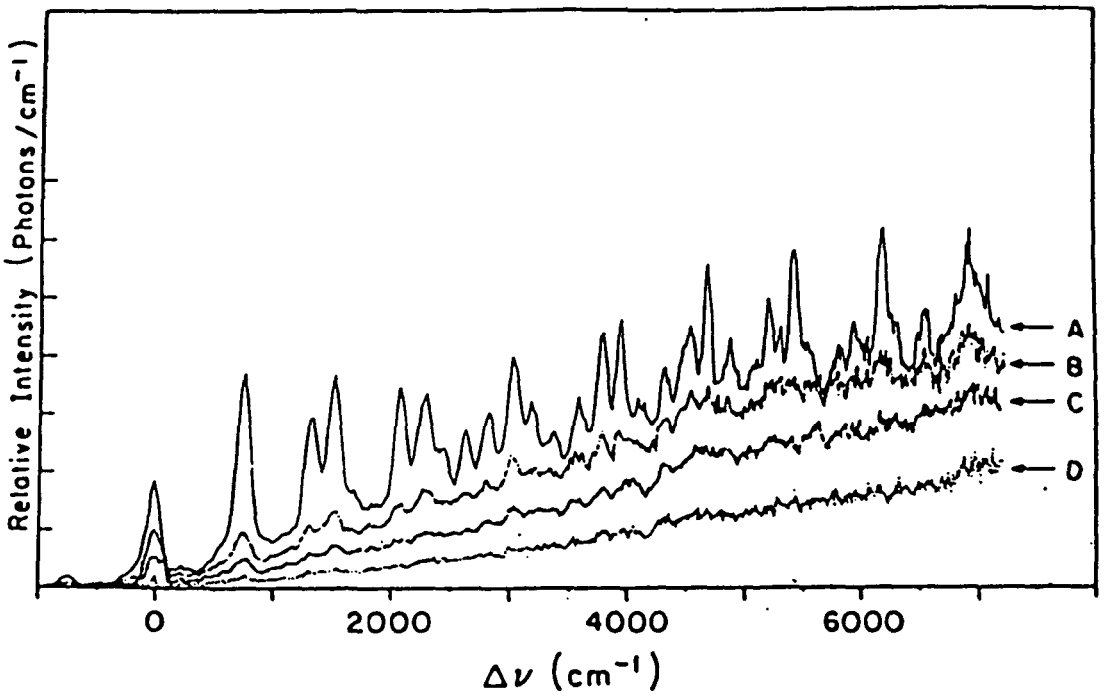

Figure 2. Fluorescence spectrum of NO_2, excited at 532 nm. The traces A to D are for increasing pressures of the buffer gas H_2.

excited state manifold to various vibrational levels of the ground state. The origin of the continuum is less obvious, but is thought to be radiation from states populated by one of several dark processes (e.g., collision-induced vibrational or rotational transfer, intrinsic energy transfer among the various molecular degrees of freedom[15]).

One wishes to objectively assess the merits of the LIF technique as well as the techniques described in subsequent sections. To that end, the signal equation is written for each technique and the molecular and experimental parameters are estimated where required.

For laser induced fluorescence, the signal rate is given by

$$S = \left[\begin{array}{l}\text{overlap integral of laser line} \\ \text{and molecular line}\end{array}\right] \cdot \left[\begin{array}{l}\text{an instrumental} \\ \text{weighting function}\end{array}\right] \cdot [\text{concentration of } NO_2] \qquad (2\text{-}1)$$

More formally

$$[\text{overlap integral}] = \int_{\text{line}} F(\nu - \nu_e)\, g(\nu - \nu_e)\, d\nu \qquad (2\text{-}2a)$$

$$\left[\begin{array}{l}\text{instrumental} \\ \text{weighting function}\end{array}\right] = \frac{\Delta\Omega}{4\pi} \cdot MP \cdot l \cdot \int_0^{\nu_e} \frac{\phi(\nu_e,\nu)\, T(\nu)\, \eta(\nu)\, d\nu}{1 + a_M(\nu_e,\nu)[M]} \qquad (2\text{-}2b)$$

$F(\nu-\nu_e)$ is the excitation lineshape function (photons $\sec^{-1}$ Hz^{-1}) and $g(\nu-\nu_e)$ is the absorption lineshape function (cm^2). Both F and g have Gaussian lineshapes characterized by widths $\Delta\nu_L$ and $\Delta\nu_D$, respectively. The maximum overlap is obtained when the Gaussian envelopes are coincident, whereupon the integral is simple:

$$\int_{\text{line}} F(\nu-\nu_e)\, g(\nu-\nu_e)\, d\nu = F_0 \sigma_0 \left[\frac{4 \ln 2}{\pi}\right]^{1/2} \left[\frac{1}{\Delta\nu_L^2 + \Delta\nu_D^2}\right]^{1/2} \qquad (2\text{-}3a)$$

$$= F_0\sigma_{peak}\left[\frac{\Delta(/_D^2}{\Delta(/_L^2 + \Delta(/_D^2}\right]^{1/2} \qquad (2\text{-}3b)$$

where

σ_0 = integrated absorption (cm^2 Hz) = $\int g((/-(/_e)d(/$

σ_{peak} = absorption at peak (cm^2) = $\sigma_0\left[\frac{4\ \ln\ 2}{\pi}\right]^{1/2}\Delta(/_D^{-1}$

F_0 = integrated intensity (photons sec^{-1}) = $\int F((/-(/_e)d(/$

In the limiting case when the full width at half maximum (FWHM) of the laser lineshape $\Delta(/_L$ is much smaller than the Doppler width of the absorption $\Delta(/_D$,

$$[\text{overlap integral}] \simeq F_0\sigma_{peak}\left[1 - \frac{1}{2}\left[\frac{\Delta(/_L}{\Delta(/_D}\right]^2\right] \qquad (2\text{-}4)$$

Because NO_2 fluoresces over a large range to the red of the excitation frequency $(/_e$, the instrumental weighting function involves a complicated convolution integral. The quantum efficiency $\phi((/_e,(/)$ and the quenching constant $a_M((/_e,(/)$ are of course molecular parameters, yet both are biased by the detection apparatus and must be included in the convolution integral. Other more straightforward components of the instrumental weighting function are:

$\frac{\Delta\Omega}{4\pi}$ = fraction of 4π sr intercepted by the detection apparatus

MP = number of passes in a multipass cell

1 = length of excitation beam viewed by detection optics (cm)

$T((/)$ = transmission function of detection optics

$\eta((/)$ = quantum efficiency of photodetector.

Fluorescence from NO_2 is isotropic and the assumption is made that a simple Stern-Volmer relationship is adequate to describe the complex quenching mechanism.[15]

In the spirit of an upper bound calculation, numerical values for the various components of the signal equation are assigned as follows. The choice of laser source hinges on ruggedness and efficiency, so of the many possible laser systems, this calculation employs a copper vapor laser pumped dye laser operating at 585 nm. Average power is 500 mW in 30 ns pulses at a repetition rate of 17 KHz. The integrated intensity is therefore 1.4×10^{18} photons sec^{-1}. The dye laser[16] produces photons with a Gaussian frequency spread of width $\Delta\nu_L \simeq 500$ MHz (= 0.017 cm^{-1}). The laser system is a minor modification of the system employed by this laboratory to detect stratospheric OH[17]. The peak absorption cross section at 585 nm is unknown, but low resolution measurements by Zare and coworkers[9] indicate a value of 2.5×10^{-20} cm^2. The cross section at the peak of a rotational line will be higher, but the density of the absorption spectrum argues for a 'true' peak cross section value not much higher than the low resolution value, and thus $\sigma_{peak} \simeq 5 \times 10^{-20}$ cm^2. The Doppler width $\Delta\nu_D$ of NO_2 is 920 MHz at 295 K and 810 MHz at the typical mid-stratospheric temperature of 230 K. Thus

$$[\text{overlap integral}] \simeq F_0 \sigma_{peak} \left[1 - \frac{1}{2}\left[\frac{\Delta\nu_L}{\Delta\nu_D}\right]^2\right]$$

$$= 5.7 \times 10^{-2} \text{ photons cm}^2 \text{ sec}^{-1} \text{ at 230 K}$$

An efficient optical collection apparatus collects approximately 20% of

the fluorescence radiated from the central 1 cm region of a multipass cell[18]. This cell is formed by two concentric mirrors and passes the beam at least 50 times with negligible reflective loss. The photon sensor of choice for highest sensitivity in the near infrared is a photomultiplier tube with a gallium arsenide (GaAs) photocathode. Gallium arsenide has a quantum efficiency of 10% independent of wavelength to 850 nm, rapidly dropping in efficiency to near zero at 950 nm. The transmission function $T(\lambda)$ is at least 0.9 throughout the near infrared for most transmissive and reflective optics. The quenching constant a_M for the dominant quenchers $M = N_2, O_2$ is roughly 50 per torr[8] with an uncertainty of about a factor of 1.5. The value of ϕ is the order of ten percent[19]. Hence

$$\begin{bmatrix}\text{instrumental} \\ \text{weighting function}\end{bmatrix} = \frac{\Delta\Omega}{4\pi} \cdot MP \cdot l \cdot \int_0^{\lambda_e} \frac{\phi(\lambda_e,\lambda)T(\lambda)\eta(\lambda)d\lambda}{1 + a_M(\lambda_e,\lambda)[M]}$$

$$= 1.8 \times 10^{-4} \text{ counts cm photon}^{-1}$$

at [M] = 10 torr

and

$$S = [\text{overlap integral}] \times \begin{bmatrix}\text{instrumental} \\ \text{weighting function}\end{bmatrix} \times [NO_2]$$

$$= 1.0 \times 10^{-5} \text{ counts cm}^3 \times [NO_2]$$

Stratospheric models[20] predict mid-stratospheric abundances of NO_2 to be 1×10^9 cm^{-3}, and thus the upper bound count rate for the LIF experiment is

$$S_{\text{upper bound}} = 1 \times 10^4 \text{ counts sec}^{-1}. \qquad (2\text{-}5)$$

The principal advantage of the LIF technique is its fundamental

character. Photons are absorbed and reradiated, although the reradiation involves a dense upper state manifold. Many years of experimental and theoretical development have laid a solid foundation for characterization of the physics of the process. Hardware complexity is not severe. The principal disadvantage of laser induced fluorescence for the detection of NO_2 is the extensive congestion of absorption lines. Low resolution measurements show few distinct peaks to provide an adequate 'tune-on, tune-off' null experiment.

Resonant Two Photon Ionization (R2PI)

Multiphoton molecular spectroscopy has been discussed quite widely in the literature[21]. The absorption of n photons via intermediate virtual states or at most (n-1) real states raises the molecule from its ground state to the ground state of the molecular ion (see Figure 3). Resonant enhanced multiphoton ionization (REMPI) (i.e., via at least one real state) is several orders of magnitude higher in cross section than ionization via virtual states. One can detect single atoms with REMPI[22]. Molecules are more difficult to ionize; the most sensitive techniques utilize only two photons and a resonant intermediate state (R2PI), in effect picking out the largest and lowest order of nonlinearity in the molecule.

The three and four photon ionization spectrum of NO_2 has been investigated by Grant and coworkers[23]. Highest ion currents were recorded when ionization proceeded through a real intermediate state (Figure 3) , but overall the process is insensitive, in part due to competing processes at various stages of absorption. For example, NO_2 excited at 500 nm absorbs two quanta and then may either dissociate into

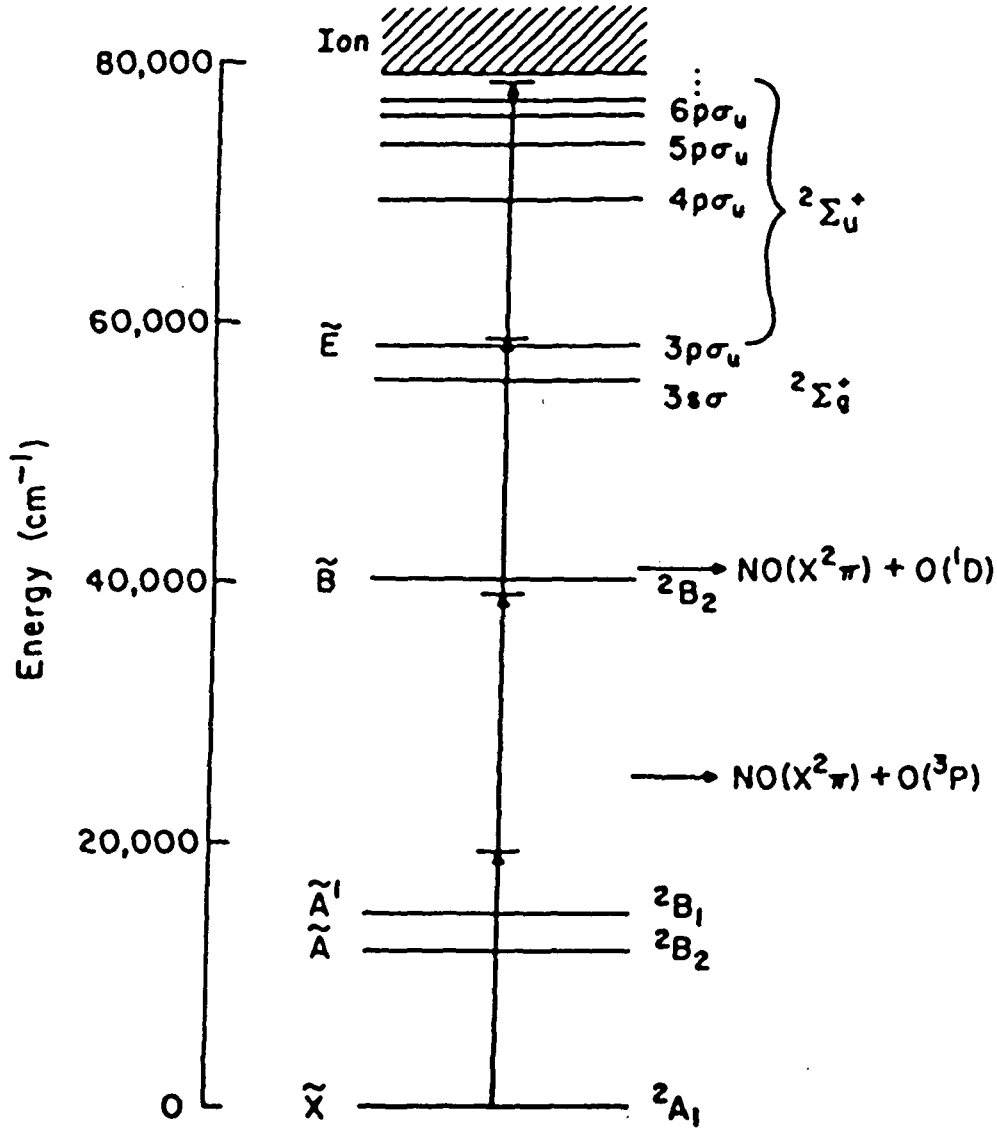

Figure 3. Partial listing of known electronic states of NO_2; from ref. 23. Shown is a four photon ionizing transition, three photon resonant.

NO ($\tilde{X}\ ^2\Pi$) and $O(^3P)$ or absorb another quantum. The relatively low observed signals as well as the significant amounts of NO^+ in the ion current show that the dissociation pathway is the preferred channel throughout much of the visible MPI spectrum of NO_2. Coupled with this insensitivity is the unstructured character of the ionization spectrum, reflecting to large measure the congested nature of the absorption at the one photon level (see Figure 1).

Two photon ionization spectra of NO_2 have not been obtained. Generation of the spectra would require high peak power tunable laser output in the mid ultraviolet (< 253 nm; ionization potential of NO_2 is 9.78 eV). However, Slanger and coworkers[24] have tuned an injection locked KrF excimer laser from 247.8 to 249.5 nm with a linewidth of 0.003 nm; this range encompasses the lowest vibrational level of the $\tilde{B}\ ^2B_2$ state of NO_2. As in the three and four photon case, dissociation is a competing channel, but the narrowness of the absorption at this wavelength[25] indicates that this state is relatively long lived (compared to strongly predissociated higher vibrational levels of this state (cf. Herzberg[26]) , or the dissociative states in the near ultraviolet, for example).

Assessment of the sensitivity and specificity of R2PI requires a quantitative model for the two photon process. If the phase coherence of both the radiation field and the molecular system play an insignificant role in the multiphoton ionization dynamics, one can avoid the more accurate density matrix formalism[27] for the equations of motion, and instead employ a more intuitive kinetic model[28]. Ion production rates inferred from the kinetic model are higher than those calculated from an

explicit formalism incorporating the spatial and temporal coherence of the laser field, so the following calculation represents an upper bound. Consider a 1 + 1 photon ionization process $\tilde{C} \leftarrow \tilde{A} \leftarrow \tilde{X}$ proceeding through an intermediate state $\tilde{A}$ as in Figure 4. The rate equations are written as

$$\dot{n}_x = -(\sigma_{A\leftarrow X} I)n_x + (\sigma_{A\leftarrow X} I + \tau_f^{-1})n_a \quad (2\text{-}6a)$$

$$= -\alpha n_x + (\alpha + \gamma)n_a \quad (2\text{-}6b)$$

$$\dot{n}_a = (\sigma_{A\leftarrow X} I)n_x - (\sigma_{A\leftarrow X} I + \sigma_{C\leftarrow A} I + \tau_f^{-1} + \tau_{ni}^{-1})n_a \quad (2\text{-}7a)$$

$$= \alpha n_x - (\alpha + \beta + \gamma + \delta)n_a \quad (2\text{-}7b)$$

$$\dot{n}_c = \sigma_{C\leftarrow A} I n_a \quad (2\text{-}8a)$$

$$= \beta n_a \quad (2\text{-}8b)$$

subject to the initial conditions

$$n_x(t = 0) = f_{species} \cdot V \cdot [species] \quad (2\text{-}9a)$$

$$= n_{x0}$$

$$n_a(t = 0) = 0 \quad (2\text{-}9b)$$

$$n_c(t = 0) = 0. \quad (2\text{-}9c)$$

Here $\alpha = \sigma_{A\leftarrow X} I$ (sec^{-1}), $\beta = \sigma_{C\leftarrow A} I (sec^{-1})$, $\gamma = \tau_r^{-1}$ is the fluorescence rate from state $\tilde{A}$ to state $\tilde{X}$ (sec^{-1}), $\delta = \tau_{ni}^{-1}$ is the transition rate for any process that does not ionize (sec^{-1}), $\sigma_{A\leftarrow X}$ is the absorption cross section for the $\tilde{A} \leftarrow \tilde{X}$ transition (cm^2), $\sigma_{C\leftarrow A}$ is the cross section for the ionization step (cm^2), and I is the photon flux (photons cm^2 sec^{-1} $pulse^{-1}$). The initial concentration of participating ground state molecules n_{x0} is the product of the fraction of molecules participating $f_{species}$, the interaction volume V, and the species number density [species].

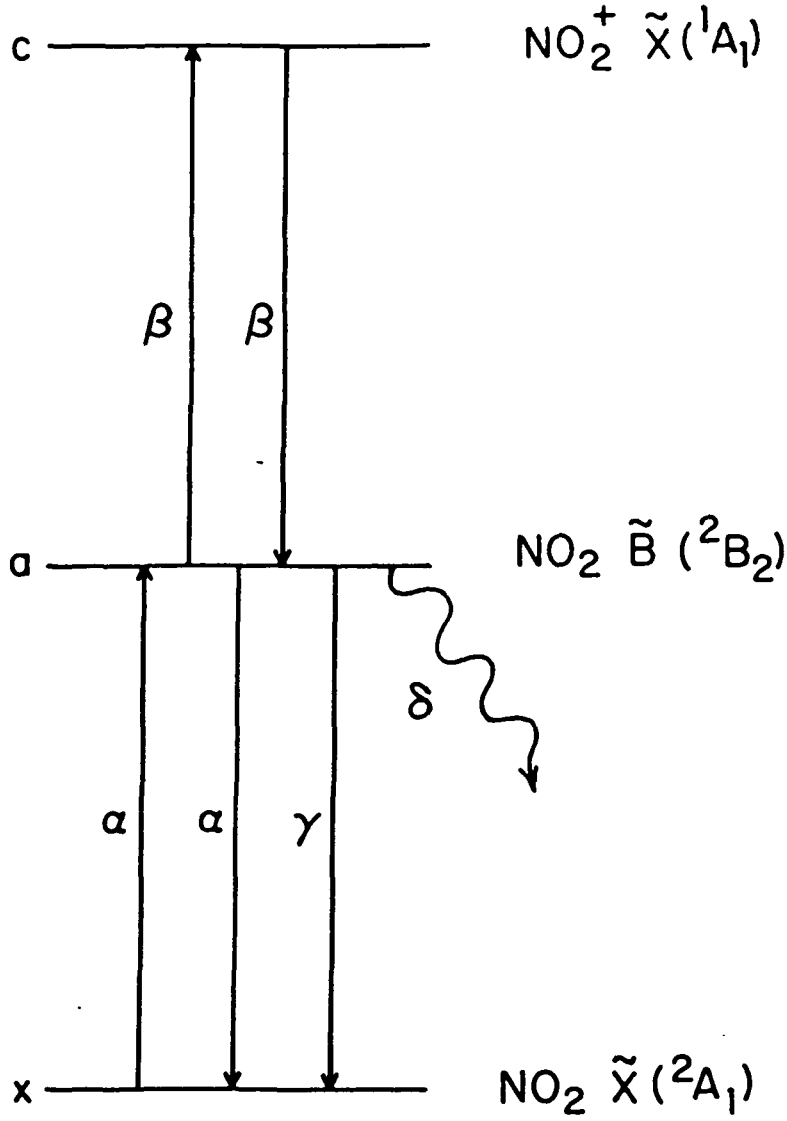

Figure 4. Energy level scheme for resonant two photon ionization.

If excitation consists of square pulses of length τ, the solution[28] for the ion concentration is

$$n_c = \beta n_{x0}\left[\frac{1}{1 + (\delta/\beta)}\right]\left[1 + \frac{L}{K - L}e^{-K\tau} - \frac{K}{K - L}e^{-L\tau}\right] \qquad (2\text{-}10)$$

where

$$Y = 2\alpha + \beta + \gamma + \delta$$

$$Z = \beta + \delta$$

$$\begin{bmatrix} K \\ L \end{bmatrix} = \frac{Y}{2}\begin{bmatrix} + \\ - \end{bmatrix}\frac{Y}{2}\left[1 - \frac{4\alpha Z}{Y^2}\right]^{1/2} .$$

This general result has two important limiting forms. If all processes occur on a time scale much longer that the pulse duration (i.e. the low flux or short time limit), the ion concentration is

$$n_c = \frac{1}{2}\alpha\beta\tau^2 n_{x0}$$
$$= \frac{1}{2}\sigma_{A\leftarrow X}\sigma_{C\leftarrow A}I^2\tau^2 f_{species}V[species] . \qquad (2\text{-}11)$$

Equation (2-11) is just the perturbation theory expression. In the high flux or long time limit, the figure of merit is the ratio of intermediate state leakage to up-pumping (δ/β) :

$$n_c = \frac{\beta n_{x0}}{1 + (\delta/\beta)}$$
$$= \sigma_{C\leftarrow A}I(1 + (\tau_{ni}^{-1}/(\sigma_{C\leftarrow A}I)))^{-1}\cdot f_{species}\cdot V\cdot[species]. \qquad (2\text{-}12)$$

To calculate the ion count rate produced in an 'ideal' experiment, the laser independent parameters are estimated first. Since no fluorescence has ever been observed from $NO_2(\tilde{B}\ ^2B_2)$, $\gamma \ll \delta$. The predissociative lifetime of 42 psec[25] implies that $\delta \simeq 2.4 \times 10^{10}$ sec^{-1}. The cross section $\sigma_{A\leftarrow X}$ is unknown. An appropriate area to pump is the $^qR_1$

bandhead at 249.2 nm , as just to the red of this bandhead the NO_2 cross section at low resolution appears two orders of magnitude smaller and hence this area might provide an adequate 'tuning off' null experiment. A low resolution absorption measurement by Hall and Blacet[29] yields a rough peak absorption cross section of about 1 x 10^{-19} cm^2. The uncalibrated higher resolution measurement of Hallin and Merer[18] shows that this bandhead is fairly dense; it is probable that peak cross sections of individual rotational lines are no more than 1 x 10^{-18} cm^2. Similarly, the cross section $\sigma_{C<-A}$ is unknown. This cross section represents a transition from a bent state to the linear ionic ground state (NO_2^+ ($\tilde{X}$ $^1A_1$)), and as such can be qualitatively compared to the photoionization transition in NO_2 (NO_2^+ ($\tilde{X}$ $^1A_1$) <- NO_2 ($\tilde{X}$ $^2A_1$)). Single photon photoelectron spectra show a broad diffuse maximum at 11.25 eV with weak ionization starting at 9.8 eV[30]. The photoionization cross section at 124.6 nm (corresponding to the same energy disposal in the ion as in the two photon scheme) is about 3 x 10^{-20} cm^2 at low resolution[31]; as an upper limit, this value is chosen as a low resolution value for $\sigma_{C<-A}$.

However, the appropriate value of $\sigma_{C<-A}$ as the excitation linewidth is decreased is even more speculative. One can advance the following qualitative argument. The cross section of an individual rotational state going to the continuum is independent of rotational quantum number and principally depends upon the Franck-Condon overlap of the initial state vibrational eigenfunction with the vibrational eigenfunctions of the repulsive upper state. Thus, within a vibrational band, the ionization cross sections are approximately the same for each individual rotational state. Now light of very small linewidth will pump all of the

rotational levels to the continuum , by definition. Light of broader linewidth but the same intensity will pump all the levels as well, but each infinitesimal segment in frequency space will pump fewer levels. The result is that the inferred low resolution cross section is the appropriate high resolution cross section, but all molecules are pumped; if the upper state were discrete, only some fraction of the initial state molecules would be pumped by narrow linewidth excitation and the appropriate high resolution cross section would be higher. Therefore, $\sigma_{C<-A}$ is assigned the value 3×10^{-20} cm^2.

Commercial KrF excimer lasers produce 500 millijoules per pulse in 30 ns pulses at 50 Hz. At 249 nm, this corresponds to 2.1×10^{24} photons sec^{-1} $pulse^{-1}$. Excimer lasers do not generally possess diffraction limited output. Focussed light from such lasers produces a roughly cylindrical ion production region of radius 0.01 cm and length 0.1 cm; ion production falls off rapidly outside of this cylinder. The flux over this 0.1 cm is therefore 6.7×10^{27} photons $cm^{-2} sec^{-1} pulse^{-1}$.

Substitution of these values into equations shows that the excimer laser intensities force the calculation into the latter of the two limits discussed: all processes occur on a time scale short compared with the laser pulse length. Therefore

$$n_c \approx \frac{\beta n_{x0}}{1 + (\delta/\beta)} = 8.3 \times 10^{-3} \cdot f_{NO_2} \cdot V \cdot [NO_2]$$

The $^qR_1$ bandhead is comprised of nine rotational lines; specifically, N" = 2 through 18, N" even, K_a" = 1. The well known formulae[32] for the fractional population of an approximate symmetric top, together with the known rotational constants[25] of ground state NO_2 yield a value for f_{NO_2} of 1.3×10^{-2}. The interaction volume V is 3.1×10^{-5} cm^3. For the canonical case, $[NO_2] = 1 \times 10^9$ cm^{-3}, and therefore

$$n_c = 3.4 \text{ ions pulse}^{-1}$$
$$= 170 \text{ ions sec}^{-1} \text{ at 50 Hz.} \qquad (2\text{-}13)$$

With the sensitivity of current techniques of ion detection, all of these ions should be observable. The ambient stratospheric ion concentration is ca. $10^2 - 10^3$ ions cm^{-3}, but the anticipated signal can be differentiated from this noise source by tuning off the $^qR_1$ bandhead. The advantages of R2PI for detection of NO_2 reside in the sensitivity of ion detection techniques and the existence of a good null experiment. A major disadvantage is the low count rate, as evidenced by the preceding calculation. The production of ions from an unknown source in the focal region is possible, as it is difficult to restrict multiphoton processes to a particular order. The theoretical foundation for nonlinear interactions has progressed from initial qualitative observations to semiquantitative detail. Hardware complexity is high.

Two Photon Fluorescence (TPF)

Detection of two photon processes is not limited to ionization. Absorption of two photons often can be observed as fluorescence from the prepared state. The fluorescent photons are generally significantly removed in energy from the incident photons, with resultant discrimination benefits. Here, as in R2PI, the highest sensitivity is obtained when the intermediate state is real.

Recent work by Slanger and coworkers [24] on the photodissociation dynamics of NO_2 in the mid-ultraviolet has shown that for excitation energies below the $NO(\tilde{X}\ ^2\Pi) + O(^1D)$ threshold (243.9 nm) the excess energy resides principally in vibrational excitation of the nascent NO.

This nonstatistical distrubtion is of course very different from thermally equilibrated NO. The vibrationally excited nascent NO can then be exicted by antoher UV photon to low vibrational levels of the $\tilde{A}^2\Sigma^+$ or $\tilde{B}^2\Pi$ state of NO, and fluorescence is observed when the upper state radiatively decays. A candidate technique for the detection of stratospheric NO_2 is as follows: one photon dissociates the NO_2 molecule in the mid-ultraviolet; the resulting vibrationally excited NO is pumped to the $\tilde{A}$ or $\tilde{B}$ state of NO; whereupon the fluorescence back to the ground state is monitored at wavelengths shorter than the second photon wavelength. For a stratospheric experiment, hardware simplicity demands that the two photons be from the same laser, although in principle such a constraint is unnecessary.

There is a fairly unique region where a <u>two</u> photon fluorescence experiment can be performed. The long wavelength limit is 285.9 nm, which corresponds to the $\tilde{A} \leftarrow \tilde{X}$ (0-5) band. Photons of longer wavelength can only pump NO transitions in $v \geq 6$ which cannot be formed (see Table 1). The short wavelength limit is probably 259.0 nm, which corresponds to the $\tilde{B} \leftarrow \tilde{X}$ (4-6) band. Photons of shorter wavelength populate high vibrational levels that the second photon cannot sample. Furthermore, the region 259.0-275.0 nm is quite congested, containing the $\tilde{B} \leftarrow \tilde{X}$ (4-6), (5-7), (3-6), (1-5), (2-6), and (0-5) transitions, and the $\tilde{A} \leftarrow \tilde{X}$ (3-7), (2-6), (1-5), and (0-4) transitions (see Figure

Table 1

Threshold Wavelengths (nm) for Production of NO $\tilde{X}\ ^2\Pi$, v = n from NO_2 $\tilde{X}\ ^2A_1$, $v_1=v_2=v_3=0$

Vibrational level	$^2\Pi$ sublevel	Wavelength
0	1/2	397.9
	3/2	395.9
1	1/2	370.2
	3/2	368.5
2	1/2	346.5
	3/2	345.0
3	1/2	325.9
	3/2	324.6
4	1/2	307.9
	3/2	306.8
5	1/2	292.1
	3/2	291.0
6	1/2	278.0
	3/2	277.0
7	1/2	265.4
	3/2	264.5
8	1/2	254.0
	3/2	253.3
9	1/2	243.8
	3/2	243.1

5). The $\tilde{A} \leftarrow \tilde{X}$ (0-5) band at 285.9 nm, however, is free from nearby bands with consequent opportunity for a good null experiment. The tabulated Franck-Condon factor for the $\tilde{A} \leftarrow \tilde{X}$ (0-5) band is within a factor of 2 of the numerically highest of the possible vibrational band Franck-Condon factors. Hence, the $\tilde{A} \leftarrow \tilde{X}$ (0-5) band is a more or less optimal choice for NO_2 detection.

As in the previous section, a simple kinetic model is appropriate to assess the upper bound sensitivity of the suggested two photon fluorescence technique. The relevant rate equations as derived from inspection of Figure 6 are

$$\dot{n}_x = -\sigma_{NO_2} I n_x + \sigma_{NO_2} I n_a \qquad (2\text{-}14a)$$

$$= -\alpha n_x + \alpha n_a$$

$$\dot{n}_a = \sigma_{NO_2} I n_x - (\tau_{diss}^{-1} + \sigma_{NO_2} I) n_a \qquad (2\text{-}14b)$$

$$= \alpha n_x - (\delta + \alpha) n_a$$

$$\dot{n}_c = \tau_{diss}^{-1} n_a + \sigma_{NO} I n_d - (\sigma_{NO} I n_c + \tau_v^{-1}) n_c \qquad (2\text{-}14c)$$

$$= \delta n_a + \beta n_d - (\beta + Q_1) n_c$$

$$\dot{n}_d = \sigma_{NO} I n_c - (\sigma_{NO} I n_d + \tau_f^{-1} + \tau_e^{-1}) n_d \qquad (2\text{-}14d)$$

$$= \beta n_c - (\beta + \gamma + Q_2) n_d$$

where $\alpha = \sigma_{NO_2} I$ (sec^{-1}) is the stimulated absorption (or emission) rate for the first photon, $\beta = \sigma_{NO} I$ (sec^{-1}) is the stimulated absorption (or emission) rate for the second photon, $\gamma = \tau_f^{-1}$ (sec^{-1}) is the spontaneous emission (fluorescence) rate of $NO(\tilde{A}\ ^2\Sigma)$, $\delta = \tau_{diss}^{-1}$ (sec^{-1}) is the dissociative rate for excited NO_2 yielding the fragments $NO(\tilde{X}\ ^2\Pi,\ v'')$ and $O(^3P)$, $Q_1 = \tau_v^{-1}$ (sec^{-1}) is the vibrational quenching rate of $NO(\tilde{X}\ ^2\Pi,\ v'')$, $Q_2 = \tau_e^{-1}$ (sec^{-1}) is the electronic quenching rate of

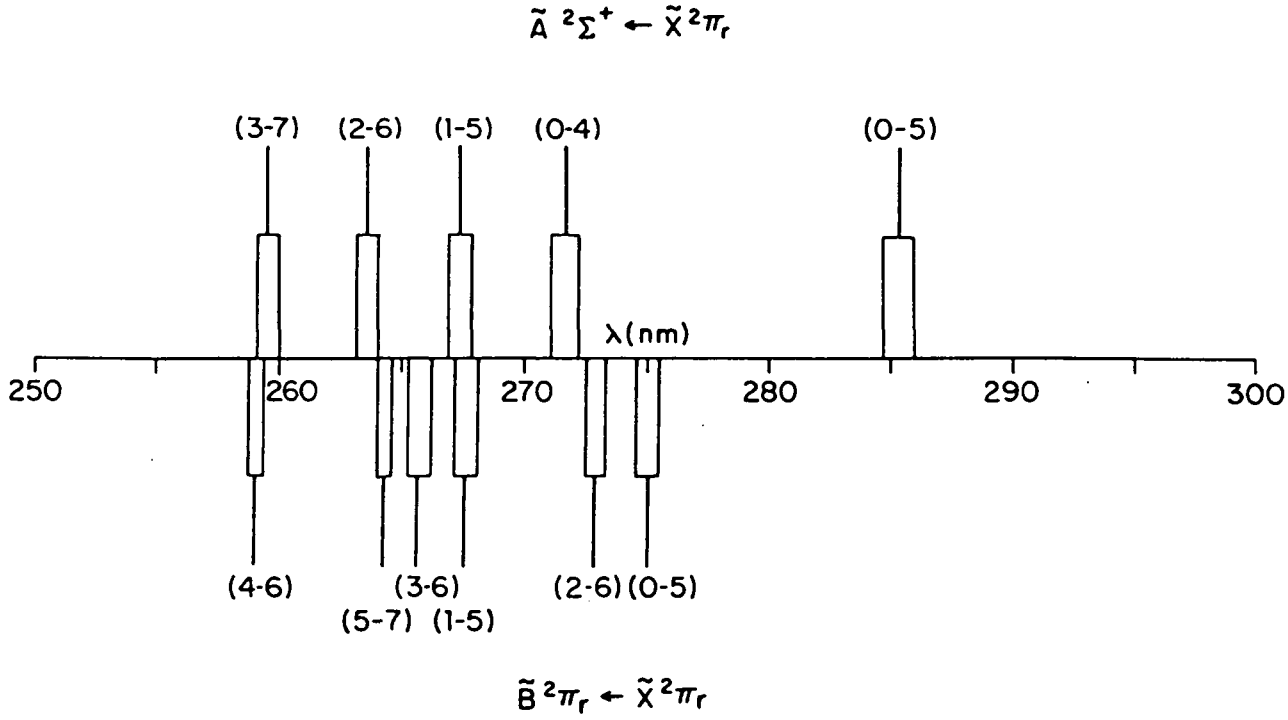

Figure 5. NO bands in the middle ultraviolet.

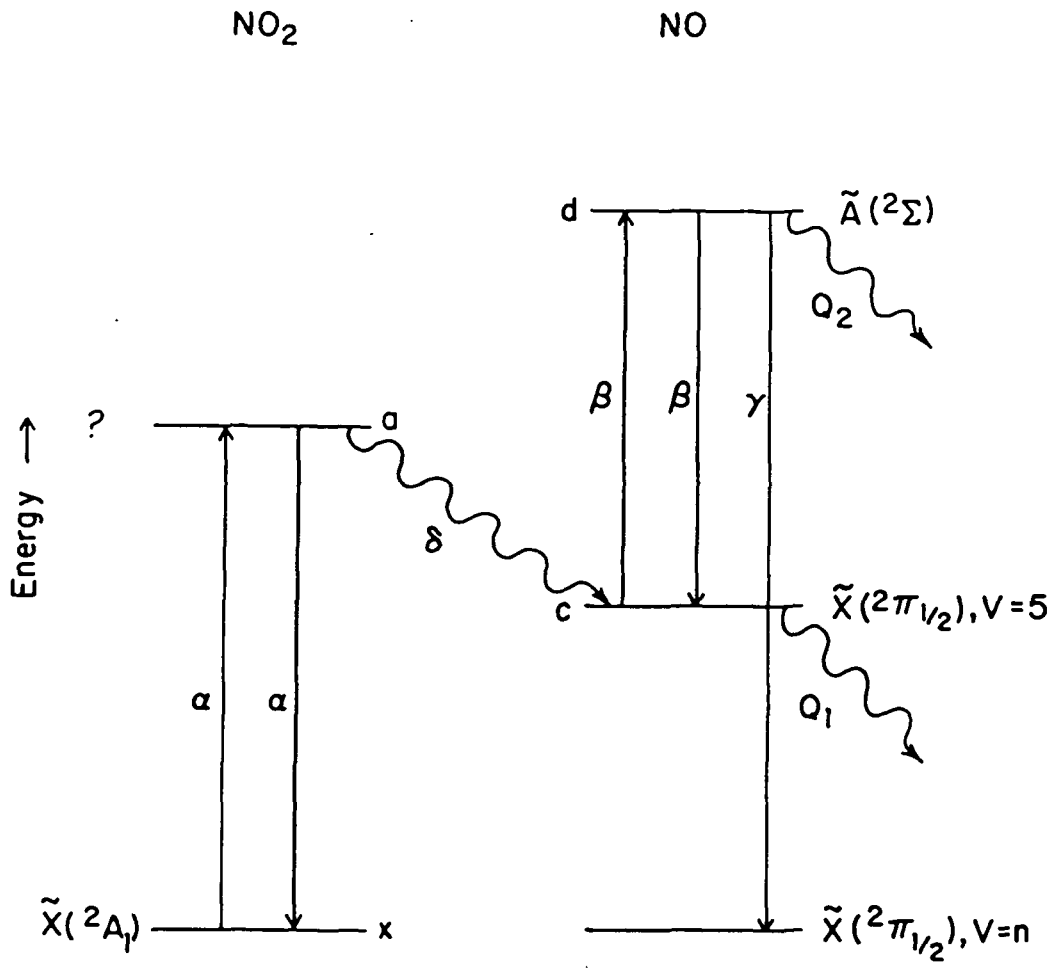

Figure 6. Energy level scheme for two photon fluorescence.

$NO(\tilde{A}\ ^2\Sigma)$, σ_{NO_2} and σ_{NO} (cm^2) are the relevant peak cross sections, and I is the laser flux (photons cm^{-2} sec^{-1} $pulse^{-1}$). Solution of this system for the number of fluorescent photons per pulse F, defined by

$$\dot{F} = \tau_f^{-1} n_d = \gamma n_d$$

is straightforward but lengthy. The initial conditions are

$$n_x(t = 0) = n_{x0} = f \cdot V \cdot [NO_2] \qquad (2\text{-}15a)$$

$$n_a(t = 0) = n_c(t = 0) = n_d(t = 0) = 0; \qquad (2\text{-}15b)$$

the solution for a square pulse of length τ is the sum of two terms: fluoresence emitted during the pulse plus fluorescence after the pulse. The result is derived in detail in Larabee[33], but in abbreviated form,

$$F = [\text{number of fluorescent photons emitted during pulse}] + [\text{number of fluorescent photons emitted after pulse}] \qquad (2\text{-}16)$$

$$= [\alpha\beta\gamma\delta n_{x0}(\text{large sum of exponentials})] + [\alpha\beta\delta n_{x0}\ (1 + (Q_2/\gamma))^{-1}\ (\text{another sum of exponentials})]$$

$$= [\sigma_{NO_2}\sigma_{NO} I^2 \tau_f^{-1} \tau_{diss}^{-1} \cdot f \cdot V \cdot [NO_2]\ (\text{large sum})] + [\sigma_{NO_2}\sigma_{NO} I^2 \tau_{diss}^{-1} (1 + (\tau_e^{-1}/\tau_f^{-1}))^{-1} \cdot f \cdot V \cdot [NO_2]\ (\text{another sum})]$$

As before, the laser independent parameters are estimated first. The spontaneous emission rate τ_f^{-1} is in general a function of upper state vibration and rotation values:

$$(\tau_f(v' = 0, K'))^{-1} = \sum_{v'', K''} A(v' = 0, v'': K', K'')$$

where A is the Einstein A coefficient for spontaneous emission. The lifetime τ_f of NO($\tilde{A}\ ^2\Sigma$) is approximately independent of upper state K' values and therefore $\gamma = (\tau_f(v' = 0))^{-1} = 4.6 \times 10^6\ sec^{-1}$ [34]. The dissociation parameter δ is not known quantitatively but certainly must be of the order of an NO_2 vibrational frequency; hence $\delta = \tau_{diss}^{-1} \approx 10^{13}\ sec^{-1}$. The rates of quenching of NO($\tilde{X}\ ^2\Pi$, v = 1) by atmospheric constituents are slow [35]. Rates for NO($\tilde{X}\ ^2\Pi$, v = 5) quenching are unmeasured, but extrapolation from the v = 1 data indicate that V-V transfer to N_2 or O_2 is the most effective vibrational quenching process in terms of overall rate. There are no v = 1 data for quenching by O_2 since experimental conditions generally allow some formation of NO_2, possibly via

$$NO + O_2 + M \rightarrow NO_3 + M$$
$$NO_3 + NO \rightarrow NO_2 + NO_2.$$

Ground state NO_2 quenches NO($\tilde{X}\ ^2\Pi$, v = 1) very well [35]. The vibrational frequency mismatch between an NO(v = 5 -> v = 4) quantum (1764 cm^{-1}) and an O_2 (v = 1 -> v = 0) quantum (1556 cm^{-1}) is less than with an N_2 (v = 1 -> v = 0) quantum (2331 cm^{-1}). Elementary theory [36] would predict a hundredfold enhancement in the quenching rate of NO(v = 5 -> v = 4) by O_2 than with N_2. As an upper limit for the number of fluorescent photons produced in the two photon process, the rough value [36]

$$k_{Q_1} = 1 \times 10^{-15}\ cm^3\ mol^{-1}\ sec^{-1}$$

is employed and therefore at 30 km

$$Q_1 = k_{Q_1}[M]$$

$$\simeq (1 \times 10^{-15} \text{ cm}^3 \text{ mol}^{-1} \text{ sec}^{-1})(4 \times 10^{17} \text{ mol cm}^3)$$
$$= 4 \times 10^2 \text{ sec}^{-1}.$$

Quenching of $NO(\tilde{A}\ ^2\Sigma^+)$ by O_2 is extremely fast, proceeding at near gas kinetic rates[37]:

$$Q_2 = k_{Q_2}[O_2]$$
$$\simeq (1.5 \times 10^{-10} \text{ cm}^3 \text{ mol}^{-1} \text{ sec}^{-1})(1 \times 10^{17} \text{ mol cm}^{-3})$$
$$= 1.5 \times 10^7 \text{ sec}^{-1} .$$

It is obvious that quenching of the $\tilde{A}$ state of NO is far more important than vibrational quenching of the intermediate $\tilde{X}$ state in determination of the two photon fluorescence yield.

Two cases are considered in determining the laser dependent parameters α and β. Case (1) will employ a Nd:YAG laser pumped dye laser, doubled into the ultraviolet, producing 100 milliwatts average power at 10 Hz in 10 ns pulses. At 285.9 nm and assuming a beam diameter of $\simeq$ 3 mm, the photon flux for case (1) (I_1) is 2.05×10^{25} photons $\text{cm}^{-2}\ \text{sec}^{-1}\ \text{pulse}^{-1}$. Case (2) will employ a copper vapor laser pumped dye laser, doubled into the ultraviolet, producing 100 milliwatts average power at 17 kHz in 30 ns pulses. At 285.9 nm and assuming a beam diameter of $\simeq$ 3 mm, the photon flux for case (2) (I_2) is 4.03×10^{21} photons $\text{cm}^{-2}\ \text{sec}^{-1}\ \text{pulse}^{-1}$. The rationale for considering the two cases is twofold: the flux produced in case (1) saturates the second step completely ($\sigma_{NO} I \gg \tau_f^{-1}$), whereas case (2) is an intermediate case ($\sigma_{NO} I \simeq \tau_f^{-1}$); and in case (1) the pump laser is an electrically inefficient ($\simeq$ .1%) Nd:YAG laser as a pump, while case (2) utilizes a relatively efficient (1%) copper vapor laser as a pump.

Hall and Blacet[29] have measured the cross section σ_{NO_2} and have found σ_{NO_2} at 286 nm to be 1 x 10^{-19} cm^2. Determination of σ_{NO} proceeds as follows. The laser wavelength overlaps the K' = 6-10 levels of the $^0{}_{12}$ branch of the $\tilde{A}\ ^2\Sigma^+$ (v' = 0) <- $\tilde{X}\ ^2\Pi_{3/2}$ (v' = 5) transition[24]; this branch is the bandhead and represents a good choice for a null experiment. The mode structure of the UV laser pulse in general completely overlaps this 0.03 nm section of the band on a pulse average basis. The peak cross section of an individual rotational line is given by Friedl and coworkers[38] as

$$\sigma^{0-5}_{J''J'} = \frac{2}{\Delta\nu_D}\left[\frac{\ln 2}{\pi}\right]^{1/2}\frac{\pi e^2}{mc^2}\frac{S_{J''J'}}{4(2J''+1)}\frac{g(J')}{g(J'')}f_{0-5} \qquad (2\text{-}17)$$

where the Doppler broadened line has a FWHM of $\Delta\nu_D$, e and m are the charge and mass of an electron, c is the speed of light, $S_{J'',J'}$ is the rotational line strength factor[39] f_{0-5} is the vibrational band oscillator strength, and g(J) is the electronic degeneracy. J'' and J' refer to rotational quantum number in the $\tilde{X}\ ^2\Pi$ and $\tilde{A}\ ^2\Sigma^+$ states, respectively. The (0-5) band oscillator strength is obtained from

$$f_{0-5} = f_{0-0}\frac{\bar{\nu}(0-5)}{\bar{\nu}(0-0)}\frac{q(0-5)}{q(0-0)}\frac{|\bar{R}_e(0-5)|^2}{|\bar{R}_e(0-0)|^2} \qquad (2\text{-}18)$$

where $\bar{\nu}(m,n)$, q(m,n), and $\bar{R}_e$ (m,n) are the wavenumber, Franck-Condon factor, and electronic transition moment, respectively, for the m <- n transition. The transition moment variation with r-centroid is not known for the (0-5) band, but maximum variations of $|\bar{R}_e|^2$ for other bands are typically a factor of two[40]. Using this number, the Franck-Condon factors of Nicholls[41], and the measured oscillator strength for

the (0-0) band of 4.0×10^{-4} (cf. Weinstock and others[42] and references therein),

$$f_{0-5} \approx 3.4 \times 10^{-4} .$$

The Doppler width $\Delta\nu_D$ depends on the translational temperature of the nascent NO, but if none of the excess energy appears as translation, T = 240 K (mid-stratosphere) and therefore $\Delta\nu_D = 0.07$ cm^{-1}. The rotational line strength factors $S_{J''J'}$ for a $^2\Sigma - {}^2\Pi$ transition were derived by Earls[43]. Substitution of the appropriate constants for NO produces peak rotational cross sections ranging from 4.6×10^{-16} cm^2 for the O_{12} (K" = 10) line to 5.4×10^{-16} cm^2 for the O_{12} (K" = 6) line. With an average peak cross section of 5.0×10^{-16} cm^2 for the entire bandhead, the pumping rates are

$$\sigma_{NO} I_1 = 1.0 \times 10^{10} \text{ sec}^{-1}$$
$$\sigma_{NO} I_2 = 2.0 \times 10^{6} \text{ sec}^{-1}.$$

Substitution of these values into equation (2-16) yields

$$F_1 = 2.5 \times 10^{-3} \cdot f \cdot V \cdot [NO_2] \quad \text{(photons pulse}^{-1}\text{)} \qquad (2\text{-}20a)$$
$$F_2 = 2.8 \times 10^{-7} \cdot f \cdot V \cdot [NO_2] \quad \text{(photons pulse}^{-1}\text{)} \qquad (2\text{-}20b)$$

The fraction f of NO_2 molecules participating in the two photon transition is composed of two parts

$$f = f_{NO_2} f_{NO}$$

where f_{NO_2} is the fraction of NO_2 molecules involved in the first photon transition and f_{NO} is the fraction of nascent NO molecules involved in the second photon transition. By an argument analogous to that

presented in the section on two photon ionization, f_{NO_2} is identically unity. The fraction f_{NO} is defined as

$$f_{NO} = [\text{fraction of nascent NO in } v = 5] \times [\text{fraction of nascent NO in } {}^2\Pi_{3/2} \text{ sublevel}] \times [\text{fraction of nascent NO in } K'' = 6 \text{ through } 10]$$

Slanger and coworkers[24] have found that approximately 40% of the dissociating NO_2 appears in the highest accessible vibrational level, a distinctly nonstatistical distribution. This nonequilibrium disposal of the excess energy has been observed throughout the ultraviolet[44]. There seems no a priori reason for the dissociation process to favor either spin-orbit sublevel, so the nascent populations of $^2\Pi_{1/2}$ and $^2\Pi_{3/2}$ are assumed equal. The rotational temperature of the nascent NO is 130 K for $K'' \leq 8$ and 750 K for $K'' > 9$[24]. Using the diatomic rotational term values and distribution, substitution of the NO ground state constants yields $f_{NO} = 2.4 \times 10^{-3}$. The final result for fluorescent photon production rate is

$$F_1 = 4.2 \times 10^{-7} [NO_2] \text{ photons pulse}^{-1} = 4.2 \times 10^{-6} [NO_2] \text{ photons sec}^{-1}, \quad (2\text{-}21a)$$

$$F_2 = 4.7 \times 10^{-11} [NO_2] \text{ photons pulse}^{-1} = 8.0 \times 10^{-7} [NO_2] \text{ photons sec}^{-1}. \quad (2\text{-}21b)$$

The counterpart of equation (2-1) for this technique is

$$S = [\text{fluorescent photon production rate}] \cdot [\text{instrumental weighting function}] \quad (2\text{-}22)$$

where the fluorescent photon production rate (photons sec^{-1}) is given by equations (2-21). The instrumental function is

$$\begin{bmatrix}\text{instrumental} \\ \text{weighting function}\end{bmatrix} = \frac{A\Omega}{4\pi} \cdot \int_0^{\nu_{(0-0)}} \phi(\nu_e, \nu) T(\nu) \eta(\nu) d\nu \quad (2\text{-}23)$$

where the various components have been defined in the section on laser induced fluorescence. Fluorescence from $NO(\tilde{A}\ ^2\Sigma^+, v' = 0)$ is predominantly in the γ vibrational bands $(0 \leftarrow 0)$, $(1 \leftarrow 0)$, $(2 \leftarrow 0)$, $(3 \leftarrow 0)$ and $(4 \leftarrow 0)$, so the integral in equation 2-23 may be replaced by a sum without loss of accuracy. The fraction of total fluorescence emitted into any one vibrational band is the ratio of the Einstein A coefficient for the specific band to the total probability for spontaneous emission:

$$\phi = \frac{A(v', v'')}{A(v')} \quad (2\text{-}24)$$

$$= \frac{\bar{\nu}^3(v', v'') q(v', v'') |\bar{R}_e(v', v'')|^2}{\sum_{v''} \bar{\nu}^3(v', v'') q(v', v'') |\bar{R}_e(v', v'')|^2}$$

where all factors are defined as in equation 2-20. Table (2) lists the five vibrational bands with their respective fractional intensities. The optics transmission function $T(\nu)$ is dominated by the characteristics of the interference filter employed to block laser scatter and red-shifted contaminant fluorescence. An ideal filter would transmit with no loss in the region between 220 nm $(0 \leftarrow 0)$ and 272 nm $(4 \leftarrow 0)$ and have infinite blocking elsewhere. The most advantageous 'real' filter is a 239 nm bandpass filter with FWHM of 10 nm, peak transmission of 12%, and extinction of 10^4 at 222.6 nm. Typical photomultiplier efficiencies in the middle ultraviolet are 15% and roughly independent

Table 2

Band Intensities of the NO ($\tilde{A}\ ^2\Sigma^+ \rightarrow \tilde{X}\ ^2\Pi$) Transition

Band	Band origin (nm)	Fractional intensity[a]
(0, 0)	227.5	0.15
(0, 1)	237.6	0.25
(0, 2)	248.5	0.26
(0, 3)	260.3	0.18
(0, 4)	273.0	0.10
(0, 5)	286.8	0.04
(0, 6)	301.9	0.01

[a]Calculated from equation (2-24) of the text, utilizing the data of Callear and others[40] and Nicholls[41].

of wavelength. If the same optical cell as described in the LIF section is utilized, the value of the instrumental weighting function is 7.2×10^{-2} counts photon^{-1}. Therefore

$$S_1 = 3.0 \times 10^{-7}\ [NO_2]\ \text{counts sec}^{-1}$$
$$S_2 = 5.8 \times 10^{-8}\ [NO_2]\ \text{counts sec}^{-1}$$

For the benchmark case of $[NO_2] = 1 \times 10^9$ mol cm^{-3},

$$S_1 = 300\ \text{counts sec}^{-1} \qquad (2\text{-}25a)$$
$$S_2 = 58\ \text{counts sec}^{-1} \qquad (2\text{-}25b)$$

as upper bounds.

The advantage of the two photon fluorescence scheme lies chiefly in the ability of this technique to eliminate laser scatter and red-shifted fluorescence as noise sources. The technique is specific, as NO ($\tilde{X}\ ^2\Pi$, v = 5) does not exist in appreciable quantities in ambient NO, and experimentally one can tune off the O_{12} bandhead in the second step to perform a null experiment in any event. Disadvantages are the low sensitivity and, in case (1), the low electrical efficiency of Nd:YAG lasers. Hardware complexity is moderate.

Photofragment Fluorescence (PFF)

Radiation of sufficient energy may dissociate a molecule and leave one of the fragments in an excited state, which can then subsequently fluoresce. The kinetics of the vacuum ultraviolet photodissociation of NO_2 have been treated in detail by Nee[45]. The count rate expression is

$$S = I_0(QY\cdot\sigma_0)\cdot\frac{\Delta\Omega}{4\pi}\cdot l\cdot\frac{[NO_2]}{1 + a_M[M]}\cdot\phi(\lambda_e)\cdot\int_0^{\lambda_e} T(\lambda)\eta(\lambda)d\lambda \quad (2\text{-}26)$$

where the absorption is assumed optically thin. In this equation, I_0 is the intensity of excitation in units of photons sec^{-1}, QY is the quantum yield of excited NO, σ_0 (cm^2) is the peak absorption cross section of NO_2 at the excitation frequency, $\Delta\Omega$ is the solid angle subtended by the detector, T is the transmission of the collection optics including any interference filter, η is the quantum efficiency of the detector, l (cm) is the distance over which the VUV photons are absorbed and fluorescent photons are emitted, $a_M = k_q\tau$ is the quenching coefficient ($torr^{-1}$), k_q is the quenching rate constant and τ is the mean lifetime (radiative and predissociative) of the nascent NO, [M] (torr) is the concentration of quencher M, and ϕ is the quantum yield of fluorescence as before.

Vacuum ultraviolet radiation is strongly absorbed by molecular oxygen and hence PFF excitation sources (in the stratosphere) are limited to 'windows' in the O_2 absorption spectrum. Such a window exists at the atomic hydrogen Ly-α line, 121.6 nm[46]. Radiation of this energy can dissociate NO_2 and form NO in the $\tilde{a}\ ^4\Pi_i$, $\tilde{A}\ ^2\Sigma^+$, $\tilde{B}\ ^2\Pi_r$, $\tilde{b}\ ^4\Sigma^-$, $\tilde{C}\ ^2\Pi_r$, $\tilde{D}\ ^2\Sigma^+$ electronic states (see Table 3). The branching ratios are unknown, but experiments by Nee have detected fluorescence from both the $\tilde{A}$ and $\tilde{B}$ states. There is some indication that the $\tilde{B}$ state may be formed in higher yield than $\tilde{A}$ state, with a quantum yield QY of $\simeq$ 2.8%. The quenching of β fluorescence bands from the $\tilde{B}\ ^2\Pi$ state exhibits an anomalous pressure dependence, which has been interpreted[45] as collision induced curve crossing from nascent $\tilde{b}\ ^4\Sigma$ to $\tilde{B}\ ^2\Pi$.

Estimation of the numerical values in equation (2-26) is straightforward. A well-made Lyman-α lamp excited by a microwave discharge will produce 10^{15} photons sec^{-1} in a fairly well collimated beam. The absorption cross section of NO_2 at 121.6 nm is 9.8×10^{-18} cm^2 [31]; as an upper limit , QY is set to 6% to allow for the unknown (but $<$ 0.5) branching ratio to NO ($\tilde{A}\ ^2\Sigma^+$). The quantum yield of fluorescence ϕ is assigned the value unity. As in the previous sections, an optimal collection cell is assumed: $\Delta\Omega/4\pi \simeq 0.2$. The fluorescence spectrum of nascent NO formed by 121.6 nm photolysis consists largely of β bands, NO ($\tilde{B}\ ^2\Pi_r$, v' = 0 -> $\tilde{X}\ ^2\Pi_r$, v'' = n) and γ bands, NO ($\tilde{A}\ ^2\Sigma^+$, v' = 0 -> $\tilde{X}\ ^2\Pi_r$, v'' = n). To eliminate contaminant fluorescence as a noise source, the appropriate bandpass filter transmits fluorescence in the most intense few bands as before. The γ bands are the most intense and thus the most acceptable filter is that chosen for the two photon fluorescence experiment. The photodetector quantum efficiency η is

Table 3

Threshold Wavelengths (nm) for Photodissociation of NO_2 into Products

NO/O	^3P	^1D	^1S
$\tilde{X}\ ^2\Pi_r$	397.9	243.9	169.7
$\tilde{a}\ ^4\Pi_i$	157.3	125.9	102.7
$\tilde{A}\ ^2\Sigma^+$	144.7	117.7	
$\tilde{B}\ ^2\Pi_r$	140.7		
$\tilde{b}\ ^4\Sigma^-$	135.4		
$\tilde{C}\ ^2\Pi_r$	129.4		
$\tilde{D}\ ^2\Sigma^+$	127.9		
$\tilde{B}'\ ^2\Delta_i$	117.0		

O_2/N	^4S	^2D	^2P
$\tilde{X}\ ^3\Sigma_g^-$	275.1	180.0	153.4
$\tilde{a}\ ^1\Delta_g$	225.9	157.6	136.8
$\tilde{b}\ ^1\Sigma_g^+$	201.8	145.5	127.6
$\tilde{c}\ ^1\Sigma_u^-$	144.1	112.9	101.8
$\tilde{A}'\ ^3\Delta_u$	140.8		
$\tilde{A}\ ^3\Sigma_u^+$	139.4		
$\tilde{B}\ ^3\Sigma_u^-$	116.1		

again 0.15. The dominant quencher of $\tilde{A}$ state NO is O_2, for which a_M is 1.2 $torr^{-1}$ [37]. Quenching rates of $\tilde{B}$ state NO in O_2 are unknown. A lower limit for quenching coefficient and hence an upper bound for the photofragment fluorescence signal is obtained by assuming N_2 is the dominant quencher of $\tilde{B}$ state fluorescence. The quenching coefficient a_M in nitrogen is 0.06 $torr^{-1}$. With [M] = 4×10^{17} mol cm^{-3} $\simeq$ 30 km altitude and $[NO_2] = 1 \times 10^9$ mol cm^{-3},

$$S = 5.3 \times 10^{-7} [NO_2]$$
$$= 530 \text{ counts } sec^{-1}.$$

The advantages of photofragment fluorescence as a detection technique for stratospheric NO_2 lie in the relatively high cross sections and quantum yields, and the hardware simplicity of the experiment. The disadvantage is principally the lack of a null experiment; there is no wavelength agility and hence no logically conclusive way to prove that the detected photons originated from photofragmentation of NO_2. Isolation of fluorescent photons to specifically γ band fluorescence implicates NO_2 as the source species, but does not differentiate this signal from an undetermined continuum source, for example.

B. An Evaluation

Table 4 is a summary of the results of the section on candidate techniques. Each technique has advantages and disadvantages. The highest weight must be placed on ultimate sensitivity, since the ability to differentiate signal from noise is problematic without adequate signal levels. Given the upper bound nature of the preceding calculations, the laser induced fluorescence technique is very likely the most sensitive technique. Specificity hopefully rests in narrow linewidth excitation; a comprehensive search for isolated lines in the yellow and orange portions of the visible spectrum is the subject of the next section.

Table 4

Summary of Candidate Techniques for
in situ
Detection of Stratospheric NO_2

Technique	Upper limit to signal at $[NO_2] = 1 \times 10^{-3}$ mol cm^{-3} sec^{-1} counts	Sensitivity	Specificity	Hardware Complexity
Laser induced fluorescence (LIF)	10000	Good	Poor (possibly good)	Medium
Two photon ionization (R2PI)	170	Fair	Good	High
Two photon fluorescence (TPF)				
a. Nd:YAG pump	300	Fair	Good	Medium
b. Cu vapor pump	58	Poor	Good	Medium
Photofragment fluorescence (PFF)	530	Fair	Poor	Low

C. Quantification of the Laser Induced Fluorescence Technique

The design goal of a sensitive and specific in situ detection instrument for stratospheric NO_2 requires quantification of each of the parameters in equation (2-1). The individual components break into two classes: structly molecular parameters such as the fluorescence cross section and quenching coefficients, and instrument-specific parameters. This section addresses the components of equation (2-1) specific to the NO_2 molecule, whereas the final section details an optimization of the hardware associated with NO_2 detection.

Molecular Properties of NO_2

The absorption cross section σ is a function of excitation frequency, whereas the quantum yield of fluorescence ϕ and quenching constant a_M are functions of both excitation frequency and detection frequency. An ideal experiment would quantify the cross section σ and investigate independently the dependences of ϕ and a_M on ν_e and ν (and completely remove the instrumental weights). Since the 'visible' spectrum of NO_2 extends from the ultraviolet to the photographic infrared, this ideal experiment subtends a large parameter space.

A set of experiments that provide the requisite information to quantify equation (2-1) and yet retain a tractible parameter space is difficult to define. However, Kaufman and coworkers[45] have found that NO_2 fluorescence quenching is approximately independent of excitation

frequency. Thus one may take excitation spectra (varying the frequency of excitation and collecting all fluorescence within the experimental bandpass) while maintaining constant quencher pressures and obtain information on the fluorescence cross section ($\phi\sigma$). Then at selected laser frequencies, one can perform quenching experiments. Within these assumptions, this set of experiments pinpoints the optimal excitation frequency as a function of cross section, quantum yield, and susceptibility to quenching.

Both low and high resolution spectra of NO_2 show that the line congestion in the blue (< 500 nm) is much higher than toward the red (> 500 nm). The line overlap generally prevents quantitative determination of individual peak cross sections for rotational lines in the blue, so it is not clear a priori whether the high (low resolution) cross section found in the blue is the result of rotational lines with intrinsically high cross section or simply overlapping lines. An adequate null experiment requires a low line density. Based on the low and high resolution spectra of Zare and coworkers[46], the 565 to 595 nm region of the NO_2 visible system was examined with Doppler limited resolution with the apparatus to be described in the following section. Choice of spectral region was dictated by several considerations. Small sections of this region (particularly near 593 nm) have been investigated at high resolution by many authors[47] and thus the work in this thesis could be dovetailed with the previous work. At the outset of experimentation, an extensive literature search was made to gauge (on both theoretical and experimental grounds) the likelihood of finding a region of the NO_2 spectrum with adequate separation of rotational lines; the 565-600 nm region is thought to encompass the transition region between 'high' and

'low' density. And lastly, from an experimental viewpoint, the laser dye Rhodamine 590 is most efficient in this region. Since this dye is one of the most efficient of all dyes, a source of excitation photons with adequate strength and linewidth is more probable in this region of the spectrum than in other regions of the spectrum.

Experimental Apparatus

Flow System

Excitation of NO_2 molecules took place in a fluorescence cell fabricated from stainless steel and pumped along one axis by either a Varian NRC diffusion pump (Model HSA-150) or a Sargent-Welch vacuum pump (Model 1397). Typically a 2% dilution of NO_2 in a buffer gas was prepared in a stainless steel, Teflon, and glass manifold. The dilute NO_2 flowed into the cell via a needle valve (Hoke 1656) and roughly two meters of 1.5 mm diameter Teflon tubing acting as a conductance limiter. The thin tubing was threaded through a stainless steel tee and ended approximately 4 cm from the center of the fluorescence cell. Buffer gas entered the cell through the main body of the tee. Measurements of the NO_2 flow rate with a Hastings 100 sccm mass flowmeter (Model LF-100) indicated no back pressure effects on the flow from the manifold (to 1.2 torr buffer gas pressure). After passing through the cell, the NO_2 was trapped by a glass trap cooled to 77 K by liquid nitrogen.

NO_2 was obtained from Matheson (stated purity 99.5%) and subjected to several freeze-pump-thaw cycles at 195 K to remove NO impurity. NO_2 samples were stored in a large reservoir shielded from ambient light.

Repurification of the NO_2 sample was performed every two or three days at first, but as experimentation proceeded the repurification period was extended to approximately every five days with (verifiably) no experimental effect. The buffer gases were (1) Airco pre-purified N_2 (stated purity 99.995%) for the quenching and cross section experiments and (2) Matheson HP helium (stated purity 99.995%) for some initial survey excitation spectra; neither buffer gas was repurified.

Pressures in both the cell and manifold were monitored by either a 10 torr absolute MKS Baratron (222-HS-A) capacitance manometer or a 1000 torr absolute MKS Baratron (227-AHS-B) capacitance manometer. Pressures of NO_2 were corrected for dimer formation. Base pressure in the cell was 5×10^{-6} torr. The gas handling system is depicted in Figure 7(a).

Optical Train

Two separate laser systems served as sources of excitation photons. For the excitation spectra, a Coherent Model 699-29 actively stabilized cw ring dye laser pumped by a Coherent Model CR-18 argon ion laser was employed. This dye laser system is referenced to an absolutely calibrated optical activity monochromator, and addresses a particular visible frequency with 200 MHz accuracy. Scan rates and data intervals are switch selectable, with total continuous scan widths of 10 THz ($\simeq$ 330 cm^{-1}) possible. The laser linewidth is quoted by the manufacturer as less than 500 KHz and was observed to be less than 50 MHz (note that an NO_2 Doppler width at 295 K is 920 MHz). Both the active stabilization components and the birefringent tuning element are controlled by an Apple II+ microcomputer with software provided by Coherent. Up to

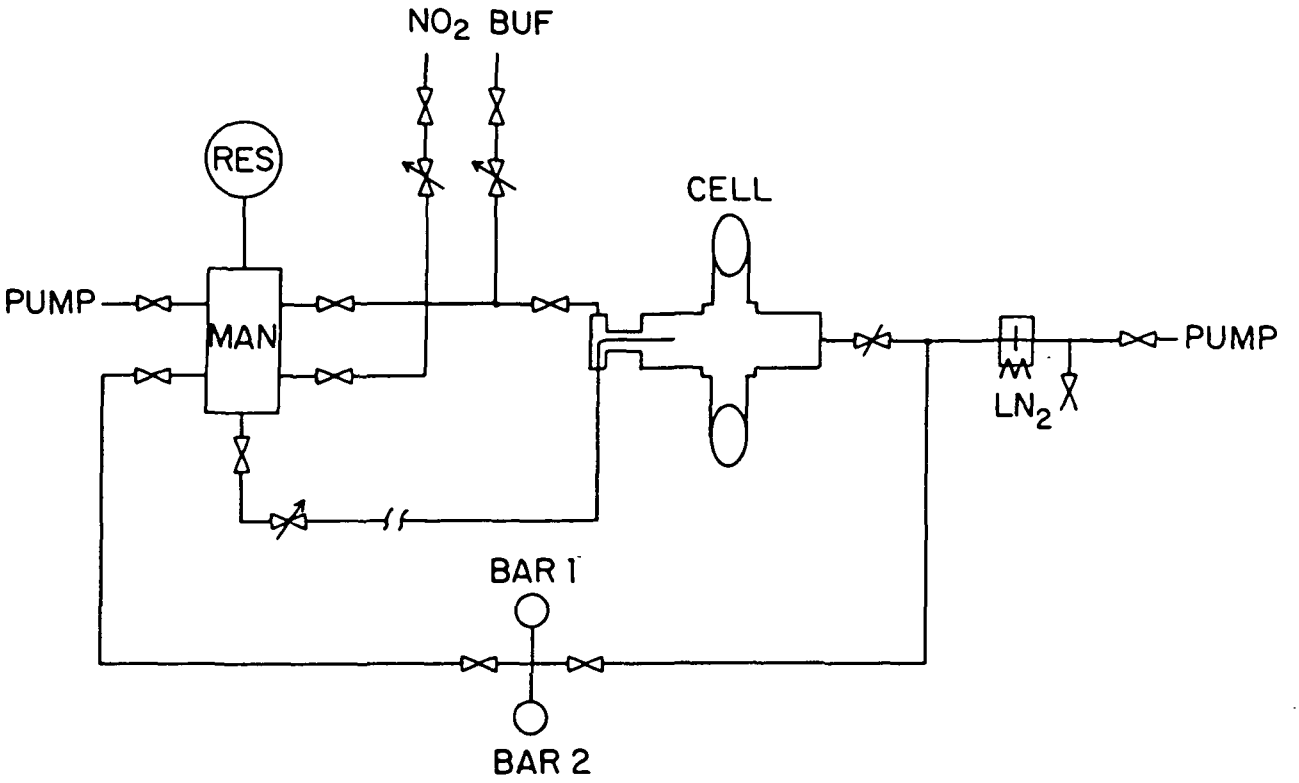

Figure 7(a). Flow geometry for excitation spectra and quantitative measurements. RES = two liter reservoir; MAN = stainless steel manifold; and BAR1 and BAR2 are MKS Baratron pressure transducers.

three analog data channels are digitized and stored in the Apple's virtual memory. Screen display and permanent storage on 5 1/4'' floppy disk are both available.

The second laser system was a Coherent Model 599-21 actively stabilized cw dye laser pumped by a Coherent Model 52 argon ion laser. This system had linewidth and stability attributes comparable to the Model 699-29 system, but was limited in 'hands-off' tuning to 30 GHz = 1 cm^{-1} = 0.035 nm at 590 nm.

These dye lasers are optically sophisticated, reliable, but very alignment-sensitive. Both dye laser systems incorporate intracavity etalons as line narrowing elements. The intracavity assembly (ICA) is comprised of two etalons, a thin etalon and a piezotranslator driven thick etalon. These etalons are sufficient to suppress multimode oscillation with careful alignment. The output of the laser is passed through an oven stabilized reference spherical interferometer, generating composite frequency and amplitude information. This signal is compared to a signal containing only amplitude information to form a discriminant with only frequency information. The derived error signal is used to adjust the cavity length by driving a high frequency piezo-mounted cavity mirror and an intracavity scanning Brewster plate. The electronic circuitry is sufficient to maintain 'lock' under most operating conditions. However, scanning the dye laser frequency by tuning any of the frequency-selective cavity elements necessarily upsets the efficiency of other elements. The CR-599-21 system scans approximately 30 GHz before one must shift another thin etalon mode and relock. The advantage of the CR-699-29 system is that this bookkeeping is controlled

by computer. The computer system automatically shifts etalon modes to connect 30 GHz scans and maintain output power levels. At the start of a new scan the laser frequency is adjusted to the value stored at the end of the previous scan. Nonetheless, the servo loops that allow the computer to control the various etalons, plates, and filters are occasionally saturated. Seamless scans of 15 cm^{-1} could be obtained, but in practice there were usually slight frequency hops and glitches, especially at the extremes of the dye gain curve. The moral is to provide some sort of absolute frequency calibration despite the manufacturer's claims and thus not depend upon etalon fringes as the sole calibration agents.

The single mode character of the output from the dye lasers was monitored by a Tropel Model 240-1 spectrum analyzer driven by a Tropel Model 251 Spectrum Analyzer Controller. The spectrum analyzer is a mode-degenerate confocal spherical Fabry-Perot interferometer with a 7.5 GHz free spectral range and 50 MHz resolution. Typical single mode output powers were 60 mw for the 599-21 system (at 3.5 watts multiline input from the Model 52 ion laser) and 400 mW for the 699-29 system (at 7 watts multiline from the CR-18), as measured by a Scientech calorimeter (Model 36-0001). Absolute wavelength calibrations were obtained by synchronous I_2 absorption spectra and subsequent comparison with the I_2 line atlas of Gerstenkorn and Luc .[48]

Laser photons entered the fluorescence cell on an axis of symmetry orthogonal to the flow axis. To minimize scattered light, quartz Brewster windows and baffles were mounted on both entrance and exit apertures, and interior of the cell was painted black with Solarcoat 50

(Zuel Corporation). Fluorescence was observed from the center of a sphere of 2.5 cm radius; molecules could travel 2.5 cm radially outward before encountering a wall.

NO_2 fluorescence was monitored on the third orthogonal axis. The photodetector was a baffled photomultiplier tube with an S-20 photocathode (EMR Model 542 E-06) mounted in a photon counting package (Spacom SE 324). A 20 cm black tube was mounted opposite the PMT photocathode to serve as a target. A red-pass filter (Oriel # 5130) with cut-on wavelength 550 nm served to eliminate room light, though not laser light. Rayleigh scattering was used to calibrate the cell (see below) and thus laser scatter was minimized by good design rather than brute force filtering. Pulses from the photon counting package were accumulated for 1 sec intervals by a Hewlett Packard counter (Model 5300B), converted to an analog voltage with a Hewlett Packard digital-to-analog converter (Model 5311), and fed to either a strip chart recorder or one of the three analog inputs to the Apple data acquisition system. The complete optical train is shown schematically in Figure 7(b).

Excitation Spectra

Doppler-limited excitation spectra in the 565 nm, 571 nm, 580 nm, 585 nm, and 593 nm regions are shown in Figures 8, 9, 10, 11(a) through (2), and 12, respectively. The spectra are normalized to incident laser intensity. Concentrations of NO_2 and M are held constant for all spectra.

Assignment of the vibrational and rotational quantum numbers for each of the individual rotational lines in the 565-590 nm region is a quite difficult if not impossible task, at least based on the spectra

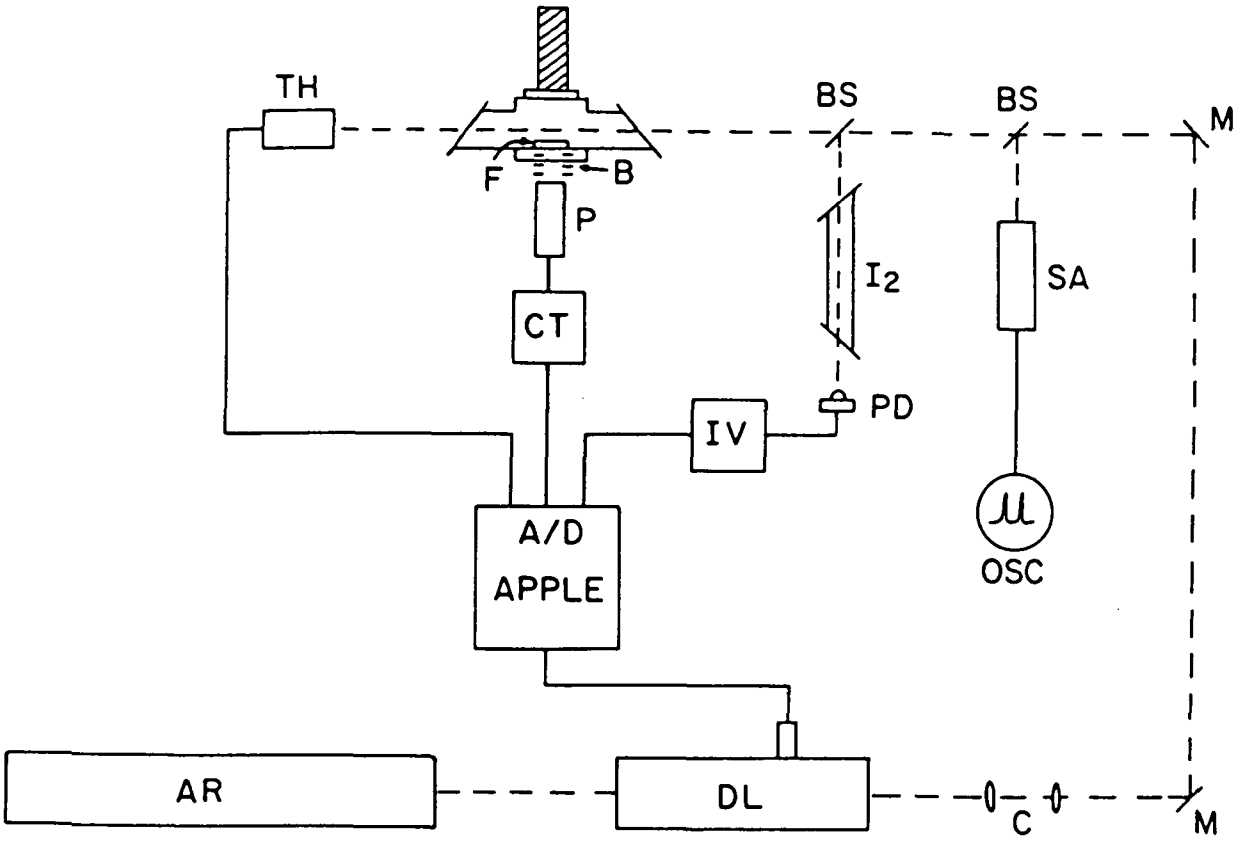

Figure 7(b). Optical geometry for excitation spectra and quantitative measurements. AR = argon ion laser; DL = dye laser; C = collimating optics; M = mirrors; BS = beam splitter; SA = spectrum analyzer; OSC = oscilloscope; I_2 = iodine absorption cell; PD = photodiode; IV = current to voltage converter; F = long pass optical filter; B = baffle; P = photomultiplier tube in photon counting package; CT = counter; and TH = thermopile.

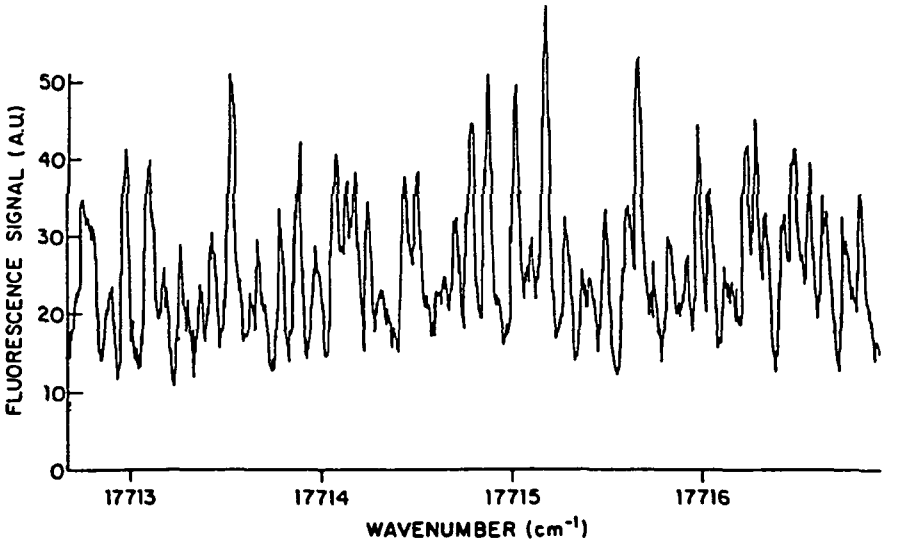

Figure 8. Excitation spectrum of NO_2 in the 565 nm region, at room temperature and low pressure ($[NO_2] = 1.7 \times 10^{-3}$ torr, $[NO_2]/[M] = 0.021$). Spectrum is normalized to incident intensity.

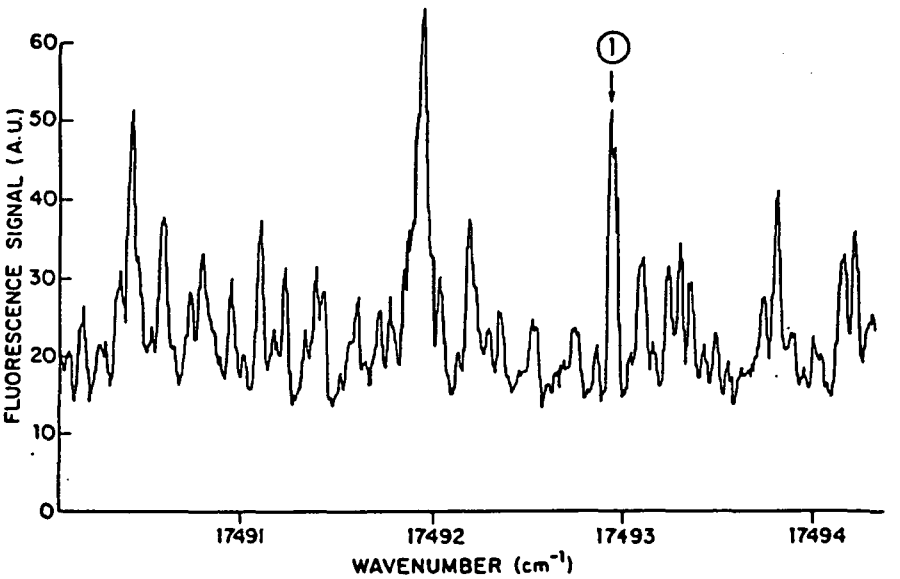

Figure 9. Excitation spectrum of NO_2 in the 571 nm region; *same experimental conditions as for Figure 8.*

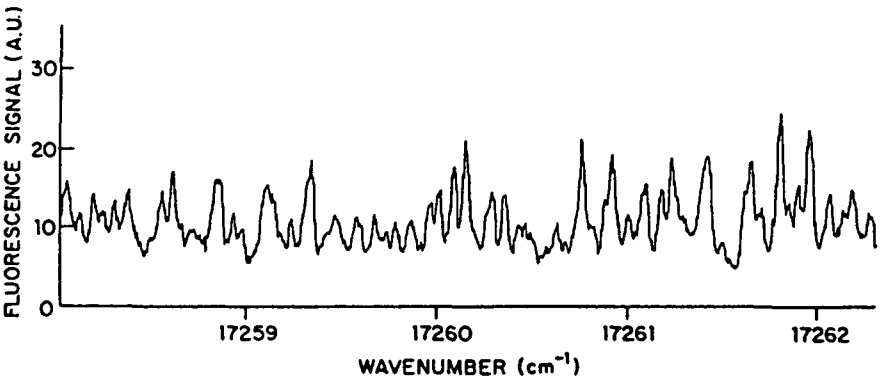

Figure 10. Excitation spectrum of NO_2 in the 580 nm region; same experimental conditions as for Figure 8.

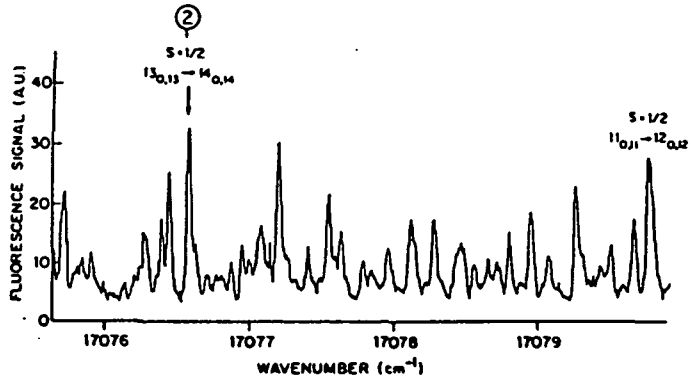

Figure 11(a). Excitation spectrum of NO_2 in the 585 nm region; same experimental conditions as for Figure 8.

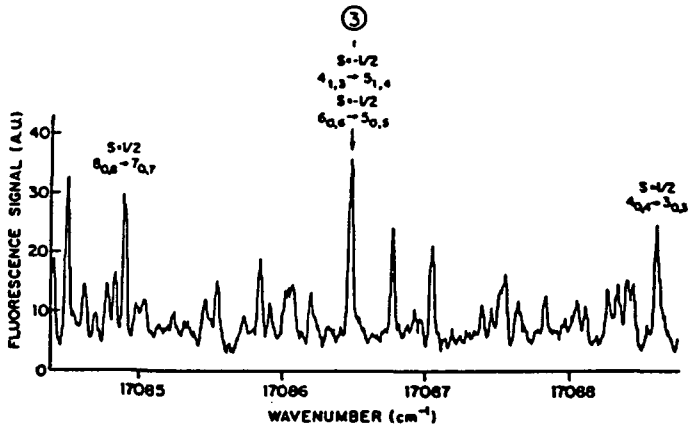

Figure 11(b). Excitation spectrum of NO_2 in the 585 region; same experimental conditions as for Figure 8. The peaks with signals greater than 15 are all assigned P branch transitions; the assignments are omitted for clarity.

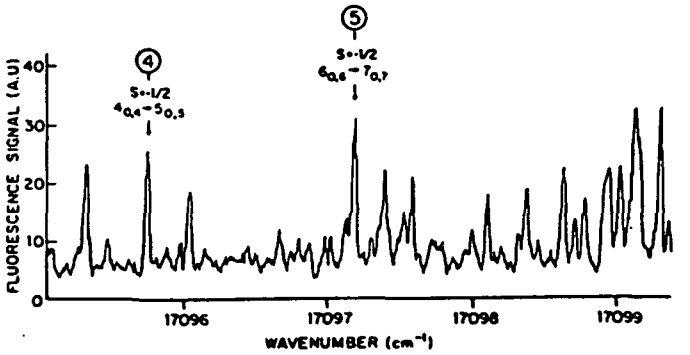

Figure 11(c). Excitation spectrum of NO_2 in the 585 region; same experimental conditions as for Figure 8. The peaks with signals greater than 15 are assigned R branch transitions; the assignments are omitted for clarity.

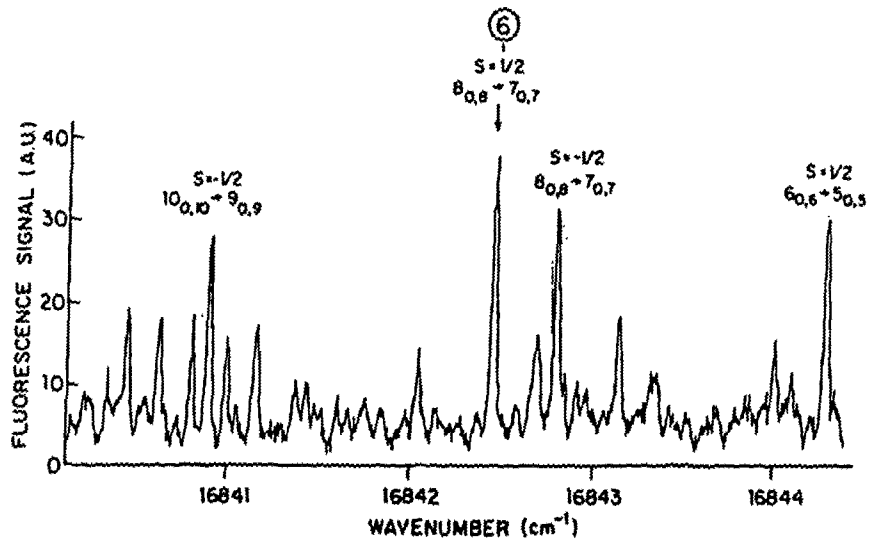

Figure 12. Excitation spectrum of NO_2 in the 593 nm region; same experimental conditions as for Figure 8. All prominent lines with intensities greater than 15 have been assigned by Stevens and Zare.[9]

obtained here. Tentative vibrational analysis of the $\tilde{A}^2B_2 \leftarrow \tilde{X}^2A_1$ absorption system has recently been performed by Bolduan and Jodl.[49] By entraining NO_2 molecules in solid Xe matrices, they have simplified the absorption spectrum by removing most of the initial state vibrational and rotational excitation, much as in a supersonic effusive beam. Many of the $\tilde{A}(n_1n_2n_3) \leftarrow \tilde{X}(000)$ transitions were identified for the first time. In addition, rotational analysis of the 585 nm band has recently been performed by Persch[50] to supplement the well known rotational assignments[47] of the 593 nm band. These rotational assignments are confirmed to within approximately 250 MHz by this work and are listed where possible.

The 565 nm and 571 nm bands are clearly too dense for an adequate null experiment, though specific peaks are approximately two times higher in cross section than peaks in the other three bands. Certain peaks, marked in Figures 11 and 12, were adjudged to be suitable compromises between high cross section and line congestion. Approximately 850 'strong' lines in the 565-595 nm region were surveyed. The chosen lines were then subjected to quantitative quenching and cross section measurements.

Quenching of NO_2 Fluorescence

The classical Stern-Volmer model for quenching of fluorescence by a buffer gas must be modified when transitions within the upper manifold can occur. Laser photons of frequency $\Delta\nu_e$ coherently excite NO_2 molecules, initially in a state $|k\rangle$, to an excited state $|m\rangle$. The

excited molecules can either fluoresce to the ground state manifold (with radiative rate k_f), undergo a shift in rotational quantum number at the expense of the other degrees of freedom (with rate k_{int} [51]), or exchange energy with a collision partner (with quenching rates k_Q and k_{SQ} for collisions with a buffer gas or NO_2, respectively). The resulting states in the upper manifold can then fluoresce or exchange energy, and so on. The mechanism is schematically shown in Figure 13. The process described by k_{int} violates both energy and angular momentum conservation in an isolated NO_2 molecule, but becomes allowed when the molecule suffers collisions. The rates k_Q and k_{SQ} model the more common vibrational and rotational energy exchange mechanisms (see, e.g., Callear [52]). The mechanism in Figure 13 ignores electronic quenching, as this process is known to be two orders of magnitude slower in NO_2 than vibrational, rotational or internal processes [53].

Each time a molecule makes a transition within the upper manifold, there is a probability P_i that this transition results in fluorescence to the ground state:

$$P_i = \frac{k_{fi}}{k_{fi} + (k_{int} + k_Q)[M] + k_{SQ}[NO_2]}$$

The observed fluorescence signal S is proportional to a sum over states $|i\rangle$:

$$S(\nu_e, \nu) \propto \int_0^{\nu_e} T(\nu)\eta(\nu) \sum_{i=m}^{\infty} f_i P_i(\nu_e, \nu)[NO_2^*]_i \, d\nu \qquad (3\text{-}1)$$

where the probability P_i is in general a function of excitation and detection frequency, and $[NO_2^*]_i$ designates the upper state population in a state $|i\rangle$. The function f_i monotonically decreases from 1 for i

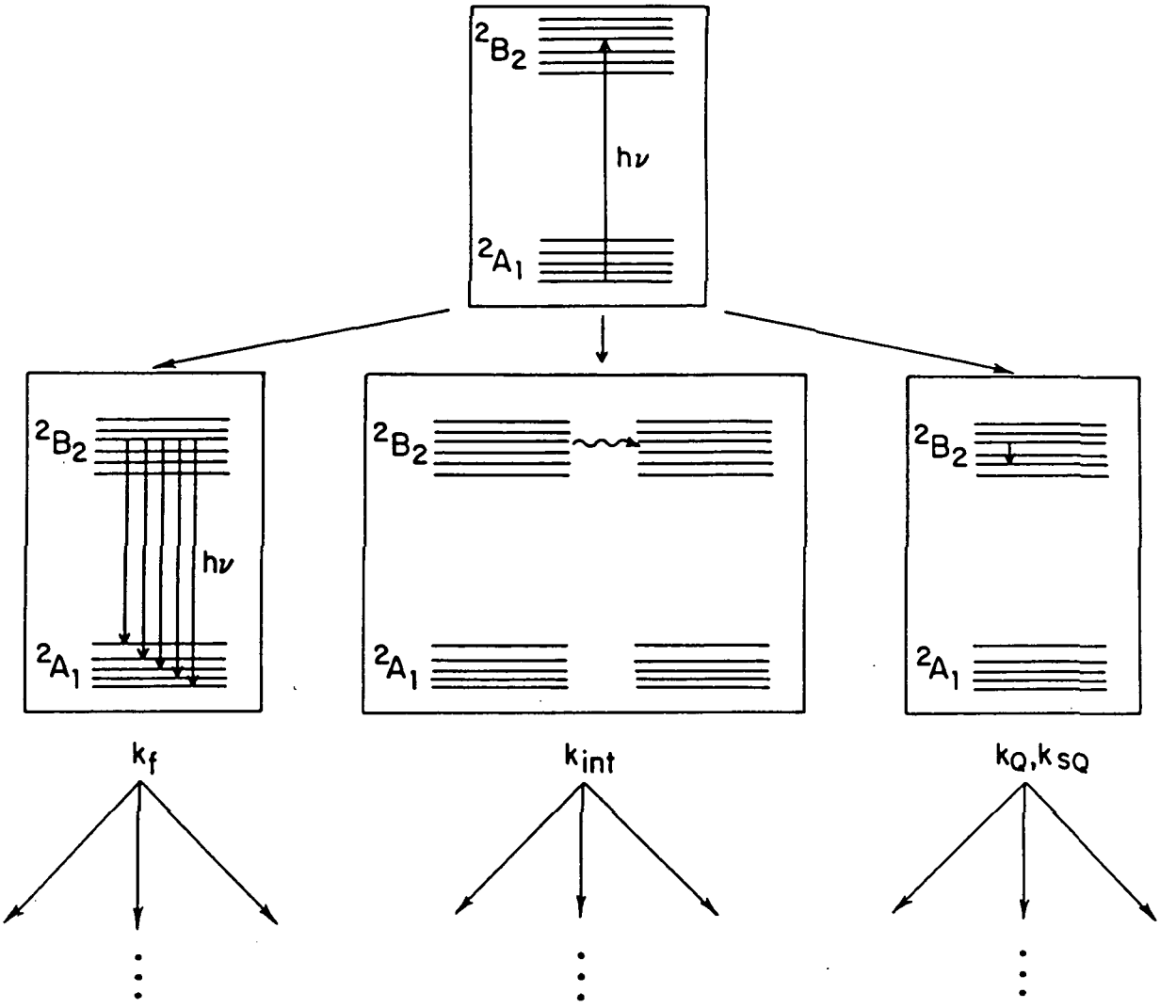

Figure 13. Schematic of NO_2 fluorescence dynamics.

near m and becomes 0 for large i . This function results from the finite experimental bandpass -- molecules near the cutoff emit a larger portion of their fluorescence outside the bandpass. The factors T(ν) and η(ν) are the same as in equation (2-1b). Rearranging equation (3-1) yields the generalized Stern-Volmer equation,

$$\frac{NO_2}{S(\nu_e, \nu)} = K(\nu_e)[NO_2]\left[\int_0^{\nu_e} T(\nu)\eta(\nu) \sum_{i=m}^{\infty} f_i P_i(\nu_e, \nu)[NO_2^*]_i \, d\nu\right]^{-1} \quad (3\text{-}2a)$$

where K is an experimental constant containing the laser intensity, the absorption cross section, the quantum yield, and geometric factors. The signal S(ν_e, $\Delta\nu$) for a given displacement $\Delta\nu$ from the excitation frequency $\Delta\nu_e$ is derived from equation (3-2a) by replacing the infinite sum with a partial sum:

$$\frac{[NO_2]}{S(\nu_e, \Delta\nu)} = K(\nu_e)[NO_2]\left[T(\Delta\nu)\eta(\Delta\nu) \int_0^{\nu_e} \sum_{i}^{n} f_i P_i(\nu_e, \nu)[NO_2^*]_i \, d\nu\right]^{-1} \quad (3\text{-}2b)$$

At high resolution the P_i are functions of detection frequency for a given excitation frequency.[51] Vibrational peaks in the fluorescence spectrum are quenched largely by the internal redistribution process (k_{int}), whereas the underlying continuum is quenched via the vibrational/rotational cascade process (k_Q and k_{SQ}). Donnelly, Keil and Kaufman found that k_{int} was roughly independent of which vibrational peak was monitored. Furthermore, k_Q and k_{SQ} were roughly constant throughout much of the fluorescence spectrum, with k_{int} about six times larger than k_Q or k_{SQ}. Hence at moderate buffer gas pressures the vibrational structure is damped, leaving a structureless continuum

quenched at a rate independent of detection frequency ν. Keyser, Levine, and Kaufman found that quenching constants were roughly independent of ν and ν_e for detection at a given displacement $\Delta\nu$ at moderate to high pressures. Thus the P_i are roughly independent of ν_e and ν at moderate to high pressures, and therefore equations (3-2a) and (3-2b) can be rewritten as

$$\frac{[NO_2]}{S(\nu_e)} = K(\nu_e)[NO_2](1 + a_M[M] + a_{NO_2}[NO_2])\left(\sum_{i=m}^{\infty} f_i[NO_2^*]_i\right)^{-1} \quad (3\text{-}3a)$$

$$\frac{[NO_2]}{S(\nu_e, \Delta\nu)} = K'(\nu_e)[NO_2](1 + a_M[M] + a_{NO_2})\left(\sum_{i}^{n} f_i[NO_2^*]_i\right)^{-1} \quad (3\text{-}3b)$$

where $a_M = k_Q/k_f$, $a_{NO_2} = k_{SQ}/k_f$ and the instrumental factors have been absorbed in the constants of proportionality.

Both radiative and quenching processes are statistically random. The NO_2 population density in any state $|i\rangle$ is on average proportional to the population of the initially prepared state $|m\rangle$. The initial state population is in turn proportional to $[NO_2]$ under optically thin conditions. Thus

$$\frac{[NO_2]}{S(\nu_e)} = K(\nu_e)(1 + a_M[M] + a_{NO_2}[NO_2])\left(\sum_{i=m}^{\infty} f_i g_i\right)^{-1} \quad (3\text{-}4a)$$

$$\frac{[NO_2]}{S(\nu_e, \Delta\nu)} = K'(\nu_e)(1 + a_M[M] + a_{NO_2}[NO_2])\left(\sum_{i}^{n} f_i g_i\right)^{-1} \quad (3\text{-}4b)$$

where g_i is an unspecified function of i. Quenching experiments generally absorb this sum into the experimental constant. Equation (3-4b) reproduces the variation of quenching constants with $\Delta\nu$ as reported by Keyser, Levine and Kaufman[53], since the partial sum is in general dependent upon the specific states $|i\rangle$ summed.

At low pressures, both the assumption that $[NO_2^*]_i = g_i[NO_2^*]_m$ and the assumption that the P_i are independent of I_e and I are invalid. A typical Stern-Volmer plot, obtained from the working equation

$$\frac{[NO_2]}{S(I_e)} = K((I_e)(1 + a_M[M] + a_{NO_2}[NO_2]) \qquad (3\text{-}5)$$

shows the attendant nonlinearity (see Figure 14). High pressure values of a_M for the peaks marked in Figures 11 and 12 are presented in Table 5 . These values were obtained by a weighted least squares analysis of equation (3-5), discussed below.

The mechanism described ignores collisionally induced vibrational excitation, radiative transfer among the states $|i\rangle$ in the upper manifold, and diffusive loss. These processes are relatively slow, though diffusive loss may become important at approximately 50 mtorr buffer gas pressure. At low buffer gas pressures, excited NO_2 molecules can diffuse large distances in a radiative lifetime. Diffusive loss resulted in significant errors in early lifetime measurements[54] of the $\tilde{A}\ ^2B_2$ state of NO_2. Diffusion coefficients for NO_2 in N_2 are unknown, but an upper bound value for the coefficient is that of self-diffusion in N_2:

$$D_{N_2\text{-}N_2} \simeq 1.3 \times 10^{-4}\ \text{torr}^{-1}\ \text{cm}^2\ \text{sec}^{-1}.$$

The dipole moment of NO_2 increases the effective collision cross section relative to N_2-N_2 collisions and slows the diffusive transport. The relevant diffusion length is $(2D\tau)^{1/2}$, where τ is the radiative lifetime ($\simeq$ 100 μs). This length is 0.5 cm at 50 mtorr of nitrogen. The onset of nonlinearity in the Stern-Volmer plots at 50 mtorr buffer gas pressure is consistent with, though not proof of, diffusive loss as a bias-

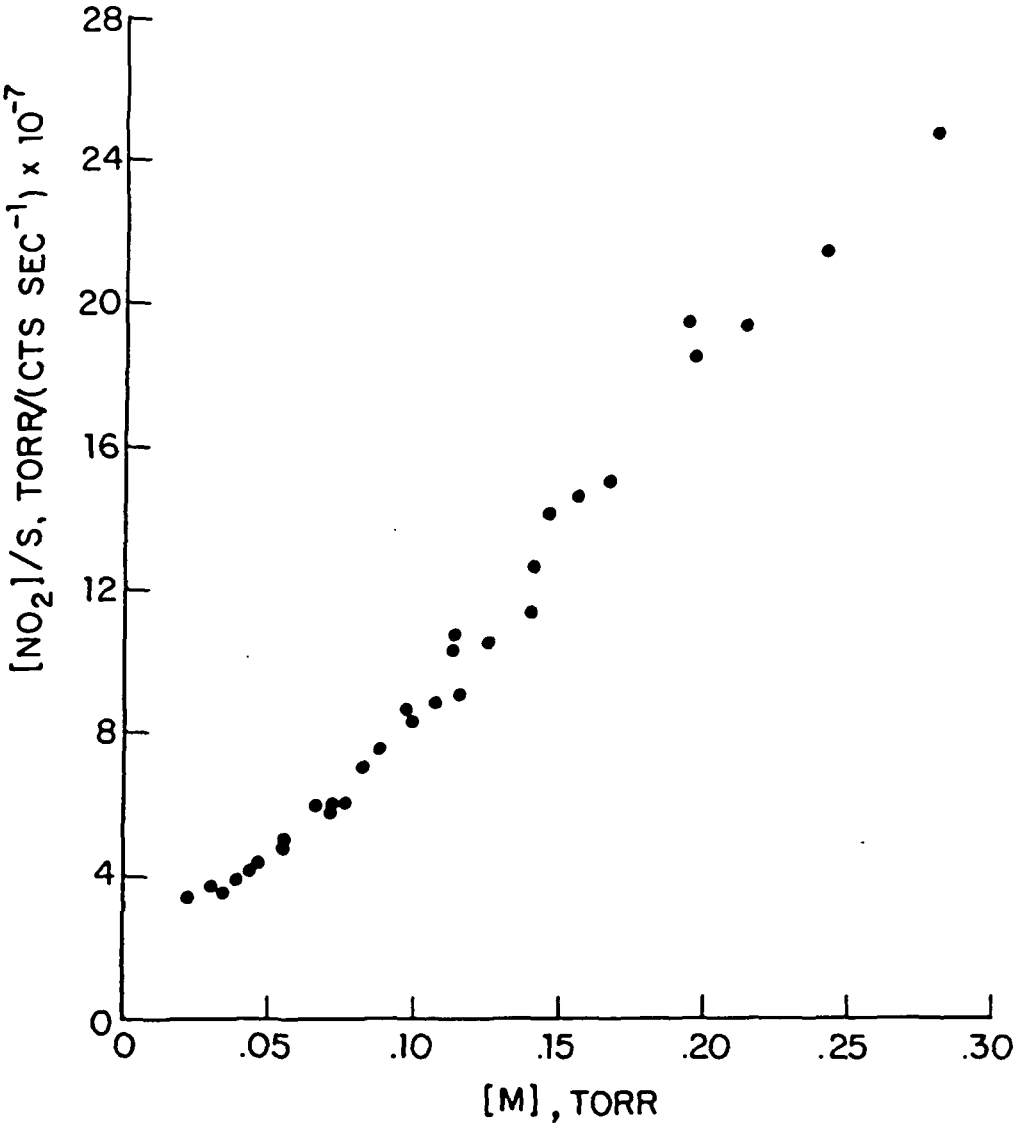

Figure 14. Stern-Volmer plot for NO_2 fluorescence.

Table 5

Cross Section and Quenching Data
on Selected NO_2 Spectral Features

Peak	Wavenumber (cm^{-1})	Assignment[a]	Cross section[b] (10^{-22} cm^2)	a_M ($torr^{-1}$)
1	17493.0	Vibrational and rotational assignment unknown	13.1 ± 2.1	45 ± 8
2	17076.6	(000) -> (430), $^{14}_{0,14} \rightarrow {}^{13}_{0,13}$, $S = 1/2$	15. ± 4.2	93 ± 30
3	17086.5	(000) -> (430), overlap of $^{6}_{0,6} \rightarrow {}^{5}_{0,5}$, $S = -1/2$ and $^{4}_{1,3} \rightarrow {}^{5}_{1,4}$, $S = -1/2$	6.2 ± 0.6	32 ± 4
4	17095.7	(000) -> (430), $^{4}_{0,4} \rightarrow {}^{5}_{0,5}$, $S = -1/2$	9.4 ± 2.3	69 ± 20
5	17097.2	(000) -> (430), $^{6}_{0,6} \rightarrow {}^{7}_{0,7}$, $S = -1/2$	7.0 ± 0.9	34 ± 4
6	16842.5	(000) -> (142), $^{8}_{0,8} \rightarrow {}^{7}_{0,7}$, $S = 1/2$	12. ± 1.7	53 ± 9

[a] Vibrational numeration is that of Bolduan and Jodl[49]; rotational numeration in the 17091 cm^{-1} region is that of Persch[50] rotational numeration in the 16850 cm^{-1} region is that of Stevens and Zare[47]. The spin quantum number S is (J - N). Vibrational quantum numbers of the lower and upper states are listed as $(n_1 n_2 n_3)$; rotational quantum numbers are listed as $N_{K_a K_c}$.

[b] NO_2 fluorescence is assumed isotropic; see text. Quoted error limits include estimates of systematic errors as well as 1σ statistical errors.

ing mechanism for these experiments at low buffer gas pressure.

Fluorescence Cross Sections

Many of the instrumental parameters in equation (2-1) can be eliminated by calibration of the detection apparatus via Rayleigh scattering signals. The signal equation for Rayleigh scattering in nitrogen is

$$S_{ray}(\theta) = C \cdot F_0 \cdot \frac{d\sigma}{d\Omega}\Big|_{ray}(\theta) \cdot T(\lambda_e) \cdot \eta(\lambda_e) \cdot [N_2] \qquad (3\text{-}6)$$

where C is an experimental constant, F_0 is the laser intensity (photons sec^{-1}), $\frac{d\sigma}{d\Omega}\Big|_{ray}(\theta)$ is the differential Rayleigh scattering cross section in nitrogen, $T(\lambda_e)$ is the transmission function of the detection optics at the excitation frequency λ_e, η is the quantum efficiency of the photodetector at λ_e, and $[N_2]$ is the number density of nitrogen molecules.

The Rayleigh cross section for dipole scatterers can be derived from first principles; the derivation is treated in detail in McCartney [55], for example. For linearly polarized incident radiation,

$$\frac{d\sigma}{d\Omega}(\theta) = \frac{9\pi^2}{N^2\lambda^4}\left[\frac{n^2 - 1}{n^2 + 2}\right]^2 \sin^2\theta \qquad (3\text{-}7)$$

where N is the number density of scatterers, λ is the appropriate wavelength, n is the refractive index of the medium, $(n^2 - 1)^2$ is proportional to N^2, and θ is the polar angle measured from the y-axis to the x-axis where the incident wave is polarized in the x-y plane. In the fluorescence cell experiments, the chosen laser polarization maximized the Rayleigh scattering signal and thus to within 5%, θ = 90 degrees.

The classical Rayleigh theory is generally corroborated by absolute

cross section measurements[56]. The difficulty of the experiment may have resulted in some systematic error. Certain experiments by George and coworkers[57] employing high peak power ruby laser pulses as excitation are in disagreement with the classical theory, but the discord may be due to sound wave excitation in the neutral gas and subsequent shifts in the refractive index of the gas.

Elimination of the instrumental parameters is performed by rearranging equation (3-5) to obtain

$$\frac{[NO_2]/[M]}{S} = K(\nu_e)\left[[M]^{-1} + a_M + a_{NO_2}\frac{[NO_2]}{[M]}\right]. \qquad (3\text{-}8)$$

At constant $[NO_2]/[M]$, the slope of $[NO_2]/[M]/S$ plotted *vs.* $1/[M]$ is $K(\nu_e)$. Replotting the data in the form of equation (3-5) allowed determination of a_M and a_{NO_2}. For all the peaks shown in Figures 11 and 12, the values of a_{NO_2} were 1.5 to 2.2 times the reported value of a_M. At low dilutions of NO_2 in N_2, the intercept-slope ratio of equation (3-8) is therefore a_M within experimental error. The slope of Rayleigh scattering signal *vs.* N_2 pressure is

$$C \cdot F_0 \cdot \left.\frac{d\sigma}{d\Omega}\right|_{ray}(\theta) \cdot T(\nu_e) \cdot \eta(\nu_e).$$

The fluorescence signal slope and Rayleigh scattering signal slope, as determined by experimental data, are multiplied to give a number N:

$$N = K(\nu_e) \cdot C \cdot F_0 \cdot \left.\frac{d\sigma}{d\Omega}\right|_{ray}(\theta) \cdot T(\nu_e) \cdot \eta(\nu_e) \quad .$$

The 'constant' $K(\nu_e)$ is

$$K(\nu_e)^{-1} = C \cdot F_0 \cdot \sigma_{peak}(\nu_e)\left[1 - \left[\frac{\Delta\nu_L}{\Delta\nu_D}\right]^2\right] \cdot \frac{1}{\Delta\nu} \int_{\Delta\nu} \phi(\nu_e, \nu) T(\nu) \eta(\nu) d\nu \qquad (3\text{-}9)$$

and therefore with $\Delta\lambda_L \ll \Delta\lambda_D$,

$$\sigma_{peak}(\lambda_e)\frac{1}{\Delta\lambda}\int_{\Delta\lambda}\phi(\lambda_e,\lambda)T(\lambda)\eta(\lambda)d\lambda = N^{-1}\frac{d\sigma}{d\Omega}\Big|_{ray}T(\lambda_e)\eta(\lambda_e). \quad (3\text{-}10)$$

To extract the true fluorescence cross section at λ_e into a bandpass $\Delta\lambda$

$$\sigma_{peak}(\lambda_e)\frac{1}{\Delta\lambda}\int_{\Delta\lambda}\phi(\lambda_e,\lambda)d\lambda$$

the λ dependence of ϕ must be determined [58]. Cross sections derived from equation (3-10), assuming ϕ is independent of λ and utilizing the manufacturer's curves for $T(\lambda)$ and $\eta(\lambda)$, are reported in Table 5. These cross sections are underestimates of the true fluorescence cross section, since ϕ is known to increase to the red.

This cross section determination combined with the quenching measurements has (a) isolated regions of the NO_2 visible system suitable for a specific <u>in situ</u> experiment, and (b) allowed quantitative determination of expected signal levels in the stratosphere based upon experimental observation rather than estimates. The next section discusses the calculated and observed signal levels for the flight prototype instrument, as well as expected and observed interference signals.

D. Design and Evaluation of a Prototype Flight Instrument

With the molecular constants in hand, this section discusses the theoretical reasoning behind and the physical realization of a prototype flight instrument. The desired result is an instrument with a signal-to-noise ratio of 50:1 throughout the altitude region of interest while retaining the 'null' capability of the laser-induced fluorescence technique. The specific instrumental goals are (1) maximization of interrogated volume, and (2) efficiency of fluorescence collection and detection. Premiums are placed on these goals, since the results of the previous section illustrate the dramatic differences between atomic or diatomic spectroscopy and the spectroscopy of polyatomic molecules. Most germane from the point of view of trace detection, the strength of electric dipole allowed transitions in diatomics is three to five orders of magnitude higher than in NO_2. Nitrogen dioxide is one of the simplest polyatomics. Nonetheless, its radiative properties are radically different from the hydroxyl radical [OH], for example.

To obtain acceptable detection limits, one therefore must carefully conserve every NO_2 fluorescence photon. The greatest advantage which the instrument designer has in fulfilling this end is the fact that both excitation and fluorescence wavelengths are in the visible or near infrared. This spectral region has a number of advantages:

- dye lasers are both powerful and efficient in the visible;
- glasses and optical coatings attain approximately ideal

qualities in the visible and near IR; and

- photomultiplier tubes retain high quantum efficiency throughout the visible, with a certain few types efficient to nearly 950 nm.

Nitrogen dioxide is stable against wall destruction (though adsorbed strongly by some wall surfaces) and thus sampling of stratospheric air need not be via a manicured nacelle[59]. Because of this stability, the path whereby air is sampled need not be a path for entrance of solar photons. In short, the excitation photon density is quite high; clever optical design can collect a substantial percentage of the emitted fluorescence photons; and instrumental noise is minimal. These declarations require substance and objective assessment.

Design

Laser Excitation

The excitation spectra of the previous section clearly define the need for narrow linewidth laser excitation. To have simultaneously quite high average powers taxes the limits of current laser technology. Larabee[33] describes fully an approach for generation of narrow linewidth laser light. Quite modest (Nd:YAG) pump laser powers yield conversion efficiencies in the neighborhood of 5%, with no obstacles to extrapolation to more powerful pump lasers. Because the dye laser of Larabee[33] operates in a single longitudinal cavity mode most reliably near laser threshold, the generation of high laser power is best obtained in an oscillator-amplifier configuration.[60]

Detection Optics

The optical design of the prototype comprises two subsystems - a multipass cell to amplify the excitation volume, and optics to efficiently collect fluorescence photons emanating from that volume while discriminating against scattered laser photons. Another approach to efficient use of laser photons would be to place the sampling volume intracavity, taking advantage of the higher circulating power within the laser resonator. This approach was deemed unacceptable as the resultant lengthened laser cavity considerably increases the difficulty of single cavity mode operation.

The multipass cell is a spherical mirror interferometer of the type investigated by Herriott and coworkers.[61] The two coaxial mirrors have the same radius of curvature and are dielectric coated for high reflectivity (99.8%) at the laser wavelength. Laser light enters the cell via a 3 mm diameter aperture displaced 12 mm from the center of one mirror, ideally with spherical wavefronts of the same radius as the mirrors. This ray is directed to a point 12 mm from the center of the opposite mirror; the reflected ray is then directed to a spot just above the entrance aperture. Subsequent reflections 'walk' around the mirrors, forming a circular spot pattern in the degenerate case but more generally an ellipse. This pattern will only be generated for focal lengths f and mirror separations d such that

$$0 < \frac{d}{f} < 4.$$

For $2f < d < 4f$, the ray bundle in the interior of the cell limns a hyperboloidal shell, desirable from the point of view of fluorescence

collection. Misalignment or deviations from sphericity on the part of the mirrors results in more complicated spot patterns in the form of Lissajous figures. For ease in quantitative assessment, the mirrors are usually aligned to produce the simple elliptical pattern. This pattern corresponds to one circuit around the mirror and exit through the aperture - the re-entrant condition - and one can easily count the number of passes in the cell. However, the maximum number of passes within the cell is ultimately limited only by the size of the entrance aperture and the reflectivity of the mirrors. Photographs of the spot patterns for both a re-entrant and a more complicated condition are shown in Figure 15 .

Fluorescence collection efficiency is basically a function of total solid angle subtended, the degree of concentration of collected photons, and any aperturing by field stops and/or the photocathode area. The design chosen in this work employs a large (15 cm diameter) elliptical mirror, coated for high reflectivity in the red and near IR. The primary and secondary foci are 6.3 cm and 11.4 cm from the center of the mirror, respectively. The ray bundle is positioned at the primary focus, and a slightly enlarged (magnification = 1.8) image of the bundle is delivered to the photocathode at the secondary focus. The aberrations induced by aspherical mirrors are quite large. Though paraxial rays and all rays intersecting the primary focus are easy to analyze, the behavior of an extended source is difficult to determine by ray tracing. To determine the optimum position of the photocathode, light from a diffuse extended source (positioned at the primary focus) was photographed at various displacements from the secondary focus. The minimum

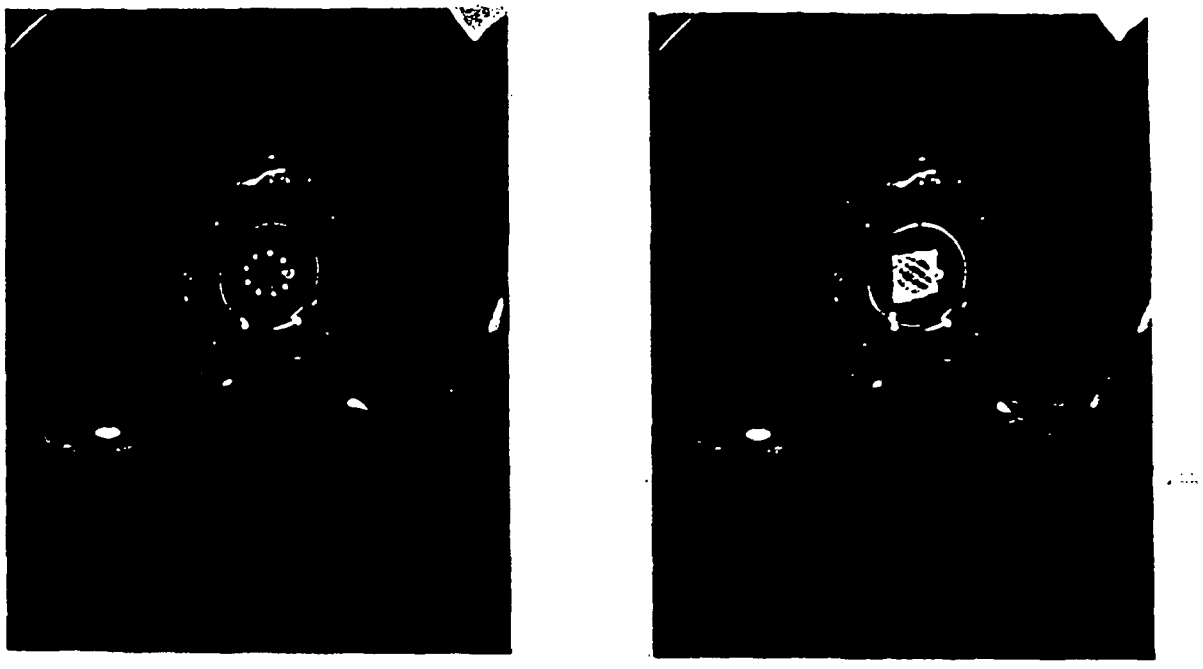

(a) (b)

Figure 15. Spot patterns on the entrance mirror of the multipass cell for the (a) re-entrant condition, and (b) a more general Lissajous figure.

image size was found approximately 0.5 cm from the secondary focus toward the primary focus, though positioning to within 1 cm is demonstrably adequate. Theoretically, the reflector subtends 37% of 4π steradians; the extended nature of the light source reduces this number to an effective value near 10-20% with some degree of uncertainty.

Collected fluorescence photons impinge upon a gallium arsenide photocathode after transmission through a 7.5 cm diameter long wavelength pass filter (Hoya R-70). The photomultiplier tube (RCA C31034-02) is connected to a high voltage supply/amplifier/discriminator package (EGG Princeton Applied Research Model 1191). Because the PMT has a quite high dark count (10000-20000 cts sec^{-1}) at room temperature, the tube is cooled by convection (in dry nitrogen) from a brass coolant jacket maintained at approximately -30^{o} C; whereupon the dark count is typically tens of counts per second. The quantum efficiency of the GaAs photocathode as derived from the manufacturer's curve is depicted in Figure 16.

To aid in the visualization of the optical subassembly, a schematic of the design is reproduced as Figure 17.

Gas Flow

Because of the low reactivity of NO_2 with system walls, gas may be introduced to the sampling region in a relatively simple manner. A known partial pressure of NO_2 in a particular buffer gas is driven by a small Roots blower along an axis orthogonal both to the collection optics and the multipass ray bundle. The entire optical system save the PMT is enclosed in a large vacuum tight aluminum 'tank' of 32 cm inner

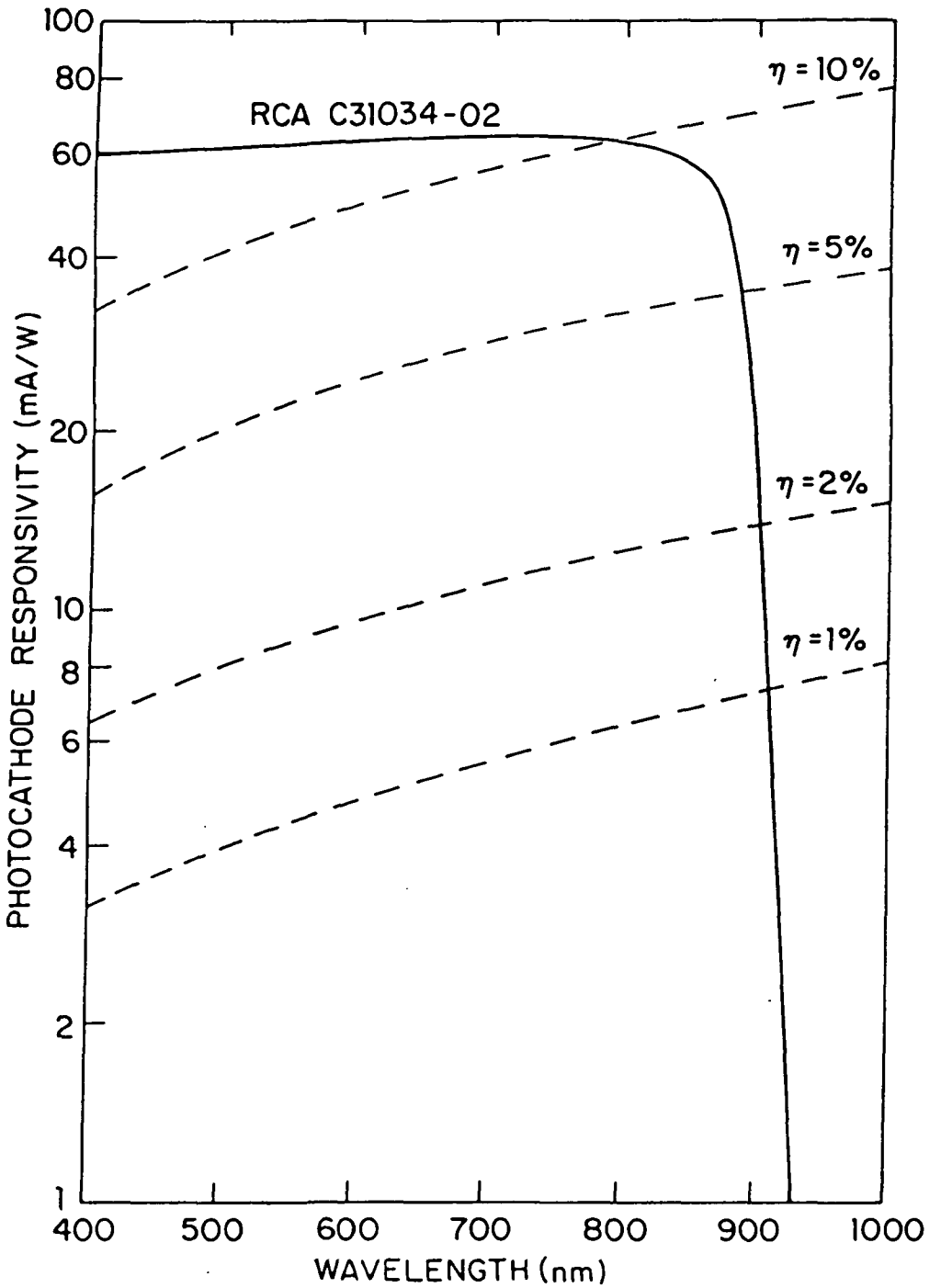

Figure 16. Typical spectral response of a gallium arsenide photocathode. Lines of constant quantum efficiency are marked. From RCA Photomultiplier Catalog, 1984.

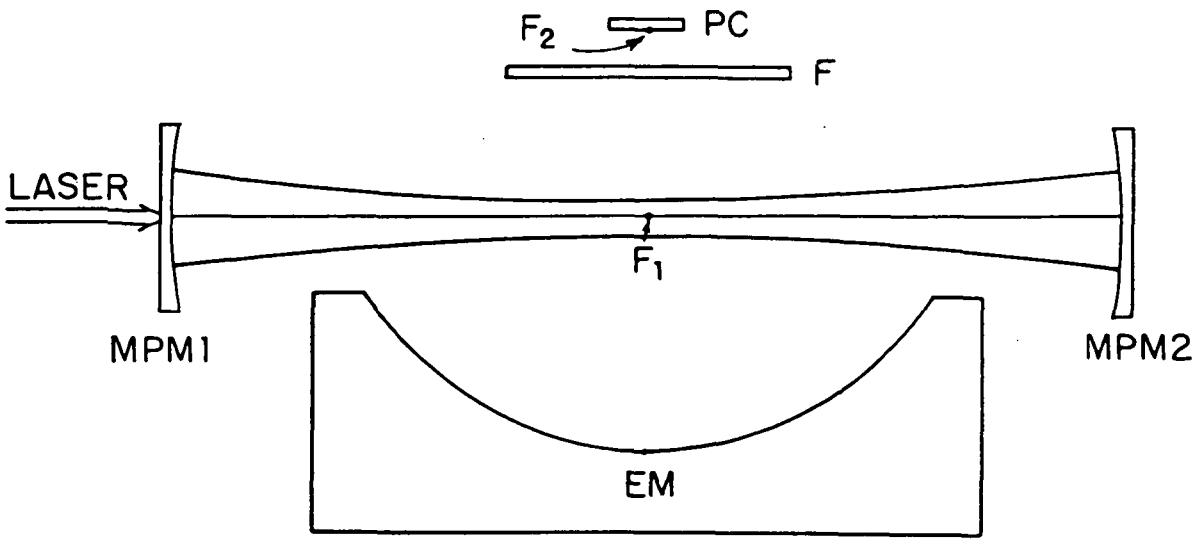

Figure 17. Schematic of the optical collection subassembly. MPM1, MPM2 = multipass cell mirrors; EM = elliptical mirror; F_1, F_2 = primary and secondary focus, respectively; F = long wavelength pass filter; and PC = photocathode. Gas flow is normal to the plane of the figure.

diameter, sandblasted and anodized to form a flat black finish. Gas enters and exits via 1.2 cm diameter stainless steel tubing interior to the tank; the gap between the entrance and exit tubes is variable and can be as small as 3.8 cm. Channeling the gas flow in this manner minimizes radial diffusion, and any diffusive effects can be determined directly by varying the gap distance and/or the Roots blower motor speed. To obtain the true NO_2 number density in the sampling region, both temperature and pressure are monitored in both the tank and source flows.

The production of a known number density of NO_2 molecules is simple and a technique long familiar to experimental gas kineticists[62]. Gas flow in a six inch diameter flow tube is produced by a large Roots blower (Leybold Heraeus RA-7001, forepumped by Model TR-630). Pressure in the flow tube is monitored by a calibrated MKS Baratron capacitance manometer; bulk gas flow rates are measured by a Hastings mass flowmeter (Matheson 8116), calibrated against a wet test meter (GCA Precision Scientific). Trace gas flows are measured from the timed pressure drop of a known volume; differential pressure is determined by a Validyne differential reluctance manometer. The trace gas flow rate from a calibrated volume in STP cm^3 sec^{-1} is

$$F_{TG} = DF \cdot V \cdot \frac{273}{T} \cdot \frac{\Delta P/\Delta t}{760}$$

where DF is the percentage dilution of the trace gas in the reservoir buffer, V is the calibrated volume in cm^3, T is the reservoir temperature in K, ΔP is the pressure drop in torr, and Δt is the time in seconds for the pressure drop to occur. The concentration [TG] (molecules cm^{-3}) of the trace gas in the bulk flow is just

$$[TG] = 2.69 \times 10^{19} \cdot \frac{F_{TG}}{\pi R^2 \bar{v}}$$

where R is the inner radius of the flow tube in cm and $\bar{v}$ is the bulk flow velocity in cm sec^{-1}. The flow velocity is given simply as

$$\bar{v} = \frac{1}{\pi R^2} \cdot \frac{760}{P_B} \cdot \frac{T}{273} \cdot F_B$$

where P_B is the bulk pressure in torr and F_B is the bulk flow rate in STP cm^3 sec^{-1}. Hence

$$[TG] = 3.47 \times 10^{18} \cdot DF \cdot \frac{V}{T^2} \cdot \frac{P_B}{F_B} \cdot \frac{\Delta P}{\Delta t}.$$

For NO_2 a small correction must be made, since dimers form in the reservoir

$$\frac{[NO_2]^2}{[N_2O_4]} = 0.141 \text{ atm}$$

but (after a short delay) become almost exclusively monomers upon insertion into the large flow tube.

Performance

Signal Levels

Evaluation of the prototype flight instrument is most straightforward if one casts equation (2-1) in the form

$$S = C_{NO_2} \cdot F \cdot Q \cdot [NO_2] \qquad (4-1)$$

where C_{NO_2} is the apparatus sensitivity (counts

sec^{-1} $milliwatt^{-1}$ $(mol\ cm^{-3})^{-1}$), F is the average laser power (milliwatts), Q is the dimensionless quenching factor, and $[NO_2]$ is the nitrogen dioxide number density (mol cm^{-3}). For the design of section 4.1 (employing 28 passes within the multipass cell), the observed sensitivity was

$$C_{NO_2} = 3.8\ (\pm\ 1.0) \times 10^{-7}\ \text{cts sec}^{-1}\ \text{milliwatt}^{-1}\ (\text{mol cm}^{-3})^{-1} \quad (4\text{-}2)$$

The observed contrast ratio of the chosen peak was about 5:1, whereas the excitation spectra of the previous section show a ratio of about 8:1; the difference is due to the increased laser linewidth (1 GHz) of this system with respect to that employed in the previous section.

Examination of equations (2-1) through (2-4) shows that the component parts of the apparatus sensitivity are

$$C_{NO_2} = 2.95 \times 10^{15} \cdot \sigma_{1/2} \cdot \frac{\Delta\Omega}{4\pi} \cdot MP \cdot l \cdot \left[\frac{\Delta\nu_D^2}{\Delta\nu_D^2 + \Delta\nu_L^2}\right] \cdot \frac{1}{\Delta\nu} \int_{\Delta\nu} T(\nu)\eta(\nu)\,d\nu \,.$$

The fluorescence cross section σ for the peak at 17086.5 cm^{-1} is taken from Table 5 . The effective solid angle subtended by the large reflector was 0.1 of 4π steradians, and was measured by placing a large black cloth over the reflector and recording the concomitant reduction in signal. The total number of traversals of the multipass cell was simply counted, since the spots were readily discernible on the mirrors. The optical trace coupled with the known aperture within the photomultiplier tube yielded a value for l of 0.8 cm. Both the laser linewidth and the Doppler width of the NO_2 spectral feature were about 1 GHz.

The convolution integral was performed by piecewise integration with manufacturer's curves, with a result of 0.042. Combining these individual components produces

$$C_{NO_2\ calc} = 1.2\ (\pm\ 0.3) \times 10^{-7}\ \text{cts sec}^{-1}\text{milliwatt}^{-1}\ (\text{mol cm}^{-3})^{-1}\ .$$

The discrepancy is likely due to the instrument-dependent value chosen for the fluorescence cross section. As discussed at the end of the previous section, the absolute fluorescence intensity per unit frequency was not determined, but rather the integrated intensity. Without knowledge of the ν_e dependence of ϕ, the true fluorescence cross section cannot be derived. Similarly, the effect of improved detector quantum efficiency cannot be determined in a quantitative manner. Figure 2 implies that an incremental increase in detector red sensitivity is quite valuable; the increased red sensitivity of GaAs photocathode is thus responsible for the 'increased' cross section and higher observed signal levels.

Noise Levels

As previously stated, dark emission from the gallium arsenide photocathode (at room temperature) is considerable, yet cooling reduces this emission by a factor of 100. The flight prototype counted only those photons (or pseudo-photons) within a 6 μs gate triggered by the firing of the laser. At the 25 Hz repetition rate of the Nd:YAG laser, the dark count was nil; even at the higher repetition rates of a metal atom laser, dark count contributions from the cooled photocathode are negligible.

The prototype instrument did suffer from laser scatter problems,

however. A glance at Figure 17 shows that the optical design therein depicted violates one of the cardinal rules of such design - no 'primary' ray should be able to intercept the photodetector. Diffuse reflections from the multipass beam spots can directly impinge upon the photocathode. Baffles were placed about the hyperboloidal shell, but the physical construction of the ellipsoid prevented significant extension toward the central observing region. Furthermore, an image of the spots is also directed toward the photocathode by one reflection at the opposite edge of the reflector. These scattered rays are small fractions of the circulating laser power within the multipass cell; excluding these photons is nominally the task of the red pass filter. Unfortunately, the filter glass has a broadband red-shifted fluorescence, readily observed by the photomultiplier. The solution for the flight prototype was to decrease laser intensity and delay by 200 ns (with respect to laser fire) the opening of the 'observing' gate. This doped glass fluorescence was the only observed interfering fluorescence in the entire apparatus.

The gas flow system exhibited some anomalous behavior as well, though properly this behavior does not constitute a noise source. The adsorptive/desorptive effects observed in the experiments of the previous section were also seen in the prototype flight instrument. Time constants on the order of 1 minute were typical when the gas delivery was via 304 stainless steel tubing. Teflon tubing is slightly less sticky, but of less uniform composition (tube to tube) and hence less informative in an estimation of its utility.

Considerations for Development into a Flight Instrument

Short Term

The instrument as currently configured has very nearly the requisite sensitivity for a flight package. For 100 milliwatts input laser power, the apparatus produces 600 cts sec^{-1} at 40 km and 30 cts sec^{-1} at 20 km. Another approximate factor of five is obtainable by increasing the number of passes within the multipass cell as discussed above.

Scattered laser light can be reduced by two methods. By increasing the multipass mirrors' radii of curvature, the mirrors can be displaced farther from the photocathode field of view and baffled with higher efficiency. Second, a better red pass filter can be found; the filter of choice is likely a highly optimized dielectric filter or an appropriate liquid, sufficient to provide high extinction at the laser wavelength without residual fluorescence.

Stray light reduction is quite important for a flight instrument. Since both NO_2 signal and laser scatter scale with laser power, the instrument can quickly become signal to noise rather than signal limited. The expedient of delaying the observing gate becomes less valuable at high quenching gas pressures.

Longer Term

Development of a flight instrument is an ongoing process. Future experimental and design must be conducted in three principal areas: high power laser systesm, wall materials, and ambient noise sources.

A flight laser system providing 100 milliwatts of single mode laser power is a nontrivial undertaking; however, the results of Larabee[33] are sufficiently positive that the limiting factor is not the physics but the technology. Of more specific interest is the requirement for frequency reference; the degree of certitude must be high for a molecule with finely spaced transitions. The following hierarchy may be appropriate:

- spectrometer for coarse absolute calibration
- optogalvanic cell for coarse relative calibration
- NO_2 reference cell for fine absolute calibration
- Fabry-Perot etalon for mode diagnostics

The etalon fringe pattern could be read on a shot-to-shot basis with a scanned photodiode array.

The area of system walls must be kept to a minimum and be constructed of a material exhibiting little affinity for NO_2; the search for such a material will probably be empirical to some extent.

Ambient noise is expected from two sources: aerosol fluorescence and Raman scattering. Logical substantiation of the LIF technique rests in its 'tune-on, tune-off' capability, which serves to distinguish NO_2 fluorescence from most other signal components. A worst case for fluorescence from aerosol particles would have the aerosol fluorescence spectrum exactly mimic NO_2 fluorescence. In any case, aerosol fluorescence may contribute to the background count rate, thereby muddying the tune-on, tune-off contrast. Raman scattering from N_2 and O_2 may also contribute to the background count rate.

Methods exist for elimination of both these noise sources. First, aerosol fluorescence has a distinct 'event' signature - a momentary large burst of photoelectrons - whereas homogeneous molecular fluorescence has a more slowly varying amplitude. Hence an anode current monitor can easily detect an aerosol event and alert the detection electronics. And second, the vibrational Raman bands of N_2 and O_2 are narrowly concentrated and thus susceptible to optical filtering. No Raman signal was ever (nor should have been) observed with the flight prototype, yet at flight laser power levels, the (unfiltered) intensity is observable.

Conclusion

Critical analysis of four possible in situ techniques for detection of stratospheric NO_2 has pointed to laser induced fluorescence as the most sensitive. The caveat of line congestion has been shown to be less important at narrow excitation linewidths, and an optimal line for performing the LIF experiment has been selected via quantitative assessment of relative cross section and quenching constant values. We have built a flight prototype (designed to maximize instrumental sensitivity) that has demonstrated part per trillion level sensitivities to stratospheric NO_2. Incorporation of the prototype into flight hardware is proceeding apace.

In-Situ Stratospheric Ozone Measurements: Recent Results and their Implications

E.M. Weinstock, C.M. Schiller, and J.G. Anderson
Department of Chemistry and
Center for Earth and Planetary Physics
Harvard University
Cambridge, Massachusetts 02138

March 1985

Introduction

It is extremely interesting to note that a relatively short time has elapsed between the identification of ozone as a trace atmospheric constituent having potentially important solar absorptive properties in the ultraviolet (Hartley, 1881); the elucidation of the mechanism for stratospheric ozone formation, destruction, and as a result the first calculated ozone altitude profile (Chapman, 1930); and the more recent disclosure concerning natural and anthropogenic perturbed ozone catalytic destruction mechanisms (see Molina and Rowland, 1974; Johnston, 1971).

Concurrent with the growth in man's understanding of the important role that ozone plays in the environment has been his ability to measure it. Ground based, rocket-borne, balloon-borne, and satellite ozone instruments have all been developed and used to determine ozone profiles in the stratosphere and troposphere. Each instrument has its own set of performance criteria — useful altitude range, altitude resolution, time response, accuracy, and precision (see Hilsenrath, 1984 for a recent review). However, the quoted accuracy and precision are usually estimated from the propagation of the uncertainties in the various parameters needed to determine ambient ozone density or mixing ratio. This approach is unavoidable for all "remote" ozone sensors, but has also been the method of expedience even for in-situ instruments which do lend themselves to laboratory calibration techniques under atmospheric conditions. It is therefore understandable that intercomparison campaigns have been used as a general approach to evaluate instrumental performance. In a truly double blind comparison, agreement between different instruments can greatly increase the credibility of each measurement.

Much of the motivation behind these intercomparisons can additionally be attributed to the relatively large systematic differences between

instrument types that have become apparent as a large data base has developed. These discrepancies were especially large and disturbing in the upper stratosphere where remote techniques typically yielded ozone mixing ratios ten to thirty percent higher than in situ instruments (Hudson, 1981; Aimedieu et al., 1983). This condition persisted even with the advent of a "Dasibi-type" UV-absorption instrument modified from one typically used as a calibration instrument at ground pressure. The generally accepted, although unproven explanation of ozone destruction in in situ instruments was virtually carved in concrete (Ainsworth et al., 1981), subsequently generalized to be applicable to all UV in situ ozone sensors, and has only recently been dispelled (Hilsenrath et al., 1985).

The ultimate goal of these intercomparisons has been to provide a means for the evaluation of global ozone measurements, and a means of distinguishing between atmospheric variability and instrumental precision and/or accuracy. An additional goal, as outlined in the Ozone Correlative Measurements Workshop (Hilsenrath, 1984), is to identify an instrument (or set of instruments) to help validate SBUV measurements, especially from 30 to 45 km, where ozone trend measurements are in progress, and additionally help identify an instrument or set of instruments capable of independent trend measurements around 40 km. With identification of possible stratospheric ozone-dstruction mechanisms in the early 1970s, a steady stream of model- and time-dependent predictions of steady state ozone depletion have been published and publicized. Credence in these time-dependent ozone depletion scenarios can only be decreased by a model's inability to match current altitude profiles of the relevant atmospheric species. In particular, the most recent calculation profiles of ozone, utilizing the newly revised O_2 cross-reactions, are systematically lower than the measured profiles in

the stratosphere above 35 km (see Crutzen and Schmailzl, 1983; Froidevaux, 1984), exactly where the models predict the largest percentage depletion. Since the measurements of stratospheric ozone have, in the past, shown large variability, these differences have been variously attributed to possible instrumental problems (Crutzen and Schmailzl, 1983) or the difficulty of comparing a seasonally averaged model calculation to "snapshot" measurements. It can be further argued that these differences are primarily due to various uncertainties in rate constants and photolysis rates which propagate through the model and not to a missing link in the ozone destruction mechanism. However, Froidevaux (1984) gives strong evidence to negate this rationalization.

With the completion of the Balloon Ozone Intercomparison Campaign (BOIC), and its conclusions, it appears that these options are no longer viable and these discrepancies must be further investigated. Using the recent results of our in situ UV-absorption measurements, the details of which we will describe here, as well as other profiles, the reliability of which has been strengthened if not established by BOIC, the extent of the problem in the upper stratosphere can be better defined.

Experimental

The design of our ozone sensor was predicated on a number of principles which distinguish it from other UV in situ absorption instruments. These are listed below with the resultant instrument requirements.

1. A signal-to-noise ratio of $\geq$ 50:1 even at 40 km, requiring the multipass cell;
2. No ozone loss, even at low pressures, requiring a high speed displacement pump ($\sim$ 50 - 100 times that of other instruments) and high conductance solenoid valves;
3. Less than 0.5 sec residence times, even with the 950 ml cell volume, requiring a high displacement pump;

4. In-flight diagnostics to verify proper instrumental performance;
5. Operation of the instrument under 1 atmosphere pressure differential for laboratory calibration purposes), requiring both a vacuum-tight absorption cell and solenoid valves.

A. The Flight Instrument

The principle of the operation of our ozone sensor is illustrated in Figure 1. Ambient air is drawn through lobe type blowers into the absorption cell alternately through a catalytic ozone scrubber to establish a reference signal (I_o) and through a suitable length of teflon inlet tube to measure the degree of O_3 absorption in the cell. The pump is driven by a Siemens Brushless DC motor (#1AD3101-0F) and controller (#TK36727) which has been voltage controlled to provide a displacement of from 0.6 to 1.8 liter/second which is virtually pressure independent. The scrubber consists of rolled MnO_2 coated copper screens supplied by the Dasibi Corporation. For initial flights, the scrubber consisted of a 5/8" I.D. stainless steel tubing containing seven screens rolled to produce minimum flow impedance and heated to ~75°C to ensure total catalytic conversion of O_3. For the more recent flights, a 12" long, 2-1/2" diameter scrubber containing about 65 rolled screens maintained at ~30°C was used, improving the thermal homogeneity of the instrument, without sacrificing scrubber efficiency, even up to ambient ozone concentrations $\geq 1 \times 10^{13}$ mol/cc. The temperature of the large volume scrubber is regulated by a heater controller with four set points which allows thorough outgassing of the MnO_2 screens at temperatures up to 75°C and ensures that no outgassing occurs during the flight.

A timing circuit controls a complete cycle of the ozone instrument by alternately activating the solenoid valves at the inlet to the absorption cell, thus establishing not only the time allowed for thoroughly

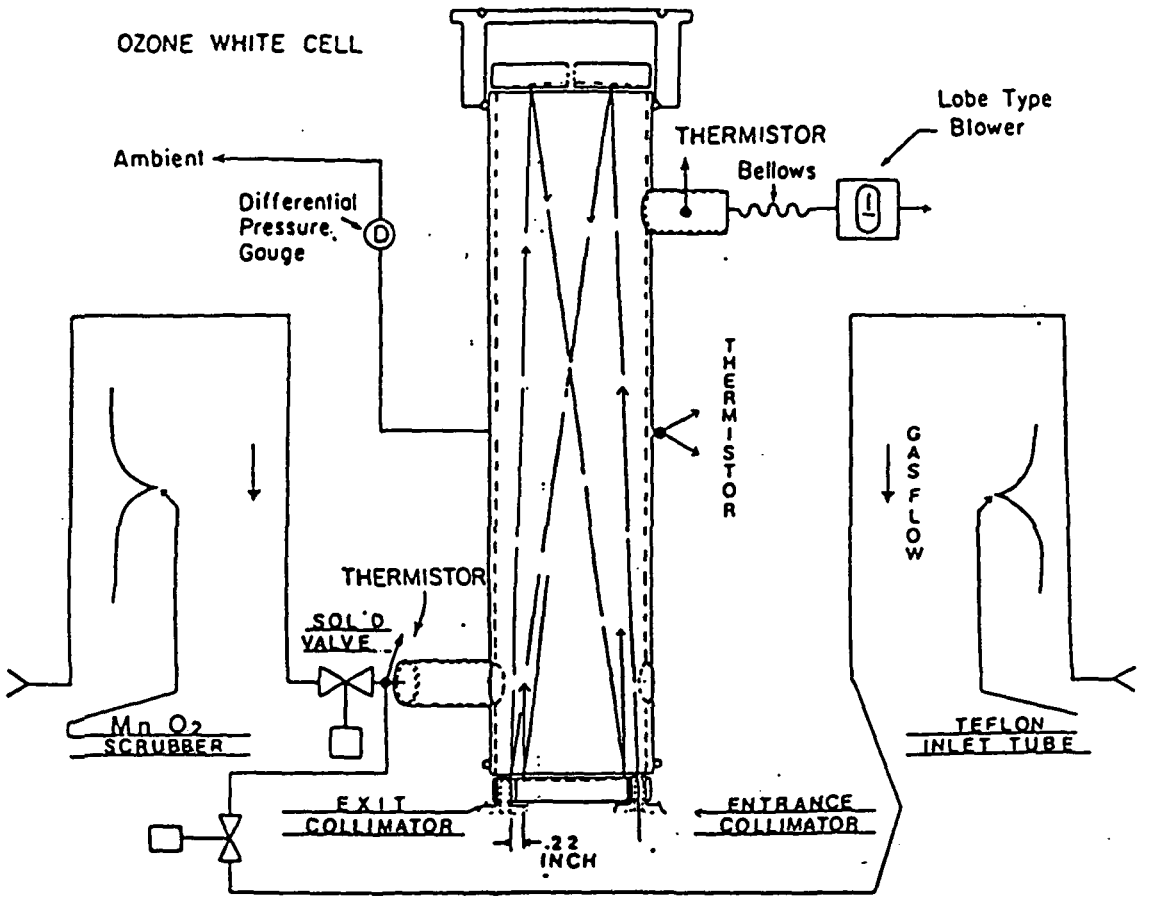

Figure 1. Schematic representation of ozone instrument.

flushing the cell but also the count up/count down down of the normalized counting system (Dasibi Electronics).

The heart of the instrument is a 40 pass "White Cell" (White, 1942), illustrated in Figure 2. The 2-1/3" diameter, 12" focal length spherical mirrors are coated to selectively provide ~ 97% reflectivity in a 200 Å bandwidth centered around 2550 Å, and are positioned at mutually conjugate foci. One mirror is split to permit alignment to the center of curvature constraints, as described by White.

All of the critical optical elements are mechanically secured to a set of three mirror rods to ensure temperature stability of the mirror spacing and alignment. Each half of the split mirror is mounted to facilitate individual alignment. The arrangement readily permits alignment for from 25 to 44 passes with typical operation of the instrument at 40 passes yielding a 1200 cm pathlength. Under these conditions the rectangular spots, approximately 1/8" by 3/16", are separated by 0.22", allowing for ease of counting as is evidence in Figure 2. Initial alignment is carried out using a Helium-neon laser, with usual observance of the number of passes and centering of the output beam in the detector collimator. The 2537 Å light source is then substituted for the laser and the alignment is completed with the output maximized and the spots again counted. A traversal from n passes to n ± 4 passes produces a valley in the output signal which is on the order of 1/3 to 1/4 the peak signal and therefore realignment with the absorption cell envelope in place without changing the number of passes is not foolproof, but can be accomplished. In addition, the mount is highly shock resistant, such that while mechanical jostling of the instrument which might occur during the shipment or flight of the instrument may affect the instrument alignment sufficiently to change the output

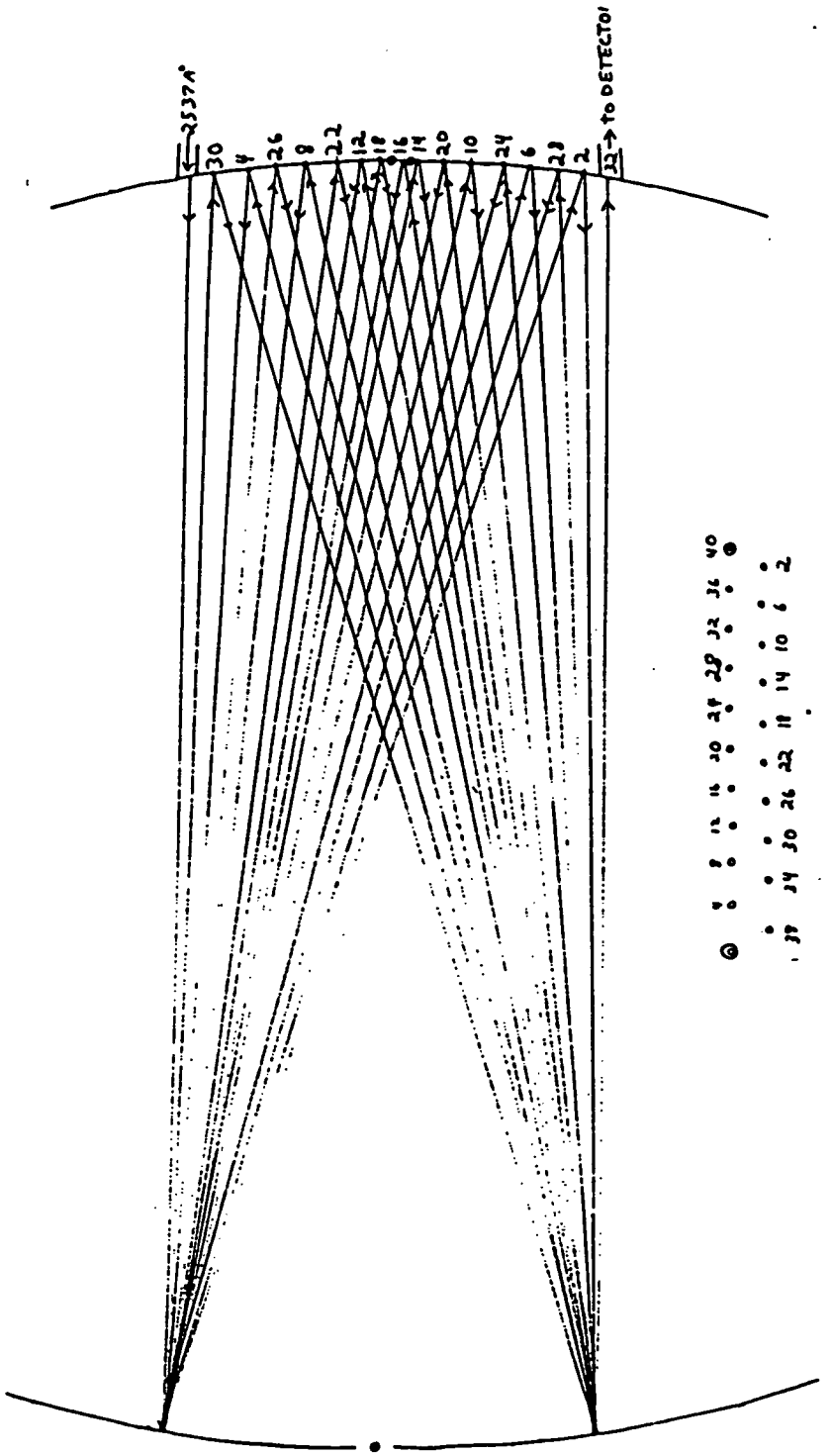

Figure 2. Schematic of White cell ray trace.

intensity, it will not change the effective pathlength or the number of passes.

The valves presently used are Balzar's bellows sealed solenoid valves (model #EVA016), with either a stainless steel (unscrubbed side) or aluminum (scrubbed side) body. These valves do limit the conductance of the instrument and will shortly be replaced by a high conductance, three-way teflon valve. The light source is a vycor sheathed, low pressure cold cathode mercury lamp (Hammamatsu Corporation) driven by an 8 kHz square wave providing a voltage of 1300 volts for turn-on and 300 volts for continuous operation. The lamp is mounted in a small cylindrical aluminum housing which provides ample temperature stability in a well shielded environment. The lamp typically takes 20 minutes to stabilize after turn on.

Two equivalent vacuum photodiodes with CsTe photodiodes are used in the instrument. One monitors the output of the lamp and provides a digitized reference signal which controls the relative lengths of the count-up and count-down phases of the measuring cycle. The other measures the intensity of light passing through the White cell. Thus, a normal cycle lasts $\sim$ 9 seconds and consists of 3.5 seconds of flushing and the count-up cycle of approximately 1 second during which ambient air is drawn through a teflon inlet tube into the cell.

The pressure in the absorption cell is continuously monitored by a 0 - 10 torr differential pressure transducer (Setra # , and more recently by a MKS Baratron 222A), which references to ambient pressures which are calibrated over a range of pressures against either an oil manometer or a pair of absolute pressure MKS capacitance manometers. The temperature of the gas in the cell is provided by thermistors located on the exterior surface of the inlet tube to the cell, as well as one in

the actual air flow of gas in the exit port of the absorption cell. The complete cell and housing is contained in an insulated aluminum box maintained at a temperature of 30°C, approximately the same temperature at which the scrubber is maintained. Under normal flight conditions the temperature gradient across the cell is $\leq$ 3°C, and thus a source of $\leq$ 1/2 percent uncertainty.

Evaluation of the operation of the instrument during flight is facilitated by a series of diagnostics:

1. Four motor speed set points which allow a range of pumping speeds from 0.60 to 1.8 liters/second;
2. Two distinct flushing times of 3.5 and 9 seconds;
3. Direct and continuous monitoring of both the reference control and absorption signal sample frequencies with 0.25 second resolution to evaluate instrument signal-to-noise throughout the flight, as well as quantifying and evaluating optical degradation of the White cell mirrors. Additionally, by turning the motor off while ozone is in the absorption cell, an estimation of ozone wall loss within the absorption cell can be made.

It is exceedingly important to have thorough testing capabilities of the instrument in the laboratory to ensure that, under controlled conditions, the instrument performs according to specifications. Ideally, the test should consist of providing the flight instrument, under stratospheric conditions, a series of "known" ozone concentrations and validating instrument performance. In practice, this task can pose as many problems as constructing the flight instrument itself, especially when looking for better than 3 percent accuracy. Additionally, the facility serves as a source for the diagnosis of all the problems that might be associated with an *in situ* UV absorption ozone sensor. Those that are peculiar to an

in situ ozone sensor are:

1. Loss of ozone on isntrument walls;
2. Incomplete ozone removal for ozone-free absorption measurement (incomplete "scrubbing");
3. Incomplete Flushing of absorption cell between "scrubbed" and "unscrubbed" cycles;
4. Scrubber emissions resulting in a negative offset;
5. Temperature inhomogeneity in the absorption cell;
6. Pressure difference between ambient and the absorption cell.

In order to be able to investigate these problems and berify their absence on an ongoing basis, a stable laboratory source at stratospheric pressures are required, allowing routine pre- and post-flight instrument performance checks.

B. The Calibration Facility

Figure 3 illustrates the current configuration of the laboratory facility at which virtually all the laboratory tests of our flight ozone sensor are made. Since it is the continual availability of the low pressure fast flow facility that allows complete diagnosis of the flight instrument, it is worthwhile discussing its operation in some detail and providing information on its gradual metamorphisis. A large Roots blower pump is capable of providing flow velocities up to 30 m/sec through a 6" diameter flow tube which is interfaced to the pump via a 6" diameter stainless steel ball valve, which provides source velocity control, and a 10" diameter stainless steel manifold. Mixtures of O_3, O_2, and N_2 are introduced into the system through a teflon loop injector and the flows are monitored with Matheson flow meters. A stainless steel screen has typically been used to help straighten or laminarize the flow. This is

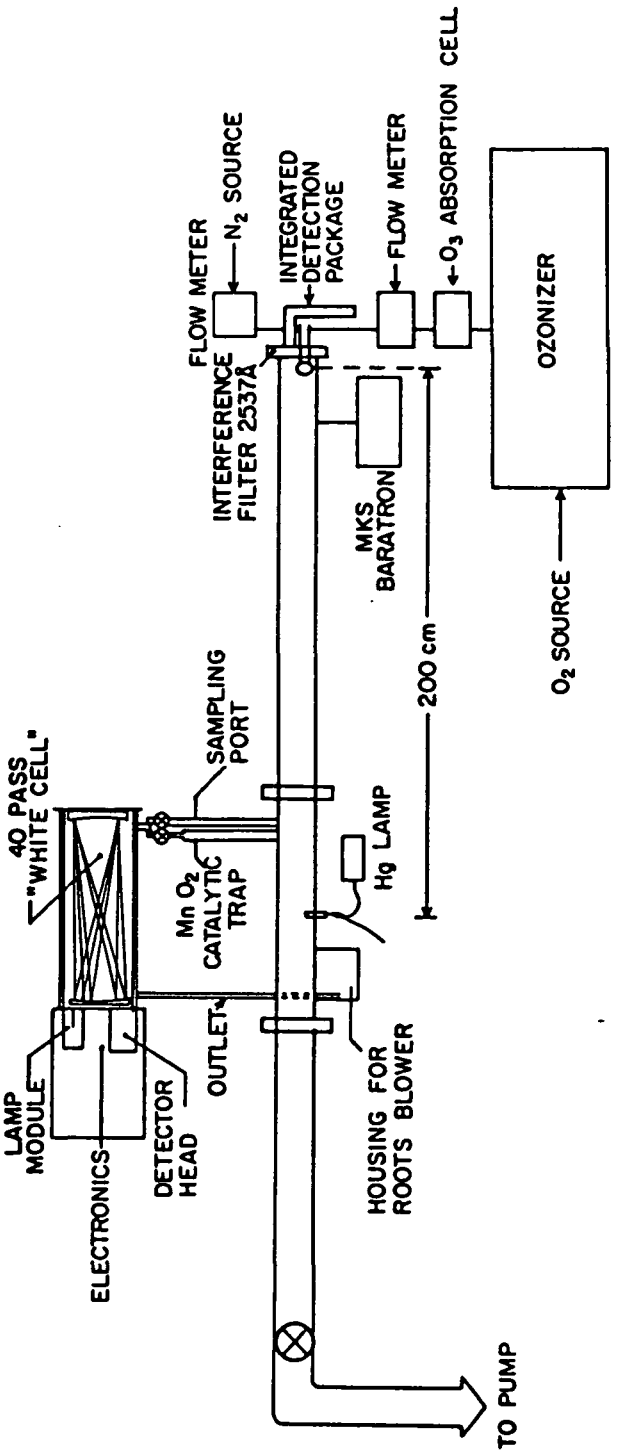

Figure 3. Ozone calibration facility.

being replaced by a teflon laminarizer made up of about 35 3/4" o.d., 2-1/2" long tubes strapped together to form a 6" diameter honeycomb. The pressure in the flow tube is measured by a 1 - 10 torr MKS Baratron capacitance manometer (low pressure range) or a Granville Phillips convector gauge checked against a Leyboldt-Heraeus Diavac gauge for the high pressure range (up to 50 torr) and more recently a 0 - 100 MKS model 222B capacitance manometer. For measurements into the summer of 1984, a vycor-sheathed low pressure mercury lamp enlcosed in an aluminum housing (the light source) is centered in the flow tube approximately 2 meters downstream from the aperture of the detector, an EMR 5410 solar blind photomultiplier used in a photon-counting mode and fitted with a bandpass filter centered at 254 nm with ~ 100 nm bandwidth. Count rates for the absorption measurements have typically been in the 175 to 225 kHz range.

As a result of the desire to improve the sensitivity of the laboratory absorption system, as well as eliminate the problems of non-linearity which recently surfaced in this system, the photomultiplier has been replaced by a vacuum photodiode, the output of which is amplified, converted to a frequency and fed into a frequency counter. To provide improved lamp stability, the lamp is situated in an insulated housing external to the vacuum system and fused silica fiber optics with a matching launching lens (Diaguide, Inc.) are used to feed the light into the flow tube and provide a slightly diverging beam of 1" diameter down the center of the flow tube, slightly overfilling a fused quartz lens which focusses the beam onto the surface of another silica fiber optic carrying the light to the photodiode. The system provides approximately 4×10^{11} photons/sec in the 215 cm absorption path with a stability of better than 5 parts in 10^5. This allows a measurement of 10^{12} O_3 moelcules/cc with 5 percent precision with 1 second averaging, a major improvement over photon counting

which is limited severely by photon shot noise.

A Welsbach gauge is used to provide ozone concentrations from 5×10^{11} to 5×10^{13} molecules/cc in a pressure regime of 2 to 50 torr and at flow velocities of from 3 to 10 m/cc. The calibration runs formerly required $[O_3] = 8 \times 10^{12}$ mol/cc, but now can be extended easily to concentrations less than 1×10^{12} mol/cc. These values are of great use in demonstrating the stability of the flight instrument and determining the stability of the ozone sources. Additionally, operating the system as a source of ozone free air is very useful in checking the signal-to-noise ratio of the instrument and the presence offsets under a wide range of conditions.

C. Laboratory Measurements

Figure 3 also contains the typical arraingement for interfacing the flight instrument to the flow system. Both the one scrubbed and two unscrubbed inlet tubes sample the gas upstream of the lamp, while the return is well downstream to avoid contaminating the measurement. The homogeneity of ozone in the flow can be checked by comparing measurements made at the two inlet points, as a function of pressure and velocity in the flow tube. Figure 4 illustrates a first order utility of the low pressure system. In 4a, the no ozone signal is represented by monitoring the intensity of I_{sample}, and the numbers printed out are the $I_o - I$ values measured by the instrument for each cycle. When the ozone in the system is turned on, the ozone concentration is measured as $2.27 \pm 0.17 \times 10^{11}$ mol/cc and represents the stability of the ozonizer under these conditions. Note the noisier character of the trace when ozone is flowing (representing ozone fluctuations), as opposed to the less severe instrument noise during the other half of the cycle. Figure 4b illustrates the stability under higher ozone flows. The important point to take note

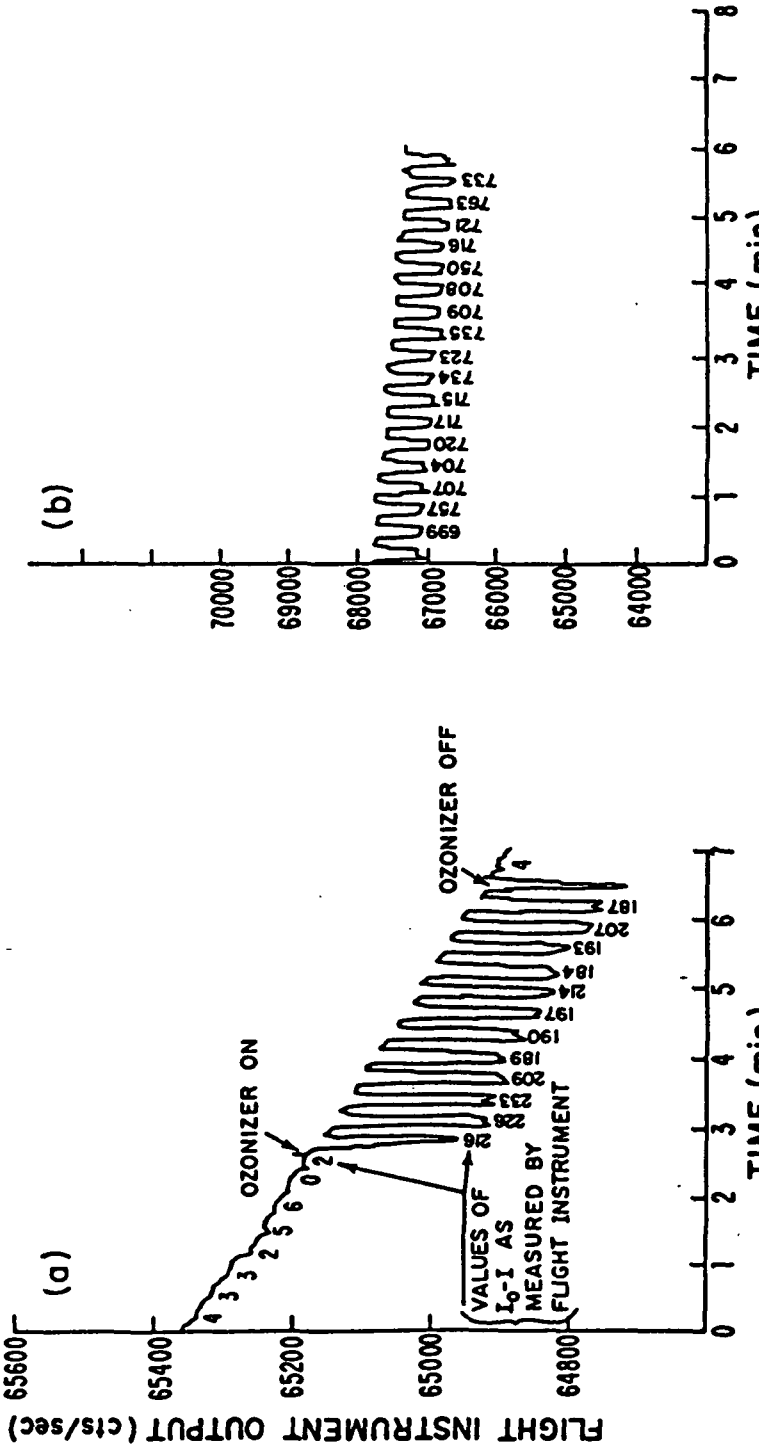

Figure 4. "White cell" ozone measurements in the flow reactor.

of is that the real signal-to-noise of the instrument is illustrated here and can be compared to that observed in flight since these data are also digitally recorded.

Table 1 illustrates a series of runs made at a variety of pressures and represents the typical agreement between the flow bench and flight instruments. It should be again emphasized that these are only calibration runs in the sense that the number of passes in the cell must be established. Subsequently, the runs demonstrate a comparison of two independent and simultaneous measurements of the same ozone concentration, subject to the limitations of the homogeneity and stability of the ozone concentration in the flow tube which should typically be 2% or better. These data were recently taken utilizing the newly improved detection system and as expected represent a statistical improvement over previous laboratory ozone measurement comparisons. One can, upon close inspection of the data, come to the following conclusions:

1. The ratio of the two measurements is independent of $[O_3]$, ambient pressure, and motor speed, except for number 4, a speed purposely included for diagnostics such as this.
2. A systematic difference of $\sim 2.5\%$ exists between the two measurements which could be caused by the sum of:
   a. Loss in the flight instrument;
   b. Flow tube inhomogeneities;
   c. Systematic error in temperature, pressure, or differential pressure measurements;
   d. Offsets or non-linearity in the counting circuit;
   e. Pathlength errors.
3. Precision of the measurement's reproducibility is $\sim 1\%$;
4. Some systematic differences, on the order of 1%, appear in the data

Table 1

Date	$\sim[O_3]$	Motor Speed	Pressure (torr)	Ratio $\left(\frac{\text{flight } O_3}{\text{lab } O_3}\right)$	Valves
2/1/85	1.24×10^{13}	1	3.25	.992	3-way TFE
	1.15×10^{13}	1	3.25	1.003	
	5.9×10^{12}	1	3.25	.983	
2/4/85	1.29×10^{13}	1	2.07	.991	↓
	1.25×10^{13}	1	2.07	.988	
	1.24×10^{13}	4	2.07	.967	
	1.15×10^{13}	4	2.07	.972	
	1.05×10^{13}	2	2.07	.976	
	1.37×10^{13}	2	5.05	.977	
	1.29×10^{13}	2	5.05	.979	
	1.25×10^{13}	4	5.09	.972	
	1.22×10^{13}	4	5.09	.965	
	1.20×10^{13}	1	5.09	.981	
2/4/85	1.25×10^{13}	1	3.06	.972	Bal-zers
	1.24×10^{13}	1	3.06	.978	
	1.23×10^{13}	4	3.06	.962	
	1.23×10^{13}	4	3.06	.964	↓
	1.22×10^{13}	2	3.06	.974	
	1.12×10^{13}	2	7.33	.976	
	1.12×10^{13}	2	7.33	.973	
	1.12×10^{13}	4	7.33	.947	
	1.12×10^{13}	1	7.33	.986	
	1.10×10^{13}	1	7.33	.988	
2/5/85	7.5×10^{12}	1	3.02	.973	
	1.01×10^{13}	1	3.02	.974	
	1.6×10^{13}	1	3.02	.970	
	1.31×10^{13}	2	3.02	.969	
	1.86×10^{13}	3	3.02	.974	
	1.04×10^{13}	3	3.02	.966	
	1.04×10^{13}	4	3.02	.967	
	1.7×10^{13}	4	3.02	.964	
	1.25×10^{13}	1	3.02	.977	
	1.9×10^{13}	1	3.02	.974	
2/7/85	1.7×10^{13}	1	3.04	.971	
	1.7×10^{13}	2	3.04	.974	
	1.7×10^{13}	4	3.04	.954	
	2.1×10^{13}	4	9.84	.948	
	8.9×10^{12}	4	9.84	.939	
	8.6×10^{12}	1	9.84	.980	
	1.6×10^{13}	2	9.84	.962	
	1.5×10^{13}	4	9.84	.917	

taken with the large throughput teflon three-way valves versus Balzer's valves. The data are limited and await further analysis. Since the high conductance, three-way teflon solenoid valves failed after a few days, substantiation of this small discrepancy has been delayed.

While further tests on the system are in progress, especially toward tracking down this systematic difference, the precision and accuracy of the instrument have been thoroughly illustrated for stratospheric applications. Extension to higher pressures are somewhat hindered by turbulence in the laboratory flow system where Reynolds number $\geq$ are in evidence and the turbulence can be viewed through chemiluminescent emission of an O + NO afterglow emission.

Additional loss tests have been carried out by studying the motor speed dependence of a series of measurements made on a stable ozone source. Figure 5 shows the results at two different pressures in which measurable loss only occurs at the slowest motor speed. Additional stopped flow tests in the laboratory verify < 1%/sec loss of ozone in the absorption cell.

D. Precision and Accuracy of the Flight Instrument

As is the case with all of the ozone photometers, the operating principle of our instrument is Beer's law where

$$I = I_o \exp(-\sigma n \ell) \qquad (1)$$

The accepted value of σ, the O_3 cross section at 253.7 nm, is 1.146×10^{-17} cm^{-2} with an accuracy of ± 2%. The pathlength in our absorption cell, ℓ, is 1205 ± 4 cm. The statistical uncertainty in the normalized counting circuitry is ± 1 count in the measurement of $I_o - I$ and $^{+\ 255}_{-\ 1}$ counts in the measurement of I_o. This propagates into an experimental uncertainty or instrument precision of $\pm 2 \times 10^{9}$ mol/cc of ozone assuming 70,000

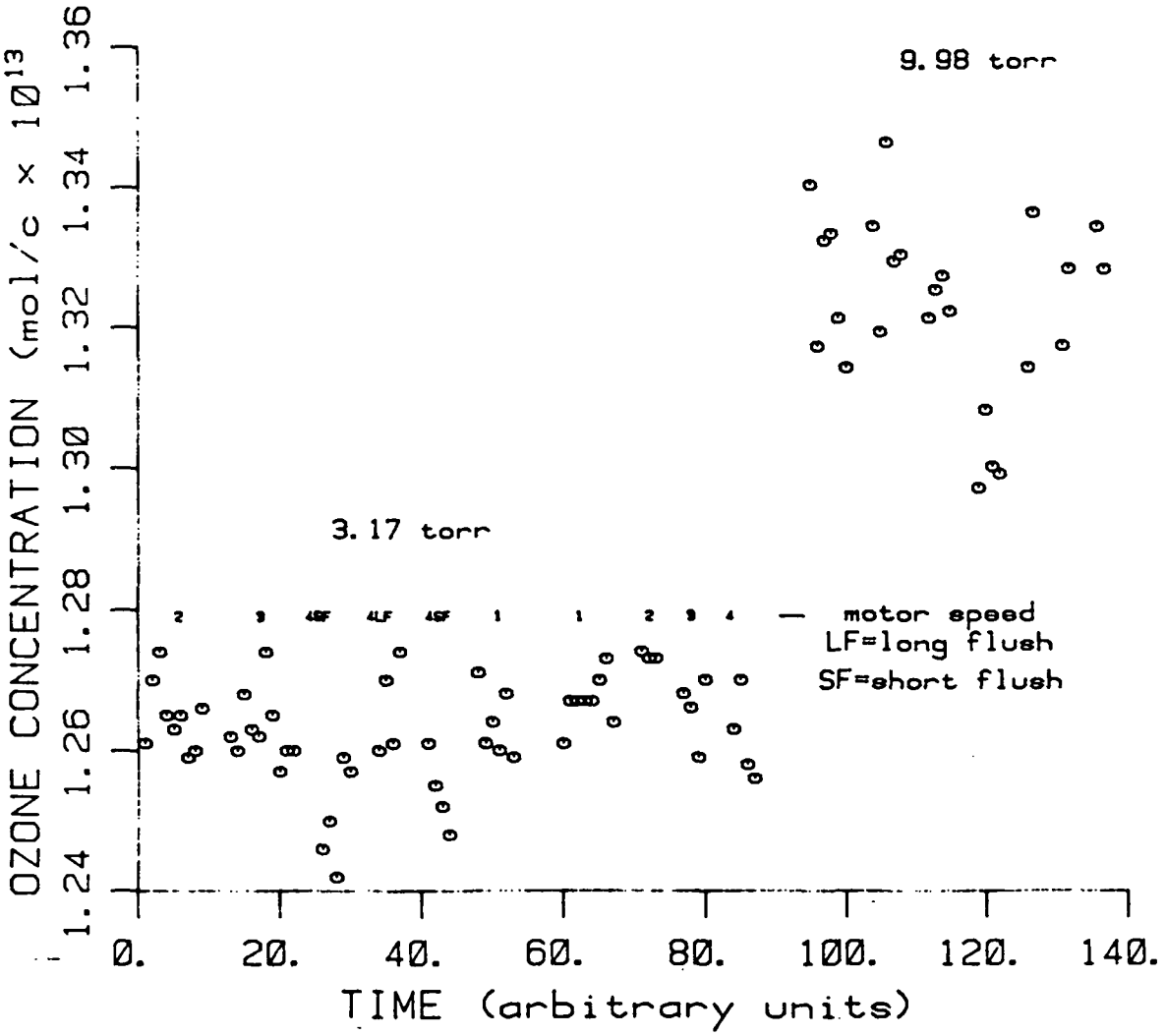

Figure 5. Variation of O_3 with motor speed.

cts/sec for I_o, and thus demonstrates the expected precision of our instrument throughout the stratosphere. However, the real test of instrumental precision and signal-to-noise is to demonstrate it during the actual operation of the instrument. Figure 4 does in fact do that for laboratory operation. However, it is more convincing to illustrate instrumental signal to noise during the flight. Figure 6 is real time data taken during the next to last flight of our instrument in March, 1984. The scans show counts/0.25 seconds of light transmitted through the absorption cell, taken during float and conclusively demonstrate the precision of the instrument. This is especially critical at 40 km and above where the ozone concentration is 5×10^{11} molecules/cc or less. Figures 5 and 6 clearly demonstrate the capability of our instrument for precise O_3 measurements up to 45 km.

The accuracy of an instrument is much more difficult to validate in flight because the ozone concentration is known only to the extent to which it can be measured. Assessment is therefore generally based on comparison with other simultaneous measurements as well as a critical evaluation of the possible systematic errors present in the instrument. It is first worthwhile noting that the most notorious sources of systematic error each reduce the measured ozone concentration and therefore create the perception that an in situ ozone photometer is unlikely if not incapable of measuring too high an ozone concentration. The in-flight diagnostics allow us to conclusively dismiss incomplete ozone scrubbing, wall loss, or incomplete flushing of the absorption cell as problems. Figure 6 demonstrates, at a float pressure of 2.5 mbar, the loss of ozone in the absorption cell in time to be $\leq$ 2%. Part of this loss of ozone is caused by diffusion of air in contact with the uncoated exit tubing into the absorption cell. It also includes the photodissociation

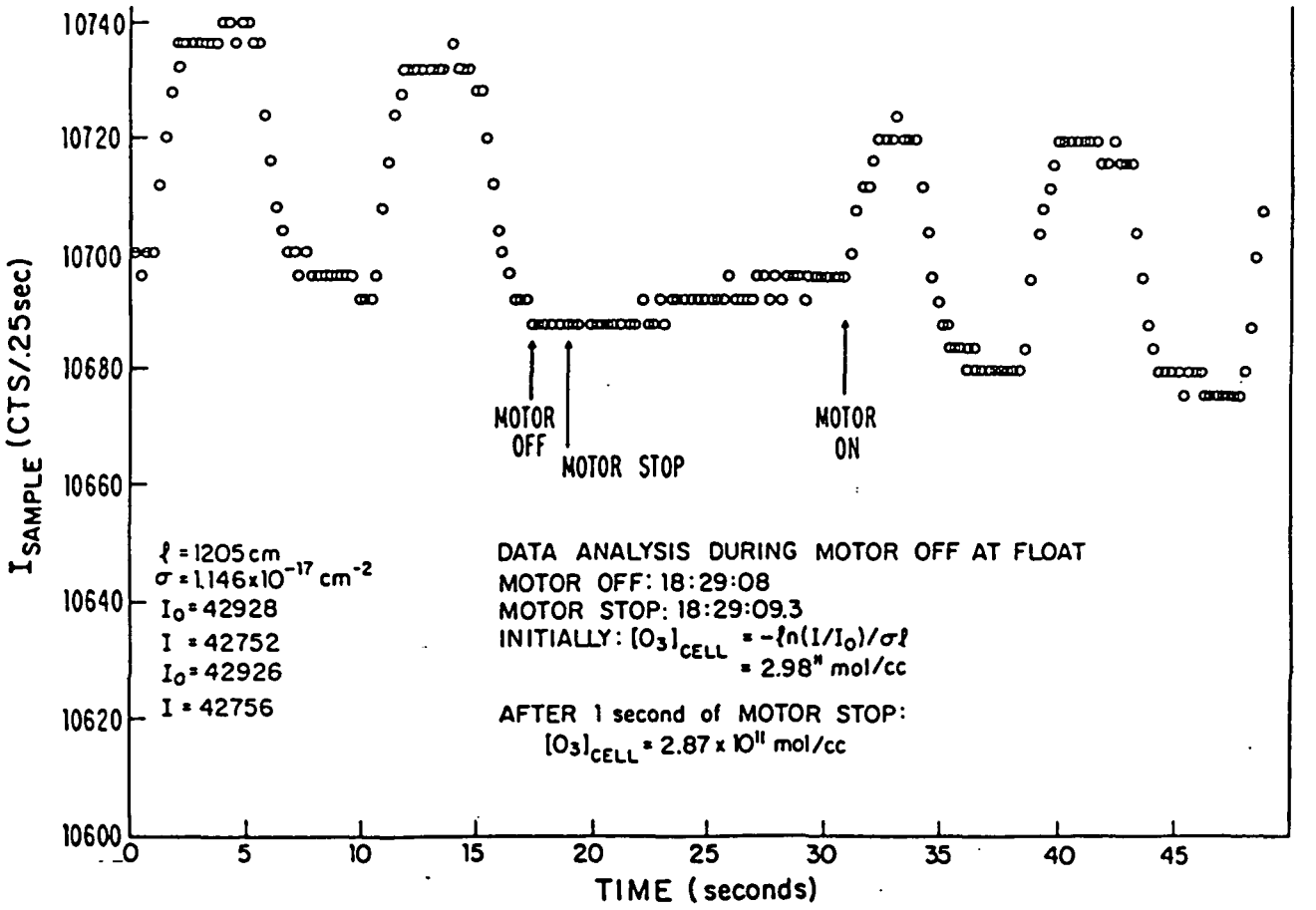

Figure 6. I_{sample} monitored during float, BOIC flight.

of ozone by the sample beam. The additional diagnostic of flow rate change of a factor of three in the instrument has never pointed to ozone loss. In addition, adequate flushing time is illustrated in Figure 6 by the shape of the sample intensity signal during the scrubbed and unscrubbed parts of the cycles. Ozone scrubbing efficiency can be evaluated by observing any changes in I_o during times of high ozone concentration, and is maintained effectively at 100 percent. At this time, no direct diagnostic is available in flight for evaluating or quantifying ozone scrubber emissions. These emissions are most likely a result of plasticizers, which are a common outgasser from plastic of all kinds. The plasticizers can be one of many phthellate esters, all of which contain a benzene ring and therefore strongly absorb around 253.7 nm. The scrubber emission during flight tends to be time dependent and is characterized by negative instrument counts during initial phases of the flight and marked difference between ascent and descent profiles. The problem, which first surfaced in 1983, can easily be controlled by thoroughly vacuum baking the scrubber during preflight tests, and then storing it in a clean environment.

Continuous monitoring of the sample intensity also provides the necessary information to correct for any changes in the ratio of I_{sample} to $I_{control}$; this, however, has never been required but does account, at least partially, for the sharp gradient in the concentration measurement after initial motor turn-on when the mirror reflectivity rises sharply. The existence of convincing evidence both from in-flight and laboratory diagnostics that the understood mechanics for measuring low ozone should remove the possible bias that might exist toward an <u>in situ</u> photometer measuring capability, most notably in the stratosphere and thus put to rest what has been a generally accepted inadequacy of this class of instrument.

Results and Discussion

The first successful flight of our ozone sensor occured over Palestine, Texas in June, 1981. The ascent and descent profiles are presented in Figure 7. Motor speed and flush time diagnotics were carried out and showed no measurable trends. The overall agreement in the two profiles supports a properly functioning instrument. In this early flight, atmospheric pressure measurements were performed by Rosemount pressure transducers provided and calibrated by the Balloon Base against a Texas Instruments Model 145 precision pressure gauge and with a quartz Bourdon tube used as a secondary standard. We present this profile as an example of high resolution data capabilities and instrument performance.

Our more recent flights, one during our participation in BOIC III, the other in September, 1984, are worthy of more detailed consideration for several reasons:

1. Improved thermal operation of the instrument;
2. Improved differential pressure measurement;
3. More reliable ambient pressure measurement using capacitance manometers;
4. Thermal diagnostics around the gondola to ensure that only data taken with unperturbed ambient air samples is considered.

Figure 8 presents approximately half km averages of the ascent and descent data for the March, 1984 flight, and ascent data for the September, 1984 flight. Based on the results of the recent BOIC intercomparison (Hilsenrath et al., 1985), these profiles may be viewed as representative of 32 N latitude Spring-Fall ozone in the stratosphere. As an additional means of comparison, we include the SBUC data of March, April, September

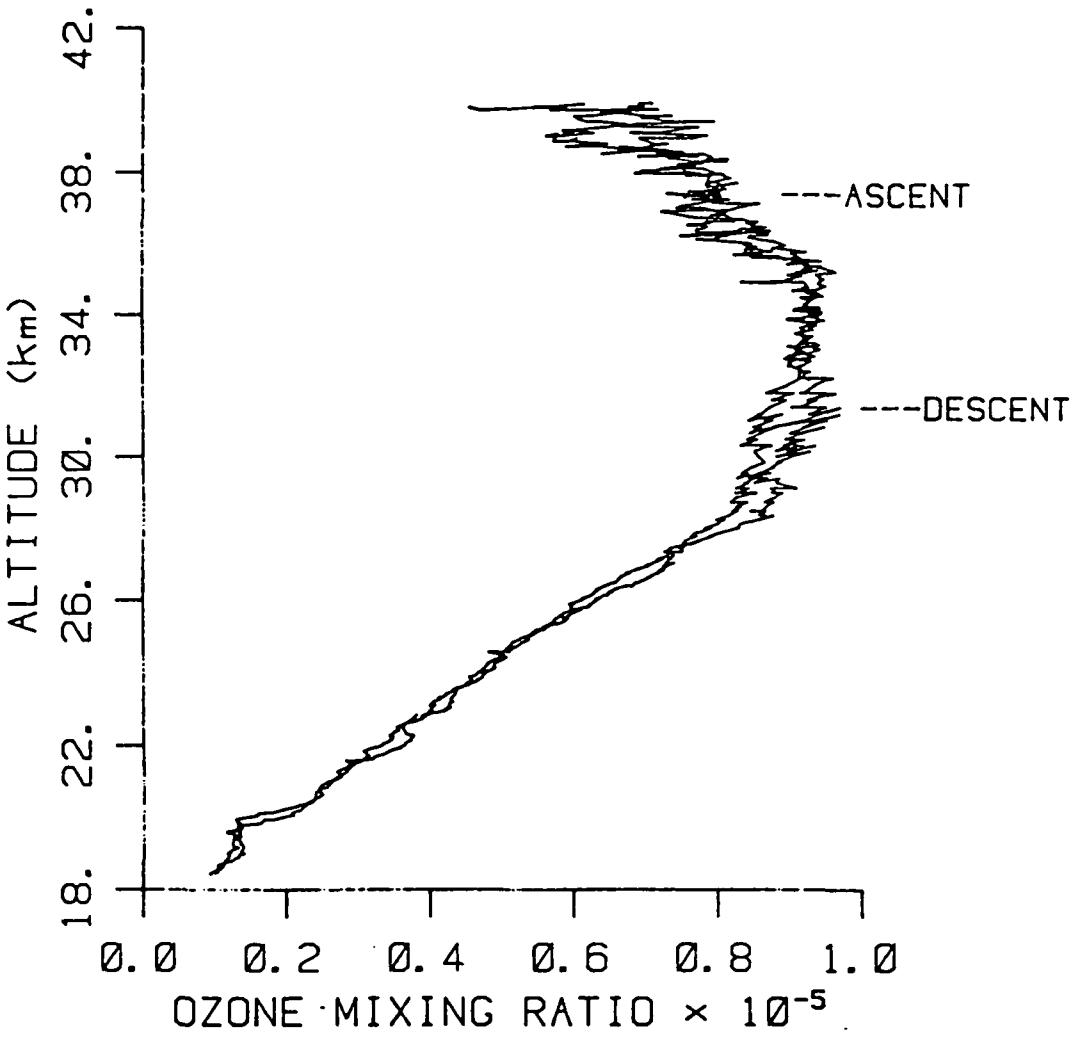

Figure 7. June, 1981 ozone profiles.

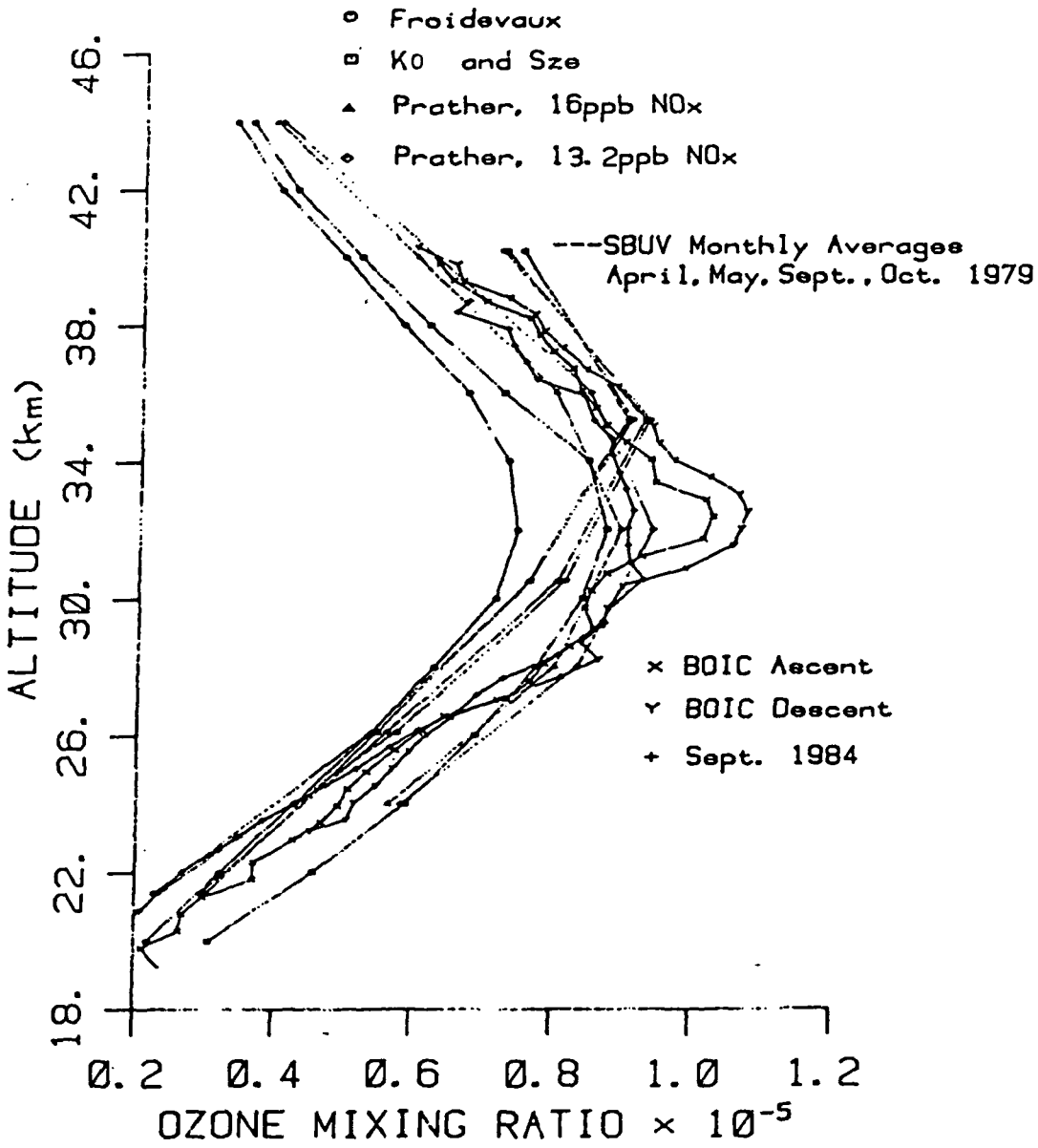

Figure 8. Comparison of experimental and modelled ozone profiles.

and October 1979, 30-40 north latitude, as tabulated by McPeters et al. (1984). The roughly 15% difference exhibited here is somewhat more than the 10% exhibited during a BOIC flight in July, 1983 (E. Hilsenrath, private communication), but nevertheless establishes a degree of consistency between in situ UV absorption, mass spectrometer, and SBUV data; and therefore a reasonable ozone profile for comparison with recent model calculations which have been updated with the most recent changes in both the O_2 absorption cross section data and relevant rate constants.

It has recently been pointed out that there exists significant differences between modeled and experimental ozone profiles (see Froidevaux, 1984; Ko and Sze, 1983). These mid-latitude, Spring-Fall equinox models, when compared to a Standard Atmosphere ozone profile (1976 Standard Atmosphere), or results from other intercomparisons reported in WMO/NASA report (Hudson, 1982), appear to be almost 50% low at 40 km, thus presenting a problem of major importance. If this large disagreement accurately represents our understanding of ozone loss and production rates in the photochemically dominated region of the stratosphere, then ozone depletion predictions must be viewed with caution. Fortunately, the Harvard 1-D model (see Prather, 1981; NAS, 1982) demonstrates acceptable agreement with the presented experimental profile. However, in 1981, agreement was obtained by reducing the H_2O mixing ratio to 2 ppm, a number we now know to be much too small; thus directly reducing O_3 catalytic destruction by OH and indirectly by ClO through conversion of HCl. The more recent comparison is made with a model which substantially underestimates NO_x around 40 km and furthermore uses a summer atmosphere which effectively pushes up the profile by 1 km. The former occurs mainly because of the scatter in the NO profiles published by various authors (see Hudson, 1981).

However, the data of Ridley et al. (see the review by Ridley and Schiff, 1980) represents our best source of knowledge for stratospheric NO and strongly suggests that the NO_x mixing ratio at 40 km should be 20-22 ppbv, thus substantially worsening the agreement of the Harvard 1-D model. In Figure 8 we present what we believe is a more realistic picture of the extent of disagreement between model and experiment. The figure contains a region representing experimental results with our in situ data verified by the BOIC flight serving as a lower bound and averaged SBUV data from March, April, September, and October, 1979 as tabulated by McPeters et al. (1984) providing the upper bound. The model profiles of Ko and Sze (1983), Froidevaux (1983), and Prather et al. (1984) with NO_x profiles normalized to 13,2 and 16 at 40 km bound the region of theoretical predicted ozone. It can now be seen that the disagreement presented here is on the order of 15-25%, and could be worse, depending on the real NO_x mixing ratio.

The results of this comparison will be more accurately quantified by both obtaining SBUV data for the time periods during or surrounding the two Palestine launches and using model calculations that incorporate the appropriate atmosphere and insolation for the particular launch dates.

Summary

Recent data from BOIC have shown the convergence of data taken by research grade in situ and remote sensors in the stratosphere around forty kilometers. The build-up of a reliable data set invites comparison with model calculations with the goal of evaluating ozone depletion scenarios. The unavoidable question is whether the lack of agreement is a result of uncertainties in photolysis rates, rate constants and measured profiles, coupled with inherent atmospheric variability; or is an indication of yet another missing link in the atmospheric puzzle.

One approach is to enlarge this data base to the extent that a comparison can be made with a seasonally averaged model. Unfortunately, the apparent variability of water vapor, methane and stratospheric radicals directly involved in the catalytic destruction of ozone, limits the viability of this averaging approach. On the other hand, simultaneous in situ measurements of ozone and a carefully chosen set of stratospheric radicals and source molecules can directly constrain model predictions of ozone reduction.

References

Aimedieu, P., A.J. Krueger, D.E. Robbins and P.C. Simon, Ozone profile intercomparison based on simultaneous observations between 20 and 40 km, Plaet. Space Sci. 7, 801, 1983.

Aimedieu, P., A.J. Kreuger, D.E. Robbins and P.C. Simons, Ozone profile intercomparison based on simultaneous observations between 20 and 40 km, Planet. Space Sci., 31, 801, 1983.

Ainsworth, J.E., J.R. Hagemeyer and E.I. Reed, Error in Dasibi flight measurements of atmospheric ozone due to instrument wall-loss, Geophys. Re. Lett., 8, 1071, 1981.

Chapman, S., A theory of upper stratosphere ozone, Mem. Roy. Met. Soc. 463, 103, 1930.

Crutzen, P.J. and U. Schmailzl, Chemical budgets of the stratosphere, Planet. Space Sci. 31, 1009, 1983.

Froidevaux, L., Photochemical modelling of the earth's stratosphere, Thesis, Cal. Inst. Techn., 1984.

Hartley, W.N., On the absorption spectrum of ozone, J. Chem. Soc. 39, 57, 1881a.

Hilsenrath, E., Ozone correlative measurements workshop, NASA Conf. Publ. 2362, 1984.

Hudson, P.D., The stratosphere 1981: theory and measurements, WMO Global Ozone Res. and Monitoring Project Report No. 11, 1981.

Johnston, H.S., Reduction of stratospheric ozone by nitrogen oxide catalysts from SST exhaust, Science 173, 517, 1971.

Molina, M.J. and F.S. Rowland, Stratospheric sink for chlorofluoromethanes: chlorine atom catalyzed destruction of ozone, Nature 249, 810, 1974.

National Academy of Sciences, Causes and effects of stratospheric ozone reduction: an update, National Research Council, National Academy Press, Washington, D.C., 1982.

Prather, M.J., Ozone in the upper stratosphere and mesosphere, J. Geophys. Res. 86, 5325, 1981.

Prather, M.J., M.B. McElroy, and S.C. Wofsy, Reductions in ozone at high concentrations of stratospheric halogens, J. Geophys. Res., to be published.

White, J.V., Long optical paths of large aperture, J. Opt. Soc. Amer. 32, 285, 1942.

WATER VAPOR

Introduction

The information necessary for the evaluation of UV-photofragment fluorescence as an approach to atmospheric water vapor measurement has been available since the first measurement of the quantum yield of $OH(^2A^+\Sigma)$ from Lyman-α photolysis of H_2O by Carrington[1] and the more recent quenching measurements of Becker and Haaks,[2] German,[3] and Lengyel and Crosley.[4]

The UV-photofragment fluorescence method for *in situ* atmospheric H_2O detection was independently developed by Kley and Stone[5] and Gertaux and Delannoy.[6] The Kley experiments were flown at night to eliminate detector background from Rayleigh scattered sunlight; and also eliminate the need for instrument "walls" serving as light baffles (which are sources of experimental contamination). The Bertaux flight dealt with the problem by using a light tight stainless steel chamber through which stratospheric air is forced by a turbine. Outgassing of the walls was achieved on ascent using dry stratospheric air and was measured at intervals during the flight by turning off the turbine. While this approach allows for a daytime flight, it does not adequately remove the effect of outgassing which had to be measured with the turbine off. Furthermore, the flight did not exceed 25 km and thus did not reach the altitude regime where water vapor concentrations are as low as 1×10^{11} molec/cc and thus outgassing is even more critical.

Since we are interested in the partitioning of the hydroxyl radical between its reservoir form, H_2O, and its free radical forms, OH and HO_2, a simultaneous and therefore daylight measurement of OH and H_2O is required. This requires an instrument which will both discriminate against

solar background and yet eliminate any possible source of H_2O contamination of the sample.

Experimental Results

In order to accomplish these objectives, we have used the design of the optical chamber previously employed to detect stratospheric OH,[7] and an aerodynamically designed nose cone,[8] both modified to allow liquid nitrogen to uniformly reduce wall temperatures to ~ 80°K and thus not only ensuring the absence of outgassing of H_2O from any instrument wall, but also removing any water from the ambient sample which collides with the cooled wall. Figure 1 is a side view illustration of the H_2O flight nacelle. The central part of this nacelle contains, as labelled, the Lyman-α light source for excitation, a movable vacuum UV photodiode to monitor its intensity, and a detector at right angles to measure the OH fluorescence. This section, with its fixed optical geometry, is used for laboratory calibrations prior to being affixed to the rest of the nacelle. All relevent surfaces in this section can be cryogenically cooled. The upper diffuser section of the nacelle houses the fan used to draw the air through the experiment at velocities up to 25 meters/sec, an anemometer to monitor the flow, as well as an array of thermistors (below the anemometer; not shown) used to characterize the quality of the flow and identify any time that an external perturbation might cause an intrusion of contaminated (cryogenically dried) air into the viewing region. The aerodynamically-shaped, cryogenically-coolable nose cone serves as the bottom section of the nacelle. Following assembly, the nacelle is fitted with flaps which allow the whole flow tube to be nitrogen-purged and thus gradually dried. This not only allows for monitoring of the lamp output

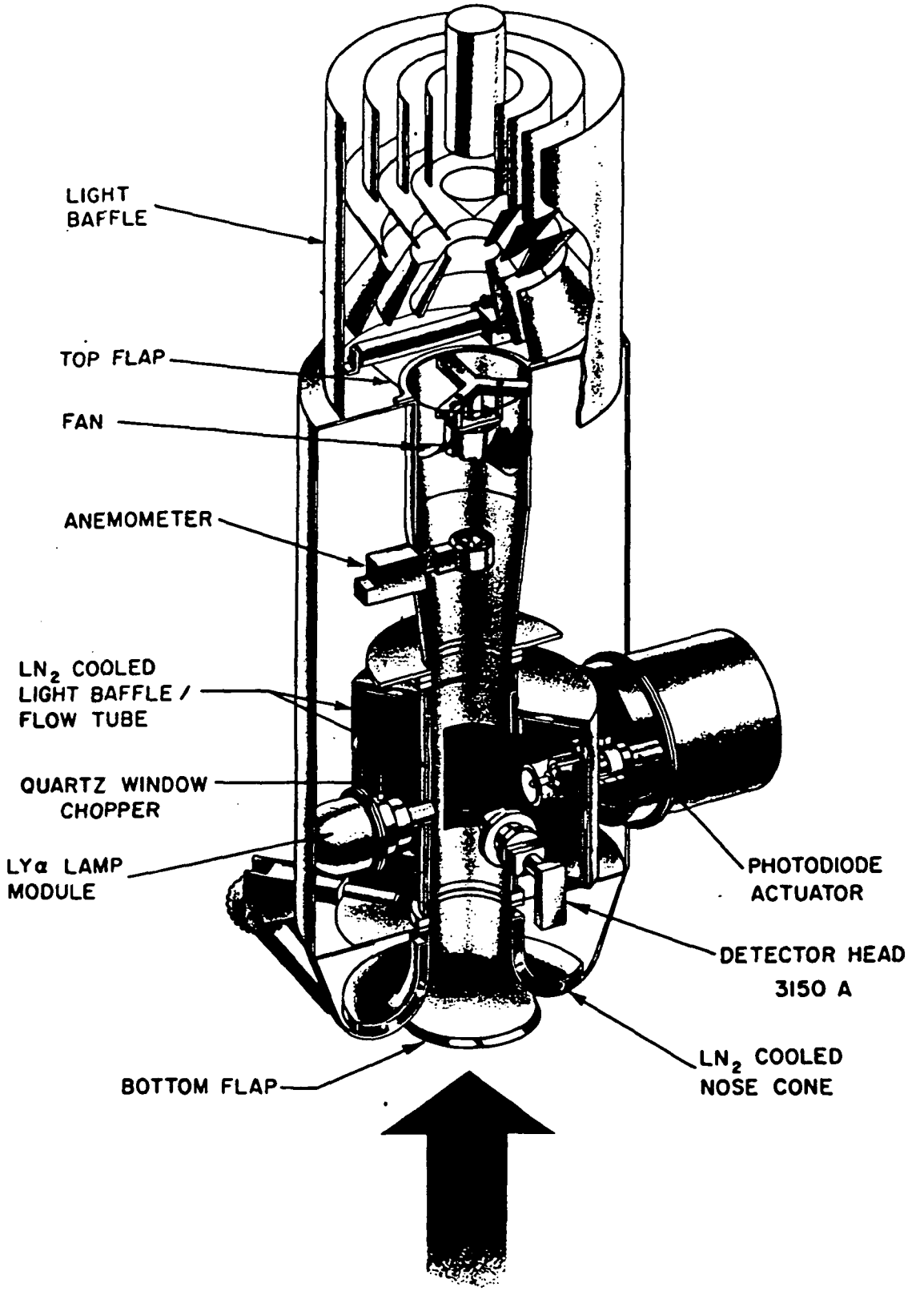

Figure 1. Side view of the cryogenic chamber and nacelle of the water vapor experiment. Also shown are the light baffles, movable UV photodiodes, anemometer, fan, and lamp module. Not shown are the sealing flaps.

during testing of the system, but also limits the icing that could occur on the nacelle walls as they are cryogenically cooled in the stratosphere. The walls of the nacelle downstream of the optical axis have been covered with aluminum honeycomb and then painted with a flat black paint (solar coat 50) to assure a minimum of backscattered sunlight into the detector. The reflective properties of an ice-layer would increase background counts unacceptably. The top of the flow tube is fitted with cylindrical light baffles to remove the possibility of intrusion of direct sunlight to the optical axis.

A fifty liter dewar is used to transport liquid nitrogen into the stratosphere. A transfer system consists of four solenoid valves rated for use at -77°C, 3/4" stainless steel tubing, and a six liter plenum maintained at 15 psi, approximately 7 psi below the dewar pressure. Thermistors in the dewar are used to monitor the level of liquid nitrogen in the dewar during the transfer and thermistors on all the nacelle surfaces are used to indicate when the transfer is complete. The fifty liters of nitrogen is sufficient to not only fill the dewar, but also allow for a refill or "top off" if dictated by a larger than desired "float" or slower than desired descent rate.

Principle of Operation

While the approach of photofragment resonance fluorescence applied to water vapor has been discussed by other authors, for completeness we shall include it here as well. Furthermore, the differences between our instrument and others will be emphasized.

Excitation and fragmentation of water vapor is accomplished by Lyman-α emission from a sealed lamp containing approximately four torr of neon and a side arm of UH_3 as a source of hydrogen. The lamp is excited via ~ 30 watts of 150 MHz RF power inductively coupled to the lamp. A vacuum photodiode monitors 4863 hydrogen radiation emitted through the rear of the lamp and serves as the control element in a feedback loop which regulates the hydrogen vapor pressure in the lamp, and thus the Lyman-α flux. A flowing oxygen filter is used to remove molecular hydrogen radiation which otherwise might contribute from 10-20% of the VUV radiation when the instrument is in the upper stratosphere.

Detection of OH fluorescence is accomplished with an EMR N-type tube preceded by a narrow band interference filter centered at 3150 Å (50 Å B.W., 30% T, Barr Associates). The expected sensitivity of the experiment can be expressed as

$$S = I\sigma_A[H_2O]Ez\eta TQ\Gamma = C_{H_2O}[H_2O]Q$$

where I is the photon flux; σ_A is the production of H_2O absorption cross section and 1216 Å and the quantum yield for formation of OH in the $A^2\Sigma^+$ state; E is the collection efficiency for the detector optics; z is the absorption pathlength; η is the quantum efficiency of the photomultiplier at 3150 Å; T is the transmission of the detector optics; Q is the fraction of unquenched radiation; and Γ is the Franck-Condon factor for the (0,0) OH band. Using typical values of $I = 5 \times 10^{13}$ photons/sec, $\alpha_A = 10^{-18}$, $E = 10^{-3}$, z = 3 cm, η = 0.20, T = 0.30, Γ = 1, $S \cong 10^{-8}$ $[H_2O]Q$, a value confirmed by laboratory calibrations.

A Hammamatsu vacuum photodiode is used to monitor the 1216 Å radiation emitted during the light and serves as a necessary check on the possible optical degradation of the MgF_2 lamp and O_2 cell windows, each subject

to optical deterioration, mostly from polymerization of contaminants on the optical surfaces by the high VUV photon flux. Since, according to Equation (1), the sensitivity is linearly proporational to flux, an in-flight measurement is necessary to correct the preflight calibration factor, C_{H_2O}, for any change in flux.

Moreover, it is desirable to measure the concentration of water vapor into the lower stratosphere, where it approaches 10^{15} molec/cc, at which point the absorption of Lyman-α radiation by water vapor is directly measurable. Additionally, as it has been shown by Kley et al.,[9] a two-path absorption measurement allows for an in-flight calibration for the fluorescence measurements. This approach is also utilized here. A timing circuit which can operate in either of two modes controls the voltage to a DC motor which moves the photodiode assembly from its normal position where the front MgF_2 window is recessed 1-1/2" from the plane of the flow tube to a position even with the wall or one 1-1/2" in front of the wall. A shaft encoder allows continuous axial measurement of the diode position to better than 0.5 mm. The normal position of the diode is chosen to not only limit scattering but also to reduce any possible outgassing effect that any of these surfaces might have.

While the exterior of the housing is cryogenically cooled to $\leq -100°C$, the diode and its complementary electronics is maintained at $\sim 0°C$. A dry nitrogen purge maintained slightly above ambient pressure helps insulate the inner assembly from the externally cooled surfaces and assures an absorption free path between the window of the photodiode and the MgF_2 window.

Temperature control of the MgF_2 window is critical as it must be cold enough not to be a source of contaminants and warm enough not to

frost. A thermistatically controlled heater with two set points assures adequate regulation. Nevertheless, the temperature restriction on this element requires it to be outgassed before data taking operations begin. The shape of the assembly was chosen to minimize the extent to which it affects the flow during the absorption measurements.

In order to determine background during the flight, a timing circuit, synchronized to the photodiode assembly timing circuit, controls the position of a quartz window which is inserted in front of the lamp for a period of 2 sec out of 8 sec.

We summarize the instrument performance by tabulating, as a function of altitude throughout the stratosphere, each of the quantities:

$$S^{FF}_{H_2O} = C_{H_2O}Q[H_2O]$$

for a typical distribution of water vapor in the stratosphere.

Alt	[M]	Q	$C^{OH(A-X)}_{H_2O}$	$[H_2O]$	$S^{F.F.}_{H_2O}$
50	2.14×10^{16}	0.72	1.5×10^{-8}	1.1×10^{11}	1190
45	4.09×10^{16}	0.57	↓	2.0×10^{11}	1710
40	8.31×10^{16}	0.40	↓	3.8×10^{11}	2280
35	1.76×10^{17}	0.22	↓	7.5×10^{11}	2475
30	3.83×10^{17}	0.125	↓	1.5×10^{12}	2813
25	8.33×10^{17}	0.062	↓	2.8×10^{12}	2604
20	1.85×10^{18}	0.029	↓	5.6×10^{12}	2436
15	4.05×10^{18}	0.014	↓	2.8×10^{13}	5880

In this table, the quenching coefficient is derived from the data of Kley and Stone,[5] who measure Q for O_2, N_2 and air at -80°C. While their Q is certainly a representative value for our flight measurement, our laboratory calibration procedure incorporates quenching measurements under conditions which duplicate flight conditions.

The instrument was calibrated and assembled for flight in preparation for a balloon launch during the summer of 1983. While the instrument was declared flight ready in Palestine, Texas, weight limitations imposed on the gondola because of the available balloon required that the water vapor experiment be removed from the gondola.

Presently, some engineering improvements are being made on the instrument in preparation for its maiden voyage for participation in a simultaneous in-situ water vapor, hydroxyl radical, and ozone measurement.

References

1. T. Carrington, J. Chem. Phys. 41, 2012 (1964).
2. K.H. Becker and D. Haaks, Z. Natur. 289, 249 (1972).
3. K.P. German, J. Chem. Phys. 62, 2584 (1975)
4. D.R. Crosley and R.K. Lengel, J. Quant. Spectr. and Radiat. Transfer 15, 579 (1975).
5. D. Kley and E.J. Stone, Rev. Sci. Instr. 49, 691 (1978).
6. J.L. Bertaux and A. Delannoy, Geophys. Res. Lett. 5, 1017 (1978).
7. Anderson, J.G., Geophys. Res. Lett. 3, 165 (1976).
8. Anderson, J.G., N.L. Hazen, S.P. Rowe, E. Thompson, C.M. Schiller, M.J. Schwab and E. Weinstock, to be published.
9. D. Kley, E.J. Stone, W.R. Henderson, J.W. Drummond, W.J. Harrop, A.L. Schmeltekopf, T.L. Thompson and R.H. Winkler, J. Atm. Sci. 36, 2513 (1979).

V. ADDITIONAL MANUSCRIPTS

The following manuscripts were written and presented during the course of this contract.

PONTIFICAL ACADEMY OF SCIENCES

CHEMICAL EVENTS IN THE ATMOSPHERE AND THEIR IMPACT ON THE ENVIRONMENT

"Role and Fate of Ozone in the Atmosphere"

James G. Anderson
Harvard University
Cambridge, MA 02138
U.S.A.

I. INTRODUCTION

A new dimension in global toxicology surfaced in the early 1970s with the introduction by Johnston[1] of the concept that rapid gas phase catalysis of ozone recombination to molecular oxygen by nitrogen oxides could alter stratospheric ozone concentrations. Not only did this provide a mechanism for reducing the atmosphere's ability to screen solar ultraviolet radiation, it also provided the means for disturbing natural patterns of heating and cooling in the upper atmosphere. In 1974, Rowland and Molina[2] presented their theory linking the surface release of fluorocarbons to the mid-stratospheric destruction of ozone by the catalytic reaction couplet:

$$Cl + O_3 \rightarrow ClO + O_2$$
$$ClO + O \rightarrow Cl + O_2$$
$$\overline{O_3 + O \rightarrow O_2 + O_2}$$

Photolytic decomposition of the fluorocarbon molecule augments the natural concentration of the Cl and ClO radicals, thereby accelerating the "odd oxygen" (ozone plus atomic oxygen) conversion to O_2.

That theory not only emphasized the importance of chlorine as a component of significant chemical importance to the unperturbed stratosphere, but also introduced the concept that the surface release of an inert and otherwise benign molecule, central to many aspects of our present society, could seriously deplete the concentration of a molecule in the upper atmosphere which is solely responsible for screening the surface of the Earth from potentially harmful near UV radiation. The work of these scientists profoundly altered our perspective of the global significance of such releases.

Important alterations to the global distribution of stratospheric ozone are currently predicted by the best available models which synthesize the chemistry, radiation and dynamics of the middle atmosphere. While these predictions have fluctuated significantly since the first crude estimates were offered in the mid-1970s[3], progress in many fields has brought a growing realization that the stratosphere may well be the first natural system to submit to the scientific method.

This tractability depends upon a rather unique and fortuitous combination of time constants which results in characteristic chemical response times being considerably shorter than dynamical time constants for many of the key mechanisms. Experimentally this means that "pure" chemical experiments can be executed in situ, to test photochemical hypotheses on the microscale within the atmosphere. On the other hand, dynamical experiments addressing the longer time scales can be conducted from Earth orbit via satellite to establish vertical and meridonal transport maps.

While evidence that the prognosis is encouraging for defining the scientific bounds of the global problem, the last decade of research has yielded mixed results. Attempts to understand the photochemical structure of the stratosphere at the level of detail required to predict trends in global ozone have challenged and often found inadequate, large areas of our understanding of gas phase photochemistry and kinetics. The stratospheric data base on trace reactive species which control the course of the chemical transformations in the atmosphere has yielded critical secrets but is in a rather primitive state.

It is not our purpose to comprehensively review the aeronomy of the stratosphere with the requisite discussion of such topics as dynamical meteorology, geochemistry, biochemical cycles, etc. Rather, we seek to

summarize our current understanding of the photochemical structure of the stratosphere by focussing on the free radicals which control the rate of transformation between different classes of reactants within the atmosphere. Achieving this objective involves a discussion of recent advances in the kinetics and photochemistry of free radicals, developments in modelling and in the measurement of free radicals in the stratosphere, and finally a means of interpreting these atmospheric measurements in the context of our present understanding of the stratosphere.

In the course of the review, several unique characteristics of the stratosphere will become apparent. We will identify examples of how the mechanistic details of a single reaction can dramatically affect predictions of stratospheric change into the next century. This is a particularly fascinating aspect of these studies — namely that while a reasonably complete (chemical) description of the stratosphere requires approximately 200 reactions, details of the reaction mechanism of a single process can alter predictions of global ozone depletion by more than a factor of three.

This sensitivity of conclusion to a single reaction coupled with the needed to distill a vast number of reactions into tractable subsets, the effect of which can be interpreted and tested by observations, restricts the strategy used to test models with field observations. We seek, therefore, to distill the orchestra of reactions into a few rate limiting steps to highlight which measurements must be made to test the mechanisms central to theories of global ozone depletion.

In the third section, we review recent developments in the field of atmospheric free radical observations so we can explore how effectively these experiments have tested our understanding of atmospheric structure.

The fourth section summarizes this progress and then presents the latest predictions of global ozone depletion resulting from fluorocarbon release. Recent and important changes have been reported in this aspect of the problem.

II. BREAKING DOWN THE REACTION SET

We first simplify the complete set of reactions needed to characterize the photochemical structure of the stratosphere, listed for reference in Appendix A, by classifying the reactants and products into three generic types: (a) "source" molecules which carry a given element to the stratosphere by upward diffusion from the lower atmosphere; (b) radicals which serve to scramble the chemical structure of the trace constituents while controlling the path and rate of transfer to (c) the "reservoir" molecules which are comprised of their terminal products of radical-radical recombination reactions. This last category is responsible for maintaining mass continuity for each element, by downward diffusion which matches the upward flux of the source molecule. Figure 1 summarizes this division superposed on a simple box model, indicating the spatial division between the surface, troposphere and stratosphere.

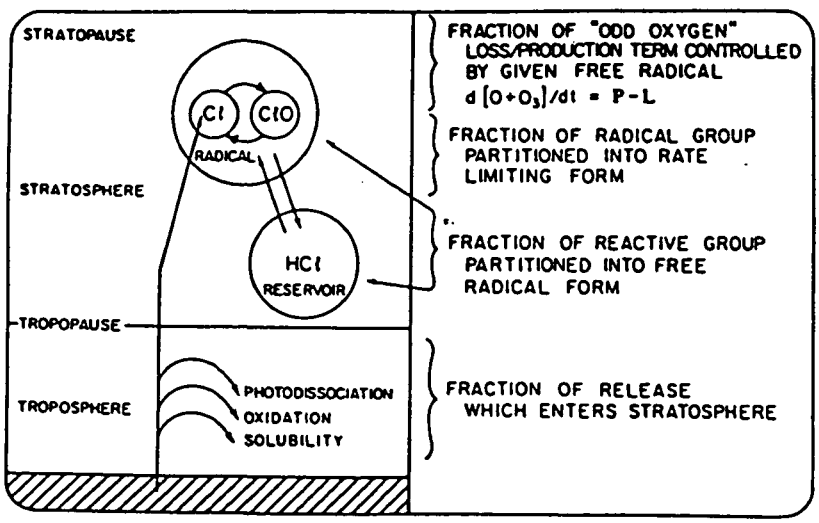

Figure 1. Box model of the middle and lower atmosphere indicating the major removal processes for source molecules carried upward from the surface. The small complement of molecules which actually reach the lower stratosphere then become the precursors for free radical chain carrying reactions which are terminated by radical-radical recombination reactions to form reservoir molecules. Downward transport to the tropopause of these reservoir molecules maintains mass continuity.

Separation of reactants and products into the three categories, SOURCE — RADICAL — RESERVOIR is done both to abstract the pattern of change in the reaction network and to distinguish the different time constants associated with each category. The spatial division indicated in Figure 1 conveniently emphasizes the filtering between the stratosphere and the Earth's surface afforded by removal processes in the troposphere.

A vast proportion of the molecules released at the surface are rapidly removed by rain-out, oxidation, or photodissociation. In order to "qualify" as a source molecule, the release rate and tropospheric lifetime against removal by the three processes noted in Figure 1 must be such that a significant flux of molecules cross the tropopause. A significant amount of theoretical analysis and observational evidence (see WMO-82, NAS-84) has isolated those few molecules which are of quantitative significance to the photochemistry of the stratosphere. Those studies are summarized in Table 1 which classifies the major source molecules according to which free radical group each sustains. The mole fraction each comprises in the troposphere is also given. Rapid horizontal and vertical mixing in the troposphere maintains, to first order, an invarient (or volume mixing ratio) mole fraction throughout that region of the atmosphere.

Table 1. Major source molecules

Free Radical Group	Source Molecule(s)	Approximate Mole Fraction @ Trop
Oxides of Nitrogen "NO_x"	N_2O	300 ppb
Oxides of Hydrogen "HO_x"	CH_4	1700 ppb
	C_2H_6	1000 - 1500 ppb
	H_2	550 ppb
	H_2O*	5000 ppb
Oxides of Chlorine "ClO_x"	CH_3Cl	650 ppb
	CF_2Cl_2	300 ppb
	$CFCl_3$	190 ppb
	CCl_4	130 ppb
	CH_3CCl_3	170 ppb
Oxides of Bromine "BrO_x"	CH_3Br	15 ppb
Sulfur, HS, HS_2	OCS	510 ppb

A brief glance at Appendix A reveals that each of the reactions involves a free radical either as a reactant or a product. Before dividing the complete reaction set into groups, we trace through the network of transformations:

SOURCE → RADICAL ⇄ RESERVOIR

for the oxides of nitrogen which is a paradigm for each of the reaction families. This will clarify the reasons behind our subsequent classification strategy.

The primary fate of N_2O in the stratosphere is reaction with $O(^1D)$ (photolysis occurs but is quantitatively insignificant). The branching ratio into products

$$N_2O + O(^1D) \xrightarrow{a} NO + NO$$
$$\xrightarrow{b} N_2 + O_2$$

and the absolute rate constant has received considerable attention in the laboratory.[5]

Nitric oxide is added to the stratosphere by the oxidation of N_2O in a rather wide altitude interval, as indicated by the observed decrease in N_2O shown in Figure 2.

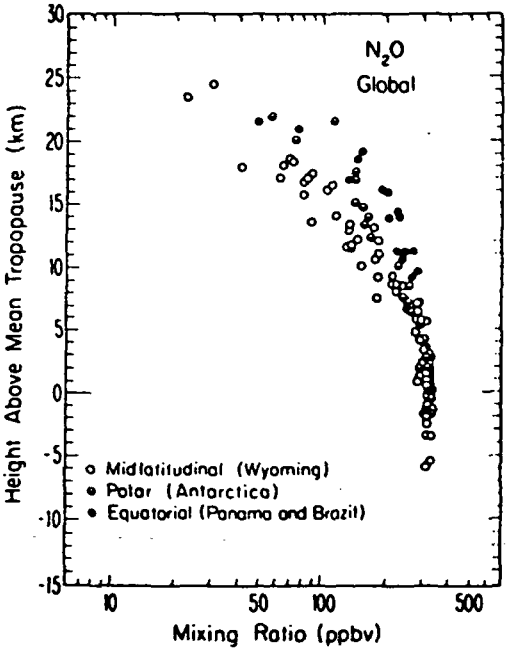

Figure 2. Altitude dependence of N_2O in the stratosphere showing the oxidation of N_2O by $O(^1D)$ which yields NO.

Release of NO into the stratosphere initiates a rapid sequence of exchange reactions which couple NO and its companion radical NO_2 on time scales of minutes throughout the stratosphere by the reaction sequence

$$NO + O_3 \rightarrow NO_2 + O_2$$

$$NO_2 + O \rightarrow NO + O_2$$

$$NO_2 + h\nu \rightarrow NO + O$$

This sequence can be represented schematically by the diagram displayed in Figure 3.

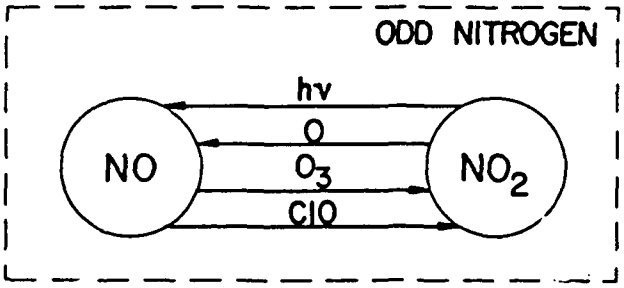

Figure 3. Schematic of the $NO-NO_2$ reaction sequence showing the catalytic couplet which accelerates the recombination of ozone and atomic oxygen to molecular oxygen.

In the absence of a removal process, the sum of $NO + NO_2$ would of course build up indefinitely. What in fact occurs is a recombination step between NO_2 and the hydroxyl radical OH to form nitric acid:

$$OH + NO_2 \rightarrow HONO_2$$

The OH radical is formed in a parallel process to that of NO with CH_4 replacing N_2O as the source molecule shown in Figure 4.

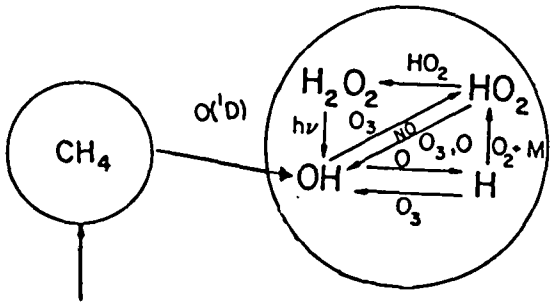

Figure 4. Production of hydrogen radicals from methane oxidation by $O(^1D)$.

Following the formation of $HONO_2$ by recombination (a mechanism which acting alone would reduce the concentration of NO and NO_2 by orders of magnitude below their observed values), an important pair of reactions

$$HONO_2 + h\upsilon \rightarrow OH + NO_2$$

$$HONO_2 + OH \rightarrow H_2O + NO_3$$

recycle the nitrogen oxides back into the free radical pool, as indicated in Figure 5.

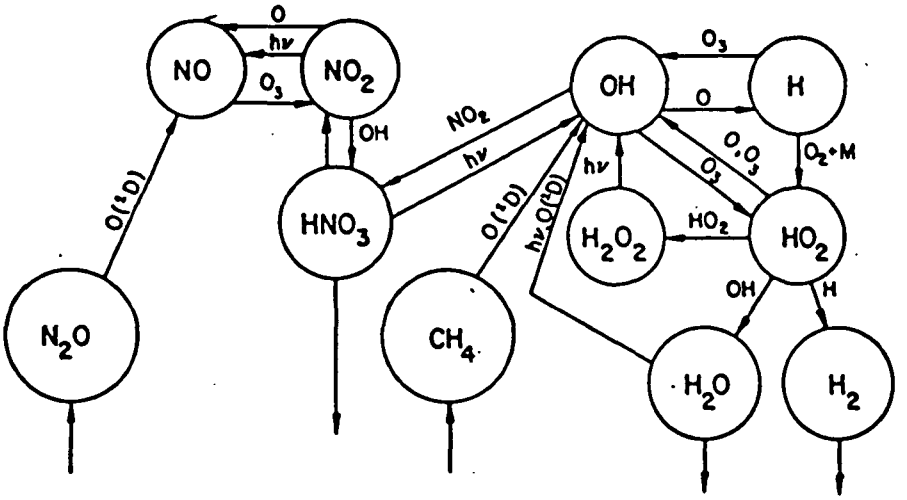

Figure 5. Coupling of the NO_x radicals to the reservoir molecules $HONO_2$ and HONO.

This completes the first order description of transfer reactions within the NO_x system. From this particular example we abstract the following characteristics which hold for all of the radical groups noted in Table 1.

1. Irreversible destruction of the source molecules to initially form the free radicals, is a slow process compared with any other exchange reactions. Conversion from the source is matched at steady state by the downward mixing of the soluable reservoir term for "wash out" below the troposphere.

2. The cyclic nature of the exchange reactions within each radical system underlies the catalytic property of these transfer reactions. For example, the exchange between NO and NO_2 catalyzes the reformation of the O_2 bond at the expense of atomic oxygen and ozone

$$NO + O_3 \rightarrow NO_2 + O_2$$
$$NO_2 + O \rightarrow NO + O_2$$
$$\overline{O + O_3 \rightarrow 2O_2}$$

There are a significant number of other catalytic cycles which interconnect radicals and which interlink the various reaction families. For example, the conversion of NO to NO_2 is catalyzed by the presence of hydrogen radicals

$$OH + O_3 \rightarrow HO_2 + O_2$$
$$HO_2 + NO \rightarrow OH + NO_2$$
$$\overline{NO + O_3 \rightarrow NO_2 + O}$$

and incidentally by the presence of free chlorine radicals

$$Cl + O_3 \rightarrow ClO + O_2$$
$$ClO + NO \rightarrow Cl + NO_2$$
$$\overline{NO + O_3 \rightarrow NO_2 + O_2}$$

3. Consideration of the transfer rates corresponding to each of the major steps within and out of/into the NO_x cycle, tabulated below as a function of altitude (where the k's are bimolecular rate constants in units of $cm^3 sec^{-1}$, bracketed quantities are concentrations in molecules cm^{-3},

and J is the photolytic rate in sec^{-1} such that each tabulated quantity is in units of molecules/cm^3-sec), underscores the fact that the conversion time within the radical group is dramatically shorter than the period for formation or removal and thus a steady state is established between NO and NO_2. Note also that from the point of view of ozone, there are two important reaction sets in the NO_x radical exchange which, when taken together, either constitute a null cycle or result in the reformation of 3 molecular oxygen bonds at the expense of two molecules of ozone: This last point begins to reveal why for the purpose of testing hypotheses of chemical links by observation of free radicals in the stratosphere, it is essential to break the full reaction complement into subsets which have a clearly defined objective of transforming compounds into or out of a given class of reactive compound. For example, as used above, those reactions which transfer oxygen into and out of the "odd oxygen" pool, or those which transfer hydrogen into or out of the "odd hydrogen" class must first be isolated as a mechanism and then the rate determining step must be established.

We close this section by summarizing the chemistry of chlorine and ozone in the Earth's stratosphere. There are three essential elements in the Rowland-Molina mechanism linking the release of fluorocarbons to the gas phase catalytic destruction of ozone in the stratosphere:

1. Release of the halogen substituted methanes, principally $CC\ell_3F$ and $CC\ell_2F_2$ (FC-11 and FC-12) into the atmosphere is

followed by rapid mixing of the compounds throughout the troposphere. To a first approximation, there are no physical or chemical removal processes at the surface or in the gas phase throughout the troposphere. This fact was established by comparing integrated release rates with global measurements by Lovelock whose shipboard observations as a function of latitude formed a cornerstone in the early formulation of the hypothesis.

2. The uniform mixing of the compounds throughout the troposphere increased the mixing ratio of chlorine at the tropopause and thereby the flux of chlorine compounds into the stratosphere. Vertical mixing continues above the tropopause although at a slower rate dictated by the permanent "temperature inversion" characteristic of the stratosphere, until the molecules reach an altitude where the penetration of solar radiation in the wavelength interval between the major absorption continuum/band system of O_2 and O_3 occurs. Photons in this interval are weakly absorbed and have sufficient energy to photodissociate both $CC\ell_3F$ and $CC\ell_2F_2$; $CC\ell_3F + h\nu \rightarrow CC\ell_2F + C\ell$ and $CC\ell_2F_2 \rightarrow CC\ell F_2 + C\ell$ releasing atomic chlorine.
3. The principal fate of the chlorine atom released is reaction with ozone to form the chlorine monoxide free radical which in turn reacts with atomic oxygen to regenerate the chlorine atom

$$Cl + O_3 \rightarrow ClO + O_2$$

$$ClO + O \rightarrow Cl + O_2$$

$$\overline{O_3 + O \rightarrow O_2 + O_2}$$

thereby forming a homogeneous gas phase catalytic cycle amplifying the rate of odd oxygen destruction. Since (1) both reactions comprising the cycle are fast bimolecular processes and the couplet is completed on the time scale of tens of seconds, and (2) each chlorine atom resides in the stratosphere for a period of years, spending a significant fraction of that time in free radical form, it follows that an amount of chlorine orders of magnitude less than that of ozone can potentially alter the rate of ozone destruction in the stratosphere.

Figure 6 traces the major exchange reactions in the SOURCE → RADICAL ⇆ RESERVOIR system. The dominant natural source of chlorine in the stratosphere is CH_3Cl; the main synthetic contribution is from CCl_4, CF_2Cl_2 and $CFCl_3$. Atomic chlorine and chlorine monoxide are the only important radicals. Exchange times between radicals and photolysis times converting the source molecules to free radicals are also summarized in Figure 6.

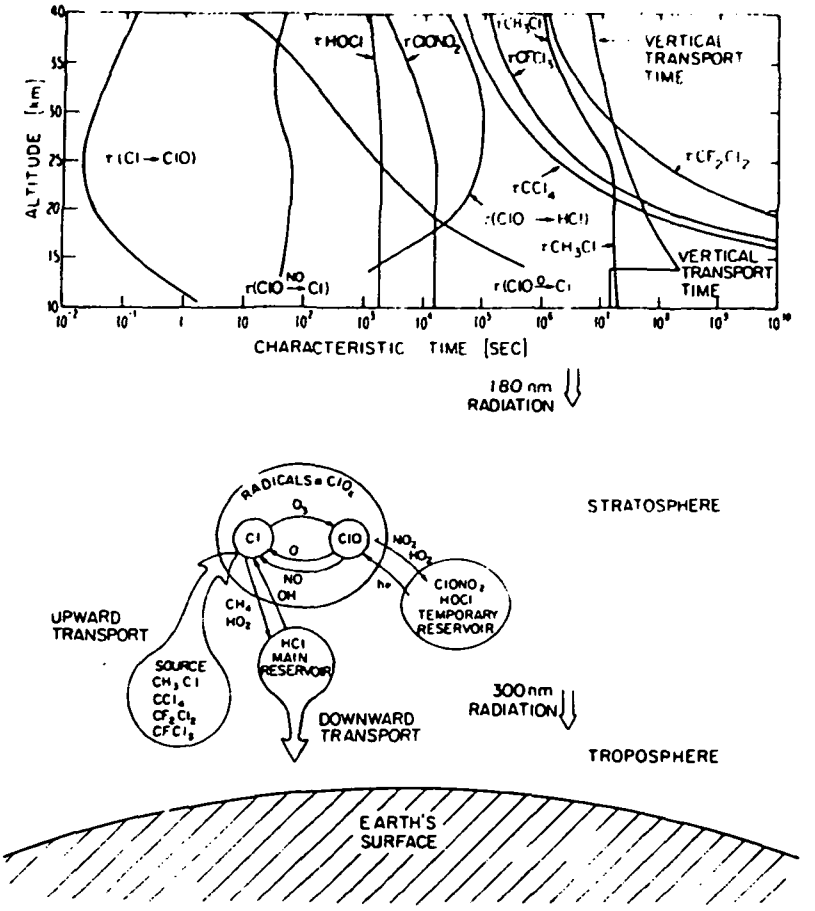

Figure 6. Schematic of the chlorine reaction system in the stratosphere with an overview of the exchange times among the various subgroups of reactants

The dominant reservoir for chlorine in the stratosphere is HCℓ which diffuses downward to maintain Cℓ atom (bound and free) continuity. Two major temporary reservoirs (those molecules with a lifetime on the order of one diurnal period) are critical to the chlorine system. Chlorine nitrate, formed by the three body reaction

$$C\ell O + NO_2 + M \rightarrow C\ell ONO_2 + M$$

and removed by photolysis

$$C\ell ONO_2 + h\nu \rightarrow C\ell O + NO_2$$

constitutes (1) a major nighttime storage tank for chlorine radicals, and (2) a critically important coupling term between the chlorine and nitrogen

systems. That single reaction is predominantly responsible for the diurnal behavior of ClO, summarized at four different altitudes in Figure 7, taken from the most recent work by Ko and Sze.[6]

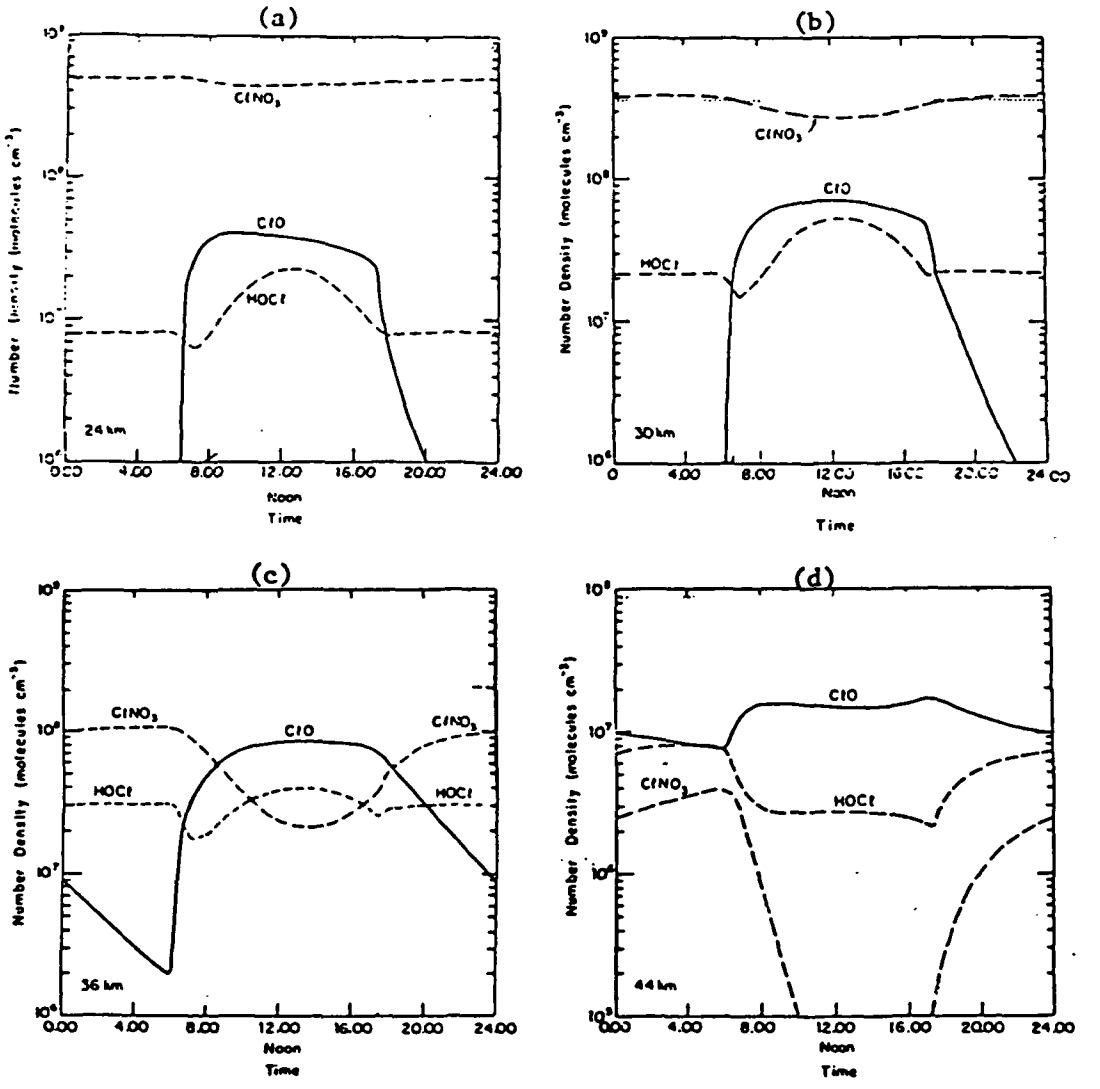

Figure 7. Diurnal trace of the ClO, $ClONO_2$ and HOCl concentrations for 4 altitudes in the stratosphere; 24, 30, 36 and 44 km. Note the rapid but easily measured decay of ClO following sunset with considerably steeper decay rates at the lower altitudes reflecting the termolecular behavior of the primary loss reaction $ClO + NO_2 + M \rightarrow ClONO_2 + M$. In the altitude interval above 40 km, the dominant diurnal behavior is the day-night exchange between ClO and HOCl. Results are from reference 6 by Ko and Sze.

The other major reservoir for chlorine compounds is HOCℓ, formed in the bimolecular reaction

$$ClO + HO_2 \rightarrow HOCl + O_2$$

and removed by direct photolysis

$$HOCl + h\nu \rightarrow OH + Cl$$

As Figure 7 implies, current theories suggest that while the altitude interval at and below 36 km is dominated by a diurnal exchange between $ClONO_2$ and ClO, above 40 km the exchange is dominated by a nighttime transition between HOCℓ and ClO.

The critical question, then, revolves on how the validity of these major hypotheses linking fluorocarbon release at the Earth's surface to (global) changes in stratospheric ozone can be established. There are five elements in the case linking CFC release to changes in stratospheric ozone:

Part 1: The CFC release rate and the rate of build up in the troposphere; are there significant losses other than upward transport to the stratosphere?

The source strength for CFC induced stratospheric ozone removal is, of course, the tropopause mixing ratio fo each of the CFC compounds. This must be known to extremely high precision at selected positions across the globe in order to predict steady state concnetrations corresponding to a given release rate. Intensive analysis of the time dependence of these mixing ratios over at least a decade is critical in order to establish a lower limit on the atmospheric lifetime.

Part 2: The fraction of halogen atoms transported across the tropopause which enter the "bank" of stratospheric halogen compounds in the middle and upper stratosphere.

The residence time for retention of compounds within the stratosphere increases very rapidly from a low and highly variable quantity in the

region just above the tropopuase, to a period approaching a decade in the lower-middle stratosphere. Thus the altitude at which CFC photolysis occurs can have important consequences concerning the transfer of halogen compounds into the chemical inventory of the stratosphere which is in turn a measure of the effectiveness of converting industrially produced halogen into active participants in the stratospheric chemistry.

Part 3: Partitioning of the halogen compounds among the reservoir, temporary reservoir, and free radical forms. Partitioning of total chlorine into the rate limiting free radical in the dominant catalytic cycle.

Given that the bottleneck establishing the rate of chlorine-induced ozone destruction is, to first order, the concentration of the rate limiting chlorine free radical in the dominant catalytic cycle destroying odd oxygen, it is essential to establish the propensity of the stratosphere for partitioning total chlorine into the rate limiting radical form. This ratio of ClO to total chlorine as a function of altitude is a quantity of *first order importance*.

Part 4: Quantitative significance of the dominant rate limiting catalytic steps to the total loss rate of odd oxygen as a function of altitude in the stratosphere.

Odd oxygen destruction rates are, of course, controlled by different free radical groups at different altitudes. The altitude dependent partitioning of the loss side of the odd oxygen budget among the hydrogen, halogen, nitrogen and pure oxygen components provides the first order test of whether current estimates of global ozone production and destruction balance. In addition, such an analysis, when based on observed radical concentrations, defines the altitude interval within which a predicted ozone change would first be observable. Of equal importance, however, is that one must have a solid quantitative understanding of rate limiting

processes in the present day atmosphere before one can confidently predict future trends. Since those trends point, in the case of CFCs, toward large changes in what is presently a rather small term in the odd oxygen balance in a limited altitude interval, establishing a detailed understanding of the dominant loss terms (i.e., the NO_2 rate limited steps) is essential.

Part 5: Chemical link between radicals and temporary reservoirs in the halogen system and the major catalytic processes controlling the rate of odd oxygen removal throughout the stratosphere.

Although the direct contribution of the chlorine rate limiting step to the odd oxygen loss rate is obviously a critical quantity, of equal importance is the coupling between the chlorine radicals and the other catalytic cycles, most notably the nitrogen system. Given the overwhelming contribution to the total ozone column from the altitude interval between 20 and 35 km where the NO_x system dominates, the large changes in chlorine mixing ratios predicted for the next century, second order coupling may prove to be the dominant consideration. This is why the temporary reservoirs hold the key to important elements in our understanding of the system and why a thorough understanding of HO_x-NO_x radical system in the middle and lower stratosphere is essential.

We turn next to the question of making those critical observations which will transform hypotheses, delineated in this section, to scientific fact. This step requires an approach of developing techniques used to make observations of and within the Earth's stratosphere.

III. RECENT ADVANCES IN ATMOSPHERIC MEASUREMENTS

Although it has been more than a decade since the scientific community was alerted to the critical need for the development of a new generation of instrumentation to address the question of global ozone depletion, it is only recently that truly novel and powerful combinations of techniques have begun to appear in the literature. The most notable of these include: (1) ground and balloon-borne mm-wave emission techniques originally developed for radioastronomy applications;[7] (2) far infrared interferometric techniques which achieve spectral resolution adequate to detect part per trillion concentrations in the stratosphere;[8] (2) satellite based high-resolution ($\sim 10^{-3}$ cm^{-1}) scanning interferometers with broad survey capabilities in the middle infrared and pressure modulated radiometry capable of mapping the global distribution of CH_4 and N_2O from Earth's orbit with vertical resolution corresponding to less than an atmospheric scale height;[9] (4) metal atom lasers and eximer lasers capable of detecting radicals at the part per trillion level in situ or by lidar from balloon platforms;[10] and (5) balloon-borne tether systems which provide repetitive vertical soundings of the stratosphere over 15 km height increments from the tropopause to the stratopause.[11]

We present here only a sampling of the most recent data obtained by those techniques to demonstrate the emerging ability of sophisticated field experiments to challenge the more fundamental hypotheses linking chemical releases at the surface with global ozone depletion.

1. Ground based mm-wave emission spectroscopy

One of the most dramatic examples of concrete progress in the field of stratospheric chemistry has come from the work of de Zafra, Solomon,

Parrish and coworkers, who adopted radio astronomy techniques to the detection of stratospheric free radicals. Three key reactive constituents have been examined: ClO emissions at both 204 and 278 GHz from a number of sites in the northern hemisphere, with a rapidly growing seasonal coverage and sufficient time resolution to examine the exceedingly important diurnal behavior of the stratospheric column; HO_2 at 266 GHz from the Mauna Kea, Hawaii Observatory; and H_2O_2 at 270 GHz, again from the Mauna Kea site.

These observations have, first of all, provided the community with a truly independent way of observing the concentration of two critically important rate limiting radicals, ClO and HO_2. The importance of having completely independent methods for establishing the concentration of radicals in the stratosphere cannot be overstated. As Section II demonstrates, the scientific case linking chemical release at the surface to ozone depletion in the stratosphere is directly testable only if the rate of catalytic conversion can be checked by observing the rate limiting step in the catalysis cycle. A vastly strongly scientific case can be established given independently acquired data sets using entirely different methods.

Table 2 summarizes the present state of knowledge obtained via the balloon-borne *in situ* optical techniques of Anderson *et al.*[12], and the ground-based mm-wave emission techniques of Solomon *et al.*[7]

In order to critique the differences between these techniques at the ± 30% level, it is necessary to consider both latitudinal, seasonal, and diurnal variation, all of which tend to improve the absolute correlation

Table 2. Average ClO column densities

Site	Period	Observed Line Frequency (GHz)	Column Density ($\times 10^{14}$ cm^{-2}) (30 to 51 km)
Massachusetts	January - February 1980	204	0.7 ± 0.2
Massachusetts	February 1981	278	$1.1^{+0.15}_{-0.2}$
Arizona	May 1981 (day)	278	0.7 ± 0.2
	(night)		0.15 ± 0.04
Hawaii	Oct (12m - 4pm) 1982	278	0.70 ± 0.15
	Dec (12m - 4pm) 1982	278	0.80 ± 0.15
	June (12m - 4pm) 1983	278	0.96 ± 0.2
	Dec (12m - 4pm) 1983	278	0.70 ± 0.2
Texas	Anderson et al. (noon) 7-flight average, excluding 07/28/76 and 07/14/77	---	1.13

between the measurements of ClO. Thus, while significant differences remain to be understood, the existence of ClO in the stratosphere at concentrations comparable to present predictions has been finally established. Such a critical step could not have been achieved with a single experimental approach.

Ground-based mm-wave emission techniques have recently provided definitive identification of HO_2 in the upper stratosphere, measurements which can be directly compared with previous in situ experiments.[13] Figure 8 presents those recent spectra. These observations can be used both to cross check in situ techniques, for which two have been reported, and to extend measurements of this key free radical above the maximum altitude attainable by balloons, specifically above 45 km. We thus find a critical combination of independent techniques with highly complementary temporal and spatial coverage evolving such that the vertical distribution

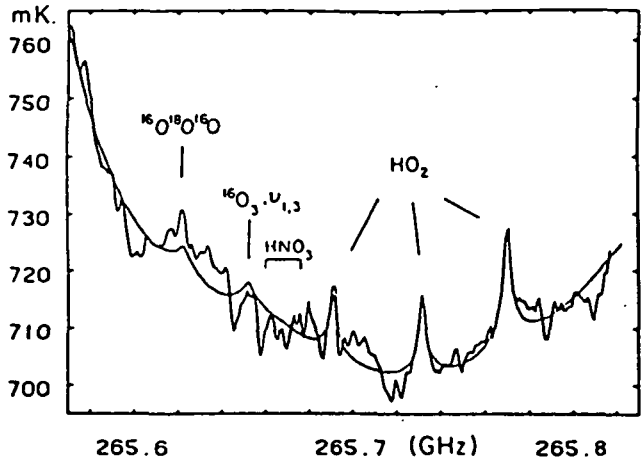

Figure 8. Ground based mm-wave emission experiments of HO_2 obtained by de Zafre et al.

of a key free radical will soon be established in the scientific literature.

Technology in mm-wave detection in the 200 to 400 GHz range has also advanced in the past three years to the point where temporal resolution from ground based observations has improved to such an extent that the diurnal behavior of several key radicals can be achieved. The most notable example is that by de Zafra,[14] who has reported vertical column ClO observations tracked throughout a series of 24-hour surveys. These results have been compared with the most recent calculations by Ko and Sze to test both the model's ability to predict the absolute concentration of ClO and its ability to predict the diurnal behavior of ClO. Providing the first step is achieved, the latter test is obviously far more stringent for it examines independently the rate of ClO production independently from the rate of destruction. The results of that comparison are summarized in Figure 9.

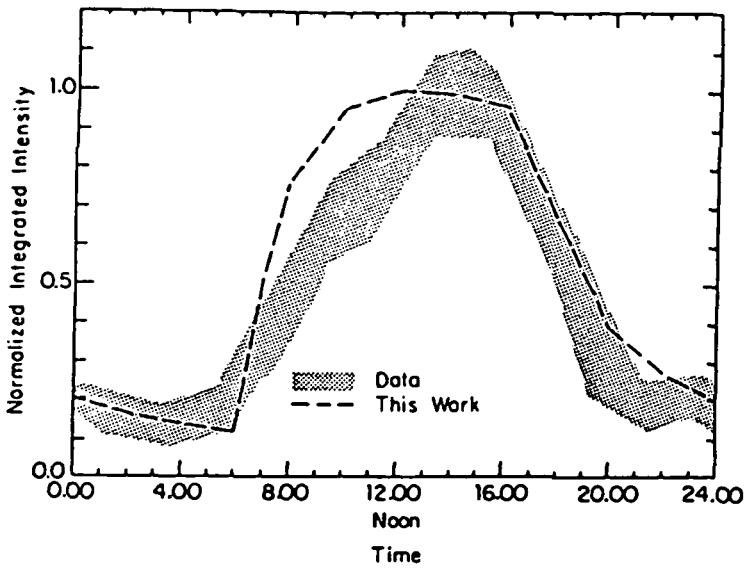

Figure 9. Comparison between the normalized observed integrated intensity of the ClO emission from Solomon et al. and the synthetic intensity derived from calculated concentrations of ClO from Ko and Sze.

Two research groups have developed Fourier transform spectrometers for high resolution balloon-borne emission observations of stratospheric trace species. Traub and Chance[15] of the Harvard-Smithsonian Center for Astrophysics have reported results on H_2O_2, HCl, and OH obtained in the 80 to 240 cm^{-1} spectral region at an (apodized) resolution of 0.064 cm^{-1}. These results have contributed directly to reported literature values on HCl, and have placed an extremely restrictive upper limit on the stratospheric H_2O_2 concentrations. Traub and Chance[16] have also reported preliminary results on OH in the critical altitude region between 18 and 48 km. These results are particularly critical to advancement in the field because (a) the absolute calibration is direct and unambiguous and (b) observations can be obtained from a balloon platform at any time of the day or night, providing key diurnal data and, in addition, the flexibility to intercompare with other techniques.

A second research group, headed by Dr. Bruno Carli of the Istituto di Ricerca sulle Onde Electtromagnetiche IROE/CNR, Via Panciatichi, 56 - 50127 Fireze, Italy have achieved a spectral resolution of 0.003 cm^{-1} in the 20 to 40 cm^{-1} spectral region using a balloon-borne Fourier transform interferometer. Preliminary results on both OH and CℓO have been reported by this group.[17] The superb spectral resolution is a critical element in both the identification of lines and in the rejection of interfering spectral features to enhance the technique's detection threshold. In the next two years, results from the two groups will advance considerably the atmospheric chemistry community's grip on several key radicals.

2. Satellite-based high-resolution interferometers and radiometers

The first laboratory quality observations made from balloon platforms were middle infrared absorption experiments of trace atmospheric species using the sun as a source. This work has now been extended to shuttle and satellite-based observations using Fourier interferometers. The ATMOS instrument developed under the leadership of C.B. Farmer and the NASA Jet Propulsion Laboratory represents the flagship of this effort.[8] The proven spectral response of this instrument will provide global maps of HCℓ, HF, $HONO_2$, CH_4, N_2O, $CF_2C\ell_2$, $CFC\ell_3$, and a number of other important reservoir molecules.

Development of satellite-based pressure-modulated radiometer (PMR) techniques by the Oxford University[9] research team has now dramatically demonstrated the power of global maps of CH_4 and H_2O for the interpretation and testing of two dimensional models. The first results of this work were reported by Jones and Pyle[9] in a comparison between satellite and in situ results using the Oxford two-dimensional model to interpret

the results. A critically important extension of this work to include the relationships between methane and water vapor has been reported by Jones. The key concept in the work is that the sum $[CH_4] + [H_2O]$ is a conserved quantity in the stratosphere so that global maps of methane can be used to deduce the water vapor composition of the atmosphere. This has critical implications for deducing free radical concentrations from satellite measurements.

The Oxford results have recently been used by Solomon and Garcia to examine the distribution of long-lived tracers and chlorine species in the middle atmosphere. This important paper has crystallized many of the issues relating the hydroxyl and chlorine species, particularly the relationship between the variability in methane concentration and the variability in ClO. Figure 10 summarizes the correlation between the two-dimensional model of Solomon and Garcia[18] and the Oxford CH_4 maps. These

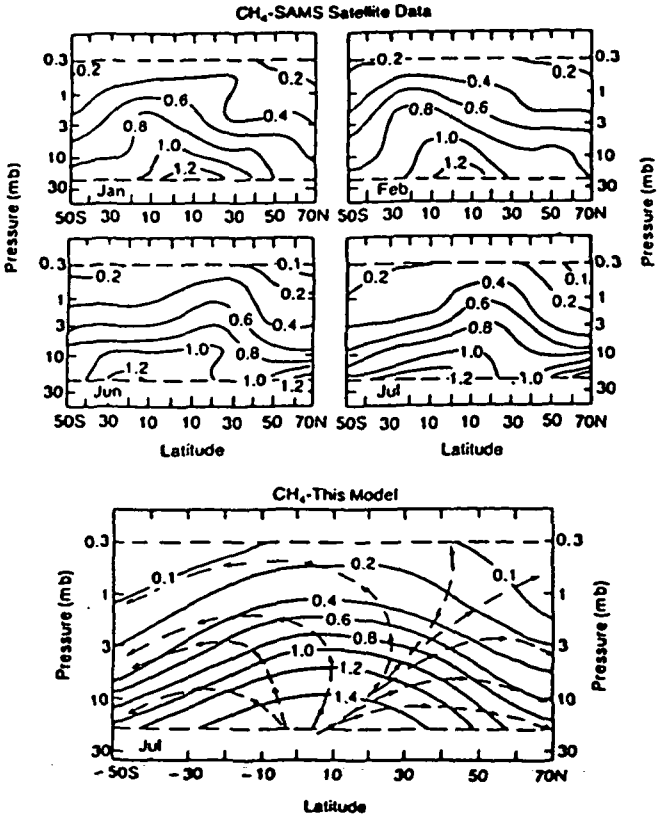

Figure 10. Some monthly averaged observed distributions of atmospheric methane from the SAMS satellite, Jone and Pyle, near solstice conditions, compared to the model distribution for July by Solomon and Garcia. Light dashed arrows indicate the residual Eulerian stream function, showing the advection pattern.

results are then used to define the expected variability in local ClO concentrations reported by in situ observations.

3. Metal atom lasers and eximer lasers for in situ and LIDAR detection of radicals

The critical need to achieve high signal-to-noise ratios for spatially resolved measurement of several free radicals has spawned a number of research efforts aimed at improving our ability to observe such radicals as OH, HO_2, NO, NO_2, etc., with orders of magnitude better sensitivity than was previously available. A major impetus behind this research has been the realization that atmospheric variability on the spatial scale of a hundred meters in the vertical drives fluctuations in several of the key reactive species which provides ample concentration variation to carry out covariance studies to establish cause and effect within subsets of free radical reaction sets.

Two groups within NASA, one at Goddard Space Flight Center, under the direction of Bill Heaps, and the other at the Jet Propulsion Lab under Laudenslager and McDermid, have respectively developed balloon-borne LIDAR methods for OH and developed eximer laser systems for extending the LIDAR method to lower detection thresholds. This research has important implications for both stratospheric and tropospheric research. Such laser ranging techniques also have important implications for intercomparison studies, particuarly with mm-wave and far infrared emission experiments.

Another approach to in situ free radical detection has been developed recently at the Harvard Center for Earth and Planetary Physics. That approach, summarized in Figure 11 employs a very high repetition rate copper vapor laser (20 kHz) to pump a dye laser which can be frequency doubled into the ultraviolet and tuned to one or more of the electronic

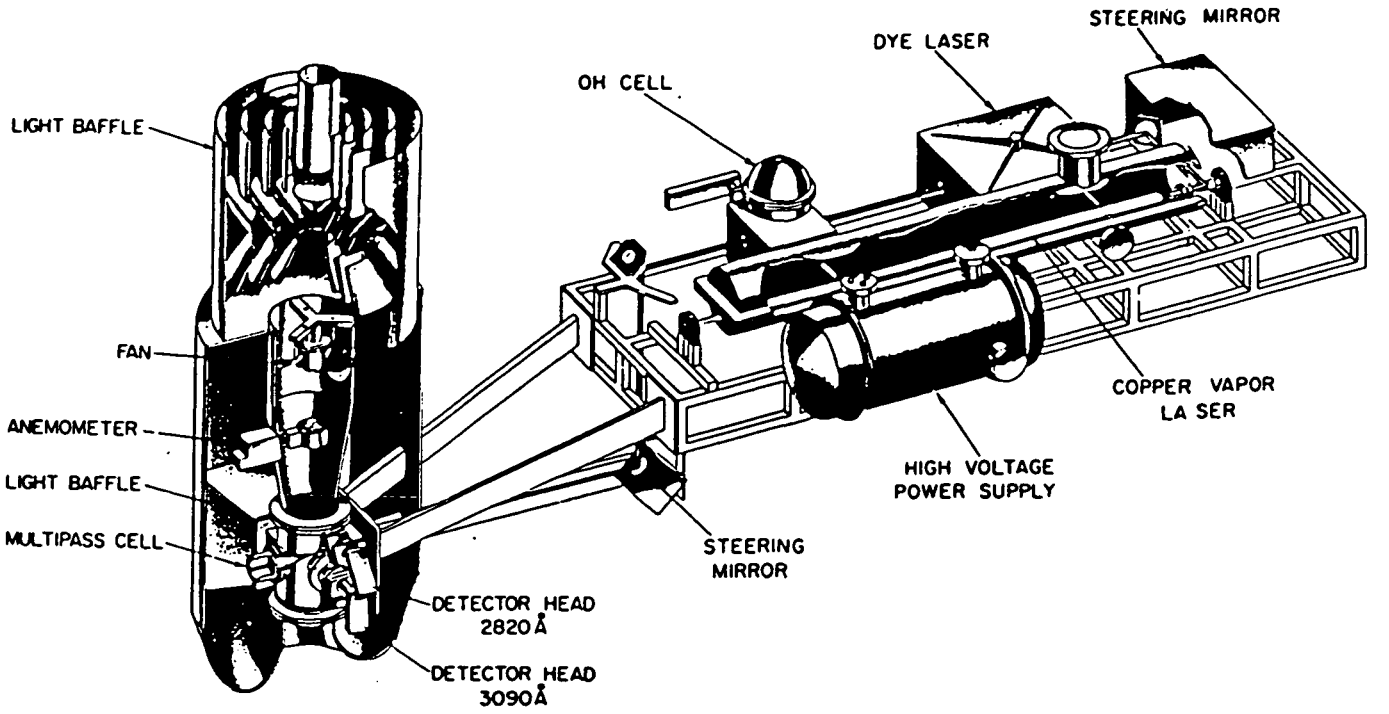

Figure 11. Schematic view of the copper vapor laser pumped dye laser system developed at Harvard for the detection of OH and HO_2 radicals in situ from balloon-borne descent probes.

absorption bands of OH, CH, NH, SH and NO_2. The objective of this approach is to provide high power levels with low peak power levels to achieve low detection thresholds by avoiding (a) saturation effects caused by laser induced depopulation of the quantum level pumped, and (b) photochemically induced OH formed by photochemical reactions initiated within the sample by the interrogating laser pulse. By confining the measurement volume to a detection chamber, two additional objectives are achieved. First, all contributions from Rayleigh scattering of solar radiation are eliminated by optical baffling techniques, and second, the contained nature of the flow allows for the option of combining chemical conversion with resonance fluorescence. For example, detection of the HO_2 radical,

which does not possess allowed electronic transitions between bond states, can be accomplished with the same hardware used to detect OH by using the rapid bimolecular reaction

$$HO_2 + NO \rightarrow OH + NO_2$$

to convert one radical to another with ease in the time scale of the experiment.

Hardware for both the LIDAR and the in situ method is either under development or has been field tested on balloon platforms. Within the next 18 months, these results will surface in the scientific literature.

4. Balloon-borne tether systems for repeated vertical scans obtained from a single balloon launch

While previously obtained "snap shots" of the free radical concentration provided first order information on concentration regimes as a function of altitude, several drawbacks exist. Problems center primarily on adequate control over flow conditions, platform stability on a given flight, and, for the chemical conversion experiments (such as for CℓO and HO_2 where nitric oxide was used to convert the radicals to Cℓ and OH, respectively), reactant gas mixing times.

Designated the "Reel Down" technique and depicted in Figure 12, a system was developed at the Harvard Center for Earth and Planetary Physics which consists of (a) a winching system borne by a helium reserach balloon to an altitude of $\sim$ 40 km (where the atmospheric pressure is approximately 2 mm Hg) and (2) an instrument cluster which is lowered on a filament of Kevlar a distance of 10 km or more, and then retracted back to the winch station. Vertical soundings can be repeated several times for a given balloon launch.

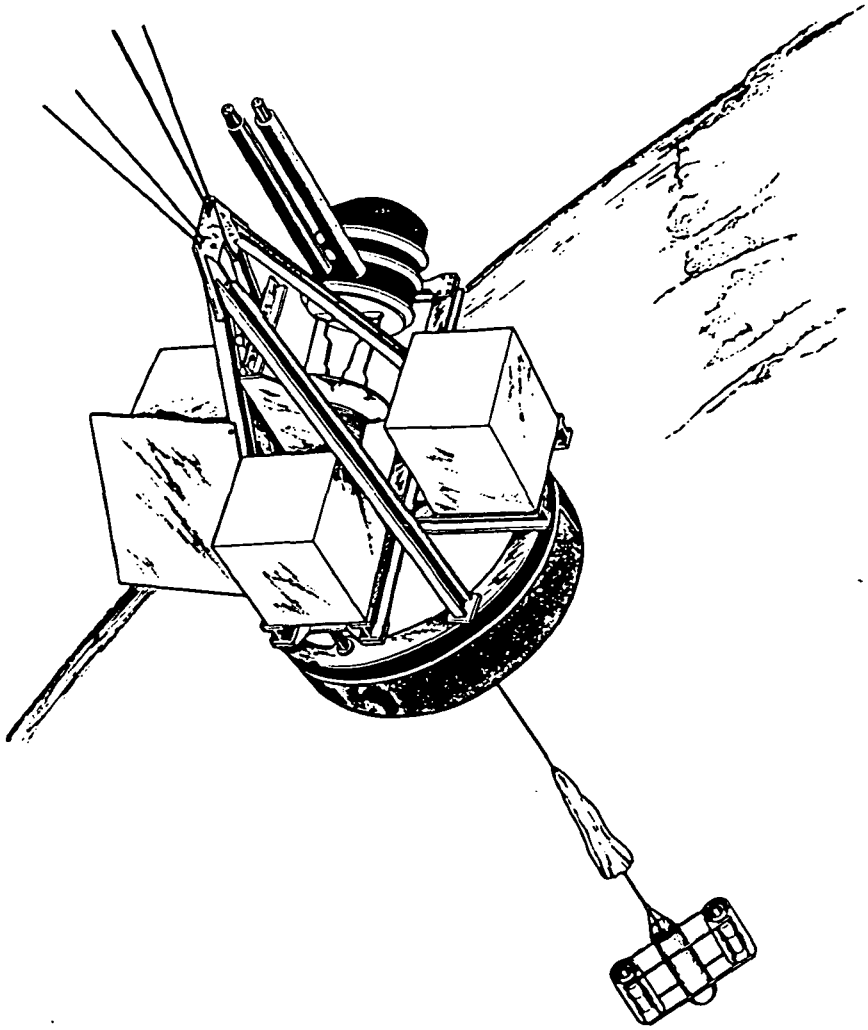

Figure 12. Rendering of the Reel Down platform with associated suspended payload. This system is capable of vertical scans of greater than 10 km from a balloon floating at or below 40 km.

Success of the Reel Down approach hinges on the stability of the system under stratospheric conditions (characterized by low pressures, but potentially large horizontal wind fields). Oscillatory motion developed in any axis of the suspended experiment cluster can compromise experimental control and thus the quality of the observations. A prototype system was constructed to test the feasibility of such a system in the stratosphere. Technical details are described in detail elsewhere.[19]

The architecture of the individual instruments used to detect atoms and small free radicals by atomic and molecular resonance fluorescence or by laser-induced fluorescence is shown in Figure 13, but is discussed in detail elsewhere. Briefly, a nacelle, hollow through the core from nose to tail with an impeller in the anterior section, provides for the laminar flow of stratospheric air around and through the instrument.

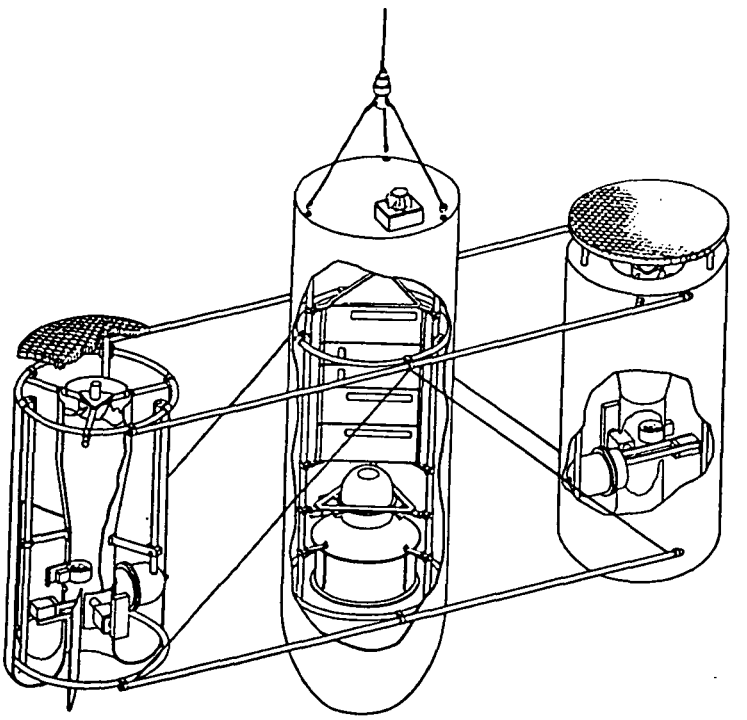

Figure 13. Cross sectional perspective schematic of the suspended payload showing a cut-away of the detection nacelles with impeller driven flow through chambers, detection head and lamp modules used in the resonance fluorescence detection of radicals.

Detection of trace species is carried out at one (or more) optical axes within the nacelle. A major subset of the important stratospheric radicals can be detected using the configuration shown in Figure 13.

The first flight of the Reel Down system took place on 15 September 1982 from the National Scientific Balloon Facility in Palestine, Texas. When the balloon was properly positioned for the descent phase of the experiment, a pin locking the suspended instrument cluster to the winching system was pulled and the controlled descent phase was initiated by releasing a magnetically controlled brake. Descent velocity was selectable by command from the ground. A line velocity of 7 ± 1 m/sec was used for the experiment reported here. A full treatment of mechanical and electronic systems, as well as the data analysis regarding the dynamics of the system, appears elsewhere.[19]

Briefly, dynamical behavior of both the suspended payload and the winching platform were documented in real time by a combination of acceleromaters, gyros, load cells, solar sensors and a downward looking video monitor on the winch platform. As the descent phase unfoleded, several critical points became apparent:

1. Longitudinal oscilations of the system were observed at the expected periods (~ 15 seconds at 12 km extension) but the amplitudes were extremely small, typically < 1% of g. Transients introduced by commanded power level changes damped rapidly. No evidence was observed for the presence of acoustical energy in the line.
2. Around the azimuthal axis, the payload described one complete revolution for the remainder of the descent. Three revolutions were recorded in the opposite direction during the last half of the descent.
3. There was a virtual absence of pendulum motion and no measurable body centered perturbations developed. Data suggest a hang-off angle of 4° resulting from wind shear of ~ 7-9 m/sec

between the balloon float altitude and the position of the suspended payload at full extension.

This new approach will be used to examine:

1. The covariance between related free radicals and ozone to establish cause and effect;
2. The diurnal behavior of the major free radicals to establish the rate of production and removal of the dominant radicals; and
3. The conversion rates for one radical to another within the same family to establish whether current coupling schemes successfully describe the quantitative conversion rates between radicals.

In summary, the past four years have witnessed a virtual revolution in the technology of stratospheric free radical and trace specie detection techniques. Sensitivities unparalleled even in the laboratory are now becoming available. Of equal importance, there is now a manifold of totally independent techniques extending from the far vacuum ultraviolet to the radio region of the electromagnetic spectrum. This research will lock down the vertical concentration of the major free radicals within the next five years — placing our understanding of the stratospheric ozone layer on a profoundly more satisfactory foundation.

IV. PREDICTIONS OF FUTURE TRENDS IN STRATOSPHERIC OZONE: A REVIEW OF RECENT MODEL RESULTS

The history of nitrogen and halogen compound induced depletion of stratospheric ozone is repleat with unpredictable changes in predicted ozone reduction figures. Every two years the National Academy of Sciences of the United States publishes a report summarizing the latest research on stratospheric ozone depletion and attempts to bound the range of predicted ozone depletion levels for steady state conditions based on present levels of fluorocarbon production. Those estimates, summarized in Table 3 below, have ranged from three percent to nearly twenty percent. These predictions are punctuated by large and episodic changes caused by inclusion of a single reaction or a change in one or a very few kinetic rate parameters.

Year	Predicted ozone depletion from CFMs at steady state	Reason for Change	Comment
1973	0		
1974	10%	Chlorine catalyzed recombination of ozone included in odd oxgyen balance	Mechanism change
1975	7%	Refinement of Cl-ClO-HCl rate constants	"Tuning" of existent calculations
1975-1976	15%	Choice of rate constant for $OH + HO_2 \rightarrow$	Significant impact on $[OH] + [HO_2]$ throughout stratosphere
1976-1977	6%	Inclusion of $ClONO_2$ in calculations	Mechanism change
1977-1978	16%	Revision in $HO_2 + NO$ rate constant	Dramatic shift in $[OH]/[HO_2]$
1978-1979	16%	No major changes	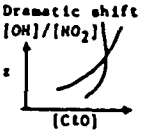
1979-1980 -1981	6%	Rate constant revision $OH + NONO_2 \rightarrow$ $OH + HO_2NO_2 \rightarrow$ $HO_2NO_2 + h\nu \rightarrow$ $OH + H_2O_2 \rightarrow$ $OH + HO_2 \rightarrow$	Dramatic change in $[OH] + [HO_2]$ in middle and lower stratosphere
1982-1983	4%	Rate constant revision $ClO + O \rightarrow Cl + O_2$ $OH + HCl \rightarrow H_2O + Cl$ $HO_2 + O \rightarrow OH + O_2$	Tuning of model
1984	4% until $[ClO]$ $[HO_2]$ sharp drop at higher ClO	Titration of HO_2 from system by ClO titration	No change in mechanism, no change in rate constant

Such oscillatory behavior does not give those concerned with translating a scientific position into legislative action a consistent vantage point. While we are all concerned, to one degree or another, with the vitality of the Earth's ozone layer, a far clearer picture of the alternatives must emerge before economically difficult decisions are warranted on an international basis.

How can the validity of these predictions be placed in perspective? What were the causes of past vacillations and are we in a significantly different position today? First, we consider what constraints existed in the period from 1974 to 1984 which could have limited the range of predicted depletion levels. Inspection of Table 3 reveals that the major shifts in predicted ozone levels into the next century are directly reflected in shifts in model calculated OH profiles of the present day atmosphere. Figure 14 sketches this coupling between the calculated OH concentration throughout the stratosphere and predicted ozone depletion levels at steady state.

This provides us with the first major test of the validity of predicted ozone depletion figures — how well do the observed and predicted middle and lower stratospheric OH concentrations in the present atmosphere correlate? The conclusion is clear. There are no dependable middle and lower stratospheric OH observations. Thus, the exceedingly important constraint remains untested. Within the next two years, however, the new observational techniques described in Section III will dramatically change this situation. Balloon-borne far-infrared emissions measurements from both the Traub et al.[16] and Carli et al.[17] research efforts will be available, as will balloon borne LIDAR data from Heaps et al. In situ measurements of OH, HO_2 and H_2O within the same volume element will be

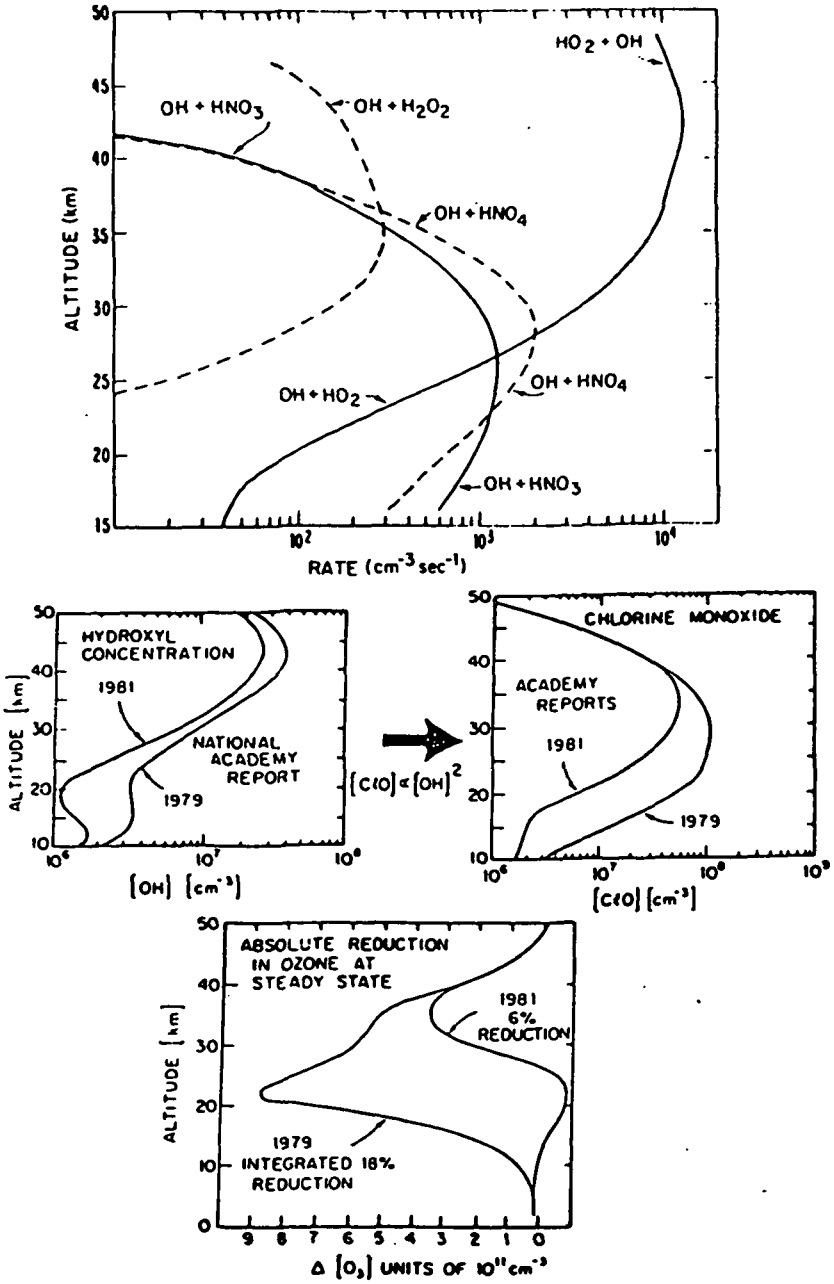

Figure 14. Coupling between the HO_x, ClO_x and ozone reaction systems shown as a sequence linking the assumed removal process for OH radicals in panel (a), dominated by the reaction set

$$OH + HO_2 \rightarrow H_2O + O_2$$
$$OH + HONO_2 \rightarrow H_2O + NO_3$$
$$OH + HO_2NO_2 \rightarrow H_2O + NO_2 + O_2$$

to the resulting concentration of OH in panel (b). OH profiles are shown with and without the nitric and pernitric acid removal mechanism for OH. The impact on the stratospheric distribution of ClO of changing the calculated OH concentration is shown in panel (c), and the subsequent impact on ozone removal as a function of altitude is shown in panel (d)

available from the Harvard group. These data, when taken together, will permanently eliminate OH as a free variable in stratospheric modelling, thus eliminating a major dimension of uncertainty.

The second major test of model validity is the predicted distribution of ClO in the stratosphere. On this particular point, the data base is considerably stronger. In situ optical techniques, ground-based and balloon-borne laser heterodyne observations have reached the literature. There is substantial agreement between the first two data sets and a major controversy surrounding the latter two. Major technical advancements already achieved will bring to the scientific literature a consensus on this key point in the next two years. In situ methods have and will employ the Reel Down approach to vastly strengthen the quality of those observations; new detector technology has improved dramatically the signal-to-noise ratio of both the ground-based and balloon-borne mm-wave emission experiments; and laboratory calibration procedures will be incorporated into the laser heterodyne radiometer field preparation. Taken together, these experiments will solidify the data base on the mid latitude vertical distribution of the key rate limiting chlorine radical between the tropopause and the stratopause. The strictness of this constraint can be grasped first by recalling from Section II the fact that ultimately the bottleneck establishing the rate of chlorine catalyzed destruction of ozone is the reaction $ClO + O \rightarrow Cl + O_2$ so the establishment of the concentration of O and ClO quantitatively defines the ozone destruction rate by chlorine. The same point can be made in a somewhat different way by examining the last two panels of Figure 14 which shows the relationship between the percentage change in ozone as a function of altitude and the ClO concentration as a function of altitude. Firmly establishing the vertical distribution of ClO

eliminates any proposed mechanism for ozone destruction which involves any change in the ClO distribution.

A third critical test for current ozone depletion calculations is the diurnal behavior of ClO as a function of altitude. Figure 15, taken from a recent treatment by Ko and Sze,[6] summarizes the distinctive signature of ClO concentration as a function of time and of altitude following sunset. This altitude dependent decay of ClO following sunset defines

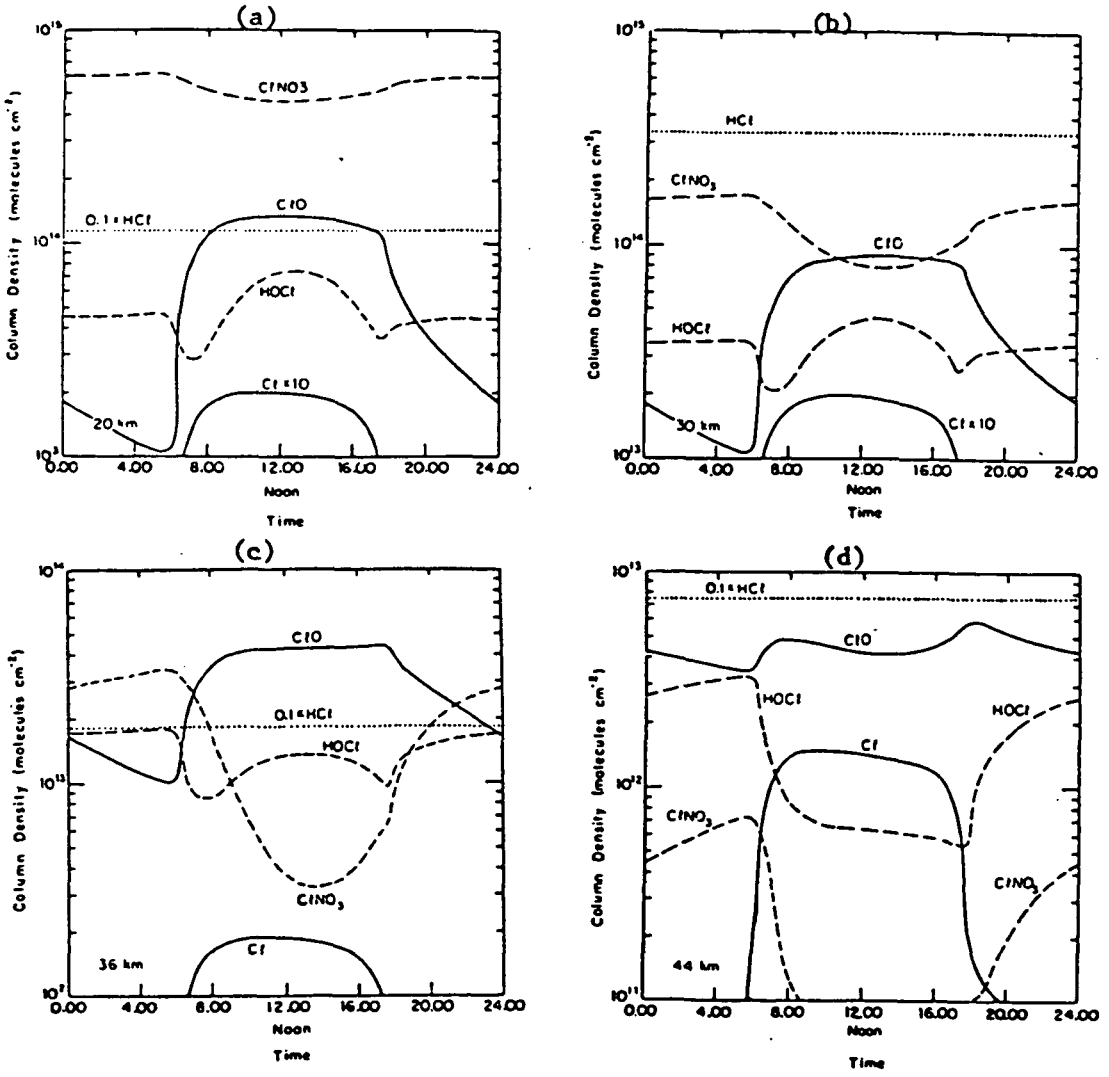

Figure 15. The diurnal variation of the column densities of HCl, ClO, Cl, $ClONO_2$ and HOCl from Ko and Sze. Calculated values are for column abundances above 20 km, 30 km, 36 km and 44 km in panels (a), (b), (c) and (d), respectively. Calculations correspond to 19°N latitude for December conditions.

with great precision the primary mechanism coupling the chlorine and nitrogen systems in the stratosphere because the removal of ClO at night occurs, it is believed, as a result of the termolecular reaction

$$ClO + NO_2 + M \rightarrow ClONO_2 + M$$

If this mechanism functions as it is currently believed to, both the observed rate of disappearance of ClO as a function of altitude (i.e., pressure) and the observed reappearance of ClO via the direct photolysis of $ClONO_2$

$$ClONO_2 + h\nu \rightarrow ClO + NO_2$$

must correlate with the calculations. Initial ground-based observations of the total column [ClO] confirms the general diurnal behavior. With both high time resolution and high spatial resolution afforded by the *in situ* techniques coupled with the Reel Down technique, the current picture can be tested with great precision.

While many other fundamentally important measurements can be described, we move on to review the most recent appraisals of ozone depletion levels because recent advances in the area have significantly changed our outlook on this subject.

With little doubt, the most significant change in our understanding of fluorocarbon induced ozone destruction, both qualitatively and quantitatively, since the Rowland-Molina proposition of radical catalyzed recombination of ozone by Cl and ClO in 1974, is described in a recent paper in *Nature* by Prather *et al.*[20] What that paper defines is the dramatically non-linear dependence of ozone depletion on added chlorine at high levels of total $Cl_x = Cl + ClO + HCl + ClONO_2 + HOCl$. The critical point is that at levels of Cl_x approaching 15 ppbv, ClO "titrates" NO_2 out of the

system via the previously described termolecular reaction

$$Cl\!O + NO_2 + M \rightarrow Cl\!ONO_2 + M \ .$$

Under conditions in which $[Cl\!O] \geq [NO_2]$, the photochemical structure of the middle and lower stratosphere undergoes a profound change. First the titration of NO_2 from the system takes all forms of NO_x with it, specifically, NO and $HONO_2$ (see pages 11-16 of this report). This eliminates the major loss mechanism for OH below 30 km, specifically the reaction

$$OH + HONO_2 \rightarrow H_2O + NO_3 \ .$$

Significantly increased levels of OH act to shift the balance of inorganic chlorine, from the non reactive form, HCl, to the reactive radicals, Cl and $Cl\!O$, via the reaction

$$HCl + OH \rightarrow Cl + H_2O \ .$$

Suppressed levels of NO act to block the conversion of $Cl\!O$ to Cl by the reaction

$$Cl\!O + NO \rightarrow Cl + NO_2$$

which both increases the $Cl\!O$ concentration directly and slows the removal of Cl radicals via the reaction

$$Cl + CH_4 \rightarrow HCl + CH_4$$

which is the dominant mechanism converting radicals back to the relatively non reactive form, HCl. Finally, enhanced levels of OH accelerate the oxidation of methane in the stratosphere and thereby suppress further the conversion of Cl and $Cl\!O$ to HCl by the above reaction.

Taken together, the effects are profound. Figure 16 from the Prather et al.[20] paper summarizes the dependence of column integrated ozone on total

Cl_x for three different mixing ratios of NO_x: 13, 16.2, and 19.5 ppb by volume. The asterisk denotes the point at which the ozone column has dropped by 10%.

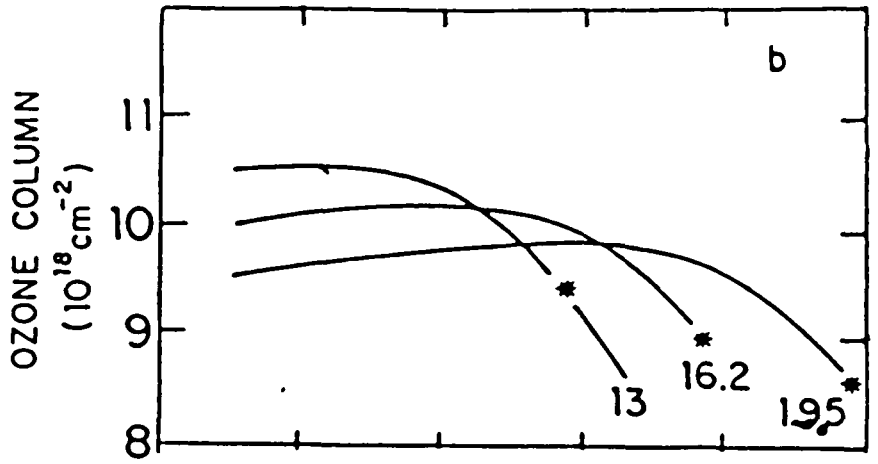

Figure 16. The column abundance of ozone as a function of stratospheric chlorine for three assumed mixing ratios (by volume) of $NO_x = NO + NO_2 + HONO_2$, taken from Prather et al.

Note that very little change in total O_3 column occurs over a broad range of Cl_x mixing ratios, but that once $[ClO] \approx [NO_2]$, a very rapid decrease is predicted. The delay between now and the time at which we approach this titration condition is summarized in Figure 17.

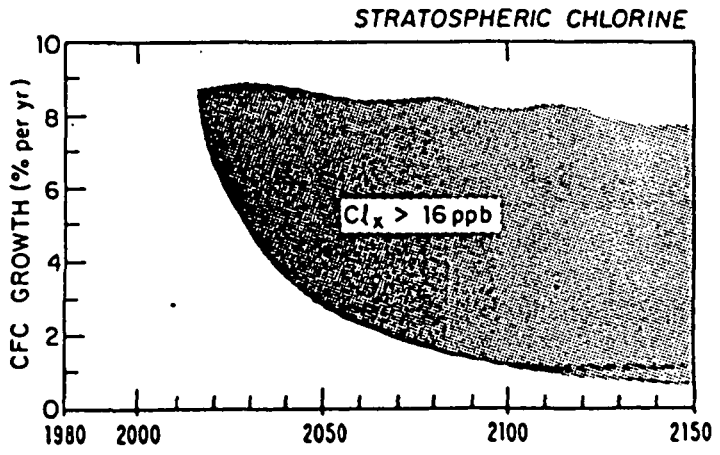

Figure 17. Relationship between the rate of increase in fluorocarbon production and the year at which the stratosphere will exceed 16 ppb of Cl_x.

At a rate of increase of 3% per year, the 16 ppbv level is reached in the middle of the next century. Quite clearly, the issue is not academic since the world is moving in a direction such that a 3% per year increase may well be conservative. We quote directly from the conclusions of Prather et al.:

> In summary, our models suggest that growth in release of chlorinated and brominated halocarbons can pose future problems for stratospheric O_3. There are reasons to believe that the chemistry of the lower stratosphere might undergo a significant change if the concentration of chlorine were to rise above that of NO_x. The concentration of OH could increase markedly and ozone could drop, with reductions potentially larger than 15% in the column density of O_3. Ozone is expected to remain relatively constant prior to the onset of the NO_x to chlorine transition below 30 km. It is important to monitor not only the total column density of O_3, but to search also for evidence of change in the chemical composition of the lower stratosphere.
>
> The large effects predicted here occur primarily below 30 km and involve major changes in the chemistry of radicals such as OH and ClO. Observational data for these species are totally inadequate at lower altitudes and are urgently required to test the validity of current models in a region containing the bulk of atmospheric O_3.
>
> The present results are based on a one-dimensional model. They should be extended to consider variations of stratospheric chemistry with latitude and season. Extension of the model to more than one dimension may be particularly important in studying the impact of high concentrations of chlorine since results should depend sensitively on details of the calculated latitudinal distributions of chlorine and NO_x.
>
> Investigations of the radical chemistry of the stratosphere have focused in past on the region above 30 km. It is clear that the emphasis must shift now to lower altitudes.

Perhaps the most profound turn of events introduced by the Prather et al. paper is the fact that these conclusions are simple, robust and testable. They depend only on the amount of OH and ClO present in the middle and lower stratosphere and on the coupling between ClO and NO_2, all directly testable using the techniques discussed in Section III.

We conclude by noting that while the subject of chemically induced changes to the ozone layer have been surrounded by uncertainty and by controversy, we stand on the edge of a series of major advances which will establish a far more profound scientific underpinning for this subject. It is now believed by students of this subject that the stratosphere may well be the first natural system of global extent which will submit to the scientific method.

REFERENCES

1. Johnston, H.S., Science 173, 517, 1971.

2. Molina, M.J. and F.S. Rowland, Nature 249, 810, 1974.

3. Symposium, International Association of Geomagnetism and Aeronomy, Aeronomy of the Stratosphere and Mesosphere, H.I. Schiff, ed., Canad. J. Chem. 52, 1381-1634, 1974.

4. World Meteorological rganization Global Ozone Research and Monitoring Project Report #11, The Stratosphere 1981: Theory and Measurements Report #11, January 1982, WMO Case Postale #5, Geneva 20, Switzerland. National Academy of Science, Causes and Effects of Changes in Stratospheric Ozone: Update 1983, National Academy Press, Washington, D.C., 1984.

5. Johnston, H.S., Chapter 4, "Odd Nitrogen Processes," in Stratospheric Ozone and Man, Vol. I, F.A. Bower and R.B. Ward, eds., CRC Press, Boca Raton, 1982.

6. Ko, Malcolm K.W. and N.D. Sze, submitted to J. Geophys. Res., March 1984.

7. Solomon, P.M., R. de Zafra, A. Parrish and J.W. Barrett, Science, in press.

8. Farmer, C.B., Jet Propulsion Laboratory Report on the ATMOS Instrument, 1983.

9. Jones, R.L. and J.A. Pyle, J. Geophys. Res. 89, 5263, 1984.

10. "Assessment of Techniques for Measuring Tropospheric H_xO_y," Proceedings of a workshop sponsored by the NASA Office of Space Science and Applications and NASA Langley Research Center, held in Palo Alto, CA, 16-20 August 1982.

11. Anderson, J.G., N.L. Hazen, S.P. Rowe, E. Thompson, C.M. Schiller, M.J. Schwab and E.M. Weinstock, submitted to Science, November 1984.

12. Anderson, J.G., H.J. Grassl, R.E. Shetter and J.J. Margitan, J. Geophys. Res. 85, 2869, 1980.

13. de Zafra, R.L., A. Parrish, P.M. Solomon and J.W. Barrett, submitted to J. Geophys. Res., 1984.

14. de Zafra, R.L., Current issues in our understanding of the stratosphere and the future of the ozone layer, Starnberger See, West Germany, 11-16 January 1984.

15. Chance, K.V. and W.A. Traub, An upper limit for stratospheric hydrogen peroxide, Starnberger See, West Germany, 11-16 January 1984.

16. Traub, W.A. and K.V. Chance, Measurements of OH from 18 to 48 km, Starnberger See, West Germany, 11-16 January 1984.

17. Carli, B., Comparison of current models of OH stratospheric concentration with far-infrared emission measurements, Starnberger See, West Germany, 11-16 January 1984.

18. Solomon, S. and R.R. Garcia, J. Geophys. Res., in press.

19. Hazen, N.L. and J.G. Anderson, A new reeling technique for very long extension scanning in the stratosphere, Paper 7.2.6 in Advances in Space Research, W. Riedler, ed., in press.

20. Prather, M.J., M.B. McElroy and S.C. Wofsy, Nature, in press.

APPENDIX A

1. $O(^1D) + N_2 \rightarrow O(^3P) + N_2$
2. $O(^1D) + O_2 \rightarrow O(^3P) + O_2$
3. $O(^1D) + N_2O \rightarrow NO + NO \rightarrow N_2 + O_2$
4. $O(^1D) + CH_4 \rightarrow OH + CH_3$
5. $OH + CH_4 \rightarrow CH_3 + H_2O$
6. $OH + CO \rightarrow CO_2 + H$
7. $CO + O + M \rightarrow CO_2 + M$
8. $O(^1D) + H_2O \rightarrow OH + OH$
9. $O(^1D) + H_2 \rightarrow OH + H$
10. $O + OH \rightarrow O_2 + H$
11. $H + O_2 \rightarrow OH + O_2$
12. $OH + O_2 \rightarrow HO_2 + O_2$
13. $HO_2 + O_2 \rightarrow OH + 2O_2$
14. $O + H_2O_2 \rightarrow O_2 + H_2O \rightarrow OH + HO_2$
15. $H + H_2O_2 \rightarrow H_2 + HO_2 \rightarrow OH + H_2O$
16. $H + HO_2 \rightarrow H_2 + O_2 \rightarrow OH + OH$
17. $H + O_2 + M \rightarrow HO_2 + M$
18. $OH + OH \rightarrow H_2O + O$
19. $O + HO_2 \rightarrow OH + O_2$
20. $OH + H_2 \rightarrow H_2O + H$
21. $O + H_2 \rightarrow OH + H$
22. $OH + H_2O_2 \rightarrow HO_2 + H_2O$
23. $OH + HO_2 \rightarrow H_2O_2 + O_2$
24. $HO_2 + HO_2 \rightarrow H_2O_2 + O_2$
25. $N + O_2 \rightarrow NO + O$
26. $OH + HCl \rightarrow H_2O + Cl$
27. $Cl + H_2 \rightarrow HCl + H$
28. $H + HCl \rightarrow Cl + H_2$
29. $O + HCl \rightarrow OH + Cl$
30. $Cl + O_2 \rightarrow ClO + O_2$
31. $Cl + Cl + M \rightarrow Cl_2 + M$
32. $ClO + NO \rightarrow Cl + NO_2$
33. $ClO + O \rightarrow Cl + O_2$
34. $ClO + NO_2 + M \rightarrow ClNO_3 + M$
35. $O + ClNO_3 \rightarrow$ products
36. $OH + ClNO_3 \rightarrow$ products
37. $H + Cl_2 \rightarrow HCl + Cl$
38. $O + Cl_2 \rightarrow ClO + Cl$
39. $H + ClO \rightarrow OH + Cl$
40. $Cl + H_2O_2 \rightarrow HCl + HO_2$
41. $Cl + HO_2 \rightarrow HCl + O_2$
42. $ClO + HO_2 \rightarrow HOCl + O_2$
43. $OH + HOCl \rightarrow H_2O + ClO$
44. $Cl + CH_4 \rightarrow CH_3 + HCl$
45. $OH + CH_3Cl \rightarrow$ products
46. $OH + CH_3CCl_3 \rightarrow$ products
47. $OH + CH_2O \rightarrow HCO + H_2O$
48. $N + NO \rightarrow N_2 + O$
49. $O + NO_2 \rightarrow NO + O_2$
50. $O_3 + NO \rightarrow NO_2 + O_2$
51. $H + NO_2 \rightarrow OH + NO$
52. $O_3 + NO_2 \rightarrow O_2 + NO_3$
53. $O + NO + M \rightarrow NO_2 + M$
54. $O + NO_2 + M \rightarrow NO_3 + M$
55. $NO + NO_3 \rightarrow NO_2 + NO_2$
56. $NO_2 + NO_3 \rightarrow NO + NO_2 + O_2$
57. $NO_2 + NO_3 \rightarrow 2NO_2 + O_2$
58. $N + NO_2 \rightarrow N_2O + O$
59. $OH + HNO_3 \rightarrow H_2O + NO_3$
60. $HO_2 + NO \rightarrow OH + NO_2$
61. $N + O_2 \rightarrow NO + O_2$
62. $OH + NO + M \rightarrow HNO_2 + M$
63. $O + HNO_3 \rightarrow OH + NO_2$
64. $H + HNO_3 \rightarrow H_2 + NO_3$
65. $O + O_2 + M \rightarrow O_3 + M$
66. $O + O_3 \rightarrow O_2 + O_2$
67. $O + O + M \rightarrow O_2 + M$
68. $NO + NO + O_2 \rightarrow NO_2 + NO_2$
69. $NO_2 + NO_3 + M \rightarrow N_2O_5 + M$
70. $N_2O_5 + M \rightarrow NO_2 + NO_3$
71. $N + OH \rightarrow NO + H$
72. $N + O \rightarrow NO + h\nu$
73. $H + H + M \rightarrow H_2 + M$
74. $NO + O \rightarrow NO_2 + M$
75. $OH + HNO_3 \rightarrow H_2O + NO_3$
76. $HO_2 + NO_2 \rightarrow HNO_2 + O_2$
77. $HO_2 + NO_2 \underline{M} HO_2NO_2$
78. $HO_2NO_2 \underline{M} HO_2 + NO_2$
79. $OH + HO_2NO_2 \rightarrow H_2O + O_2 + NO_2$
80. $OH + CH_3OOH \rightarrow CH_3O_2 + H_2O$
81. $CH_3OO + NO \rightarrow CH_3O + NO_2$
82. $CH_3OO + HO_2 \rightarrow CH_3OOH + O_2$
83. $CH_3OO + CH_3OO \rightarrow 2CH_3O + O_2$
84. $OH + NO_2 + M \rightarrow HNO_3 + M$
85. soluble gas $\rightarrow$ precipitation scavenging (CH_3OOH)
86. $NO + h\nu \rightarrow N + O$
87. $N_2O_5 + h\nu \rightarrow NO_2 + NO_3$
88. $NO_2 + h\nu \rightarrow NO + O$
89. $HNO_2 + h\nu \rightarrow OH + NO$
90. $HNO_3 + h\nu \rightarrow OH + NO_2$
91. $N_2O + h\nu \rightarrow N_2 + O(^1D)$
92. $NO_2 + h\nu \underline{1} NO + O, O \underline{2} NO_2 + O$
93. $O_3 + h\nu \rightarrow O_2 + O$
94. $O_3 + h\nu \rightarrow O + O$
95. $H_2O + h\nu \rightarrow H + OH$
96. $CH_4 + h\nu \rightarrow CH_3 + H_2$
97. $CO_2 + h\nu \rightarrow CO + O$
98. $H_2O_2 + h\nu \rightarrow OH + OH$
99. $CH_3OOH + h\nu \rightarrow CH_2O + OH$
100. $HO_2 + h\nu \rightarrow OH + H$
101. $H_2CO + h\nu \rightarrow HCO + H \rightarrow H_2 + CO$
102. $Cl_2 + h\nu \rightarrow Cl + Cl$
103. $HCl + h\nu \rightarrow H + Cl$
104. $ClO + h\nu \rightarrow Cl + O$
105. $ClNO_3 + h\nu \rightarrow ClO + NO_2$
106. $CCl_2F_2 + h\nu \rightarrow CCl_2F + Cl$
107. $CCl_3F + h\nu \rightarrow CCl_2F + Cl$
108. $CCl_4 + h\nu \rightarrow CCl_3 + Cl$
109. $CH_3Cl + h\nu \rightarrow CH_3 + Cl$
110. $CH_3CCl_3 + h\nu \rightarrow CH_2CCl_2 + Cl$
111. $HOCl + h\nu \rightarrow OH + Cl$
112. $HO_2NO_2 + h\nu \rightarrow OH + NO_2$
113. $BrONO_2 + h\nu \rightarrow Br + NO_3$
114. $BrO + h\nu \rightarrow Br + O$
115. $HOBr + h\nu \rightarrow OH + Br$
116. $Br_2 + h\nu \rightarrow Br + Br$
117. $CH_3Br + h\nu \rightarrow CH_3 + Br$
118. $Br + O_3 \rightarrow BrO + O_2$
119. $Br + HO_2 \rightarrow HBr + O_2$
120. $Br + H_2O_2 \rightarrow HBr + HO_2$
121. $OH + HBr \rightarrow H_2O + Br$
122. $O + HBr \rightarrow OH + Br$
123. $BrO + NO \rightarrow Br + NO_2$
124. $BrO + O \rightarrow Br + O_2$
125. $BrO + BrO \rightarrow 2Br + O_2$
126. $BrO + ClO \rightarrow Br + Cl + O_2$.

Stratospheric Ozone and Man

Volume I

Editors

Frank A. Bower, Ph.D.
E. I. du Pont de Nemours & Company
Haskell Laboratory for Toxicology and Industrial Medicine
Newark, Delaware

Richard B. Ward, Ph.D.
Research Associate
E. I. du Pont de Nemours & Company
Petrochemical Department
Wilmington, Delaware

CRC Press, Inc.
Boca Raton, Florida

Chapter 6

THE CHEMISTRY OF STRATOSPHERIC CHLORINE

James G. Anderson

TABLE OF CONTENTS

I. INTRODUCTION

The entry of chlorine into the mainstream of atmospheric photochemistry was in progress in the early 1970s when the Rowland-Molina hypothesis[1] linked the release of fluorocarbons at the surface to the gas phase catalytic destruction of ozone in the stratosphere. That theory not only emphasized the importance of chlorine as a component of significant chemical importance to the unperturbed stratosphere, but also introduced the concept that the surface release of an inert and otherwise benign molecule, central to many aspects of our present society, could seriously deplete the concentration of a molecule in the upper atmosphere which is solely responsible for screening the surface of the Earth from potentially harmful near UV radiation. The work of Rowland and Molina profoundly altered our perspective on the global significance of such releases.

There were three essential elements in their case:

1. Release of the halogen substituted methanes, principally CCl_3F and CCl_2F_2 (FC-11 and FC-12), into the atmosphere is followed by rapid mixing of the compounds throughout the troposphere. To a first approximation, there are no physical or chemical removal processes at the surface or in the gas phase throughout the troposphere. This fact was established by comparing integrated release rates with global measurements by Lovelock[2] whose shipboard observations as a function of latitude formed a cornerstone in the early formulation of the hypothesis.
2. The uniform mixing of the compounds throughout the troposphere increased the mixing ratio of chlorine at the tropopause and thereby the flux of chlorine compounds into the stratosphere. Vertical mixing continues above the tropopause although at a slower rate dictated by the permanent "temperature inversion" characteristic of the stratosphere, until the molecules reach an altitude where the penetration of solar radiation in the wavelength interval between the major absorption continuum/band system of O_2 and O_3 occurs. Photons in this interval are weakly absorbed and have sufficient energy to photodissociate both CCl_3F and CCl_2F_2; $CCl_3F + h\nu \rightarrow CCl_2F + Cl$ and $CCl_2F_2 \rightarrow CClF_2 + Cl$ releasing atomic chlorine.
3. The principal fate of the chlorine atom thus released is reaction with ozone to form the chlorine monoxide free radical which in turn reacts with atomic oxygen to regenerate the chlorine atom

$$\begin{aligned} Cl + O_3 &\rightarrow ClO + O_2 \\ ClO + O &\rightarrow Cl + O_2 \\ \hline O_3 + O &\rightarrow O_2 + O_2 \end{aligned}$$

thereby forming a homogeneous gas phase catalytic cycle amplifying the rate of odd oxygen destruction. Since (1) both reactions comprising the cycle are fast bimolecular processes and the couplet is completed on the time scale of tens of seconds, and (2) each chlorine atom resides in the stratosphere for a period of years, spending a significant fraction of that time in free radical form, it follows that an amount of chlorine orders of magnitude less than that of ozone can potentially alter the rate of ozone destruction in the stratosphere.

Although a great deal has been learned about the gas phase chemistry of chlorine in general and about chlorine-ozone atmospheric photochemistry in particular since that

first paper by Molina and Rowland,[1] the three essential features of their original theory remain firmly intact.

In the sections which follow we review the current state of chlorine-ozone chemistry in three parts. First, an analysis of the interplay between chemical kinetics and physical dynamics is offered in Section II, emphasizing details of the chlorine system. An understanding of several key points in that section must precede the interpretation of atmospheric observations which are reviewed in Section III. That review is approached from two complementary points of view. The first emphasizes prognostic elements of the subject by comparing observations with model calculations and the second emphasizes model independent diagnostic studies of the real atmosphere which, while far less precise than model studies, have the fundamental advantage of testing basic hypothesis of chemical cause and effect through direct observation and can thus define the (absolute) accuracy of perturbations to the system. As we will see, many aspects of the model independent approach can be effectively applied only to the chlorine-ozone system.

II. STRATOSPHERIC CHLORINE-OZONE PHOTOCHEMISTRY: A REVIEW

In this section, the essential elements of chlorine chemistry are introduced in parallel with physical transport processes which, while inseparably related to chemical changes, need not obscure or dilute crucial conclusions obtained from observations discussed in subsequent sections. The fact that the atmosphere is a fluid and thus moves in capricious patterns is too often taken to mean that chemistry experiments performed therein are relegated to a semiquantitative status. This, as we shall see, is not the case provided care is taken in the selection and execution of field experiments.

The fluorocarbon-ozone problem cannot be studied in isolation from processes involving nitrogen, hydrogen, and bromine which are discussed in other chapters. We must deal, therefore, with some 150 essential and carefully screened thermal and photolytic processes as outlined in the reaction set listed in Table 1 below taken from Logan et al.[3] augmented by the addition of bromine reactions from Yung et al.[4]

In general the change in concentration of constituent n_i with time within any volume element of the stratosphere is governed by the continuity equation

$$\frac{d[n_i]}{dt} = P_i - L_i + \nabla\cdot\phi_i$$

which expresses the time rate of change on n_i in terms of the chemical production and loss rates, P_i and L_i, respectively, and the flux divergence $\nabla\cdot\phi_i$ which represents a net flow of n_i into the volume element under consideration. A brief inspection of Table 1 indicates that each P and L term consists of between 3 and 20 terms of the form (selecting ClO as an example)

$$P_{ClO} = k_{30}[Cl][O_3] + k_{38}[O][Cl_2] + J_{ClONO_2}[ClONO_2]$$

$$L_{ClO} = \{k_{32}[NO] + k_{33}[O] + k_{34}[M][NO_2] + k_{39}[H] + k_{42}[HO_2] + k_{126}[BrO] + J_{ClO}\}[ClO]$$

where the k's represent bimolecular or termolecular reaction rate constants in units cm^3 $molecule^{-1}$ sec^{-1} or cm^6 $molecule^{-1}$ sec^{-1}, respectively, and the J's represent photodissociation rates in units of sec^{-1}. Since analytical techniques have been developed or

Table 1 (continued)
REACTIONS SET

1. $O(^1D) + N_2 \rightarrow O(^3P) + N_2$
2. $O(^1D) + O_2 \rightarrow O(^3P) + O_2$
3. $O(^1D) + N_2O \rightarrow NO + NO \rightarrow N_2 + O_2$
4. $O(^1D) + CH_4 \rightarrow OH + CH_3$
5. $OH + CH_4 \rightarrow CH_3 + H_2O$
6. $OH + CO \rightarrow CO_2 + H$
7. $CO + O + M \rightarrow CO_2 + M$
8. $O(^1D) + H_2O \rightarrow OH + OH$
9. $O(^1D) + H_2 \rightarrow OH + H$
10. $O + OH \rightarrow O_2 + H$
11. $H + O_3 \rightarrow OH + O_2$
12. $OH + O_3 \rightarrow HO_2 + O_2$
13. $HO_2 + O_3 \rightarrow OH + 2O_2$
14. $O + H_2O_2 \rightarrow O_2 + H_2O \rightarrow OH + HO_2$
15. $H + H_2O_2 \rightarrow H_2 + HO_2 \rightarrow OH + H_2O$
16. $H + HO_2 \rightarrow H_2 + O_2 \rightarrow OH + OH$
17. $H + O_2 + M \rightarrow HO_2 + M$
18. $OH + OH \rightarrow H_2O + O$
19. $O + HO_2 \rightarrow OH + O_2$
20. $OH + H_2 \rightarrow H_2O + H$
21. $O + H_2 \rightarrow OH + H$
22. $OH + H_2O_2 \rightarrow HO_2 + H_2O$
23. $OH + HO_2 \rightarrow H_2O_2 + O_2$
24. $HO_2 + HO_2 \rightarrow H_2O_2 + O_2$
25. $N + O_2 \rightarrow NO + O$
26. $OH + HCl \rightarrow H_2O + Cl$
27. $Cl + H_2 \rightarrow HCl + H$
28. $H + HCl \rightarrow Cl + H_2$
29. $O + HCl \rightarrow OH + Cl$
30. $Cl + O_3 \rightarrow ClO + O_2$
31. $Cl + Cl + M \rightarrow Cl_2 + M$
32. $ClO + NO \rightarrow Cl + NO_2$
33. $ClO + O \rightarrow Cl + O_2$
34. $ClO + NO_2 + M \rightarrow ClNO_3 + M$
35. $O + ClNO_3 \rightarrow$ products
36. $OH + ClNO_3 \rightarrow$ products
37. $H + Cl_2 \rightarrow HCl + Cl$
38. $O + Cl_2 \rightarrow ClO + Cl$
39. $H + ClO \rightarrow OH + Cl$
40. $Cl + H_2O_2 \rightarrow HCl + HO_2$
41. $Cl + HO_2 \rightarrow HCl + O_2$
42. $ClO + HO_2 \rightarrow HOCl + O_2$
43. $OH + HOCl \rightarrow H_2O + ClO$
44. $Cl + CH_4 \rightarrow CH_3 + HCl$
45. $OH + CH_3Cl \rightarrow$ products
46. $OH + CH_3CCl_3 \rightarrow$ products
47. $OH + CH_2O \rightarrow HCO + H_2O$
48. $N + NO \rightarrow N_2 + O$
49. $O + NO_2 \rightarrow NO + O_2$
50. $O_3 + NO \rightarrow NO_2 + O_2$
51. $H + NO_2 \rightarrow OH + NO$
52. $O_3 + NO_2 \rightarrow O_2 + NO_3$
53. $O + NO + M \rightarrow NO_2 + M$
54. $O + NO_2 + M \rightarrow NO_3 + M$
55. $NO + NO_3 \rightarrow NO_2 + NO_2$
56. $NO_2 + NO_3 \rightarrow NO + NO_2 + O_2$
57. $NO_2 + NO_3 \rightarrow 2NO_2 + O_2$
58. $N + NO_2 \rightarrow N_2O + O$
59. $OH + HNO_3 \rightarrow H_2O + NO_3$
60. $HO_2 + NO \rightarrow OH + NO_2$
61. $N + O_2 \rightarrow NO + O$
62. $OH + NO + M \rightarrow HNO_2 + M$
63. $O + HNO_2 \rightarrow OH + NO_2$
64. $H + HNO_2 \rightarrow H_2 + NO_2$
65. $O + O_2 + M \rightarrow O_3 + M$
66. $O + O_3 \rightarrow O_2 + O_2$
67. $O + O + M \rightarrow O_2 + M$
68. $NO + NO + O_2 \rightarrow NO_2 + NO_2$
69. $NO_2 + NO_2 + M \rightarrow N_2O_4 + M$
70. $N_2O_4 + M \rightarrow NO_2 + NO_2$
71. $N + OH \rightarrow NO + H$
72. $N + O \rightarrow NO + h\nu$
73. $H + H + M \rightarrow H_2 + M$
74. $NO + O \rightarrow NO_2 + M$
75. $OH + HNO_2 \rightarrow H_2O + NO_2$
76. $HO_2 + NO_2 \rightarrow HNO_2 + O_2$
77. $HO_2 + NO_2 \underset{}{\overset{M}{\rightleftharpoons}} HO_2NO_2$
78. $HO_2NO_2 \underset{}{\overset{M}{\rightleftharpoons}} HO_2 + NO_2$
79. $OH + HO_2NO_2 \rightarrow H_2O + O_2 + NO_2$
80. $OH + CH_3OOH \rightarrow CH_3O_2 + H_2O$
81. $CH_3OO + NO \rightarrow CH_3O + NO_2$
82. $CH_3OO + HO_2 \rightarrow CH_3OOH + O_2$
83. $CH_3OO + CH_3OO \rightarrow 2CH_3O + O_2$
84. $OH + NO_2 + M \rightarrow HNO_3 + M$
85. soluble gas $\rightarrow$ precipitation scavenging (units: s^{-1}) (HCl, HNO_3, HNO_2, HO_2NO_2, H_2O_2, H_2CO, CH_3OOH)
86. $NO + h\nu \rightarrow N + O$
87. $N_2O_5 + h\nu \rightarrow NO_2 + NO_3$
88. $NO_2 + h\nu \rightarrow NO + O$
89. $HNO_3 + h\nu \rightarrow OH + NO$
90. $HNO_2 + h\nu \rightarrow OH + NO_2$
91. $N_2O + h\nu \rightarrow N_2 + O(^1D)$
92. $NO_2 + h\nu \underset{}{\overset{1}{\rightleftharpoons}} NO + O, \underset{}{\overset{2}{\rightleftharpoons}} NO_2 + O$
93. $O_2 + h\nu \rightarrow O_2 + O$
94. $O_2 + h\nu \rightarrow O + O$
95. $H_2O + h\nu \rightarrow H + OH$
96. $CH_4 + h\nu \rightarrow CH_3 + H_2$
97. $CO_2 + h\nu \rightarrow CO + O$
98. $H_2O_2 + h\nu \rightarrow OH + OH$
99. $CH_3OOH + h\nu \rightarrow CH_3O + OH$
100. $HO_2 + h\nu \rightarrow OH + H$
101. $H_2CO + h\nu \rightarrow HCO + H \rightarrow H_2 + CO$
102. $Cl_2 + h\nu \rightarrow Cl + Cl$
103. $HCl + h\nu \rightarrow H + Cl$
104. $ClO + h\nu \rightarrow Cl + O$
105. $ClNO_3 + h\nu \rightarrow ClO + NO_2$
106. $CCl_2F_2 + h\nu \rightarrow CCl_2F + Cl$
107. $CCl_3F + h\nu \rightarrow CCl_2F + Cl$
108. $CCl_4 + h\nu \rightarrow CCl_3 + Cl$
109. $CH_3Cl + h\nu \rightarrow CH_3 + Cl$
110. $CH_3CCl_3 + h\nu \rightarrow CH_3CCl_2 + Cl$
111. $HOCl + h\nu \rightarrow OH + Cl$
112. $HO_2NO_2 + h\nu \rightarrow OH + NO_2$
113. $BrONO_2 + h\nu \rightarrow Br + NO_3$
114. $BrO + h\nu \rightarrow Br + O$
115. $HOBr + h\nu \rightarrow OH + Br$
116. $Br_2 + h\nu \rightarrow Br + Br$
117. $CH_3Br + h\nu \rightarrow CH_3 + Br$
118. $Br + O_3 \rightarrow BrO + O_2$

Table 1 (continued)
REACTIONS SET

119. $Br + HO_2 \rightarrow HBr + O_2$
120. $Br + H_2O_2 \rightarrow HBr + HO_2$
121. $OH + HBr \rightarrow H_2O + Br$
122. $O + HBr \rightarrow OH + Br$
123. $BrO + NO \rightarrow Br + NO_2$
124. $BrO + O \rightarrow Br + O_2$
125. $BrO + BrO \rightarrow 2Br + O_2$
126. $BrO + ClO \rightarrow Br + Cl + O_2$.

are currently being developed for determining the concentrations of virtually all compounds which appear in Table 1, P and L are, in principle, observable quantities within a specific volume element. The same is not true of the flux divergence term $\nabla \cdot \varnothing_i$ nor can it be given current technology, since it represents a minute difference between large and experimentally unobservable quantities.

We are confronted, therefore, by a problem of considerable chemical complexity superimposed on a constantly changing global circulation pattern, such that care is needed to cast the problem in a form which will allow a transformation of hypothesis to fact through a plausible set of observable quantities. In order to make sense of this global broth of chemical kinetics and physical dynamics, it is first necessary to categorize each constituent, i, in terms of its life expectancy against chemical transformation, τ^i_{CHEM}, which is equal to the concentration of constituent i divided by the local rate of production or destruction by photochemical processes. That chemical lifetime must then be compared with the period of time, τ_{TRAN}, required to transport that constituent to a region of the atmosphere with a measurably different radiation, temperature or pressure environment.

In general if $\tau^i_{CHEM} << \tau_{TRAN}$, then P_i and L_i vastly exceed $\nabla \cdot \varnothing_i$ and the concentration of constituent i is controlled entirely by chemical processes within the volume element. If, in addition, P_i and L_i exceed the absolute magnitude of their difference, P_i and $L_i >> |P_i - L_i|$ then $d[n_i]/dt \approx P_i - L_i \approx 0$. Constituent i is then in photochemical steady state and hypothesized chemical exchange processes can be tested within that volume element through simultaneously observed concentrations of those constituents believed to comprise P_i and L_i. These tests are of two forms, either "budget" analyses wherein simultaneous observations are used to test whether the difference between P_i and L_i equals zero or a more discriminating "covariance" analysis in which observed fluctuations in P_i and L_i are examined to discover the cause and effect relationship among the constituents. Note, incidentally, that if τ^i_{CHEM} is short compared with any other relevant time constant, we have satisfied both a necessary and a sufficient condition for the steady state assumption to hold so that we can experimentally test our hypothesis, or the mechanisms which comprise P_i and L_i, knowing their difference must closely approximate zero.

On the other hand, if $\tau_{TRAN} << \tau^i_{CHEM}$, the motion of the atmosphere dictates the distribution of constituent i and experiments testing chemical exchange mechanisms through simultaneous observations are meaningless.

We seek, then, to classify the chlorine compounds according to whether their chemical lifetime is significantly less than, comparable to, or significantly greater than their corresponding transport time. The troposphere can be dispensed with quickly because the only compounds of interest are the chlorine source molecules CH_3Cl, CH_3CCl_3, CCl_4, CCl_2F_2, CCl_3F, and $CHCl_2F$ all of which have chemical lifetimes greatly exceeding vertical transport times throughout the troposphere so their mixing ratio is approximately constant throughout that region. The solubility of HCl produced by chemical

transformations within the stratosphere ensures its rapid rainout in the troposphere and

$$\tau_{CHEM}^{HCl} < \tau_{TRAN}$$

In the stratosphere, we must consider the time constant for both horizontal and vertical mixing, noting that transport velocities in the horizontal are typically 500 to 1000 times that in the vertical. Figure 1A depicts the zonal (east-west) flow pattern of the general circulation pattern of the Earth, and Figure 1B indicates the rather more complicated meridional circulation. Although it takes $\sim$ 1 week for a given air mass to zonally circumvent the globe, equator to poleward motion requires a period of months, reflecting the slower meridional motion of Figure 1B. The poleward transport of constituents entering the stratosphere from the troposphere, principally at low latitudes, establishes surfaces of constant mixing ratio, termed isopleths, as discussed by Wofsy[7] and Logan et al.[3] The rate determining process in the stratospheric distribution of molecules released in the troposphere is therefore vertical mixing. This fact, in conjunction with the limitation of finite computer size and the large number of important photochemical processes (see Table 1), has led historically to the one dimensional (1-D) model. Those models take global averages in the zonal and meridional dimension and parameterize vertical transport in terms of an eddy diffusion coefficient, K, such that the vertical flux ϕ of constituent i is given by

$$\phi_i = -K[M]\frac{\partial f_i}{\partial z}$$

where M is the total atmospheric density, f_i is the number mixing ratio of constituent i, and z is altitude. This method of dealing with vertical transport has been a topic of major controversy and although it has serious limitations when indiscriminately applied, it constitutes an important and defensible approach for a carefully selected set of problems.

Values of the eddy coefficient, K, are inferred from the observed vertical distribution of the source molecules, which are not chemically reformed in the stratosphere, by balancing local destruction, usually oxidation or photolysis, against flux convergence with the constraint that the numerically integrated profile match that of the observations. The source molecules most intensively studied in this regard have been CH_4, N_2O, CCl_3F, and CCl_2F_2.

Although one would not expect, based upon what we know about advective motion in the stratosphere, that such an eddy diffusion coefficient could represent atmospheric transport in even a crude sense, there are observational facts which lend support to such simplified treatments. First, as Figure 2A-C taken from Goldan et al.[6] imply, a large collection of vertical soundings of N_2O, CCl_3F, and CCl_2F_2 taken between the equator and 41°N latitude show a consistent and predictable gradient and are not characterized by large random fluctuations which would be expected if large advective cells dictated vertical concentration profiles of the source molecules. The concern, of course, is that while values of K so inferred may be appropriate for upward transport of source molecules, contributions from advective motion could lead to asymmetries in vertical fluxes, affecting the downward transport of compounds produced in the stratosphere. Although much work remains to be done on this point, it is clear from a considerable body of observational data that such 1-D treatments adequately distribute the source molecules. We adopt, for our order of magnitude appraisal of vertical transport times, the value of K displayed in Figure 3A which closely approximates that used in Logan et al.[3] and several recently published model results.[8]

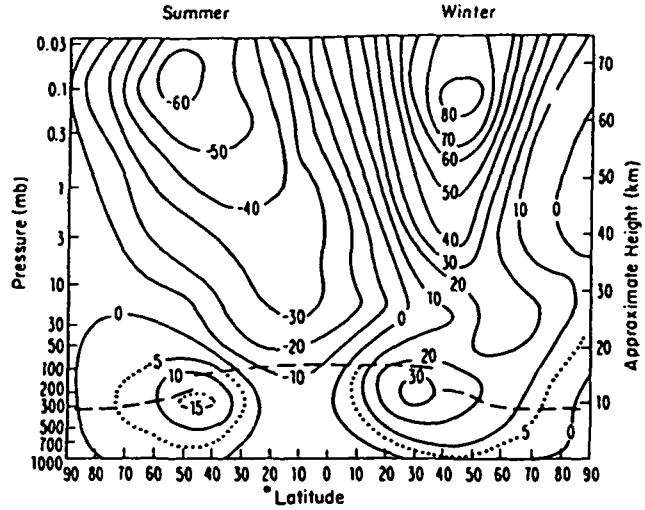

FIGURE 1A. Schematic latitude-height section of the mean zonal wind in m/sec at the solstices. (From Murgatroyd, R. J., *The Global Circulation of the Atmosphere*, Corby, G. A., Ed., London Royal Meteorological Society, 1969, 194. With permission.)

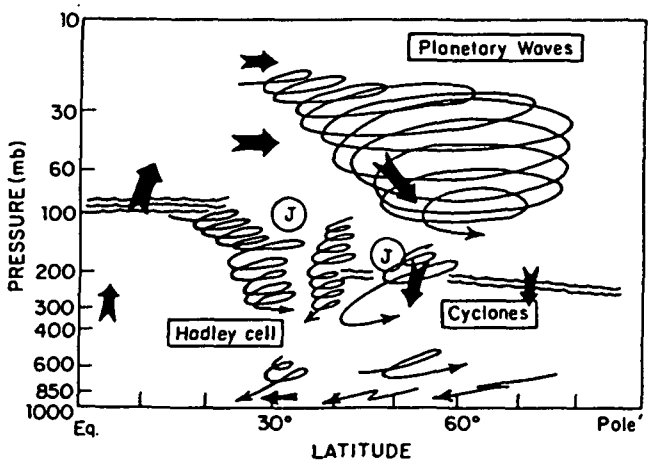

FIGURE 1B. Lagrangian mean meridional circulation, heavy arrows showing contributions by the Hadley cell, extratropical cyclones; jet streams, J; planetary waves and small scale motions. (From Wallace, J. M., *J. Atmos. Sci.*, 35, 554, 1978. With permission.)

From that vertical profile of the eddy diffusion coefficient, K, a vertical transport time $\tau^{v}_{TRAN} = H^2/K$ where H is the atmospheric scale height (or e-folding distance) is determined and presented in Figure 3B.

We proceed then to compare τ^{v}_{TRAN} with τ_{CHEM}, the lifetime against chemical transformation for each chlorine compound, considering first the source molecules CH_3Cl, CCl_4, CCl_2F_2, and CCl_3F. For carbon tetrachloride, CCl_2F_2 and CCl_3F, the dominant loss process is photodissociation and the chemical lifetime is calculated directly from the altitude dependent photodissociation rate

$$J_i(Z) = \int_{\text{absorption band}} F_\infty(\lambda) \exp\left(-\sum_j \sigma_j(\lambda)\eta_j(Z)\right) \sigma_i(\lambda) d\lambda$$

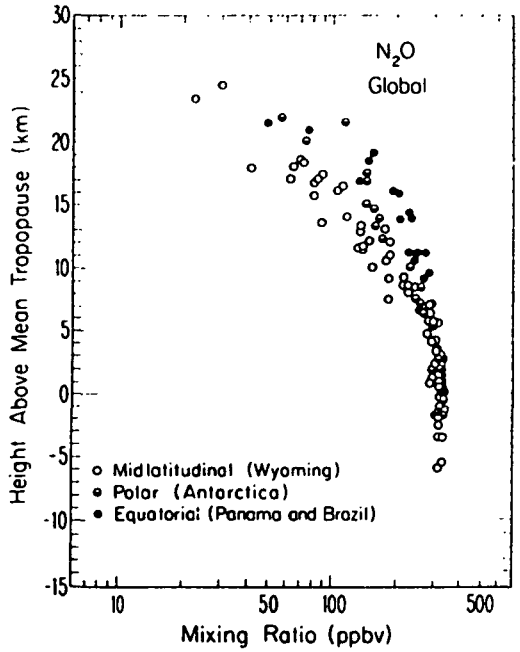

FIGURE 2A. Global N_2O mixing ratio versus height above the mean tropopause for all flights. (From Goldan, P. D., Kuster, W. C., Albritton, D. L., and Schmeltekopf, A. L., *J. Geophys. Res.*, in press.)

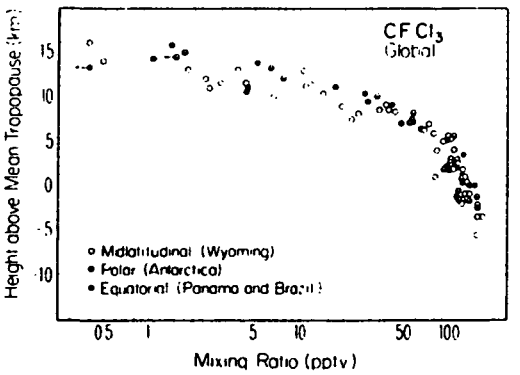

FIGURE 2B. Global CCl_3F mixing ratio versus height above the mean tropopause from all flights. Arrows indicate upper limits. (From Goldan, P. D., Kuster, W. C., Albritton, D. L., and Schmeltekopf, A. L., *J. Geophys. Res.*, in press.)

where $F_\infty(\lambda)$ is the solar flux at the top of the atmosphere, $\sigma_i(\lambda)$ is the cross section for the photodissociation process under consideration, $\sigma_j(\lambda)$ is the absorption cross section for all molecules which contribute to the opacity of the atmosphere above level Z and $\eta(Z)$ is the column density of species j above that altitude. Figure 4A presents values of J_i for the three compounds from Logan et al.[3] For methyl chloride, reaction 45 with OH must be considered in addition to photodissociation. The sum of J_{CH_3Cl} and $k_{45}[OH]$ are displayed in Figure 4A. Figure 4B presents the corresponding photochem-

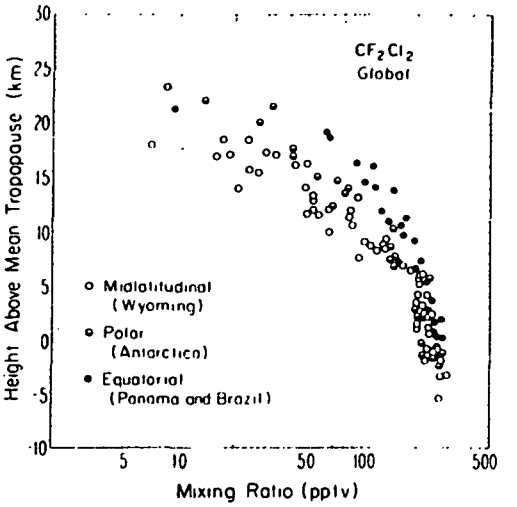

FIGURE 2C. Global CCl_2F_2 mixing ratio versus height above the mean tropopause from all flights. Note the dramatically more rapid fall off in the CCl_3F profiles. (From Goldan, P. D., Kuster, W. C., Albritton, D. L., and Schmeltekopf, A. L., *J. Geophys. Res.*, in press.)

ical lifetime τ_{CHEM}^{i} at each altitude Z superimposed on the characteristic time for vertical transport from Figure 3B. A brief inspection of Figure 4B indicates that below ~20 km, the vertical transport time is significantly shorter than the photochemical lifetime for all four compounds, implying that the mixing ratio (mole fraction) of each should be independent of altitude. At approximately 20 km

$$\tau_{CHEM}^{CCl_3F} \approx \tau_{TRAN}^{V}$$

and the mixing ratio of CCl_3F should begin to decrease with increasing altitude.

Although this occurs for each compound at a slightly different altitude the same statement is true for each of the major stratospheric chlorine source molecules. Figure 5 presents the calculated vertical distribution of the four compounds, which agree reasonably well with the observed distribution as noted in Figure 2A-C, indicating that the mixing ratios behave as expected with the overwhelming fraction of the chlorine released between the altitudes of 20 and 35 km.

The chlorine radicals Cl and ClO, formed from the photolytic decomposition of the chlorine source molecules form a second distinct subset when classified according to chemical destruction time. Atomic chlorine, for example, is converted to ClO principally by Reaction 30 with a time constant

$$\tau_{CHEM}^{Cl \rightarrow ClO} = \frac{[Cl]}{k_{30}[O_3][Cl]} = \frac{1}{k_{30}[O_3]}$$

which is shown as a function of altitude in Figure 6. The chlorine monoxide radical, on the other hand, is converted back to Cl by Reaction 32 and 33 so

$$\tau_{CHEM}^{ClO \rightarrow Cl} = \frac{[ClO]}{(k_{32}[NO] + k_{33}[O])[ClO]} = \frac{1}{k_{32}[NO] + k_{33}[O]}$$

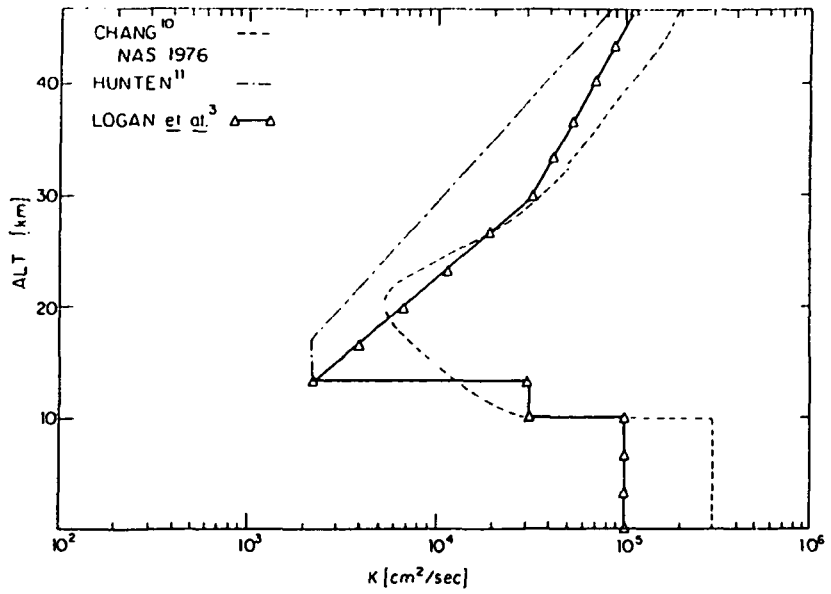

FIGURE 3A. Examples of eddy diffusion, K_z coefficient with height from Chang and Dickinson,[10] Hunten,[11] and Logan et al.[3]

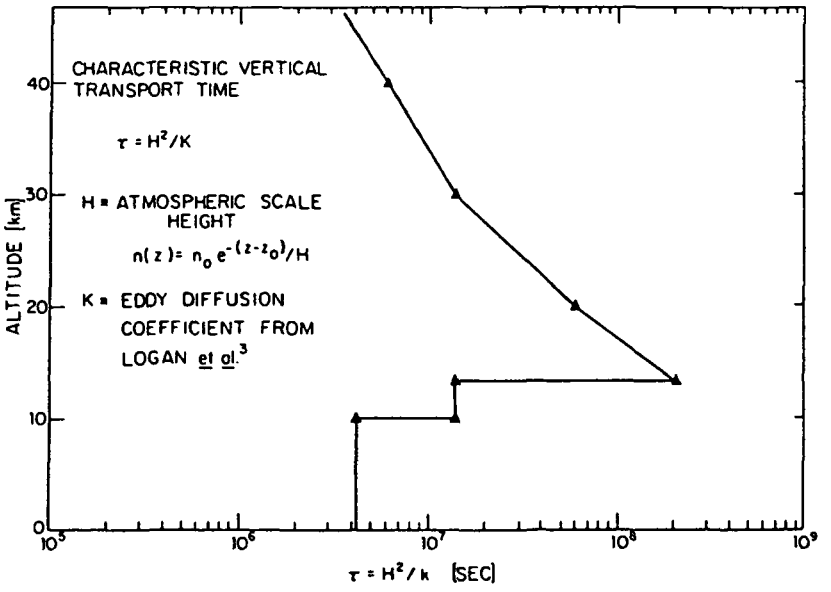

FIGURE 3B. Characteristic Vertical Transport time using the mid-latitude eddy diffusion coefficient of Logan et al.[3]

which is also displayed in Figure 6. Thus the ratio of [Cl] to [ClO] is established under daytime conditions within seconds throughout the stratosphere and the two radicals are, therefore, in strict photochemical steady state with respect to each other.

The sum $[ClO_x] = [Cl] + [ClO]$ is controlled by those reactions which recombine chlorine into its more stable forms HCl, $ClONO_2$, and HOCl by the reactions $Cl + CH_4 \rightarrow HCl + CH_3$; $Cl + HO_2 \rightarrow HCl + O_2$; $ClO + NO_2 + M \rightarrow ClONO_2 + M$; $ClO + HO_2 \rightarrow HOCl + O_2$.

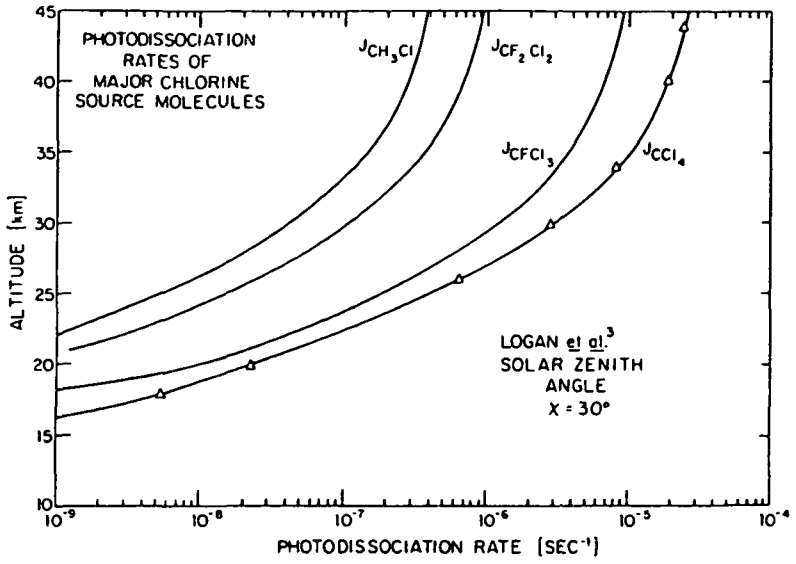

FIGURE 4A. Photodissociation rates of the four major chlorine source molecules CH_3Cl, CCl_3F, CCl_2F_2, and CCl_4. From Logan et al.[3]

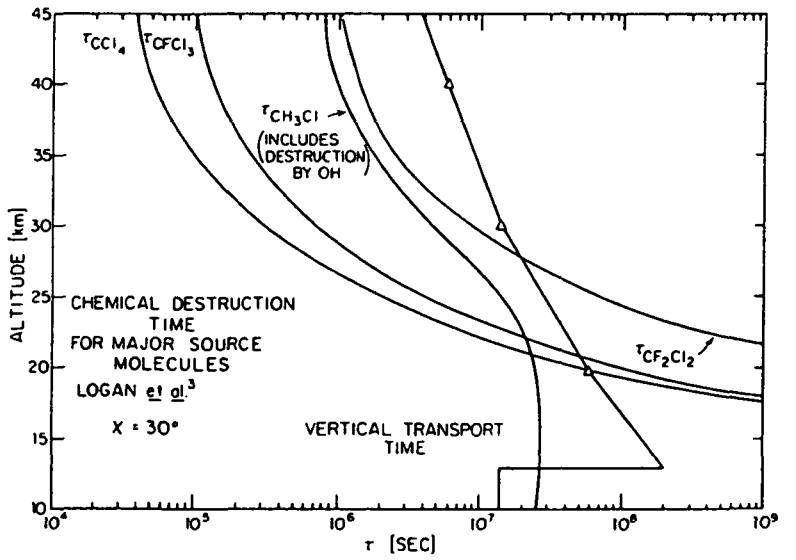

FIGURE 4B. Photochemical destruction times for CH_3Cl, CCl_2F_2, CCl_3F, and CCl_4 taken from the photodissociation rates of Figure 4A.

Before calculating

$$\tau_{CHEM}^{ClO_x}$$

we consider first the chemical lifetime of three chlorine containing products of the above reactions. Chlorine contained in HCl is returned to free radical form by the reaction HCl + OH → H_2O + Cl which is also the dominant chemical destruction process for HCl so

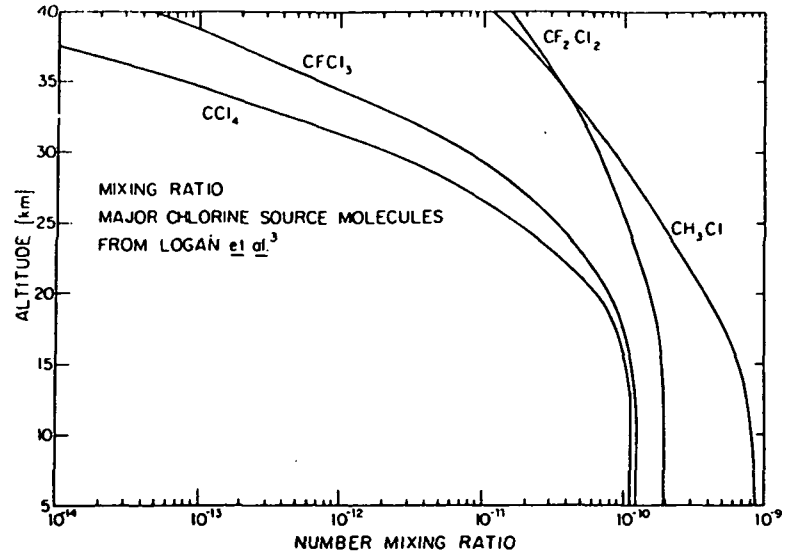

FIGURE 5. Vertical distribution of source molecule mixing ratios using the eddy diffusion coefficient from Figure 3a and the photodissociation rates from Figure 4a.

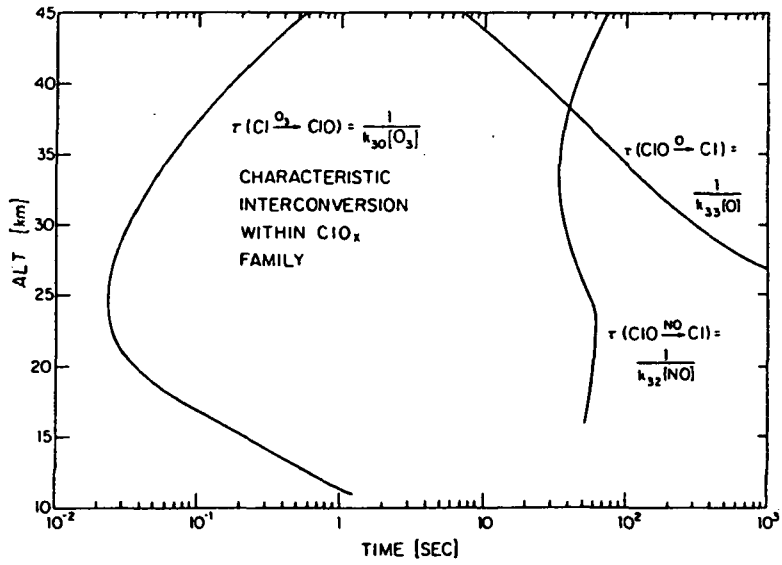

FIGURE 6. Characteristic interconversion times among free radicals in the ClO, system.

$$\tau_{CHEM}^{HCl} = \frac{1}{k_{16}[OH]}$$

a quantity displayed in Figure 7. Both $ClONO_2$ and HOCl are removed predominantly by photolysis so their lifetimes are simply the inverse of J_{ClONO_2} and J_{HOCl}, which are also displayed in Figure 7. Both chlorine nitrate and hypochlorous acid have lifetimes significantly shorter than 1 day and thus both serve as a temporary reservoir for chlorine. They are rapidly reconverted into the ClO_x-HCl reaction system after sunrise. Thus we believe the dominant reservoir for chlorine is HCl. The time constant for the con-

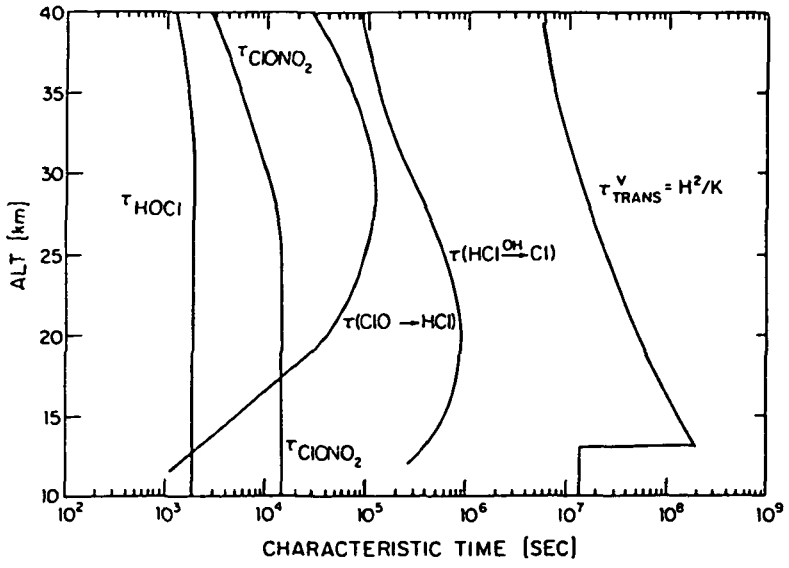

FIGURE 7. *Characteristic interconversion times between the reservoir terms HCl, $ClONO_2$, and HOCl and the free radical family ClO_x. The vertical transport time is from Figure 3B.*

tainment of chlorine in the form of ClO_x is thus

$$\tau^{ClO_x \rightarrow HCl}_{CHEM} = \frac{[ClO_x]}{\left\{k_{44}[CH_4] + k_{41}[HO_2]\right\}[Cl]}$$

which is displayed in Figure 7.

An inspection of that figure reveals that

$$\tau^{ClO_x \rightarrow HCl}_{CHEM}$$

and

$$\tau^{HCl \rightarrow ClO_x}_{CHEM} << \tau^{V}_{TRAN}$$

so the ratio $[ClO_x]/[HCl]$ is chemically controlled and thus susceptible to examination by simultaneous observations within a defined volume element smaller than the scale of atmospheric variability. Care must be taken, however, with high latitude, winter hemisphere intrusions from the polar vortex which can transport air masses rapidly equatorward.

The five chlorine compounds Cl, ClO, HCl, $ClONO_2$, and HOCl thus comprise a group within which chemical exchange occurs on a time scale much shorter than the time required for vertical transport and thus the hypothesized mechanistic links can be tested directly. However, because there is no known chemical loss process for the sum $[Cl] + [ClO] + [HCl] + [ClONO_2] + [HOCl]$, *the vertical distribution of that* sum is controlled by vertical transport.

If one considers chlorine in all forms, the mixing ratio of Cl, bound or free, will be very nearly constant above the tropopause with the upward flux of chlorine in the

"organic" forms CH_3Cl, CCl_4, CH_3CCl_3, $CHClF_2$, CCl_3F, and CCl_2F_2 balanced by the downward flux of inorganic HCl formed in the stratosphere by the chemical transformations discussed above. Because of recent increases in the release rate of some of these compounds, the upward flux will exceed slightly the downward flux until a new steady state is achieved.

In summary: (1) the major chlorine source molecules mix vertically, establishing altitude independent number mixing ratios up to an altitude at which their characteristic lifetimes against photochemical decomposition diminish to the point where τ^V_{CHEM} becomes comparable with the time scale for vertical mixing, above which their respective mixing ratios decrease rapidly, (2) the chlorine radicals formed in that decomposition have chemical lifetimes with respect to intraconversion orders of magnitude less than the period required for vertical transport, (3) the exchange time between ClO, and $ClONO_2$ or HOCl is three orders of magnitude less than τ^V_{TRAN} such that chemical transformations dictate the exchange between ClO, and these two temporary reservoir terms, (4) the exchange between ClO, and the major chlorine reservoir, HCl, occurs in a period 1 to 2 orders of magnitude less than τ^V_{TRAN} and finally, (5) the sum Cl + ClO + $ClONO_2$ + HOCl + HCl has no known chemical destruction mechanism so the mixing ratio of that sum is established by vertical transport and is approximately independent of height above the source region at ~20 to 25 km. Figure 8 represents these characteristics schematically.

III. TRANSPOSING HYPOTHESIS TO FACT: THE MODEL DEPENDENT AND MODEL INDEPENDENT APPROACHES

The suggestion of sizable ozone total column depletion resulting from usage of FC-11 and FC-12 at or near current levels requires that we consider carefully our current ability to predict future trends in the total column concentration of ozone and to consider how discriminating our current diagnoses are based on direct observations of the real atmosphere. Although obviously our perceptions of what reactions dominate a specific aspect of stratospheric chemistry can only be tested by a comparison between calculated and observed constitutent distributions, the explicit formulation of the problem and the choice of conditions and constituents selected for those observations distinctly affects the clarity of the conclusions which result.

We note first that models are the only tool we have for predicting secular trends in global ozone. As will be described in Section A, models currently available systhesize all that is presently known about the chemical kinetics and photochemistry of stratospheric ozone and deal in a pragmatic but, for our purposes, effective way with the mean transport processes. Second, if the objective of the model is to predict future changes in ozone, a comparison between observed and model-calculated concentrations of constituents in the stratosphere is not a test of the model's predictive power. History is replete with examples of models (econometrics, chemical kinetics, for example) which explain available data successfully but have a demonstrated lack of predictive power. This results, of course, from the fact that while it is a necessary condition that a model reproduce certain observable quantities, such agreement is not sufficient to prove uniqueness or completeness. While models are precise (ozone trends are presented to three significant figures[12]) and they represent our only means of prediction, they cannot be used to test the absolute accuracy of our mechanistic picture of the real atmosphere in a truly diagnostic (i.e., cause and effect) investigation. We can establish cause and effect only through correlated observations.

Although logically diagnosis must precede prognosis, we note that for historical reasons the latter is far more advanced than the former and we thus consider first the model dependent approach.

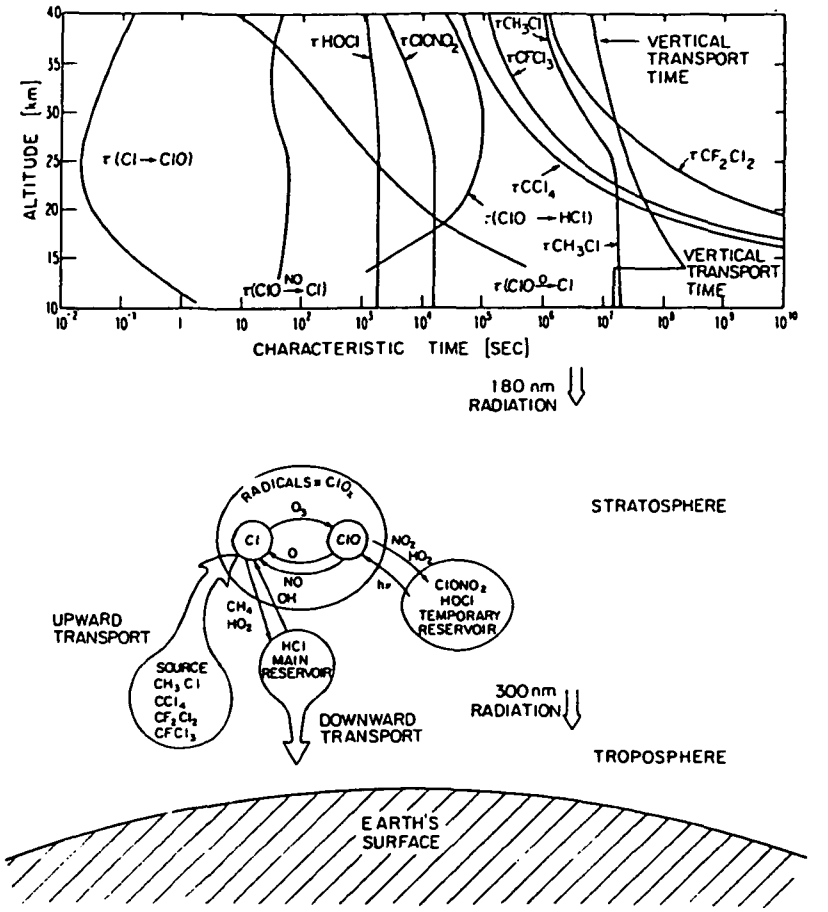

FIGURE 8. Schematic of the chlorine reaction system in the stratosphere with an overview of the exchange times among the various subgroups of reactants.

A. Model Dependent Studies: A Comparison Between Observed and Calculated Vertical Distributions of HCl, $ClONO_2$, HOCl, ClO, and Cl

Considerable experience with the photochemical modeling of planetary atmospheres preceded the stratospheric ozone-fluorocarbon problem[13-15] and reasonably advanced models were available in the mid 1970s[16-19] which combined extensive chemical reaction schemes with vertical transport as described in Section II. Because of finite computer size, it has been necessary either to emphasize photochemical processes[3,7,16,20-23] or the three dimensional (3-D) general circulation[24,25] accepting, in the latter approach, simplified chemical reaction sets. We note also that there are two dimensional (2-D) treatments which can, for some specific problems, offer an effective compromise between chemical complexity and realistic vertical and meridional transport.[26-28]

For the past decade, the burden for predicting secular changes in global ozone has been borne principally by the 1-D photochemical models which synthesized what we knew about ozone photochemistry using a carefully selected but nevertheless extensive set of thermal and photolytic reactions as noted in Table 1. A first order examination of the validity of such models requires a careful comparison between calculated and observed vertical distributions (as well as diurnal, seasonal and latitude variations where applicable) of key compounds such as CCl_2F_2, CCl_3F, CH_3Cl, CCl_4, HCl, $ClONO_2$, ClO, and Cl.

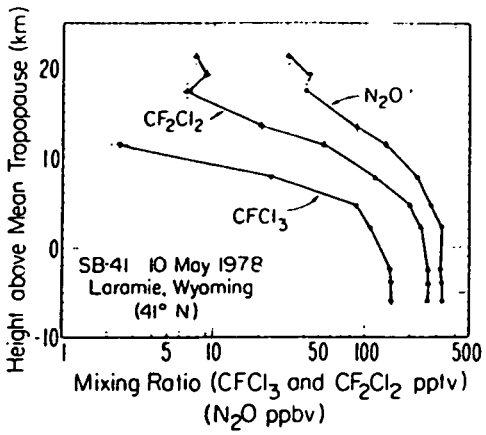

FIGURE 9. Mixing ratios of CCl_3F, CCl_2F_2, and N_2O observed on a single flight by Goldan et al.[8] showing the effects (apparently) of mass motion approximately 17 km above the tropopause.

We proceed with this comparison by first recalling the discussion in Section II which established, by contrasting calculated and observed mixing ratios of the source molecules, that the global distribution of chlorine initially injected into the stratosphere is adequately represented by the 1-D models. There is of course a circular aspect to this approach because just such a comparison was made at mid-latitude to determine the altitude dependence of the eddy diffusion coefficient. Inspection of Figures 2A-C clearly indicates that large scale advection does not control the average distribution of the source molecules. There must of course be adjustments to the altitude of the tropopause as a function of latitude[3,7,8] and on rare occasions there is evidence of profile "folding" in the lower-midstratosphere as indicated in Figure 9 below taken from the recent paper by Goldan et al.[8]

This general consistency in the vertical and meridional distribution of the source terms, coupled with the fact that mixing within the stratosphere is significantly more rapid than removal from the stratosphere of the Cl atom released by photolysis, is of considerable importance. We conclude that significant uncertainties in predicting secular trends in global ozone will not result from uncertainties in the vertical distribution of chlorine source molecules.

We can, therefore, concentrate on comparing the calculated and observed partitioning of chlorine among its chemically active forms which are created and transformed by the reactions described in Section II. We consider first the most recently available data on the primary reservoir term HCl, which is currently thought to maintain mass continuity in the stratospheric chlorine system by transporting, from the stratosphere to the troposphere, a flux of chlorine approximately equal to that transported upward from the troposphere by the source molecules.

1. HCl

Three analytical methods have been used to determine the vertical distribution of HCl in the stratosphere:

1. High resolution absorption spectroscopy from balloon borne platforms viewing the Earth's limb during sunset.[29-33] The geometry shown below with a sample spectrum from Raper et al.[32] demonstrates the clearly resolved rotation-vibrational features of both isotopes of HCl.

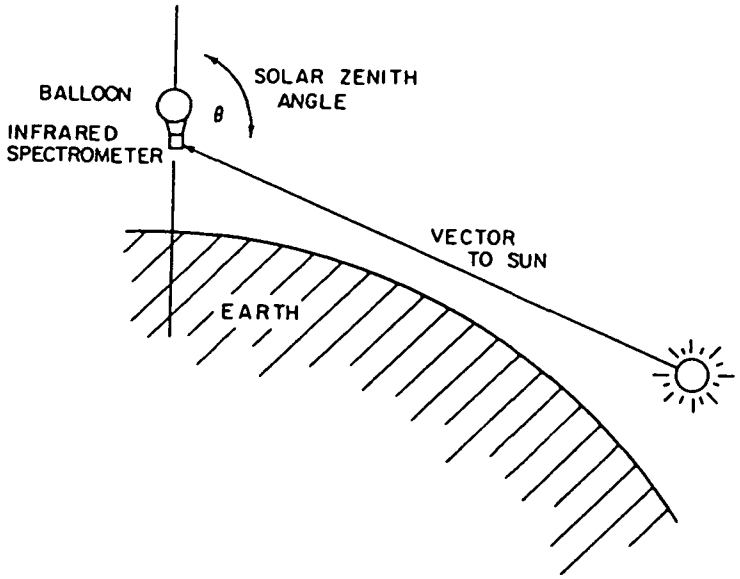

FIGURE 10A. Geometry used for long path infrared solar absorption measurements at and slightly after sunset.

Although little information about the vertical distribution of constituents can be retrieved from the region above the balloon float altitude, for molecules such as HCl a major portion of the profile is accessible from balloon float altitudes. The direct and irrefutable spectroscopic evidence provided by this method has placed the observations at the foundation of our understanding of stratospheric chlorine. The methods are continuously being refined through the use of such techniques as Fast Fourier Transform Interferometry and a growing catalogue of laboratory absorption data so the full potential of the method has not been realized. It is also important to note that fully one half of the observed absorption features in the near infrared are at this time unidentified!

2. Pressure modulated radiometry, which has been applied to trace constituent analysis in the stratosphere using the same geometry depicted in Figure 10, has been extended from initial observations of the more abundant constituents H_2O and O_3 to include species such as HCl[34] using narrow pass band filter elements in tandem with the pressure modulation cell. The method can achieve spectral resolution comparable to the width of individual spectral lines, can be flown in satellite packages of limited weight and has sufficient collection efficiency to allow measurements to be rapidly acquired.
3. *In situ* filter collection methods followed by wet chemical analysis for total acidic chlorine has been used by Lazrus et al.[35]

Results obtained by the three methods are summarized in Figure 11. Several points are important to note. Given the uncertainties of ~30% in the region between 20 and 30 km and ~50% at the profile extremities, the scanning high resolution infrared absorption methods exhibit a high degree of consistency. Since the *in situ* filter trapment methods detect total acidic chlorine and are thus an upper limit when total observed concentration is identified as HCl, it is inconsistent that the Lazrus et al.[35] results fall below the IR data which are specific to HCl. This difference may of course result from real atmospheric variability but it is a point which bears attention. The radiometer data lie above the interferometer-spectrometer data between 30 to 35 km.

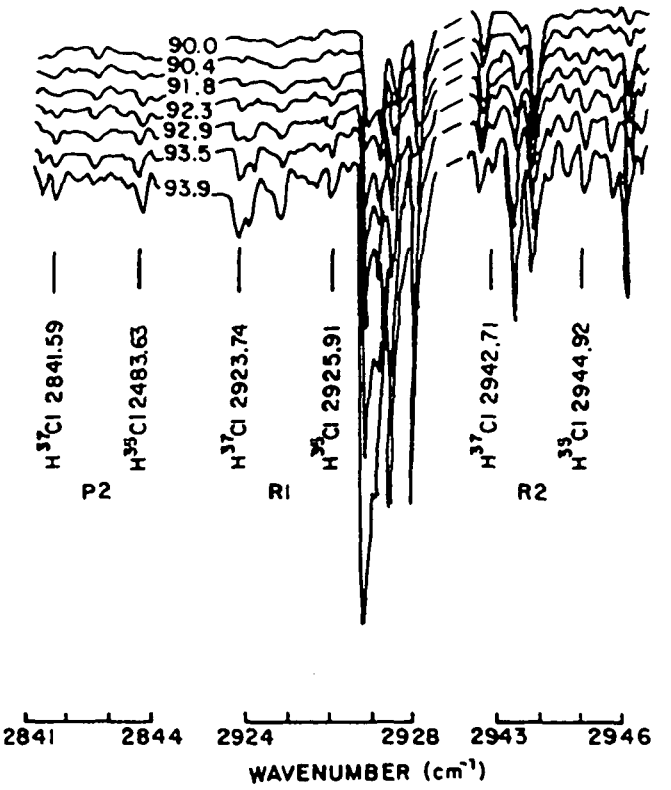

FIGURE 10B. Portions of the set of stratospheric spectra covering the P2, R1, and R2 lines of the 1-0 HCl transition obtained during the balloon flight on May 18, 1976, near Palestine, Texas. The line positions for both the $H^{35}Cl$ and $H^{37}Cl$ isotopes are shown in the figure; the three $H^{37}Cl$ lines are blended with features of other atmospheric gases, principally methane, and were not used for the quantitative analysis. The angles shown are the (astronomical) solar zenith angles at which the spectra were recorded. In this figure the individual spectra have been offset for clarity. The baseline in each figure is the zero line for the lowest trace.

We select for comparison with the calculations of Logan et al.[3] the spectro-interferometric infrared results from Figure 11A which are shown in Figure 12 as a cross hatched band that encompasses the observations and indicates the extremity of the experimental uncertainties cited in the references in Figure 11. Also shown in Figure 12 is the mean of the high resolution infrared spectrophotometric data which is compared in Figure 13 with the calculated HCl distribution.

Considering the small number of profiles available and the difficulty of deconvolving details in the vertical distribution from long path absorption data, the agreement implied in Figure 13 is striking and encouraging. While significant differences in the HCl profiles exist among the three principal techniques, the mean of the three methods is very similar to that of the high resolution spectro-interferometric data since the distinct minimum of the Lazrus et al.[33] data occurs in the same altitude interval as the maximum in the pressure modulated radiometer data of Eyre and Roscoe[34] and each bounds the Farmer et al.[33] data by an equal interval. Little can be learned about such differences without a simultaneous observation of the same air mass. It remains to be seen whether the agreement implied by Figure 13 withstands the next generation of observations.

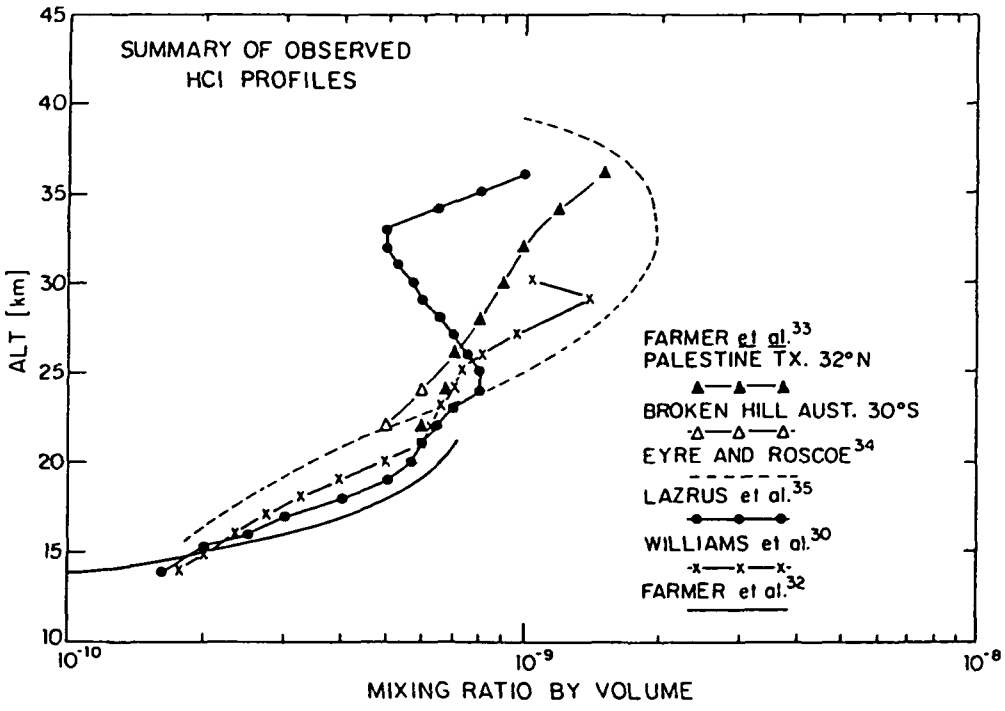

FIGURE 11. HCl profiles extending from the tropopause to 40 km. References are indicated on the figure.

2. $ClONO_2$

Recently significant progress has been reported in the search for $ClONO_2$ in the stratosphere by Murcray et al.[36] who used a high resolution Michelsen interferometer with 0.02 cm^{-1} resolution to observe the absorption feature of $ClONO_2$ at 1292 cm^{-1} near sunset from a balloon platform. The flight took place on 27 October 1978 from Holloman AFB, observations were made at sunset. Spectra from that flight are shown in Figure 14.

The broad $ClONO_2$ spectral feature noted in Figure 14 is of course more difficult to use close to the detection limit than the normal, (narrow) rotation-vibration lines characterized in Figure 10. Nevertheless, Murcray et al.[36] have reported the deconvolved $ClONO_2$ distribution shown in Figure 15 which is compared (Chapter 4 of Hudson[9]) with the $ClONO_2$ mixing ratio band determined using the currently available range of pressure and temperature dependence[37] for the three body reaction $ClO + NO_2 + M \rightarrow ClONO_2 + M$. *It is important to note that considerable laboratory data are still needed in the 10 to 100 torr pressure range between 210 and 300°K for Reaction 34.* There are also unresolved questions about the products of 34 because kinetic studies have as yet not observed the rate of product formation simultaneously with the disappearance of reactants. For these reasons the excellent agreement implied by Figure 14 must be viewed with caution.

3. HOCl

There are, at this time, no reported observations of HOCl in the stratosphere. The molecule is formed by the bimolecular reactions[38] $HO_2 + ClO \rightarrow HOCl + O_2$ and $OH + ClONO_2 \rightarrow HOCl + NO_3$. Laboratory infrared spectra of the 3600 cm^{-1} and 1240 cm^{-1} bands of HOCl have been reported[39] which provide frequencies for the individual transitions but only approximate line strengths since the absolute concentra-

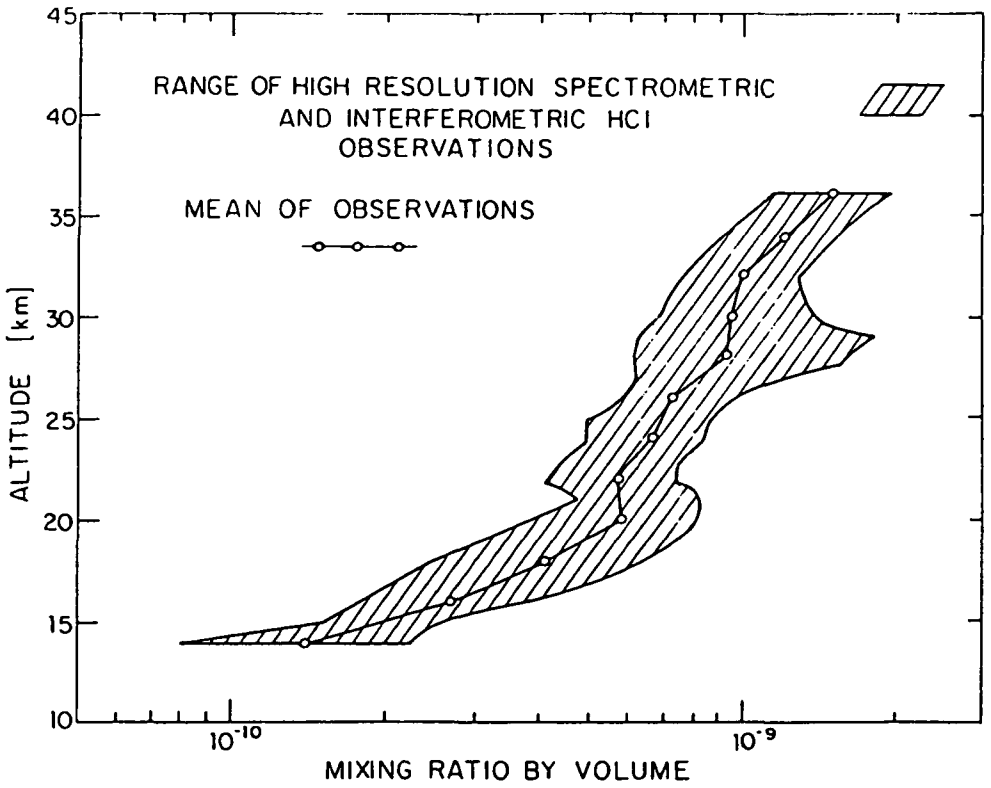

FIGURE 12. Range of HCl mixing ratios obtained using the high resolution, spectrometric and interferometric long path infrared solar absorption technique indicated schematically in Figure 10A. The mean of the observations is also indicated.

tion of HOCl in the laboratory absorption cell was not determined in those experiments. High resolution ($\sim$0.02 cm^{-1}) balloon spectra are potentially capable of providing stratospheric observations of this molecule.

Although HOCl drew considerable attention as a possible major reservoir for stratospheric chlorine when details of the long wavelength photolysis cross section were in doubt, it now appears that the lifetime of HOCl against photolysis is less in the lower stratosphere[37,40] (see Figure 7), but considerable work remains to be done.

4. The Sum HCl + $ClONO_2$ + HOCl

It is currently believed that HCl, $ClONO_2$, and HOCl comprise the dominant chemical reservoir terms of chlorine in the stratosphere. It is instructive to combine the mean of the observed profiles of the two major forms, HCl and $ClONO_2$, and compare that sum with the calculated HCl and $ClONO_2$ profiles from Logan et al.[3] It must of course be borne in mind that insufficient data are available to allow clear conclusions to be extracted from such a comparison; it is also important to note developing trends. Figure 16A shows the calculated HCl and $ClONO_2$ mixing ratios, with HOCl included for completeness and to show that, with the most recent photolysis cross sections, it is not believed to contribute measurably to the chlorine budget. Figure 16B displays the mean HCl and $ClONO_2$ distribution along with the sum. Figure 16C compares the calculated sum with the observed sum. The comparison is of course carried out at sunset to match conditions of the observations.

The agreement implied by Figure 16C reflects the close agreement implied in Figures 13 and 15. It remains to be demonstrated whether the agreement implied in Figure 16C

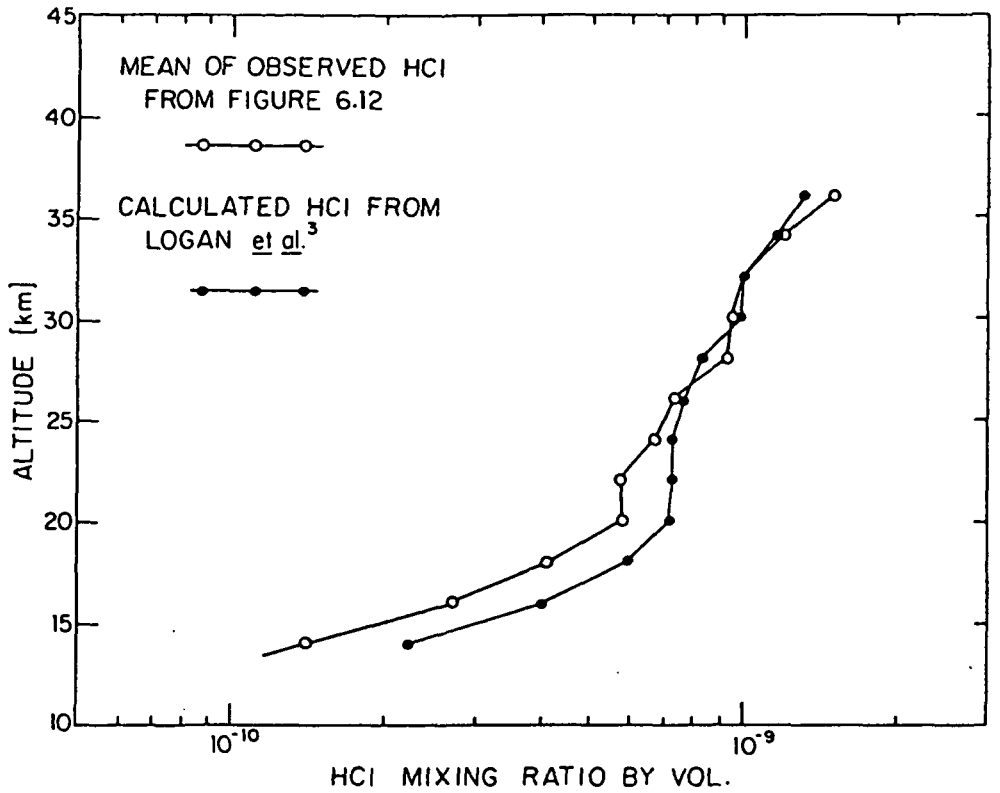

FIGURE 13. *Comparison between the mean of the observations from Figure 12 and the calculated distribution from Logan et al.*[3]

will withstand the test of an expanded observational data base and refined laboratory data but it does imply that data on the chlorine reservoir terms show striking agreement with the calculated distribution. This represents a conclusion of major significance if observations of total chlorine (i.e., the sum of all chlorine atoms bound or free in a given volume element of the stratosphere) confirm that all major chlorine reservoir terms are accounted for in the sum HCl + $ClONO_2$. Perhaps the most important implication is that the 1-D models appear to distribute the major chlorine reservoir species successfully, at least at mid-latitude. Because of the close chemical coupling between the free radical forms of chlorine (which react directly with odd oxygen) and the reservoir terms as discussed in Section II, we can focus attention on the partitioning of chlorine between its free radical and reservoir terms with considerable confidence that, at least in a time averaged sense, the latter are distributed appropriately by the model.

5. The Radical Forms Cl and ClO

Chemical transformations within the chlorine family are dictated by reaction of the O_x, HO_x, and NO_x free radicals with Cl and ClO as an inspection of Figure 8 reveals. It is impossible to quantify the rate of chemical exchange without knowledge of the absolute concentration of Cl and ClO which exist at the ppt and ppb level, respectively, in the middle and upper stratosphere. While such trace levels present detection problems, two methods have been used to observe free chlorine radicals in the stratosphere.

An important and versatile method which can be used for long path absorption experiments to detect polyatomic radicals, that of laser heterodyne radiometry, was

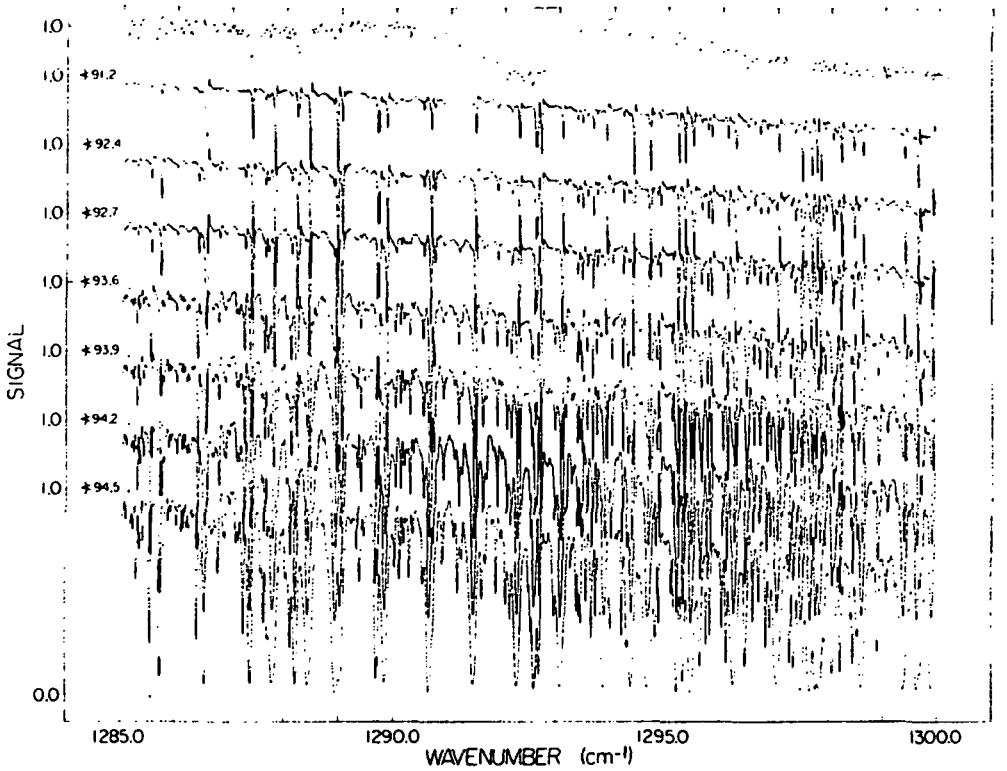

FIGURE 14. Top curve: laboratory absorption spectrum of $ClONO_2$ in a 5 cm cell. Total pressure in the cell is 1.5 mmHg and includes HNO_3 impurity. Lower curves: balloonborne sunset spectra obtained on October 27, 1978 from Alamogordo, New Mexico, with a Bomem interferometer at 0.02 cm^{-1} resolution. Individual scans are displaced for clarity. All the scans were obtained from float altitude of 39.1 km. Zenith angles are indicated for each scan. Note that signal levels are the raw data amplitude and not transmittance.[24]

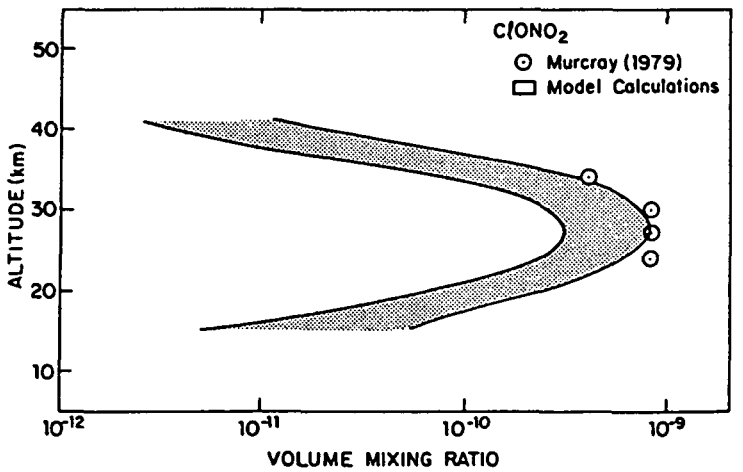

FIGURE 15. From Hudson.[9] A comparison between recent model calculations of $ClONO_2$ (differences in pressure and temperature dependence of chlorine nitrate formation rate is reflected in the width of the band) and the observed profile from Murcray et al.[24]

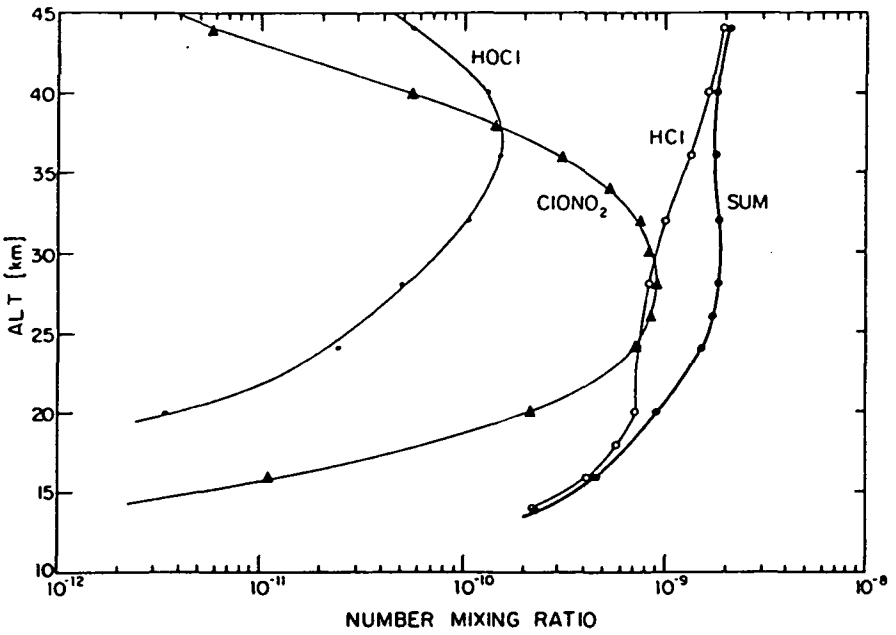

FIGURE 16A. Calculated distribution of HCl, $ClONO_2$, and HOCl in the stratosphere corresponding to mid-latitude, sunset conditions from Logan et al.[3] Also displayed is the sum [HCl] + [$ClONO_2$] + [HOCl].

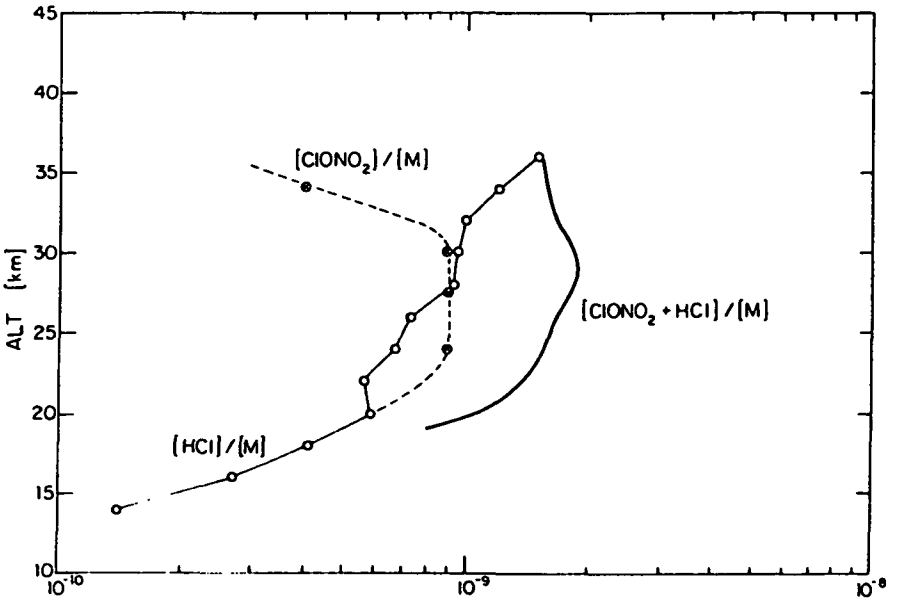

FIGURE 16B. Observed mean of the long path infrared solar absorption measurements of HCl from Figure 13, ClONO, from Figure 15 and the sum [HCl] + [$ClONO_2$] expressed as a number mixing ratio.

introduced for the detection of ClO by Menzies.[41] That method provides extremely high resolution ($<10^{-4}$ cm^{-1}) absorption measurements (note the geometry in Figure 10A) using a reference frequency from an isotope doped CO_2 laser which is mixed with

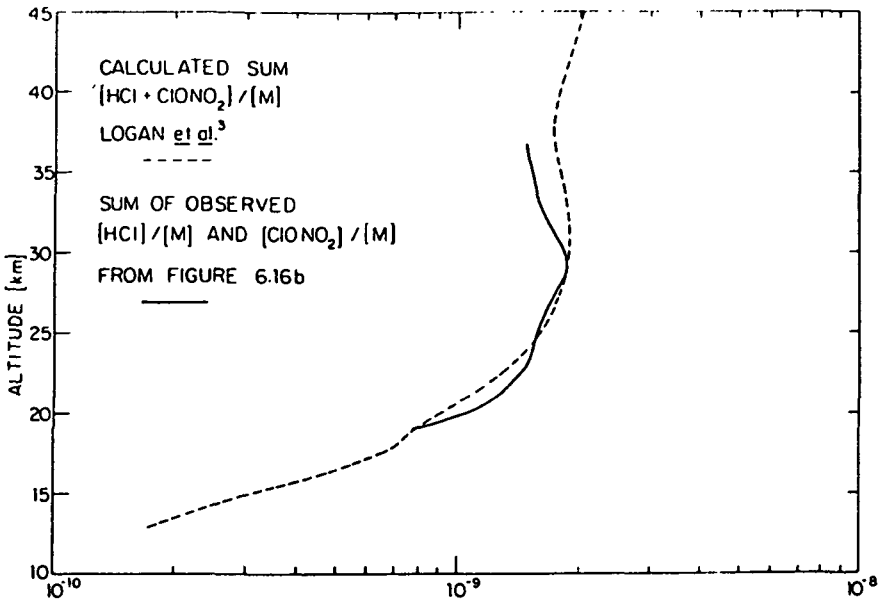

FIGURE 16C. Comparison between the calculated and observed sum [HCl] + [ClONO$_2$] from Figures 16A and 16B.

solar radiation after passage through a narrow band interference filter at 853.2 cm^{-1}. By deconvoluting the absorbed signal as a function of solar zenith angle the altitude distribution of ClO is inferred.

Atomic and molecular resonance fluorescence lends itself to the detection of small radicals at the ppt level within a defined volume of ~1 cm^3 because of the exceedingly large absorption cross sections linking bound electronic states through electric dipole allowed transitions. This method has been used to determine the stratospheric distribution of O(^{3}P), OH, HO_2, NO, Cl, and ClO.[42-48] The application of this technique in situ must be carried out such that heterogeneous destruction of radicals resulting from collisions with the detection chamber wall are eliminated. *In situ* resonance fluorescence, as it has thus far been applied to stratosphere detection, employs a high velocity flow of stratospheric air, formed by dropping a hollow, aerodynamically shaped pod or "nacelle" vertically through the stratosphere on a stabilized parachute deployed from a balloon platform at the stratopause. That flow, which passes unrestricted through the center of the hollow nacelle shown in Figure 17A, is probed by a beam of photons resonant with an allowed transition between two bound electronic states of the radical. Photons reasonantly scattered from the beam are counted by a photomultiplier operated in the pulse mode. As indicated in Figure 17A, the photon beam formed in a low pressure (~5 torr) He plasma discharge containing a trace quantity of molecular chlorine, is orthogonal to both the flow direction and the detector field of view. For a detailed discussion of the experimental technique see Anderson et al.[46]

Because each detection system is relatively light in weight (~45 lbs) several nacelles can be grouped, as shown in Figure 17B, on a single platform, to make simultaneous observations within the same cubic meter of space.

The flow is contained within the nacelle to isolate the detector from the radiation environment of the stratosphere and to provide the capability for controlled chemical conversion within the sample. The chemical conversion can be used either to (1) remove a fluorescing species from the sample in order to determine the instrument background

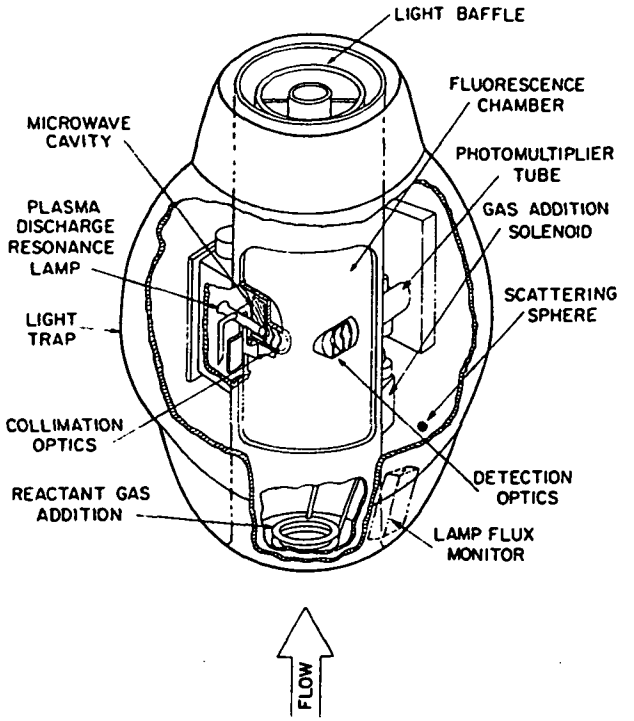

FIGURE 17A. Detection chamber used for the *in situ* measurement of atoms and diatomic radicals in the stratosphere.

count rate in the absence of the radical or to (2) convert a radical which does not fluoresce to one which does. An example of case (1) is the removal of Cl from the flow by the addition of ethane; an example of case (2) is the conversion of ClO, which predissociates in all vibrational levels of the $A^2\pi$ state, to $Cl(^2P)$ by the addition of NO to the flow.

Figure 18 summarizes all available observations of Cl and ClO which includes two *in situ* measurements of Cl, 10 *in situ* measurements of ClO and one laser heterodyne observation of ClO. All observations were made from balloonborne platforms launched from the National Scientific Balloon Facility, Palestine, Texas, 32°N latitude.

Several points summarized in Figure 18 require comment. First the observed *in situ* ClO profiles fall into two well defined regimes: An envelope containing 8 of the 10 observations and a pair of observations clearly divorced from and decidedly greater in concentration than the envelope. Second, the profile observed on 28 July 1976 differs appreciably in shape from the other observations exhibiting a broad maximum in mixing ratio between 30 and 36 km. The observation of 7/14/77 peaks at or about 41 km at 8 ppb, a factor of three above current estimates of the total chlorine mixing ratio (time averaged) in the stratosphere. Although it was not clear during the evolution of the data set how relevant the exceedingly high observed concentration of 7/14/77 was to a "normal," mid-latitude ClO distribution, it is clear now that the observation has little relationship to the mean chemical morphology of that region of the atmosphere. The distinction between establishing a "typical" ClO distribution and establishing the chemical link between chlorine and ozone is of course profound.

A comparison between the laser heterodyne absorption measurement, done at a solar zenith angle of 95°, and the midday *in situ* ClO observations requires an altitude de-

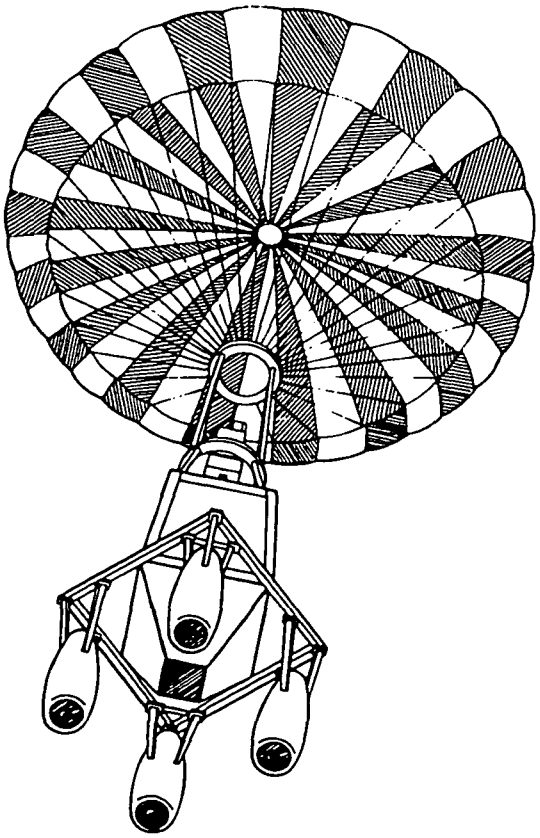

FIGURE 17B. Detection chambers clustered on the flight package for the simultaneous measurement of radicals within the same volume element.

pendent correction term resulting from the rapid, pressure dependent, termolecular recombination ClO + NO_2 + M → $ClONO_2$ + M which reduces the ClO concentration by a factor of ~2.5 at 29 km and ~1.3 at 35 km based on the diurnal calculation of Logan et al.[3] With that correction applied, the laser heterodyne results exhibit an altitude distribution in substantial agreement with the mean of the eight resonance fluorescence observations within the envelope shown in Figure 18 but an absolute concentration ~3 times that of the mean.

Figure 19 displays a comparison between the mean of the *in situ* observation, excluding the observation of 7/14/77, and the calculated distribution of Logan et al.[3] The most obvious disparity is that the observed distribution exhibits a much steeper mixing ratio gradient below the peak than does the calculated distribution. The steep ledge in the ClO mixing ratio taken in conjunction with the data previously presented on HCl, $ClONO_2$, and HOCl implies strongly that currently accepted photochemical mechanisms partition chlorine improperly into its free radical form. Specifically, the comparison suggests that either ClO reacts with (or clusters to) one or more atmospheric constituents to form a product which is not $ClONO_2$ or HCl but which has a mixing ratio comparable with the difference between observed and calculated ClO shown in Figure 19. Alternatively the OH concentration, which dictates the rate of formation of chlorine free radicals via the reaction HCl + OH → Cl + H_2O may be significantly less than currently accepted in the lower stratosphere.

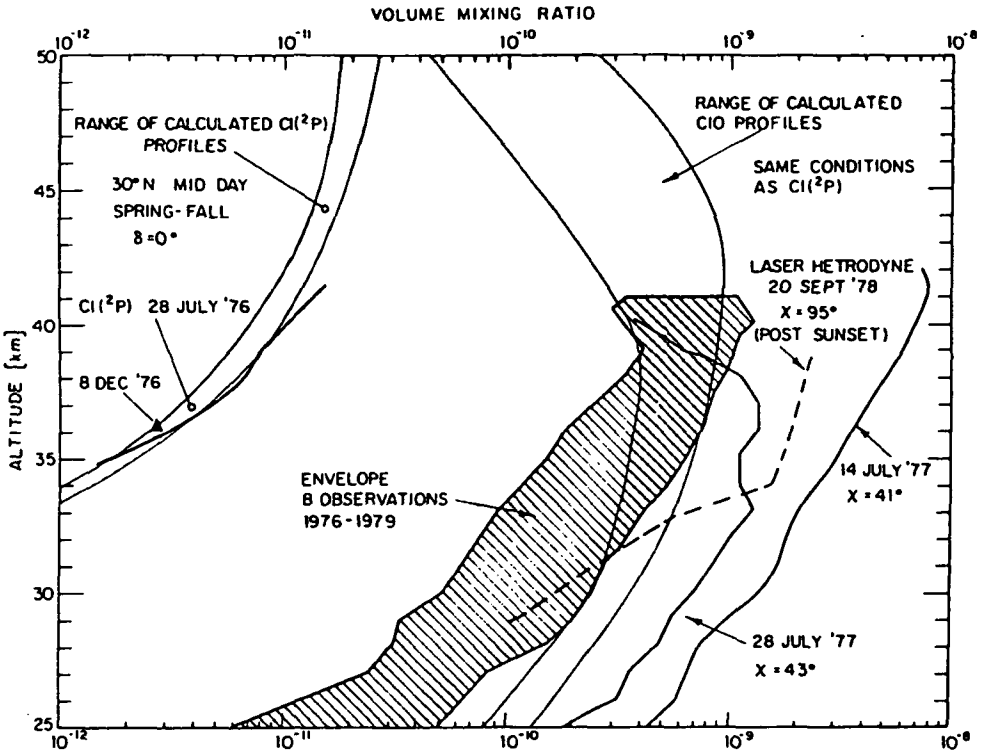

FIGURE 18. Summary of the *in situ* Cl and ClO observations compared with the laser heterodyne observations and the range of recent model calculation from Hudson.[9]

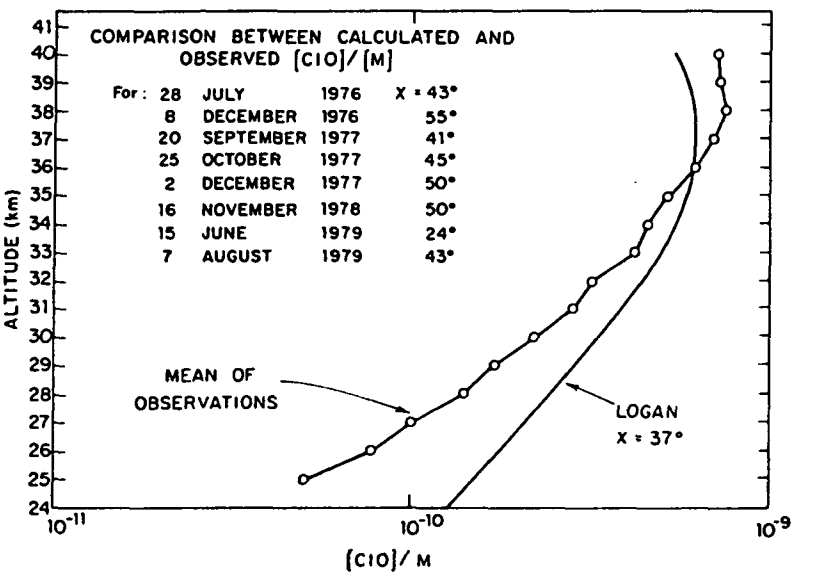

FIGURE 19. Comparison between calculated and observed [ClO]/[M] excluding the 7/14/77 observations of ClO. Calculated distribution is the most recent model of Logan et al.[1]

Prasad[49] has suggested O_2 clustering with ClO may account for the discrepancy implied by Figure 19, $ClO + O_2 + M \rightleftharpoons ClO\,O_2 + M$, but considerable background work remains to be done before such processes can be accepted.

Simultaneous observations of Cl and ClO within the same volume element have been made on two occasions using *in situ* resonance fluorescence.[46] Because of the extremely rapid exchange between Cl and ClO, governed by the three reactions $Cl + O_3 \rightarrow ClO + O_2$, $ClO + O \rightarrow Cl + O_2$, and $ClO + NO \rightarrow Cl + NO_2$ the observed Cl/ClO ratio can be compared directly with the steady state ratio

$$[Cl]/[ClO] = \frac{k_{33}[O] + k_{32}[NO]}{k_{30}[O_3]} \qquad (1)$$

using either observed values for $O(^3P)$, NO, and O_3 or calculated distributions (see Hudson[9] for a recent review of observed and calculated stratospheric distributions). In the region above 35 km, where the [Cl]/[ClO] ratio measurement exists, Reaction 30 and 33 dominate the rate of exchange and thus Equation 1 simplifies to $[Cl]/[ClO] \approx (k_{33}/k_{30})([O]/[O_3])$.

Since both k_{30} and k_{33} are well-known[50] and the $[O(^3P)]/[O_3]$ ratio has been determined through simultaneous observations to be in close agreement with the calculated ratio[46] it is a simple matter to test our mechanistic picture of the reaction linking Cl to ClO. A comparison between the calculated and observed [Cl]/[ClO] is shown in Figure 20 which indicates that agreement to within a factor of two exists. The observed presence of Cl, ClO, $O(^3P)$, and O_3 demonstrates conclusively that (1) the chlorine free radicals which comprise the catalytic agents in the homogeneous gas phase recombination (destruction) of odd oxygen exist in the stratosphere, and (2) the rate of O_x destruction by ClO_x is equal to twice the rate of the slower catalytic step (Reaction 2) so that a gross rate of odd oxygen destruction equal to $2k_{33}[O][ClO]$ occurs in this region of the stratosphere. This latter point will be discussed in Section III B in detail.

Experimental uncertainty in the observed ratio prevents one from concluding that only Reactions 30, 32, and 34 link Cl to ClO.

B. Diagnostic Examination of the Stratosphere: The Model Independent Approach

Without a comprehensive data base on the stratospheric distribution of the key free radicals and reservoir terms, we are forced to test our perceptions of the chemical processes which dictate the rate of production and destruction of chemically active stratospheric constituents by "spot" checks between observed and calculated distributions. Lest we accept such "model verification" comparison studies as the only alternative for testing our understanding, we consider in this section a model independent approach designed to examine our first order understanding of the stratospheric photochemical system, emphasizing directly observed cause and effect studies which form the foundation for a fundamental understanding of the problem. The usefulness of this approach is predicated on our ability to formulate the problem in terms of the kinetic processes which control the rate of a given event (such as breaking or reforming the O_2 bond) and on our ability to simultaneously observe those free radicals involved as reactants in the rate limiting steps so identified.

We begin a discussion of this approach by citing an example of one of the questions we wish to answer, noting that while the question may be narrow in its perspective, it cannot be answered by model comparison studies, yet an answer to it must precede a thorough understanding of chlorine-ozone photochemistry in the stratosphere. We ask: Does an increase in the concentration of ClO_x (by any means) between 30 and 45 km lead to a reduction in O_x?

Formulation of an answer must obviously be based on defining the rate of odd

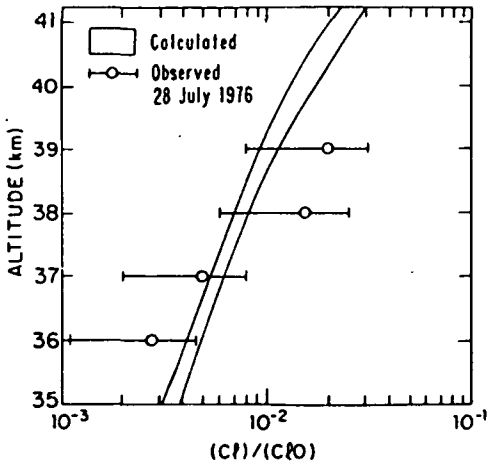

FIGURE 20. Comparison between observed [Cl]/[ClO] and the band of calculations from the most recent models reported in Hudson et al.[9]

oxygen production and destruction in terms of (a reasonable number of) simultaneously observable quantities. If that cannot be done, the question as formulated cannot be answered. We begin by noting that the continuity equation for O,

$$d[O_x]/dt = P_{O_x} - L_{O_x} + \nabla \cdot \phi_{O_x}$$

may be significantly simplified in this region of the atmosphere (see Section II) since

$$\nabla \cdot \phi_x << P_{O_x}, L_{O_x}$$

$$\text{and } |P_{O_x} - L_{O_x}| << P_{O_x}, L_{O_x} \text{ so that}$$

$$d[O_x]/dt = P_{O_x} - L_{O_x} \approx 0$$

We are then faced with two alternatives for defining the functional form of P_{O_x} and L_{O_x}: (1) we can scan through Table 1 to identify all reactions which produce or destroy $O(^3P)$ and O_3, defining each term in P and L, or (2) we can search for sets of reactions which, when taken together, result in the severance or reformation of the O_2 bond.[51] It is immediately obvious that the first approach, while crucial for modelling the problem, is inappropriate here because one cannot design a tractable experiment to observe the required 20 odd constituents simultaneously. In addition many of the terms cancel so we must subtract two large numbers in the hope of accurately determining a small difference (as the saying goes, "One way to determine the weight of a ship's captain is to weigh the ship and captain and then the ship alone.") The second approach has the potential (and profound) advantage that (1) if the reaction groups which sever and reform the O_2 bond are each comprised of a small number of reactions, (2) if we can demonstrate which reaction in each set determines the period of time required to complete the reaction sequence and, finally, (3) if we can simultaneously observe each reactant in the slowest step in the reaction chain in the stratosphere, then we can formulate the problem in terms of rate limiting steps and test directly both the cause and effect relationship between rate limiting radicals and O, as well as the completeness of

our formulation. Neither option is available to us in conventional model verification studies.

We therefore seek first to identify those reactions (or reaction sets) which result in the severance or formation of the O_2 bond. There are two immediate candidates

$$O_2 + h\nu \xrightarrow{J_{O_2}} O + O \text{ and}$$

$$O + O_3 \xrightarrow{k_{66}} O_2 + O_2 \qquad (2)$$

If the rate of occurrence of Reaction 2 is competitive with the overall rate of odd oxygen formation then $2J_{O_2}$ must appear in P_{O_x} and similarly if $2k_{66}[O][O_3]$ is competitive with the overall rate of odd oxygen destruction then that term must appear in L_{O_x}.

Focusing first on sets of thermal reactions which form O, by breaking the O_2 bond, we note reaction sequences in the methane oxidation chain which result in the formation of O, from O_2, for example

$$OH + CH_4 \rightarrow H_2O + CH_3$$

$$CH_3 + O_2 + M \rightarrow CH_3OO + M$$

$$CH_3OO + NO \rightarrow CH_3O + NO_2$$

$$CH_3O + O_2 \rightarrow H_2CO + HO_2$$

$$H_2CO + h\nu \rightarrow H_2 + CO$$

$$O_3 + h\nu \rightarrow O_2 + O(^1D)$$

$$O(^1D) + H_2O \rightarrow OH + OH$$

$$OH + CO \rightarrow CO_2 + H$$

$$OH + H_2 \rightarrow H_2O + H$$

$$2(H + O_2 + M \rightarrow HO_2 + M)$$

$$2(HO_2 + NO \rightarrow OH + NO_2)$$

$$3(NO_2 + h\nu \rightarrow NO + O)$$

$$3(O + O_2 + M \rightarrow O_3 + M)$$

$$OH + HO_2 \rightarrow H_2O + O_2$$

$$\overline{CH_4 + 5O_2 \rightarrow CO_2 + 2H_2O + 2O_3}$$

In the altitude range of interest here, however, the rate of O, formation by this reaction set is orders of magnitude smaller than $2J_{O_2}[O_2]$ and can thus be ignored in the O, continuity equation. The only known production term of O, that is of quantitative importance between 30 and 45 km is the direct photolysis of O_2 so L_{O_x} takes the simple form

$$P_{O_x} = 2J_{O_2}[O_2]$$

We must of course acknowledge that we have not demonstrated completeness within the context of the natural system; that must await direct observation. However, completeness can be inferred within the context of the model (see Johnston and Podolske[51]). Thus

$$P_{O_x} \geq 2J_{O_2}[O_2] \tag{3}$$

We turn next to the identification of those elementary reactions which, when taken together, result in the reformation of the O_2 bond. We can quickly identify four such sets, they are the principle catalytic cycles previously discussed:

$$\begin{array}{l} NO + O_3 \xrightarrow{k_{50}} NO_2 + O_2 \\ NO_2 + O \xrightarrow{k_{49}} NO + O_2 \\ \hline O + O_3 \rightarrow O_2 + O_2 \end{array} \qquad \begin{array}{l} Cl + O_3 \xrightarrow{k_{30}} ClO + O_2 \\ ClO + O \xrightarrow{k_{33}} Cl + O_2 \\ \hline O + O_3 \rightarrow O_2 + O_2 \end{array}$$

$$\begin{array}{l} OH + O_3 \xrightarrow{k_{12}} HO_2 + O_2 \\ HO_2 + O \xrightarrow{k_{19}} OH + O_2 \\ \hline O + O_3 \rightarrow O_2 + O_2 \end{array} \qquad \begin{array}{l} OH + O_3 \xrightarrow{k_{12}} HO_2 + O_2 \\ HO_2 + O_3 \xrightarrow{k_{13}} OH + 2O_2 \\ \hline 2O_3 \rightarrow 3O_2 \end{array}$$

The period of time required to complete each reaction pair is of course determined by the slower of the two reactions. This defines the "bottleneck" or rate limiting step. Note that once identified, the elementary reaction which defines the rate limiting step must be represented in L_{O_x} because within each volume element the rate of O_2 bond reformation (and thus O_x destruction) is in fact dictated by these few rate limiting processes. We cannot reformulate the problem to alter that physical fact and thus we immediately define an important subset of rate limiting free radicals. How difficult is it to unambiguously define which of the two reactions in each set is rate limiting? In most cases it is trivial, requiring only a rough definition of reactant concentrations.

For example, in the first catalytic cycle above, $k_{49}[NO_2][O]$ is nearly an order of magnitude smaller than $k_{50}[NO][O_3]$ because NO_2 photolysis dominates the conversion of NO_2 to NO so only the crudest knowledge of $[O_3]$, $[O]$, $[NO]$ and $[NO_2]$ is required to establish that $2k_{49}[NO_2][O]$ must appear in L_{O_x} (the factor of 2 accounts for the fact that whenever the rate limiting step takes place, the reaction couplet is complete). Note that as long as we simultaneously measure $[NO_2]$ and $[O]$ within a volume element which is smaller than the spatial variability of each, we need know only that $NO + O_3 \rightarrow NO_2 + O_2$ is the faster step; we need no additional information to establish the necessity that $2k_{49}[NO_2][O]$ appear in L_{O_x}.

In the case of the two HO_x cycles, it is easy to establish through available observation of OH, HO_2, O, and O_3 that $k_{12}[OH][O_3] > k_{19}[HO_2][O]$ and $k_{12}[OH][O_3] > k_{13}[HO_2][O_3]$ and thus that $2k_{19}[HO_2][O]$ and $2k_{13}[HO_2][O_3]$ must also appear in L_{O_x}.

In the case of ClO, catalysis, the choice is not quite as simple in the upper stratosphere (above $\sim$ 36 km) because the catalytic reaction pair dominates the exchange between Cl and ClO and thus $k_{33}[ClO][O] \approx k_{30}[Cl][O_3]$. Below 36 km Reaction 32, $ClO + NO \rightarrow Cl + NO_2$ dominates Reaction 33 and thus $ClO + O \rightarrow Cl + O_2$ is clearly rate limiting. However, we are in the enviable position that, in the region where we need extremely accurate measurements of Cl, ClO, O, and O_3 in order to choose the slower step because $k_{33}[ClO][O] \approx k_{30}[Cl][O_3]$, the choice becomes academic. We thus choose $2k_{33}[ClO][O]$ at all altitudes, and insert it into L_{O_x} such that our simple

accounting to this point allows us to write

$$L_{O_x} \geq 2k_{66}[O][O_3] + 2k_{49}[NO_2][O] + 2k_{33}[ClO][O] + 2k_{19}[HO_2][O] + 2k_{13}[HO_2][O_3] \quad (4)$$

Although an inspection of all reactions and reaction sets currently considered important for stratospheric ozone photochemistry reveals no other rate limiting steps of quantitative importance between 30 and 45 km (see the detailed discussion by Johnston and Podolske[51]) we note the inequality in Equation 4 simply as a reminder that we have not as yet proven completeness in the real atmosphere.

To this point we have written the odd oxygen production and destruction rates in terms of constituent concentrations without mention of how those concentrations are related to the instantaneously observed values. The distinction is important because of the diurnal dependence of each term in 3 and 4. Since the chemical lifetime of O, is significantly greater than one day at all altitudes of interest here, the quantities needed for a consideration of the odd oxygen budget are the diurnal averages of the products

$$J_{O_2}[O_2], k_{66}[O][O_3], k_{49}[NO_2][O], \text{ etc.}$$

which comprise Equations 3 and 4. Thus for a detailed comparison of O_x production and destruction rates we will consider the quantities

$$\overline{J_{O_2}[O_2]} = \frac{1}{\tau}\int_0^\tau J_{O_2}[O_2]dt \qquad \overline{k_{66}[O][O_3]} = \frac{1}{\tau}\int_0^\tau k_{66}[O][O_3]dt$$

$$\overline{k_{49}[NO_2][O]} = \frac{1}{\tau}\int_0^\tau J_{O_2}[O_2]dt \qquad \overline{k_{33}[ClO][O]} = \frac{1}{\tau}\int_0^\tau k_{33}[ClO][O]dt$$

where τ corresponds to a diurnal period.

It is instructive to consider the temporal behavior[3] of the quantities in the integrals of Equation 5. The photolysis of O_2 is of course absent at night and because $O(^3P)$ is formed by the photolysis of O_3 and destroyed by the rapid termolecular Reaction 65, atomic oxygen decays precipitously at sunset, returning to its steady state value equally rapidly at sunrise. Thus both the production and destruction of odd oxygen terminate at sunset; the concentration of ozone remains invariant throughout the night. The radicals NO_2, ClO, and HO_2 require approximately 2 hr to achieve their midday steady state values following sunrise.[3] This fact, coupled with slower build up time for J_{O_2} compared with J_{O_3} due to the shorter wavelength (224 nm) required for the former, means that the snape of the diurnal profiles of J_{O_2} and [O][R] are similar to first order.

We have thus defined the rate limiting steps for the production and destruction of odd oxygen, given our present understanding of the stratosphere, and we can now ask: is $P_{O_x} - L_{O_x}$ less than, equal to, or larger than zero when

$$P_{O_x} = \overline{2J_{O_2}[O_2]} \text{ and}$$

$$L_{O_x} = \overline{2k_{66}[O][O_3]} + \overline{2k_{49}[NO_2][O]} + \overline{2k_{33}[ClO][O]} + \overline{2k_{19}[HO_2][O]} + \overline{2k_{13}[HO_2][O_3]}$$

Table 2
PARTITIONING OF ODD OXYGEN DESTRUCTION RATES FROM MEAN OF SIMULTANEOUS OBSERVATIONS ON 9-20-77, 10-25-77, and 12-2-77 NORMALIZED TO $J_{O_2}[O_2]$

Altitude	$k[O_3][O]$	$k[NO][O]$	$k[ClO][O]$	$k[HO_2][O]$	$k[HO_2][O_3]$	Sum
43	—	—	—	—	—	—
40	0.12	0.36	0.53	0.15*	0.0*	1.17
39	0.14	0.49	0.41	0.13*	0.0*	1.17
37	0.13	0.52	0.27	0.10	0.01	1.03
35	0.10	0.51	0.15	0.07	0.01	0.84
33	0.07	0.37	0.10	0.08	0.06	0.68
31	0.08	0.39	0.08	0.06	0.06	0.71
29	0.09	0.39	0.08	0.04	0.09	0.70
27	0.10	0.73*	0.09	0.05	0.13	1.10
25	0.11	0.37*	0.06	0.03	0.22	0.80

Note: Fractional removal of odd oxygen by O_x, NO_x, ClO, and HO_x normalized to $J_{O_2}[O_2]$ based on *in situ* observations of O_3, $O(^3P)$, NO, ClO and HO_2 corrected for diurnal mean destruction rates as described in the text. Asterisks indicate the substitution of calculated quantities which lie outside the altitude range of the observations.

given a simultaneous measurement of [O], $[O_3]$, $[NO_2]$, [ClO], $[HO_2]$ and J_{O_2} in the same volume element? This approach has been explored through a series of simultaneous observation of [O], $[O_3]$, [NO], [ClO], and $[HO_2]$, using the steady state relationship between NO and NO_2 to convert observed [NO] to $[NO_2]$ (a major weakness in the approach since it requires significantly more information about the photochemical exchange processes to define $[NO]/[NO_2]$ than to know that Reaction 49 is rate limiting) and is discussed in detail elsewhere (see Anderson et al.[48]). Those results are summarized in Table 2 which defines the partitioning of O_x destruction rates by the rate limiting steps in L_{O_x} given above. Direct measurements of J_{O_2} are not currently available, but development of a measurement technique is in progress.[52] Detailed studies of P_{O_x} and L_{O_x} as a function of altitude are obviously in their infancy and there is significant room for progress.

A second approach, which is a far more direct method of answering the question posed at the outset of this discussion, is to cast the steady state relation

$$d[O_x]/dt = P_{O_x} - L_{O_x} = 0$$

in terms of expression 3 and 4 for P_{O_x} and L_{O_x}, respectively, and solve the resulting algebraic expression for $[O_3]$ or [O]. In order to simplify somewhat the resulting expression to make our point, we note from Table 1 that L_{O_x} is dominated by Reactions 19, 33, and 49 and thus

$$P_{O_x} - L_{O_x} \approx J_{O_2}[O_2] \quad [O]\left\{k_{49}[NO_2] + k_{33}[ClO] + k_{19}[HO_2]\right\} = 0$$

Thus

$$[O(^3P)] \approx \frac{J_{O_2}[O_2]}{\left\{k_{49}[NO_2] + k_{33}[ClO] + k_{19}[HO_2]\right\}}$$

and we are in a position to test whether fluctuations in the observed concentration of each of the rate limiting radicals (which is the rule rather than the exception in such

measurements) are reflected in fluctuations in $[O(^3P)]$ and thus in O_3. We must of course simultaneously observe each term in the denominator of the above expression.

The change in the observed concentration of $O(^3P)$, $\Delta[O(^3P)] = [O(^3P)]_1 - [O(^3P)]_2$ resulting from changes in the mean ClO concentration, $\overline{[ClO]}$, where $[ClO]_1 = \overline{[ClO]} - \Delta[ClO]$ and $[ClO]_2 = \overline{[ClO]} + \Delta[ClO]$ is just

$$\Delta[O(^3P)] = [O(^3P)]_1 - [O(^3P)]_2 =$$

$$J_{O_2}[O_2]\left\{\frac{1}{k_{49}[NO_2] + k_{33}([ClO] - \Delta[ClO]) + k_{19}[HO_2]}\right.$$

$$\left. - \frac{1}{k_{49}[NO_2] + k_{33}([ClO] + \Delta[ClO]) + k_{19}[HO_2]}\right\}$$

$$= J_{O_2}[O_2]\left\{\frac{2k_{33}\,\Delta[ClO]}{(k_{49}[NO_2] + k_{33}[ClO] + k_{19}[HO_2])^2}\right\}$$

So

$$\frac{\Delta[O(^3P)]}{[O(^3P)]} = \frac{2\Delta[ClO]}{\overline{[ClO]}}\left\{\frac{1}{1 + \frac{k_{49}[NO_2]}{k_{33}[ClO]} + \frac{k_{19}[HO_2]}{k_{33}[ClO]}}\right\} \tag{6}$$

A glance at Table 2 indicates that in the vicinity of 40 km where ClO_x has its maximum effect on O_x, the fractional terms in the denominator of expression 6 are less than 1. This is of considerable importance because we have formulated the partial derivative of $[O(^3P)]$ with respect to $[ClO]$ and we must account for changes in $[NO_2]$ and to a lesser degree $[HO_2]$.

As a practical point, we note that because O_3, can be detected *in situ* with a precision of ±3% and an accuracy of ±5%, which is superior to corresponding figures for atomic fluorescence measurements of $O(^3P)$, we can rewrite Equation 6 in terms of O_3 rather than $O(^3P)$ so

$$\frac{\Delta[O_3]}{\overline{[O_3]}} = \frac{2\Delta[ClO]}{\overline{[ClO]}}\left\{\frac{1}{1 + \frac{k_{49}[NO_2]}{k_{33}[ClO]} + \frac{k_{19}[HO_2]}{k_{33}[ClO]}}\right\}$$

Thus we have a simple expression for the partial derivative of $[O_3]$ with respect to $[ClO]$, cast in terms of simultaneously observable quantities,

$$\frac{\partial[O_3]}{\partial[ClO]} = \left(\frac{\Delta[O_3]}{\Delta[ClO]}\right)_{ClO} = \frac{\overline{[O_3]}}{\overline{[ClO]}}\left\{\frac{1}{\left(1 + \frac{k_{49}[NO_2]}{k_{33}[ClO]} + \frac{k_{19}[HO_2]}{k_{33}[ClO]}\right)}\right\}$$

which has the implicit advantage that when implemented, conclusions will be based on the *precision* of the observations rather than on the (absolute) *accuracy*. In addition, the striking variability observed in the free radicals which has historically frustrated detailed comparison between model calculations and observations, is just the ingredient needed to demonstrate cause and effect between ClO_x and O_x.

Although a determination of $(\Delta[O_3]/[ClO])_{ClO}$ as a function of altitude by direct

observation will answer the question posed at the outset of this section, it is but a first step linking $CFCl_3$ and CF_2Cl_2 release at the surface to a total column ozone change in the stratosphere.

There are, however, several characteristics unique to the chlorine system which can be exploited for the purpose of linking surface release of any chlorine compound to *first order* changes in stratospheric ozone using observable quantities only. These characteristics are:

1. The first order destruction of ozone by chlorine occurs in the upper stratosphere where the O_x system is in photochemical steady state.
2. Chlorine is a trace component ($\sim$ few ppb) at all altitudes in the stratosphere so that an accurate measurement of total chlorine in the stratosphere (i.e., an accounting of Cl atoms bound or free in any volume element) can be simply and unambiguously interpreted.
3. The altitude at which significant photolytic decomposition of the major industrially related fluorocarbons occurs is sufficiently far above the tropopause that all chlorine atoms transported across the tropopause in source molecules safely enter the stratospheric chlorine "bank".
4. The ratio of the rate limiting chlorine radical, ClO, to total chlorine is independent of total chlorine. This will of course be checked but its first order validity results from the fact that the ratio of [Cl] to [HCl] depends principally upon $[OH]$, $[HO_2]$ and $[CH_4]$ which are not a function of the chlorine concentration.

The fractional change in O_x (or O_3) at any altitude z resulting from changes in Cl_x via the release of a chlorine containing compound at the surface can be expressed as

$$\left(\frac{\Delta[O_3]}{[O_3]}\right)_z^{Cl_x} = \left(\frac{\Delta[Cl_x]\ \left(\frac{[ClO]}{[Cl_x]}\right)\ \left(\frac{\Delta[O_3]}{\Delta[ClO]}\right)_{ClO}}{[O_3]}\right)_z$$

where the numerator on the right is the product of three quantities:

$\Delta[Cl_x]$, the change in total chlorine mixing ratio resulting from the enhancement in chlorine following the release of chlorine compounds at the surface,

$$\left(\frac{[ClO]}{[Cl_x]}\right)$$

the ratio of the chlorine rate limiting radical to total chlorine and

$$\left(\frac{\Delta[O_3]}{\Delta[ClO]}\right)_{ClO}$$

the observed partial derivative of ozone with respect to the rate limiting radical.

The last quantity has been fully discussed above and we simply add that the localized destruction of O_x by ClO in the upper stratosphere represents a profound simplification not only because the effect peaks at an observable level comparable to the total rate of O_x production but also because the O_x system is in photochemical steady state at that altitude.

The second term, $[ClO]/[Cl_x]$, is directly observable because analytical techniques

exist for both constituents, although measurements of total chlorine have not yet been published. Equally important, chlorine is a rare and clearly discernable chemical component of the stratosphere (a condition which is not satisfied by HO_x or NO_x).

The first term, $\Delta[Cl_x]$, represents the change in total chlorine resulting from the surface release of any chlorine compound, i. It is thus a summation over all contributions such that

$$\Delta[Cl_x] = \sum_i \Delta[i]$$

each component of which may have a different ratio of stratospheric to tropospheric lifetime. We note however that considerable effort has been expended on the identification of tropospheric loss processes which are potentially capable of diminishing $\Delta[Cl_x]$ below that implied by the enhanced tropospheric mixing ratio of total chlorine and within the next few years remaining small uncertainties should be eliminated for the purposes of our discussion here.

In concluding this discussion, we note first that while the analytical techniques exist for such covariance studies, the proper combination of observations has not yet been achieved. Second, although such studies may be tedious they do have the fundamental advantage that (1) they depend upon instrumental precision rather than accuracy, (2) large variability both in O, and the rate limiting radicals will be used to establish cause and effect which cannot be determined by any other approach, and (3) as the studies develop not only will the variability of $[O_3]$ be determined, but also (and more importantly) we will understand why O_3 varies.

ACKNOWLEDGMENTS

The calculations of photodissociation rates and constituent profiles in Figures 3 to 5, 13, 16, and 19 were kindly made available by Drs. J. Logan, M. J. Prather, S. C. Wofsy, and M. B. McElroy of Harvard. Special thanks go also to Ms. Judy Banks for expert assembling and typing of the chapter.

REFERENCES

1. Molina, M. J. and Rowland, F. S., Stratosperic sink for chlorofluoromethanes: chlorine atom catalyzed destruction of oxone, *Nature (London)*, 249, 810, 1974.
2. Lovelock, J. E., Maggs, R. J., and Wade, R. J., Halogenated hydrocarbons in and over the Atlantic, *Nature (London)*, 241, 194, 1973.
3. Logan, J. A., Prather, M. J., Wofsy, S. C., and McElroy, M. B., Atmospheric chemistry: response to human influence, *Philos. Trans. R. Soc. London*, 290, 187, 1978. Calculations presented herein were done using the following revised rate constants:

$HO_2 + O_2 \longrightarrow OH + 2O_2$	$1.4 \times 10^{-14} \exp(-580/T)$ cm.^{3}sec.$^{-1}$
$HO_2 + HO_2 \longrightarrow H_2O_2 + O_2$	3×10^{-12}
$HO_2 + ClO \longrightarrow HOCl + O_2$	4.5×10^{-12}
$HO_2 + NO \longrightarrow OH + NO_2$	$3.3 \times 10^{-12} \exp(255/T)$

4. Yung, Y. L., Pinto, J. P., Watson, R. T., and Sander, S. P., Atmospheric bromine and ozone perturbations in the lower stratosphere. Manuscript 1979.
5. Murgatroyd, R. J., The structure and dynamics of the stratosphere, in *The Global Circulation of the Atmosphere*, Corby, G. A., Ed., London Royal Meteorological Society, 1969, 194.

6. Hidejii, K., A numerical investigation of the atmospheric general circulation and stratosphheric - tropospheric mass exchange. II. Lagrangian motion of the atmosphere, *J. Meteorol. Soc. Jpn .*, 55, 71, 1977
7. Wofsy, S. C., Temporal and latitude variations of stratospheric trace gases: a critical comparison between theory and experiment, *J. Geophys. Res.*, 83, 364, 1978.
8. Goldan, P. D., Kuster, W. C., Albritton, D. L., and Schmeltekopf, A. L., Stratospheric $CFCl_3$, CF_2Cl_2 and N_2O height profile measurements at several latitudes, *J. Geophys. Res.*, in press.
9. Hudson, R. D., Ed., The stratosphere: present and future, NASA reference publication #1049, December 1979.
10. Chang, J. S. and Dickenson, R., private communication, 1979.
11. Hunten, D. M., Vertical transport in atmospheres, *Atmospheres of Earth and the Planets*, McCormac, B. M., Ed., Kluwer Boston, Hingham, MA, 1975.
12. Schiff, H., Stratospheric ozone depletion by halocarbons: chemistry and transport, National Academy of Sciences, 1979.
13. Strobel, D. F., Odd nitrogen in the mesosphere, *J. Geophys. Res.*, 76, 8384, 1971.
14. Crutzen, P. J., Ozone production rates in an oxygen-hydrogen-nitrogen dioxide atmosphere, *J. Geophys. Res.*, 76, 7311, 1971.
15. McConnell, J. C. and McElroy, M. B., Odd nitrogen in the atmosphere, *J. Atmos. Sci.*, 30, 1465, 1973.
16. Liu, S. C., Donahue, T. M., Cicerone, R. J., and Chameides, W. L., Effect of water vapor on the destruction of ozone in the stratosphere perturbed by Cl, or NO, pollutants, *J. Geophys. Res.*, 81, 3111, 1976.
17. Stolarski, R. S. and Cicerone, R. J., Stratospheric chlorine: a possible sink for ozone, *Can. J. Chem.*, 52, 1610, 1974.
18. Crutzen, P. J., A review of upper atmospheric photochemistry, *Can. J. Chem.*, 52, 1569, 1974.
19. Wofsy, S. C. and McElroy, M. B., HO_x, NO, and ClO_x: their role in atmospheric photochemistry, *Can. J. Chem.*, 52, 1582, 1974.
20. Crutzen, P. J., Isaksen, I. S. A., and McAfee, J. R., The impact of the chlorocarbon industry on the ozone layer, *J. Geophys. Res.*, 83, 345, 1978.
21. Chang, J. S., Duewer, W. H., and Wuebbles, P. J., The atmospheric nuclear tests of the 1950's and 1960's: a possible test of ozone depletion theories, *J. Geophys. Res.*, 84, 1755, 1979.
22. Miller, C., Filkin, D. L., and Jesson, J. P., The fluorocarbon-ozone theory. VI. Atmospheric modeling: calculations of the diurnal steady state, *Atmos. Environ.*, 13, 381, 1979.
23. Turco, R. P. and Whitten, R. C., A note on the diurnal averaging of aeronomical models, *J. Atmos. Terr. Phys.*, 40, 13, 1978.
24. Cunnold, D., Alyea, F., Phillip, N., and Prinn, R., A three dimensional dynamical-chemical model of atmospheric ozone, *J. Atmos. Sci.*, 32, 170, 1975.
25. Mahlman, J. D. and Moxim, W. J., Tracer simulation using a global general circulation model: results from a midlatitude instantaneous source experiment, *J. Atmos. Sci.*, 35, 1370, 1978.
26. Harwood, R. S. and Pyle, J. A., A two dimensional mean circulation model for the atmosphere below 80 km, *Q. J. R. Meteorol. Soc.*, 1001, 723, 1975.
27. Hidalgo, J. and Crutzen, P. J., The tropospheric and stratospheric composition perturbed by NO, emissions of high altitude aircraft, *J. Geophys. Res.*, 82, 5833, 1977.
28. Borucki, W. J., Whitten, R. C., Woodward, H. T., Capone, L. A., Riegel, C. A., and Gaines, S., Stratospheric ozone decrease due to chlorofluoromethane photolysis: predictions of latitude dependence, *J. Atmos. Sci.*, in press.
29. Williams, W. J., Kostus, J. J., Goldman, A., and Murcray, D. G., Measurements of the stratospheric mixing ratio of HCl using an infrared absorption technique, *Geophys. Res. Lett.*, 3, 383, 1976.
30. Ackerman, M., Frimont, D., Girard, A., Gottignier, M., and Muller, C., Stratospheric HCl from infrared spectra, *Geophys. Res. Lett.*, 3, 81, 1976.
31. Farmer, C. B., Raper, O. F., and Norton, R. H., Spectroscopic detection and vertical distribution of HCl in the tropopause and stratosphere, *Geophys. Res. Lett.*, 3, 13, 1976.
32. Raper, O. F., Farmer, C. B., Doth, R. A., and Robbins, B. D., The vertical distribution of HCl in the stratosphere, *Geophys. Res. Lett.*, 4, 531, 1977.
33. Farmer, C. B., Raper, O. F., Muller, C., Robbins, B. D., and Noth, R. A., Simultaneous spectroscopic measurements of stratospheric species O_3, CH_4, CO, CO_2, N_2O, H_2O, and HCl at northern midlatitudes, *J. Geophys. Res.*, 85, 1621, 1980.
34. Eyre, J. R. and Roscoe, H. K., Radiometric measurement of stratospheric HCl, *Nature (London)*, 266, 243, 1977.
35. Lazrus, A. L., Gandrud, B. W., Greenberg, J., Bonelli, J., Mroz, E., and Sedlacek, W. A., Midlatitude seasonal measurements of stratospheric acidic chlorine vapor, *Geophys. Res. Lett.*, 4, 587, 1977.
36. Murcray, D. G., Goldman, A., Murcray, F. H., Murcray, F. J., and Williams, W. J., Stratospheric distribution of $ClONO_2$, *Geophys. Res. Lett.*, 6, 857, 1979.

37. DeMore, W. B., Stief, L. J., Kaufman, F., Golden, D. M., Hanpson, R. F., Kurylo, M. J., and Margitan, J. J., Kinetic and photochemical data for use in stratospheric modelling, JPL Publication 79-27, 1979.
38. Stimpfle, R. M., Perry, R. A., and Carleton, J. H., Temperature dependence of the reaction of ClO and HO_2 radicals, *J. Chem. Phys.*, 71, 5183, 1979.
39. Wells, J. S., Sams, R. L., and Lafferty, W. J., The high-resolution infrared spectrum of the υ_1 band of hypochlorous acid, *J. Mol. Spectrsc.*, 77, 349, 1979.
40. Molina, L. T. and Molina, M. J., Ultraviolet spectrum of HOCl, *J. Phys. Chem.*, 82, 2410, 1978.
41. Menzies, R. T., Remote measurement of ClO in the stratosphere, *Geophys. Res. Lett.*, 6, 151, 1979.
42. Anderson, J. G., The absolute concentration of $O(^3P)$ in the earth's stratosphere, *Geophys. Res. Lett.*, 2, 231, 1975.
43. Anderson, J. G., The absolute concentration of $OH(X^2)$ in the earth's stratosphere, *Geophys. Res. Lett.*, 3, 165, 1976.
44. Anderson, J. G., The detection of atoms and diatomic radicals in the earth's stratosphere, *Atmos. Technol.*, 9, 55, 1978.
45. Anderson, J. G., Margitan, J. J., and Stedman, D. H., Atomic chlorine and the chlorine monoxide radical in the stratosphere: three *in situ* observations, *Science*, 198, 501, 1977.
46. Anderson, J. G., Grassl, H. J., Shetter, R. E., and Margitan, J. J., Stratospheric free chlorine measured by balloon borne *in situ* resonance fluorescence, *J. Geophys. Res.*, 85, 2869, 1980.
47. Anderson, J. G., Grassl, H. J., Shetter, R. E., and Margitan, J. J., *in situ* measurements of HO_2 in the earth's stratosphere, *Geophys. Res. Lett.*, in press.
48. Anderson, J. G., Grassl, H. J., Shetter, R. E., and Margitan, J. J., NO, HO_2, ClO and $O(^3P)$ in the earth's stratosphere: do the rates of odd oxygen production and destruction balance? *J. Atmos. Sci.*, in press.
49. Prasad, S. S., Possible existence and chemistry of $ClOO_2$ in the stratosphere, *Nature (London)*, 285, 152, 1980.
50. Zahniser, M. S. and Kaufman, F., Kinetics of the reactions of ClO with O and with NO, *J. Chem. Phys.*, 66, 8, 1977.
51. Johnston, H. S. and Podolske, J., Interpretations of stratospheric photochemistry, *Rev. Geophys. Space Phys.*, 16, 491, 1978.
52. Schmeltekopf, A. L., private communication, 1979.

from Causes and Effects of Stratospheric Ozone Reduction: An Update, Environmental Studies Board, Commission on Natural Resources, National Research Council, National Academy Press, Washington, D.C., 1982.

Appendix D

THE MEASUREMENT OF TRACE REACTIVE SPECIES IN THE STRATOSPHERE: A REVIEW OF RECENT RESULTS

J.G. Anderson
Harvard University

INTRODUCTION

The central objective of this report is to review critically the data base on trace species observations in the stratosphere for the specific purpose of testing predictions of global ozone depletion resulting from the release of compounds containing chlorine and nitrogen into the lower atmosphere. A corollary objective is to appraise prospects for significant advances in the next five years and to suggest a strategy for that research.

Achieving the first objective in a reasonably concise document must confront the often incompatible elements of data quality, quantity, and applicability to theory. For example, a large body of data may exist on a particular radical that is of demonstrably superior quality with respect to the analytical method, but that, if not taken at the proper time of day and referenced to the local tropopause height, may be uninterpretable in terms of a modeled distribution. We will deal with the sheer volume of information by referencing the recent WMO/NASA report document, "The Stratosphere 1981: Theory and Measurements," whenever possible while attempting to maintain reasonable continuity in this report (Hudson et al. 1982).

The species that are of interest to the stratospheric photochemistry of ozone are divided into groups and listed in Table D.1. The ordering of groups and of the species within each group in the table is rather arbitrary, but the choice seeks to represent the fact that the central objective of this report is an assessment of the effect of fluorocarbon release on stratospheric ozone. Thus, the photochemically active chlorine components are treated first.

TABLE D.1 Chemical Species of Interest in the Stratospheric Chemistry of Ozone

	Species							
Group	1	2	3	4	5	6	7	8
1	ClO	Cl	ClOO	OClO	HCl	HOCl	$ClONO_2$	
2	OH	HO_2	H	H_2	H_2O_2	H_2O		
3	$O(^3P)$	$O(^1D)$	$O_2(^1\Delta)$	$O_2(^1\Sigma)$	O^*_2 (other)	O_3		
4	NO	NO_2	N	NO_3	N_2O_5	$HONO_2$		
5	BrO	Br	BrO_2	OBrO	HBr	HOBr	$BrONO_2$	
6	FO	F	FO_2	OFO	HF			

A review of the data appears first. Then we examine how well the current data base constrains model predictions of ozone reduction. That analysis first summarizes uncertainties in the reaction rate constant data by defining a series of six "cases," tracing the impact of rate constant assumptions on the key free radicals and on the altitude dependence of odd oxygen destruction. The objective is first to correlate each case with the observed vertical distribution of the key free radicals to determine whether a consistent picture evolves, and, second, to identify the altitude regime in which the maximum impact on ozone occurs, resulting from changes in total chlorine or reactive nitrogen.

Finally we abstract from the analysis a series of questions that must be addressed by measurement of trace species in the stratosphere. The answers are essential for significant progress to be realized in the near future. Following each question is an appraisal of the prospects for progress in the next three years.

REVIEW OF DATA BASE ON TRACE SPECIES

Group 1: Reactive Trace Constituents Containing Chlorine

While the case linking fluorocarbons released at the earth's surface to the global distribution of ozone is made up of innumerable elements, the single most important observable in the stratosphere for a first-order appraisal of ozone destruction rates resulting from the decomposition of fluorocarbons is the concentration of the chlorine monoxide free radical, ClO. The reason for this is that ClO is the rate limiting (RL) chlorine constituent in the

major catalytic cycles (see the recent discussion by Weubbles and Chang (1981)):

$$Cl + O_3 \rightarrow ClO + O_2$$
$$ClO + O \rightarrow Cl + O_2 \quad (RL)$$

$$O + O_3 \rightarrow 2O_2$$

$$Cl + O_3 \rightarrow ClO + O_2$$
$$ClO + HO_2 \rightarrow HOCl + O_2 \quad (RL)$$
$$OH + O_3 \rightarrow HO_2 + O_2$$
$$HOCl + h\nu \rightarrow OH + Cl$$

$$O_3 + O_3 \rightarrow 3O_2$$

$$Cl + O_3 \rightarrow ClO + O_2$$
$$NO + O_3 \rightarrow NO_2 + O_2$$
$$ClO + NO_2 + M \rightarrow ClONO_2 + M$$
$$\left.\begin{array}{l} ClONO_2 + h\nu \rightarrow NO_3 + Cl \\ NO_3 + h\nu \rightarrow NO + O_2 \end{array}\right\} (RL)$$

$$O_3 + O_3 \rightarrow 3O_2.$$

ClO has thus been the focus of experimental attention since Molina and Rowland (1974) first linked fluorocarbon release to global ozone reduction. In addition, because ClO dominates the chlorine free radical system with respect to concentration, reaching nearly 1 part per billion (ppb) in the middle to upper stratosphere (its reactive partner, Cl, for example, reaches only 1 part per trillion [ppt] in the stratosphere), it is amenable to a broader class of observational techniques. Four other chlorine-containing constituents are of central importance: HCl, Cl, HOCl, and $ClONO_2$ (with possible isomeric forms).

Chlorine Monoxide (ClO)

Three methods have been successfully applied to the detection of stratospheric ClO (listed here in the chronological order of their application):

1. Balloon-borne in situ resonance fluorescence methods (Anderson et al. 1977, 1980; Weinstock et al. 1981).
2. Ground-based millimeter(mm)-wave emission spectroscopy of the ClO total column at 204 GHz (Parrish et al. 1981).

3. Balloon-borne, mm-wave emission spectroscopy of ClO at 204 GHz (Waters et al. 1981). Aircraft-borne observations by this group had previously established an upper limit on stratosphere ClO (Waters et al. 1979).

A fourth method, that of balloon-borne, laser heterodyne radiometry (see Menzies 1978, Menzies et al. 1981), has been applied to the problem, but ambiguities in spectral line position prevent an interpretation of the results.

While a clear consensus on several aspects of the stratospheric ClO distribution has not emerged, the last two years have witnessed several crucial steps toward a first-order understanding of [ClO] (where square brackets indicate concentration) at middle latitudes.

We consider first results from the two balloon-borne techniques that provide a direct determination of the altitude dependence of [ClO]. Figure D.1 summarizes 10 observations reported by Weinstock et al. (1981) obtained using method 1. All observations contained in Figure D.1 represent midday conditions at 32°N latitude; variations in solar zenith angle primarily reflect changes in solar declination.

The in situ observations fall into two classes; 8 of the 10 define an envelope with deviations limited to about ±50 percent about the observed mean; two of the observations, both obtained in July, fall clearly outside of the envelope and are not representative of the mean distribution of ClO at middle latitudes. Without independent substantiation, the two July observations cannot be included in the data base defining the mean distribution of ClO.

In Figure D.2, the envelope of in situ observations is superposed with the recent balloon-borne observations of Waters et al. (1981) using mm-wave emission techniques. Included in the in situ array is an observation (June 1, 1978) not included in the Weinstock et al. (1981) publication because it was obtained using an instrument with no previous flight history; the results are not at variance and are included for completeness.

The consistency in both absolute magnitude and gradient between the two techniques is one of the most important results to be achieved since the last NRC report (NRC 1979). It underscores the importance of using independent techniques to cross-calibrate observational methods for all of the key radicals involved directly in processes that control the rate of odd oxygen destruction.

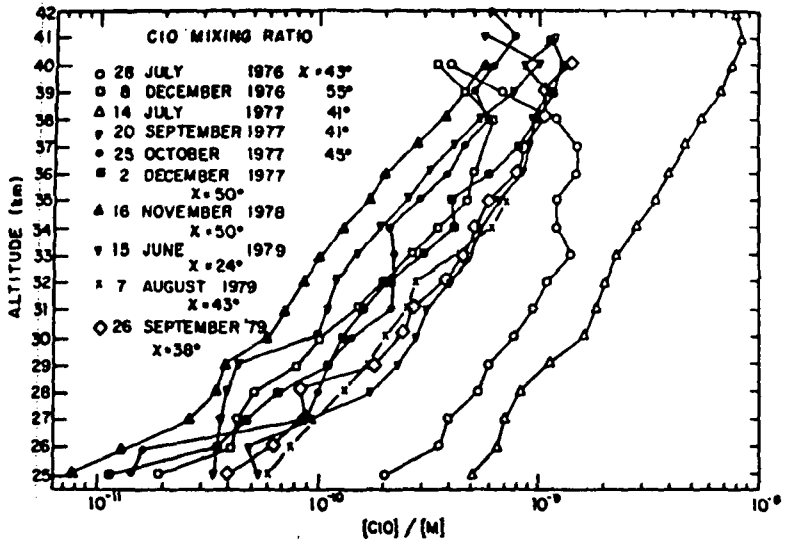

FIGURE D.1 Summary of the vertical distribution of ClO obtained between July 28, 1976, and September 26, 1979, using in situ resonance fluorescence methods (from Weinstock et al. 1981).

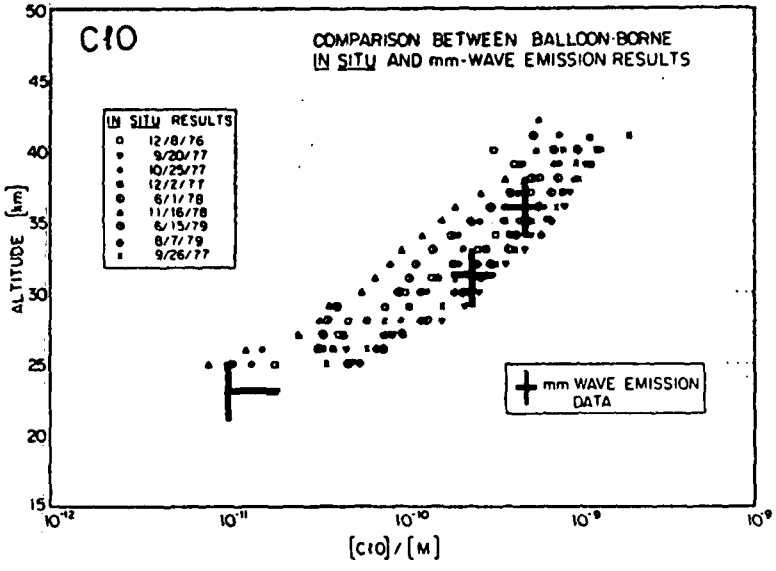

FIGURE D.2 Comparison between balloon-borne in situ and mm-wave emission observations of ClO (from Weinstock et al. 1981, Waters et al. 1981).

It also should be pointed out that while the envelope of ClO data appears to be rather well defined, the dispersion about the mean exceeds ±50 percent; the cited experimental uncertainty is ±30 percent. As we will see, when the results are applied to the problem of constraining model-predicted ozone reduction, this dispersion constitutes a serious impediment. In anticipation of that fact, we represent the nine in situ observations from Figure D.2 in a somewhat different way. Figure D.3 displays a composite of the data converted to absolute concentration to eliminate the steep gradient, and in each frame a single profile is highlighted against the background array. The variety in profile shape is significant, with clear evidence of vertical structure on the order of 2 km in some cases, but nearly absent in others. In addition, the top-side shape of [ClO] exhibits significant variation.

We summarize next the results recently reported by Parrish et al. (1981) using the ground-based, mm-wave emission technique noted earlier (method 2), which were obtained between 10 a.m. and 4 p.m. on 17 separate days (between January 10, 1980, and February 18, 1980) at 43°N latitude from the Five College Radio Astronomy Observatory, Amherst, Massachusetts. Such ground-based observations, which employ purely rotational transitions, are affected by collisional (pressure) broadening by approximately 4 MHz/mb at stratospheric pressures. This is both a blessing, in that low-resolution altitude information can be extracted from the emission line shape, and a curse, in that one must have a first-order estimate of the shape of the emitting layer in order to obtain the absolute column concentration for the observed brightness temperature as a function of frequency. In practice, however, the balloon-borne observations have provided the information on the layer shape, and thus absolute column measurements can be extracted. It should be noted, however, that even without knowledge of the shape of the emitting layer, some information on absolute concentration can be extracted.

Parrish et al. (1981) have taken the mean of seven in situ profiles, specifically those appearing in the envelope of Figure D.2, excluding the last profile obtained on September 26, 1979, and the June 1, 1978, data (which do not alter the conclusions to be drawn), scaled those results by 0.8, integrated the signal that would have resulted, and then overlayed that profile with the observed brightness as a function of frequency. The

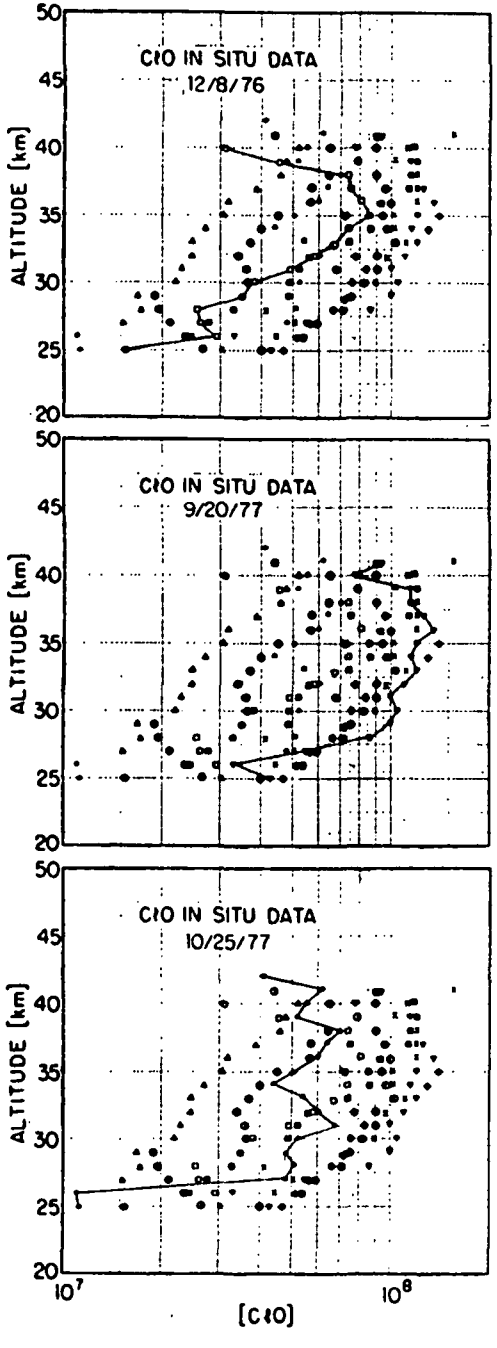

FIGURE D.3a Composite of the ClO profiles, 12/8/76, 9/20/77, and 10/25/77.

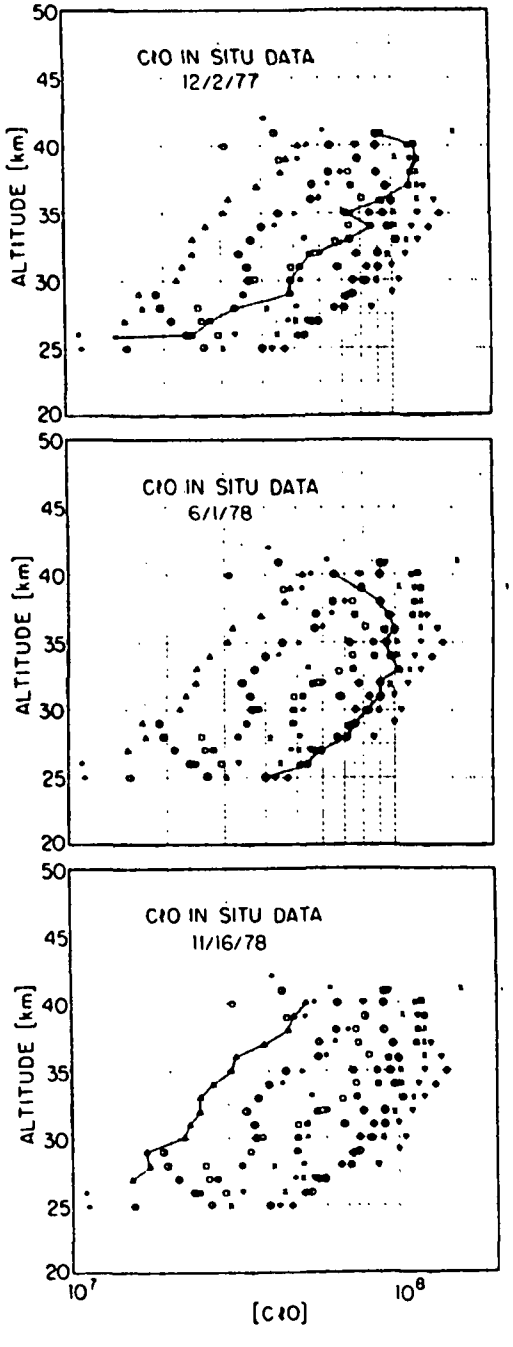

FIGURE D.3b Composite of the ClO profiles, 12/2/77, 6/1/78, and 11/16/78.

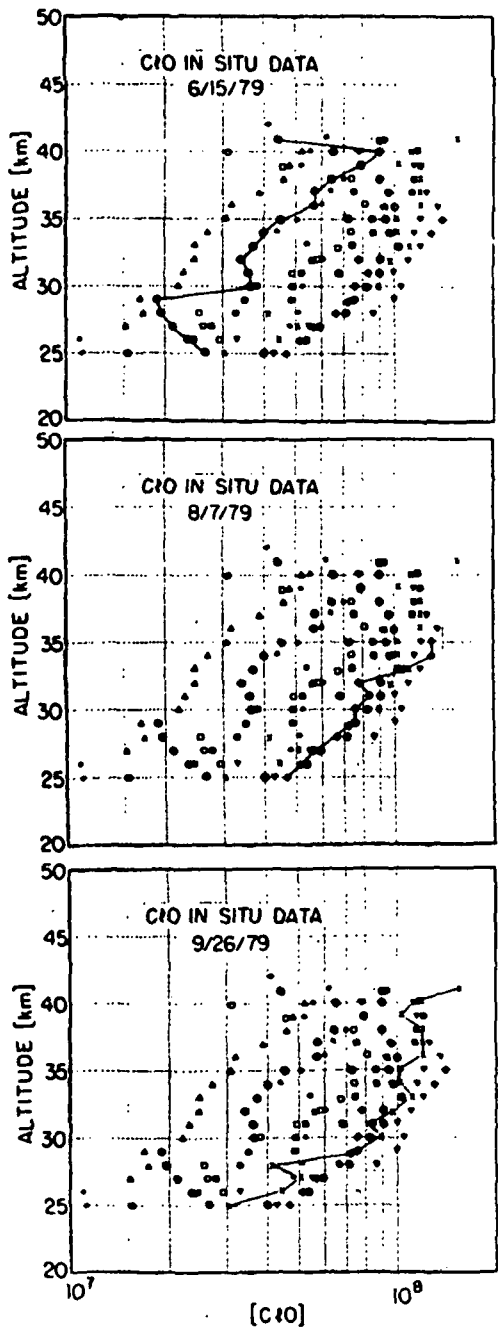

FIGURE D.3c Composite of the ClO profiles, 6/15/79, 8/7/79, and 9/26/79.

results are shown in Figure D.4. The first conclusion to be drawn is that substantial agreement exists with respect to absolute magnitude, since both techniques quote uncertainties of greater than or equal to 25 percent. However, it must be noted that the ground-based observations were done at a latitude 10° northward of the balloon measurements, and are confined to a relatively short period of time in midwinter. A broader data base and observations done in the same latitude band are clearly needed. Parrish et al. (1981) report that no single day of observation exceeded the average by more than a factor of 2.5, and tentative evidence for variations on the order of a factor of 2 in total ClO column density occurred on a time scale of a few days.

An inspection of Figure D.4 indicates a point of major importance: The mm-wave, emission line shape is consistent with the distribution determined by both balloon-borne techniques.

The ability of the ground-based observations to discriminate among the available model calculations is demonstrated in the three panels of Figure D.5. These figures compare the line shape that would be observed for three modeled cases: Case (a) with a mixing ratio of 2.7 ppb for total chlorine, a chemical reaction scheme comparable to that used for the previous NRC report, and an elevated stratospheric water vapor mixing ratio of 8 ppm (uniform from troposphere to stratosphere, as discussed in Logan et al. (1978)); Case (b) with 2.6 ppb for total chlorine and a "normal" mixing ratio for H_2O of 5 ppm (see Sze and Ko 1981); and, finally, Case (c) with 1.3 ppb for total chlorine and 5 ppm H_2O (see Crutzen et al. 1978). The point is not that those ground-based observations cast new light on the selection of a preferred combination of total chlorine and water; the determination of total chlorine (Berg et al. 1980) and H_2O (see Kley et al. 1980) had established that point. Rather, the line shape resulting from the calculated distribution of ClO using chemistry consistent with the previous NRC report (Case a) is distinctly broader than that observed by the mm-wave method. This reflects the larger concentration of ClO calculated by the model at lower altitudes in the stratosphere.

A reasonably thorough discussion of the experimental uncertainties associated with each of the methods discussed above appears in Chapter 1 of Hudson et al. (1982).

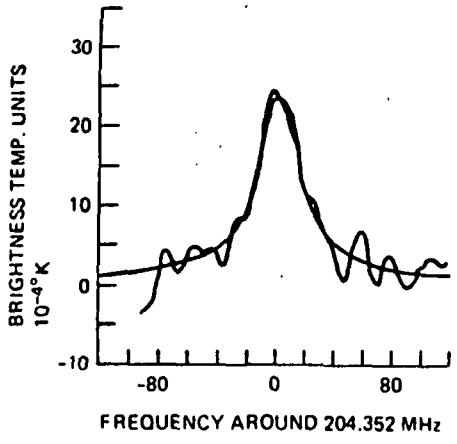

FIGURE D.4 An overlay of the ground-based mm-wave emission data of Parrish et al. (1981) and the signal that would result from an integral of the mean of the balloon-borne in situ observations multiplied by 0.8. The mean was taken excluding the July 28, 1976, and July 14, 1977, in situ ClO profiles.

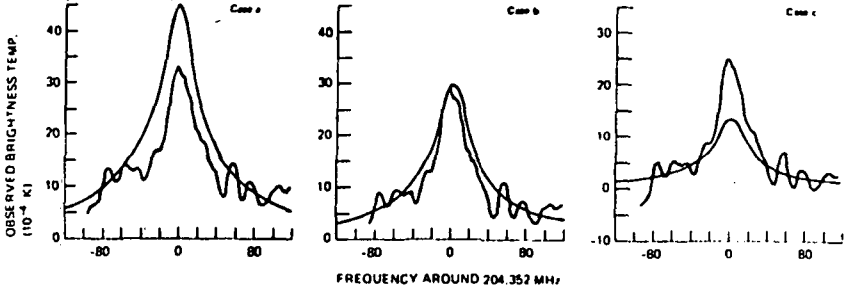

FIGURE D.5 A comparison between the ground-based mm-wave emission data of Parrish et al. (1981) and three modeled predictions: Case a from Logan et al. (1978) with 8 ppm H_2O throughout the stratosphere; Case b with 5 ppm H_2O and 2.3 ppb total chlorine from Sze and Ko (1981); and Case c for 5 ppm H_2O and 1.3 ppb total chlorine from Crutzen et al. (1978).

Chlorine (Cl)

There have been no further measurements of atomic chlorine since those reported by Anderson et al. (1977), which were noted in the last NRC report. However, the ratio of [Cl]/[ClO] was explicitly discussed in a recent paper (see Anderson et al. 1980); those results are summarized in Figure D.6.

A more complete discussion of atomic chlorine appears in Hudson et al. (1982), along with a detailed critique of experimental uncertainties. There are several reasons for the paucity of the data in this important area. The first is that attention has been focused on its rate limiting partner, ClO, and the second is that the exceedingly low concentrations of Cl make the observations exceedingly difficult. It is critical that progress be made in the study of atomic chlorine, particularly in conjunction with studies of ClO and HCl.

Chlorine Dioxide Radical (ClOO)

There have been no reported observations of the radical ClOO in the stratosphere, and there have been no concerted attempts to observe it. Because of its large cross section for photolysis, it is expected to exist at extremely small concentrations, well below currently available detection techniques.

Symmetrical Chlorine Dioxide (OClO)

The more stable form of chlorine dioxide has not been observed and at predicted concentrations of 10 to 100 cm^{-3} in the stratosphere will probably so remain in the foreseeable future.

Hydrochloric Acid (HCl)

Table D.2 summarizes the partitioning among the various chlorine compounds given our current understanding of the reactions that govern the chemical exchange of these constituents. The budget is clearly dominated by [HCl], and it has thus rightfully received a considerable amount of attention in experiments.

TABLE D.2 Partitioning Among Chlorine Compounds (Concentrations Correspond to Case 6 as Described in the Text)

$\Sigma = [HCl] + [ClO] + [ClONO_2] + [HOCl] + [Cl]$						
Altitude	HCl/Σ	ClO/Σ	$ClONO_2/\Sigma$	HOCl/Σ	Cl/Σ	Σ
50	0.97	0.016	8.44×10^{-8}	0.002	0.007	0.4323×10^{8}
45	0.92	0.056	6.27×10^{-6}	0.01	5.3×10^{-3}	0.8258×10^{8}
40	0.78	0.15	0.0007	0.05	2.2×10^{-3}	0.16477×10^{9}
35	0.69	0.17	0.02	0.09	6.4×10^{-4}	0.3332×10^{9}
30	0.72	0.10	0.10	0.06	1.4×10^{-4}	0.6692×10^{9}
25	0.83	0.03	0.11	0.01	3.0×10^{-5}	0.1164×10^{10}
20	0.95	0.008	0.034	0.001	7.5×10^{-6}	0.1098×10^{10}
15	0.98	0.004	0.008	0.001	2.9×10^{-6}	0.6454×10^{9}
10	0.98	0.004	0.001	0.009	2.07×10^{-6}	0.3717×10^{9}

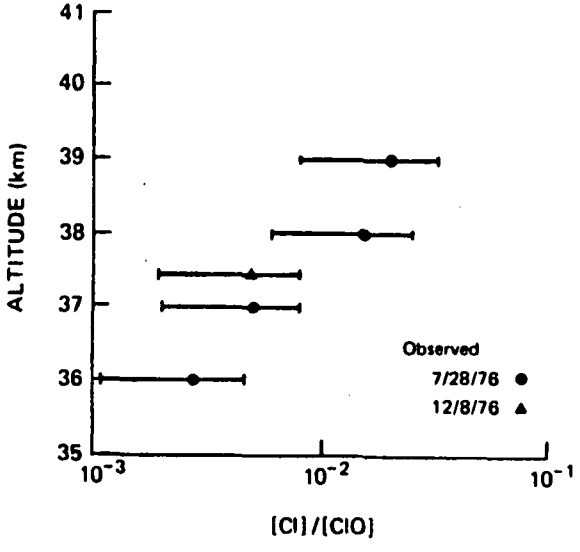

FIGURE D.6 Comparison between the observed and the calculated ratio of atomic chlorine to ClO (from Anderson et al. 1980).

Four remote sensing techniques and one in situ method have been employed from balloon platforms for the detection of HCl in the stratosphere. These include (1) high-resolution, middle infrared solar absorption (see, for example, Farmer et al. 1980, Zander 1980, Buijs et al. 1980); (2) mid-infrared emission (Bangham et al. 1980); (3) pressure-modulated infrared radiometry (Eyre and Roscoe 1977); and (4) far-infrared emission measurements with Fourier transform techniques (Chaloner et al. 1978). The only in situ method used thus far is the base impregnated filter collection method of Lazrus et al. (1977).

Results from those five data sets can best be summarized in two groups. First, the high-resolution middle infrared absorption data obtained by five independent research groups constitute a consistent data set that is reviewed in Figure D.7.

The uniformity of these middle IR results is not reflected in the survey of the other four methods, the results of which are reviewed in Figure D.8. In particular, the base impregnated filter data of Lazrus, which should provide an upper limit on [HCl], since any acidic chlorine compound should be collected, indicate significantly lower concentration in the critical 25- to 35-km altitude region. On the other hand, the pressure-modulated radiometer data lie considerably above the IR absorption data in the altitude region above 22 km. The far-infrared result of Traub lies below the band of middle IR absorption data, but well within the scatter of the results shown in Figure D.8.

Given the paramount importance of HCl in the total chlorine budget, and thus the need to understand in detail the distribution of HCl throughout the stratosphere, it is essential that those discrepancies be eliminated.

Hydrogen Oxychloride (HOCl)

Although HOCl has been searched for in the library of middle infrared sunset absorption data at 1238 cm^{-1} (D.G. Murcray, University of Denver, personal communication, 1981), no observable absorption has been found. This corresponds to an upper limit of 10 ppb at 25 km, which is approximately a factor of 1000 above current model predictions.

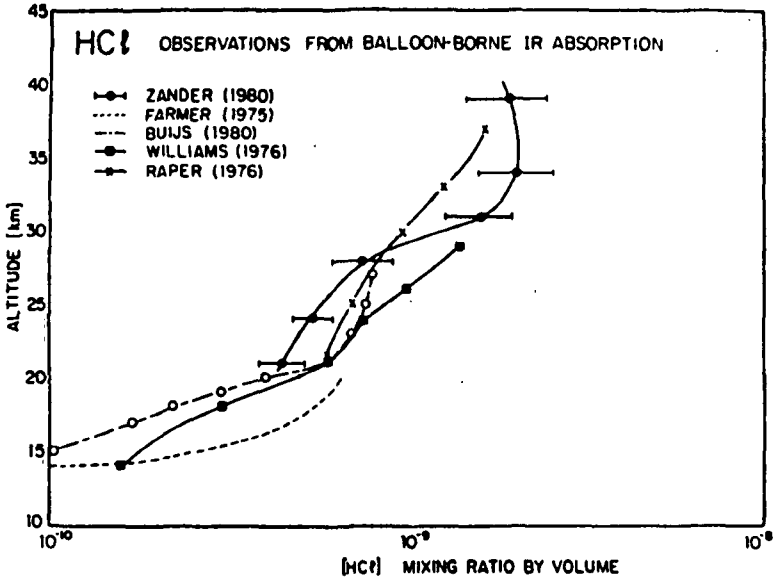

FIGURE D.7 HCl observations from balloon-borne IR absorption spectroscopy.

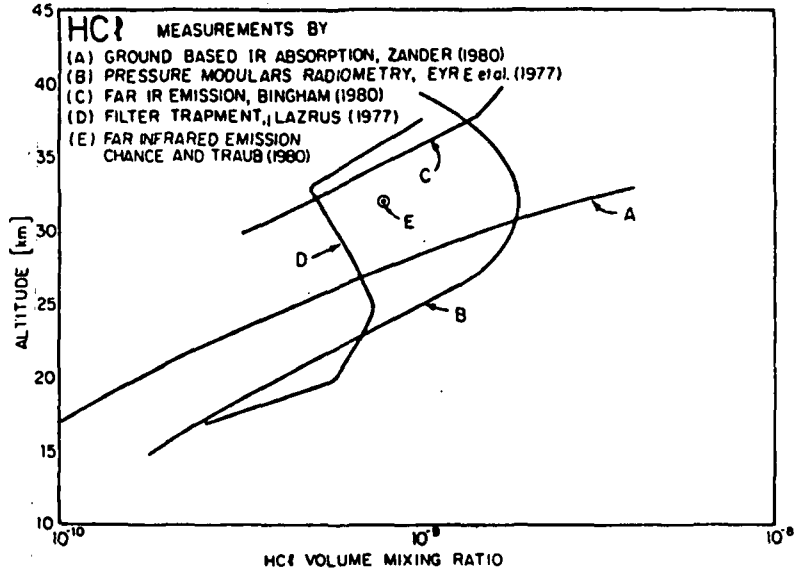

FIGURE D.8 HCl measurements by ground-based spectroscopy, pressure-modulated radiometry, far IR emission, and in situ filter collection.

The importance of HOCl to our understanding of stratospheric chlorine chemistry results from the fact that it is formed by the reaction,

$$HO_2 + ClO \rightarrow HOCl + O_2$$

and is thus a test of the coupling between the hydrogen and chlorine families. An unambiguous determination of its vertical concentration profile at low or middle latitudes would be of very significant value.

Chlorine Nitrate ($ClONO_2$)

A single observation of chlorine nitrate has been reported (see Murcray et al. 1979). As discussed in the WMO/NASA report (Hudson et al. 1982), the measurement is an exceedingly difficult one, given the broad nature of the $ClONO_2$ absorption feature and interferences from absorption bands of N_2O, CH_4, and H_2O that mask the chlorine nitrate feature. A review of these factors led the WMO/NASA panel to conclude that an upper limit of 1 ppb for $ClONO_2$ between 25 and 35 km was a defensible position at this time. Since the upper limit falls above current model predictions for chlorine nitrate in this altitude interval, the measurement cannot be used to establish whether isomers other than $ClONO_2$ are found in the recombination reaction,

$$ClO + NO_2 + M \rightarrow ClONO_2$$
$$\rightarrow \text{other isomeric forms.}$$

Group 2: Reactive Trace Species Containing Hydrogen

The Hydroxyl Radical (OH)

Hydroxyl has been observed in the stratosphere by four independent techniques noted in the chronological order of their application:

1. Solar flux induced resonance fluorescence observed by a rocket-borne spectrophotometer (Anderson 1971, 1975), which provides a local concentration measurement by determining the change in total column emission rates as a function of altitude.

2. Balloon-borne in situ molecular resonance fluorescence using a plasma discharge resonance lamp to induce fluorescence. The fluorescence chamber is lowered through the stratosphere on a parachute to control the altitude and velocity of the probe (Anderson 1975, 1980).

3. Ground-based high-resolution solar absorption by a PEPSIOS (Poly-Etalon Pressure Scanned Interferometer) instrument, which resolves a single rotational line in the (0-0) band of OH at 309 nm. The total column density of terrestrial OH between the instrument and the sun is observed and is dominated by the altitude interval of 25 to 65 km (Burnett 1976, 1977; Burnett and Burnett 1981).

4. Balloon-borne laser-induced detection and ranging (LIDAR) in which a pulsed laser system coupled to a telescope is used to observe the backscattered fluorescence from OH. The laser is tuned to the (0-1) band of the A-X transition at 282 nm and the fluorescence at 309 nm (the 0-0 band) is observed as a function of time following the laser pulse (Heaps et al. 1981).

Four methods have been employed for the detection of tropospheric OH:

1. Aircraft-borne laser-induced fluorescence wherein a contained atmosphere sample is passed through an enclosed detection chamber and is probed by a pulsed laser tuned to the (0-1) band of the A-X transition at 282 nm. Fluorescence is observed at 309 nm (Davis et al. 1976, 1979).

2. Aircraft-borne laser-induced fluorescence using an "open" optical arrangement in which a telescope is used to observe the backscattered fluorescence outside the boundary layer of the fuselage, but in the near vicinity of the aircraft (Wang et al. 1981).

3. Measurements of carbon 14 labeled CO oxidation rates by OH in which the sample is drawn into a Teflon-coated vessel of 10-liter volume. All reported observations were taken in the boundary layer (Campbell et al. 1979).

4. Long path (7.8 km) absorption of laser radiation at 308 nm (the Q(2) line of the $A^2\Sigma^+$, $v = 0$, $x^2\Pi v = 0$ transition). The experiment employs a double pass (3.9 km per leg) optical arrangement in which the beam is returned by a spherical mirror to a double monochrometer located at the laser (Perner et al. 1976).

Although the subject of tropospheric OH is one of central importance to the photochemical structure of the atmosphere, it cannot be dealt with in adequate detail in this document. We extract from the above work, and from tropospheric lifetime studies of methyl chloroform (see Logan et al. 1981 and references therein) that the tropospheric contribution to total column OH does not exceed 5×10^{12} cm^{-2} and is thus a negligible contribution to the total OH column density measured from the ground.

Restricting the discussion to stratospheric OH, we first review the comparison between the in situ observations and the ground-based total column measurements; second, we summarize a considerable body of new information taken from the recent ground-based observations of Burnett and Burnett (1981).

For the purpose of summarizing the in situ results, Figures D.9, D.10, and D.11 present a three-panel display of (a) the upper stratosphere-mesosphere rocket data from Anderson (1975); (b) the stratosphere balloon data using in situ resonance fluorescence (Anderson 1980); and (c) a composite of the two data sets with an upper limit on the mean tropospheric OH concentration taken from the methyl chloroform lifetime studies and the tropospheric laser experiments noted above.

We note several features of the profile that will be referred to throughout this section. First, the total column concentration of OH determined from an integral of the in situ observations and an estimate of the upper mesospheric profile is 6.9×10^{13} cm^{-2}. The fractional contribution to this figure for each 15 km interval between 0 and 90 km is given in Table D.3. Second, the altitude interval over which the balloon and rocket data extend, 30 to 70 km, encompasses all but 13 percent of the total column concentration so that ground-based observations provide an excellent cross check on the absolute concentration determined in situ. Third, within the region between 30 and 70 km, the dominant source is $O(^1D) + H_2O \rightarrow 2OH$, and the dominant loss is $OH + HO_2 \rightarrow H_2O + O_2$. Thus the in situ observations and the comparison between the integrated in situ data and the total column observations relate primarily to the balance between these two reactions and do not involve in a sensitive way the question of OH reactions with nitric acid and pernitric acid.

Although the ground-based data will be discussed in detail in the remainder of this section, we extract from

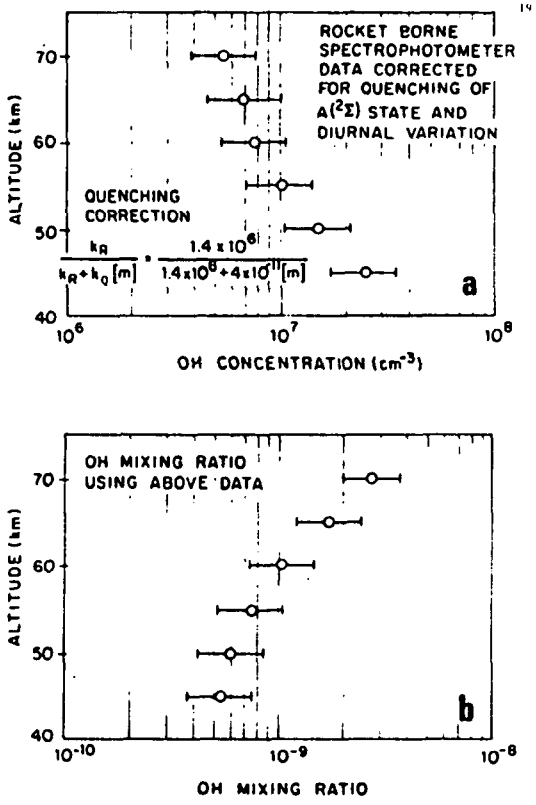

FIGURE D.9 (a) Concentration and (b) mixing ratio of OH in the upper stratosphere and mesosphere obtained by rocket-borne spectrophotometer (Anderson 1975). Data are corrected for collisional deactivation (see German 1975, 1976) and for diurnal behavior (see Logan et al. 1978). Zenith angle at time of rocket flight was 86°; data are corrected to midday steady state condition.

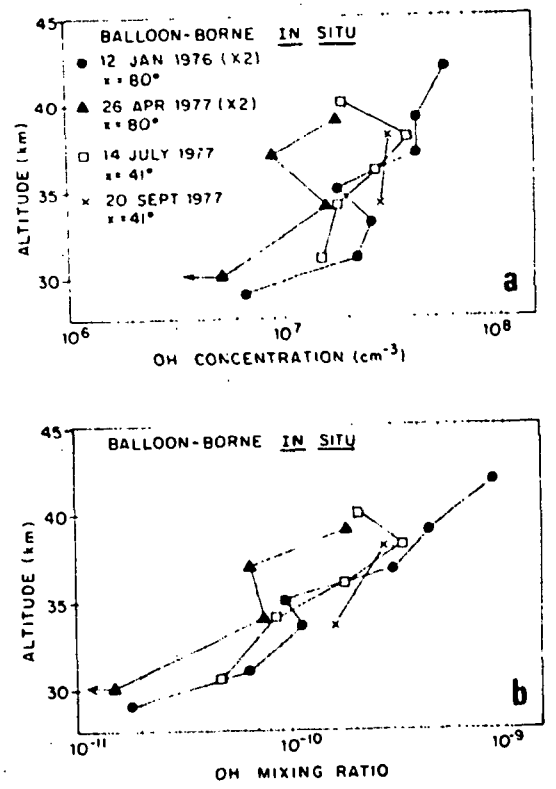

FIGURE D.10 (a) Concentration and (b) mixing ratio of stratospheric OH obtained in situ by molecular resonance fluorescence within a chamber lowered through the stratosphere at a controlled velocity on a parachute (Anderson 1980).

that discussion the key quantity for comparison with the in situ data, the total column density of OH observed by the PEPSIOS and reported in Burnett and Burnett (1981). Based on a total of 270 observing days extending from December 1976 to December 1979, the midday abundance of OH averaged over all seasons is 5.7×10^{13} cm^{-2}. All reported PEPSIOS observations were done at Fritz Peak, Colorado, 40°N latitude. Given the cited uncertainty of the in situ observations of ±30 percent and of the total column observations of ±25 percent, the observed absolute concentrations summarized in Table D.4, are consistent.

We turn next to a more detailed discussion of the ground-based observations recently reported in Burnett and Burnett (1981). As previously noted, all ground-based observations of OH were made from Fritz Peak Observatory, west of Boulder, Colorado, at 40°N latitude. All observations were taken between a solar zenith angle of 70° following sunrise through noon to a zenith angle of 70° prior to sunset. The period of observation was from 1976 to 1979, with a total of 270 observing days, which yielded 900 data sets with equal to or less than one-hour time resolution. The diurnal behavior of the column density was fit to a curve in sec χ, which is characterized by an overhead sun maximum of 7.1×10^{13} cm^{-2} decreasing to 4.9×10^{13} cm^{-2} at sec $\chi = 2$ (solar zenith angle 60°). Midday abundance averaged over all seasons is 5.7×10^{13} cm^{-2}. The following systematic departures from the mean were observed:

1. An annual increase of 1×10^{13} cm^{-2} in total column.
2. A gradual decrease of about 25 to 30 percent between spring and fall.
3. Diurnal oscillation observed with systematic changes of 30 to 40 percent that show a clear solar flux dependence on both a diurnal and an annual basis.

The observed and predicted diurnal behavior of total column OH with respect to shape and absolute magnitude is summarized in Figure D.12. A representative data set is also shown in Figure D.13, indicating the scatter about the mean.

Burnett and Burnett (1981) briefly discuss both an annual and a seasonal departure from the reported mean values. We consider first the observed year-to-year trends.

TABLE D.3 Contribution of Each Altitude Interval to the Integrated Column

Altitude Interval	Contribution to Total Integral	Fraction of Total Integral	Integrated Column Density
0-5	1.5×10^{12}	0.02	
15-30	3.4×10^{12}	0.05	
30-45	3.2×10^{13}	0.46	6.9×10^{13} cm^{-2}
45-60	1.9×10^{13}	0.28	
60-75	8.8×10^{12}	0.13	
75-90	4.3×10^{12}	0.06	

TABLE D.4 Summary of the Comparison Between the Integrated *In Situ* Results from Balloon and Rocket Data and the Ground-Based Total Column Observation

Composite of the *In Situ* OH Data	Ground-Based Total Column OH
6.9×10^{13} cm^{-2}	5.7×10^{13} cm^{-2}
Uncertainty: ±40 percent	Uncertainty: ±25 percent
Conditions: Midday, 32°N	Conditions: Midday, 40°N

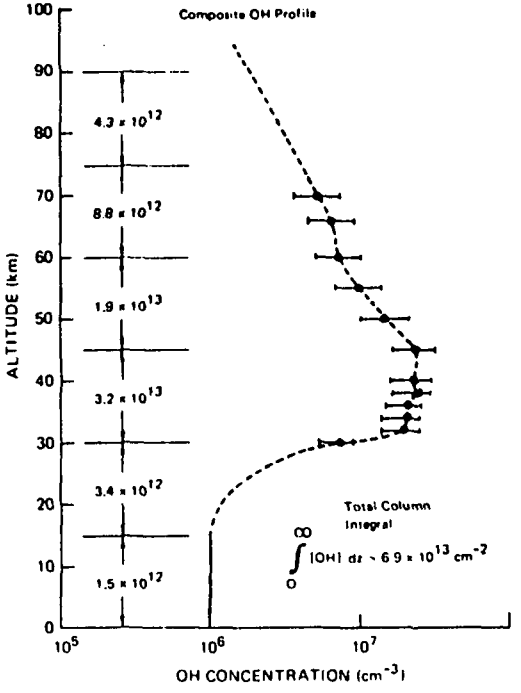

FIGURE D.11 Composite of OH profile.

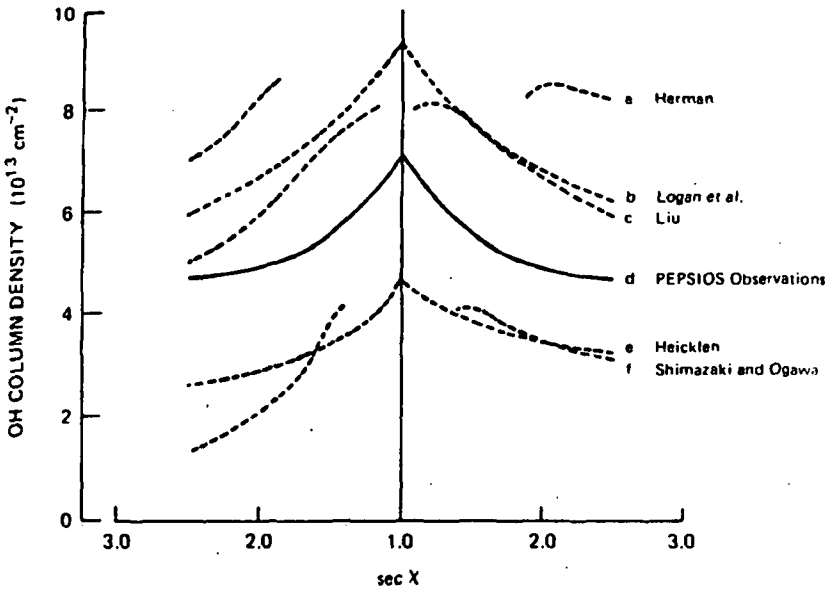

FIGURE D.12 The correlation between OH total column density and solar zenith angle expressed as sec X comparing the observed and modeled behavior (from Burnett and Burnett 1981).

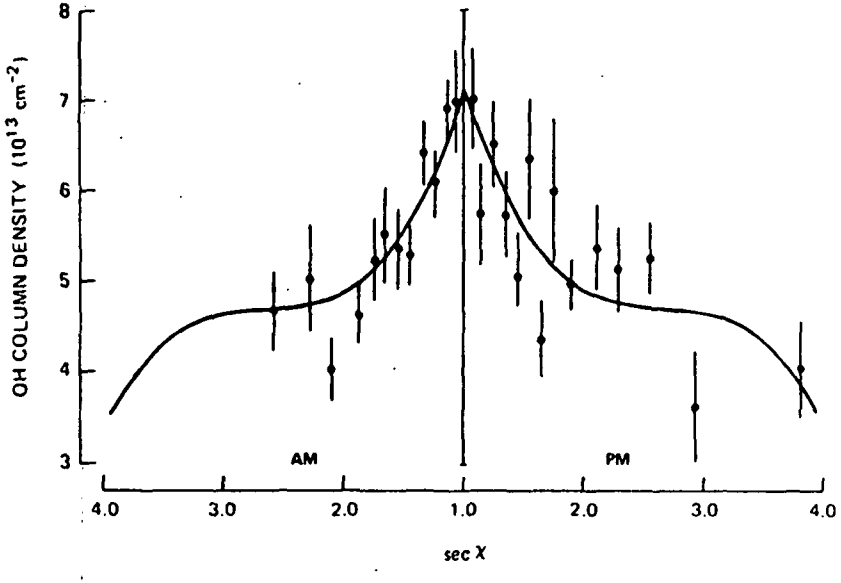

FIGURE D.13 An indication of the scatter about the mean of individual observations taken with the ground-based PEPSIOS (from Burnett and Burnett 1981).

A reanalysis of the December 1976 data (from Burnett 1977) using more advanced methods for baseline determination established 3.1 ± 0.6 x 10^{13} cm^{-2} for a midday mean. In Figure D.14, the evolution of the monthly mean from December 1976 to December 1979 is summarized. There is an apparent increase of approximately 1 x 10^{13} cm^{-2} per year during that three-year period. Correlating such an increase to the 11-year solar cycle was suggested by Burnett and Burnett (1981), but such a dramatic change seems difficult to rationalize and will require more extensive data coverage and a far more thorough analysis of solar cycle flux variations with an associated mechanistic hypothesis before it can be accepted.

The seasonal behavior in the total column of OH is a recurring and extremely interesting feature of the data in Figure D.14. There is the clear suggestion of a springtime maximum in OH and a fall minimum. One very important advantage to be gained from a more extensive geographic coverage with such ground-based observations would be an examination of this seasonal behavior as a function of latitude. The correlation of the dependence with other constituents such as O_3, H_2O, NO_2, and ClO would be of significant importance.

An unexpected and as yet unexplained aspect of the ground-based observations involves the appearance, particularly in the summer 1978 data set, of a zenith angle dependent pattern exemplified in Figure D.15. In particular, there is a distinct minimum in the observed column following local noon. The early afternoon decrease shows an abrupt drop of 4.5 x 10^{13} cm^{-2} with a subsequent increase of 3.5 x 10^{13} cm^{-2} followed by the conventional decrease into sunset. This feature has lead to a careful critique of the data by the authors, who believe that it is not an artifact of the data reduction or of instrumental performance. The oscillatory behavior shown in Figure D.15 persisted into the late summer of 1978, but was not apparent in the 1979 data set, which was taken with the same instrument at the same site using the same data reduction method. There was also a systematic progression of the position of the maximum and minimum as the 1978 season progressed.

In summary, an analysis of (a) balloon and rocket data on OH in the stratosphere and (b) ground-based total column observations provide the following conclusions:

1. There is substantial agreement among the three techniques; the in situ data provide a consistent picture

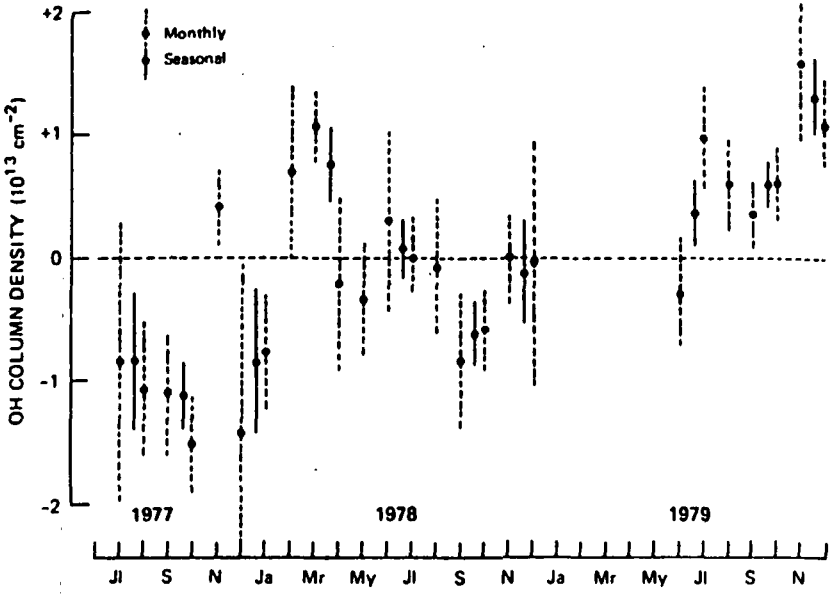

FIGURE D.14 Summary of the observed fluctuations in OH total column measured from the ground.

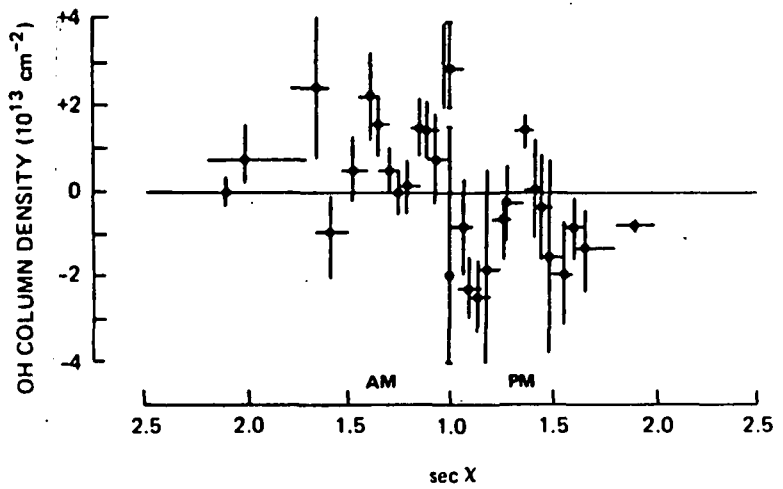

FIGURE D.15 Typical example of the oscillatory diurnal behavior of the OH total column, which was a characteristic signature of the summer 1978 data and does not appear to be an instrumental artifact (from Burnett and Burnett 1981).

of the altitude dependence of [OH] between 30 and 70 km, implying a peak concentration at 40 km of 2.4 x 10^7 cm^{-3} and a total column density at midday of 6.9 x 10^{13} cm^{-2}. The midday total column abundance determined from the ground is 5.7 x 10^{13} cm^{-2}, as summarized in Table D.4.

2. There is a systematic increase of approximately 1 x 10^{13} cm^{-2} per year between December 1976 and December 1979 and a suggestion of a yearly spring maximum and fall minimum. The spring-to-fall decrease is approximately 30 percent.

3. It is clear that knowledge of the OH distribution between 15 and 30 km, which is absent, is of the highest priority. This need results not only from the fact that HO_x becomes an increasingly important component of the odd oxygen destruction rate below 30 km, but also because the photochemical partitioning of chlorine and nitrogen depends currently on the OH concentration.

The Hydroperoxyl Radical (HO_2)

Two techniques thus far have been used for the detection of HO_2 in the stratosphere:

1. Balloon-borne cryogenically captured matrix isolation followed by laboratory detection of HO_2 by EPR methods. The experiment is carried out by drawing a stratospheric sample into an evacuated flask, collecting the sample on a "cold finger" at a given balloon float altitude, closing the flask, and returning it to the laboratory for analysis (Mihelcic et al. 1978).

2. Balloon-borne chemical conversion-molecular resonance fluorescence detection wherein HO_2 is converted to OH by the rapid bimolecular reaction $HO_2 + NO \rightarrow OH + NO_2$. The product OH is then detected by molecular resonance fluorescence using a microwave-sustained plasma discharge lamp to induce fluorescence in the (0-0) band of the $A^2\Sigma$-$X^2\Pi$ transition at 309 nm. Chemical conversion and detection are done within a chamber lowered through the stratosphere at a controlled velocity on a parachute (Anderson 1980, Anderson et al. 1980).

A total of four HO_2 observations have appeared in the literature, one by the matrix isolation technique, and three by the resonance fluorescence method. Those

observations are summarized in Table D.5, in chronological order.

As noted in Table D.5, the Mihelcic sample collection was initiated immediately following sunrise at a solar zenith angle of 85°. The conversion to midday for comparison with models and other observations was carried out using the diurnal calculation of Logan et al. (1978). That correction factor is significant--a factor of 2--and attempts to account for the period over which the sample was collected.

The data summarized in Table D.5 are presented graphically in Figure D.16. There is significant scatter evident in those observations that should not be attributed to atmospheric variability until (a) the signal-to-noise ratio of the observations is improved, and (2) simultaneous observations of photochemically related species such as OH or H_2O demonstrate a correlation in concentration fluctuations.

Atomic Hydrogen (H)

There are no reported observations of atomic hydrogen in the stratosphere. Although atomic resonance scattering can detect concentrations of H in the range of 10^5 cm^{-3}, current models predict a distribution shown in Figure D.17 so it is detectable only above 45 km.

Molecular Hydrogen (H_2)

Molecular hydrogen has received careful attention for more than 10 years. The most comprehensive work is that by Ehhalt and coworkers (see Ehhalt et al. 1977, Schmidt 1978, Schmidt et al. 1980). The tropospheric distribution is uniform with a slight interhemispheric asymmetry at the tropopause. The average mixing ratio in the northern hemisphere is 0.576 ppm by volume, and in the southern hemisphere 0.552 ppm.

Hydrogen Peroxide (H_2O_2)

The only reported observation of H_2O_2 is a tentative detection by Waters et al. (1981), which is noted here primarily to indicate that an analytical technique is under development that should provide empirical evidence

TABLE D.5 Summary of Experimental Parameters for the HO_2 Observations

	Altitude					Experimental Uncertainty
	37	35	33	31	29	
Mihelcic et al. (1980), Launch Date 8/8/76, Latitude 53°N, Solar Zenith Angle 85°						factor of 3
Observed NO_2 mixing ratio corrected to midday				1.0×10^{-10} [a]		
Anderson et al. (1980), Launch Date 9/20/77, Latitude 32°N, Solar Zenith Angle 41°						±45%
Resonance fluorescence $^SHO_2$	17	9	13	8	2	
HO_2 mixing ratio	7.1×10^{-10}	1.84×10^{-10}	8.5×10^{-11}	$\leq 8.0 \times 10^{-11}$	$<7.0 \times 10^{-11}$	
Detection threshold	1.1×10^{-10}	8.2×10^{-11}	7.0×10^{-11}	7.6×10^{-11}	6.4×10^{-11}	
Anderson et al. (1980), Launch Date 10/25/77, Latitude 32°N, Solar Zenith Angle 45°						±45%
Resonance fluorescence $^SHO_2$	3	3	9	5	–	
HO_2 mixing ratio	3.6×10^{-10}	8.7×10^{-10}	6.9×10^{-10}	2.1×10^{-10}	1.0×10^{-10}	
Detection threshold	1.6×10^{-10}	1.5×10^{-10}	1.5×10^{-10}	1.0×10^{-10}	1.0×10^{-10}	
Anderson et al. (1980), Launch Date 12/2/77, Latitude 32°N, Solar Zenith Angle 50°						±45%
Resonance fluorescence $^SHO_2$	33	25	20	22	16	
HO_2 mixing ratio	3.4×10^{-10}	2.3×10^{-10}	4.2×10^{-10}	3.4×10^{-10}	1.7×10^{-10}	
Detection threshold	8.1×10^{-11}	6.0×10^{-11}	4.6×10^{-11}	8.8×10^{-11}	8.7×10^{-11}	

[a] Datum taken at an altitude of 31.8 km.

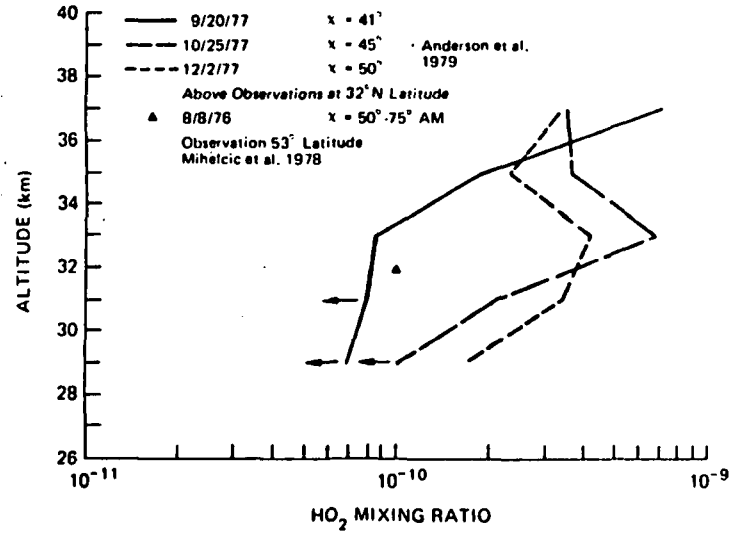

FIGURE D.16 The observed midday HO_2 mixing ratio from three in situ resonance fluorescence balloon flights (chemical conversion to OH followed by resonance fluorescence) and one in situ sample collection experiment (cryogenic sampling with EPR analysis).

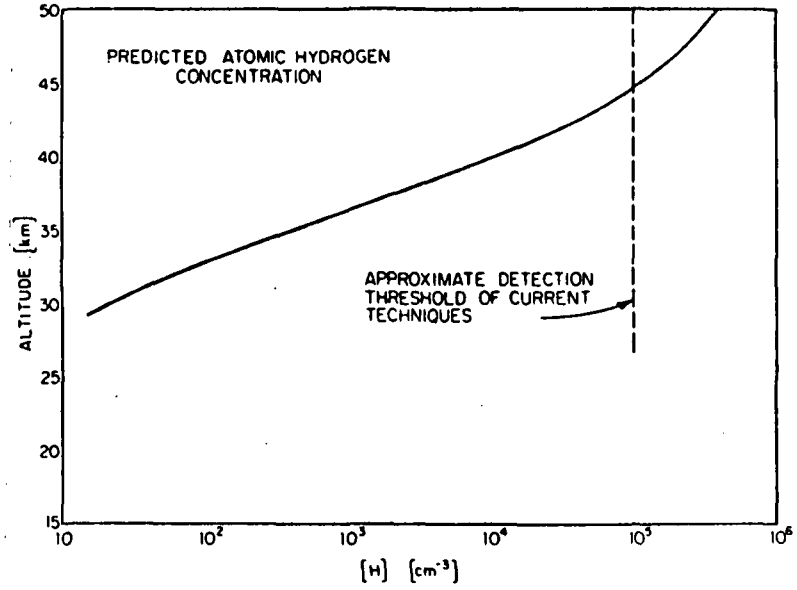

FIGURE D.17 Detection threshold of H atom experiment compared with predicted concentrations. H atom density is only approximate but parallels Cases 5 and 6 described in text.

in the near future (Figure D.18). Given that hydrogen peroxide is principally formed in the reaction

$$HO_2 + HO_2 \rightarrow H_2O_2 + O_2$$

and destroyed by photolysis, it constitutes an important component of HO_x chemistry and observational evidence is clearly needed.

Water Vapor (H_2O)

The subject of stratospheric H_2O is of sufficient size to preclude its treatment in this summary. The topic is, however, treated in considerable detail in Hudson et al. (1982).

Group 3: Oxygen

Atomic Oxygen in the Ground State ($O(^3P)$)

Atomic oxygen, $O(^3P)$, is of particular interest to the photochemistry of stratospheric ozone. First, it is believed to be in strict photochemical steady state with ozone through the rapid exchange reactions,

$$O_3 + h\nu \xrightarrow{J_{O_3}} O(^3P) + O(^3_2\Sigma)$$

$$\rightarrow O(^1D) + O_2(^1\Sigma)$$

$$O(^1D) + M \rightarrow O(^3P) + M$$

$$O(^3P) + O_2 + M \xrightarrow{k_1} O_3 + M$$

such that the ratio

$$[O(^3P)]/[O_3] = J_{O_3}/k_1[M][O_2]$$

should be obeyed throughout the stratosphere. Second, atomic oxygen is the reactive partner with ozone in the direct recombination step,

$$O(^3P) + O_3 \rightarrow O_2 + O_2,$$

which establishes the rate of odd oxygen destruction apart from any catalyzed recombination. Third, atomic oxygen is the odd oxygen reactant in virtually all catalytic rate limiting steps in the middle and upper stratosphere.

There are six reported observations of $O(^3P)$ in the stratosphere, all obtained using balloon-borne, parachute descent, in situ atomic resonance (Anderson 1980). These results are given in Figure D.19.

Several points are readily apparent from Figure D.19. First, there is both local structure within and absolute displacement among observed distributions that exceed, respectively, the precision and accuracy of the measurements. It should also be noted that the local structure does not consistently appear. For example, the profiles observed on October 25, 1977, and December 2, 1977, display a small degree of local structure, typically less than ±20 percent variation over an interval of ±1 km above approximately 34 km. Below that altitude, significantly greater local structure is apparent, though seldom more than ±50 percent. On the other hand, the remaining four observations exhibit at least one example of major (factor of 2) variation over a ±2-km interval with an increasing structural development below the 33- to 35-km interval. Although this local structure makes a detailed profile-by-profile comparison with modeled distributions difficult, a comparison with the mean of the observed $O(^3P)$ distribution can be made. Thus, in Figure D.20, we display the observed mean.

Atomic Oxygen in an Excited State ($O(^1D)$)

There are no reported observations of $O(^1D)$ in the stratosphere.

Singlet Delta Molecular Oxygen ($O_2(^1\Delta)$)

Although there are currently no known reaction mechanisms that involve $O_2(^1\Delta)$, its predicted concentration, substantiated by a limited number of rocket observations, is such that its number mixing ratio reaches 1 ppm at 50 km (dropping by 2 orders of magnitude in the interval between 50 and 35 km), and it is thus a potentially impor-

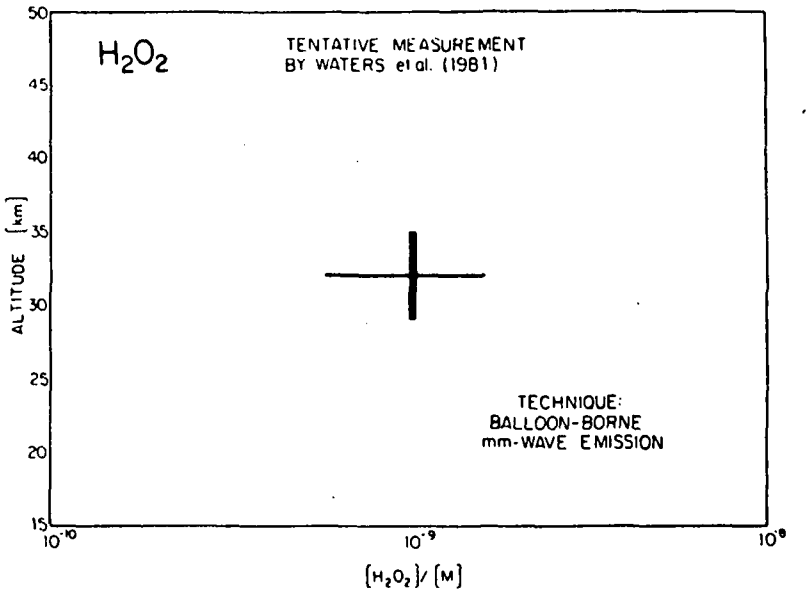

FIGURE D.18 Tentative measurement of H_2O_2 by Waters et al. (1981) using balloon-borne mm-wave emission techniques.

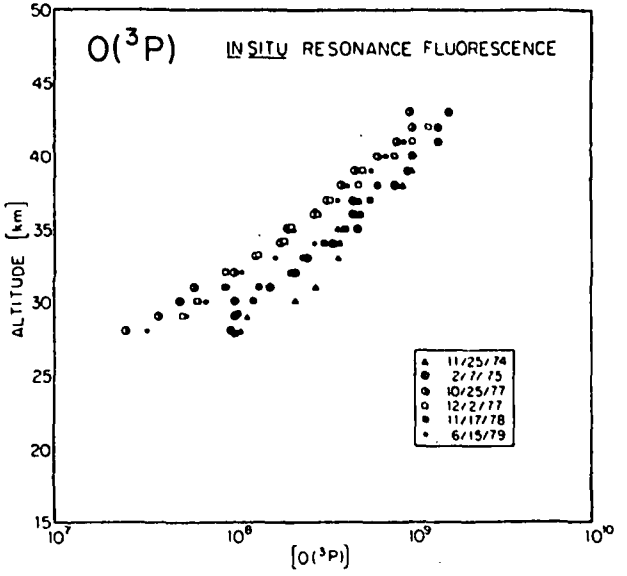

FIGURE D.19 Summary of the in situ $O(^3P)$ data obtained by atomic resonance fluorescence methods (Anderson 1980).

tant minor species. Numerous rocket measurements of the infrared atmospheric system of $O_2(^1\Delta)$ have been made and interpreted in terms of $O_2(^1\Delta)$ concentrations. Most of these are mesospheric and auroral studies, and only a few are applicable to the stratosphere. Two rocket measurements of the day airglow in the 1.27-μm band with a rocket photometer are shown in Figure D.21 (Evans and Llewellyn 1970). They are in essential agreement. Aircraft measurements (Noxon 1968) and balloon measurements (Evans et al. 1969) of the integrated dayglow intensity are in agreement with these rocket measurements. Below 30 km, new balloon ascent measurements would be required to obtain good estimates of $O_2(^1\Delta)$ concentrations. New measurement techniques such as photoionization mass spectrometry could be applied. $O_2(^1\Delta)$ is produced by ozone photolysis and resonance phosphorescence, is quenched by molecular species, and is reasonably simple to model.

Singlet Sigma Molecular Oxygen ($O_2(b^1\Sigma)$)

The $O_2(b^1\Sigma)$ state contains nearly 2 eV of excess energy over the $^3\Sigma$ ground state, but $O_2(b^1\Sigma)$ is not involved in any known reaction of stratospheric significance. Interest in its vertical distribution has been confined to auroral regions; there are few measurements applicable to the stratosphere. Results of the only relevant rocket measurements by Wallace and Hunten (1968) are given in Table D.6. The observations have a large radiative transfer correction; hence the concentrations of $O_2(b^1\Sigma)$ below 50 km are quite uncertain. Balloon ascent measurements would be required to obtain more accurate data. The main production processes are $O(^1D)$ energy transfer and resonance fluorescence.

Other Electronically Excited States of Molecular Oxygen (O_2^*)

There are no known observations of $O_2(^3\Delta_u)$, $O_2(^3\Sigma_u^+)$, or $O_2(^1\Sigma_u^-)$ in the stratosphere. These electronically excited states of O_2 contain approximately 4.5 eV in energy above that in the $^3\Sigma_g^-$ ground state, and are thus of potential importance to all of the free radical reactions in the stratosphere. The quantum

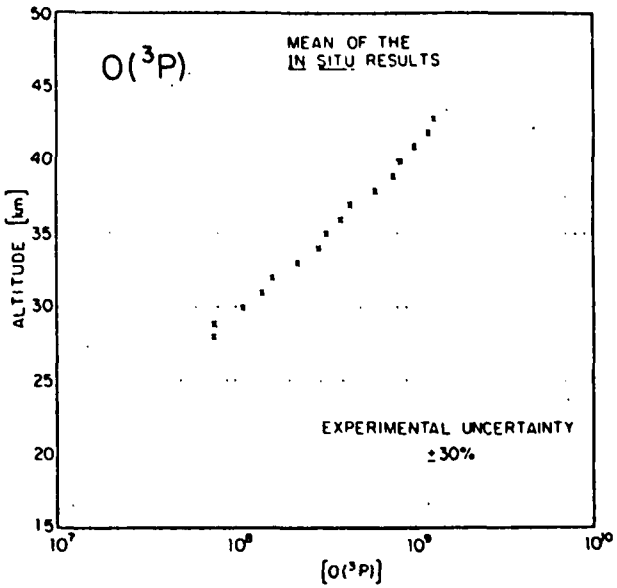

FIGURE D.20 Mean of the six in situ $O(^3P)$ observations displayed in Figure D.19.

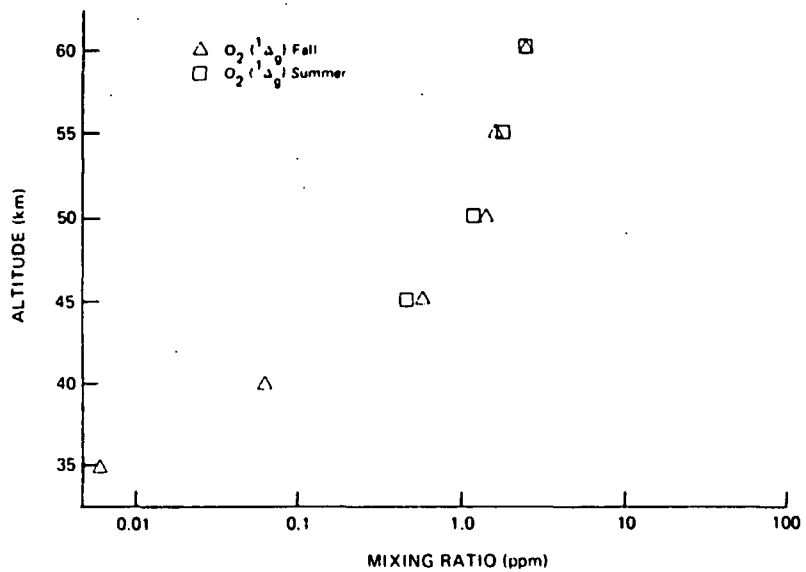

FIGURE D.21 Fall and summer profiles of $O_2(^1\Delta g)$. The uncertainty estimate is ±20 percent (Evans and Llewellyn 1970).

TABLE D.6 Data Reported by Wallace and Hunten (1968) from a Rocket-Borne Spectrometer Flown on October 11, 1966, at a Solar Zenith Angle of 75.5° and at a Latitude of 33°N

Molecule (State)	Concentration at Altitude (cm^{-3})					
	35 km	40 km	45 km	50 km	55 km	60 km
$O_2(^1\Sigma)$	0.4×10^5	0.5×10^5	1.8×10^5	1.8×10^5	1.6×10^5	1.2×10^5

yields from O_3 photolysis, collisional deactivation rates, and reaction rates are, however, unknown.

Ozone (O_3)

Although the sheer volume of ozone data prevents a comprehensive review of the subject in this document (see Hudson et al. 1982), new in situ results using three different techniques have recently become available. Those observations are of critical importance to the subject of trace species observations, for they signify the arrival of highly accurate (and precise) in situ methods that have sensitivity and altitude resolution sufficient for detailed analysis of those factors controlling the local production and destruction rates of odd oxygen as a function of altitude.

Two of the techniques have been cross-calibrated by flying the instruments on the same gondola on three separate occasions. Those results, obtained with an open source mass spectrometer and a modified Dasibi ultraviolet absorption experiment at Palestine, Texas, 32°N latitude, are presented in Figure D.22 (Mauersberger et al. 1981). The altitude resolution is better than 0.5 km for the UV absorption method, and is approximately 1 km for the mass spectrometer.

A third technique, using a "White cell" to amplify absorption within a confined volume has been developed by Anderson and coworkers, and was flown in June 1981 from Palestine, Texas. That experiment provides a vertical resolution of about 30 m with a signal-to-noise ratio greater than 100. Those results are compared with the Mauersberger et al. (1981) profile obtained at the same location and season in Figure D.23.

These data provide the opportunity to examine the ratio of $O(^3P)$ to O_3 between 28 and 40 km. Those

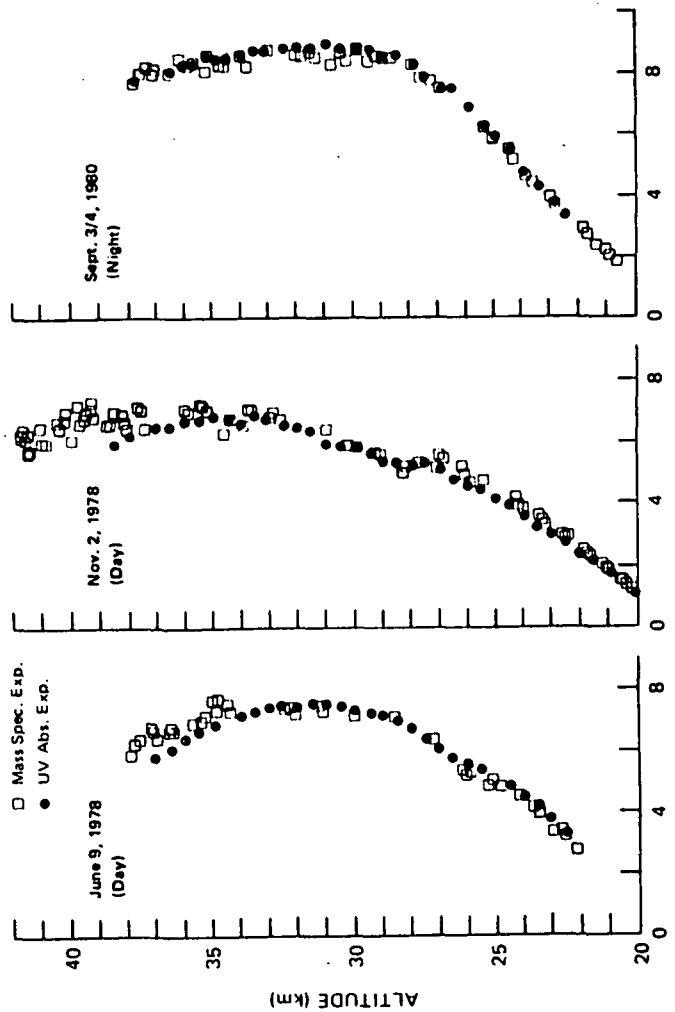

FIGURE D.22 A comparison of ozone volume mixing ratios measured simultaneously during balloon descent by the mass spectrometer beam experiment and UV absorption instrument (Mauersberger et al. 1981).

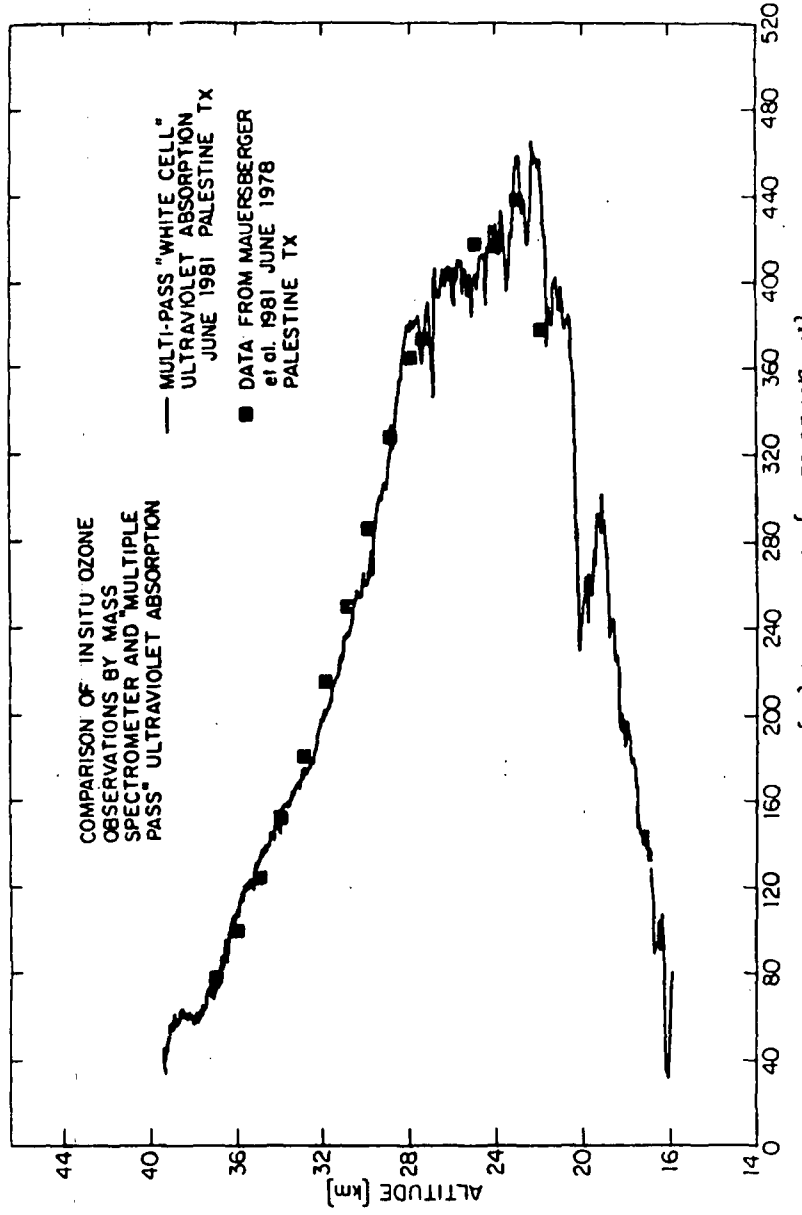

FIGURE D.23 Comparison between the in situ multipass "White cell" data and the in situ mass spectrometer data.

results will be discussed at the end of the section on the relationships between observational data and predictions of models.

Group 4: Reactive Trace Constituents Containing Nitrogen

Nitric Oxide (NO)

Concerns raised nearly 10 years ago about stratospheric ozone depletion resulting from supersonic transport flights above the tropopause placed early emphasis on measurements of NO and NO_2 in the stratosphere. NO has emerged as the most extensively studied radical in the stratosphere in terms of the variety of techniques applied, the number of observations reported, and the latitude coverage available. A critique of the nitric oxide data base is thus not a question of interpreting a limited number of observations, but rather a problem of selecting those observations that (a) are of demonstrated analytical quality, and (b) are useful for testing hypotheses in the chemical reaction schemes used in the stratospheric models.

We adopt here an approach that closely parallels that taken by the WMO/NASA review committee on trace species: Only those data on NO will be accepted that have been obtained by research groups who have repeatedly applied the method and have done the laboratory calibration tests required for a defensible absolute calibration.

Measurement techniques for NO can be separated into the usual categories of in situ and remote. Remote absorption techniques, however, are of little value for a detailed comparison with model calculations because remote techniques are confined to the period at and immediately following sunset/sunrise because of the very small optical depth of NO. NO is rapidly converted to NO_2 at sunset by the reaction

$$NO + O_3 \rightarrow NO_2 + O$$

and reformed rapidly from NO_2 by the direct photolysis

$$NO_2 + h\nu \rightarrow NO + O$$

at sunrise. Emission techniques in the infrared need not suffer from this problem, but there is an insufficient

data base for these methods to warrant selection at this time. For an extensive treatment of this subject, the reader is referred to the WMO/NASA report (Hudson et al. 1982).

We are left, therefore, principally with in situ measurements to test the model-calculated NO height profile under midday conditions. Several techniques have contributed significantly to the in situ data base: balloon-borne chemiluminescence (Ridley and Howlett 1974, Drummond et al. 1977, and an extensive series of reports by Ridley and co-workers), aircraft chemiluminescence (see Loewenstein et al. 1978a,b and references therein), rocket-borne chemiluminescence (Horvath and Mason 1978), photoionization mass spectroscopy (Aiken and Maier 1978), spin flip laser absorption (Patel et al. 1974), and balloon-borne pressure-modulated radiometry (Chaloner et al. 1978).

Since the techniques listed above have not been cross-calibrated to isolate unknown systematic instrumental discrepancies, on the one hand, we must explore the overall consistency of the data sets, but on the other, any detailed analysis of vertical profiles is most effectively approached by considering a given set of internally consistent results. We simply note, therefore, that within the quoted experimental uncertainties of the observations there are no large discrepancies, but only one data set is extensive enough to warrant detailed consideration with respect to the vertical profile of NO in the stratosphere, the work of Ridley and co-workers (Roy et al. 1980, Ridley and Schiff 1981, Ridley and Hastie 1981).

The observations of particular interest are a series of six flights made with a chemiluminescence instrument that incorporated direct in-flight calibration procedures to eliminate the possibility of heterogeneous removal in the inlet/chamber section of the instrument. The excellent internal consistency of the data set is evident in Figure D.24.

Note, in particular, the nearly coincident half-filled symbols, which represent data gathered from three different flights at 32°N in the fall, but in two different years. Also, the data taken in two flights at nearly identical latitude in the southern hemisphere and equivalent season are only slightly lower than the corresponding northern hemisphere results. As noted in Hudson et al. (1982), since differences between the results of the flights are very nearly equal to variations

within any one of the flights, the data present no evidence of systematic patterns over the ranges of season, latitude, and hemisphere. However, it is essential to caution against extracting statistically significant conclusions from but six observations. What can be concluded, however, is that very significant progress has been made in the analytical area: high-quality in situ observations of NO are technically feasible.

It will become apparent when attempting to use these data, that differences between profiles of a factor of 2 are of considerable importance when applying the NO results to modeled distributions. Thus, in anticipation of this, we replot the data points from Figure D.24 with higher resolution in the abscissa; those results are given in Figure D.25 in terms of absolute calibration.

This is the data set that will be used later to determine whether the NO_x data set provides a quantitative constraint on predictions of ozone depletion resulting from changes in N_2O.

We can quickly summarize the conclusions extracted from a consideration of the other data on NO in Figure D.26, which presents the range of observed NO as a banded region extending from the tropopause to the lower-middle stratosphere.

Diurnal Variation of NO. The qualitative features that one would expect for the diurnal behavior of NO based upon the current mechanistic links partitioning the reactive nitrogen family, as summarized in the flow diagram of Figure D.27, have been confirmed:

- NO decays following sunset at a rate comparable to that expected from the conversion to NO_2 via

$$NO + O_3 \rightarrow NO_2 + O_2.$$

- NO increases rapidly at sunrise as one would expect from the direct photolysis of NO_2
- NO increases slowly throughout the day consistent with the formation of $NO + NO_2$ from the back conversion of N_2O_5, which serves as a temporary reservoir.

The most extensive set of diurnal observations is from the in situ studies of Ridley and co-workers using balloon-borne chemiluminescence. The sunset measurements (Ridley and Schiff 1981) are shown in Figure D.28, and an analogous data set for sunrise is shown in Figure D.29.

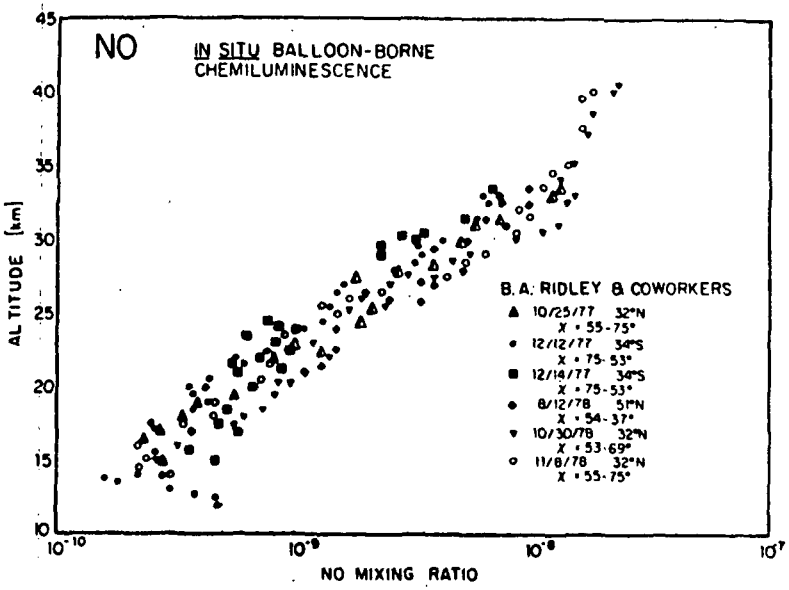

FIGURE D.24 Summary of six in situ NO observations by Ridley and co-workers obtained with a chemiluminescent probe (Roy et al. 1981, Ridley and Schiff 1981, Ridley and Hastie 1981).

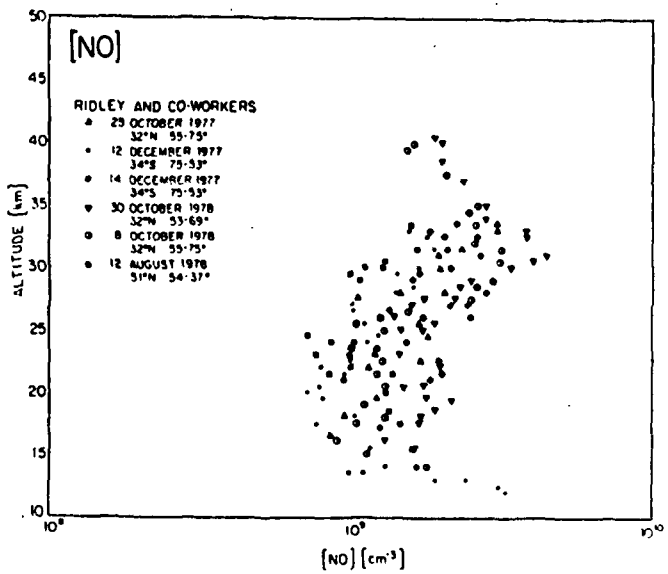

FIGURE D.25 Nitric oxide data of Figure D.24 converted to absolute concentration.

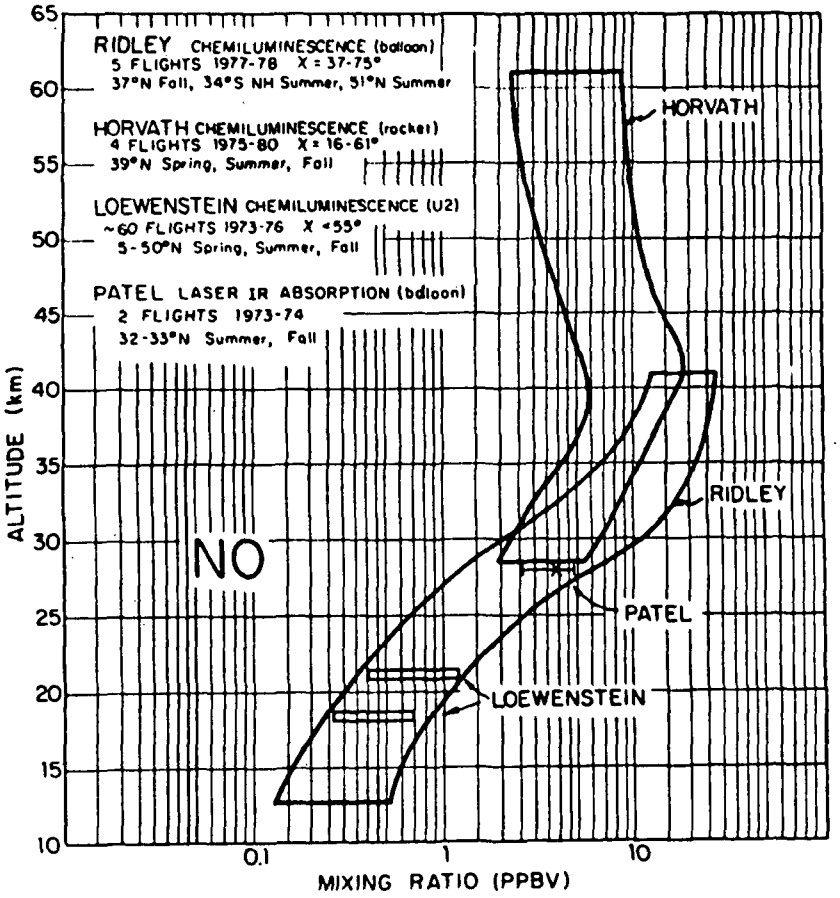

FIGURE D.26 In situ NO mixing ratio measurements reported by four research groups, which encompass the stratosphere and mesosphere.

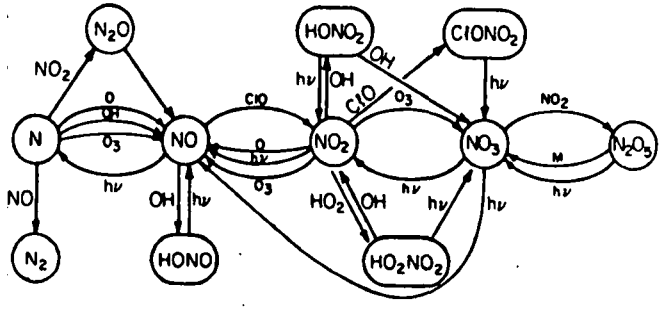

FIGURE D.27 Partitioning of the reactive nitrogen family.

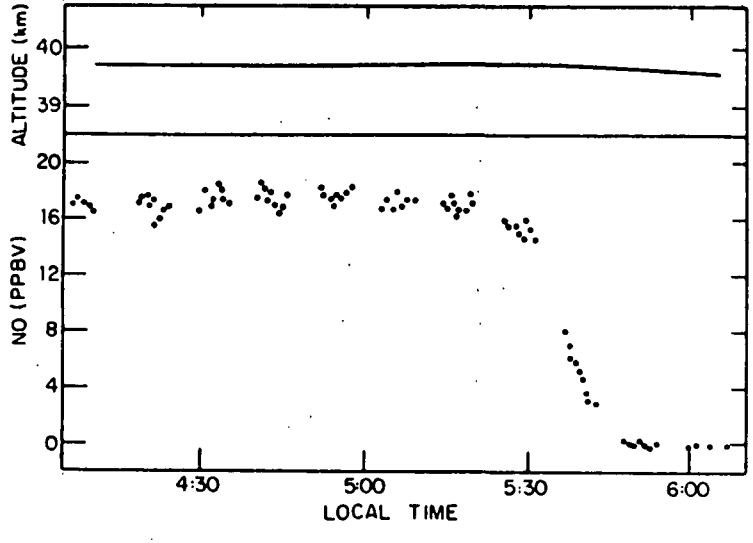

FIGURE D.28 Sunset observation of NO determined in situ by Ridley and Schiff (1981).

The sunrise data were obtained in 1975, before the improved inlet and calibration procedures were added, but the asymptote in the NO mixing ratio is consistent with that obtained by the improved analytical techniques, so the temporal behavior is almost certainly representative. The detail revealed by those two data sets is superb and demonstrates in principle how such data can be used to test rates of production and destruction within any given chemical mechanism.

Patel et al. (1974) have employed the laser Raman spin flip technique to the NO diurnal dependence. The results, not inconsistent with those presented above, are discussed in Hudson et al. (1982).

What these diurnal data do make clear is that the rapid fall off of NO at sunset obviates the possibility of using long-path absorption techniques for detailed measurements of nitric oxide.

Nitric Oxide Seasonal Variability. There is currently an insufficient data base on NO to establish any statistically meaningful seasonal dependence. However, the aircraft measurements of Loewenstein et al. (1978b) at 18 and 21 km extending over a period of four years have revealed two significant effects. The first is a rather sharp winter minimum that lasts just 2 to 3 months at 40°N latitude in the vicinity of 21 km. The second is a rather broad summer maximum that exhibits a duration of 7 to 8 months at 40°N, 21-km altitude. The observations are summarized in Figure D.30. A similar trend has been found at 18 km, although fewer data are available at that altitude.

Given that the observed winter minimum is a factor of 3 to 4 lower than the summer maximum, clearly exceeding the cited uncertainties and demonstrated reproducibility of the balloon-borne chemiluminescent technique, it is unfortunate that vertical profiles of NO at 40°N during December and January are not available. A great deal could be learned from such a data set. Vertical column (integrated) measurements of NO from aircraft (Coffey et al. 1981) include higher ratios of NO in summer than in mid-February by a factor of 1.4. However, as Figure D.30 reveals, the deep minimum occurs before mid-February. In addition, the almost certain altitude dependence of the effect may well erode the vertically integrated effect.

It is crucial to point out that such a deep, short-lived minimum presents an excellent opportunity to carry out diagnostic experiments to elucidate response of the

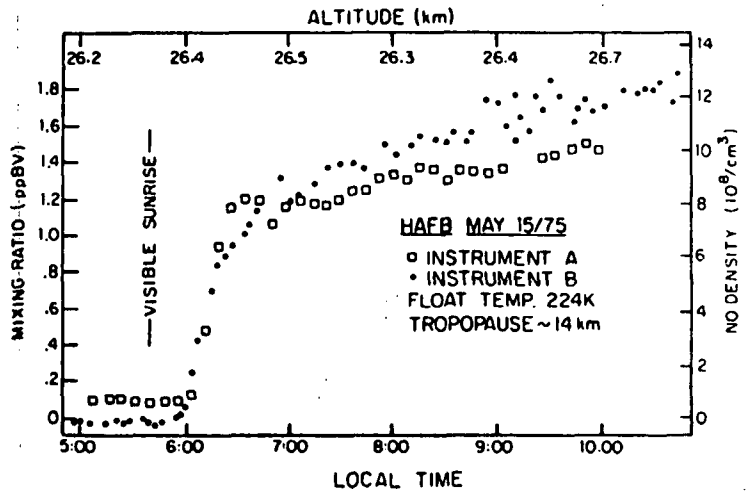

FIGURE D.29 Sunrise in situ measurements of NO by Ridley using two chemiluminescent instruments on a balloon platform at 33°N latitude.

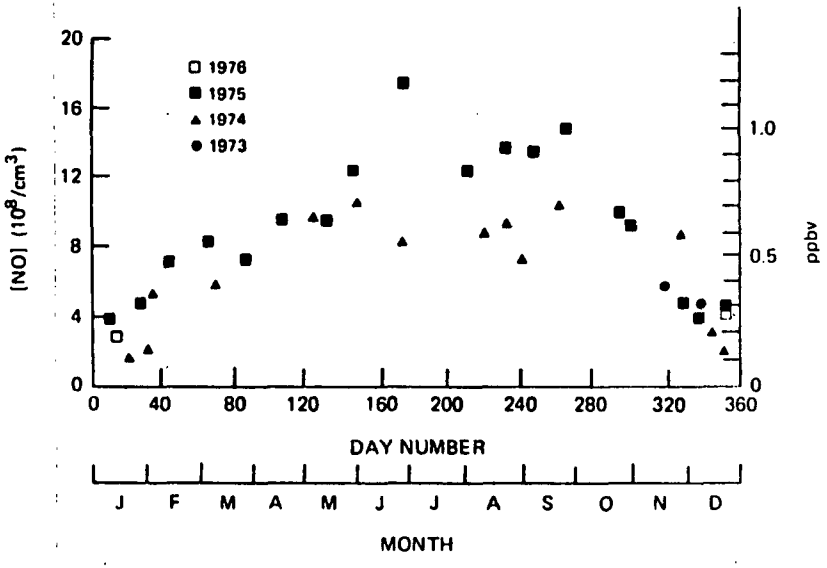

FIGURE D.30 Nitric oxide seasonal data (122°W, 40°N) summary at 21.3 km. The in situ NO measurements of Loewenstein et al. (1978) were obtained with a chemiluminescent instrument flown near 40°N, 122°W, and 21.3 km.

NO_x systems to perturbation, and the subsequent response of O_3 to these changes.

There is another marked seasonal/latitude dependent feature discovered by Loewenstein et al. (1978b). Specifically, above approximately 65°N latitude in the 18-km altitude aircraft flights, [NO] transits from a winter maximum to a fall minimum with a concentration excursion of more than an order of magnitude. Between 5° and 50°N latitude in contrast, the variation of NO is not large in the lower stratosphere. The vertical column data of Mankin and co-workers (see Coffey et al. 1981) exhibit very little latitude variation between 5° and 45°N latitude.

Nitrogen Dioxide (NO_2)

Given our current picture of the reactions that control the rate of odd oxygen production and destruction in the stratosphere, summarized in Figure C.6a of Appendix C, the concentration of NO_2 is the single most important radical for determining whether we have a quantitative understanding of the odd oxygen production/destruction budget. An inspection of Figure C.6a in Appendix C reveals that the NO_x catalytic cycle

$$\begin{aligned} NO + O_3 &\rightarrow NO_2 + O_2 \\ NO_2 + O &\rightarrow NO + O_2 \\ \hline O + O_3 &\rightarrow O_2 + O_2 \end{aligned}$$

constitutes 60 to 70 percent of the total loss rate for odd oxygen between 20 and 35 km. We are thus particularly interested in the NO_2 data base as a test of ozone destruction rates.

The first fact that emerges from an investigation of available NO_2 data is that there are no in situ observations of the molecule, so that conclusions we draw will be based exclusively on remote sensing techniques. The remote sensing techniques, predominantly visible and infrared absorption, are strictly limited to the sunrise and sunset periods. This does not prevent conclusions from being drawn that are accurate to within a factor of 2 in the altitude range from 25 to 35 km, but at lower and higher altitudes the conversion of NO to NO_2 at sunset dramatically shifts the ratio such that the modeled diurnal behavior becomes critically involved.

This is summarized quantitatively in Figure D.31, which indicates that the sunset/noon ratio of $[NO_2]$ approximates 1.5 between 20 and 35 km. Thus sunset observations of NO_2 are very difficult to interpret accurately in terms of midday steady state NO_2 concentration. It is also essential to realize that $[NO_2]_{90°}/[NO_2]_{30°}$ is greater than unity primarily because of the slow build-up of NO_2 during the day resulting from N_2O_5 decomposition. Thus we must correct the sunset observation back to midday if we are to compare them with modeled distributions close to local noon as is done for all other radicals.

We select for particular attention the data set collected at 34°N latitude by infrared solar absorption (Murcray et al. 1974, Goldman et al. 1978, Blatherwick 1980) and by visible absorption (Fischer et al. 1982) because of the extensive analysis afforded the IR results and because of the existence of two independent measurement techniques. It is also true, as we will discuss later in this section, that seasonal and latitude data have the greatest probability of being unbiased by variability on any given day.

We display in Figure D.32, therefore, the results from five different flights obtained between 1967 and 1980 using two independent methods, IR and visible absorption, all taken at sunset. Also displayed are the infrared pressure-modulated radiometer (PMR) data of Roscoe et al. (1981), which represent a time average from approximately 2 hours before local noon to sunset. We would expect these results to be about 20 to 25 percent below the sunset data, all other things being equal, because of the diurnal behavior of NO_2. Figure D.32 presents the mixing ratio data, a figure identical to that which appears in the WMO/NASA report with the pressure-modulated radiometer data added, and Figure D.33 presents the same set of data expressed in terms of absolute concentrations in an expanded abscissa.

Given the diurnal correction of about 25 percent to the pressure-modulated radiometer data, the extremely limited number of results in Figure D.33 yield surprisingly consistent results. The range in mixing ratio appears to be less than a factor of 2 using three independent experimental techniques. When one begins to probe within this factor of 2 envelope, it is advantageous to examine the absolute concentration data, which removes the gradient in NO_2 with altitude and offers a more discriminating examination of the data spread, as shown in Figure D.33.

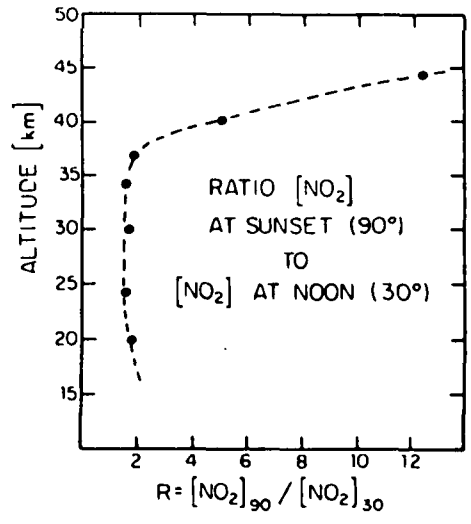

FIGURE D.31 Calculated ratio of $[NO_2]$ at sunset to that at noon.

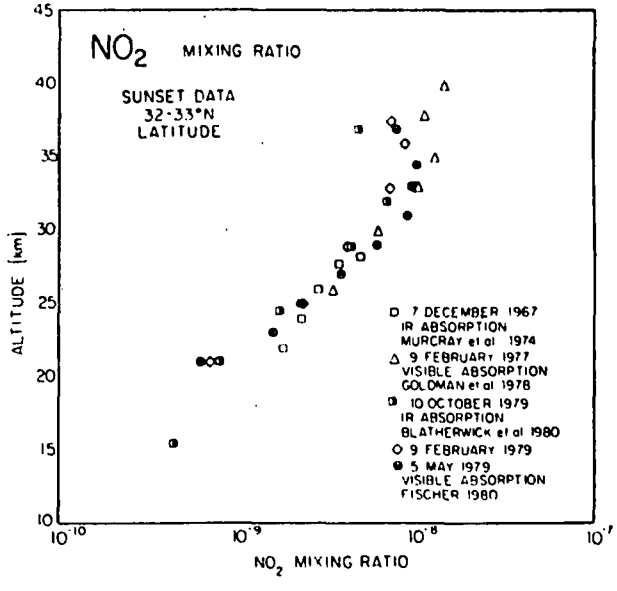

FIGURE D.32 Summary of sunset mid-latitude NO_2 data between 20 and 40 km. The midday to sunset mean reported by Roscoe et al. (1981) is included for completeness.

When we compare these results with model calculations, it becomes clear that it is the level of detail shown in Figure D.33 that is needed to discriminate between predicted ozone reduction levels between 2 and 15 percent. In addition, given the dominance of NO_x catalyzed destruction of O_x, which is rate limited by NO_2, factors of 2 are crucial to the question of odd oxygen balance.

We summarize the higher latitude data in Figure D.34 obtained at 45° to 50°N and at 51° to 58°N.

The same comments are applicable to the higher latitude data: There is a serious shortage of coverage in seasonal and diurnal dependence, but what data there are show a remarkable consistency.

The most obvious feature extracted from a comparison of Figures D.30 and D.32 is that there is an indication of larger mixing ratios of NO_2 at high latitude in the altitude region between 20 and 30 km where the concentration of nitrogen dioxide peaks. The difference between 32°N and 51° to 58°N corresponds to a 50 percent increase in mixing ratio over this latitude range. It is essential to verify this difference, and the seasonal dependence of it, preferably with the same array of cross-calibrated techniques on the same observation platform.

We turn next to an exceedingly important component of our experimental picture of global NO_2--the ground-based data set obtained by Noxon (see, for example, Noxon 1978, 1979, 1980; Noxon et al. 1979) using the visible absorption technique he pioneered. Noxon reports NO_2 vertical column densities that are a factor of 2 larger at night than during the day, which confirms in a semiquantitative way the conversion of NO_2 to N_2O_5 via NO_3 as outlined in our previous discussion of NO:

$$NO \underset{O,\ h\nu}{\overset{ClO,\ O_3}{\rightleftharpoons}} NO_2 \underset{h\nu}{\overset{O_3}{\rightleftharpoons}} NO_3 \underset{M,\ h\nu}{\overset{NO_2}{\rightleftharpoons}} N_2O_5$$

In addition, Noxon has defined the seasonal and latitudinal morphology of stratospheric NO_2 in a four-year series of data collection at four northern latitude sites. Those results are summarized in Figure D.35. The regularity of the winter minimum and summer maximum is dramatic, as is the distinct factor of 5 change in NO_2 total column at latitudes of 50°N over the period of a year.

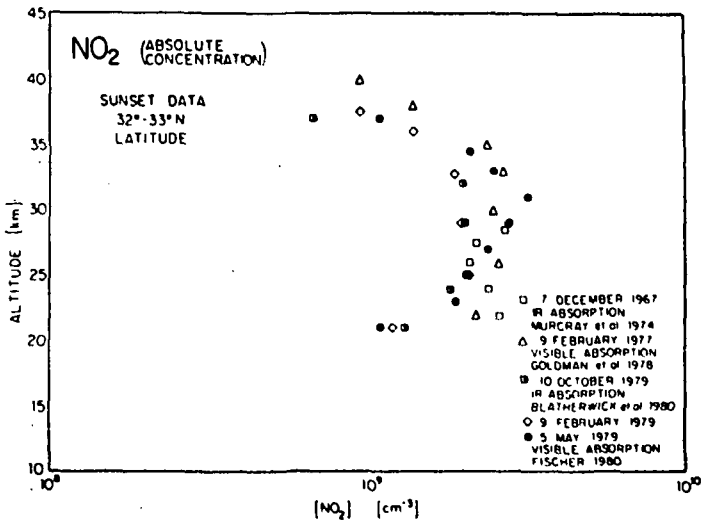

FIGURE D.33 Data from Figure D.32 converted to absolute concentration and presented with an expanded abscissa. The PMR data are not included.

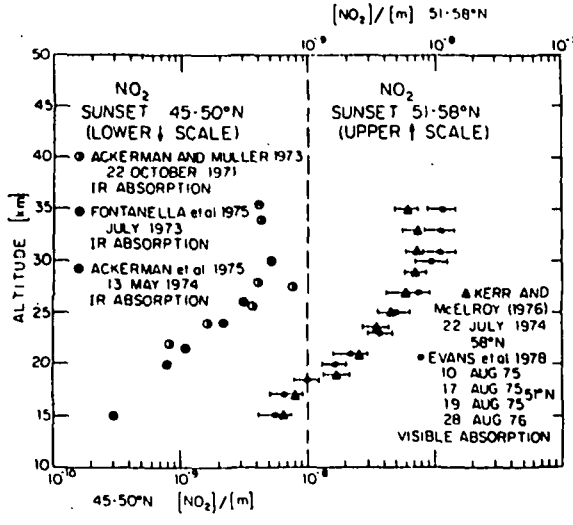

FIGURE D.34 NO_2 sunset 45°-50°N (lower scale) and NO_2 sunset 51°-58°N (upper scale).

It was Noxon's observations of NO_2 at high latitude that first identified the extremely low NO_2 concentrations in the polar regions (both northern and southern latitudes) with a distinct "ledge" in NO_2 vertical column densities as a function of latitude at 45°N, as summarized in Figure D.36.

Diurnal, Latitude, and Seasonal Dependence of Stratospheric [NO_2]. Although stratospheric [NO_2] depends critically on all these factors, the evolving picture can, to first order, be deconvoluted in the following way.

The diurnal dependence has been examined by four independent research groups. Two groups used ground-based visible absorption (Noxon et al. 1979, Noxon 1980, Girard et al. 1978/1979, A. Girard, Office National d'Etudes et de Recherches Aerospatiales, personal communication to D. Albritton, 1981). One group used aircraft-based infrared absorption (Coffey et al. 1981), and one used balloon-borne visible absorption (Evans et al. 1978). Both ground-based data sets report a factor of 2 larger NO_2 column amounts at night than during the day at middle latitudes. The aircraft data of Coffey et al. (1981) shown in Figure D.37 provide an interesting picture of the sunset-sunrise asymmetry, between 40° and 50°N latitudes, confirming the ground-based data.

The time dependence of the day/night conversion is highly altitude and time dependent following sunset. The obvious question, of course, is: In which altitude region does this diurnal variation appear? A first, and very informative, look at this question was reported by Evans et al. (1978), who examined the sunrise-sunset NO_2 profiles in four separate flights from Yorkton, Saskatchewan (51°N). Their results are summarized in Figure D.38.

The latitude and seasonal variations are convoluted, but the basic trend is captured in Figure D.39, which represents the recent aircraft observations of Coffey et al. (1981). To first order, the NO_2 column increases monotonically with latitude (at least to 45°N) during summer, and follows a similar pattern to 30°N in winter. At higher latitudes during the winter, however, there is a strong divergence to much lower total column concentration. This time-dependent transition between these two cases is, at least in part, exemplified by the exceedingly interesting "cliff" features discovered by Noxon and summarized previously in Figure D.36.

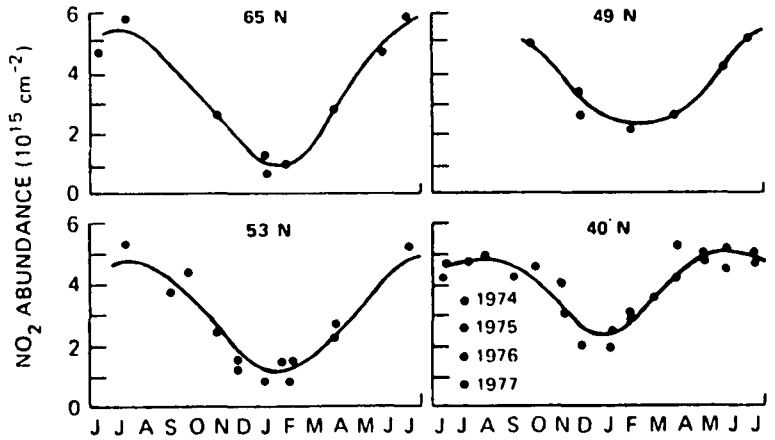

FIGURE D.35 Seasonal variation of late afternoon NO_2 at four latitudes, as given by the ground-based visible absorption spectroscopic measurements of Noxon (1979). The abundance should be multiplied by 1.25 (Noxon 1980).

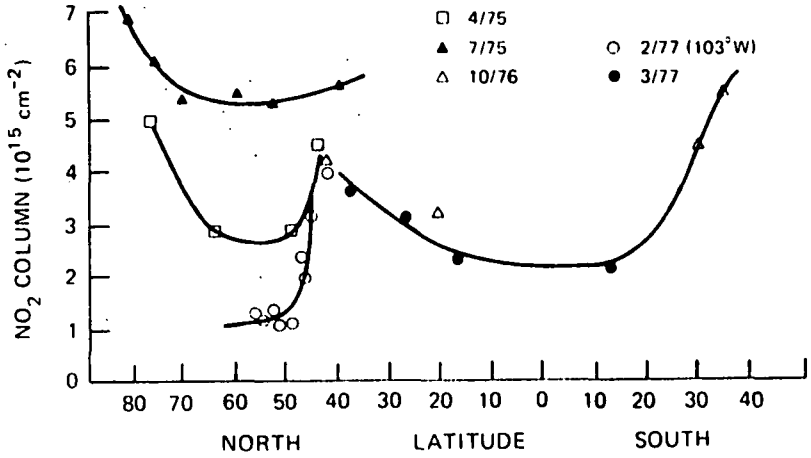

FIGURE D.36 Latitudinal and seasonal variations of the late afternoon vertical column of NO_2, as measured by Noxon (1979) using ground-based visible absorption techniques. The values represented by the open and solid circles should be multiplied by 1.6, and all others by 1.25 (Noxon 1980).

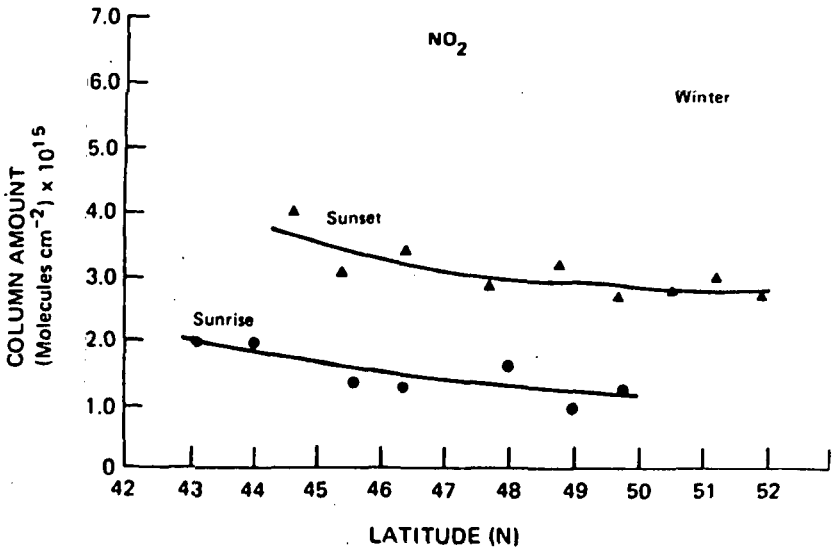

FIGURE D.37 Sunrise and sunset vertical-column measurements of NO_2 by Mankin and co-workers, who used an infrared absorption apparatus on an aircraft platform (Coffey et al. 1981).

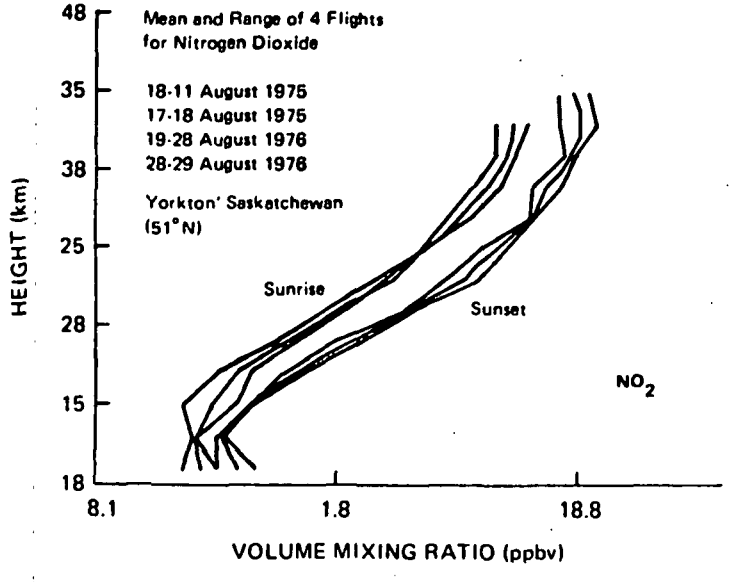

FIGURE D.38 The sunrise and sunset altitude profiles of NO_2 reported by Evans et al. (1978) from the Canadian stratosphere flight series. The upper and lower limits indicate the maximum observed deviations from the mean. The measurements were made using a balloon-borne visible absorption apparatus.

In closing this brief discussion of the NO_2 data base, we note a final point made by Noxon (1979, 1980) that NO_2 has been observed to change by a factor of 2 within the time span of a few days, as illustrated in Figure D.40.

Atomic Nitrogen (N)

There are no reported observations in the stratosphere of atomic nitrogen in either its ^2D or ^4S states. Although atomic resonance fluorescence could detect, in situ, N atom concentrations in the 10^5 cm^{-3} range, current predictions place its expected concentration well below that, and no experiments have been attempted.

The Nitrate Radical (NO_3)

The chemical link between the NO_x catalytic radicals NO and NO_2 and the higher oxides of nitrogen is believed to be NO_3, and yet there are very few data on this important intermediate. There are no daytime observations available (the only analytical technique used thus far for NO_3 is visible absorption--a technique identical to that used for NO_2). A single nighttime profile has been reported, obtained at 43°N latitude from a balloon-borne visible spectrophotometer using Venus as a light source. That profile is shown in Figure D.41.

If the data in Figure D.41 are integrated, one obtains a vertical column between 20 and 40 km of 3.5×10^{13} cm^{-2}. This figure is not inconsistent with the only other data available, that of Noxon, who estimates, based on ground-based visible absorption data, a column density of 10^{14} cm^{-2} in the spring and an upper limit in the summer of 4×10^{13} cm^{-2}.

While it may well turn out to be irrelevant due to the very different moisture level, total pressure, and heterogeneity of the troposphere, it should be noted that NO_3 currently represents an enigma to tropospheric NO_x studies in that dramatically less NO_3 is observed (when simultaneous NO_2 measurements are made) than one would predict given current models. The implication is that a large sink for NO_3 exists because the source is well established.

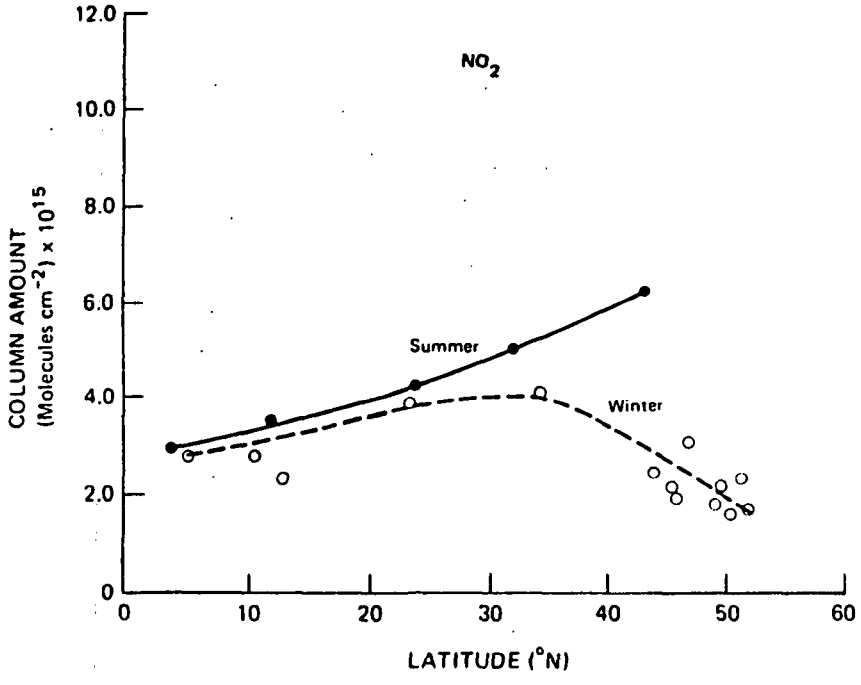

FIGURE D.39 Latitudinal and seasonal variations of the late afternoon vertical column of NO_2, as measured by Mankin and co-workers using aircraft-borne infrared absorption techniques (Coffey et al. 1981).

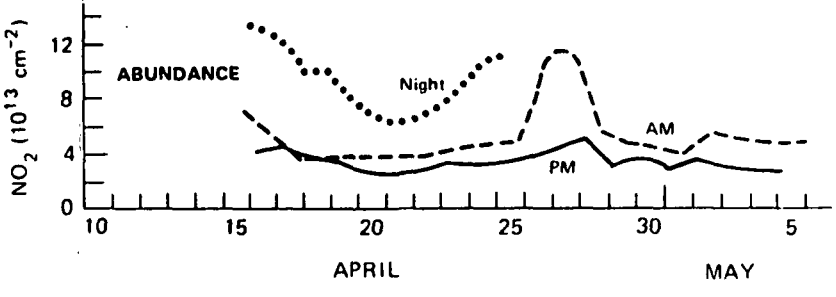

FIGURE D.40 The daily variation of the vertical column of the nighttime, late afternoon, and early morning NO_2 at 40°N in April and May 1976 as seen by Noxon et al. (1979), using ground-based visible absorption spectroscopy. The abundances should be multiplied by 1.25 (Noxon 1980).

Dinitrogen Pentoxide (N_2O_5)

Although dinitrogen pentoxide is recognized to be of major importance to our understanding of atmospheric NO_x chemistry, and has received increasing attention from the experimental community, there have been no new results reported beyond those presented in Hudson and Reed (1979). In that document, Evans et al. report a tentative detection of 2 ppbv at 30 km and Murcray reported an upper limit of 1.2×10^{15} cm^{-2} above 18 km in February.

Nitrous Acid (HONO)

The nitrous acid molecule, formed in the recombination reaction of OH and NO, is rapidly photolyzed in the stratosphere and thus is expected to be present at concentrations several orders of magnitude below the detection threshold of the high-resolution infrared absorption experiments. It does not possess a strong, well-defined electronic transition and is thus not amenable to resonance fluorescence techniques.

Thus, although it has been searched for in the IR absorption data, there are no reported observations, and the upper limits one would extract from the data are incapable of testing our understanding of hydrogen-nitrogen oxygen photochemistry.

Nitric Acid ($HONO_2$)

Nitric acid has, since the inclusion of reactive nitrogen compounds into stratospheric chemistry, been recognized as the dominant chemical "reservoir" for the oxides of nitrogen and has thus received considerable attention. Four analytical methods are currently available for the detection of $HONO_2$, two in situ and two remote.

In situ observations were first reported by Lazrus and Gandrud (1974) using a filter collection technique deployed on a balloon to determine the vertical profile of $HONO_2$ between the tropopause and 38 km. Those observations were taken in the spring season in three consecutive years: 1971, 1972, and 1973. Those results appear in Hudson and Reed (1979). Results using a second in situ technique, a rocket-borne ion-sampling method developed by Arnold and co-workers, have been recently reported (see Arnold et al. 1980).

Remote observations have been reported employing both infrared absorption (Fontanella et al. 1975 and H. Fischer, personal communication to D. Albritton for the WMO/NASA report, 1980) and infrared emission (Harries et al. 1976, Evans et al. 1978, and D.G. Murcray, University of Denver, personal communication to D. Albritton for the WMO/NASA report, 1980).

Although the data of Lazrus and Gandrud (1974), Harries et al. (1976), and Fontanella et al. (1975) have appeared in previous reports by both NASA and the NRC, we include those results with the more recent data to appraise the entire data base defining the mid-latitude, northern hemisphere vertical distribution of nitric acid. We present both the mixing ratio data in Figure D.42 (which is identical to the figure appearing in the WMO/NASA report) and the absolute concentration data in Figure D.43, the latter with an expanded abscissa (a format required for a detailed comparison with modeled distributions, as we will see in the sections that follow).

Given that four independent analytical techniques were employed by seven research groups, the consistency of the $HONO_2$ data is exceptional. It remains, of course, to employ the methods simultaneously for soundings of the same air mass and to standardize the deconvolution techniques in order to establish whether the scatter represents experimental uncertainty or atmospheric variability.

A particularly important point regarding the long path absorption sunrise-sunset data is that the chemical time constant of nitric acid is much longer than a diurnal period, and thus those data can be immediately interpreted in terms of the model calculations without reference to details of the diurnal dependence.

Figure D.43 constitutes the most important body of evidence available for testing our understanding of the nitric acid distribution in the stratosphere, and we will recall the figure later. However, there are other important experimental results that have been obtained for nitric acid.

First, the combined seasonal and latitude scans using aircraft-borne total column infrared measurements, summarized in Figure D.44, demonstrate a notable lack of seasonal dependence in the characteristic monotonic increase in $HONO_2$ from equator to pole, up to 40°N. This is, of course, in sharp contrast to the corresponding results for NO_2.

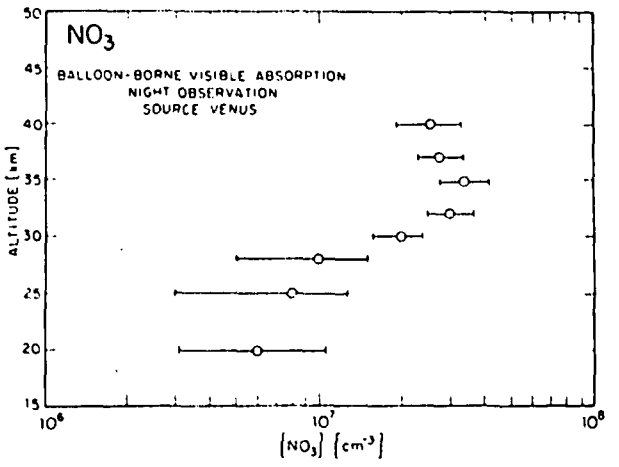

FIGURE D.41 Vertical distribution of NO_3 in the stratosphere at night obtained by balloon-borne absorption techniques in the visible using Venus as the source.

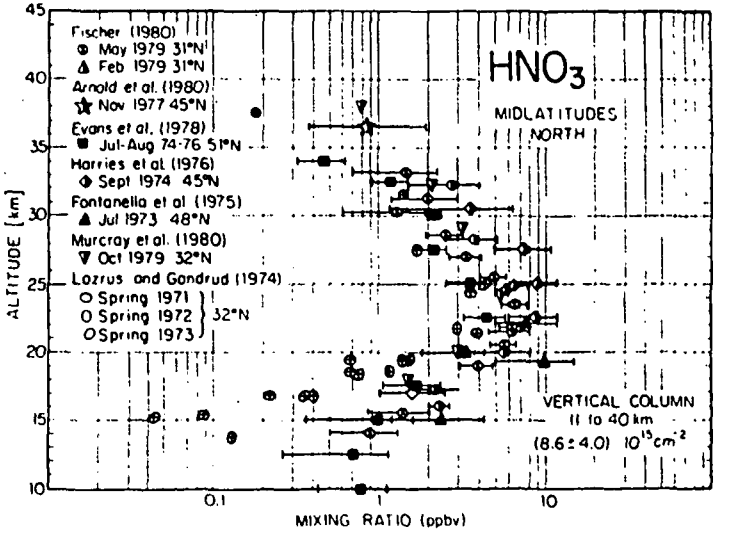

FIGURE D.42 In situ and remote measurements of the HNO_3 mixing ratio at northern mid-latitudes.

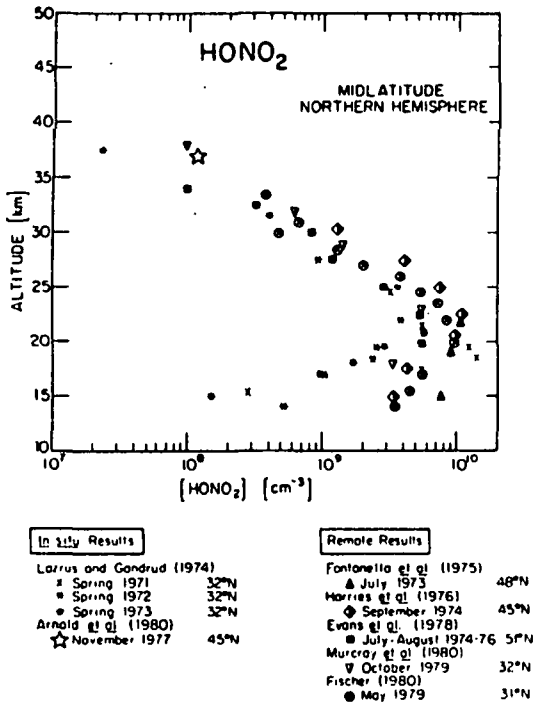

FIGURE D.43 Mid-latitude $HONO_2$ data expressed in terms of absolute concentration.

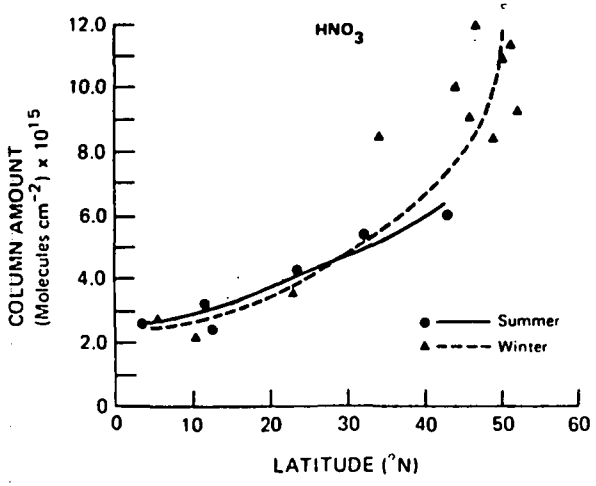

FIGURE D.44 Evidence for the lack of a seasonal variation in the vertical column density of HNO_3 at latitudes less than 40°N, as measured by Coffey et al. (1981) using infrared absorption.

The aircraft vertical column data substantiate the general morphology of the nitric acid total column concentration first reported by Murcray et al. (1974). There is a strong increase in the vertical column density with increasing latitude, in both the northern and the southern hemispheres. Above about 60°N latitude, there appears to be a pronounced seasonal variation. In the winter at high latitudes, the vertical column concentration of $HONO_2$ is distinctly larger than in early summer.

Group 5: Reactive Trace Constituents Containing Bromine

The Bromine Monoxide Radical (BrO)

There are no reported observations of BrO in the stratosphere. It should be amenable to detection by laser heterodyne techniques in the middle infrared, by mm-wave emission and by in situ chemical conversion resonance fluorescence. BrO is the pivotal radical in the bromine-ozone system.

Atomic Bromine (Br)

There are no reported observations of atomic bromine in the stratosphere.

The Bromine Dioxide Radical (BrO_2)

There are no reported observations of BrO_2 in the stratosphere.

Bromine Dioxide (OBrO)

There are no reported observations of OBrO in the stratosphere.

Hydrogen Bromide (HBr)

No direct observations of HBr have been reported. However, a recent publication by Berg et al. (1980)

report observations of total bromine using neutron activation techniques applied to an activated charcoal sampling matrix deployed from both aircraft and balloon platforms. Initial results from six aircraft flights and one balloon mission in the lower stratosphere are presented for latitudes between 16° and 67°N. Five total bromine values showed substantial variability ranging from 7 ± 4 ppt by volume to 40 ± 11 ppt. If the assumption that HBr dominates the total bromine budget in the middle and upper stratosphere is correct, these figures should reflect the HBr concentration in that region.

Hydrogen Oxybromide (HOBr)

There are no reported observations of HOBr in the stratosphere.

Bromine Nitrate ($BrONO_2$)

There are no reported observations of $BrONO_2$ in the stratosphere.

Group 6: Reactive Trace Constituents Containing Fluorine

Fluorine Monoxide (FO)

There are no reported observations of FO in the stratosphere.

Atomic Fluorine (F)

There are no reported observations of atomic fluorine in the stratosphere.

The Fluorine Dioxide Radical (FO_2)

There are no reported observations of FO_2 in the stratosphere.

Fluorine Dioxide (OFO)

There are no reported observations of OFO in the stratosphere.

Hydrogen Fluoride (HF)

Hydrogen fluoride has received considerable attention both because it possesses a strong IR absorption spectrum in the middle infrared and because it provides a very important check on the amount of fluorine released from the chlorofluorocarbons. Since the strength of the HF bond is sufficiently strong that no radical reacts with HF to any measurable degree, it is also of interest to compare ratios of HF and HCl in the same air mass.

Table D.7, taken from Hudson et al. (1982), summarizes the data, latitude, altitude range, method, and experimenter for each of the reported HF observations.

The two measurements that can be most directly compared are, as in the case of HCl, the high-resolution infrared absorption measurements of Farmer et al. (1980) and Buijs et al. (1980). The techniques are identical; the results are shown in Figure D.45. Although the slopes correlated reasonably well, the Buijs results are a factor of 2 greater than those of Farmer. It is unfortunate that such a large latitude discrepancy exists between the observations (although HF should not depend sensitively on latitude). It may well be that an adjustment for tropospheric height could remedy the disparity significantly.

Two additional profiles for HF have been obtained by Bangham et al. (1980) and Marche et al. (1980a), the former from balloon-borne observations at 32°N in emission and the latter from ground-based absorption measurements at 42°N. These two profiles cover different altitude regions in the stratosphere, but at the one common altitude of 30 km differ by about a factor of 5 (see Figure D.45). As was the case for HCl, however, the emission data values shown here are preliminary and, in particular, are likely to increase at the lower altitudes when a more rigorous analysis of the data is performed. Should this be the case, they may well be in agreement with the Buijs et al. (1980) data at lower altitudes.

The remaining remote sensing measurements are those of Zander et al. (1981), who report total column abundances above three different float altitudes from balloon flights

TABLE D.7 Summary of HF Measurements (Hudson et al. 1982)

Experimenter	Observation Date	Latitude	Altitude Range	Method	Reference
Zander	September 1974		above 27 km	IR absorption	Zander (1975)
Zander	May 1976	32°N	above 27 km	IR absorption	Zander (1980)
Buijs	May 1976	65°N	15-30 km	IR absorption	Buijs et al. (1980)
Mroz	February to November 1976	30°-33°N	15-37 km	In situ (filter)	Mroz (1977)
Farmer	March 1977	30°S	14-40 km	IR absorption	Farmer et al. (1980)
Zander	October 1978	32°N	above 30 km	IR absorption	Zander (1980)
Carli	April 1979	32°N	30-40 km	IR emission	Bangham et al. (1980)
Marche	May 1979	49°N	20-30 km	IR absorption (ground-based)	Marche et al. (1980)
Zander	September 1979	32°N	above 36 km	IR absorption	Zander (1980)

made over a period of four years. These measurements were made at successively higher altitudes and yield increasingly larger values for the total HF burden above the balloon, which, if interpreted as a profile, produce the result shown in Figure D.46. They may also be indicative of a long-term increase in the stratospheric HF, which Zander has observed in the course of the IR absorption studies. The possibility of such an increase renders even more difficult intercomparisons between measurements in a data base acquired over a period of six years and clearly demonstrates the need to establish a reliable baseline profile for HF against which future measurements can be assessed.

The in situ data of Mroz et al. (1977) shown in Figure D.45 are the average of four seasonal sets of measurements made in 1976. Although the shapes of the profiles are different, the total stratospheric burdens for HF that can be deduced from the data of Mroz and co-workers and of Farmer et al. (1980) appear to be in reasonably good agreement. However, the sampling technique used by Mroz and co-workers is stated to be sensitive to total fluoride, including COF_2 and COFCl: Depending on the model used, this implies that as much as one third of the collected material could have been in the form of these two gases. Thus, the HF in situ results are similar to those for HCl in that they are generally lower than the results obtained using remote sensing techniques.

HOW WELL DOES THE CURRENT DATA BASE ON STRATOSPHERIC REACTIVE TRACE SPECIES CONSTRAIN MODEL PREDICTIONS OF OZONE REDUCTION LEVELS?

Progressing beyond the demonstration that the basic tenets of a given ozone reduction theory have a reasonably high probability of being qualitatively correct requires a significant advance in both the quality of the data available and the manner in which those data are employed.

What we mean by "demonstration that the basic tenets . . . have a reasonably high probability of being qualitatively correct . . ." is that direct observations have verified that

- a given catalytic cycle enhancing the rate of ozone recombination occurs in the stratosphere, e.g., by observing NO, NO_2, O and O_3, or Cl, ClO, O and O_3;

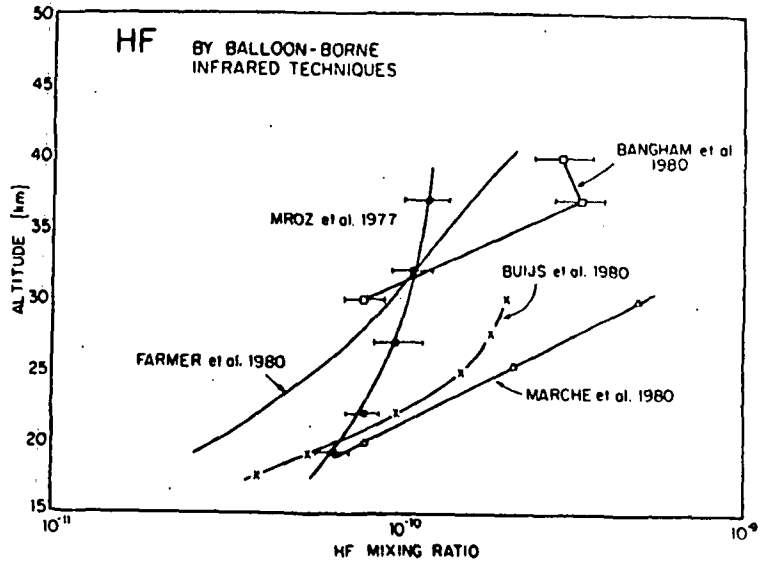

FIGURE D.45 Stratospheric HF profile measurements.

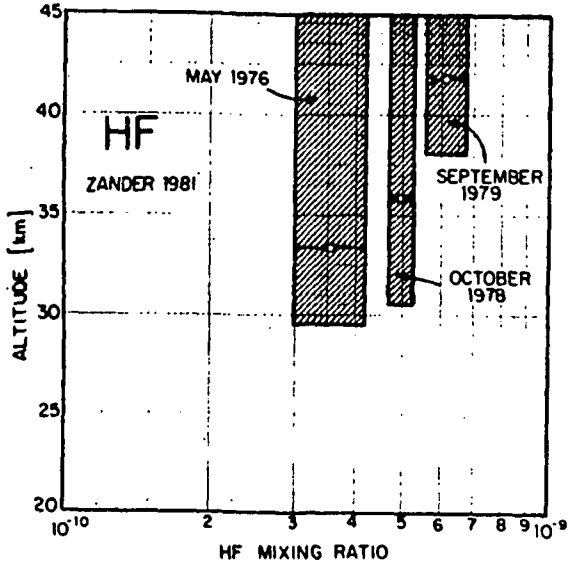

FIGURE D.46 HF mixing ratio reported by Zander (1981). The shaded areas were deduced from near and subhorizontal observations for each of the three flights indicated. Comparison with Figure D.45 indicates a marked change between 20 and 30 km.

- the radicals that make up a given catalytic cycle exist in approximately the model-calculated proportion to their reservoir terms;
- the source molecules that are believed to augment the concentration of a given family of reactants--e.g., N_2O or CH_3Cl, $CFCl_3$, CF_2Cl_2--penetrate the stratosphere approximately as calculated based on their assumed mechanism of destruction; and
- the observed total budget comprising source, reservoir, and free radical concentrations (e.g., CH_3Cl, CH_3CCl_3, $CFCl_3$, CF_2Cl_2; HCl, $ClONO_2$; and Cl, ClO) is in line with modeled predictions.

A review of the data base summarized earlier and treated in detail in Hudson et al. (1982) demonstrates that these criteria have been met for the nitrogen and chlorine systems throughout much of the stratosphere limited to the catalytic cycles:

$$\begin{array}{rcl} NO + O_3 & \rightarrow & NO_2 + O_2 \\ NO_2 + O & \rightarrow & NO + O_2 \\ \hline O + O_3 & \rightarrow & O_2 + O_2 \end{array} \qquad \begin{array}{rcl} Cl + O_3 & \rightarrow & ClO + O_2 \\ ClO + O & \rightarrow & Cl + O_2 \\ \hline O + O_3 & \rightarrow & O_2 + O_2 \end{array}$$

and for the hydrogen system in the middle stratosphere for the cycles

$$\begin{array}{rcl} OH + O_3 & \rightarrow & HO_2 + O_2 \\ HO_2 + O & \rightarrow & OH + O_2 \\ \hline O + O_3 & \rightarrow & O_2 + O_2 \end{array} \qquad \begin{array}{rcl} OH + O_3 & \rightarrow & HO_2 + O_2 \\ HO_2 + O_3 & \rightarrow & OH + O_2 + O_2 \\ \hline O_3 + O_3 & \rightarrow & 3O_2 \end{array}$$

The central issue is whether we have the experimental evidence to test

1. the quantitative change in ozone for a given change in the source molecule concentration given the set of reactions currently adopted in the best models of the stratosphere; and
2. whether that reaction set is complete with respect to those mechanisms that can directly affect odd oxygen.

We will discover that the data currently available in large measure fail on both counts, but there are important exceptions. Demonstrating precisely why the data fail is important not only to define the limits of our current understanding of the stratosphere, but also to

serve as an important lesson for future measurement strategies, a topic discussed in the next section.

The approach adopted here is to trace the impact of the various assumptions about the rate constants through the model-predicted free radical concentrations to the predicted ozone depletion profiles, as summarized in Figure D.47.

In order to correlate the rate constant data, the free radical concentration, and the resulting ozone reduction profiles, we define the following six model cases, which encompass the major uncertainties in laboratory rate data.

Case 1: A set of rate constants identical to that recommended in Hudson and Reed (1979). See Table D.8. This case references all modeled distributions to those employed in the last NRC report.

Case 2: Rate constants similar to those in Case 1 with changes as tabulated in Table D.8. All of the changes are of minor significance for stratospheric modeling (although not for tropospheric modeling).

Case 3: Rate constants identical to those of Case 2, except a temperature-dependent rate constant for the reaction

$$OH + HONO_2 \rightarrow H_2O + NO_3$$

of $k = 1.5 \times 10^{-14} \exp(650/T)$ cm^3 s^{-1} is used in place of the temperature independent rate,

$$k = 8.5 \times 10^{-14} \exp[(0 + 100)/T] \text{ cm}^3 \text{ s}^{-1}$$

Case 4: Rate constants identical to those of Case 3, except the rate constant for the reaction

$$OH + HO_2HO_2 \rightarrow H_2O + NO_2 + O_2$$

is assumed to be 5 times that of Case 2.

Case 5: Rate constants identical to those of Case 4, except the rate constant for the reaction

$$OH + HO_2 \rightarrow H_2O + O_2$$

is assumed to be twice that of Case 2.

Case 6: Rate constants the same as those of Case 5, except with a "slow" formation rate for $ClONO_2$. It is assumed in this case that other isomeric forms are rapidly photodissociated following sunrise. See Hudson et al. (1982) for details.

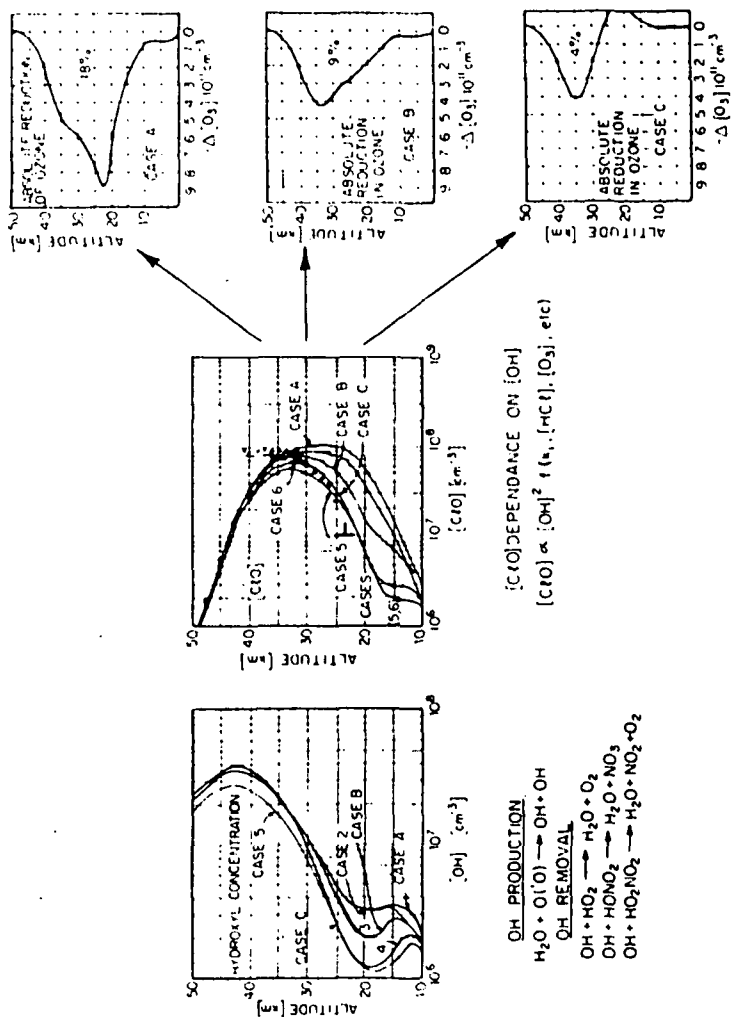

FIGURE D.47 Schematic representation linking the dependence of [ClO] on [OH] and the resulting altitude dependence of ozone depletion as a function of altitude.

TABLE D.8 Reaction Rates of Cases 1 and 2 (cm^{-3} s^{-1})

Reaction	Case 1: NASA 1049	Case 2
$OH + H_2O_2 \rightarrow H_2O + HO_2$	$1.0 \times 10^{-11} \exp[(-750 \pm 350)/T]$	$2.7 \times 10^{-12} \exp[(-145 \pm 100)/T]$
$OH + O \rightarrow H + O_2$	$4.0 \times 10^{-11} \exp[(0 \pm 300)/T]$	$2.3 \times 10^{-11} \exp[(-110 \pm 200)/T]$
$HO_2 + O \rightarrow OH + O_2$	$3.5 \times 10^{-11} \exp[(0 \pm 350)/T]$	$4.0 \times 10^{-11} \exp[(0 \pm 350)/T]$
$ClO + NO \rightarrow NO_2 + Cl$	$7.8 \times 10^{-11} \exp[(+250 \pm 100)/T]$	$6.5 \times 10^{-12} \exp[(+280 \pm 100)/T]$
$O(^1D) + \begin{Bmatrix} N_2O \\ H_2O \\ CH_4 \\ N_2 \\ O_2 \\ CO_2 \end{Bmatrix} \rightarrow$ Product	See NASA 1049	See JPL Publication 81-3
$HO_2 + HO_2 \rightarrow H_2O_2 + O_2$	$2.5 \times 10^{-12} \exp\left[\left(-0 + \frac{0}{1245}\right)/T\right]$	2.5×10^{-12}
$HO_2 + NO \rightarrow OH + NO_2$	$4.3 \times 10^{-12} \exp[(200 \pm 200)/T]$	$3.5 \times 10^{-12} \exp[(+250 \pm 100)/T]$
$OH + OH \rightarrow H_2O + O_2$	$1.0 \times 10^{-11} \exp[(500 \pm 400)/T]$	$4.5 \times 10^{-12} \exp[(-275 \pm 275)/T]$
$OH + HOCl \rightarrow H_2O + ClO$	$3.0 \times 10^{-12} \exp[(-800 \pm 500)/T]$	$3.0 \times 10^{-12} \exp\left[\left(-150 + \frac{350}{-150}\right)/T\right]$
$Cl + CH_4 \rightarrow HCl + CH_3$	$9.9 \times 10^{-12} \exp[(-1359 \pm 150)/T]$	$9.6 \times 10^{-12} \exp[(-1350 \pm 150)/T]$
$Cl + HO_2 \rightarrow HCl + O_2$	$4.5 \times 10^{-11} \exp[(0 \pm 250)/T]$	$4.8 \times 10^{-11} \exp[(0 \pm 250)/T]$
$ClO + HO_2 \rightarrow HOCl + O_2$	5.2×10^{-12}	$4.6 \times 10^{-13} \exp[(+710 \pm 250)/T]$
$NO_3 + h\nu \rightarrow NO + O_2$ $\rightarrow NO_2 + O$	See NASA 1049, page 23	See discussion in this appendix
$OH + HONO_2 \rightarrow$ Products	$8.5 \times 10^{-14} \exp[(0 \pm 100)/T]$	Same as Case 1
$OH + HO_2NO_2 \rightarrow$ Products	5.0×10^{-13}	8×10^{-13}
$OH + HO_2 \rightarrow H_2O + O_2$	$4 \times 10^{-11} \exp[(0 \pm 250)/T]$	Same as Case 1

Briefly, these six cases can be summarized by noting that Case 1 corresponds approximately to the reaction and rate constant set used at the time of the previous NRC report. Case 2 catalogs all the refinements in reported rate constants that do not have a significant effect on the calculated distribution of any key reactive species in the stratosphere. Cases 3, 4, and 5 define the impact of, respectively, the faster low-temperature rate constant for OH + $HONO_2$, the faster overall rate for OH + HO_2NO_2, and the faster overall rate for OH + HO_2. Case 6 isolates the impact of assuming the formation of isomers other than $ClONO_2$ in the termolecular recombination of NO_2 and ClO.

Given that the most immediate concern of this report is an assessment of the ozone reduction resulting from the release of fluorocarbon compounds, we treat the chlorine-ozone question first.

Chlorine-Induced Destruction of Ozone

The [ClO] Profile

Figure D.48 compares the model calculated [ClO] profiles for each of the six cases defined above, with the corresponding altitude dependence of ozone reduction for steady state conditions given 1976 release rates of fluorocarbons and 1979 release rates for chloroform. These results were provided by D.J. Wuebbles and J.S. Chang of the Lawrence Livermore National Laboratory. Also cited in the figure are the integrated column reduction percentages for each of the six cases.

The most obvious conclusion to be drawn from Figure D.48 is that both the altitude distribution and the integrated reduction in ozone are exceedingly sensitive to the rate constants selected for the HO_x reactions. This results from the quadratic dependence of [ClO], the rate limiting radical in the dominant chlorine catalytic cycle:

$$\begin{aligned} Cl + O_3 &\rightarrow ClO + O_2 \\ ClO + O &\rightarrow Cl + O_3 \\ \hline O_3 + O &\rightarrow 2O_2 \end{aligned}$$

on [OH], as noted in Appendix C. The second conclusion is that, for the diminished OH concentration in the lower

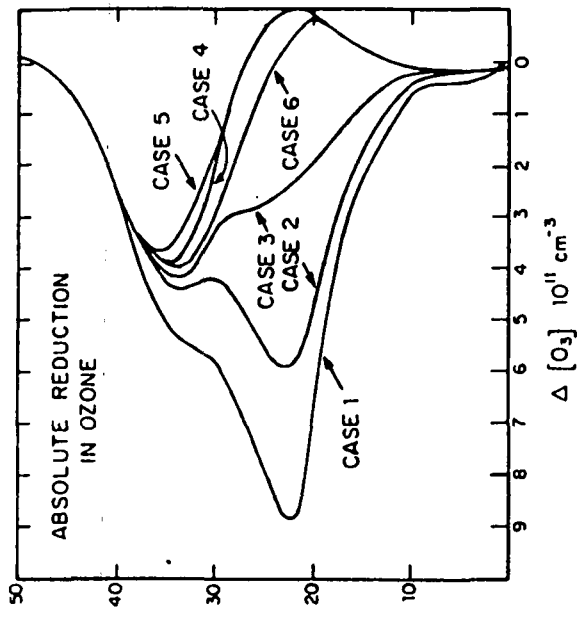

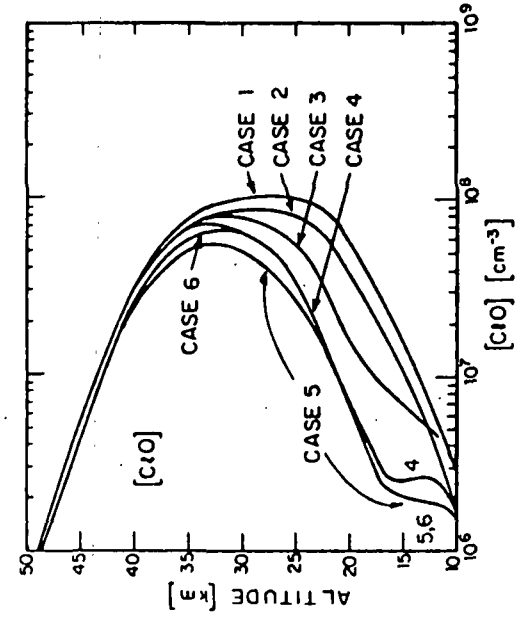

Case	Predicted Ozone Reduction
1	18%
2	14%
3	9%
4	4%
5	3%
6	5%

FIGURE D.48 Predictions of stratospheric ClO concentration and ozone reduction for the six cases described in the text.

stratosphere corresponding to Cases 4, 5, and 6, the chlorine-induced destruction of ozone is confined to the altitude region above 30 km with less than 10 percent of the integrated effect occurring at lower altitudes. The bimodal distribution in $\Delta[O_3]$ as a function of altitude for Cases 1, 2, and 3, which results from the contribution of the catalytic cycles (see Wuebbles and Chang 1981)

$$\begin{aligned} Cl + O_3 &\rightarrow ClO + O_2 \\ ClO + HO_2 &\rightarrow HOCl + O_2 \\ OH + O_3 &\rightarrow HO_2 + O_2 \\ HOCl + h\nu &\rightarrow OH + Cl \\ \hline O_3 + O_3 &\rightarrow 3O_2 \end{aligned}$$

$$\begin{aligned} Cl + O_3 &\rightarrow ClO + O_2 \\ ClO + NO_2 &\rightarrow ClONO_2 \\ NO + O_3 &\rightarrow NO_2 + O_2 \\ ClONO_2 + h\nu &\rightarrow Cl + NO_3 \\ NO_3 + h\nu &\rightarrow NO + O_2 \\ \hline O_3 + O_3 &\rightarrow 3O_2 \end{aligned}$$

below 30 km, disappears entirely for Cases 4, 5, and 6, which are characterized by 10 times lower [ClO] at 20 km. The isolation of chlorine-induced ozone destruction to the middle and upper stratosphere greatly simplifies the interpretation of ozone destruction by chlorine both because the chemical time constant for ozone (defined here as the ozone concentration divided by the rate of odd oxygen production) is much shorter than transport times in the middle and upper stratosphere, and thus local chemical production and destruction rates determine the ozone concentration. The cases characterized by low [ClO] also represent a significant decoupling of the chlorine system from hydrogen and nitrogen in the lower stratosphere.

Can we, based on the available ClO data, select which of the six cases most accurately reflects conditions in the real atmosphere? Figure D.49 displays Cases 1 through 6 superposed with the in situ data that comprise the envelope of observations critiqued earlier. The spread in the in situ observations is approximately ±50 percent about the mean, but there is a clear indication that: (a) the measurements strongly favor the calculated distributions characterized by a rapid decrease in [ClO] below 30 km; and (b) the rapid decrease in [ClO] above 35 km predicted by all six model cases is not substantiated by the data.

Next, in Figure D.50, we superpose the mean of the nine in situ observations shown in Figure D.49 with the balloon-borne mm-wave emission data of Waters et al.

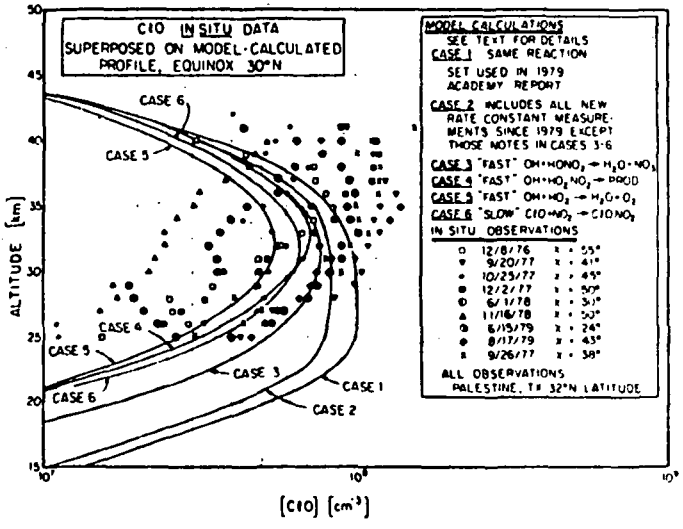

FIGURE D.49 ClO in situ data superposed on model-calculated profile, equinox 30°N.

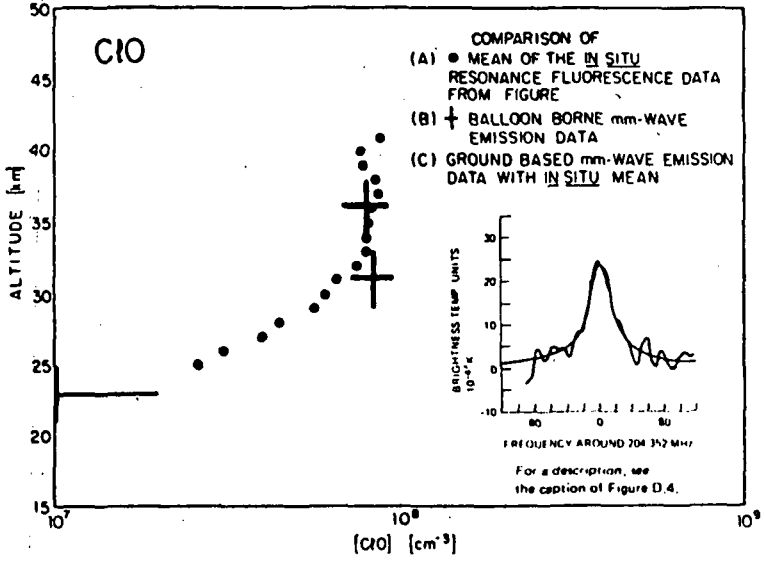

FIGURE D.50 Summary of the comparison between the ground-based mm-wave emission data of Parrish et al. (1980), the balloon-borne mm-wave emission data of Waters et al. (1981), and the in situ data of Anderson and co-workers.

(1981) and note with an inset the comparison between the mean of the in situ data and the ground-based mm-wave emission data of Parrish et al. (1981).

We conclude from Figure D.50 that to first order the three independent ClO detection methods provide very consistent results. A comparison between those data, represented by the balloon-borne observations that directly observe the distribution of [ClO] with altitude, and the six modeled cases is presented in Figure D.51.

Taken as a whole, the data clearly support the calculations that predict the minimum ClO concentration below 30 km, i.e., Cases 4 through 6. This is a conclusion of considerable importance, not only because, if accepted, it alters the predicted ozone reduction levels very significantly (see Figure D.48), but also because it seriously constrains any proposed mechanism involving chlorine radicals in the lower stratosphere. Such a proposed mechanism might involve either a catalytic cycle that is involved directly in the recombination of odd oxygen or a reaction linking the chlorine system to another family of reactants (e.g., bromine, nitrogen, hydrogen, etc.); in either case, the factor of 10 lower ClO concentration in the lower stratosphere seriously reduces the probability that such a mechanism can be of quantitative significance.

We are thus limited to Cases 4 to 6, which isolate the chlorine-induced destruction of ozone to altitudes above 30 km (where the ozone density is controlled predominantly by local chemical production and destruction). In this altitude regime, it is clear that observed [ClO] exceeds the calculated distribution by nearly a factor of 3 at 40 km. The first-order importance of this can be represented by an "overlap integral" between the altitude dependence of chlorine-induced ozone destruction, $\Delta[O_3]$ versus altitude, and the ratio of calculated to observed [ClO]. This is summarized in Figure D.52.

The implication of Figure D.52 is that a mechanism not currently included in the models exists that converts HCl (the dominant form of chlorine at 40 km) to the free radical form ClO. If that mechanism does not enter directly in a rate limiting process for ozone production or destruction, then Figure D.52 implies that the chlorine-induced destruction of ozone will deepen and shift to higher altitudes. If the missing mechanism does involve odd oxygen production or destruction directly, then one cannot conclude even the sign of the effect resulting from the inclusion of the mechanism.

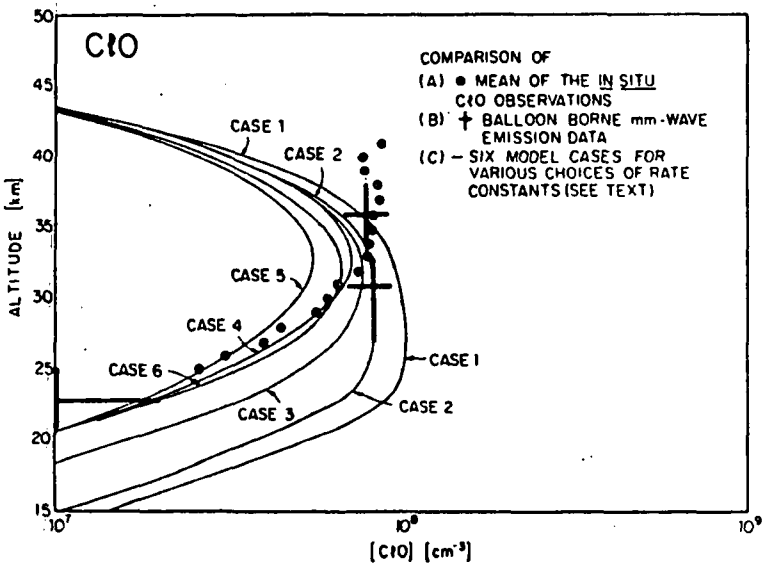

FIGURE D.51 Superposed balloon-borne observations of ClO and the six model-calculated cases defined in the text.

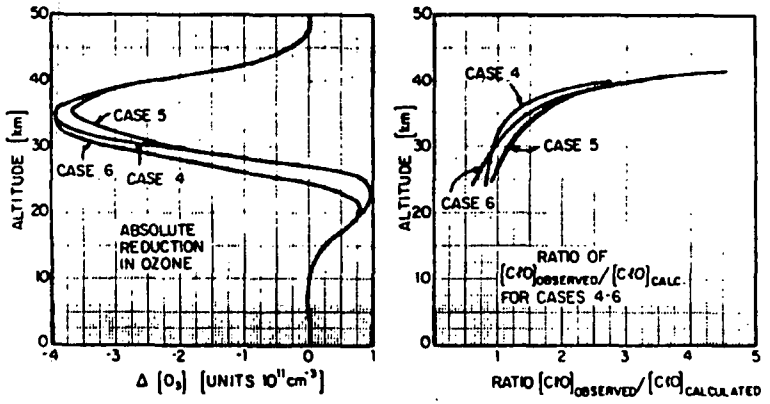

FIGURE D.52 Correlation between the model-calculated altitude dependence of ozone depletion (resulting from 1976/1979 release rates, as noted in the text) and the ratio of calculated to observed [ClO] in the stratosphere.

The [OH] Profile

Given the direct relationship between the ClO concentration profile and the predicted reduction in ozone, we consider next whether other observations substantiate or refute the selection of Cases 4 to 6 as those most appropriately representative of stratospheric photochemistry for the cases considered. The most obvious test is, of course, the correlation between calculated and observed [OH] because (a) the ClO concentration depends quadratically on [OH] below 30 km, as discussed in Appendix C; and (b) it is the $HO_x \equiv OH + HO_2$ concentration that is altered by the various rate constant assumptions for

$OH + HONO_2 \rightarrow N_2O + NO_3$	Case 3
$OH + HO_2NO_2 \rightarrow$ products	Case 4
$OH + HO_2 \rightarrow H_2O + O_2$	Case 5

Figure D.53 summarizes the constraints placed on the six cases by the available OH data, represented here by the in situ balloon-borne data. We select those data because they are consistent with the ground-based total column measurements of OH and they provide the only information available on the shape of the [OH] distribution in the stratosphere. The conclusion, however, is disappointing. The observations are insufficient in number, (absolute) accuracy, and altitude coverage to distinguish between any of the available cases. In the most important region below 30 km, no data exist.

If we consider the other HO_x radical, HO_2, we find the same situation; the data are too scattered and of insufficient altitude coverage to test this critical question of lower stratospheric OH_x (Figure D.54).

A gap of considerable importance thus exists in the case linking low ClO concentrations in the region below 30 km to low OH concentrations, which are in turn explained by exhanced HO_x destruction via reactions of OH with nitric and pernitric acid.

We can, of course, search elsewhere for clues regarding the destruction of OH in the lower stratosphere, most notably in the nitrogen system. Before doing this, however, we turn to a brief review of the nitrogen-catalyzed destruction of odd oxygen and the perturbation of O_3 resulting from the doubling of N_2O.

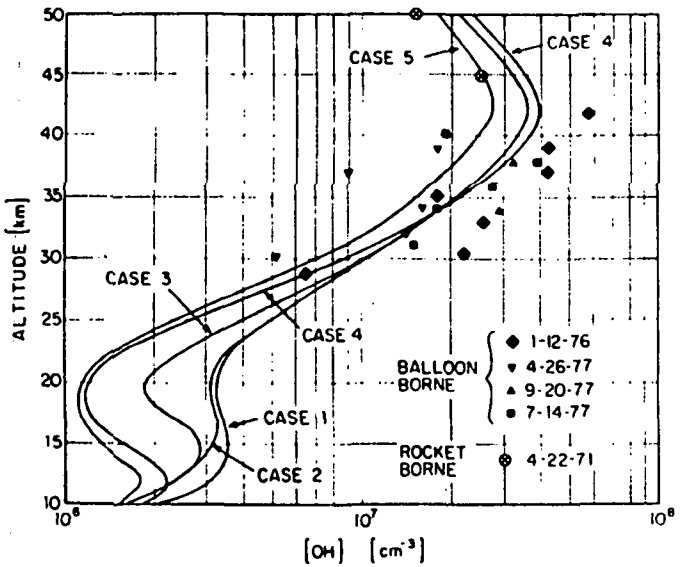

FIGURE D.53 Comparison between observed and calculated OH for the six model cases. Case 6 matches the profile for Case 5.

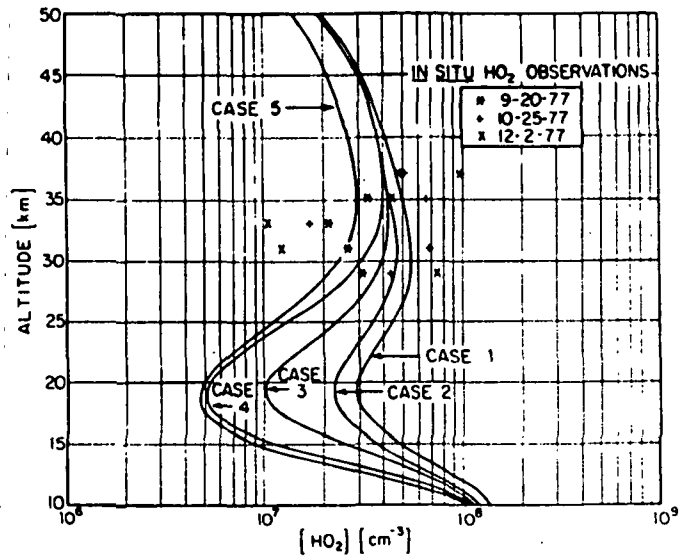

FIGURE D.54 Summary of the correlation between observed and calculated HO_2.

Nitrogen-Induced Destruction of Ozone

The $[NO_2]$ Profile

We first define, in Figure D.55, the response of ozone, as a function of altitude, to a doubling of N_2O for each of the six cases, previously defined. Also included in that figure is the corresponding altitude distribution of the rate limiting radical, NO_2. Cases 1 and 2 are characterized by (nearly) equal but opposite lobes in ΔO_3 that virtually cancel when integrated. This behavior underlines the important connection between the nitrogen and hydrogen catalytic systems. Positive values of ΔO_3 for Cases 1 and 2 below 25 km result from a decrease in the rate of O_x catalysis (not a production of odd oxygen!) by HO_x for increased levels of NO_x because the reaction

$$HO_2 + NO \rightarrow OH + NO_2$$

shifts the available HO_x from the O_x catalytic rate limiting form HO_2 to OH. This behavior is observed only under conditions in which there is sufficient HO_x to dominate the budget of O_x and the behavior is simply one of a deepening of the ozone destruction profile with increasing NO_2. Note that, as OH decreases, the concentration of NO_2 increases since NO_x is removed predominantly by the recombination of OH with NO_2 to form nitric acid.

In Figure D.56, we present the overlay of the 32°N latitude NO_2 data (corrected to midday conditions) with the six modeled $[NO_2]$ profiles. Several points are immediately apparent. First, the range in calculated NO_2 is significantly smaller than that for ClO and thus, while the spread in the NO_2 data is less than that for ClO, it is decidedly more difficult to extract a clear conclusion. The implication, however, is that Cases 1 to 3 correlate better with the data than do Cases 4, 5, and 6. This is obviously a point of considerable importance, not only as a clue to the question of lower stratospheric HO_x and the consistency of our picture of ClO concentration below 35 km, but also from the point of view of the total odd oxygen balance. As noted in Appendix C (Figure C.6a), approximately 70 percent of the total production rate of odd oxygen between 20 and 35 km is balanced by NO_x catalysis (rate limited by NO_2) for a reaction rate constant set corresponding to Case 5, so differences of even ±50 percent are of major import.

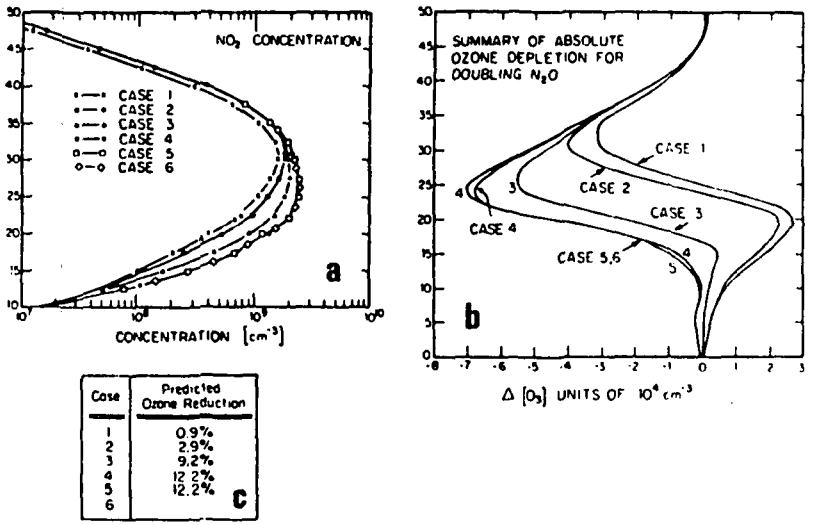

FIGURE D.55 (a) Calculated NO_2, (b) ozone reduction as a function of altitude for a doubling of NO_2, and (c) the integrated column reduction of ozone for each of the six cases defined in the text.

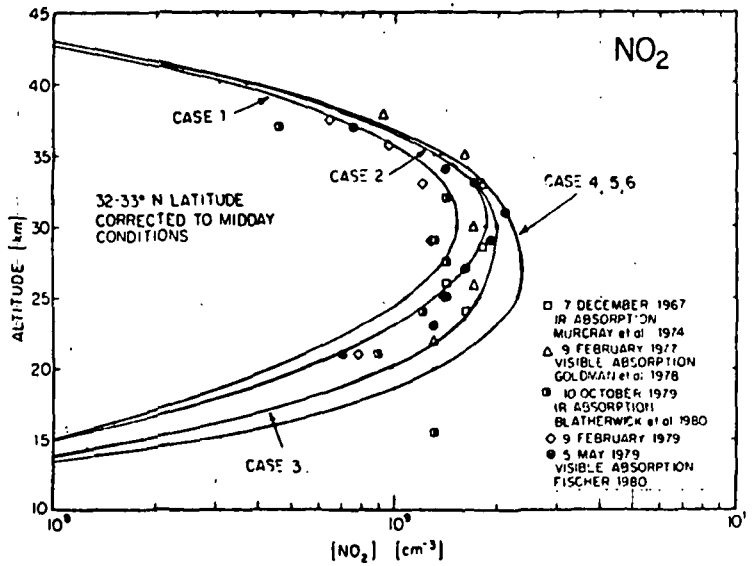

FIGURE D.56 Summary of the correlation between NO_2 observed at midday and the six modeled cases defined in the text. The model calculations here do not include the effect of the spherical earth on multiple scattering at large zenith angles. This effect is important below 30 km.

Examination of the correlation between observed and calculated middle-latitude NO is summarized in Figure D.57, using the most consistent data set available, that of Ridley and co-workers. Although Figure D.57 reflects the significantly larger data base available for NO than for NO_2 (note, also, that the in situ observations were done at midday and thus do not need to be "corrected" for diurnal differences), the superposition of observations and theory is inconclusive. One cannot discriminate, based on the best available data, between NO concentrations corresponding to column-integrated ozone reduction figures from 1 to 12 percent.

The $[HONO_2]$ Profile

We consider next the correlation between calculated and observed $HONO_2$, singling out the mid-latitude data previously presented in Figure D.57. It is clear from Figure D.58 that the nitric acid concentration below 25 km is insensitive to the particular choice of rate constants partitioning reactive nitrogen among NO, NO_2, NO_3, N_2O_5, and $HONO_2$ because nitric acid dominates the reactive nitrogen budget. In the upper stratosphere, nitric acid is only weakly dependent on [OH], and thus there is little hope of using such data to constrain current models with respect to ozone reduction prediction. It is of considerable interest, however, to note the clear divergence between all six cases and the envelope of observations at altitudes above 25 km. This has been a persistent and unresolved feature and while the nitric acid data above 25 km are not as direct a check on the odd oxygen budget as are observations of NO and NO_2, such differences are very clearly of concern.

The Profile of the Ratio of $[O(^3P)]$ to $[O_3]$

We conclude this section by comparing the calculated and observed ratio of $[O(^3P)]$ to $[O_3]$. We display in Figure D.59 the calculated ratio and the mean of the $O(^3P)$ in situ observations and the most recent in situ ozone observations obtained in June (1978 and 1981) at Palestine, Texas, from Figure D.20. The in situ ozone data, discussed earlier, was obtained using three different methods that agree within the uncertainty of the techniques, which is less than 10 percent.

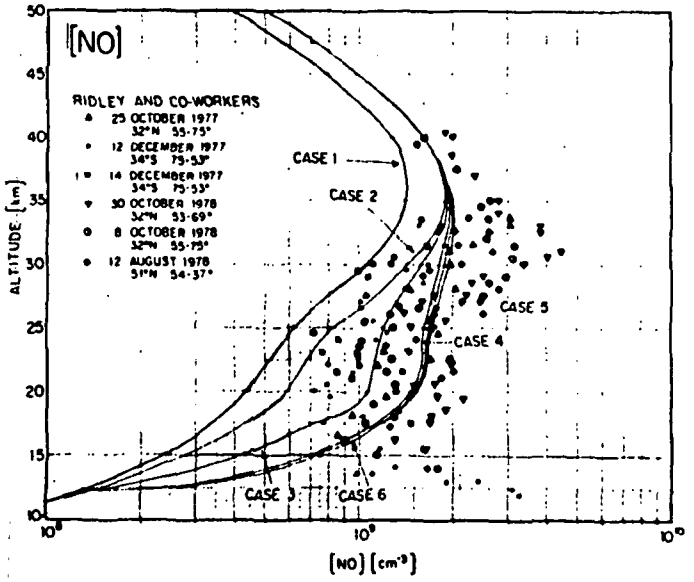

FIGURE D.57 Comparison of calculated and observed NO at mid-latitude.

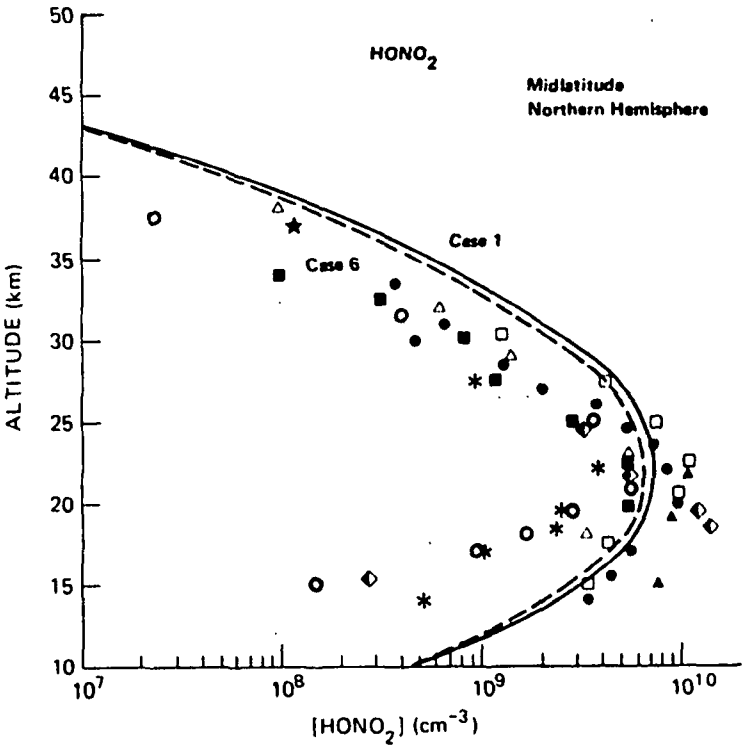

In situ Results

Lazrus and Gandrud (1974)
- ◐ Spring 1971 32°N
- ✱ Spring 1972 32°N
- O Spring 1973 32°N

Arnold et al. (1980)
- ★ November 1977 45°N

Remote Results

Fontanella et al. (1975)
- ▲ July 1973 48°N

Harries et al. (1976)
- □ September 1974 45°N

Evans et al. (1978)
- ■ July-August 1974-76 51°N

Murcray et al. (1980)
- △ October 1979 32°N

Fischer (1980)
- ● May 1979 31°N

FIGURE D.58 Comparison of calculated and observed $HONO_2$ at mid-latitude.

The $[O(^3P)]/[O_3]$ ratio predicted by all six cases is indistinguishable because none of the rate constants involve the exchange of $O(^3P)$ and O_3. Given that the ratio is followed over more than 2 orders of magnitude, the agreement is of considerable significance.

STRATOSPHERIC TRACE SPECIES MEASUREMENTS: PROSPECTS FOR THE NEXT THREE YEARS

A comparison between this paper and the trace species sections in either NRC (1979) or Hudson and Reed (1979) reveals that, while the total number of observations has not expanded dramatically in the past two years, the number of independent techniques has, in several key instances, brought much more clearly into focus a number of important questions. Those questions range from the more qualitative issues such as "typical" atmospheric variability of trace species (e.g., the newest generation of (six) in situ NO measurements exhibits much greater consistency than did previous observations, while the H_2O, OH, and ClO results are characterized by sets of data that are reproducible, but for which clear exceptions exist) to the quantitative problem of constraining ozone reduction predictions by eliminating certain classes of stratospheric models (e.g., those that predict "high" [OH] and [ClO] concentrations in the lower stratosphere).

In this section, we discuss prospects for progress in the next three years by defining the evolving set of problems that can be directly addressed by stratospheric trace species measurements. This is done by formulating a series of questions abstracted from earlier discussions. The emphasis is placed almost entirely on photochemical mechanisms involving the higher reactive trace species that either couple the chemical families (i.e., nitrogen, hydrogen, chlorine, etc.) together by radical-radical recombination steps or enter directly into the rate-determining processes for odd oxygen production/destruction. This bias eliminates in large measure the exceedingly important topic of satellite observations, a subject that has been recently reviewed in detail in Hudson et al. (1982).

Following a statement of the questions that must be addressed by stratospheric measurements in the near future, an appraisal of the prospects for making significant progress in the next three years is presented.

QUESTION 1: Is the cause of the large discrepancy between the observed and calculated [ClO] profile above 35 km an experimental problem or is there an important mechanism missing in the models that converts chlorine to the free radical ClO?

This discrepancy is critical because it coincides in altitude with the peak in the chlorine-induced odd oxygen destruction profile (see Figure D.52). It also has a great deal in common with a similar divergence between calculated and observed [ClO] below 30 km that existed at the time of the last NRC report, a situation summarized in Figure D.60.

In the past two years, both the balloon-borne microwave emission data and the ground-based mm-wave emission data have confirmed the in situ results below 30 km. Of perhaps greater importance was that a plausible mechanism for the cause of the discrepancy evolved out of laboratory measurements of the reaction rate constant data for OH + $HONO_2$ and OH + HO_2NO_2, as noted in the definition of Cases 3 and 4.

Without a resolution to Question 1, there will remain two schools of thought on quantitative predictions of fluorocarbon-induced ozone reduction, because the latter is a sensitive function of the vertical distribution of the rate limiting radical, ClO, in the chlorine-catalyzed destruction of ozone.

PROSPECTS: Several advances in ClO detection methodology will, with high probability, settle the remaining questions concerning the vertical distribution of ClO at mid-latitudes. Progress is forecast in three areas. First, the cross-calibration of the balloon-borne techniques (which within the next two years will include in situ chemical conversion-resonance fluorescence, mm-wave emission, and laser heterodyne radiometry) will define the experimental uncertainties of the three methods. It is already clear from the intercomparison of the mm-wave and in situ methods that agreement within the cited uncertainties of ±30 percent exists. Extensive laboratory simulation work, the use of redundant instruments on each flight, and the addition of several in-flight calibration checks coupled with more careful control of descent velocities will reduce the experimental uncertainties of the in situ methods to about ±10 or 15 percent. Similar figures are the planned objective of the remote techniques.

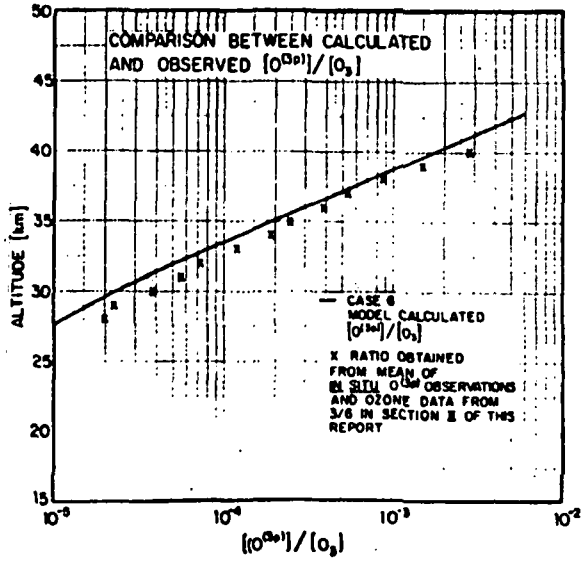

FIGURE D.59 Comparison between observed and calculated $[O(^3P)]/[O_3]$.

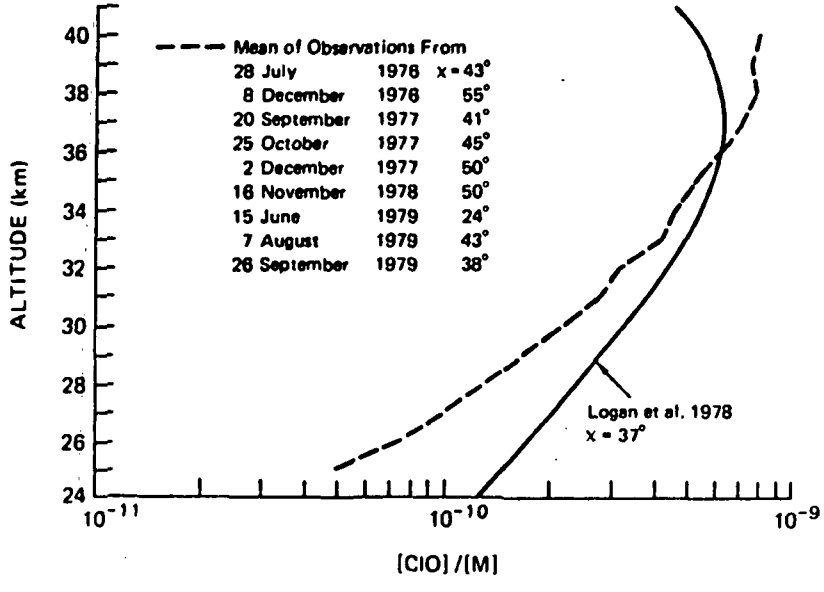

FIGURE D.60 Comparison between the mean of all in situ ClO observations, excluding July 14, 1977, and the calculated ClO distribution from Logan et al. (1978).

The ClO distribution above 35 km must be explored with the balloon-borne mm-wave emission measurements to determine, in particular, the total ClO column density above 40 km. This is most effectively done simultaneously with in situ observations obtained with multiple vertical scans using the reel down/reel up deployment technique currently under development.

It is important to note that all the measurement techniques provide data that are easiest to interpret in the low-pressure region of the upper stratosphere, so that if the middle and lower stratospheric profiles are correct, the probability is large that the high-altitude end of the profile is correct.

Second, the development of ground-based mm-wave emission techniques provides the means for obtaining much better temporal coverage to search for the occurrence of enhancements reported by the in situ methods--the only impediment currently preventing the initiation of that coverage is the serious attenuation of 204-GHz radiation by water vapor in the troposphere, which maximizes during the summer months, encompassing July when both high values were observed.

Careful delineation of the diurnal behavior of ClO should also be accomplished in the next five years using both the mm-wave emission technique and the multiple vertical scan in situ technique. These results should cast light on the question of isomer formation from the reaction of ClO with NO_2. This is not suggested as a substitute for direct laboratory data, but rather as a complementary approach to establish the temporal behavior of ClO as a function of altitude throughout the night and following sunrise.

<u>QUESTION 2: Is the stratosphere most accurately characterized by "high" [OH] below 30 km, as represented by Cases 1 and 2 in Figure D.53, or by "low" [OH], as defined by Cases 4 and 5 in the same figure?</u>

From the standpoint of understanding perturbations to stratospheric ozone, this question is of unequaled importance because an unequivocal answer will establish (a) whether the rate of ozone destruction in the lower stratosphere is controlled by catalytic cycles involving HO_x or NO_x radicals, and (b) whether the chlorine radicals Cl and ClO have any measureable impact on the odd oxygen budget below 30 km. Without direct observations of OH (with an excellent signal-to-noise ratio) in the region

between 15 and 30 km, obtained simultaneously with measurements of H_2O, an intolerable gap will remain in the case linking chemical perturbation to ozone reduction in the stratosphere.

PROSPECTS: Two methods have been developed to extend previous OH measurements in the upper stratosphere to lower altitudes. A lidar method, employing a pulse laser with time-resolved detection, has been initially tested in the stratosphere and should yield the first balloon-borne remote measurements in the next five years. In addition, an in situ method employing a high repetition rate (20,000 Hz) tuneable laser has been developed to determine the OH concentration in situ throughout the stratosphere with approximately 1000 times the signal-to-noise ratio of the experiments reported earlier. The in situ method also promises to provide observations of HO_2 by using chemical conversion (the addition of NO) to convert HO_2 to OH, followed by laser-induced fluorescence detection of OH. This "simultaneous" detection of OH and HO_2 with the same absolute calibration will establish the sum of the two major HO_x species and the ratio with an altitude resolution of less than or equal to 0.5 km and a signal-to-noise ratio greater than or equal to 10 throughout the stratosphere.

Development of cryogenically cooled detection chambers for the measurement of H_2O by fragment fluorescence under daylight conditions should, within two years, provide the first data on the ratio of $[HO_x]$ to $[H_2O]$.

QUESTION 3: What is the mean distribution of NO_2 as a function of altitude between 15 and 45 km determined to an (absolute) accuracy of ±10 percent throughout the day at equatorial, lower mid-latitude, and upper mid-latitude locations?

Given our current picture of odd oxygen destruction rates, as summarized in Figure C.6a of Appendix C, catalytic destruction of odd oxygen by NO_x constitutes at least 70 percent of the ozone budget between the tropopause and 35 km. That catalytic cycle is rate limited by NO_2 at all altitudes, yet we do not have high-accuracy data on this critical radical as a function of altitude and latitude.

PROSPECTS: High-accuracy/precision NO_2 observations with excellent signal-to-noise ratios have not been

reported, but a recent experiment employing photolytic conversion of NO_2 to NO followed by the chemiluminescent detection of NO holds promise of making a considerable contribution to this exceedingly serious shortcoming in our observational data base. A particularly attractive feature of the technique is that it provides a measurement of NO with the same absolute calibration, so highly precise ratios of NO to NO_2 should result. In addition, on-board NO and NO_2 calibrated samples should yield exceedingly accurate absolute results.

There are other methods currently under study in the laboratory for both NO and NO_2 including laser-induced fluorescence, double photon ionization, and double photon fluorescence. Those in situ methods may well yield the first "cause and effect" studies of the odd oxygen budget by correlating local fluctuations in NO_2 and O_3 in the middle stratosphere, where the loss rate of O_3 is controlled almost entirely by the NO_x catalytic cycle.

The infrared methods that are not plagued by the restriction of sunset-sunrise geometries may also, if cross-calibrated in the same air mass, yield important results that will address Question 3.

QUESTION 4: Do the infrared techniques applied to the "reservoir" terms HCl and $HONO_2$ yield results within the stated experimental accuracies when applied simultaneously to the same air mass?

An exceedingly important check on the models used for ozone reduction calculation comes from a comparison between calculated and observed concentrations of the chlorine and nitrogen compounds of intermediate lifetime (about a few months) in the middle and lower stratosphere. This is because these compounds, primarily HCl and $HONO_2$, dominate the total budget of reactive chlorine and nitrogen in the lower and middle stratosphere and are transport controlled and thus sensitive to model assumptions regarding vertical and horizontal transport.

PROSPECTS: An extensive series of cross-calibration flights, wherein the major infrared remote techniques for HCl and $HONO_2$ detection are used to interrogate the same air mass, is scheduled for the next two years. Experiments from both Europe and North America will be included, and a standard series of deconvolution programs will be applied to the data with careful comparison of the resulting profiles.

This flight series should make major advances toward narrowing the experimental uncertainties in the observation of both HCl and $HONO_2$. It has generally been found that a few carefully orchestrated observations are more effective for testing models than a large number of observations with questionable absolute calibration. It is equally true that the observation of a given trace reactant by as many independent methods (with comparably defensible absolute calibration) is essential for acceptance by the scientific community. This joint flight of the analytical techniques for HCl and $HONO_2$ is in response to that fact, and the results will be applicable to a broad range of molecules that can, at present, only be observed by remote IR methods.

QUESTION 5: What is the diurnal behavior of ClO, NO_2, NO, OH, and HO_2 as a function of altitude between the tropopause and 45 km?

Although high-quality profiles of the major radicals at midday are of first-order importance, there is a great deal to be learned from the temporal behavior, under carefully controlled conditions, of the highly reactive trace species following sunrise and sunset. It is crucial in these studies to achieve altitude resolution of 1 to 2 km and to watch several related species simultaneously.

PROSPECTS: The need to obtain simultaneous data on the five constituents with good altitude resolution is one of the most difficult analytical challenges currently facing the field. It will require the simultaneous deployment of three sophisticated experiments with repetitive vertical scans, concentrating on the sunset and sunrise periods. While this capability will probably be within reach in the next two to three years, considerable progress will almost certainly be made using mm-wave emission techniques to examine the diurnal behavior of ClO, IR emission techniques and chemiluminescence for NO and NO_2, and balloon-borne lidar or in situ laser-induced fluorescence measurements for OH and HO_2, separately deployed in each case.

QUESTION 6: What is the spectral distribution of solar radiation between 180 and 240 nm as a function of altitude down to the tropopause?

The absence of published high-resolution data of the solar flux as a function of altitude, solar zenith angle, and wavelength is a shortcoming of major importance. Without those direct measurements, the loss rate of the critical "source" terms (e.g., $CFCl_3$, CF_2Cl_2, and CH_3Cl) cannot be checked.

PROSPECTS: Within the next year, publication of the first high-resolution data on the penetration of solar flux in the 180- to 240-nm spectral interval should begin to eliminate a serious shortcoming on the question. If this does not clear up discrepancies in the loss rates of, for example, $CFCl_3$, then it may be necessary to consider the difficult observations of dissociation rates directly measured in situ. A discussion of the discrepancies between observed and calculated source molecules (CH_4, N_2O, CH_3Cl, $CFCl_3$, ethane) appears in Appendix C.

QUESTION 7: What is the vertical distribution of ClO, NO, NO_2, OH, and HO_2 between 15 and 45 km in the equatorial latitudes?

Far too much emphasis has been placed on the analysis of mid-latitude data as a result of the concentration of experimental results on this region. However, the dominant region of global ozone production exists at latitudes below 30°N, and it is of first-order importance to discover whether [ClO], for example, exhibits the behavior characterized by a rapid decrease below 30 km as it does at 32°N. There are comparably important examples in the HO_x and NO_2 systems.

PROSPECTS: Within two years, the new generation of techniques previously discussed should have provided the first high-quality soundings of these key radicals, hopefully with simultaneous observation of H_2O and O_3 with the OH and HO_2 experiments. It will require, perhaps, another two years to establish with considerable confidence the mean distribution of those radicals, but the large observed fluctuations in H_2O above the tropopause may yield valuable insight into the chemical linking between the NO_x, HO_x, and ClO_x families by studying the covariance between these radicals. Simultaneous in situ observations of ozone may yield exceedingly important insight into the odd oxygen budget from the same series of observations.

QUESTION 8: What is the altitude distribution of the important intermediates, HOCl, $ClONO_2$, HO_2NO_2, NO_3, N_2O_5, and $HONO_2$ in the stratosphere?

The reasons that these products of radical-radical recombination reactions are important are discussed throughout this report and need not be repeated. They present a particularly difficult analytical problem, however, because they are in general large polyatomic molecules that do not possess strong electronic transitions, yet their predicted concentrations fall below the detection threshold of long-path IR absorption techniques.

PROSPECTS: The first three molecules in this group constitute an exceedingly difficult triplet from the point of view of analytical techniques that can be applied to the stratosphere. Initial detection of $ClONO_2$ has been reported, but the detection is marginally possible with the best IR methods available, and no method has reported observation of HOCl and HO_2NO_2. Significant difficulties are predicted for progress on these molecules, but the options have not been exhausted. Double photon ionization methods and fragment fluorescence may be applicable, although the ubiquitous nature of the hydrogen, nitrogen, and oxygen fragments in pernitric acid will make such measurements difficult to interpret.

Initial measurements of NO_3 at night are encouraging. Attempts to detect N_2O_5 by thermal dissociation followed by detection of the NO_x products formed have been made in the laboratory, but have not shown sufficient promise to warrant stratospheric application.

It would, in addition, be exceedingly important if an unambiguous technique for detecting $HONO_2$ in situ could be developed. This would contribute significantly to the question of the NO_2, $HONO_2$, OH chemistry of the lower stratosphere.

QUESTION 9: What is the concentration of NO_2, NO, ClO, OH and O_3 simultaneously determined in an air mass characterized by the very low NO_2 concentration observed by Noxon northward of the high-latitude ledge features, described in Figure D.34?

The apparent intrusion of polar air to northern mid-latitudes in the spring represents the opportunity to test in an interesting way the nitrogen, hydrogen, and chlorine chemistry of the stratosphere.

PROSPECTS: The analytical techniques will be available within two years to explore in situ and simultaneously the concentration of NO, NO_2, ClO, OH, HO_2, and O_3 in the vicinity of the NO_2 "ledge" reported by Noxon, based on ground-based observations of nitrogen dioxide. A detailed understanding of the free radical concentration in such an event would be an exceedingly interesting perturbation experiment.

QUESTION 10: Is water vapor the constituent responsible for inducing the variability in free radical concentrations evident in virtually all the results reported in this paper?

Given the extreme sensitivity of $[H_2O]$ to the tropopause temperature and the large observed fluctuations of water above the tropical tropopause, it seems plausible that fluctuations in H_2O, which in turn cause fluctuations in OH and HO_2, constitute a starting point for observed local changes in NO, NO_2, and ClO. The mechanistic links are discussed both here and in Appendix C.

PROSPECTS: As the signal-to-noise ratio, absolute calibration, altitude resolution, and capability to make a large number of simultaneous observations improve in the next three to four years, a wealth of information about how fluctuations in local water vapor concentrations affect the HO_x, NO_x, and ClO_x chemistry of the stratosphere will evolve. Thus correlation experiments may best be carried out in the equatorial region, where fluctuations in H_2O may be the most dramatic. If local variability reported from aircraft observations well above the tropopause hold at higher altitudes, an entirely new class of correlation experiments will evolve. Such measurements hold great promise for establishing cause-and-effect links within the complex net of reactions linking the various families through radical-radical reactions.

QUESTION 11: Does the odd oxygen production/destruction budget balance, based on observed concentrations of the rate limiting free radicals?

Although transport times in the odd oxygen continuity equation obviate the possibility of applying a purely chemical test to the balance of local odd oxygen produc-

tion and destruction in the lower stratosphere, it is essential that we continue to press the issue of improved analytical techniques for NO_2, HO_2, ClO, $O(^3P)$, and O_3 to quantify, as a function of altitude and latitude, the balance between production and destruction of odd oxygen. Although this approach cannot directly test cause-and-effect relationships with the odd oxygen budget and the approach is currently seriously diluted by large experimental uncertainties, it must be carefully pursued.

PROSPECTS: The next two years will bring considerably more accurate detection techniques for the major rate limiting radicals, NO_2, ClO, HO_2, OH, $O(^3P)$, and O_3 with cross-calibration against remote techniques and limited latitude coverage. Although such techniques can never prove completeness in our definition of ozone production and loss processes, the detailed accounting will provide important evidence suggesting the altitude dependence of proposed mechanisms.

REFERENCES

Ackerman, M. and C. Muller (1973) Stratospheric methane and nitrogen dioxide from infrared spectra. Pure and Applied Geophysics 106-108:1325-1335.

Ackerman, M., J.C. Fontanella, D. Frimout, A. Girard, N. Louisnard, and C. Muller (1975) Simultaneous measurements of NO and NO_2 in the stratosphere. Planetary and Space Science 23:651-660.

Aiken, A.C. and E.J.R. Maier (1978) Balloon-borne photoionization mass spectrometer for measurement of stratospheric gases. Review of Scientific Instruments 49:1034-1040.

Anderson, J.G. (1971) Rocket measurement of OH in the mesosphere. Journal of Geophysical Research 76:7820.

Anderson, J.G. (1975) Measurement of atomic oxygen and hydroxyl in the stratosphere. Pages 458-464, Proceedings, Fourth Conference on CIAP. Symposium No. 175. Washington, D.C.: U.S. Department of Transportation.

Anderson, J.G. (1980) Free radicals in the earth's stratosphere: A review of recent results. Pages 233-251, Proceedings of the NATO Advanced Study Institute on Atmospheric Ozone: Its Variation and Human Influences, edited by A.C. Aiken. October 1-13, 1979. U.S. Department of Transportation, Report No.

FAA-EE-80-20. Washington, D.C.: Federal Aviation Administration.

Anderson, J.G., J.J. Margitan, and D.H. Steoman (1977) Atomic chlorine and the chlorine monoxide free radical in the stratosphere: Three in situ observations. Science 198:501.

Anderson, J.G., R.E. Shetter, H.J. Grassel, and J.J. Margitan (1980) Stratospheric free chlorine measured by balloon-borne in situ resonance fluorescence. Journal of Geophysical Research 85:2869.

Arnold, F., R. Fabian, G. Henschen, and W. Joos (1980) Stratospheric trace gas analysis from ions: H_2O and HNO_3. Planetary and Space Science 28:581-585.

Bangham, M.J., A. Bonetti, R.H. Bradsell, B. Carli, J.G. Harries, F. Mencaraglia, D.G. Moss, J. Pollitt, E. Rossi, and N.R. Swann (1980) New measurements of stratospheric composition using submillimeter and infrared emission spectroscopy. (Unpublished manuscript available from A. Bonetti, University of Florence, Florence, Italy.)

Berg, W.W., P.J. Crutzen, F.E. Grabek, and S.N. Gitlin (1980) First measurements of total chlorine and bromine in the lower stratosphere. Geophysical Research Letters 7:937-940.

Blatherwick, R.D., A. Goldman, D.G. Murcray, F.J. Murcray, G.R. Cook, and J.W. Van Allen (1980) Simultaneous mixing ratio profiles of stratospheric NO and NO_2 as derived from balloon-borne infrared solar spectra. Geophysical Research Letters 7:471-473.

Buijs, H.L., G.L. Vail, G. Tremblay, and D.J.W. Kendall (1980) Simultaneous measurements of the volume mixing ratio of HF and HCl in the stratosphere. Geophysical Research Letters 7:205.

Burnett, C.R. (1976) Terrestrial OH abundance measurement by spectroscopic observation of resonance absorption by sunlight. Geophysical Research Letters 3:319.

Burnett, C.R. (1977) Spectroscopic measurements of atmospheric OH abundance. Bulletin of the American Physical Society 22:539.

Burnett, C.R. and E.B. Burnett (1981) Spectroscopic measurements of the vertical column abundance of hydroxyl [OH] in the earth's atmosphere. Journal of Geophysical Research 86:5185.

Campbell, M.J., J.C. Sheppard, and B.J. An (1979) Measurement of hydroxyl concentration in boundary layer air by monitoring CO oxidation. Geophysical Research Letters 6:175.

Chaloner, C.P., J.R. Drummond, J.T. Houghton, R.F. Jarnot, and H.K. Roscoe (1978) Infrared measurements of stratospheric composition I. The balloon instrument and water vapor measurements. Proceedings of the Royal Society of London, Series A 364:145-159.

Chance, K.V., J.C. Brasunas, and W.A. Traub (1980) Far infrared measurement of stratospheric HCl. Geophysical Research Letters 7:704.

Coffey, M.T., W.G. Mankin, and A. Goldman (1981) Simultaneous spectroscopic determination of the latitudinal, seasonal and diurnal variability of stratospheric N_2O, NO and HNO_3. Journal of Geophysical Research 86(C8):7331-7341.

Crutzen, P.J., I.S.A. Isaksen, and J.R. McAfee (1978) The impact of the chlorocarbon industry on the ozone layer. Journal of Geophysical Research 83:345.

Davis, P.D., W.S. Heaps, and T. McGee (1976) Direct measurements of natural tropospheric levels of OH via an aircraft borne tunable dye laser. Geophysical Research Letters 3:331.

Davis, P.D., W.S. Heaps, D. Philen, M. Rodger, T. McGee, A. Nelson, and A.J. Moriarty (1979) An airborne laser induced fluorescence system for measuring OH and other trace gases in the parts-per-quadrillion to parts-per-trillion range. Review of Scientific Instruments 50:1505.

Drummond, J.W., J.M. Rosen, and D.J. Hoffman (1977) Balloon-borne chemiluminescent measurements of NO to 45 km. Nature 265:319-320.

Ehhalt, D.H., U. Schmidt, and L.E. Heidt (1977) Vertical profiles of molecular hydrogen in the troposphere and the stratosphere. Journal of Geophysical Research 82:5907-5911.

Evans, W.F.J. and E.J. Llewellyn (1970) Molecular oxygen emission in the airglow. Annales de Geophysique 26:167.

Evans, W.F.J., E.J. Llewellyn, and A.V. James (1969) Balloon observations of the temporal variation of the infrared atmospheric oxygen bands in the airglow. Planetary and Space Science 17:933.

Evans, W.F.J., H. Fast, J.B. Kerr, C.T. McElroy, R.S. O'Brien, D.I. Wardle, J.C. McConnell, and B.A. Ridley (1978) Stratospheric constituent measurements from project stratoprobe. Pages 55-60, Proceedings of the WMO Symposium on the Geophysical Aspects and Consequences of Change in the Composition of the Stratosphere, WMO Publication 511. Geneva: World Meteorological Organization.

Eyre, J.R. and H.K. Roscoe (1977) Radiometric measurements of HCl. Nature 226:243.

Farmer, C.B., O.F. Raper, B.D. Robbins, R.A. Toth, and C. Muller (1980) Simultaneous spectroscopic measurements of stratospheric species: O_3, CH_4, CO, CO_2, N_2O, HCl, and HF at northern and southern mid-latitudes. Journal of Geophysical Research 85 (C3):1621.

Fischer, H., F. Fergg, and D. Rabus (1982) Radiometric measurements of stratospheric H_2O, HNO_3 and NO_2 profiles. Proceedings of the International Radiation Symposium, Fort Collins, Colorado, August 1980. (To be published in the Journal of the National Cancer Institute in 1982.)

Fontanella, J.C., A. Girard, L. Gramont, and N. Louisnard (1975) Vertical distribution of NO, NO_2 and HNO_3 as derived from stratospheric absorption infrared spectra. Applied Optics 14:825-839.

German, K.R. (1975) Radiative and predissociative lifetimes of the $V^1 = D_1 D_1$ and 2 levels of the $A^2\Sigma^+$ state of OH and OD. Journal of Chemistry and Physics 63:5252-5255.

German, K.R. (1976) Collision and quenching cross sections in the $A^2\Sigma^+$ state of OH and OD. Journal of Chemistry and Physics 64:4065-4068.

Girard, A., J. Besson, R. Giraudet, and L. Gramont (1978/1979) Correlated seasonal and climate variations of trace constituents in the stratosphere. Pure and Applied Geophysics 117:381-394.

Goldman, A., F.G. Fernald, W.J. Williams, and D.G. Murcray (1978) Vertical distribution of NO_2 in the stratosphere as determined from balloon measurements of solar spectra in the 4500 Å region. Geophysical Research Letters 5:257-260.

Harries, J.E., D.G. Moss, N.R.W. Swann, G.F. Neill, and P. Gildwarg (1976) Simultaneous measurements of H_2O, NO_2 and HNO_3 in the daytime stratosphere from 15 to 35 km. Nature 259:300-301.

Heaps, W.S., T.J. McGee, R.D. Hudson, and L.O. Caudill (1981) Balloon-borne Lidar Measurements of Stratospheric Hydroxyl and Ozone, NASA Publication X-963-81-27. Greenbelt, Md.: National Aeronautics and Space Administration.

Horvath, J.J. and C.J. Mason (1978) Nitric oxide mixing ratios near the stratopause measured by a rocket-borne chemiluminescent detector. Geophysical Research Letters 5:1023-1026.

Hudson, R.D. and E.I. Reed, eds. (1979) The Stratosphere: Present and Future. NASA Reference Publication 1049. Greenbelt, Md.: National Aeronautics and Space Administration; N80-14641-14648. Springfield, Va.: National Technical Information Service.

Hudson, R.D. et al., eds. (1982) The Stratosphere 1981: Theory and Measurement. WMO Global Research and Monitoring Project Report No. 11. Geneva: World Meteorological Organization. (Available from National Aeronautics and Space Administration, Code 963, Greenbelt, Md. 20771.)

Kerr, J.B. and C.T. McElroy (1976) Measurement of stratospheric nitrogen dioxide from the AES stratospheric balloon program. Atmosphere 14:166-171.

Kley, D., J.W. Drummond, and A.L. Schmeltekopf (1980) On the structure and microstructure of stratospheric water vapor. Pages 315-327, Atmospheric Water Vapour, edited by A. Deepak, T.D. Wilkerson, and L.H. Ruhnke. New York, N.Y.: Academic Press, Inc.

Lazrus, A.L. and B.W. Gandrud (1974) Distribution of stratospheric nitric acid vapor. Journal of Atmospheric Science 31:1102.

Lazrus, A.L., B.W. Gandrud, J. Greenberg, J. Bonelli, E. Mroz, and W.A. Sedlacek (1977) Midlatitude seasonal measurements of stratospheric and chlorine vapor. Geophysical Research Letters 4:587.

Loewenstein, M., W.J. Borucki, H.F. Savage, J.G. Borucki, and R.C. Whitten (1978a) Geographical variations of NO and O_3 in the lower stratosphere. Journal of Geophysical Research 83:1875-1882.

Loewenstein, M., W.J. Starr, and D.G. Murcray (1978b) Stratospheric NO and HNO_3 observations in the northern hemisphere for three seasons. Geophysical Research Letters 5:531-534.

Logan, J.A., M.J. Prather, S.C. Wofsy, and M.B. McElroy (1978) Atmospheric chemistry: Response to human influence. *Philosophical Transactions of the Royal Society* 290:187.

Logan, J.A., M.J. Prather, S.C. Wofsy, and M.B. McElroy (1981) Tropospheric chemistry: A global perspective. Journal of Geophysical Research 80:7210.

Marche, P., A. Barbe, C. Secroun, J. Corr, and P. Jouve (1980a) Ground-based spectroscopic measurements of HCl. Geophysical Research Letters 7:869.

Marche, P., A. Barbe, C. Secroun, J. Corr, and P. Jouve (1980b) Mesures des acides fluorhydrique et chlorhydrique dans l'atmosphere par spectroscopic

infraroque a partir du sol. Comptes Rendus Hebdomadaires des Seances de l'Academie des Sciences, Series B 290(14):369-371.

Mauersberger, K., R. Finstad, S. Anderson, and P. Robbins (1981) A comparison of ozone measurements. Geophysical Research Letters 8:361.

Menzies, R.T. (1978) Remote measurements of ClO in the stratosphere. Geophysical Research Letters 6:151.

Menzies, R.T., C.W. Rutledge, R.A. Zanteson, and P.D. Spears (1981) Balloon-borne laser heterodyne radiometer for measurements of atmospheric trace species. Applied Optics 20:536.

Mihelcic, D., D.H. Ehhalt, G.F. Kulessa, J. Klomfass, M. Trainer, U. Schmidt, and H. Röhrs (1978) Measurements of free radicals in the atmosphere by matrix isolation and electron paramagnetic resonance. Pure and Applied Geophysics 116:530.

Molina, M.J. and F.S. Rowland (1974) Stratospheric sink for chlorofluoromethanes: Chlorine-atom catalyzed destruction of ozone. Nature 249:810-812.

Mroz, E.J., A.J. Lazrus, and J. Bornelli (1977) Direct measurements of stratospheric fluoride. Geophysical Research Letters 4:149.

Murcray, D.G., A. Goldman, W.J. Williams, F.H. Murcray, J.N. Brooks, J. Van Allen, R.N. Stocker, J.J. Kosters, D.B. Barker, and D.E. Snider (1974) Recent results of stratospheric trace-gas measurements from balloon-borne spectrometers. Pages 184-192, Proceedings of the Third CIAP Conference, Report No. DOT-TSC-OST-74-15. Washington, D.C.: U.S. Department of Transportation.

Murcray, D.G., A. Goldman, F.H. Murcray, F. J. Murcray, and W.J. Williams (1979) Stratospheric distribution of $ClONO_2$. Geophysical Research Letters 6:857.

National Research Council (1979) Stratospheric Ozone Depletion by Halocarbons: Chemistry and Transport. Panel on Chemistry and Transport, Committee on Impacts of Stratospheric Change, Assembly of Mathematical and Physical Sciences. Washington, D.C.: National Academy of Sciences.

Naudet, J.P., D. Huguenin, P. Rigaurd, and D. Cariolle (1981) Stratospheric observations of NO_3 and its experimental and theoretical distribution between 20 and 40 km. Planetary and Space Science 29:707.

Noxon, J.F. (1968) Day airglow. Space Science Reviews 8:92.

Noxon, J.F. (1978) Stratospheric NO_2 in the Antarctic winter. Geophysical Research Letters 5:1021-1022.

Noxon, J.F. (1979) Stratospheric NO_2. II. Global behavior. Journal of Geophysical Research 84:5067-5076.

Noxon, J.F. (1980) Correction. Journal of Geophysical Research 85:4560-4561.

Noxon, J.F., E.C. Whipple, Jr., and R.S. Hyde (1979) Stratospheric NO_2. I. Observational method and behavior at mid-latitude. Journal of Geophysical Research 84:5047-5065.

Parrish, A., R.L. de Zafra, P.M. Solomon, J.W. Barrett, and E.R. Carlson (1981) Chlorine oxide in the stratospheric ozone layer: Ground-based detection and measurement. Science 211(4487):1158-1161.

Patel, C.K.N., E.G. Burkhardt, and C.A. Lambert (1974) Spectroscopic measurements of stratospheric nitric oxide and water vapor. Science 184:1173-1176.

Perner, D., D.H. Ehhalt, H.W. Pätz, U. Platl, E.P. Roth, and A. Volz (1976) OH radicals in the lower troposphere. Geophysical Research Letters 3:460.

Ridley, B.A. and D.R. Hastie (1981) Stratospheric odd-nitrogen: NO measurements at 51°N in summer. Journal of Geophysical Research 86(C4):3162-3166.

Ridley, B.A. and L.C. Howlett (1974) An instrument for nitric oxide measurements in the stratosphere. Review of Scientific Instruments 45:742-746.

Ridley, B.A. and H.I. Schiff (1981) Stratospheric odd-nitrogen: Nitric oxide measurements at 31°N in autumn. Journal of Geophysical Research 86:3167-3172.

Roscoe, H.K., J.R. Frummond, and R.F. Jarnot (1981) Infrared measurements of stratospheric composition III. The daytime changes of NO and NO_2. Proceedings of the Royal Society of London A 375:507.

Roy, C.R., I.E. Galbally, and B.A. Ridley (1980) Stratospheric odd nitrogen. II. Measurements of nitric oxide in the southern hemisphere. Quarterly Journal of the Royal Meteorological Society 106:887-894.

Schmidt, U. (1978) The latitudinal and vertical distribution of molecular hydrogen in the troposphere. Journal of Geophysical Research 83:941-946.

Schmidt, U., G. Kulessa, and E.P. Roth (1980) The atmospheric H_2 cycle. Pages 307-322, Proceedings of the NATO Advanced Study Institute on Atmospheric Ozone: Its Variation and Human Influences, edited by A.C. Aiken. October 1-13, 1979. U.S. Department of Transportation, Report No. FAA-EE-80-20. Washington, D.C.: Federal Aviation Administration.

Sze, N.D. and M.K.W. Ko (1981) The effects of the rate of OH + HNO_3 and $HONO_2$ photolysis on the stratospheric chemistry. Atmospheric Environment 15:1301.

Wallace, L. and D.M. Hunten (1968) Dayglow of the oxygen A band. Journal of Geophysical Research 73:4813.

Wang, C.C., L.I. Davis, Jr., P.M. Zelzer, and R. Munoz (1981) Improved airborne measurements of OH in the atmosphere using the technique of laser induced fluorescence. Journal of Geophysical Research 86:1181.

Waters, J.W., J.J. Gustincic, R.K. Kakar, H.K. Roscoe, P.N. Swanson, T.G. Phillips, T. deGraauw, A.R. Kerr, and R.J. Mattauch (1979) Aircraft search for millimeter-wavelength emission by stratospheric ClO. Journal of Geophysical Research 84:7034-7040.

Waters, J.W., J.C. Hardy, R.F. Jarnot, and H.M. Pickett (1981) Chlorine monoxide radical, ozone and hydrogen peroxide: Stratospheric measurements by microwave limb sounding. Science 214:61.

Weinstock, E.M., M.J. Phillips, and J.G. Anderson (1981) In situ observations of ClO in the stratosphere: A review of recent results. Journal of Geophysical Research 86:7273.

Wuebbles, D.J. and J.S. Chang (1981) A study of the effectiveness of the Cl_x catalytic ozone loss mechanism. Journal of Geophysical Research 86:9869.

Zander, R. (1975) Presence de HF dans la stratosphere superieure. Comptes Rendus Hebdomadaires des Seances de l'Academie des Sciences, Series B 281(12):213-214.

Zander, R. (1981) Recent observations of HF and HCl in the upper stratosphere. Geophysical Research Letters 8(4):413-416.

Zander, R., H. Lecbert, and L.D. Kaplan (1981) Concentration of carbon monoxide in the upper stratosphere. Geophysical Research Letters 8(4):365-368.

JOURNAL OF GEOPHYSICAL RESEARCH, VOL. 86, NO. C8, PAGES 7273–7278, AUGUST 20, 1981

In Situ Observations of ClO in the Stratosphere: A Review of Recent Results

E. M. WEINSTOCK, M. J. PHILLIPS, AND J. G. ANDERSON

Center for Earth and Planetary Physics and Department of Chemistry, Harvard University, Cambridge, Massachusetts 02138

A summary of the results of 10 balloon-borne in situ measurements of ClO in the stratosphere is presented. All observations were carried out close to local noon at 32°N latitude with solar zenith angles between 24° and 55°. The mean of nine of the observations, which for the most part fall within a well-defined envelope, is compared with a recently calculated [ClO] distribution between 25 and 42 km at the appropriate latitude and time of day. It is found that while reasonable agreement exists in the 35- to 40-km region, the ratio of calculated to observed [ClO] increases monotonically with decreasing altitude below 35 km, reaching approximately three at 25 km. The tenth observation exhibits a mixing ratio nearly an order of magnitude greater than the mean. An analysis of the relevant chemistry below 30 km is presented which indicates that the discrepancy between the observed mean and the calculated [ClO] distribution can be linked to uncertainties in the [OH]/[NO] ratio in the lower stratosphere. A comparison is made between the in situ resonance fluorescence observation reported here and the remote laser heterodyne radiometer measurements of Menzies. Finally, the fractional destruction of $O_x \equiv O_3 + O(^3P)$ by $ClO_x \equiv Cl + ClO$, based on the observed mean of the in situ [ClO] and [$O(^3P)$] midday observations, is presented for the altitude interval 27–41 km.

INTRODUCTION

The fluorocarbon-ozone theory of Rowland and Molina [see *Molina and Rowland*, 1974; *Rowland and Molina*, 1975] linked the surface release of halogen substituted methanes, principally fluorocarbon 11 ($CFCl_3$) and 12 (CF_2Cl_2) with the stratospheric destruction of $O_x \equiv O_3 + O(^3P)$ by the homogeneous gas phase catalytic cycle

$$Cl + O_3 \xrightarrow{k_1} ClO + O_2 \quad (1)$$

$$ClO + O \xrightarrow{k_2} Cl + O_2 \quad (2)$$

$$O + O_3 \rightarrow 2O_2$$

Both the calculated distribution of Cl, ClO, O, and O_3 [see, e.g., *Logan et al.*, 1978; *Miller et al.*, 1979 and references therein] and initial observations of the same four radicals [see Anderson et al., 1980] strongly suggest that reaction (2) occurs less frequently throughout the stratosphere than reaction (1) and is thus 'rate-limiting' in the closure of the catalytic cycle. Therefore, the term $2k_2$[ClO][O], where brackets indicate concentrations, must appear in the photochemical destruction term in the continuity equation for odd oxygen [see *Johnston and Podolske*, 1978; *Anderson et al.*, 1980]. This has placed emphasis on measurements of [ClO] as a function of altitude in the stratosphere for the assessment of chlorine-induced effects on global ozone.

We summarize in what follows the results of a series of 10 balloon-borne, in situ observations of the concentration of the chlorine monoxide free radical obtained between July 1976 and September 1979 in the altitude inerval 25–42 km at Palestine, Texas, 32°N latitude. The [ClO] observations are combined with in situ observations of atomic oxygen and knowledge of the reaction rate constant, k_2, to quantify the gross rate of O_x destruction by the catalytic reaction pair (1)–(2). The mean of the observed [ClO] distributions is compared with a calculated distribution by *Logan et al.* [1978] and with the laser-heterodyne observations of *Menzies* [1978] and *Menzies et al.* [1981].

EXPERIMENTAL

The in situ detection of ClO, by atomic resonance fluorescence of ground state $Cl(^2P)$ following conversion of ClO to Cl with the rapid bimolecular reaction

$$ClO + NO \rightarrow Cl + NO_2 \quad (3)$$

is discussed in detail elsewhere [*Anderson et al.*, 1980]. Briefly, a confined flow of stratospheric air is established by lowering a cylindrically symmetric, hollow nacelle through the stratosphere on a stabilized parachute deployed from a balloon at the stratopause (~45 km). The flow through the instrument core is probed by a photon beam, resonant with the $^2D_{5/2} - {}^2P_{3/2}$ transition of Cl at 119 nm, which is formed in a low pressure (~10 torr) helium plasma-discharge lamp. A 2.4 GHz microwave field sustains the plasma which contains a trace quantity of chlorine. Output from the lamp is passed through a cell containing molecular oxygen, thus eliminating, with the exception of the $^2D_{5/2,3/2} - {}^2P_{3/2}$ doublet, all resonance lines in the three major vacuum ultraviolet multiplets of atomic chlorine. Resonant photons, scattered perpendicular to the beam by atoms in the flow, are counted by a photomultiplier (EMR 510-G) operated in the pulse mode.

For all experiments reported here, nitric oxide was added in controlled amounts to the flowing sample through a stainless steel loop injector at the leading edge of the instrument throat. Nitric oxide flows were cycled in a four-step time sequence consisting of a low-flow segment which provided sufficient NO to convert 95% of the ClO to Cl by (3) during the period between gas injection and detection at the optical axis, a high-flow segment employing a flow rate five times that of the low flow case, and finally two zero flow, 'background' segments between each flow setting. This sequence tests (1) whether the ClO to Cl conversion is complete and (2) whether NO intrinsically contributes to the observed fluorescence.

Care is taken to eliminate the possibility of radical recombi-

Paper number 1C0276.
0148-0227/81/001C-0276$01.00

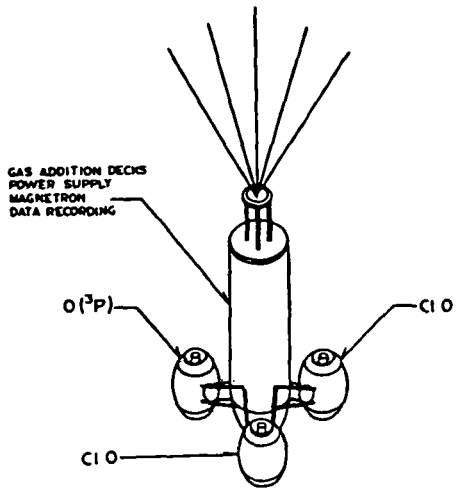

Fig. 1. Schematic of the three nacelle instruments configuration.

nation within the instrument throat by selecting the parachute descent velocity and the ratio of throat diameter to length such that the residence time of the sample between entry into the instrument and passage through the plane of the optical axis is 2 orders of magnitude shorter than the diffusion time from the center of the flow to the cylinder wall. For a detailed discussion of experimental strategy, see *Anderson et al.* [1980].

Two distinct instrument configurations were used to acquire the results reviewed here. The first, used between July 1976 and December 1977, employed a large (15 cm) throat diameter and is discussed in *Anderson et al.* [1977]. The second, used between June 1978 and September 1979, employed a smaller 10 cm throat design with a proportionally diminished distance between the throat entrance and the optical axis. That instrument array, shown in Figure 1, consisted of a three-nacelle cluster containing an atomic oxygen experiment and a pair of redundant ClO instruments. A major design criterion was the reduction of total experiment weight to provide a useful number of flights, given the observed variability of ClO and the recent and considerable increase in balloon costs. No systematic differences in the acquired data were observable between the two instrument types.

Results and Conclusions

Figure 2 summarizes the 10 available ClO observations obtained by in situ resonance fluorescence methods between 25 and 42 km. The observations fall into two distinct classes: (1) a well-defined envelope spanning the range 0.35–1.2 ppbv at 40 km decreasing to 10–60 pptv at 25 km which contains 8 of the 10 profiles and (2) a pair of observations distinctly separated from that envelope, one obtained on July 28, 1976, which exhibits a broad peak between 32 and 37 km of 1.6 ppbv decreasing to 0.1 ppbv at 25 km and a second on July 14, 1977, which exhibits approximately the same mixing ratio gradient as the major envelope but with a peak mixing ratio of 8 ppbv at 41 km. All observations were obtained close to midday at 32°N latitude; differences in solar zenith angle primarily reflect changes in solar declination. Calibration methods were uniform for all 10 flights; consideration of uncertainties in absolute calibration imply an accuracy of ±30% and an experimental precision of ±10% [see the discussion in *Anderson et al., 1980*]; so both the observed variability among the profiles and within a given profile in Figure 2 are deemed real.

Although it was not clear at the time of observation what relationship the July 14, 1977, measurement had to the mean, mid-latitude distribution of stratospheric ClO (note the chronology in Figure 2), it is now clear that it bears little resemblance to the time-averaged, mid-latitude, stratospheric ClO distribution, and we will thus exclude it when taking the mean of the observations for comparison with model calculations. It is of course important to clearly distinguish between the time-averaged distribution of ClO and the mechanistic link between chlorine radicals and ozone which is treated elsewhere [*Anderson et al., 1980*].

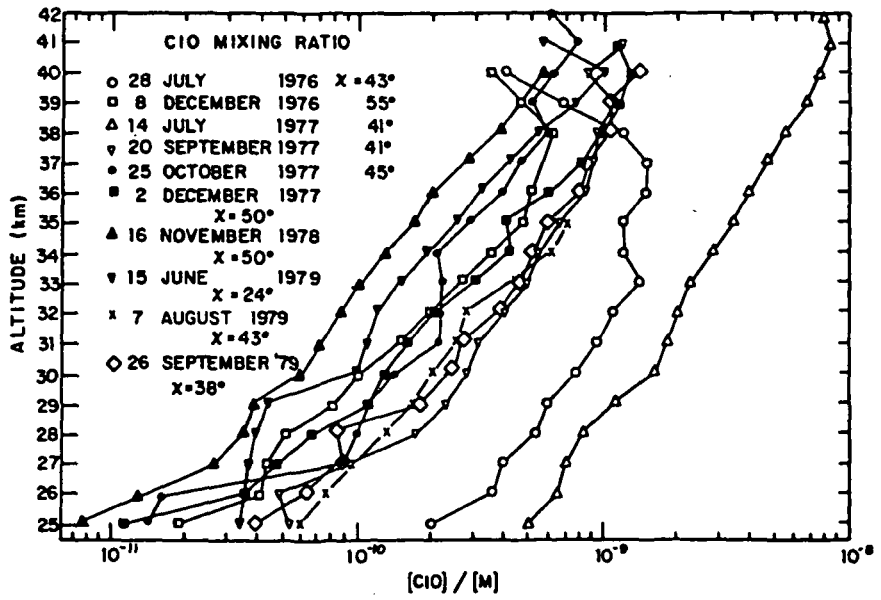

Fig. 2. Summary of the vertical distribution of ClO obtained between July 28, 1976, and September 26, 1979, using in situ resonance fluorescence methods.

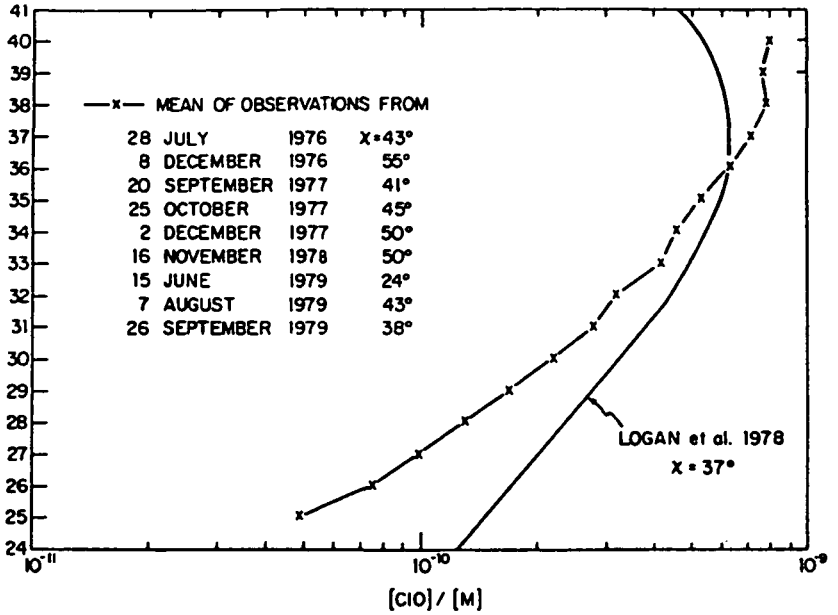

Fig. 3. Comparison between the mean of all in situ ClO observations, excluding July 14, 1977, and the calculated ClO distribution from *Logan et al.* [1978].

In Figure 3 we compare the mean of the nine remaining profiles with the calculated [ClO] distribution from the model of *Logan et al.* [1978], using the updated HO_x reaction rate constants from *DeMore et al.* [1979]. The comparison demonstrates that while significant agreement exists in the vicinity of 40 km, there is a clear divergence between the calculated and the observed mean [ClO] below 30 km. The ratio of calculated to observed [ClO] increases monotonically with decreasing altitude, to approximately 3 at 25 km. This is a major discrepancy and results either from improper partitioning between $ClO_x \equiv Cl + ClO$ and $ClX \equiv HCl + ClONO_2 + HOCl$ by virtue of an incomplete chemical description by the model or from the improper distribution of ClX with altitude by the one-dimensional, parameterized transport used in the model.

A comparison between calculated and observed ClX, using the most recent data available for the chlorine reservoir terms [see *Anderson*, 1980], however, implies that the model does in fact properly distribute ClX as a function of altitude, at least at mid-latitudes. Therefore, the discrepancy between calculated and observed ClO apparently lies in the chemical partitioning between the major forms of ClO_x (i.e., ClO) and ClX (i.e., HCl). The [ClO] to [HCl] ratio is believed to be controlled below 35 km by reactions (1), (2), and the noncatalytic coupling reactions

$$ClO + NO \rightarrow Cl + NO_2 \quad (3)$$

$$Cl + CH_4 \rightarrow HCl + CH_3 \quad (4)$$

$$Cl + HO_2 \rightarrow HCl + O_2 \quad (5)$$

$$HCl + OH \rightarrow H_2O + Cl \quad (6)$$

such that in steady state

$$[ClO]/[HCl] = \frac{[Cl]}{[HCl]}\left\{\frac{[ClO]}{[Cl]}\right\} = \frac{k_6[OH]}{k_4[CH_4] + k_5[HO_2]} \left\{\frac{k_1[O_3]}{k_2[O] + k_3[NO]}\right\} \quad (7)$$

In the altitude interval under consideration here (i.e., below ~30 km) reaction (4) dominates reaction (5) and thus $k_5[HO_2]$ can be ignored in the denominator of the right-hand side of (7) [see *Anderson et al.*, 1981]. In addition, since k_3 [NO] $\gg k_2$ [O] in this region, (2) can be ignored in comparison with (3) and thus

$$[ClO]/[HCl] \approx \frac{k_6[OH]}{k_4[CH_4]}\left\{\frac{k_1[O_3]}{k_3[NO]}\right\} \quad (8)$$

Given the assumption that the above reaction set linking ClO and HCl is complete (an as yet untested hypothesis), the alternatives available as an explanation for the discrepancy between calculated and observed ClO below 30 km involve uncertainties in the [OH]/[NO] ratio in (8). The reason for this is that the kinetics of (1)–(6) are well characterized [*DeMore et al.*, 1979], and high quality data for both O_3 [see *Hudson and Reed*, 1979] and CH_4 [see *Fabian et al.*, 1979] are available throughout the 20–30 km interval and are in close agreement with modeled distributions. (In some models, observed $[O_3]$ and $[CH_4]$ are de facto independent variables.)

We briefly review, therefore, our present knowledge of the [OH] and [NO] distribution between 20 and 30 km, considering hydroxyl first. No direct observations of OH exist in this altitude interval. Above 30 km there are both in situ observations extending up to 70 km and integrated total column measurements which agree within the respective experimental uncertainties, and are reviewed by *Hudson and Reed* [1979]. The distribution of OH observed in situ between 30 and 70 km is consistent with current models. If, however, the hydroxyl distribution from those models is used in the 20–30 km region, three discrepancies result: (1) the observed $[HNO_3]/[NO_2]$ ratio lies significantly below predictions based on modeled distributions [*McConnell and Evans*, 1978; *Harries*, 1978], (2) the observed [HF]/[HCl] ratio lies significantly above that currently calculated by models [*Sze*, 1978; *Buijs et al.*, 1980], and (3) the observed SO_2 concentration at 20 km and the OCS concentration at 30 km exceed predicted levels and the con-

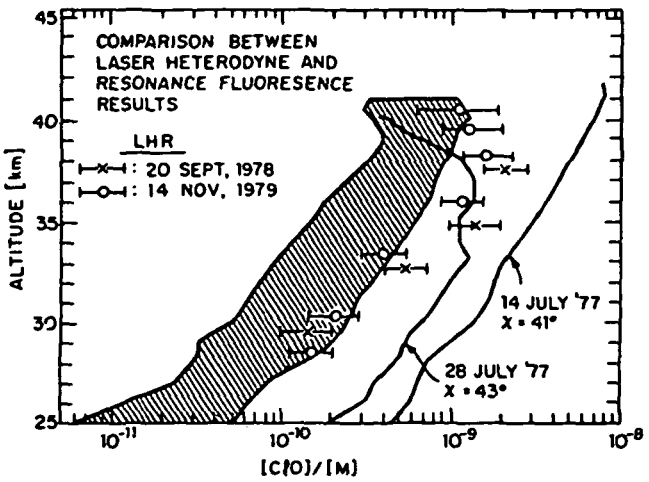

Fig. 4a. Comparison between in situ resonance fluorescence observations obtained at midday and the post sunset laser-heterodyne radiometer observations. The shaded envelope represents 8 of the 10 in situ experiments summarized in Figure 2.

centration of large ($d > 0.15$ cm) aerosols at 20 km is significantly less than predicted [*Turco et al.*, 1980]. Although much of the evidence is indirect, both discrepancies would be resolved in large measure by an OH concentration which decreases significantly more rapidly with decreasing altitude below 30 km than is currently predicted. Noting that [OH] appears in the numerator of (8), a reduction in [OH] sufficient to alleviate points 1 and 2 above would significantly diminish the divergence below 35 km apparent in Figure 3.

Turning next to NO, we note that from the point of view of direct observations, the situation is significantly better defined than for OH in the lower stratosphere and is characterized by an expanding data base at mid-latitude, northern hemisphere locations [see the review by *Ridley and Schiff*, 1980]. Recent observations of NO by those authors using chemiluminescent techniques, with improved in situ calibration methods and pyrex sample inlets, imply an NO concentration approximating the upper bound of the modeled distributions reported in *Hudson and Reed* [1979]. The upper bound is approximately a factor of 2 higher than the NO profile in the *Logan et al.* [1978] model (corrected for recent changes in HO_x reaction rate constant) which was used to calculate the ClO distribution shown in Figure 3. It remains, of course, to be determined whether the difference between observed and calculated [NO] will survive a more extensive data base. It is essential that further observation of the vertical distribution of NO be made to characterize this difference accurately.

Since the NO concentration appears in the denominator of (8), the larger observed than calculated [NO] implies a diminished [ClO]/[HCl] ratio, thus diminishing the discrepancy below 30 km summarized in Figure 3.

In concluding this discussion we note that the [ClO]/[HCl] ratio is particularly sensitive to the OH profile below 30 km, not only because of the direct proportionality expressed in (8) but also because of the inverse dependence of [NO] on [OH] resulting from NO_2 recombination to HNO_3 via $OH + NO_2 + M \rightarrow HNO_3 + M$. The suggestion [see *McConnell and Evans*, 1978; *Sze*, 1978; *Turco et al.*, 1980] that the OH concentration below 30 km is decidedly (2 or 3 times) less than is currently predicted by models is thus of considerable importance, both to our understanding of stratospheric chlorine chemistry and to our confidence in the ozone-depletion prognoses which depend critically on the chemical link between nitrogen and hydrogen radicals.

We next compare the results of the in situ observations of ClO with the laser-heterodyne radiometer measurements of *Menzies* [1978] and *Menzies et al.* [1981]. Figure 4a summarizes, as a shaded band, the eight in situ midday ClO observations within the envelope of Figure 2. It also presents, individually, the July 28, 1977, and July 14, 1977, profiles and displays the post-sunset heterodyne radiometer profiles of *Menzies* [1978] and *Menzies et al.* [1981].

A direct comparison between the data sets requires that proper account be taken of the recombination of ClO to chlorine nitrate by the termolecular reaction

$$ClO + NO_2 + M \xrightarrow{k_9} ClONO_2 + M \qquad (9)$$

following sunset. The results of using the diurnal model of *Logan et al.* [1978] to convert the post-sunset data back to midday steady state values (note that the rate of recombination is decidedly more rapid in lower stratosphere since the pressure is higher and the temperature lower) is shown in Figure 4b. The corrected ClO profiles are compared with the mean of the in situ observations previously given in Figure 3. There is substantial agreement with respect to the mixing ratio gradient between the two techniques, but a clear difference in absolute value is apparent. It remains to distinguish between observed variability and systematic experimental differences through simultaneous observations of the same air mass.

We turn, finally, to the question of the rate of odd oxygen destruction by the catalytic reaction pair (1)–(2) noting, as is discussed in the introduction, that reaction (2) is rate limiting in the closure of the catalytic cycle. Thus if [ClO] and [O] are simultaneously observed within the same stratospheric volume element, the local loss rate of odd oxygen by ClO_x is $2k_2$ [ClO][O]. Although major experimental advances will be required to define accurately the altitude dependence of ClO_x-catalyzed recombination of O_x, we present here the results of a simplified, first-order determination of O_x destruction by ClO_x which is as accurate as the present observations merit (±30%). We employ the mean of the available in situ observations of ClO with the mean of the midday in situ $O(^3P)$ observations reported in *Anderson* [1980] and the bimolecular rate constant k_2 from *DeMore et al.* [1979]. The product $2k_2[ClO][O(^3P)]$, determined from those three quantities, is normalized to the odd oxygen production term $2J_{O_2}[O_2]$ at each altitude to establish the fractional removal of O_x by ClO_x.

Since the temporal dependence of J_{O_2} and [ClO][O] are similar but not identical, it is necessary to distinguish between the instantaneous midday (observed) product k_2 [ClO][O] and the diurnally integrated quantity

$$\frac{1}{T}\int_0^T k_2\,[ClO][O]\,dt$$

which, within any given air mass, determines the destruction of O_x by ClO_x. This is accomplished by dividing the diurnal period into 24 equal intervals, i, and employing the time-dependent shape of $[ClO]_i$, $[O]_i$, and $J_{O_2,i}$ from *Logan et al.* [1978] to establish the calculated ratio $\sum_{i=1}^{24} k_2[ClO]_i[O]_i / \sum_{i=1}^{24} J_{O_2,i}[O_2]$. That ratio is then scaled by the ratio of the ob-

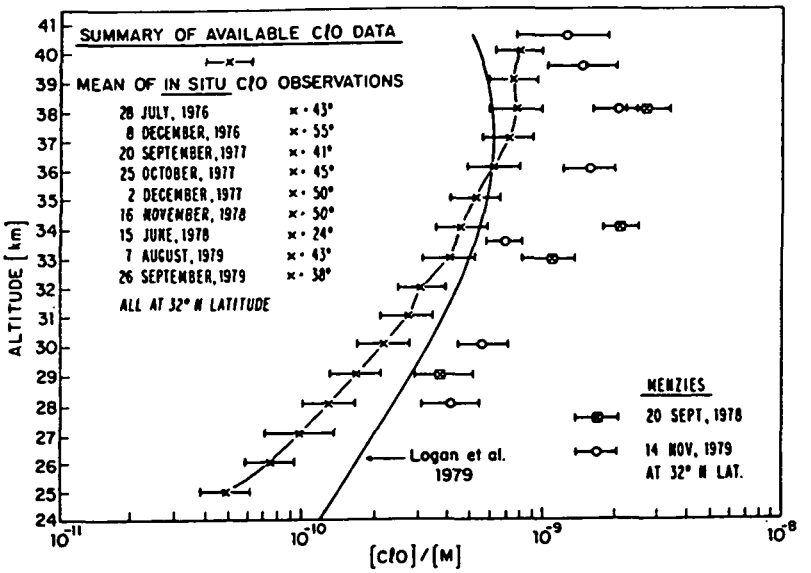

Fig. 4*b*. Comparison between the mean of the in situ resonance fluorescence observations and the laser-heterodyne radiometer data corrected (approximately) from post sunset ($\chi = 93°$) conditions to midday. Also shown is the calculated distribution of *Logan et al.* [1978] at the appropriate solar zenith angle.

served quantity k_2 [ClO][O] to the calculated product k_2 [ClO]$_i$[O]$_i$ at the solar zenith angle corresponding to each experiment. Thus the (~10%) correction for the difference between the instantaneous and diurnally averaged values of k_2 [ClO][O]/J_{O_2}[O$_2$] is accomplished to first-order by using only the shape of the diurnally calculated profiles scaled to observed, absolute concentrations.

Table 1 presents the fractional destruction of O_x by ClO_x as a function of altitude between 25 and 41 km based on the mean of the available in situ ClO and O(^3P) observations corrected for the difference between instantaneous midday and diurnally averaged ratios of [ClO][O(^3P)] to J_{O_2} as noted above.

Two conclusions are summarized in Table 1. First, the gross destruction of O_x by ClO_x (note that these experiments, as executed, cannot establish a net destruction) maximizes at the upper altitude extremity of the observations and reaches approximately half of the O_x production rate by O_2 photolysis. Second, the ClO_x-catalyzed O_x destruction diminishes rapidly below 40 km so that it makes a negligible direct contribution to the O_x budget in the midstratosphere.

TABLE 1. Fractional Rate of O_x Destruction by the Catalytic Reaction Pair $Cl + O_3 \rightarrow ClO + O_2$, $ClO + O \rightarrow Cl + O_2$ at Each Altitude Based on Observed ClO and O Distributions

Altitude	Fractional Destruction of O_x by ClO_x
41	0.45
39	0.40
37	0.30
35	0.20
33	0.15
31	0.15
29	0.10
27	0.10

The instantaneous observations were corrected for the diurnal dependence of rate limiting step for chlorine catalyzed destruction as discussed in the text. Figures are rounded off to the nearest 0.05.

SUMMARY

Three conclusions emerge from an analysis of the 10 balloon-borne, in situ observations of ClO reported here:

1. While the agreement between calculated and observed ClO concentrations between 35 and 40 km is acceptable, there is a clear divergence at lower altitudes such that the ratio of calculated to observed [ClO] at 25 km approaches three. Consideration of (1) the reaction which govern the [ClO]/[HCl] ratio below 35 km, (2) the apparent success of the one-dimensional model in predicting the vertical distribution of [HCl] at mid-latitudes, and (3) the quality and extent of current observational evidence for [O_3], [CH_4], [OH], and [NO] suggests that uncertainties in the [OH]/[NO] ratio in the lower stratosphere may be the major factor contributing to the observed discrepancy in [ClO]/[HCl].

2. A comparison between in situ resonance fluorescence measurements and remote laser-heterodyne radiometer observations implies substantial agreement in the ClO mixing ratio gradient below 40 km but differences in absolute magnitude exceed significantly the stated accuracy (±30%) of each method. This discrepancy may result either from natural variability (each method reports profile fluctuations which exceed the stated accuracy) or from systematic errors in absolute calibration.

3. The fraction destruction of O_x by the catalytic reaction pair

$$\begin{array}{l} Cl + O_3 \rightarrow ClO + O_2 \\ \underline{ClO + O \rightarrow Cl + O_2} \\ O + O_3 \rightarrow 2O_2 \end{array}$$

determined from the mean of observed [ClO] and [O(^3P)] reaches a maximum of 0.45 at 41 km, the upper extremity of the observations, and decreases monotonically below that altitude, reaching 0.10 at 27 km.

REFERENCES

Anderson, J. G., The chemistry of stratospheric chlorine, in *Man and Stratospheric Ozone*, edited by F. A. Bower and R. B. Ward, CRC, Cleveland, 1980.

Anderson, J. G., J. J. Margitan, and D. H. Stedman, Atomic chlorine and the chlorine monoxide free radical in the stratosphere: Three in situ observations, *Science, 198*, 501, 1977.

Anderson, J. G., R. E. Shetter, H. J. Grassl, and J. J. Margitan, Stratospheric free chlorine measured by balloon borne in situ resonance fluoresence, *J. Geophys. Res., 85*, 2869, 1980.

Anderson, J. G., H. J. Grassl, R. E. Shetter, and J. J. Margitan, HO_2 in the stratosphere: Three in situ observations, *Geophys. Res. Lett, 8*, 2869–2887, 1981.

Buijs, H. L., G. L. Vail, G. Tremblay, and D. J. W. Kendall, Simultaneous measurement of the volume mixing ratios of HCl and HF in the stratosphere, *Geophys. Res. Lett., 7*, 205, 1980.

DeMore, W. B., L. I. Stief, F. Kaufman, D. M. Golden, R. F. Hampson, M. J. Kurylo, J. J. Margitan, M. J. Molina, and R. T. Watson. Kinetic and photochemical data for use in stratospheric modelling, *Publ. 79-27*, Jet Propul. Lab., Pasadena, Calif., 1979.

Fabian, P., R. Borchers, K. H. Weiler, U. Schmidt, A. Volz, D. H. Ehhalt, W. Seiler, and F. Muller, Simultaneously measured vertical profiles of H_2, CH_4, CO, N_2O, $CFCl_3$, and CF_2Cl_2 in the mid-latitude stratosphere and troposphere, *J. Geophys. Res., 84*, 3149, 1979.

Harries, J. F., Ratio of HNO_3 to NO_2 concentration in daytime stratosphere, *Nature, 274*, 235, 1978.

Hudson, P. D., and E. I. Reed, The stratosphere: Present and future, *NASA Ref. Publ. 1049*, 1979.

Johnston, H. S., and J. Podolske, Interpretations of stratospheric photochemistry, *Rev. Geophys. Space Phys., 16*, 491, 1978.

Logan, J. A., M. J. Prather, S. C. Wofsy, and M. B. McElroy, Atmospheric chemistry: Response to human influence, *Phil. Trans. R. Soc., 290*, 187, 1978.

McConnell, J., and W. F. J. Evans, Implications of low stratospheric hydroxyl concentrations for CFM and SST scenario calculation of ozone depletion, *Eos Trans. AGU, 59*, 1078, 1978.

Menzies, R. T., Remote measurements of ClO in the stratosphere, *Geophys. Res. Lett., 6*, 151, 1978.

Menzies, R. T., C. W. Rutledge, R. A. Zanteson, and D. L. Spears, Balloon-borne laser heterodyne radiometer for measurements of stratospheric trace species, *Appl. Opt., 20*, 536, 1981.

Miller, C., D. L. Fildin, and J. P. Jesson, The fluorocarbon-ozone theory VI atmospheric modelling: Calculations of the diurnal steady state, *Atmos. Environ., 13*, 381, 1979.

Molina, M. J., and F. S. Rowland, Stratospheric sink for chlorofluoromethanes: Chlorine atom catalyzed destruction of ozone, *Nature, 249*, 810, 1974.

Ridley, B. A., and H. I. Schiff, Stratospheric odd nitrogen: Nitric oxide measurements at 32°N in autumn, submitted to *J. Geophys. Res.*, 1980.

Rowland, R. S., and M. J. Molina, Chlorofluoromethanes in the environment, *Rev. Geophys. Space Phys., 13*, 1, 1975.

Sze, N. D., Stratospheric fluorine: A comparison between theory and measurement, *Geophys. Res. Lett. 5*, 781, 1978.

Turco, R. P., R. C. Whitten, O. B. Toon, E. C. Y. Inn, and P. Hamill, Stratospheric hydroxyl radical concentration: New limitations suggested by observations of gaseous and particulate sulfur, *J. Geophys. Res., 86*, 1129, 1981.

(Received September 10, 1980;
revised February 17, 1981;
accepted February 18, 1981.)